IntechOpen

Hydrodynamics
Theory and Model

Edited by Jinhai Zheng

HYDRODYNAMICS – THEORY AND MODEL

Edited by **Jinhai Zheng**

Hydrodynamics - Theory and Model
http://dx.doi.org/10.5772/2114
Edited by Jinhai Zheng

Contributors

Mohammed Seaid, Mapundi Kondwani Banda, Yousef Hassanzadeh, Giorgio Domenico Maria Micale, Antonio Busciglio, Giuseppa Vella, Nwabueze Emekwuru, Guo-Hai Dong, Yun-Peng Zhao, Bi Chun-Wei, Tiao- Jian Xu, Sergey Nikolaevich Kharlamov, Lelio Luzzi, Antonio Cammi, Manuele Aufiero, Carlo Fiorina, Liehui Zhang, Jingjing Guo, Qiguo Liu, Haitao Wang, Indradi Wijatmiko, Keisuke Murakami, Karmakar, Jesorka, Jin - Hai Zheng, Gang Wang, Chi Zhang, Yingqi Liu

Notice

First published in Croatia, 2012 by INTECH d.o.o.
eBook (PDF) Published by IN TECH d.o.o.
Place and year of publication of eBook (PDF): Rijeka, 2019.
IntechOpen is the global imprint of IN TECH d.o.o.
Printed in Croatia

Legal deposit, Croatia: National and University Library in Zagreb

Additional hard and PDF copies can be obtained from orders@intechopen.com

Hydrodynamics - Theory and Model
Edited by Jinhai Zheng

p. cm.

ISBN 978-953-51-0130-7

eBook (PDF) ISBN 978-953-51-4963-7

Meet the editor

Jinhai Zheng received his Doctoral Degree in Coastal Engineering from Hohai University of China in 1998. He has been Chair Professor of Harbor, Waterway, Coastal, and Offshore Engineering in the same University since 2007. His research interests cover estuarine and coastal processes, harbor and waterway engineering, coastal engineering, and environment. He carries out numerical and experimental studies that have dealt with characteristics of water wave, tidal flow, and sediment transport and their responses to engineering projects in the Yangtze River Estuary, the Pearl River Delta, the Min River Estuary, and along the southeast coasts in China. An author of about 100 academic publications, he is one of the main members engaged in the preparation and translation of General Rules for Design of Port and Waterway Works, a standard code of practice of China. He is actively involved in several international and domestic professional societies, such as the IAHR, the Chinese Ocean Engineering Society, and the China Water Transportation Construction Association.

Contents

Preface XI

Part 1 The Recent Research Achievements in Fundamental Theory 1

Chapter 1 **Hydrodynamics of Dual Fluidized Beds 3**
M.K. Karmakar and P.K. Chatterjee

Chapter 2 **Hydraulics of Sediment Transport 23**
Yousef Hassanzadeh

Chapter 3 **Study on the Interaction Between Tsunami Bore and Cylindrical Structure with Weir 59**
I. Wijatmiko and K. Murakami

Chapter 4 **Using the General Gamma Distribution to Represent the Droplet Size Distribution in a Spray Model 79**
Nwabueze G. Emekwuru

Chapter 5 **Well Responses in Three-Zone Linear Composite Dual-Porosity Reservoirs 95**
Jing-Jing Guo, Lie-Hui Zhang, Hai-Tao Wang and Qi-Guo Liu

Part 2 The New Technology in Laboratory Experiments, Numerical Models, and Engineering Applications 117

Chapter 6 **Thermo-Hydrodynamics of Internally Heated Molten Salts for Innovative Nuclear Reactors 119**
Lelio Luzzi, Manuele Aufiero, Antonio Cammi and Carlo Fiorina

Chapter 7 **Measurement of Multiphase Flow Characteristics Via Image Analysis Techniques: The Fluidization Case Study 143**
Antonio Busciglio, Giuseppa Vella and Giorgio Micale

Chapter 8 **Hydrodynamically Confined Flow Devices 167**
Alar Ainla, Gavin Jeffries and Aldo Jesorka

Chapter 9 **Actual Problems of Hydrodynamics at Internal Not-Isothermal Flows in Fields of Mass Forces 183**
Sergey Kharlamov

Chapter 10 **Numerical Wave Flumes Based on Smoothed Particle Hydrodynamics 233**
Jinhai Zheng, Gang Wang, Chi Zhang and Yingqi Liu

Chapter 11 **Lattice Boltzmann Simulation for Shallow Water Flow Applications 255**
Mapundi K. Banda and Mohammed Seaid

Chapter 12 **The Numerical Simulation of Hydrodynamics of Fishing Net Cage 287**
Yunpeng Zhao, Tiaojian Xu, Chunwei Bi
Guohai Dong and Shengcong Liu

Preface

Hydrodynamics has experienced a long history. A substantial growth of knowledge in this field has been happening since the 18th century. It is applicable in a wide variety of areas, such as ocean engineering, environmental engineering, water conservancy, energy exploration, and chemical engineering, to name a few. Over the past several decades, good progress has been made in physical models, computational methods, and theoretical studies, which significantly expanded the understanding and the engineering implications of hydrodynamics. The aim of this book is to present a collection of the advances and trends in hydrodynamics from countries around the globe. There are exciting new findings in this field of scientific research, and real-world applications are analyzed in countries like Iran, Sweden, India, China, Mexico, the United Kingdom, Japan, Italy and South Africa. The book is intended to provide useful references to scientists and engineers working in this field. The book consists of twelve independent chapters, and it can be divided into two main parts: the first five chapters present the recent research achievements in fundamental theory, while the last seven chapters describe the new technology in laboratory experiments, numerical models, and engineering applications.

We begin at Chapter 1, which gives a brief idea about the dual fluidized beds system, experimental set up, and the hydrodynamic model using L-valves in down comer and return leg. Chapter 2 examines the theoretical and experimental studies of hydraulics of sediment transport, hydraulic formulas for fluid flow and sediment computation in open channels, and analyzing the flow and sediment characteristics of the water motion. Chapter 3 focuses on the interaction of tsunami bore with cylindrical structure in three-dimensions, in which the effect of the protective weir existence is investigated. The proliferation of spray producing devices for use in the various applications of sprays has led to a keen interest in the hydrodynamics of sprays, and Chapter 4 presents the application of a general Gamma distribution to represent the droplet size distribution in a moments spray model. Based on the Warren and Root's natural fracture model, Chapter 5 presents a new well test model for linear composite dual-porosity reservoirs, considering formation thickness and reservoir properties variations in plane. Molten Salt Reactors have more potentialities and favorable features than conventional solid-fuelled reactors for their improved sustainability, inherent safety, and unique characteristics in terms of actinide burning and waste reduction. Chapter 6 investigates their thermo-hydrodynamics of internally heated

fluids through focusing on the heat transfer coefficient prediction and the natural circulation characteristics.The analysis of complex multiphase systems is usually conducted by a powerful experimental method-digital imaging technique. Chapter 7 describes several new techniques based on digital image analysis for the measurement of the mixing behavior in the fluidized bed. Hydrodynamically confined flow devices are a young research area with demonstrated potential for practical application in surface processing, assay development, single cell research, and pharmacology. Chapter 8 displays different fabrication strategies for these multilayered devices, including theoretical and conceptual studies, as well as fully developed automated systems. Chapter 9 is devoted to the discussion of actual problems of complex physical, mathematical, and numerical modeling of hydrodynamics and heat transfer in high-swirled internal luminaries flows. Smoothed Particle Hydrodynamics is a mesh-free Lagrangian method widely used in many fields of research, including astrophysics, ballistics, volcanology, and oceanography. Chapter 10 gives an overview on this method applied in numerical wave flumes. The lattice Boltzmann method is an alternative and promising numerical scheme for simulating fluid flows and modeling physics in fluids, and it is particularly successful in fluid flow applications involving interfacial dynamics and complex boundaries. Chapter 11 details the method and its application to the simulation of depth-averaged models in flow hydraulics and dispersion. Knowledge of the hydrodynamic behavior of fish net cage under the action of waves is the basis of the design and management of net cage in the open sea. Chapter 12 numerically investigates the hydrodynamic behavior of fish net cage in waves.

Jinhai Zheng
Hohai University
China

Part 1

The Recent Research Achievements in Fundamental Theory

1

Hydrodynamics of Dual Fluidized Beds

M.K. Karmakar and P.K. Chatterjee
CSIR-Central Mechanical Engineering Research Institute, Durgapur, West Bengal, India

1. Introduction

A dual fluidized beds system essentially comprises of two fluidized bed reactors coupled together with a provision of gas or materials transfer in between. It may be a combination of circulating-circulating or bubbling-circulating or bubbling-bubbling type systems. A noble application is in a gasification process for coal or biomass where nitrogen of air is not allowed to dilute the product gas. In a dual fluidized bed gasifier of bubbling-circulating type system, a bubbling fluidized bed (BFB) reactor acts as the gasifier where steam is used as gasifying medium to get medium heating value syngas and the circulating fluidized bed is a combustor using air as fluidizing medium. The energy demand for the endothermic gasification reaction is met by the combustion of residual char in the fast bed combustor. The circulating bed materials act as heat carrier between the two fluidized beds and maintain the required temperature in gasifier. Therefore, the hydrodynamics of such a dual fluidized beds system needs to be thoroughly understood for successful design and operation of the system for industrial application.

In literature, the studies on hydrodynamics of bubbling fluidized bed and circulating fluidized bed systems are available separately. However, the studies on hydrodynamics of combined system of these, a dual fluidized beds system loop predictions are scanty. The flow structure of gas-solids mixture is very complex in CFB system. Variety of models of fluidized bed system have been classified into three broad groups: (i) models predicting solids suspension density in axial variation, but not in radial direction, (ii) models predicting axial and radial variations by assuming two or more regions, such as core-annulus or clustering annulus flow models and (iii) models which employ the fundamental equations of fluid dynamics to predict the two phase gas-solids flow (Harris & Davidson, 1994). Of the three classifications, the type (iii) seems to be most rigorous, but the mathematical complexity of solving the equations limits its usefulness from practical design perspective. According to literature (Pugsley & Berruti, 1996a, 1996b), it is suggested that type (i) and type (ii) models are the best suited as a design tool for CFB to investigate the effects of operating conditions and riser dimensions on the flow structure. A dual fluidized beds system was also investigated (Bai et al., 1997) with two risers, two downcomers and two valves. The model shows how the solids circulation fluxes are affected by the operating conditions such as superficial gas velocities, particle diameter, density, solids inventory and fractional opening of solids flow control valves as well as by geometry. The hydrodynamics of a dual fluidized beds system were also studied (Loffler et al. 2003; Kaiser et al., 2003) which consisted of a fast bed riser with the downcomer, a

bubbling bed gasifier and a transfer pipe. They used the loop seals arrangement for solids flow control in the system.

2. Description

In this section, the hydrodynamics of a dual fluidized beds has been discussed using the almost similar system as described in (Loffler et al. 2003; Kaiser et al., 2003) except the mechanism for the solids transfer between the vessels. Loop seal device has been used in the studies described in (Loffler et al. 2003; Kaiser et al., 2003). In the current study, two L-valves, in place of loop seals, have been installed between the coupled reactors. The L-valves absorb a part of pressure that is built up due to static head of solids in the downcomer. Depending upon the pressure absorbed in L-valves, the solid circulation rate changes to adjust the pressure balance of the loop.

2.1 Experimental test set up

The dual fluidized beds experimental set up is made of transparent perspex material. The system consists of a fast bed riser, a cyclone to separate the solids, a down comer with a L-valve, a bubbling fluidized bed and a return pipe with another L-valve. The system is shown schematically in Fig 1. The solids after passing through the fast bed riser gets separated in the cyclone, descend downwards through the down comer and enter the bubbling bed reactor through the L-valve. A part of bed materials in the bubbling bed system are then transferred back into the riser through the inclined return leg fitted with the other L-valve. Circulation of material takes place in this way. The major dimensions of test set-up and the range of operating flow rates are presented in Table 1.

Parameter	Value	Unit
Height of riser	5.95	m
Inside diameter of riser	0.050	m
Height of Secondary air injection above distributor	0.300	m
Height of bubbling fluidized bed vessel	1.200	m
Inside diameter of bubbling fluidized bed vessel	0.100	m
Length of downcomer stand pipe	4.0	m
Inside diameter of downcomer stand pipe	0.025	m
Connecting pipe diameter: fast bed and bubbling bed	0.025	m
Primary air flow in fast bed riser	1.5 – 5.0	m^3/hr
Secondary air flow in fast bed riser	25-50	m^3/hr
Air flow in bubbling fluidized bed vessel	3-16	m^3/hr

Table 1. Dimensions and air flow rates of dual FB system cold model set up

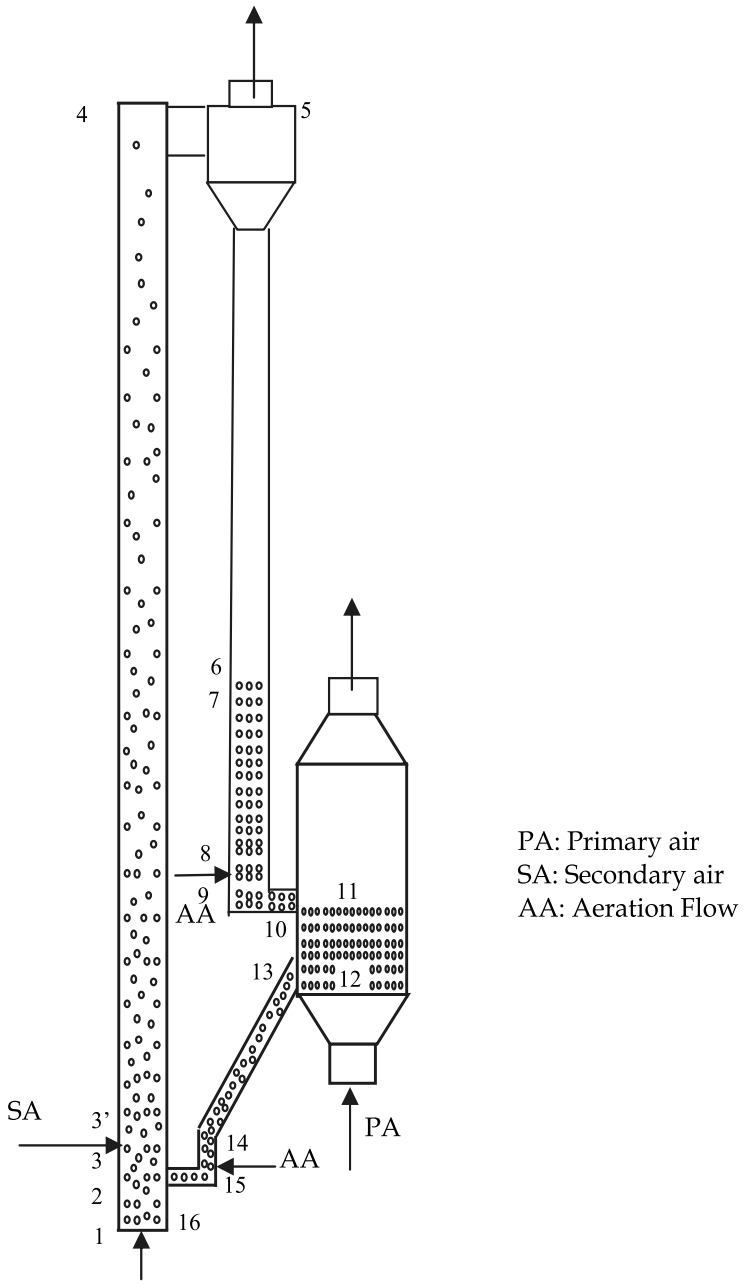

Fig. 1. Schematic diagram of dual FB system: 1-2: Dense zone, 2-3: Splash zone, 3-3′: Secondary air injection, 3′-4: Transport zone, 4-5: Cyclone separator, 5-6: Downcomer above sand accumulation column, 6-7: Air Sand Interface 7-8: Sand accumulation in downcomer, 8-9: Aeration point, 9-10: Aeration point to solid discharge point, 10-11: Solid discharge to bubbling bed, 11-12: bubbling fluidized bed gasifier, 12-13: Connector junction, 13-14: Connector from bubbling to Aeration point, 14-15: Aeration point, 15-16: Aeration point to solid discharge to fast bed

The description of the cold model set up is discussed below.

Fast bed riser: The system consists of a 5.95 m high and 0.05 m inner diameter riser made of transparent perspex. It is fitted with a perforated type distributor plate at the bottom. There are two air flow systems in riser. The primary air is given through the distributor plate where the flow is controlled by a regulator valve for maintaining the bottom bed at bubbling fluidizing state. The secondary air is injected in fast bed riser above the connector point from the bubbling bed vessel at a height of 0.3 m above the distributor plate. The size of secondary air port is 0.025 m in the riser. The secondary air helps to pneumatically transport the sand particles to the top of riser before entering into the cyclone separator. The flow rates of primary and secondary air in riser and the fluidizing air to bubbling bed vessel were measured by the orifice meters.

Cyclone: The cyclone separates the silica sands from the gas-solid mixture and feeds the solid material to the down comer. The entry duct to cyclone is placed tangentially with the cyclone body so that the gas-solids mixture experiences a rotational movement forming a vortex inside the cyclone causing the heavier particles to fall down. The air leaves through the upward escape pipe. The outside diameter of cyclone is 0.1 m while the delivery pipe is 0.05 m in diameter. The figure of the cyclone is shown in Fig 2.

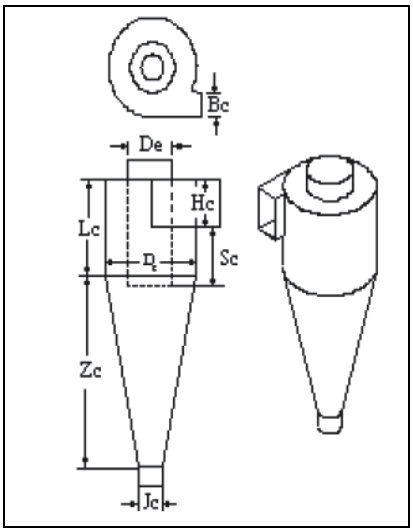

Bc = 25 mm
Hc = 50 mm
Dc = 100 mm
De = 50 mm
Lc = 200 mm
Zc = 300 mm
Jc = 25 mm

Fig. 2. Cyclone dimensions in dual FB system

Downcomer and L-valve: The down comer is a transparent perspex pipe of inner diameter of 0.025 m. The height of downcomer pipe is 4.0 m. There is a L-valve at the bottom of downcomer pipe. The L-valve is meant for controlling the solid sand flow to the gasifier by means of air flow regulation. The port size of L-valve is 0.006 m for air injection. The length of horizontal leg of L-valve is 0.1 m which extends upto the bubbling bed vessel.

Bubbling bed system: The bubbling fluidized bed is also made of perspex pipe of inside diameter 0.1 m and of 1.2 m high. There is a distributor plate at the bottom of the gasifier. The distributor plate is a single perforated plate. There is an opening for under-bed feeding of fresh sand inside the vessel. The primary air flow from a blower keeps the bed in bubbling condition.

Connector and L-valve: The connector is an inclined transparent pipe of inner diameter of 0.03 m. The vertical height is 1.3 m with a L-valve arrangement. The solids sand materials in the bubbling bed chamber are transferred to the fast bed riser through the aeration flow regulated by L-valve. The port size in the L-valve is 0.006 m for auxiliary air injection. The length of horizontal leg of L-valve is 0.1 m through which the fast bed riser is connected to complete the loop.

Feeding system of bed materials: The bed material feeding system consists of a screw feeder and a lock hopper, the screw feeder is connected to a variable speed motor. The screw feeder feeds the solid bed materials directly into the bubbling bed at the height of 0.1 m above the distributor. The sand particles ranging from 0.147 mm to 0.416 mm in mean diameters have been used as bed materials. The hopper is refilled manually with bed materials periodically.

There are eight numbers of pressure taps along the riser height to measure the static heads. Similarly, there is one pressure tap at cyclone, five in downcomer and L-valve section, two in bubbling fluidized bed and three in the connection pipe. The pressure heads have been measured using water manometers. A blower has been used to supply air to the system.

2.2 Materials and method

To investigate the hydrodynamic behaviour, four silica sand samples (group-B particles as per Geldart classification) of different Sauter mean diameters have been taken during the experiments. These samples are prepared by screening the materials through a set of wire mesh sieves. The characteristics of bed material are presented in Table 2. The cumulative percentage distribution for each mean particle size is shown in Fig 3.

Material	Sand I	Sand II	Sand III	Sand IV
Size range, μm	50-300	75-425	106-500	150-600
Mean diameter, μm	147	211	334	416
Sphericity	0.86	0.86	0.86	0.86
Particle density, kg/m^3	2650	2650	2650	2650
Bulk density, kg/m^3	1696	1696	1710	1722
Voidage at min. fluidization, ε_{mf}	0.46	0.44	0.41	0.40
Min fluidization velocity at 27 ^{0}C, m/s	0.018	0.037	0.091	0.138
Particle terminal velocity at 27 ^{0}C, m/s	1.2	1.7	2.7	3.4
Archimedes' number	281	835	3292	6347
Group of Geldart's classification	B	B	B	B

Table 2. Characteristics of the bed materials used during cold model analysis

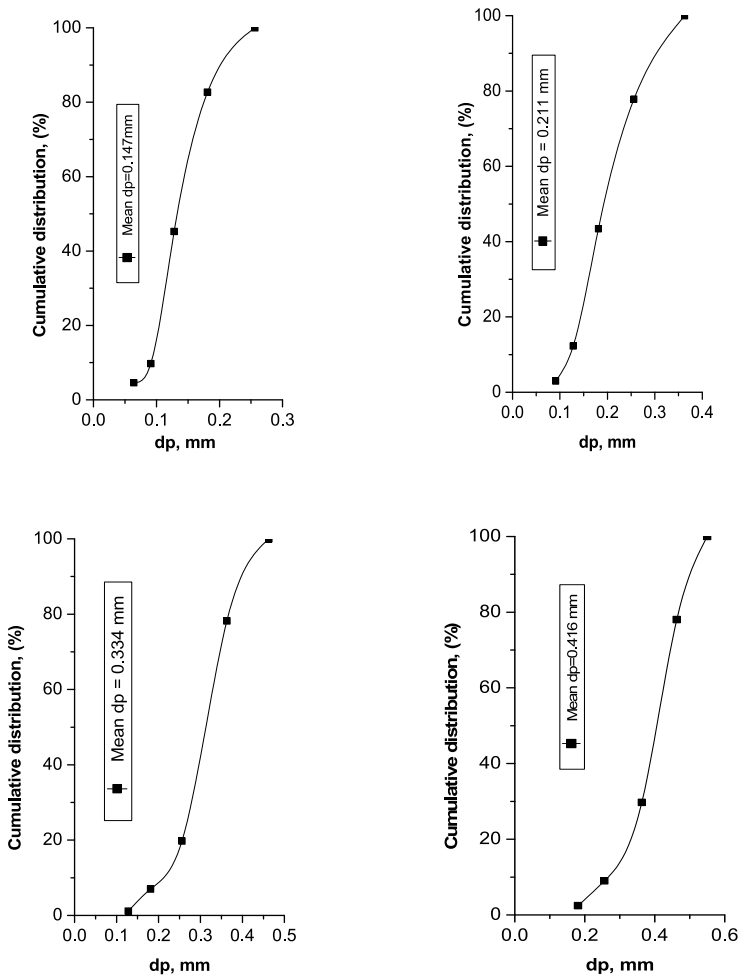

Fig. 3. Cumulative particle size distribution of silica sand samples

Separate aeration flows have been used through two L-valves to maintain the material circulation in the dual bed system. The aeration taps are placed near the valve bend in downcomer which yields the maximum solids flow. The solids do not begin to flow immediately upon injecting aeration flow; there is a threshold aeration rate to produce a drag force sufficient to initiate solids flow. When this drag force exceeds the force required to overcome the resistance to solids moving through the constricting bend and gravity of the particles, the solids begin moving through this non-mechanical valve (Knowlton, 1997).

Each run was characterized at a fixed primary air flow with variations in secondary air and aeration flow. The solids inventory in all runs was maintained at 6.0 kg. The solid circulation rate is an essential parameter in a dual fluidized bed system and hence, its measurement is an important experimental input. It may be measured through a very simple way. In this study, when the gas-solids flow was fully established in the system, the flow of material in downcomer was suddenly stopped by closing the L-valve for a short duration. The increase in height of materials, piled up in downcomer, was measured to determine the solid circulation.

Under steady state conditions during experiment, the solids circulation rate, primary and secondary air in riser and the readings at static pressure points are noted. By varying the riser air velocity and aeration flow, the solids circulation rate and the system pressure at different points are taken at different operating conditions.

2.3 Modeling

2.3.1 Riser

The axial pressure profile in riser is a key parameter and an important characteristic of CFB; the prediction of such profile is a major task in modeling the system. The pressure drop in riser is usually contributed by the pressure heads for solids suspension, gas solids friction and particle acceleration.

The current model assumes the CFB riser to be divided into three regions: dense bottom zone, splash zone and dilute transport zone. When the gas passes through the bottom zone, a distinct bed surface separates the bed which enables some particles of solids to entrain into the splash zone. A part of these entrained particles becomes decelerated and return back to the bottom zone, while the rest of the particles are accelerated to the transport zone. It is most likely that acceleration on a time average is compensated for by the corresponding deceleration. The only net acceleration is that caused by the secondary air, and it is small in the present case. Secondary air helps in the process of solids transportation and the axial voidage is the major factor for determining the solids circulation in the system.

Dense zone: The dense bottom bed operates in bubbling fluidized mode and it comprises of two phases, namely, a dense or emulsion phase and a bubble phase. The volume fraction of solids in such bed is obtained by applying modified two phase theory (Johnsson et al., 1991). The emulsion phase is formed by the bed particles as well as the interstitial gas flow in bed particles. The gas velocity, U_{mf}, and the voidage, ε_{mf}, at minimum fluidizing condition is determined from literature (Ergun, 1952).

$$U_{mf} = \frac{\mu_g}{d_p \rho_g}\left[\left(33.7^2 + 0.0408\,\frac{d_p^3 \rho_g \left(\rho_s - \rho_g\right) g}{{\mu_g}^2}\right)^{\frac{1}{2}} - 33.7\right] \tag{1}$$

and

$$\frac{\Delta p}{L_{mf}} = \left(1 - \varepsilon_{mf}\right)\left(\rho_s - \rho_g\right)\frac{g}{g_c} \tag{2}$$

The bubble phase consists of up rising gas bubbles, assumed to be free of solids. The net voidage in the dense zone, ε_{dz}, is expressed as follows.

$$\varepsilon_{dz} = \delta_b + (1 - \delta_b).\varepsilon_{mf} \tag{3}$$

where, the bubble volume fraction, δ_b, can be calculated as:

$$\delta_b = \frac{1}{1 + \frac{1.3\,(\,0.15\, + U_{pa} - U_{mf}\,)^{0.33}}{0.26\, + 0.7\exp\,(\,-3.3\,d_p\,)}.(\,U_{pa} - U_{mf}\,)^{-0.8}} \tag{4}$$

The bottom zone is characterized by a constant pressure drop for a particular bed height. This constant pressure drop, ΔP_{dz}, is determined by static heads of bed particles with the assumption that solids acceleration and deceleration compensates each other as well as negligible friction forces exist amongst solid bed particles and particles to wall. Therefore, it is given as follows:

$$\Delta P_{dz} = (1 - \varepsilon_{dz})\,\rho_s\,h_{dz}\,g \tag{5}$$

where, h_{dz} is the bed height in dense bubbling zone.

Splash zone: The splash zone is assumed to exist when the gas velocity is below the terminal velocity, U_t, of a single particle above the dense zone. The bubbles erupt ejecting solids above dense bed, some of which fall back again into the bed. This zone extends to secondary air injection level, above which the gas velocity exceeds the terminal velocity. The bed voidage in splash zone, ε_{sz}, is calculated using the following correlation (Kaiser et al., 2003).

$$\frac{\varepsilon_{sz} - \varepsilon}{\varepsilon_{dz} - \varepsilon} = \exp[\,-k(h_{sz} - h_{dz})\,] \tag{6}$$

Since this zone has been considered up to secondary air injection point and the gas velocity in the splash zone is below the single particle terminal velocity, the value of ε has been taken as unity (Loffler et al. 2003). Since this splash zone originates from the upper surface of dense bed, the actual bed height may be taken as (h_{sz} – h_{dz}). The decay factor, k, for the zone has been taken (Johnsson & Leckner, 1995) as

$$k = \frac{C\,U_t}{U_{pa}} \tag{7}$$

where, C = 10 m^{-1}.

For pressure drop estimation in splash zone, one has to consider the local solids hold up. However, there is experimental evidence that the solids acceleration significantly affects the pressure drop across the splash zone (Schlichthaerle & Werther, 1999). Further work is still needed on this issue. The following equation gives the pressure drop in splash zone for solids hold up (Loffler et al. 2003).

$$\Delta P_{sz} = \int_{h_{dz}}^{h_{sz}} (1 - \varepsilon_{sz})\,\rho_s\,g\,dh \tag{8}$$

Now, the ε_{SZ} in eqn. (8) can be represented by ε(h) as a function of height in the splash zone and the equation may be rewritten as

$$\Delta P_{sz} = \int_{h_{dz}}^{h_{sz}} (1 - \varepsilon(h))\,\rho_s\,g\,dh \tag{9}$$

Substituting the value of ε_{sz} from eqn. (6) as unity (Loffler et al. 2003), one gets

$$\Delta P_{sz} = \int_{h_{dz}}^{h_{sz}} \left(1 - \left(1 - (1 - \varepsilon_{dz}) \cdot e^{-k(h - h_{dz})}\right)\right) \rho_s \, g \, dh \tag{10}$$

$$\Rightarrow \Delta P_{sz} = \int_{h_{dz}}^{h_{sz}} \left((1 - \varepsilon_{dz}) \cdot e^{-k(h - h_{dz})}\right) \rho_s \, g \, dh \tag{11}$$

$$\Rightarrow \Delta P_{sz} = (1 - \varepsilon_{dz}) . \rho_s . g . e^{k.h_{dz}} \int_{h_{dz}}^{h_{sz}} e^{-k.h} dh \tag{12}$$

$$\Rightarrow \Delta P_{sz} = \left(\frac{(1 - \varepsilon_{dz}) . \rho_s . g . e^{k.h_{dz}}}{-k}\right) \left[e^{-k.h_{sz}} - e^{-k.h_{dz}} \right] \tag{13}$$

$$\Rightarrow \Delta P_{sz} = \left(\frac{(1 - \varepsilon_{dz}) . \rho_s . g . e^{k.h_{dz}}}{k}\right) \left[\frac{1}{e^{k.h_{dz}}} - \frac{1}{e^{k.h_{sz}}} \right] \tag{14}$$

Transport zone: The axial distribution of voidage profile in transport zone may be obtained from the exponential correlation based on entrainment model (Zenz & Weil, 1958).

$$\frac{\varepsilon_{tz} - \varepsilon_{\infty}}{\varepsilon_{sz} - \varepsilon_{\infty}} = \exp\left[-a \, (h_{tz} - h_{sz}) \right] \tag{15}$$

where α is the decay factor of solids fraction and h_{tz} is the height of any point in transport zone.

Various correlations for the decay factor, α, are available in the literature. The present study is dimensionally almost similar to an experiment (Adanez et al., 1994) conducted in a circulating fluidized bed system. They used sand and coal as bed materials under group B of Geldart classification and proposed a correlation for the decay factor.

$$a(U - U_t)^2 \, D^{0.6} = 0.88 - 420 \, d_p \tag{16}$$

This correlation has been chosen for the present study as the current operating conditions fall within the range described in literature (Adanez et al., 1994).

The far upstream voidage in transport section, ε_{∞}, in eqn. (15), depends on superficial gas velocity, particle terminal velocity, particle density and elutriation rate. The voidage at infinity is taken as described in (Loffler et al., 2003).

$$(1 - \varepsilon_{\infty}) = \frac{K_{\infty}}{\rho_S \, (U - U_t)} \tag{17}$$

where, K_{∞} is the particle elutriation rate constant for mono-sized bed materials and it is obtained using following correlation (Wen & Chen, 1982).

$$K_{\infty} = \rho_S \, \alpha_i \, (U - U_t) \tag{18}$$

where,

$$\alpha_i = 1 - \left(1 + \frac{f_s \, (U - U_t)^2}{2 \, g \, D} \right)^{-\frac{1}{4.7}} \tag{19}$$

Here, the co-efficient of friction, f_s, is evaluated from the correlations (Wen & Chen, 1982).

$$\frac{f_s \, \rho_S}{d_p^2} \left(\frac{\mu_g}{\rho_g} \right)^{2.5} = 5.17 \left[\frac{\rho_g \, (U - U_t) \, d_p}{\mu_g} \right]^{-1.5} D^2 \qquad for \quad \frac{\rho_g \, (U - U_t) \, d_p}{\mu_g} \leq \frac{2.38}{D} \tag{20}$$

and

$$\frac{f_s \, \rho_S}{d_p^2} \left(\frac{\mu_g}{\rho_g} \right)^{2.5} = 12.3 \left[\frac{\rho_g \, (U - U_t) \, d_p}{\mu_g} \right]^{-2.5} D \qquad for \quad \frac{\rho_g \, (U - U_t) \, d_p}{\mu_g} \geq \frac{2.38}{D} \tag{21}$$

The eqns. (18) to (21) were recommended for bed particles having diameters in the range of 37 to 3400 μm and density of 860 to 7850 kg/m^3 with superficial velocity in the range of 0.1 to10 m/s in riser with diameters in the range of 0.034 to 2.06 m (Wen & Chen, 1982). The input parameters of present investigation fall within the range as mentioned (Wen & Chen, 1982) and thus, the similar correlations have been used.

The pressure drop in transport zone of riser is determined from the solids hold up which can be represented by the following formulations.

$$\Delta P_{tz} = \int_{h_{sz}}^{h_{tz}} (1 - \varepsilon_{h_{tz}}) \, \rho_s \, g \, dh \tag{22}$$

$$\Rightarrow \Delta P_{tz} = \int_{h_{sz}}^{h_{tz}} \left(1 - \varepsilon(h)\right) \rho_s \, g \, dh \tag{23}$$

$$\Rightarrow \Delta P_{tz} = \int_{h_{sz}}^{h_{tz}} \left[1 - \left(\varepsilon_{\infty} - (\varepsilon_{\infty} - \varepsilon_{sz}) \, . \, e^{-a\left(h - h_{sz}\right)} \right) \right] \rho_s \, g \, dh \tag{24}$$

$$\Rightarrow \Delta P_{tz} = \int_{h_{sz}}^{h_{tz}} \left[\left(1 - \varepsilon_{\infty}\right) + (\varepsilon_{\infty} - \varepsilon_{sz}) \, . \, e^{-a\left(h - h_{sz}\right)} \right] \rho_s \, g \, dh \tag{25}$$

$$\Rightarrow \Delta P_{tz} = \int_{h_{sz}}^{h_{tz}} \left[\left(1-\varepsilon_{\infty}\right) \rho_s \, g \right] dh + \int_{h_{sz}}^{h_{tz}} \left[\left(\varepsilon_{\infty} - \varepsilon_{sz}\right) . e^{-a\left(h-h_{sz}\right)} \right] \rho_s \, g \, dh \tag{26}$$

$$\Rightarrow \Delta P_{tz} = \left(1-\varepsilon_{\infty}\right) \rho_s \, g \left(h_{tz} - h_{sz}\right) + \left(\varepsilon_{\infty} - \varepsilon_{sz}\right) . \rho_s . g . e^{a h_{sz}} . \int_{h_{sz}}^{h_{tz}} \left[e^{-ah} \right] dh \tag{27}$$

$$\Rightarrow \Delta P_{tz} = \left(1-\varepsilon_{\infty}\right) \rho_s \, g \left(h_{tz} - h_{sz}\right) + \left(\frac{\left(\varepsilon_{\infty} - \varepsilon_{sz}\right) . \rho_s . g . e^{a.h_{sz}}}{a} \right) \left[\frac{1}{e^{a.h_{sz}}} - \frac{1}{e^{a.h_{tz}}} \right] \tag{28}$$

The pressure drop due to solids friction is obtained (Loffler et al., 2003) as follows:

$$\Delta P_{tz,fric} = \int_{h_{sz}}^{h_{tz}} f_s \frac{U_S^2}{2} \frac{4}{D} \left(1 - \varepsilon_{h_{tz}}\right) \rho_s \, g \, dh \tag{29}$$

Since the transport section in riser appears to behave like a fully developed dilute-phase vertical pneumatic zone, the correlation for estimating particle velocity beyond the acceleration region (Yang, 1978) has been employed.

$$U_s = U - U_t \sqrt{\left(1 + \frac{f_s U_s^2}{2 g D} \right)} \, \varepsilon_{tz}^{4.7} \tag{30}$$

where,

$$f_s \frac{\varepsilon_{tz}^{\,3}}{\left(1-\varepsilon_{tz}\right)} = 0.0126 \left[\left(1-\varepsilon_{tz}\right) \frac{U_t}{U_s} \right]^{-0.979}, \quad for \quad \frac{U_t}{U_s} > 1.5 \tag{31}$$

and

$$f_s \frac{\varepsilon_{tz}^{\,3}}{\left(1-\varepsilon_{tz}\right)} = 0.0410 \left[\left(1-\varepsilon_{tz}\right) \frac{U_t}{U_s} \right]^{-1.021}, \quad for \quad \frac{U_t}{U_s} < 1.5 \tag{32}$$

The equations (15) to (32) are solved iteratively to evaluate the voidage ε_{tz}, the solid friction factor, f_s, and the solid velocity, U_s.

The solids circulation rate, G_s, has been determined from the following correlation:

$$G_s = \rho_s \left(1 - \varepsilon_{tz}\right) U_s \tag{33}$$

2.3.2 Riser exit and cyclone

Riser exit: The pressure drop in horizontal section between riser and cyclone has been considered as available in literature (Patience et al., 1990).

$$\Delta P_{RE} = G_s \left(2.84 + 0.0108\, U_h^2 \right) \tag{34}$$

where, G_s and U_h are the solid mass flux and the gas velocity in this section respectively.

Cyclone: The cyclone pressure drop is directly proportional to the square of inlet velocity and it is employed (Gimbun et al., 2005).

$$\Delta P_{CYC} = \alpha \, \frac{\rho_g U_{CYC}^2}{2} \tag{35}$$

where, α is a function of cyclone dimension and it is expressed in (Gimbun et al., 2005) as.

$$\alpha = 16 \, \frac{a_{CYC} . b_{CYC}}{D_e^2} \tag{36}$$

2.3.3 Down comer and L-valve

The determination of gas flow rate and the corresponding pressure drop through the down comer and L-valve sections of a circulating fluidized bed system is not an easy task (Daous & AI-Zahrani, 1998).

Variations of voidage in downcomer depend on solids flow mode. Non-fluidized bed flow is divided into a packed bed and transitional packed bed flow. In present study, the solids movement in downcomer was considered to be transitional packed bed flow in presence of aeration flow through L-valves. When these aeration taps are turned off, the solids form a packed bed in the downcomer causing no solids flow. While the aeration flow is on, air flows through the particles and the relative movement between gas and solids produces a drag force on the particles in the direction of flow. This phenomenon was also observed in literature (Zhang & Rudolph, 1991) that the transitional packed bed flow occurs when the solids flow by aeration.

During the transitional packed bed flow, the voidage increases linearly with slip velocity. The voidage in downcomer is more than compact bed voidage (ε_c), but less than voidage at minimum fluidization condition (ε_{mf}). Therefore, this voidage above the aeration point is taken as per the correlation (Tong et al., 2003).

$$\varepsilon_{DC} = \frac{1}{2} \left(\varepsilon_{mf} + \varepsilon_c \right) \tag{37}$$

Pressure drop due to solids flow by aeration is a function of slip-velocity as suggested in (Ergun, 1952; Knowlton & Hirsan, 1978).

$$\frac{\Delta P_{DC}}{L_{DC}} = \frac{150\, \mu \left(1 - \varepsilon_{DC} \right)^2 U_{SLDC}}{\left(\phi\, d_p \right)^2 \varepsilon_{DC}^2} + \frac{1.75\, \mu \left(1 - \varepsilon_{DC} \right) U_{SLDC}^2}{\left(\phi\, d_p \right) \varepsilon_{DC}} \tag{38}$$

The slip velocity for gas flowing up the downcomer can be expressed as:

$$U_{SLDC} = \frac{G_s}{\rho_S (1 - \varepsilon_{DC})} + \frac{U_{GDC}}{\varepsilon_{DC}} \tag{39}$$

The slip velocity for gas flowing down the downcomer can be expressed as:

$$U_{SLDC} = \frac{G_s}{\rho_S (1 - \varepsilon_{DC})} - \frac{U_{GDC}}{\varepsilon_{DC}} \tag{40}$$

For the pressure drop across the L-valve section, ΔP_{LV}, between the aeration point and the solids discharge point to the gasifier can be correlated with the solid mass flux (G_S), L-valve diameter (D_{LV}), mean particle size (d_p) and length of valve (L_{LV}). This correlation is as follows (Geldart & Jones, 1991).

$$\frac{\Delta P_{LV}}{L_{LV}} = 216\, G_s^{0.17}\, D_{LV}^{-0.63}\, d_p^{-0.15} \tag{41}$$

This correlation has been used in the present study because the input operating parameters match with those of (Geldart & Jones, 1991). They carried out measurements of valve pressure drops between the aeration and the solids discharge taking silica sand materials with diameters 68-341 μm with density 2550 kg/m^3 and showed that the values estimated by eqn. (41) were close enough with the experimental data.

2.3.4 Bubbling fluidized bed system

The gasifier is considered as bubbling fluidized bed, thus the correlations for pressure drop and voidage are the same as described in article 2.3.1 for dense zone of the riser.

2.3.5 Connector between bubbling and fast bed

The main task of the connector is to prevent the gas slip between the gasifier and the combustor, and excess aeration at L-valve must be avoided to prevent the dilution of product gas in gasifier. The solids circulation from bubbling fluidized bed to fast bed riser is done by an inclined connector pipe with a L-valve. The determination of gas flow rate and the corresponding pressure drop through this inclined connector and L-valve sections of a dual fluidized beds system is done in line with article 2.3.3 (Knowlton & Hirsan, 1978). In this case, the angle of inclination has been taken into account while calculating the pressure drop.

The pressure drop in L-valve has been determined in the same way as described in article 2.3.3.

2.4 Experimental observation

This part describes the experimental investigations which were carried out on hydrodynamics of dual fluidized beds system. The study focused on the axial voidage, the pressure drops across various components and the solid circulation under different

operating conditions. A mathematical model of the system to study its hydrodynamic behavior has been presented. The experimental data have been compared with the mathematical model as discussed in article 2.3.

2.4.1 Voidage profile

The effect of bed particles of mean diameters 0.147 mm and 0.416 mm on voidage along the riser has been predicted as shown in Fig 4, where the primary air flows were maintained at 0.16 m/s and 0.59 m/s respectively at the bottom zone to maintain the bed in fluidized state. It is evident from part A of Fig 4 that the voidage at the dense zone is more for smaller particles compared to larger particles at low air velocity. This can be explained by the fact that both the large and fine particles are present at the bottom zone and fine particles are embedded in larger diameter particles which decreases the voidage.

Due to the secondary air injection, the voidage in the acceleration zone of riser increases to the level of 0.998 as shown in part B of Fig 4. Beyond this acceleration zone, the flow is fully developed and behaves like a dilute-phase vertical pneumatic transport system. It is seen in part C of Fig 4 that, for the superficial gas velocities of 4.43–4.45 m/s, the voidage is more in case of 0.416 mm diameter particle as compared to 0.147 mm diameter particles. This results in lower mass flux for larger particles.

Fig 5 shows the axial voidage of dual fluidized beds system using sand # II. The system has two major sub-systems, (a) the fast bed section – riser, and (b) the section comprising of downcomer, L-valve to bubbling bed, the bubbling bed and the connector to fast bed riser. The voidage along the riser has been indicated from point-1 to point-4 and the voidage in downcomer, L-valve to bubbling bed, the bubbling bed, connector and the L-valve to fast bed riser is shown from point-7 to point-16.

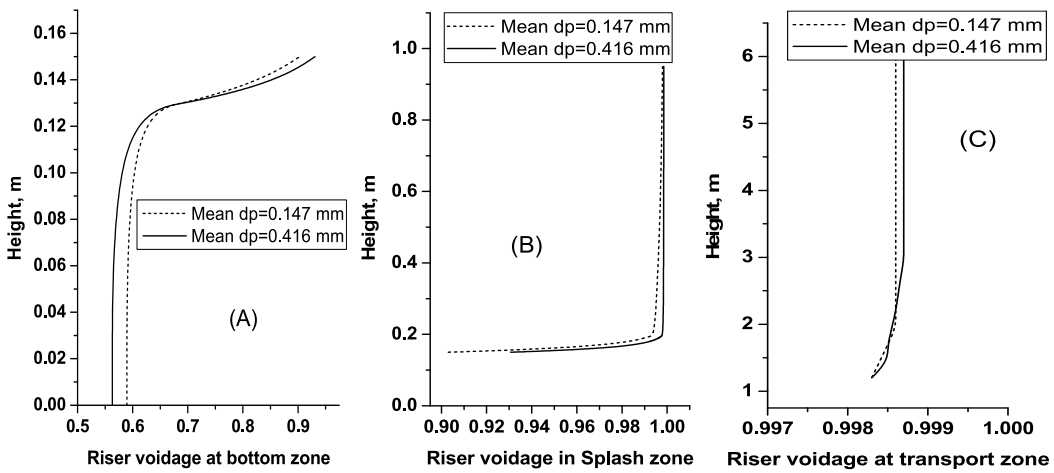

Fig. 4. Riser voidage for sand # I and sand # IV A) at bottom zone (Primary air velocity: 0.16 m/s for sand # I and 0.59 m/s for sand # IV), B) at secondary air injection in splash zone, and C) at transport zone (superficial velocity of 4.43-4.45 m/s)

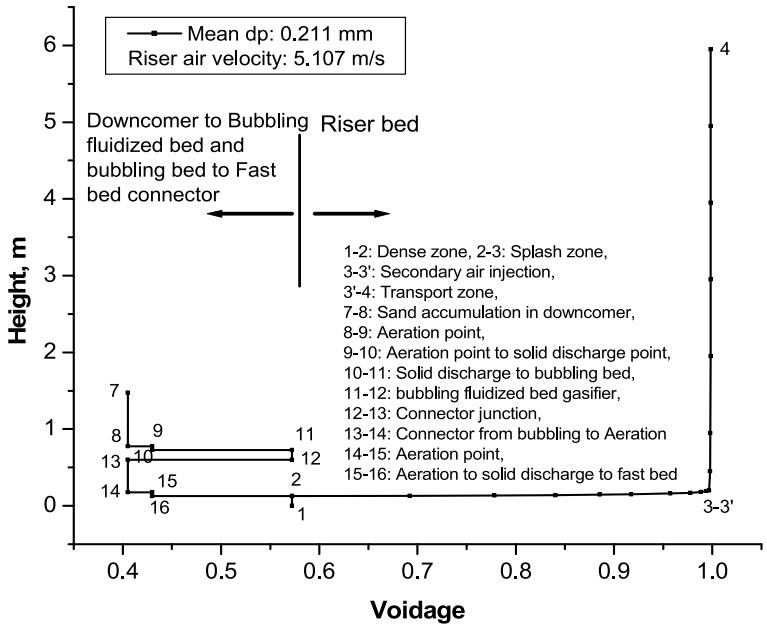

Fig. 5. Axial voidage in Dual Fluidized Bed system for sand # II

2.4.2 Pressure profile

The basic assumption is that the hydrostatic head of solids contributes to the axial pressure drop. The suspension density is related to the pressure drop through the axial distance. During the experiment, the static heads were measured along the riser, at the cyclone, along the downcomer and L-valve, the bubbling fluid bed, the connector and L-valve for every run. It was observed that the pressure drops in components of the loop were affected due to changes in superficial air velocity or solid mass flux.

Fig 6 shows the predicted and experimental values of static pressure for sand # II particles at superficial air velocity 3.85 m/s with solid mass flux of 6.94 kg/m^2-s. The figure indicates that the highest pressure is at downcomer L-valve aeration tap in the loop.

In Fig 7, the static pressure profiles using sand # IV particles have been shown along the dual fluidized beds loop at different rates of mass flux. The figure shows that the pressure drop in L-valve is greater at higher mass flux due to higher aeration flow. This is due to increase in the contribution of drag and weight forces caused by solids flow. This behaviour agrees with (Arena et al. 1978). It is also studied (Kim et al., 1999) that, at constant solids inventory, the pressure drop across the down comer increases with increasing solid circulation rate.

According to literature (Knowlton & Hirsan, 1978), the L-valve pressure drop does not depend on the particle diameter, but, later on, it was reported that the pressure drops in L-valve are less for larger particle diameters (Arena et al. 1978). They attributed this behaviour to the fact that coarser particles produce larger inter particle voidage, thus reducing the resistance to the gas flow. In Fig 8, it is seen that, in the same range of G_s, the L-valve pressure drop was more when smaller particles were used. However, further investigation should be conducted in order to confirm the results.

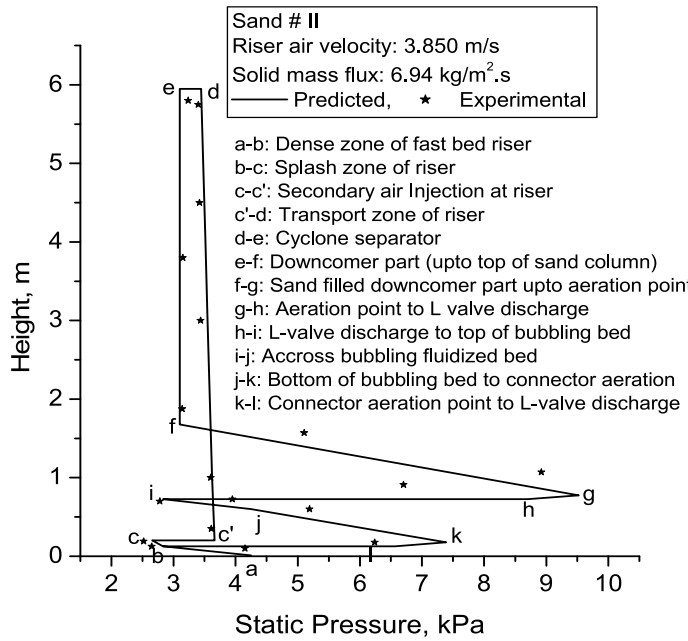

Fig. 6. Predicted and experimental pressure profiles of dual fluidized bed for sand # II

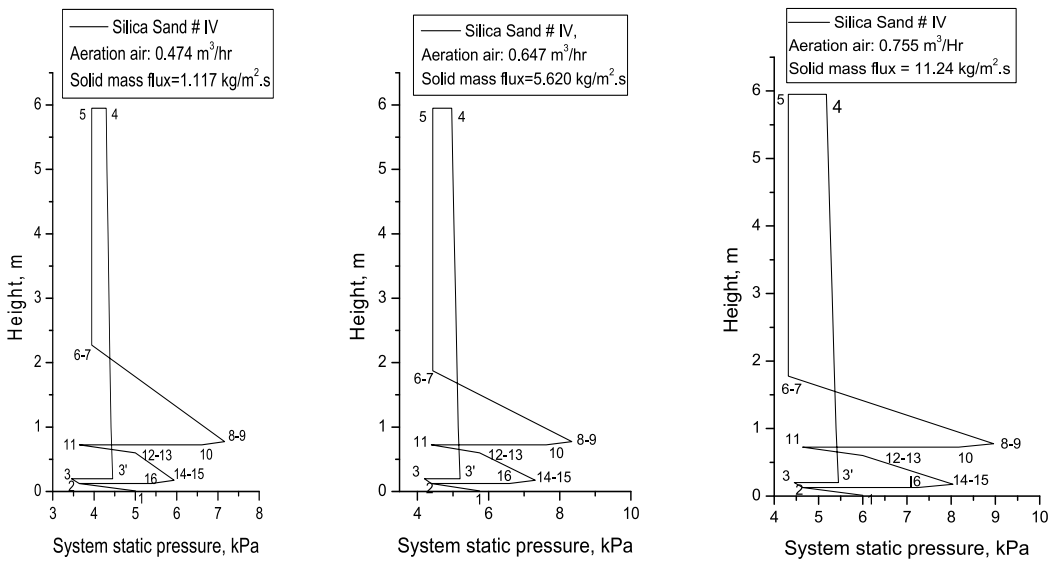

Note: 1-2: Dense zone, 2-3: Splash zone, 3-3': Secondary air injection, 3'-4: Transport zone, 4-5: Cyclone separator, 5-6: Downcomer above sand accumulation column, 6-7: Air Sand Interface 7-8: Sand accumulation in downcomer, 8-9: Aeration point, 9-10: Aeration point to solid discharge point, 10-11: Solid discharge to bubbling bed, 11-12: bubbling fluidized bed gasifier, 12-13: Connector junction, 13-14: Connector from bubbling to Aeration point, 14-15: Aeration point, 15-16: Aeration point to solid discharge to fast bed

Fig. 7. Predicted pressure profiles of dual fluidized bed for sand # IV at different riser air velocities

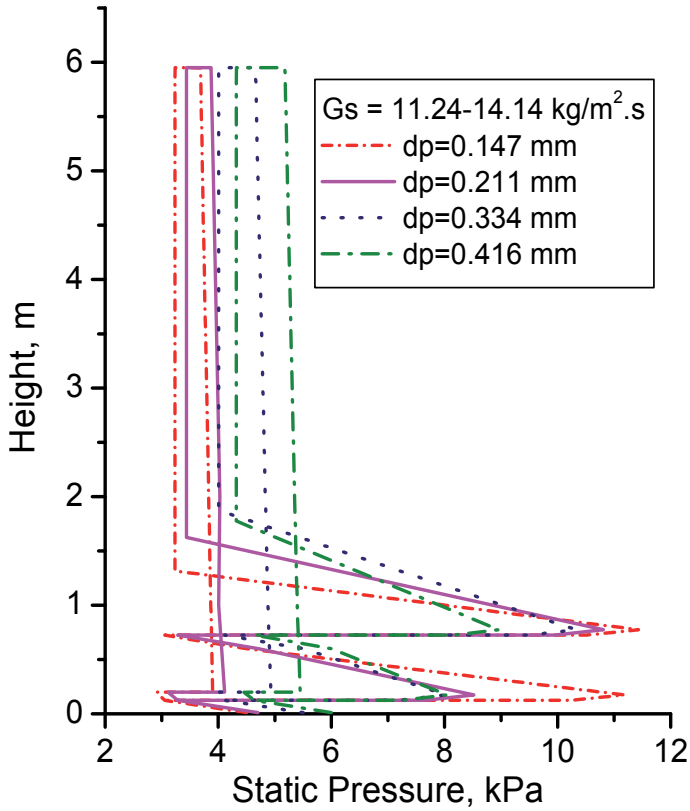

Fig. 8. Predicted pressure profiles in dual fluidized bed for sand # I, II, III and IV

2.4.3 Solid circulation

Fig 9 shows the variations of solid mass flux with the change in aeration flow and superficial gas velocity for different sizes of particles. The predicted values and experimentally observed values of solid mass flux were compared and it was found to be in good agreement between them. The solid circulation increases with increase in superficial gas velocity and this may be explained by the fact that, the increase of upward drag forces resulted in increase of net rising particle velocity ($U - U_t$). The curves also show that the requirement of aeration flow was more for larger particles to initiate solids transport in the system. The aeration rates, which were needed to cause the minimum solids flow, were 0.08 m^3/h and 0.268 m^3/h for sand # I and sand # IV, respectively. At higher solid mass fluxes, the aeration flows were more than the minimum air flow required to initiate the solids flow.

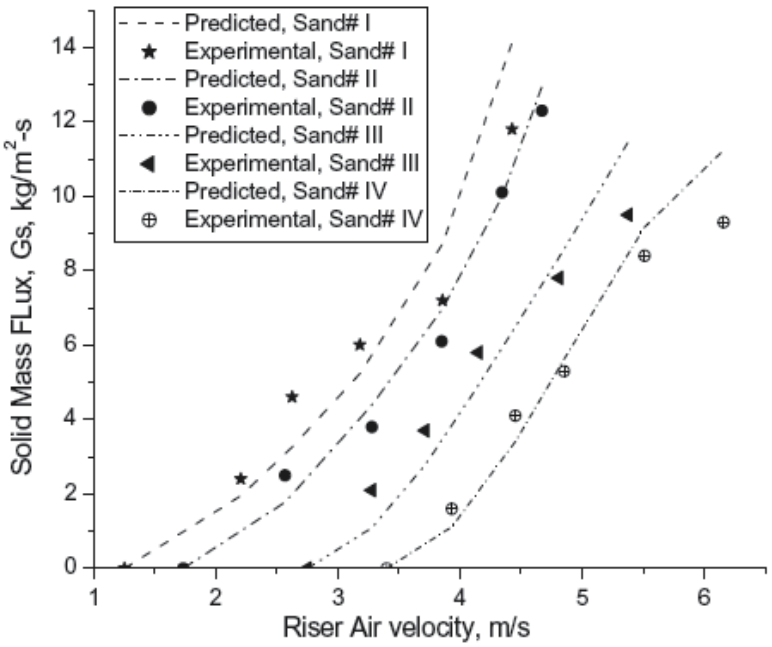

Fig. 9. Experimental and predicted mass fluxes (G_s) of samples at various riser air velocities.

3. Conclusion

The chapter gives a brief idea about the dual fluidized beds system, its experimental set up and the hydrodynamic model using L-valves in down comer and return leg. This model describes the essential features of the gas–solid flow structure. It was observed that the longitudinal voidage profiles in riser exhibit an exponential decay nature. Evaluation with experimental data shows sufficient accordance of the model regarding the pressure profile and the solids circulation. The solid circulation rate increases with increase in aeration flow and also with increase in superficial velocity. It was also discussed that, for lower size particles, the solid circulation is higher with the same superficial air flow. The L-valve aeration air requirement increases with increase in bed particle size and the pressure drop across L-valve is more for higher solid mass flux.

4. Acknowledgment

The authors thankfully convey heartfelt gratitude to Prof. Gautam Biswas, Director, CSIR - Central Mechanical Engineering Research Institute, Durgapur, India for his support during this research work..

5. References

Adanez, J. ; Gayan, P. ; Gracia-Labiano, F. & Diego, L. F. (1994). Axial voidage profiles in fast fluidized beds, *Powder Technology*, vol. 31, 259-268

Arena, U. ; Langeli, C.B. & Cammarota, A. (1998). L-Valve behavior with solids of different size and density, *Powder Technology* 98 231.

Bai, D. ; Issangya, A. S. ; Zhu, J. X. & Grace, J. R. (1997). Analysis of the overall pressure balance around a high-density circulating fluidized bed. *Industrial and Engineering Chemistry Research*, 36, 3898

Daous, M. A. & AI-Zahrani, A. A., (1998). Modeling solids and gas flow through an L-valve, *Powder Technology* vol 99, 86-89

Ergun, S. (1952) Fluid Flow Through Packed Columns. *Chem. Eng. Prog*., 48(2), 89

Geldart, D. & Jones, P. (1991). The behaviour of L-valves with Granular Powders, *Powder Technology*, 67 163-174

Gimbun, J. ; Chuah, T. G. ; Fakhru'l-Razi, A. & Choong, T. S. Y. (2005). The influence of temperature and inlet velocity on cyclone pressure drop: a CFD study, *Chem. Eng. and Processing* vol. 44, 7–12

Harris, B. J. & Davidson, J. F. (1994). Modeling options for circulating fluidized beds: A core/annulus deposition model, in A. A. Avidan (Ed), *Circulating fluidized bed technology IV*, 32-39, New York, AIChE.

Johnsson, F. ; Andersson, S. & Leckner, B. (1991). Expansion of a freely bubbling fluidized bed, *Powder Technology*, vol. 68, 117-123

Johnsson, F. & Leckner, B. (1995). Vertical distribution of solids in a CFB furnace, *13th Int. Conf. fluidized bed combustion*, 671-679, New York, ASME

Kaiser, S. ; Loffler, G. ; Bosch, K. & Hofbauer, H. (2003). Hydrodynamics of a dual fluidized-bed gasifier—Part II: simulation of solid circulation rate, pressure loop and stability, *Chemical Engineering Science*, vol.58, 4216 – 4223

Knowlton, T. M. (1977). Standpipe and return system in Circulating Fluidized Beds, 1st ed.; Grace, J. R., Avidan, A. A., Knowlton, T. M., Eds.; Blackie: London,; Chapter 7, p 240

Loffler, G. ; Kaiser S. ; Bosch, K. & Hofbauer, H. (2003). Hydrodynamics of a dual fluidized-bed gasifier—Part I: simulation of a riser with gas injection and diffuser, *Chemical Engineering Science*, vol.58, 4197 – 4213

Pugsley, T. S. & Berruti, F. (1996). A predictive hydrodynamic model for circulating fluidized bed risers, *Powder Technology*, vol. 89, 57-69

Pugsley, T. S. & Berruti, F. (1996).The circulating fluidized bed catalytic reactor; Reactor model validation and simulation of the oxidative coupling of methane, *Chem. Eng. Sci*., vol. 51, 2751-2756

Kim, W. K. ; Namkung, W. & Kim, S. D. (1999). Solid flow characteristics in loop-seal of a circulating fluidized bed, *Korean Journal of Chemical Engineering* 16 (1) 82–88.

Knowlton, T. M. & Hirsan, I. (1978). L-Valve Characterized for Solids Flow – Design Parameters Examined for Valve Use in Coal Gasification. *Hydrocarbon Processing*. Vol. 57, 149

Patience, G. S. ; Chaouki, J. & Grandjean, B. P. A. (1990). Solids Flow Metering from Pressure Drop Measurement in Circulating Fluidized Beds. *Powder Technology*. 61, 95

Schlichthaerle, P. & Werther, J. (1999). Axial pressure profiles and solids concentration distributions in the CFB bottom zone. *Chemical Engineering Science*, 54, 5485–5493

Tong, H. ; Hongzhong, L. ; Xuesong, L. & Qiayu, Z. (2003). Hydrodynamic modeling of the L-valve, *Powder Technology* vol 129, 8– 14

Wen, C. Y. & Chen, L. H. (1982). Fluidized bed freeboard phenomena: entrainment and elutriation, *AIChE Journal*, vol. 28, 117-128

Yang, W. (1978). A correlation for solid friction factor in vertical pneumatic conveying lines, *AIChE Journal*, vol. 24, 548-552

Zhang, J. Y. & Rudolph, V. (1991). Transitional Packed bed Flow in Standpipes, *Can. J. of Chem. Eng.*, 69, 1242

Zenz, F. A. & Weil, N. A. (1958). A theoretical-emperical approach to mechanism of particle entrainment from fluidized beds, *AIChE Journal*, vol 4, 472-479

2

Hydraulics of Sediment Transport

Yousef Hassanzadeh
Faculty of Civil Engineering, University of Tabriz, Tabriz, Iran

1. Introduction

This chapter deals with the theoretical and experimental considerations of hydraulics of sediment transport, involved in identifying the hydraulics formulas for fluid flow and sediment computation in open channels, and analyzing the flow and sediment characteristics of the water motion. In general, the field of sediment transport is very complex, and the engineers in this field should refer to more comprehensive works to better understand the computational basis.

The hydraulics of flow in a river and its sediment transport characteristics are the two basic phenomena that determine it's geometric and plan form shape. There are many variables that affect the hydraulics of flow and the nature of sediment transport in a natural stream. As indicated Yang et al. (1996), the Yellow River in China is notorious for enormous amount of sediment it carries. The total average annual sediment discharge to the sea in China is about 1.94×10^9 t. of which 59% comes from the Yellow River. A concentration of 911kg/m^3 was measured on September 7, 1977, at the Saumenxia Station near the entrance of the lower Yellow River.

The condition of incipient sediment motion is important in a large variety of problems associated with sediment transport. For more than two centuries workers in this field have attempted to formulate the conditions of incipient motion.

Many research programs have been devoted to the study of the sediment transport in channels. Extension can be found by Vanoni (1984), Yallin (1963, 1972) and Yang (1972, 1973). Yallin (1963, 1972) developed a bed load equation incorporating reasoning similar to Einstein (1942, 1950), but with a number of refinements and additions. Yang (1972, 1973) approached the total transport from the energy expenditure point of view and related the transport rate to stream power. Shen and Hung (1972) derived a regression equation based on laboratory data for the sand-sized particles. Using the same concept, Ackers and White (1973) defined sediment transport functions in terms of three dimensionless groups namely, size, mobility and transport rate of sediments. His functions are based on flume data carried out with flow depths up to 0.4 meters. One of the most extensive field and laboratory studies of sediment transport is that by Van Rijn (1984). He has presented a method which enables the computation of the bed load transport as the product of the saltation height, the particle velocity and the bed load concentration.

More recently, Hassanzadeh (2007) based on the dimensional analysis and the Buckingham Π-theorem in reasoning and discussion of bed load phenomenon has presented a dimensionless semi-empirical equation on the bed load. Comparisons have been made between this formula with common ones on sediment hydraulics after their unified descriptions. It is showed that, the latest formula agrees well with the measured data and could be regarded as optimal, compared with other common formula.

The theoretical equation for the distribution of suspended sediment in turbulent flow has been given by H. Rouse. Further useful information on the modification of the theory can be found in Einstein and Chien (1955), Vanoni (1984), Hassanzadeh (1985, 1979), and many others (Graf 1971, 1998 and Raudkivi 1976). A special study on the hyperconcentrated fluid mud in rivers is also reported by Mei et al. (1994).

Utilizing the data obtained from the Vanyar gauging station on Adji-chai River in Tabriz, Iran, and by means of regression analysis on the relationship between the suspended load and water discharge, Hassanzadeh (2007) has given two empirical equations with high regression coefficient to calculate the river's suspended load for the wet and dry seasons. This chapter presents a comprehensive analysis of the hydraulics of sediment transport. The effort is focused on those aspects of the study that will produce the best overall results within given constraint of time. This chapter briefly reviews hydraulics formulas for fluid flow in open channels and several fundamental sediment computations and contains the following subjects:

1. Sediment properties
2. Threshold of Particle Transport
3. Channel Roughness and Resistance to Flow
4. The Sediment Load

2. Sediment properties

The dynamic problems of liquid - solid interaction are greatly influenced by the sediment properties. The description of the latter, however, is exceedingly complex and one is forced to make many simplifying assumptions. The first of which is the subdivision into cohesive and non- cohesive sediments.

In cohesive sediments the resistance to erosion depends on the strength of the cohesive bond between the particles which may far outweigh the influence of the physical characteristics of individual particles. The problem of erosion resistance of cohesive soils is a very complex one and at present our understanding of the physics of it is very incomplete.

The non- cohesive soils generally consist of larger discrete particles than cohesive soils and the movement of these particles depends on the physical properties of the individual particles, such as size, shape and density.

2.1 Particle size, shape and density

Particle size. The most important physical property of a sediment particle is its size.

It has a direct effect on the mobility of the particle and can range from great boulders, which are rolled only by mountain torrents, to fine clays, which once stirred uptake days to settle.

The size of particles can be determined in a number of ways. The nominal diameter refers to the diameter of a sphere of same volume as the particle, usually measured by the displaced volume of a submerged particle. The sieve diameter is the minimum length of the square sieve opening through which a particle will fall. The fall diameter is the diameter of an equivalent sphere of specific gravity δ= 2.65 having the same terminal settling velocity in water at 24˚C.

Shape. Apart from size, shape affects the transport of sediment but there is no direct quantitative way to measure shape and its effects. McNown (1951) suggested a shape factor S.F. = $c/\sqrt{(ab)}$, where c is the shortest of the three perpendicular axes (a, b, c,) of the particle. The shape factor is always less than unity, and values of 0.7 are typical for naturally worn particles.

Density. Density of the particles is important and must be known. A large variation in density affect sediment transport by segregation, e.g. the armoring effect of the heavy minerals on dune crests. The mass density of a solid particle, ρ_s, describes the solid mass per unit volume. The particle specific weight, γ_S, corresponds to the solid weight per unit volume of solid. The specific weight of a solid, γ_S, also equals the product of the mass density of a solid particle, ρ_S, times the gravitational accelerating, thus:

$$\gamma_S = \rho_S \cdot g \tag{1-1}$$

Submerged specific weight of a particle, $\gamma_S^{'}$. Owing to Archimedes' principle, the specific weight of a solid particle, γ_S, submerged in a fluid of specific weight, γ, equals the difference between the two specific weights, thus,

$$\gamma_S^{'} = \gamma_S - \gamma = (\rho_S - \rho)g \tag{1-2}$$

Where ρ is the mass density of fluid.

The ration of the specific weight of a solid particle to the specific weight of a fluid at a standard reference temperature defines the specific gravity δ. With common reference to water at 4˚C, the specific gravity of quarts particles is

$$\delta = \frac{\gamma_S}{\gamma} = \frac{\rho_S}{\rho} = 2.65 \tag{1-3}$$

The specific gravity is a dimensionless ratio of specific weights, and thus its value remains independent of the system of units.

2.2 The fall velocity

The fall or settling velocity of a particle is assumed to be a steady- state motion. It is also a function of size, shape, density and viscosity of fluid.

In addition it depends on the extent of the fluid in which it falls, on the number of particles falling and on the level of turbulence intensity. Turbulent conditions occur when settling takes place in flowing fluid and can also occur when a cluster of particles is settling. For grain diameter d greater than 2mm, the fall velocity w can be approximated by the following equation:

$$w = 3.32\sqrt{\mathrm{d(mm)}} \tag{1-4}$$

Falling under the influence of gravity the particle will reach a constant velocity named the terminal velocity, when the drag equals the terminal velocity, i. e. difference of the solid and fluid velocities, V_s- V= w; we obtain the following equation:

$$C_D \frac{\pi d^2}{4}\frac{\rho w^2}{2} = \frac{\pi d^3}{6} g(\rho_S - \rho) \tag{1-5}$$

or

$$w^2 = \frac{4}{3}\frac{1}{C_D} gd(\frac{\rho_S - \rho}{\rho}) \tag{1-6}$$

Thus, the problem reduces to finding the value of the drag coefficient, C_D, for the particle in question. For spherical particles of diameter d in a viscous fluid of dynamic viscosity μ, the drag coefficient is fairly well defined. In laminar flow region, for Re < 0.5 and approximately for up to 1.0, where Re = wd/ν , we have the stokes' solution of

$$F_D = 3\pi\mu dw \text{ , and } C_D = \frac{24}{\mathrm{Re}} \tag{1-7}$$

The Stokes' solution may be considered if either the viscosity of fluid is very large (heavy oil) or the particle is very small (dust particle). Stokes, in solving the general differential equation of Navier- Stokes, neglected the inertia terms completely. Oseen (1927) seems to have been the first who successfully included, at least partly, the inertia terms in his solution of the Navier- Stokes equation. The Oseen's solution in approximate form is

$$C_D = \frac{24}{\mathrm{Re}}(1 + \frac{3}{16}\mathrm{Re}) \tag{1-8}$$

Goldstein (1929) provides a more complete solution for Oseen approximation and gives the drag coefficient in the form of

$$C_D = \frac{24}{\mathrm{Re}}(1 + \frac{3}{16}\mathrm{Re} - \frac{19}{1280}\mathrm{Re}^2 + \frac{71}{20480}\mathrm{Re}^3 + ...) \tag{1-9}$$

For $\mathrm{Re} \le 2$.

The value of drag coefficient, C_D, depends strongly on the level of free stream turbulence, apart from turbulence caused by the particle itself. It also depends on whether or not the surface of the sphere is hydraulically smooth or rough.

Schiller and Naumann (1933) suggest a formula that gives good results for Re <800, or

$$C_D = \frac{24}{\mathrm{Re}}(1 + 0.150\,\mathrm{Re}^{0.687}) \tag{1-10}$$

Schiller and Naumann (1933) also multiplied Eq. (1-6) by $(d/\nu)^2$ and obtained

$$C_D\,\mathrm{Re}^2 = \frac{4}{3} g \frac{\rho_S - \rho}{\rho} \frac{d^3}{\nu^2} \tag{1-11}$$

Olson (1961) suggests that the drag coefficient can be well represented by the following equation, for Re <100,

$$C_D = \frac{24}{\mathrm{Re}}\left(1 + \frac{3}{16}\mathrm{Re}\right)^{\frac{1}{2}} \tag{1-12}$$

2.3 Effect of viscosity

The effect of the viscosity of the fluid on the dray coefficients, fall velocities, etc., enters through the Reynolds number. However, when dealing with suspensions it may be necessary to consider the effective viscosity of the suspension rather than that of the fluid. For dilute suspensions of spheres, Einstein developed the following equation.

$$\frac{\mu_{susp}}{\mu} = 1 + k_e C \tag{1-13}$$

Where

μ_{susp}= Viscosity of the suspension
μ = Viscosity of the liquid medium
k_e= Einstein's viscosity constant
C = Volumetric concentration of the solid phase.
k_e = 2.5 for C < 2-3%.

The kinematic viscosity of a Newtonian mixture, ν_m, is obtained by dividing the dynamic viscosity of a Newtonian mixture, μ_m, by the mass density of the mixture, ρ_m, or

$$\nu_m = \mu_m \Big/ \rho_m \tag{1-14}$$

2.4 Colloids and flocculation

Suspensions of fine particles are known as colloidal system. These very small particles are made up of cohesive material. If many of the very small particles come together and form flocs, the effective weight of such an agglomerate would increase and sedimentation will occur. This entire process is frequently referred to as flocculation. This phenomena plays an important part in the formation of estuarine muds and deltas. These fine materials form soil-water complexes which have physical properties quite different from those of their elementary particles. The behavior of these materials is controlled by electro-chemical forces and most the clay-water phenomena are interpreted in terms of these electro-chemical forces.

3. Threshold of particle transport

The Motion of a fluid flowing across its bed tends to move the bed material downstream. A submerged grain on the surface is subjected to a weight force and the hydrodynamic forces. For analysis all forces are resolved into normal and tangential components. The tangential components maintain the forward motion. Below some critical hydraulic condition, the hydrodynamic forces will be so small that particles submerged weight will move very rarely or not at all. However, a slight increase in flow velocity above this hydraulic critical condition will initiate appreciable motion by some of the particles on the bed. This hydraulic critical condition is termed the condition of initiation of motion and is computed in terms of either mean flow velocity in the vertical or the critical bed shear stress (also known as the tractive force or the drag force).

3.1 Velocity criteria

In the study of hydraulics of alluvial channels the engineers are often interested in finding the quantity of water and the sediment load carried by the stream under given hydraulic conditions.

The condition of incipient motion for an assembly of solid particles is given in terms of the forces acting on the particle by the following relation

$$\tan\phi = \frac{F_t}{F_n} \tag{1-15}$$

Where F_t and F_n are the forces parallel and normal to the angle of repose ϕ. In this study F_t and F_n are resultants of the hydrodynamic drag F_D, the lift force F_L and the submerged weight.

Equation (1-15) for the condition of incipient motion under the action of these three forces becomes

$$\tan\phi = \frac{W\sin\alpha + F_D}{W\cos\alpha - F_L} \tag{1-16}$$

Where angle α is the inclination of the bed from the horizontal at which incipient sediment motion takes place. Fig. 1.1 shows the situation of these three named forces. The drag F_D and lift F_L forces may be expressed as

$$F_D = C_D K_1 d^2 \frac{\rho u_b^2}{2} \tag{1-17}$$

$$F_L = C_L K_2 d^2 \frac{\rho u_b^2}{2} \tag{1-18}$$

Where u_b = fluid velocity at the bottom of the channel

C_D, C_L= drag and lift coefficients, respectively
d= particle diameter
K_1, K_2 = particle shape factors
ρ = liquid density

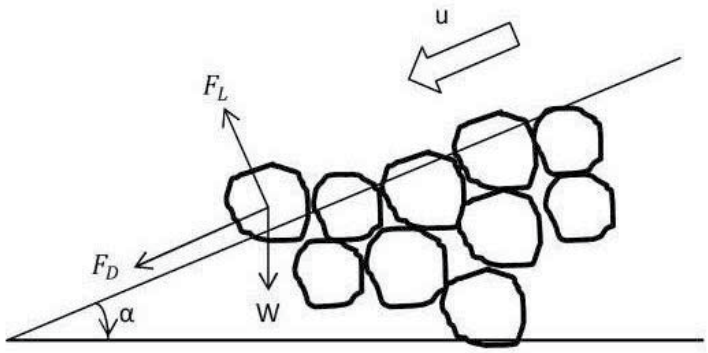

Fig. 1.1. Force diagram on particles in a cohesionless sediment

The submerged weight of the particle is given by

$$W = K_3(\rho_S - \rho)gd^3 \tag{1-19}$$

With K_3 being another shape factor and ρ_s being the solid particle density.

Introducing Eqs. (1-17), (1-18), and (1-19) into Eq. (1-16) yields

$$\frac{(u_b^2)_C}{(\rho_S/\rho - 1)gd} = \frac{2K_3(\tan\phi\cos\alpha - \sin\alpha)}{C_D K_1 + C_L K_2 \tan\phi} \tag{1-20}$$

Where $(u_b)_c$ is the critical bottom velocity at which incipient sediment motion takes place. The quantity of the right- hand side in Eq. (1-20) is referred to as the sediment coefficient A',

$$A' = \frac{2K_3(\tan\phi\cos\alpha - \sin\alpha)}{C_D K_1 + C_L K_2 \tan\phi} \tag{1-21}$$

The sediment coefficient A' depends on the particles properties, the dynamics of the flow, the channel slope, and the angle of repose. The angle of repose is the slope angle formed with the horizontal by granular material at the critical condition of incipient sliding. The angle of repose ϕ which is given by Lane (1953), in Figure 1.2 depends on particle size.

For more than two centuries the hydraulicians have attempted to formulate the conditions of incipient motion. One of the earliest relations is due to Brahms (1753). Brahms gave the critical velocity V_c of water as

$$V_c = kW^{1/6} \tag{1-22}$$

Where k is an empirical constant and W is the weight of the grain.

Fortier et al. (1926) report on a most extensive study on "permissible canal velocities", the maximum permissible value of the mean velocities.

Erosion, transportation, and deposition phenomenon have studied by Hjulström (1935) for uniform material on a loose bed (Fig. 1.3).

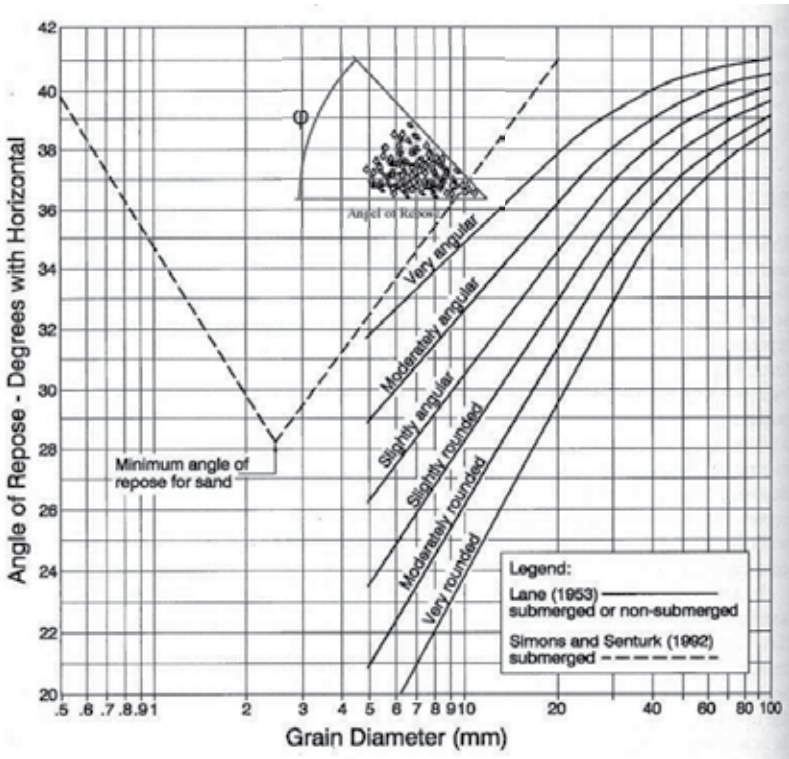

Fig. 1.2. Angle of repose for uniform non cohesive sediment (Lane, 1953)

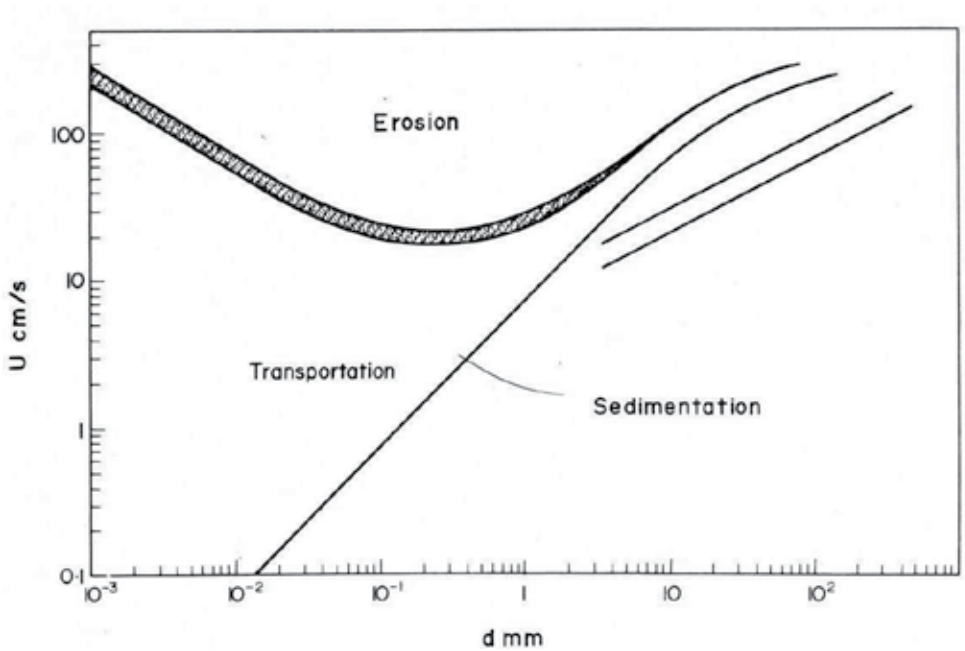

Fig. 1.3. Erosion and deposition criteria for uniform particles (Hjulström, 1935)

Neil (1967) gave the following relation for uniform material.

$$\frac{u_c^2}{(\rho_S/\rho-1)gd} = 2.50(d/h)^{-0.20} \tag{1-23}$$

Where h is the depth of uniform flow.

Based on the incipient motion data, Carstens (1966) proposed an equation such as

$$\frac{u_c^2}{(\rho_S/\rho-1)gd} = 3.61(\tan\phi\cos\alpha - \sin\alpha) \tag{1-24}$$

The latest is by Yang (1973, 1996) who used the conventional drag and lift concepts combined with the logarithmic velocity distribution and arrived at

$$\frac{V_c}{w} = \frac{2.5}{\log\frac{u_* d}{\nu} - 0.06} + 0.66 \quad ; \quad 0 < \frac{u_* d}{\nu} < 70 \tag{1-25}$$

Where the numerical constants are from empirical curve fitting. The above equation is valide for the hydraulically smooth and transition zones and for the hydraulically rough region the relationship is:

$$\frac{V_c}{w} = 2.05 \qquad , \qquad R_{e^*} > 70 \tag{1-26}$$

It should be noted that, Eq.1.25 yields $V_c/w \approx \infty$ when $u_* d/\nu \approx 1.48$ .This would means that particles just a little finer than 100 μ_m will behave as a fixed boundary because $w \neq 0$ for this grain size. It is likely that the formula will give acceptable results for the shear velocity Reynolds number R_{e^*} > 1.5 or 2.

In the turbulent range, for R_{e^*}> 70, Yang's expression states that particles on a bed will begin moving when the average velocity is twice the particle settling velocity.

3.2 Bed shear stress or tractive force criteria

In a steady uniform flow, the component of the gravitational force exerted along the slope direction which causes downstream motion is balanced by the bed shear stress or tractive force per unit surface τ_0, which is the frictional force exerted on the moving fluid at its boundary. For the small slopes, the bed shear stress in a channel can computed as

$$\tau_0 = \gamma R_h S = \rho g R_h S \tag{1-27}$$

Where R_h= hydraulic radius, and S = bed slope. In a wide open channel, the hydraulic radius R_h is equal to the depth of flow h; hence

$$\tau_0 = \gamma h S = \rho g h S \tag{1-28}$$

The relationship between the friction velocity u_* and shearing stress τ_0 is given by

$$u_* = \sqrt{\tau_0 / \rho} = \sqrt{R_h g S} \tag{1-29}$$

The first research in the mechanics of sediment transport, using the foregoing concept, was reported by Shields (1936). Shields determined that the critical condition could be related to two dimensionless parameters: the dimensionless shear stress or the Shields parameter F_*, and the boundary Reynolds number or the shear Reynolds number $\mathrm{Re}_* = \frac{u_* d}{\nu}$. The Shields parameter F_* reflects the ratio of the force producing sediment motion to the force resistance motion and may be computed by:

$$F_* = \frac{\tau_0}{(\gamma_S - \gamma)d} \tag{1-30}$$

Use of the Shields diagram requires that the critical value of the Shields parameter F_{*c} be determined. To facilitate computations when grain size is known, the dimensionless diameter d_* may be computed by Jullien (1995) equation:

$$d_* = d\left[\frac{(\delta - 1)g}{\nu^2}\right]^{\frac{1}{3}} \tag{1-31}$$

Where d= sediment diameter, δ= specific gravity of sediment, and ν = kinematic viscosity.

The Shields diagram (Fig. 1.4) is a widely used method to determine the condition of incipient motion based on bed shear stress. Points lying above the curve representing the critical condition correspond to sediment motion, and points below the curve correspond to no motion. Three somehow distinct zones can be noticed in Fig. 1.4. It should be mentioned that, many hydraulic engineering problems deal with flow in the turbulent range and sediment having d >1 mm, the value of Shields parameter may be considered F_{*c} = 0.047 for critical condition in the range of boundary Reynolds number $\mathrm{Re}_* > 40$ (Yalin and Karahan, 1979). For this condition Eq. (1-28) is rearranged as

$$\tau_c = F_*(\gamma_S - \gamma)d = 0.047(\gamma_S - \gamma)d \tag{1-32}$$

In Shields diagram, a value for $\mathrm{R}_{e^*} \geq 400$ is obtained as

$$\frac{\tau_c}{(\gamma_S - \gamma)d} = 0.06 \tag{1-33}$$

Zeller (1963) finds this constant to be too high, and he obtained a value of 0.047.

The simplest method for estimating the critical condition for the movement of cohesionless sediment is using the linear relationship between critical bed shear stress τ_c and grain size d given by Julien (1995).

$$\tau_c(g/m^2) = 80 d_{50}(mm), \quad \text{for } \mathrm{d}_{50} > 0.30mm \tag{1-34}$$

A similar linear relationship is also suggested by Leliavsky (1955):

$$\tau_c(g/m^2) = 166 d_{50}(mm), \quad \text{for} \quad d_{50} < 3.4mm \tag{1-35}$$

These equations are approximately valid for d_{50} > 0.3 mm, and can be used as a quick check against other methods and to help determine the hydraulic roughness regime.

Considerable field data are used by Lane (1953) to establish the critical tractive force diagram on function of grain size, as shown in Fig. 1.5. This diagram concern of allowable tractive force in channels as a function of grain size, for the range of fine to coarse noncohesive materials. As can be seen in Fig. 1.5, the critical shear stress τ_c for clear water is considerably lower than for water with a low or high content of sediments. The Lane diagram summarizes much of the important research done and, hence, should prove very helpful for the hydraulician engaged in stable channel design.

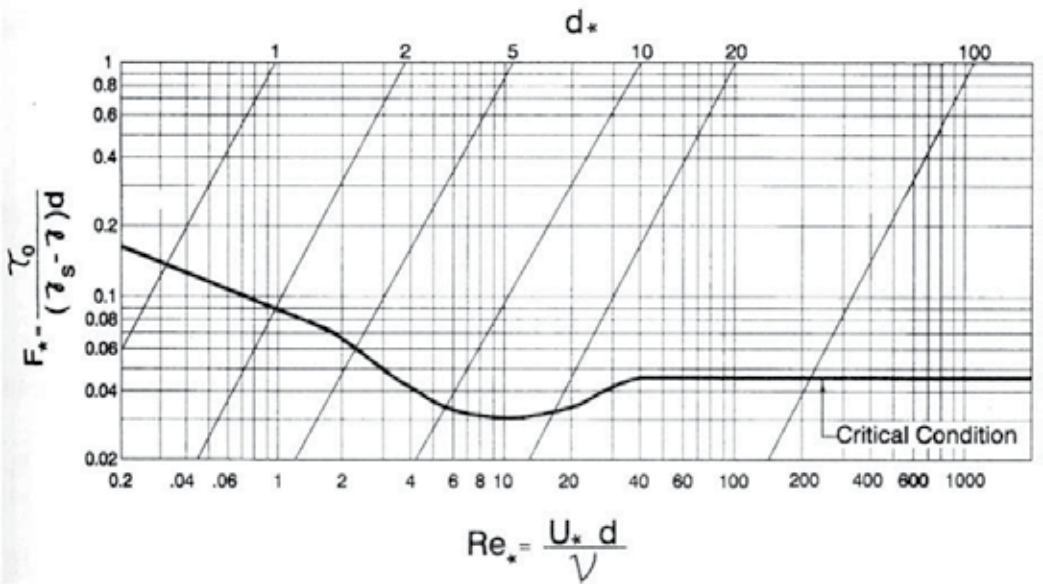

Fig. 1.4. Modified Shields diagram (Yalin and Karahan, 1979).

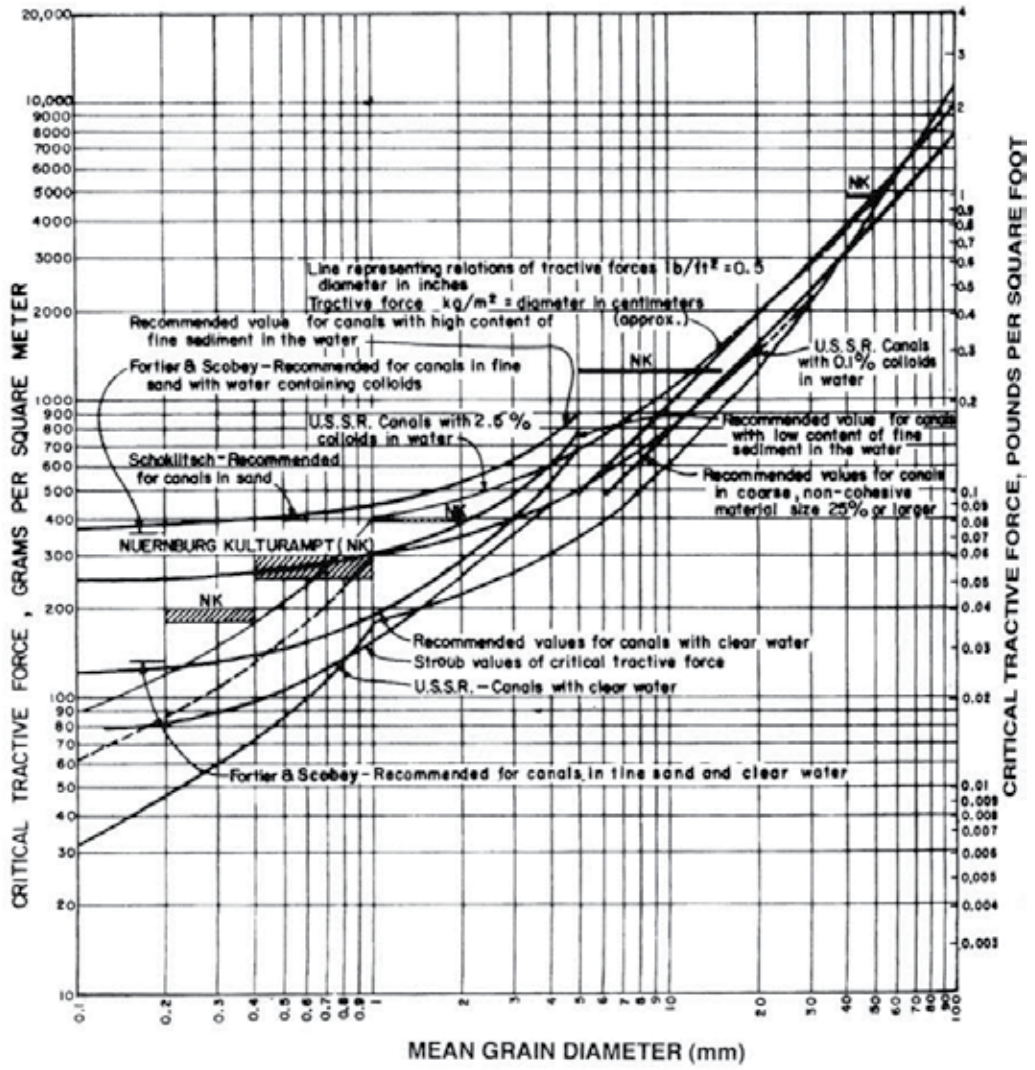

Fig. 1.5. Allowable tractive force in channels as a function of grain size (Lane, 1955).

It should be noted that the initiation of significant motion within a bed of mixed sediment can be affected by factors such as hiding of smaller grain by the larger ones and armoring. Graf (1971) indicated that for materials which are not uniformly sized or contain cohesive materials, the critical bed shear stress for incipient motion should be higher than predicted in the Shields diagram. Also, the shear stress is not distributed evenly accros a cross section. For a straight prismatic trapezoidal channel, Lane (1953) determined the shear stress distribution shown in Fig. 1.6 and concluded that in trapezoidal channels maximum shear stress for the bottom and sides is approximately equal to $0.97\,\gamma hS$ and $0.75\,\gamma hS$, respectively.

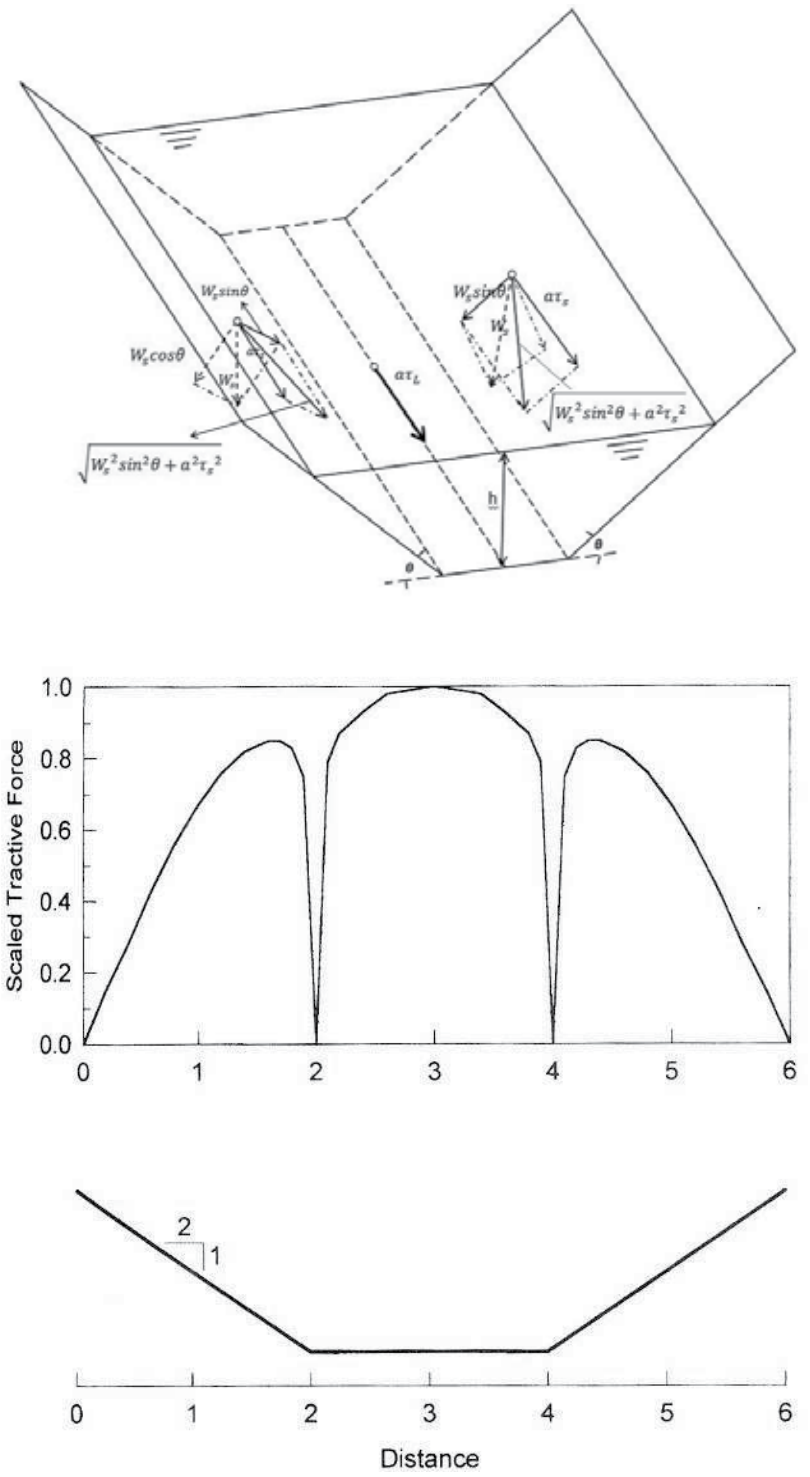

Fig. 1.6. Shear stress distribution in a trapezoidal channel section (Lane, 1955).

The boundary shear stress distribution for a curved trapezoidal channel was experimentally measured by Ippen and Drinker (1962) who found that the maximum shear stresses τ_{max}, occur at the outer toe of the bank immediately downstream of the curve. Shear stress in the curved reach will be 2 to 3 times greater than the shear in a straight channel. The ratio of maximum local boundary shear stress, τ_{max}, in a curved reach to the average boundary shear stress in a approach straight channel τ_0, is given by

$$\frac{\tau_{\max}}{\tau_0} = 2.65\left(\frac{r_c}{B}\right)^{-0.5} \tag{1-36}$$

Where r_c = centerline radius of the bend, and B = water surface top width at the upstream end of the curved reach.

3.3 Shear stress ratio

It is remarkable that, on a channel bank, the gravity force that causes the particle to move down the sloping sides of the channels must be considered. On a soil particle resting on the sloping side of a channel section (Fig. 1.6) in which water is flowing, two forces are acting: the tractive or shear stress force $a\tau_s$, which try to move the sediment particle down the channel in the direction of flow, and the gravity- force component $W_s \sin\theta$, which tends to cause the particle to roll down the side slope. The resultant of these two forces, which are at right angles to each other, is

$$\sqrt{W_S^2 \sin^2\theta + a^2\tau_S^2}$$

where a = effective area of the particle, τ_s = unit tracrive force or shear stress on the side of the channel, W_s = submerged weight of the particle, and θ = angle of the side slope. When this force is large enough, the particle will move. On the other hand, the resistance to motion of the particle is equal to the normal force $W_s \cos\theta$ multiplied by the coefficient of friction, or $\tan\phi$, where ϕ is the angle of repose. Hence, by the principle of friction motion in mechanics, we have

$$W_S \cos\theta \tan\phi = \sqrt{W_S^2 \sin^2\theta + a^2\tau_S^2} \tag{1-37}$$

Solving for the unit tractive force τ_c that causes impending motion on a sloping surface,

$$\tau_S = \frac{W_S}{a}\cos\theta\tan\phi\sqrt{1-\frac{\tan^2\theta}{\tan^2\phi}} \tag{1-38}$$

Similarly, when motion of a particle on the level surface is impending owing to the tractive force $a\tau_L$, the following is obtained from Eq. (1-37) with $\theta = 0$:

$$W_S \tan\phi = a\tau_L \tag{1-39}$$

Solving for the unit tractive force τ_L that causes impending motion on a level surface

$$\tau_L = \frac{W_S}{a}\tan\phi \tag{1-40}$$

The ratio of τ_s to τ_L is called the tractive or shear stress force ratio; which is an important ratio for design purposes. From Eqs. (1-38) and (1-40) the ratio is

$$K = \frac{\tau_S}{\tau_L} = \cos\theta\sqrt{1 - \frac{\tan^2\theta}{\tan^2\phi}} \tag{1-41}$$

Simplifying

$$K = \sqrt{1 - \frac{\sin^2\theta}{\sin^2\phi}} \tag{1-42}$$

It can be seen that this ratio is a function only the inclination of the sloping side θ and of the angle of repose of the material ϕ. The Eq. (1-41), is the form given by Lane (1953), has been suggested for the use in channel designs. Both of these expressions give the ratio of shear stress required to start motion on the slope to that required on the level surface of the same material.

By knowing the critical shear stress on the bottom, with the aid of Shields diagram the critical wall shear stress can be calculated, provided information on the angle of repose is available.

It is evident that, for a bank to be stable, the angle of the bank θ, must be less than of the angle of repose ϕ, or in other words, for stability reasons, $\phi > \theta$.

3.4 Annandale's erodibility index method

The erodibility index method has been developed recently by Annandale (1995) and may be used to compute the hydraulic conditions under which erosion will be initiated in a wide range of materials.

The erodibility index method is based on unit stream power, τV, the erosive power of water, according to the relationship:

$$\tau V = f(K_h) \tag{1-43}$$

Where τV = unit stream power (W/m^2), and $f(K_h)$ is the erodibility index. Erosion will occur when $\tau V > f(K_h)$, but not when $\tau V < f(K_h)$. The rate of energy dissipation per unit of bed area is determined by:

$$\tau V = \gamma h S V \tag{1-44}$$

Where γ = unit weight of water, h = depth, V = velocity and S = energy slope. For loose granular material, $0.1 < d_{50} < 100$ mm, the relationship between unit stream power at the critical erosion condition τV_c and the erodibility index K_h may be given by

$$\tau V_c = 480 K_h^{0.44} \tag{1-45}$$

Erosion occurs if unit stream power exceeds the value of τV_c. For cohesionless granular sediment, the erodibility index value may be related to grain diameter by:

$$K_h = 20 d_{50}^3 \tan\phi \tag{1-46}$$

Where ϕ = angle of repose (Annandale, 1994).Fig. 1.7 shows the eroding and noneroding conditions based on the erodibility index method given by Annandale (1996).

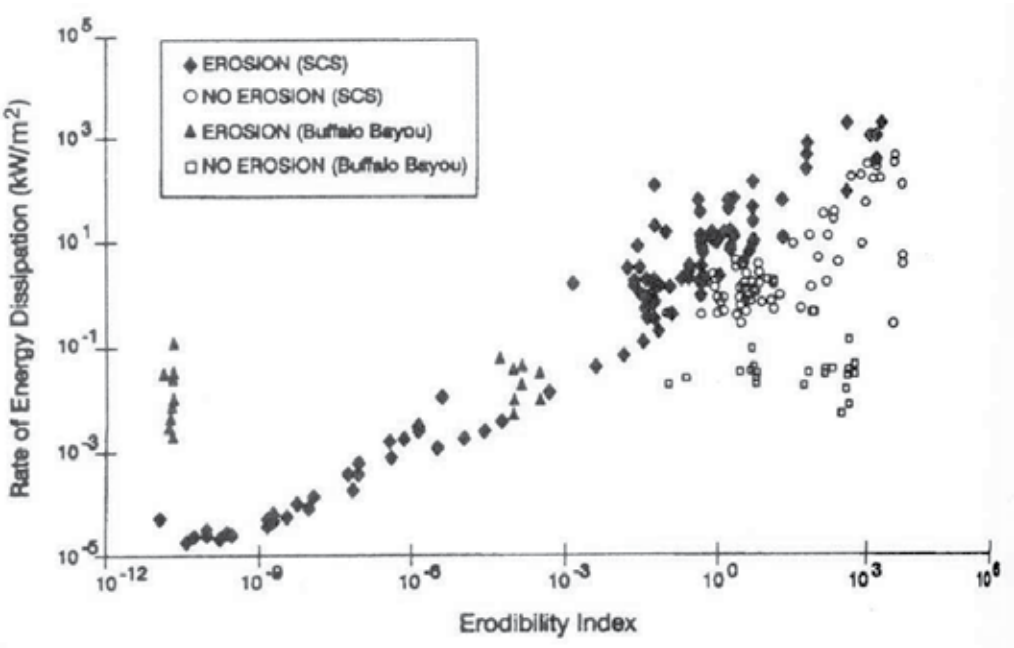

Fig. 1.7. Eroding and noneroding conditions based on the erodibility index method (Annandale, 1996).

4. Channel roughness and resistance to flow

The resistance to flow in a channel of fixed geometry carrying clear water in steady uniform flow can be predicted quiet accurately. But when the same channel carries clear water in non-uniform state of flow the resistance problem becomes very complicated. The shape of the channel in alluvium changes with flow conditions; bed features may form and the cross-section of the channel may become displaced laterally. These changes affect the drag caused by surface roughness and introduce form drag caused by the bed features, as well as energy losses due to secondary currents. The problem is further complex by the sediment motion along the bed and in suspension, since the mixture of water and sediment does not behave as clear water.

4.1 Flow resistance equations

4.1.1 Chézy equation

In 1775, the French engineer Chézy has given the relationship bearing his name, the first equation to successfully relate uniform open-channel flow to bed resistance. Chézy related the average velocity V of steady uniform open-channel flow to three parameters: channel

slope S the hydraulic radius R_h, and a coefficient which expresses the boundary roughness. The Chézy equation is usually written in the form:

$$V = C\sqrt{R_h S} \tag{1-47}$$

in which C=Chézy coefficient of friction with the dimensional equation of $[C] = L^{1/2}T^{-1}$.

4.1.2 Manning equation

The equation developed in 1889 by the Irish engineer Robert Manning may be derived from the Chézy equation if the Chézy friction coefficient is set equal to $C = \frac{1}{n} R_h^{1/6}$. The Manning equation has the following form in SI units:

$$V = \frac{1}{n} R_h^{2/3} \sqrt{S} \tag{1-48}$$

In which n= Value in the Manning equation shows the roughness or flow-resistance characteristics of the boundary surface with the dimensional equation of $[n] = L^{-1/3}T$.

By multiplying both sides of the equation by the wetted cross-sectional area A, Manning's equation can be solved for discharge in SI units:

$$Q = \frac{1}{n} A R_h^{2/3} \sqrt{S} \tag{1-49}$$

This equation is widely used in open channel water flow computations.

4.1.3 Darcy-Weisbach equation

The nature of the boundary resistance in open channel flow is identical with that of full pipe flow and the Darcy-Weisbach and Colebrook-White equation for non-circular section may be applied. Noting that the energy gradient S_f is equal to the bed slope S in uniform flow:

$$V = \sqrt{\frac{8g}{\lambda}} \cdot \sqrt{R_h S} = C\sqrt{R_h S} \tag{1-50}$$

or

$$V = \sqrt{\frac{8}{\lambda}} \; u_* \tag{1-51}$$

With

$$C = \sqrt{8g/\lambda} \quad , \quad \text{and} \quad \lambda = 8g/C^2 \tag{1-52}$$

Unlike the friction coefficient in the Chézy and Manning equations, the Darcy-Weisbach friction factor λ is dimensionless, and can be read from Moody diagram.

4.2 Hydraulic flow-resistance factors

Hydraulic flow resistance has two components: grain roughness and form loss. Grain roughness is due to the tractive force created by sediment materials, vegetations, or other roughness elements at the flow boundary surface.

Form loss is the large-scale turbulent loss caused by the irregularity of the channel geometry along its length because of bed forms, expansions, constrictions, bends, and similar geometric features. Both types of flow resistance are important in natural channels.

A large information on n value determination for common engineering materials and natural channels may be found in chow (1959), Barnes (1967), and Arcement and Schneider (1989).

4.2.1 Grain roughness

The Strickler formula, developed in 1923, defined Manning's n value for grain roughness as a function of particle size:

$$n = \frac{d_{50}^{1/6}}{21.1} \tag{1-53}$$

Where d_{50}= median sediment particle diameter in meter (Morris and Fan, 1998).

Muler (1943) proposes to calculate the roughness coefficient K which is a result of the friction of the top layer of the grains,

$$K = \frac{26}{d_{90}^{1/6}} \quad (m^{1/3} / \sec) \tag{1-54}$$

Where d_{90} represents the size of the sediment in the bed for which 90 percent of the material is finer. This is certainly a reasonable diameter, since the top layer, being made up of the largest grains and is armoring the bed.

Specific procedures that can be used to determine Manning's n values for channels and flood plains, described by Arcement and Schneider (1989), are based on Cowan's (1956) method, research on channel roughness by Aldridge and Garrett (1973) and flood plain studies.

Cowan's procedure determines roughness values using a base n value which is then modified to incorporate additional factors which influence flow resistance.

4.2.2 Effect of vegetation on flow resistance

Vegetation presents a special problem in hydraulic computations because the boundary roughness changes greatly as a function of factors such as flow depth, velocity, and the biomechanical characteristics of the vegetation.

The sediment roughness value n can change remarkably during flow events as vegetation is inclined of flattened by the flow. Torres (1997) collected data from 452 experiments in grassed channels with flow depths from 0.018 to 0.81 m and vegetation height ranging from

0.05 to 0.9 m. The variation in Manning's n value with respect of channel mean velocity V, and submerged ratio (h/h_v), for grass channels is given by Torres (1997) in Fig 1.8. In which h and h_v represents water depth and the vegetation height, respectively.

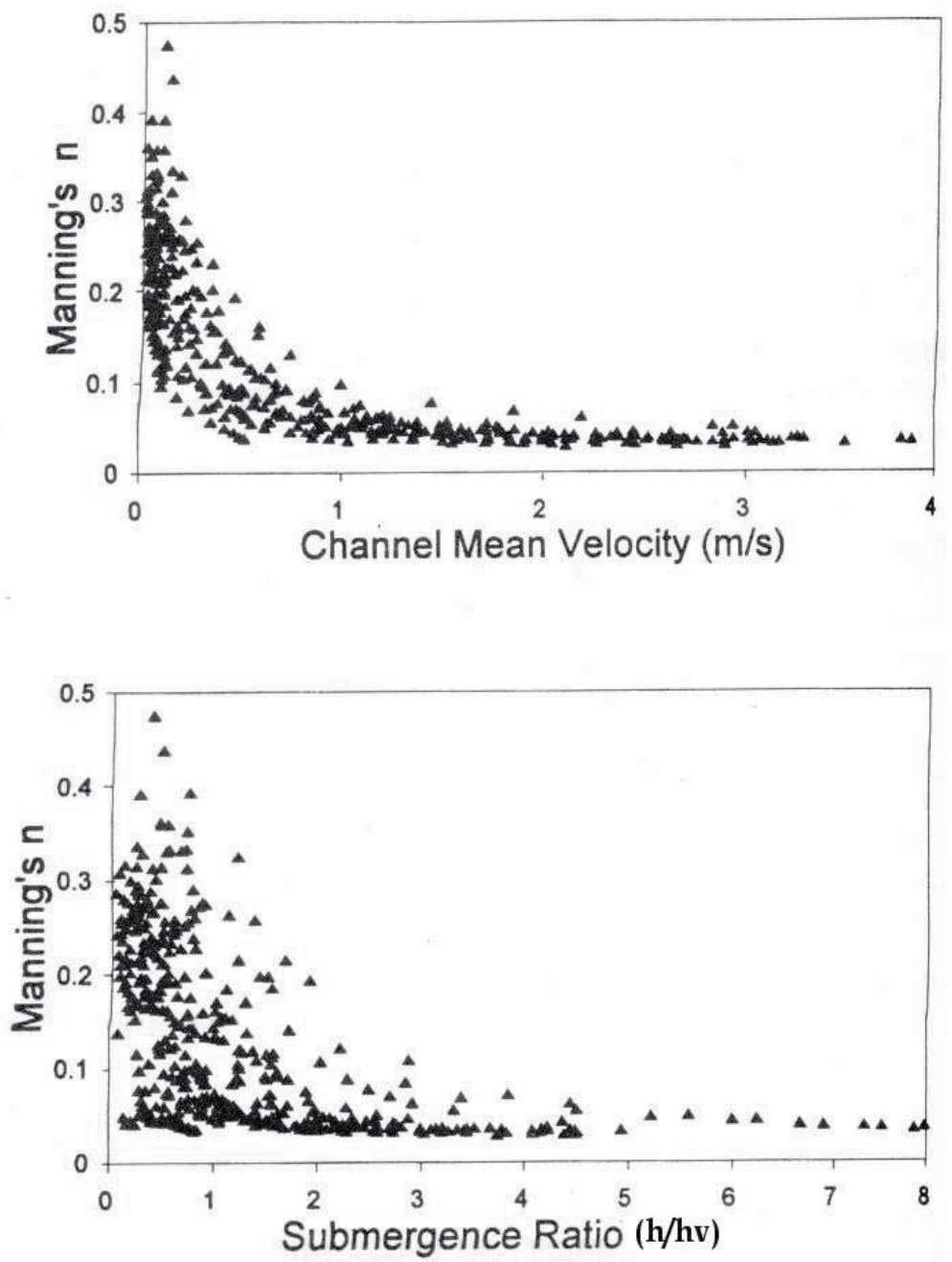

Fig. 1.8. Variation in Manning n value for grass channels (Torres, 1997)

4.3 Bedforms

When the sediment materials enter motion, the random patterns of erosion and sedimentation generate very small perturbations of the bed surface elevation. In many instances, these perturbations grow until various surface configurations known bed forms cover the entire bed surface. Resistance to flow, which depends largely on bed form configuration, directly affects water surface elevation in alluvial channel. As flow velocity increases, an initially flat sand bed develops first ripples and then dunes. With additional velocity, as illustrated in Fig.1.9, the stream subsequently transitions into a plain bed form, and finally forms antidunes with standing waves which may or may not crest and break. Transition from the lower flow regime, where bed forms dominant roughness, to the upper regime produces a dramatic drop in roughness and will produce a discontinuous discharge rating curve.

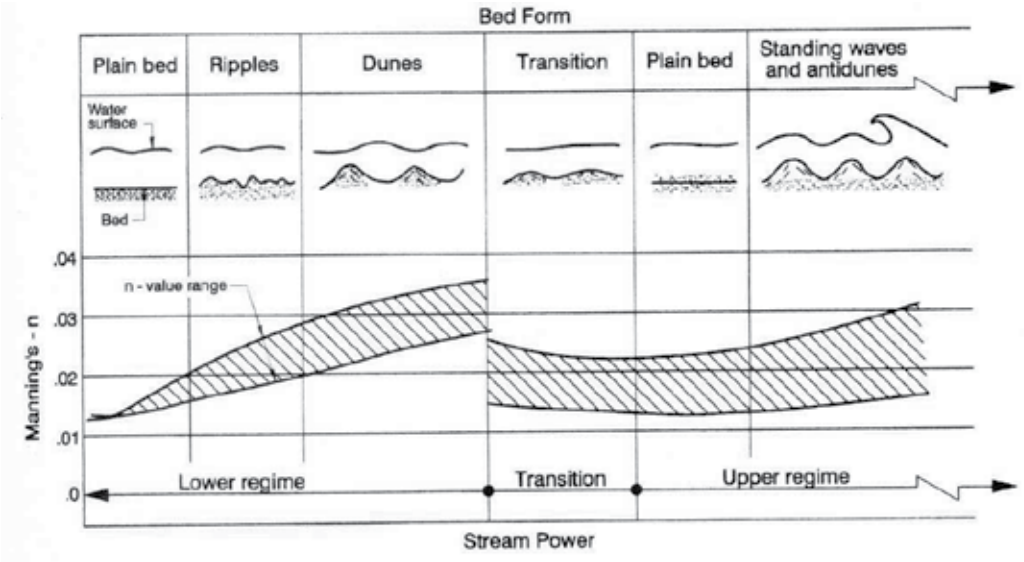

Fig. 1.9. Bed forms encountered in movable bed streams.

Various bed form configurations and geometry define the boundary roughness and resistance to flow in alluvial channels. The primary variables that affect bed form configuration and geometry are the slope of the energy grade line, flow depth, bed particle size, and particle fall velocity. Flat bed, or plain bed, refers to a bed surface without bed forms. Ripple shapes is small bed form, vary from nearly triangular to almost sinusoidal. Dunes are larger than ripples and are out of phase will the water surface waves.

Bedforms are classified into lower and upper flow regimes based upon their shape, resistance to flow, and mode of sediment transport (Simons and Richardson, 1963, 1966). A transition zone exists between the two flow regimes, where bedforms range from washed-out dunes to plain bed or standing waves. The relationship between bedform and stream power developed by Simons and Richardson (1966) shown in Fig. 1.10 can be used to determine the flow regime. Because of the non-uniform conditions in natural channels, different flow regimes and bed forms can coexist in different areas of the same channel.

The Simons and Richardson (1966) proposed predictor bed form encompassing both lower and upper regimes when plotting the stream power ($\tau_0 V$) as a function of particle diameter d. Their bedform predictor based on extensive laboratory experiments is quite reliable for shallow stream but deviates from observed bed forms in deep streams.

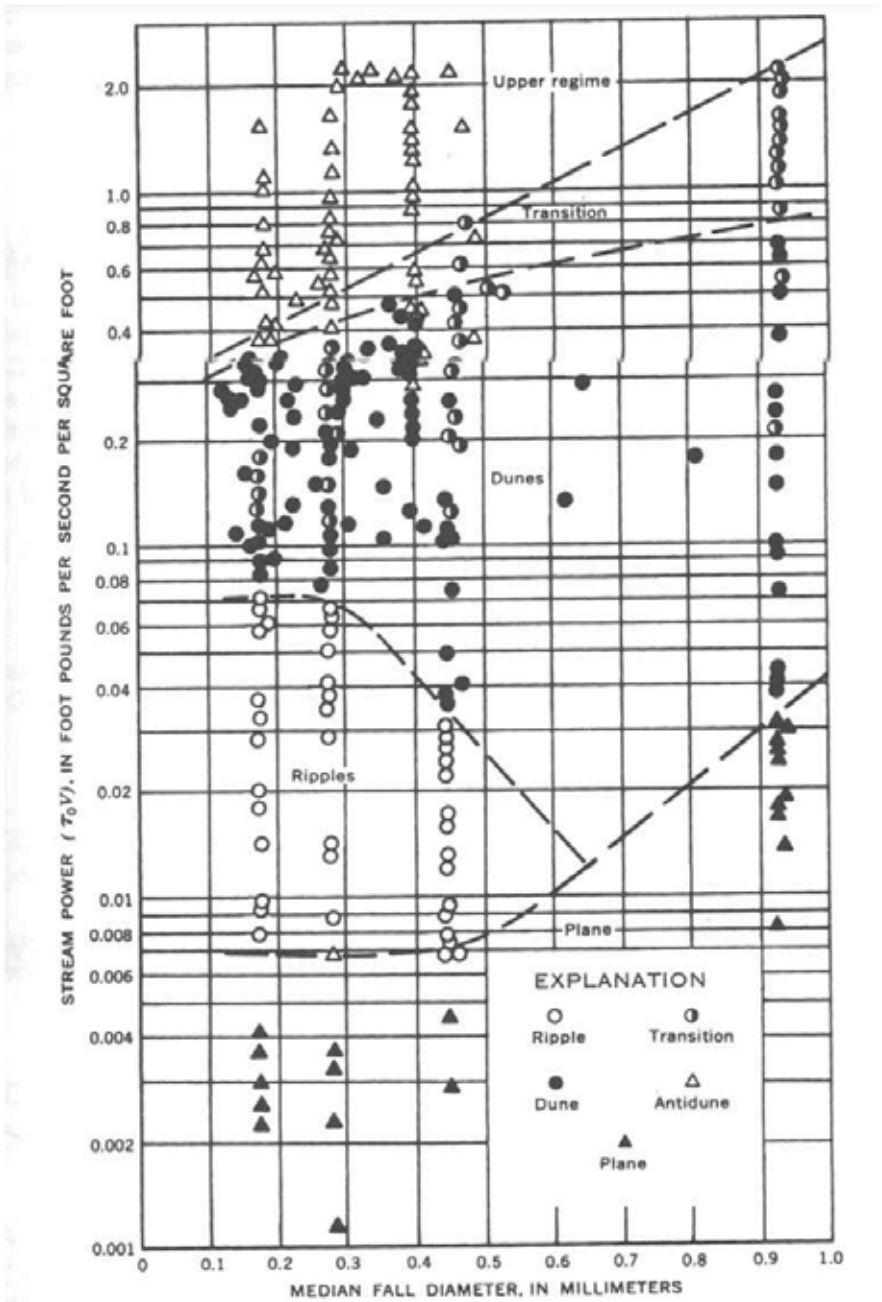

Fig. 1.10. Predictional bed form type based on stream power (Simons and Richardson, 1966)

Example 1. 1. Determine critical grain size for noncohesive sediment in a wide channel with the following characteristics:

T= 20°C ($\nu = 1\times10^{-6}\, m^2/s$)
h= 0.8 m ; V= 1.25 m/s ; n=0.03

$$\gamma_S = 2650 kg/m^3 = 25996\ \mathrm{N/m^3};\quad \gamma = 1000 kg/m^3 = 9810\ \mathrm{N/m^3}$$

Solution. Use Manning's equation and assume R_h=h, since the channel is wide, and rearrange to compute: $V = S^{1/2}h^{2/3}/n$

$$S = \frac{V^2.n^2}{h^{4/3}} = \frac{(1.25)^2(0.03)^2}{0.8^{4/3}} = 0.0019$$

Solve for bed shear stress:

$$\tau_0 = \gamma hS = 9810\times0.8\times(0.0019) = 14.9 N/m^2 \cong 1520\, gr/m^2$$

Empirical Relationships:

Use Eq. 1.34 by letting $\tau_0=\tau_c$, compute d_{50}:

$$d_{50} = \tau_c/80 = 1520/80 = 19mm$$

From the Fig. 1.5, a diameter of approximately 20 mm is obtained.

Using the known values, determine the flow regime.

$$\mathrm{Re}_* = \frac{u_* d}{\nu} = \frac{(gR_hS)^{1/2}d}{\nu} = \frac{(9.81\times0.8\times0.0019)^{1/2}\times0.02}{1\times10^{-6}} = 2442$$

The flow regime is strongly turbulent; i.e., $\mathrm{Re}_* \rangle\rangle 70$.

Yang's Method: In the turbulent range rearrange the Yang's Eq. 1.24 to obtain:

$$w = \frac{V_c}{2.05}$$

Let V=V_c ; solve for $w = 1.25/2.05 = 0.61 m/s$

Estimating that the particle diameter is greater than 2 mm, rearrange Eq. 1. 4 to solve for the particle diameter:

$$d = \left(\frac{w}{3.32}\right)^2 = \left(\frac{0.61}{3.32}\right)^2 = 0.034m = 34mm$$

It should be noted that, for particle in this grain size, viscosity effects are negligible.

Using Shields diagram and letting $\tau_0=\tau_c$, in the turbulent flow range, from Fig. 1.4, we have F_{*C}= 0.047. Rearrange Eq. 1.32 to solve for diameter:

$$d = \frac{\tau_c}{F_{*C}(\gamma_s - \gamma)} = \frac{14.9}{0.047(25966 - 9810)} = 0.019m = 19mm$$

Erodibility Index Method. Compute stream power:

$$\tau V = \gamma hSV = (9810)(0.8)(0.0019)(1.25) = 18.64 \quad W/m^2$$

Determine the critical K_h value from stream power by rearranging Eq. 1.45:

$$K_h = (\frac{\tau V}{480})^{2.27} = (\frac{18.64}{480})^{2.27} = 6.3 \times 10^{-4}$$

Determine the value of the critical grain diameter by letting $\tan\phi$=0.8 and rearranging Eg.1.46 to solve for diameter:

$$d_{50} = (\frac{K_h}{20\tan\phi})^{1/3} = (\frac{6.3 \times 10^{-4}}{20 \times 0.8})^{1/3} = 0.034m = 34mm$$

Example 1.2. Determine critical grain size for noncohesive sediment in a wide channel at 20°C ($\nu = 10^{-6} m^2/s$) with the following characteristics:

h=5 m ; V= 1.25 m/s ; n= 0.03

$$\gamma_S = 2650 \quad kg_f/m^3 \quad ; \quad \gamma = 1000 \quad \text{kg}/m^3$$

Solution. Using the Manning's equation to solve for S:

$$S = \frac{V^2.n^2}{R_h^{4/3}} = \frac{(1.25 \times 0.03)^2}{(5)^{4/3}} = 0.00016$$

Solve for bed shear stress:

$$\tau_0 = \gamma hS = (9810)(5)(0.00016) = 7.85 \quad \text{N/m}^2 = 0.8kg/m^2 = 800 \quad \text{g/m}^2$$

Solve as before using the Shields diagram:

$$d = \frac{\tau_c}{F_{*c}(\gamma_S - \gamma)} = \frac{7.85}{0.047(25996 - 9810)} = 0.01m = 10mm$$

A similar value is obtained from Fig 1.5, and using Eq. (1.32). For the erodibility index method, compute stream power:

$$\tau V = \gamma hSV = (9810)(5)(0.00016)(1.25) = 9.81 \quad \text{W/m}^2$$

$$k_h = (\frac{\tau V}{480})^{2.27} = (\frac{9.81}{480})^{2.27} = 1.46 \times 10^{-4}$$

$$d_{50} = (\frac{K_h}{20\tan\phi})^{1/3} = (\frac{1.46 \times 10^{-4}}{20 \times 0.8})^{1/3} = 0.021m = 21mm$$

The above approaches all predict a reduction in the critical grain size as flow depth increases, with average velocity remaining unchanged. However, mean velocity approaches will predict a grain size identical to that in Example 1.1 because the mean velocity remain unchanged between the two examples.

5. The sediment load

The analysis of hydraulic sediment transport is usually seperated into two sediment parts: suspended load and bed load. The total load could be obtained by summing these two loads.

It should be noted that the fine fractions flowing into the river bed from its catchment area are usually transported in suspension and are defined as wash load. The latter is a very fine organic material transported by rivers over long distances and then deposited at the river mouth as a result of energy dissipation.

Suspended load is defined as that part of sediment load which is being remained in suspension for a considerable time by upward components of turbulent flows.

Bed load is defined as part of sediment within the bed layer moved by saltation (jumping), rolling, or sliding. The bed layer is a flow layer in several grain diameters thick immediately above the bed. Its thickness is usually taken as 2 times of grain diameters. Bed load transport occurs when the flow conditions exceed the criteria for incipient motion.

This subdivision does not rest on a physical basis and, in practice, it is at times very difficult to define where the suspended load starts and bed load stops (Vanoni 1984).

In the past, numerous bed load equations have been proposed, but some of them are very similar. There are essentially four slightly different approaches to the bed load problem. They are:

i. The Du Boys-type equations

Du boys (1879) introduced the tractive force or bed shear stress which was an entirely new concept. He expressed transport rate in terms of shear stress and the critical shear stress for initiation of sediment motion.

ii. The Schoklitsch-type equations

The bed load formula of A Schoklitsch (1926) is based on discharge relationship, and represents essentially the same form as the Du Boys formula.

iii. The Einstein-type equations

Introducing probability concepts of sediment movement and statistical considerations of the lift forces, Einstein (1942-1950) developed his empirical relationship. The contributions by Einstein (1942-1950) to the problem of bed load transportation represent also somehow a departure from the Du Boys-type and Schoklitsch-type equations.

iv. The Hassanzadeh-type equations

More recently, based on the dimensional analysis and the Buckingham Π – theorem, Hassanzadeh(2007) has presented a dimensionless semiempirical equation on the bed load.This latest dimensionless bed load equation has been given as a function of the hydrodynamic-immersed gravity force ratio.

Extensive discussions on this subject has been given by Vanoni (1984), Yallin (1963, 1972) and Yang (1972, 1973). Yallin (1963, 1972) developed a bed-load equation incorporating reasoning similar to Einstein but with a number of refinements and additions. Yang (1972, 1973) approached the total transport from the energy expenditure point of view and related the transport rate to stream power. Shen and Hung(1972) derived a regression equation based on laboratory data for the sand-sized particles. Using the same concept, Ackers and White(1973) defined his sediment transport functions in terms of three dimensionless groups namely, size, mobility and transport rate of sediments. His functions are based on flume data carried out with uniform or near uniform sediments with flow depths up to 0.4 meters. One of the most extensive field and laboratory studies of sediment transport is that by Van Rijn(1984). He has presented a method which enables the computation of the bed-load transport as the product of the saltation height, the particle velocity and the bed-load concentration.

5.1 Bed load

Bedload particles roll, slide, or saltate along the bed. The sediment transport thus occurs tangential to the bed. For determiniation of bed load several empirical equations from laboratory flume data have been given by many investigators with the basic assumptions that the sediment is homogeneous and noncohesive. The results differ appreciably but it is not recommended in practice to transfer the information to outside the limits of the experiments. However, one can discern general trends of the sediment transport rate by using several formulae, with some theoretical background.

The dimensional analysis and the Buckingham Π-theorem in reasoning and discussion of bed load phenomenon has been used here.

Mathematically, the physical problem of bed load per unit width q_s in turbulent free surface flow depends upon bed shear stress τ_0 , sediment diameter d, gravity acceleration g, slope S, immersed specific weight of solid γ'_s and specific weight of fluid γ. It would be written then:

$$F(q_s, \tau_0 , d , \gamma'_s , g , \gamma , S) = 0 . \tag{1-55}$$

In the Eq.1.55, $\tau_0 = \gamma h S$ and $\gamma'_s = \gamma_s - \gamma = (\rho_s - \rho) g$

are used to replace respectively depth of flow h and specific weight of solids γ_s.

Chosen γ'_s , d and g as the repeating variables and using the Buckingham Π-theorem procedure, we obtaine the following expression:

$$\psi\left(\frac{q_s}{\sqrt{gd^3}}, \frac{\tau_0}{\gamma'_s d}, \frac{\gamma}{\gamma'_s}, S\right) = 0. \tag{1-56}$$

So, the Π-independent, dimensionless and significant terms are as follows:

$$\Pi_1 = \frac{q_s}{\sqrt{gd^3}} \quad ; \quad \Pi_2 = \frac{\tau_0}{(\gamma_s - \gamma)d} = \frac{U_*^2}{(\frac{\gamma_s}{\gamma} - 1)gd}$$

$$\Pi_3 = \frac{\gamma}{\gamma'_s} = \frac{\gamma}{(\gamma_s - \gamma)} = \frac{\rho}{\rho_s - \rho} ; \ \Pi_4 = S$$

where ρ_s and ρ represent density of solids and fluid respectively, and $u_* = \sqrt{\tau_0/\rho}$ is shear velocity. Using the Buckingham Π-theorem procedure, the bed load equation may be expressed as:

$$\frac{q_s}{\sqrt{agd^3}} = \phi\left(\frac{\tau_0}{\gamma_s - \gamma)d}\right) , \tag{1-57}$$

where $a = (\gamma_s - \gamma)/\gamma = \gamma_s'/\gamma$ shows the immersed sediment specific gravity. The hydrodynamic-immersed gravity force ratio is obtained from:

$$f = \frac{\tau_0}{(\gamma_s - \gamma)d} = \frac{U_*^2}{(\frac{\gamma_s}{\gamma} - 1)gd} . \tag{1-58}$$

Based on the properties of the Buckingham Π-theorem and neglecting the mild slope S, $q_s/\sqrt{agd^3}$ may be obtained as follows:

$$\frac{\Pi_1}{\sqrt{\Pi_3}} = \frac{q_s}{\sqrt{gd^3}} \cdot \frac{1}{\sqrt{\gamma_s'/\gamma}} = \frac{q_s}{\sqrt{agd^3}} .$$

The variation of dimensionless sediment discharge in unit width, $q_s/\sqrt{agd^3}$ with respect of $f = \tau_0/(\gamma_s - \gamma)d$ has been presented in Figure 1.11, and compared with field measured data obtained from Vanyar guaging station on Adji - chai river (with a = 1.65 , d = 2.5 – 10 mm, S = 1.1 *10^{-3} and width of B=29.9-39.35m).

The Hassanzadeh (2007) bedload equation which agrees closely with the measured data has been expressed as follows:

$$\frac{q_s}{\sqrt{agd^3}} = 24 f^{2.5} . \tag{1-59}$$

Comparison have been made between the last proposed equation (1.59) with common ones on sediment hydraulics after their unified descriptions.

For comaprison reason the common formulae on sediment hydraulics after their unified description are given in Table 1.1 and Fig.1.11.

As Figure 1.11 and Table 1.1 show, the Hassanzadeh (2007) equation (1.59) agrees well with the measured data and could be considered as an optimum one compared with the formulae given by the others (Graf, 1971, Julien, 1995 and Larras, 1972).

Example 1.3. Determine the rate of bed load transport in a rectangular cross section river with the following hydraulic characteristics:

Average flow depth h= 5.87 m
River bed slope S= 6.5 × 10^{-4}

Width B= 46.52 m
Chézy coefficient C= 56.
Median size of bed materials d_{50}= 0.012 m =12 mm

$$\gamma_S = 2650kg/m^3, \qquad \gamma = 1000\text{kg/m}^3.$$

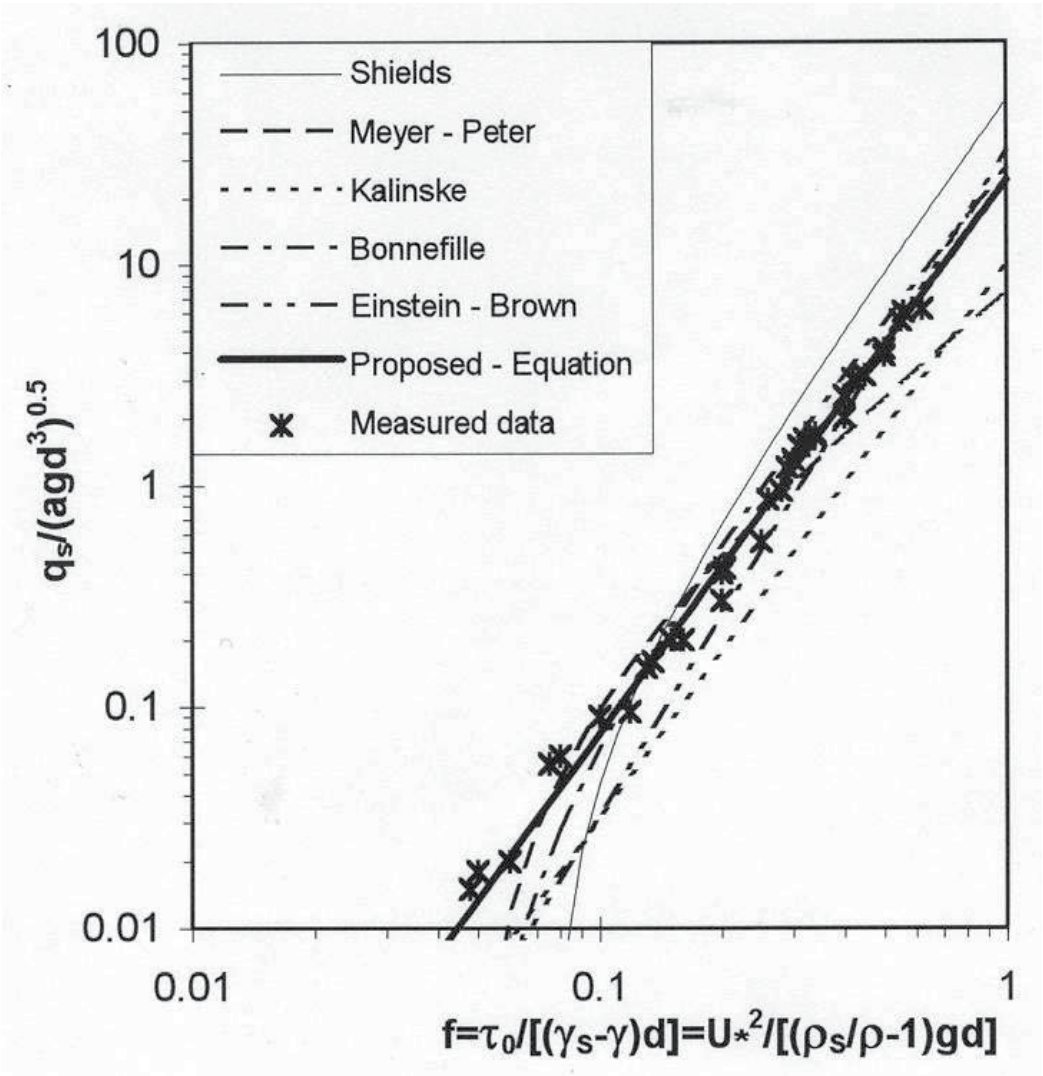

Fig. 1.11. Comparison of dimensionless bed load formulas (Hassanzadeh, 2007)

Solution: Use the Hassanzadeh-type equations. Assume R_h=h, since the river is wide. Determine the values of: f, a, $\sqrt{agd^3}$ and C_* as bellows respectively:

$$f = \frac{\tau_0}{(\gamma_S - \gamma)} = \frac{\gamma hS}{(\gamma_S - \gamma)d} = \frac{(1000)(5.87)(6.5\times10^{-4})}{(2650-1000)(0.012)} = 0.193$$

$$a = \frac{\gamma_S - \gamma}{\gamma} = \frac{2650-1000}{1000} = 1.65$$

$$\sqrt{agd^3} = \sqrt{1.65(9.81)(0.012)^3} = 5.29\times10^{-3}\, m^2/s$$

$$C_* = \frac{C}{\sqrt{g}}.\frac{\gamma}{\gamma_S} = \frac{56}{\sqrt{9.81}}.\frac{1000}{2650} = 6.75$$

Using the Hassanzadeh (2007) type of common dimensionless formulas on the hydraulics of sediment transport, the rate of bed load has been calculated and given in Table 1.1.

Author	Formula	$\frac{q_S}{\sqrt{agd^3}}$	$Q_S(kg/s) = \gamma_s B q_S$
Meyer-Peter (1934)	$\frac{q_S}{\sqrt{agd^3}} = 8(f-0.047)^{1.5}$	0.446	291.05
Shields (1936)	$\frac{q_S}{\sqrt{agd^3}} = 10C_*(f-0.076)f^{1.5}$ $C_* = \frac{C}{\sqrt{g}}.\frac{\gamma}{\gamma_S}$	0.67	436.68
Einstein-Brown (1942)	$\frac{q_S}{\sqrt{agd^3}} = 23.6f^3$	0.17	110.64
Kalinske (1947)	$\frac{q_S}{\sqrt{agd^3}} = 10f^{2.5}$	0.164	106.72
Bonnefille (1963)	$\frac{q_S}{\sqrt{agd^3}} = 5.5f^{1.5}(4.26f^{0.5}-1)^{1.25}$	0.393	256.08
Hassanzadeh (2007)	$\frac{q_S}{\sqrt{agd^3}} = 24f^{2.5}$	0.393	256.12

Table 1.1. Dimensionless existing formulas to estimate bed load (Hassanzadeh, 2007)

5.2 Suspended load

The mechanics of the process of suspension of particles more dense than liquid is still inadequately explained. Engineers and scientists had long been interested in the phenomenon of sediment suspension in water flows. The theoretical equation for the vertical distribution of suspended sediment in turbulent flow has been given by H. Rouse. Vertical distribution of sediment concentration under condition of steady state uniform flow, the tendency for sediment to settle under the influence of gravity, is offset by the vertical component of turbulence in the water column, a process called as turbulent diffusion. The upward-moving water comes from the deeper zone with higher concentration, partially of setting the settling of the sediment and creating a vertical concentration gradient which can be described using the Rouse (1937) equation:

$$\frac{C}{C_a} = \left(\frac{h-y}{y} \times \frac{a}{h-a}\right)^Z , \tag{1-60}$$

$$Z = \frac{w}{ku_*} \qquad \text{or} \qquad Z = \frac{\mathrm{w}}{\beta \mathrm{ku}_*} \tag{1-61}$$

Where C and C_a= concentration of sediment having fall velocity w at vertical distances y and a above the bed and h=total depth, k=0.4 is von Karman's constant. β is of the order of unity for fine sediment and appears to decrease with increasing particle size. If β=1 and K=0.4 the ratio $w/u_* = 1$ corresponds to Z=0.4. Eq.1.60 represents the state of equilibrium between the upward rate of sediment motion due to turbulent diffusion and the downward volumetric rate of sediment transfer per unit area due to gravity. This equation can be used to determine the concentration C at any height y above the bottom relative to the known concentration Ca at height a above the bed. The value of Z will decrease as fall velocity w decreases; producing a vertical distribution will exist for each size class. Vertical concentration distributions for several values of Z are illustrated in Fig 1.12, assigning a concentration distribution C_a=1 at height a=0.05 h. For given shear stress, Z is proportional to w, which means that fine-grained material has small values of Z and the particles are fairly uniformly distributed throughout the depth, whereas coarse grains will be near the bed.

Equation (1.60) has been found that to give a better fit to the observed distribution β must be taken to 0.6 (Hassanzadeh, 1985 and 1979).

To formulate river sediments, data from Vanyar guaging station on Adji-chai river, near Tabriz city, were collected for 8 years. All the suspended sediment data were collected by the surface water departement of Tabriz water organization. The collected data consist of the instantaneous water discharges and the corresponding sediment load.

Through the use of the instantaneous values of suspended sediment load, Q_s , and water discharge, Q, regression equations for dry and wet seasons were developed. Fig.1.13 represents the average monthly water discharge Q_m (m^3/s), and suspended load, Q_{sm} (tons/day) with respect of time in months from October 1.

The inspection of this figure shows that reasonable correlations do exist between the average monthly water discharge Q_m and suspended load Q_{sm} for a period of 8 years, from october

1974 through september 1982 water years. It is obvious from this figure that at some time during the year a good correlation between the average monthly water discharge Q_m and the sediment load Q_{sm} exists . However, for 6 months, the sediment load was quite low even though the water discharge remained fairly high. Thus an exact correlation between water discharge and sediment load did not exist throughout the whole water year. It should be stated that, in Fig.1.13 the values of monthly and annual water discharge Q_m (m^3/s) and the corresponding suspended sediment load Q_{sm} (tons/day) are related respectively to the left and right axis.

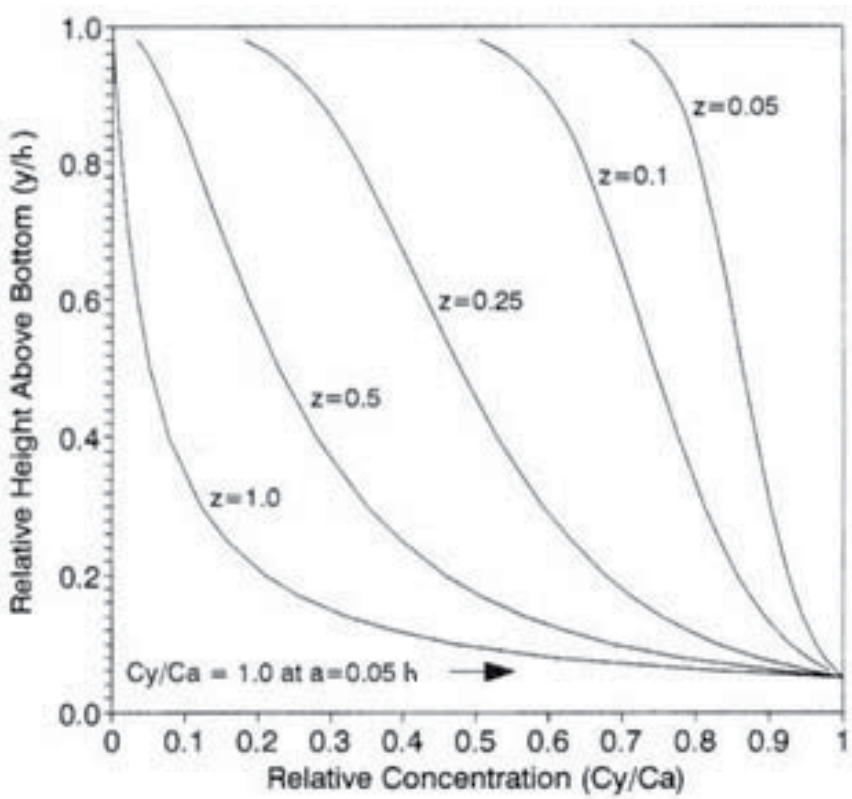

Fig. 1.12. Distribution of suspended sediment in a flow according to Eq.1.60

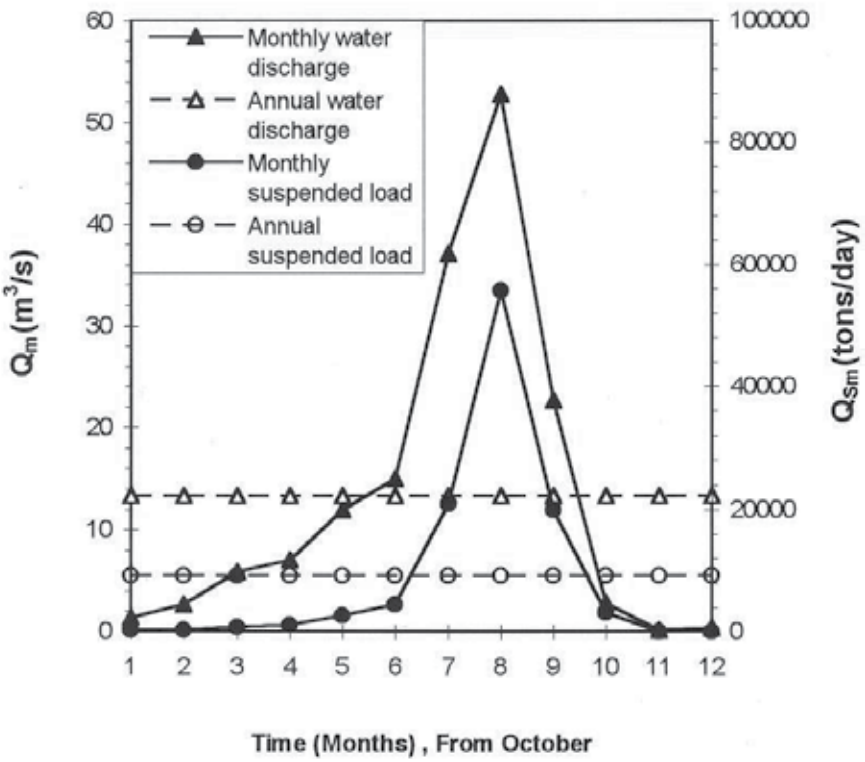

Fig. 1.13. Relationship between Q_{sm} and Q_m with time in months for a period of 1974-1982 (Hasaanzadeh, 2007)

Fig.1.14 shows the relationship between the percentage of the cumulated annual suspended load moving past the Vanyar guaging station in a given number of days for the four water years. An examination of Fig.1.14 will reveal that the bulk of the sediment load has been moved during storm events. Since the number of storm events in a water year is small and the duration of the storm events are generally short, the bulk of the suspended load passes through station during the relatively small number of days in a water year.

Fig.1.15 shows the variation of daily suspended load Q_s (tons/day) with the corresponding water discharge Q (m^3/s) for the dry and wet seasons of the 1974-1982 water years, for the Vanyar guaging station on the Adji-chai river. Throught the use of these instantaneous values of suspended load, Q_s , and water discharge, Q, regression equations for the wet and dry seasons were developed.

The resulted equations are as follows:

For wet seasons ($Q>15 m^3/s$):

$$Q_s \text{ (tons/day)} = 16.67Q^{1.91} \quad (1\text{-}62)$$

For dry seasons ($Q\leq 15 m^3/s$):

$$Q_s \text{ (tons/day)} = 47.48Q^{1.42} \quad (1\text{-}63)$$

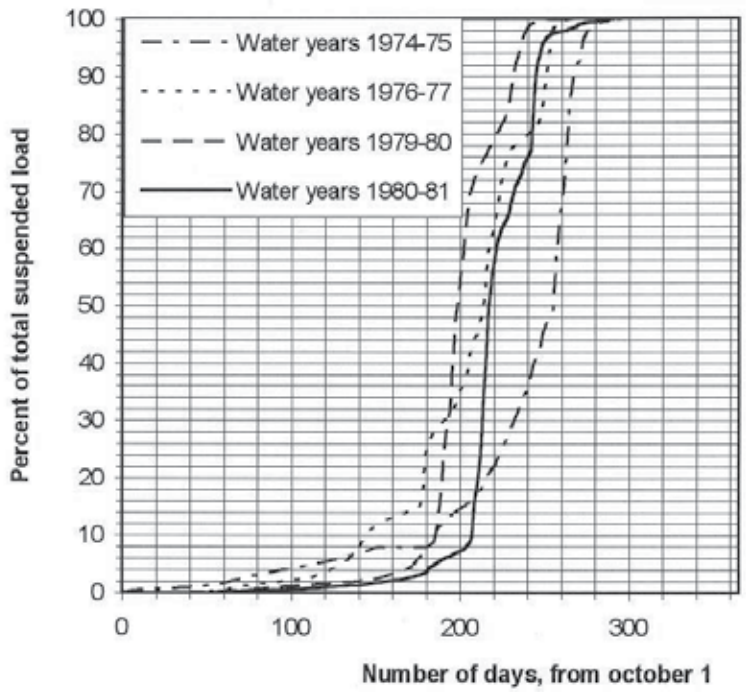

Fig. 1.14. Annual suspended load carried in a given number of days (Hasaanzadeh, 2007)

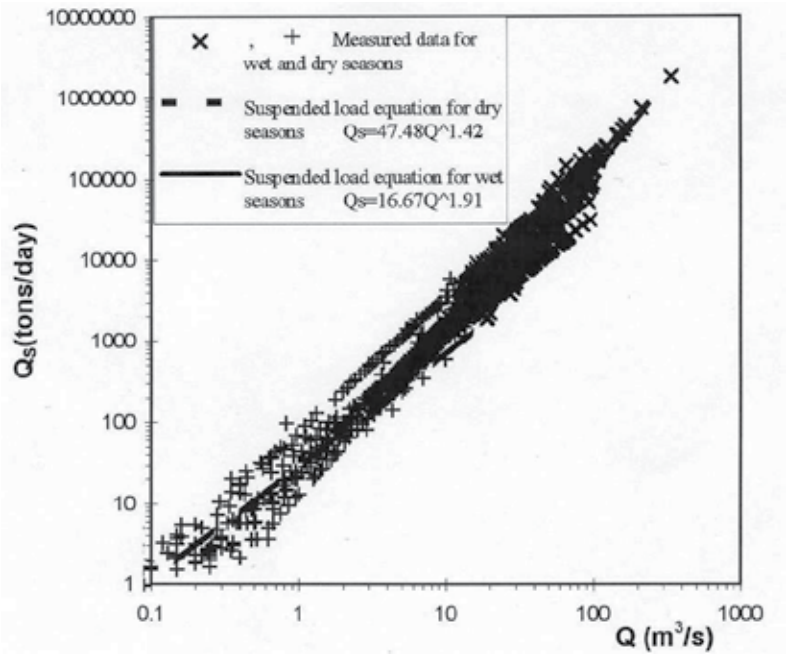

Fig. 1.15. Variation of suspended load Q_s with respect to water discharge Q (Hasaanzadeh, 2007)

6. Nomenclatuers

a	reference level; radius of particle; particle effective area; one of the triaxial dimensions of a particle; immersed sediment specific gravity
A	wetted cross-section area
A′	sediment coefficient
b	one of the triaxial dimensions of a particle
B	water surface top width
c	one of the triaxial dimensions of a particle
C	concentration of sediment at vertical distance y, Chézy coefficient
C_a	concentration of sediment at vertical distance a
C_D	drag coefficient
C_L	lift coefficient
C_*	Chézy coefficient en dimensionless form
d	particle diameter
d_*	dimensionless diameter
F	force
F_D	drag force
F_L	lift force
F_n	normal force to the angle of repose
F_t	parallel force to the angle of repose
F_r	Froude number
F_*	Shields parameter
f	hydrodynamic-immersed gravity force ratio
g	gravitational acceleration
h	water depth
h_v	vegetation height
k	constant, von Karmman's constant
K_1, K_2, K_3	particle shape factor
K	Strickler coefficient, tractive- force ratio
K_h	erodibility index
n	Manning coefficient
P	length of wetted perimeter, pressure
Q	water discharge
q_s	rate of bedload in volume per unit time and unit width
Q_s	rate of bedload in weight per unit time, daily suspended load
Q_m	average monthly water discharge
Q_{sm}	average monthly suspended load
r	radius
Re	Reynolds number
Re_*	boundary Reynolds number
Re_c	critical Reynolds number
R_h	hydraulic radius
S	bed slope
S.F.	shape factor
S_f	energy gradient
t	time

T	temperature
$\tan\phi$	coefficient of friction
u	velocity in x-direction
u_*	shear velocity
u_b	liquid velocity at the bottom of the channel
V	mean velocity over depth
V_c	liquid critical velocity
V_s	velocity of solids
w	fall or settling velocity
W	grain weight
x	coordinate direction
y	coordinate direction
z	coordinate direction
Z	exponent in the suspension distribution
α	angle of the inclination of the bed form from the horizontal
β	constant
γ	liquid specific weight
γ_s	solid particle specific weight
γ_s'	solid particle submerged specific weight
δ	specific gravity
θ	angle of the side slpe
λ	friction factor
μ	liquid dynamic viscosity
μ_{susp}	dynamic viscosity of the suspension or mixture
ν	liquid kinematic viscosity
ν_m	kinematic viscosity of the suspension or mixture
π	dimensionless group
ρ	liquid mass density
ρ_s	solid particle mass density
τ	unit shear stress or tractive force
τ_c	critical unit shear stress
τ_0	unit shear stress at a solid boundary
τ_L	unit shear stress on the level surface
τ_s	unit shear stress on the side of the channel
τV	unit steam power
ϕ	angle of repose of the materials

7. Subscripts

none	liquid phase
b	at bed or at bottom
c	critical condition, center line
L	level surface

susp	suspension, mixture
m	mixture, suspension, average monthly
max	maximum value
v	vegetation
s	solid phase, side of channel, suspension
sm	average monthly suspended load
y	at a distance y
0	at boundary (y=0)
*	shear value
1,2,..	index
∞	at infinity

8. References

Ackers, P., and White, W.R. 1973."Sediment Transport: New Approach and Analysis", Journal of the Hydraulics Division, ASCE, No. HY11.

Annandale, G.W, 1996. "Prediction of Sediment Distribution in a Dry Reservoir: A Stochastic Modeling Approach", PP.I.85-I.92, proc. 6th Federal Interagency sedimentation Conf. Las Vegas.

Annandale, G.W., 1995. "Erodibility", Journal of Hydraulic Research, IAHR, 33(5): 471-494.

Arcement, G.J.J, and Schneider, V.R., 1989. "Guide for Selecting Mannings Roughness Coefficients for Natural Channels and Flood Plains", USGS Water Supply Paper 2339, Washington, D.C.

Barnes, H.H, 1467. "Roughness Characteristics of Natural Channels", USGS water- supply paper 1849, Washington, D.C.

Carstens, M.R., 1966. "A Theory of Heterogeneous Flow of Solid in Pipes", Proc. Am. Soc. Civil Engrs., Vol. 95, no.Hy1.

Chow, V. T., 1959. "Open Channel Hydraulics", McGraw-Hill Book Company.

Cowan, W.L., 1956. "Estimating Hydraulic Roughness Coefficient", Agricultural Engineering, 37 (7): 473-475.

Einstein, H.A., and Chien, N. 1955. "Effects of Heavy Sediment Concentration near the Bed on Velocity and Sediment Distribution", M.R.D. sediment series No. 8, University of California, Institute of Engineering Research and United States Army Engineering Division, Missouri River, Corps of Engineers, Omaha, Neb.

Fortier.S, and Scobey, F.C, 1426. "Permissible canal velocities", Transactions, A.S.C.E, Vol. 89,PP.940-956.

Goldstein, S., 1929. "The Steady Flow of Viscous Fluid Past a Fixed Spherical Obstacle at 3-Small Reynolds Numbers", Proc. Roy. Soc., London, Vol. 123A.

Graf, W. H. and Altinakar, M. S., 1998. "Fluvial Hydraulics" John Wiley, U.K .

Graf, W.H., 1971. "Hydraulics of Sediment Transport" Mc Graw-Hill Book Company.

Hassanzadeh, Y., 1979. "Distribution des vitesses et des concentrations dans un écoulement diphasique liquide/solide à surface libre", La Houille Blanche, No.1, Paris.

Hassanzadeh, Y., 1985. "Hydrodynamics of Two-phase Flows" Fifteenth Congress on Large Dams, ICOLD, Lausanne, Suisse

Hassanzadeh, Y., 2007. "Evaluation of Sediment Load in a Natural River" Journal of Water International, Vol.32, No.1, Pg.145-154.

Ippen, A.T, and Drinker, P, A, 1962. "Boundary Shear Stress in Curved Trapezoidal Channels", j. Hydraulics Div. ASCE, 88 (Hy5): 143-180.

Julien, P.Y., 1995. "Erosion and Sedimentation", Combridge university press, combridge, U.K.

Lane, E.W, 1935. "Progress Report on Studies on the Design of Stable Channels of the Bureau of Reclamation", proc. A.S.C.E.79. sep.no.280.

Lane, E.W., 1955. "Design of Stable Channels", trans. ASCE, 120: 1234-1279.

Larras, J., 1972. "Hydraulique et Granulats" Eyrolles, France

Leliavsky,S., 1955. "An Introduction to Fluvial Hydraulics", constable.

McNown, J. S., 1951. "Particles in slow motion", La Houille Blanche, 6, no. 5. Leipzig.

Mei, C.C., and Liu, K., and Ng. C., 1994. "Two Models for Roll waves in a Mud Layer", Proceeding of the ICHD, 94, Wuxi, China..

Morris, G. L. and Fan J., 1998. "Reservoir Sedimentation Handbook", McGraw-Hill, New York.

Muller, R., 1943. "Theoretische Grundlagen der Fluss- und Wildbachverbauungen", Mitteil. VAWE, Eidgen. Tochn. Hochschule, Zurich, no.4.

Neil,C.R., 1467. "Mean velocity criterion for scour of coarse uniform bed material", Int. Assoc. Hydr. Res., 12th Congress, Fort Collins 3,46-54.

Olson, R., 1961. "Essential of Engeneering fluid Mechanics", chap. 11, International Textbook, Scranton.Pa.

Raudkivi, A. J., 1976. "Loose Boundary Hydraulics", pergamon press Ltd., Oxford.

Schiller, L. and Naumann, A., 1933. "Ueber die grund legenden Berechnugen beider schwerkraftaufbereituv", Z. d. V. D. I. 77

Shen, H.W. and Hung, C.S., 1971. "An Engineering Approach to Total Bed Material Load by Regression Analysis", Proc. Sedimentation Symposium, Berkeley.

Van Rijn,L.C., 1984."Sediment Transport, Part I: Bed Load Transport", Journal of Hydraulic Engineering, Vol. 110, No.10,ASCE.

Vanoni, V.A., 1984."Fifty Years of Sedimentation" Journal of Hydraulic Engineering, Vol. 110, No. 8 ASCE.

Vanoni,V.A.,1946."Transportation of Suspended Sediment by Water", Trans. A.S.C.E.,Vol.III.

Yalin,M.S., 1963."An Expression for Bed Load Transportation", ASCE 89, HY3.

Yalin,M.S., 1972. "Mechanics of Sediment Transport",Pergamon Press.

Yang,C.T., 1972."Unit Stream Power and Sediment Transport", Proc.ASCE,98, HY10, 1805-26.

Yang,C.T., 1973."Incipient Motion and Sediment Transport", Proc.ASCE99,HY10,1679-1704.

Yang,C.T, 1996. "Sediment Transport: Theory and Practice", MC Graw- Hill, New york.

3

Study on the Interaction Between Tsunami Bore and Cylindrical Structure with Weir

I. Wijatmiko and K. Murakami
University of Miyazaki
Japan

1. Introduction

The destructive power of tsunami creates catastrophic damages in large area. In order to reduce these damages, there is a need to understand the interactions between tsunami wave and structures as the basic knowledge before applying any countermeasure strategies.

Tsunami amplifies its height in shallow water area, and it may transfer into bore when it breaks and generates enormous forces (Yeh, 1991). The impact of tsunami bore to the vertical structures with two-dimensional cross section has been investigated through experiments and numerical simulations (Fukui et al., 1962; Palermo & Nistor, 2008). Those previous studies provide many useful information for the construction of coastal structures. However, the interaction between tsunami bore and structures with three-dimensional cross section have not been understood well, because tsunami flow around such structures becomes quite complex. Structures with three-dimensional section, such as a storage tank and tsunami evacuation building, can be seen as important infrastructures on many coastal areas. Especially, the recent tsunami Japan 2011 had brought serious damages on structures such as oil storages (International Energy Agency, 2011). Meanwhile, those structures are regulated by a building code to be protected by weir to restrain the spread of spilled contents (Dangerous Goods Safety Management [DGSM], 2003). This protective weir may produce quite complex flow around the structures, but the effects of the flow on the structures with weir have not been investigated well.

In the investigation of interactions between tsunami wave and cylindrical structure, a numerical simulation is very powerful tools to obtain much detail quantities such us pressures, velocities and free surface elevations, at any points with higher resolution in time and space. Recently, many numerical simulation techniques have been developed in order to simulate wave motions around three-dimensional structures (Arikawa & Yamano, 2008; Goto et al., 2009; Tomita et al., 2006; Kawasaki et al., 2006). Among those numerical models, the method based on Navier-Stokes equation and Volume of Fluid (VOF; CADMAS-SURF 3D) tends to be used as one of the common numerical technique to simulate three-dimensional interactions between wave and structures (Arikawa & Yamano, 2008).

This study investigates the validity of three dimensional numerical simulation model based on Navier-Stokes equation and VOF method to estimate hydraulic quantities around the structure. Furthermore, this study discusses the characteristics of interaction between bore type tsunami and the cylindrical structure with weir with using above numerical model.

2. Background

2.1 Previous study

An extensive summary on the bore type tsunami propagation is given by Yeh (1991). Here the focus is on the bore type tsunami behaviours and its transition process along the shore. This process is caused by the 'momentum exchange' between the bore and the small wedge-shaped water body. It has been studied that the changes of velocities and the convergence of fluid tend to accumulate turbulence on the front face of the bore when the bore reach the shoreline. In addition, the no-water condition in front of bore cause wave flow to rely on its velocity for the run-up motion, and it causes stronger turbulence on the transition process. The generated turbulence and its accumulation, together with rapidly accelerated mean flow motion, are said to be the cause of destructive tsunami energy on the dry beach surface. Mizutani & Imamura (2001) investigated the destructive tsunami pressure on the breakwaters by using the highly accurate sensor system. They categorized the type of maximum pressure such as: dynamic pressure, sustain pressure, impact standing pressure and overflowing wave pressure. The dynamic pressure occurs when an incident wave hits structures at the first attempt. After this pressure, the sustain pressure is observed due to the succeeding tsunami flow. In addition, the impact standing pressure may occur when the reflected tsunami wave coincide with incoming wave. While the overflowing wave pressure occurs when wave collide on the back of the structure. Another investigation of tsunami risk to structures had been done by Palermo & Nistor (2008). The tsunami-induced loading and its impact on the shoreline structure according to Canadian context were mainly discussed. Several physical experiments had been done for the purpose of understanding Tsunami forces acting on the structure. Several structural shapes, such as square, rectangular, diamond-shape and cylindrical shape, and also debris impact testing were discussed in this study. Through various cases of experiments, the result indicated that through various impoundment heights, the force caused by surge wave does not significantly exceed the drag force. Further, the existence of debris can generate the 'bounce back' effect on the structure, even though the magnitude of this force was smaller than the initial debris impact. This study emphasized the consideration of tsunami-induced loading for the structures.

Haritos, Ngo & Mendis in 2005 gave the brief review on the estimation of tsunami wave force on wall structures by many coastal engineers. Japanese researchers purposed estimations of wave pressure on the building face in the case of 'unbroken' and 'break-up' tsunami conditions (Okada et al., 2004). In the case of 'unbroken' tsunami condition, the hydrostatic distribution reaches up to 3 times of wave height with maximum pressures located at the bottom section of building. Meanwhile, this estimation is superimposed by 2.4 ρgh, where ρ is water density; g is gravity and h is wave height at 0.8 of maximum wave height above the ground for the case of 'break-up' tsunami. Meanwhile The U.S. Army Corps gave an assumption that the interaction between surge wave and structure consist of hydrostatic action and hydrodynamic one. In addition, the dynamic action is calculated based on the bore gradient on its face (U.S. Army Corps, 1990, as cited in Haritos, N., et al., 2005).

An extensive description of tsunami load acting on shoreline structure was provided by Yeh, H. (2007). Tsunami load was analysed with considering: 1) hydrostatic force, 2) buoyant force, 3) hydrodynamic force, 4) surge force, 5) debris impact force, and 6) wave breaking force. Among these forces, hydrodynamic force and surge force give significant contribution to the maximum force acting on structures. Further, the Federal Emergency Management Agency's Coastal Construction Manual in 2008 mentions the additional estimation beside those forces, such as uplift force and gravity loads in case of building with elevated floors.

2.2 Theoretical considerations

2.2.1 Hydrodynamic model

The evolution of tsunami wave with time can be expressed by a system of nonlinear partial differential equations. However, these equations are very difficult to solve analytically. Therefore, a numerical method that discretizes a computational domain into grids is sometimes used to obtain tsunami wave field. There are several numerical methods to solve fluid dynamic problems, e.g. the finite difference method (fdm), the finite element method (fem) and the finite volume method (fvm). The finite difference method, which discretizes a computational domain into square cells with fix width (Δx), length (Δy) and height (Δz) in a three dimensional problem, is widely used to solve many hydraulic problems. However, the square grid sometimes loses the resolution of boundary shapes, which can be seen on the structure with complex cross sections. On the other hand, the finite element method allows various grid sizes, and it can be applied to the structure with complex shape.

With the increase of computer capacity, some direct numerical simulation techniques have being developed recently in coastal engineering field to investigate the interaction problems between waves and structures. The basic equations in this direct numerical simulation are the continuity equation and momentum equations witch is called Navier-Stokes equation. This study employs a system of above equations, those are discretizes with the finite difference method to simulate tsunami flow around three-dimensional structure on arbitrary topography.

2.2.2 Governing equations

The governing equations used in this study are the continuity equations expressed in Eq.(1) and momentum ones from Eq.(2) to Eq.(4). The system of these equations is purposed by Sakakiyama & Kajima (1992), where the area porosities γ_x , γ_y , γ_z in x, y and z projections are introduced respectively in order to investigate the interactions between waves and porous structures.

$$\frac{\partial \gamma_x u}{\partial x} + \frac{\partial \gamma_y v}{\partial y} + \frac{\partial \gamma_z w}{\partial z} = \gamma_v S_\rho \tag{1}$$

$$\begin{aligned} \lambda_v \frac{\partial u}{\partial t} + \frac{\partial \lambda_x uu}{\partial x} + \frac{\partial \lambda_y vu}{\partial y} + \frac{\partial \lambda_z wu}{\partial z} = &-\frac{\gamma_v}{\rho}\frac{\partial p}{\partial x} + \frac{\partial}{\partial x}\left\{\gamma_x v_e \left(2\frac{\partial u}{\partial x}\right)\right\} + \frac{\partial}{\partial y}\left\{\gamma_y v_e \left(\frac{\partial u}{\partial y} + \frac{\partial v}{\partial x}\right)\right\} \\ &+ \frac{\partial}{\partial z}\left\{\gamma_z v_e \left(\frac{\partial u}{\partial z} + \frac{\partial w}{\partial x}\right)\right\} - \gamma_v D_x u - R_x + \gamma_v S_u \end{aligned} \tag{2}$$

$$\lambda_v \frac{\partial v}{\partial t} + \frac{\partial \lambda_x uv}{\partial x} + \frac{\partial \lambda_y vv}{\partial y} + \frac{\partial \lambda_z wv}{\partial z} = -\frac{\gamma_v}{\rho}\frac{\partial p}{\partial y} + \frac{\partial}{\partial x}\left\{\gamma_x v_e\left(\frac{\partial v}{\partial x} + \frac{\partial u}{\partial y}\right)\right\} + \frac{\partial}{\partial y}\left\{\gamma_y v_e\left(2\frac{\partial v}{\partial y}\right)\right\} + \frac{\partial}{\partial z}\left\{\gamma_z v_e\left(\frac{\partial v}{\partial z} + \frac{\partial w}{\partial y}\right)\right\} - \gamma_v D_y v - R_y + \gamma_v S_v \quad (3)$$

$$\lambda_v \frac{\partial w}{\partial t} + \frac{\partial \lambda_x uw}{\partial x} + \frac{\partial \lambda_y vw}{\partial y} + \frac{\partial \lambda_z ww}{\partial z} = -\frac{\gamma_v}{\rho}\frac{\partial p}{\partial y} + \frac{\partial}{\partial x}\left\{\gamma_x v_e\left(\frac{\partial w}{\partial x} + \frac{\partial u}{\partial z}\right)\right\} + \frac{\partial}{\partial y}\left\{\gamma_y v_e\left(\frac{\partial w}{\partial y} + \frac{\partial v}{\partial z}\right)\right\} + \frac{\partial}{\partial z}\left\{\gamma_z v_e\left(2\frac{\partial w}{\partial z}\right)\right\} - \gamma_v D_z w - R_z + \gamma_v S_w - \frac{\gamma_v \rho^* g}{\rho} \quad (4)$$

where t is the time, x and y the horizontal coordinates, z the vertical coordinate, u,v,w the velocity components in the direction of x, y and z respectively. ρ means the density of the fluid, ρ^* the relative density of the fluid, p the pressure. v_e means the kinematic viscosity (summation of molecular kinematic viscosity and eddy kinematic viscosity), g the gravity, λ_v is defined from γ_v using following relationships:

$$\lambda_v = \gamma_v + (1 - \gamma_v) C_M \quad (5)$$

where C_M is the inertia coefficient. While the resistance force Rx, Ry and Rz are described in Eq. (6), Eq. (7) and Eq. (8).

$$R_x = \frac{1}{2}\frac{C_D}{\Delta x}(1 - \gamma_x)\, u \sqrt{u^2 + v^2 + w^2} \quad (6)$$

$$R_y = \frac{1}{2}\frac{C_D}{\Delta y}(1 - \gamma_y)\, v \sqrt{u^2 + v^2 + w^2} \quad (7)$$

$$R_z = \frac{1}{2}\frac{C_D}{\Delta z}(1 - \gamma_z)\, w \sqrt{u^2 + v^2 + w^2} \quad (8)$$

where C_D is the drag coefficient; Δx, Δy are the horizontal mesh sizes and Δz is the vertical mesh sizes in porous media.

2.2.3 Boundary condition and discretization of numerical domain

Volume of Fluid (VOF) method, which was introduced by Hirt & Nichols in 1981, is used in this study to distinguish the air and water zone. A function, F, is introduced in the VOF method to define the fluid region. This function indicate the fractional volume of water which occupies each cell in the computational domain. Youngs (1982) described the algorithm to track the interface between air and water zone. In the first step, the interface is approximated by a linear line in each cell. After that, the interface is detected by solving a advection equation, which relates to the function, F, in order to get the evolution of fractional function in time series. The three-dimensional advection equation for fractional function is described in Eq. (9).

$$\gamma_v \frac{\partial F}{\partial t} + \frac{\partial \gamma_x uF}{\partial x} + \frac{\partial \gamma_y vF}{\partial y} + \frac{\partial \gamma_z wF}{\partial z} = \gamma_v S_F \quad (9)$$

This study generates the bore type tsunami in developed numerical flume. The fluid motion start from a still water condition. The initial pressure is given by hydrostatic pressure, where the water density is 998.2 kg/m^3 and air density is 1.2 kg/m^3. In this study, slip condition is applied in the interface between fluid and solid boundary.

In order to propagate bore type tsunami, time history of wave surface elevation and fluid velocity are set as the initial flow parameters in the ghost cells which is set at outside of the most upstream cells. These values will be calculated by using the governing equation for the rest of the domain.

Fukui, et.al had investigate the relations between fluid mean velocity and water surface displacement under the propagation of bore type tsunami. Through analytical investigation and a series of hydraulic experiments, they derived the following equation.

$$U = \frac{C\zeta}{H} = \zeta\sqrt{\frac{gH(H+h)}{2H(H+\eta\zeta)}} \tag{10}$$

where U is the mean velocity, g the acceleration of gravity, H=h+ζ the total depth from the datum (Refer to Fig.1), ζ the temporal bore height. η is the velocity coefficients, which equal to 1.03, and it was taken from the ratio of water level and wave height.

In this study, the water surface profile of bore type tsunami on the most upstream boundary is assumed at first, and the velocity profile on the same boundary is obtained from Eq.(10).

Finite difference method with staggered grid mesh is applied to discretize the governing equations. The velocity components are defined on the each boundary of the cell, while scalar quantities, such as pressure and F-function, are defined at the center of the cell. Finite control volume is applied to satisfy the conservation equation for momentum equation. Both central difference technique and upwind scheme are used to discretize the spatial derivative, while F-function is discretize by using forward difference method. The simplified marker and cell (SMAC) method is used to estimate the time evolution solution for continuity and momentum equations.

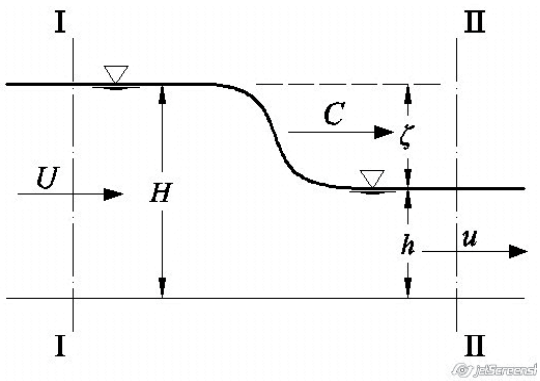

Fig. 1. Bore profile illustration

3. Hydraulic experiments for the verification of numerical simulation

In order to investigate the validity of numerical simulation, some numerical results are compared with experimental ones. This study examined the validity of numerical simulation on two series of experiment, one was conducted on the composite slope and the other was on the flat one. The former experiment was conducted for the purpose of investigating the validity of tsunami propagation on a complex sea bottom. On the other hand, the latter experiment was conducted to check the validity of tsunami pressures acting on the cylindrical structure. This chapter shows the configurations of above to weirs of experiment.

3.1 Composite slope

The experiment of composite slope topography had been conducted by Sakakiyama et al., (2009). This experiment is referred in order to investigating the validity of tsunami propagation generated with using Eq. (1) on a complex sea bottom.

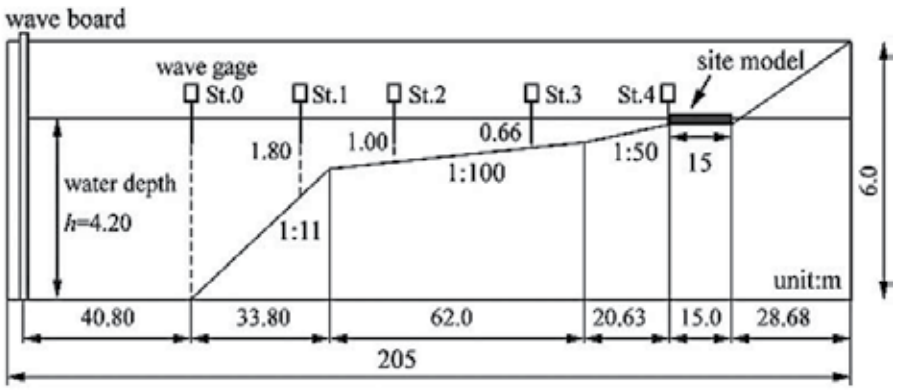

Fig. 2. Composite slope experimental setup

Two-dimensional wave flume with 205.0m in length, 6.0m in height and 3.4m in width was used in this experiment. The sea bottom consisted of several slope as shown in Fig.2. A dike with 15.0 m in length and 0.2 m in height was installed on the downstream area. The tsunami waves were generated by the wave board, which was a piston type generator, on the left hand side. In order to record the wave surface profile, wave gauges were placed at both the propagation area, i.e. η_2=-89.665m; η_3=-67.225m; η_4=-33.025m; η_5=-1.5m; η_6=-0.225m and η_7=-0.01m and in the inundation area, i.e. η_8=+0.29m and η_9=+0.532m (all locations are measured in the x-axis direction from the dike corner).

3.2 Flat bottom slop

Experiments were conducted on open channel flume with 12.0m in length, 0.4m in width and 0.4m in depth as shown in Fig. 3. Various bore heights were generated by instantaneously lifting up the division plate, which separates the downstream quiescent water from the upstream deeper water. Upstream water level (h_1) was change from 0.15m to 0.3m while the downstream water depth (h_2) was kept at 0.045m.

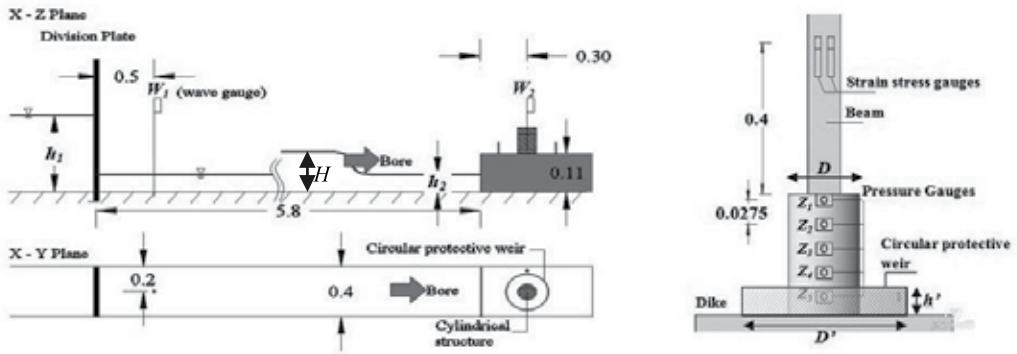

Fig. 3. Flat bottom experimental setup

At the downstream area, a dike with 0.11m height was installed 5.8m from the division plate. Cylindrical structure, which is assumed as an oil storage tank, with difference diameter (D), i.e. 0.04m, 0.08m and 0.11m, was set 0.3m from the dike's tip.

A weir, that represents the oil protective barrier, was installed around cylindrical structure to investigate its existence effects. Building code of oil weir require certain level of weir height and weir diameter to restrain any leak from the storage material. In addition, the weir volume must be more than 1.1 times of storage volume. Regarding those conditions, this study set various diameters (D') and heights (h') as described at Table 1.

						Cylindrical structures								
						Diameter (m)								
						D=0.04			D=0.08			D=0.11		
						Wave Tank Height (m)			Wave Tank Height (m)			Wave Tank Height (m)		
						h_1=0.2	h_1=0.25	h_1=0.3	h_1=0.2	h_1=0.25	h_1=0.3	h_1=0.2	h_1=0.25	h_1=0.3
Weirs	Diameter (m)	D'=0.26	Height (m)	h'=0.02	Type A_1	O	O	O	O	O	O	X	X	X
				h'=0.04	Type A_2	O	O	O	O	O	O	O	O	O
				h'=0.06	Type A_3	O	O	O	O	O	O	O	O	O
		D'=0.22	Height (m)	h'=0.02	Type B_1	O	O	O	O	O	O	X	X	X
				h'=0.04	Type B_2	O	O	O	O	O	O	O	O	O
				h'=0.06	Type B_3	O	O	O	O	O	O	O	O	O
		D'=0.16	Height (m)	h'=0.02	Type C_1	O	O	O	X	X	X	X	X	X
				h'=0.04	Type C_2	O	O	O	O	O	O	X	X	X
				h'=0.06	Type C_3	O	O	O	O	O	O	X	X	X

note: O = conducted experiment

Table 1. Experiment cases

Several measurement gauges were places on specific location for verification purposes. Three wave gauges (W_1, W_2 and W_3) and one velocity meter (V_1) were placed on the propagation area, while one wave gauges (W_4) and one velocity meter (V_2) were placed on the inundation area. As seen in Fig.5, five pressure gauges (Z_1, Z_2, Z_3, Z_4 and Z_5) were attached on the front face of cylindrical structure with 0.0275m distances between two gauges to collect direct pressure data. While four strain-stress gauges were installed on the beam to obtain horizontal forces.

4. Results and discussions

4.1 Verification of simulation

4.1.1 Experimental with composite slope

Verifications are conducted on both propagation and inundation area. Fig. 4 shows the profile of water surface elevation at propagation area, i.e. η_3, η_4 and η_5, and at inundation area (η_8). Both experimental data and numerical simulation results are fit quite well in the bore front face and maximum wave surface elevation value. The experimental data shows the detail record of fluctuation at the tail of wave profile in η_4 and η_5, which indicates the collision between incident wave and reflected one.

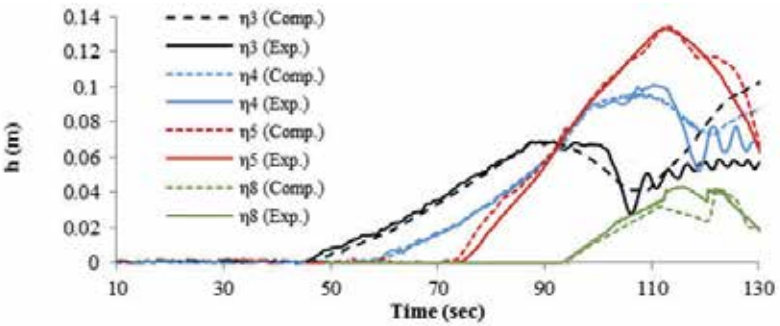

Fig. 4. Water surface elevations profiles at η_3, η_4, η_5 and η_8

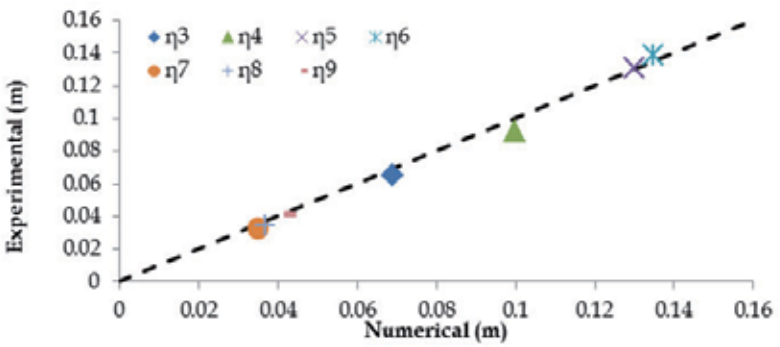

Fig. 5. Comparison of maximum water surface elevation at each measurement point

The plotted dots in the Fig. 5 are scatter close to the validity line ($h_{exp}/h_{comp.} = 1$), it means that there are good agreements on the verification of maximum water surface in propagation and inundation area.

4.1.2 Experimental with bottom flat

4.1.2.1 Water surface elevation profiles

The numerical simulation of bottom flat cases also confirms the good agreement of numerical and experimental at the propagation and inundation area. Fig. 6 shows the wave profile at propagation area with the difference impoundment height, i.e. 0.15m, 0.20m and 0.25m at W_2.

W_2 station is located 2.0m downstream side from W_1 station. In this station, water surface elevation quickly elevates when bore passes the measurement point. After sudden increase, wave constantly keeps its surface level before it fluctuates due to the collision of incident wave and reflected wave. The verifications fit well in the bore front profile, propagation phase and also the bore tail.

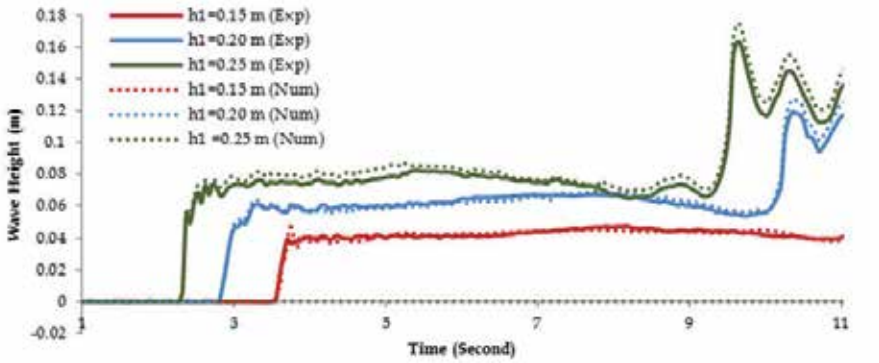

Fig. 6. Water surface elevations profiles at propagation area

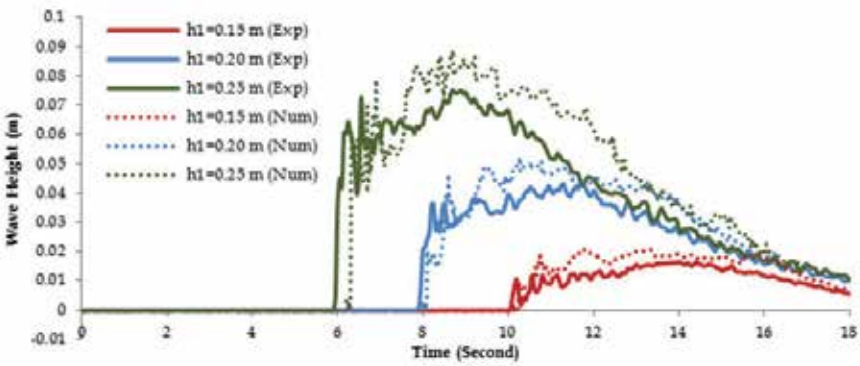

Fig. 7. Water surface elevations profiles at inundation area

Fig.7 shows the wave profile at the inundation area. Wave profile shows increasing trend after the quick raise at the beginning of measurement due to the incoming of sustain wave. Heavy fluctuations at the beginning of measurement indicate turbulence action occurs due to hydraulic wave jump hit the dike. Both experimental data and numerical result show similar trend of wave profile, though the simulations are slightly over estimate the maximum water depth after bore passes the wave gauges in the inundation area

4.1.2.2 Velocities profiles

Fig. 8 shows the verification of wave velocity with various impoundment heights in front of cylindrical structure with no weir existence. The maximum value of velocity occurs just after wave passes the current-meter. Then, the velocity profile shows the dramatic decreasing trend as the wave begins to adjust its flow after the successive waves collide with reflected ones from structure. Higher impoundment level (h_1=0.25m) cause high velocity value and quick wave arrival time (t=5.9s).

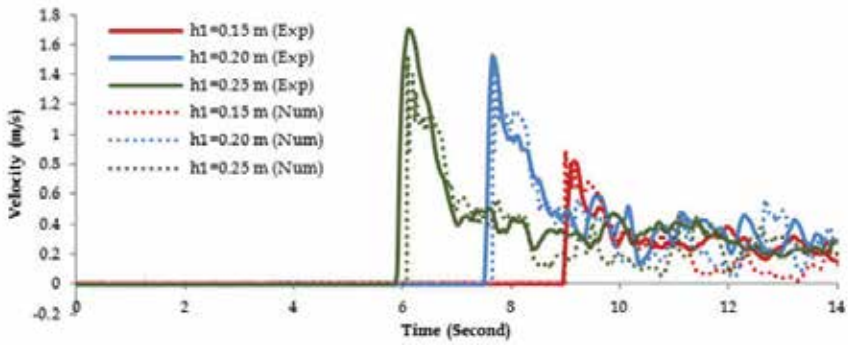

Fig. 8. Wave velocity profiles in front of cylindrical structure

Meanwhile Fig. 9 shows the wave velocity profile in the side of cylindrical structure. The quick raise velocity at the beginning of measurement also observes in this location. In addition, the slight decreasing trend indicates that the successive wave flows with less or no collision from the reflected wave.

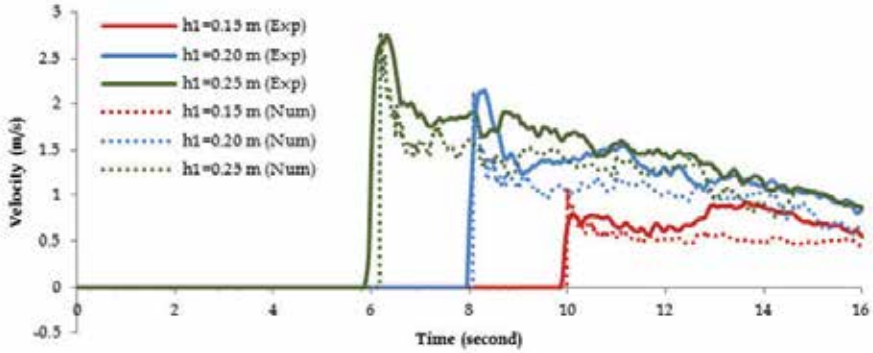

Fig. 9. Wave velocity profiles beside cylindrical structure

Fig. 8 and Fig. 9 show that even under these complicate flow conditions, the numerical results show good agreement with the experimental ones. Though at the side of structure, the numerical simulations appear to slightly overestimate the experimental results.

4.1.2.3 Force profiles

The verification of wave force acting on the 0.11m of structure diameter with various impoundment levels can be seen in Fig. 10. Both experimental and numerical results record sharp increase of initial force at the beginning of measurement as a result of wave hit the structure at the first attempt. Although the initial impact produces significant force value, it only occurs at very short period of time. Therefore there is high possibility to miss the peak of initial impact force during the observation. While sustain force, which occurs due to the accumulation of continuous incident waves, can be easily observe either in experimental or numerical results. The good agreement on these both forces can be seen in Fig. 10, while the comparison on the other maximum initial forces and maximum sustain ones can be seen in Fig. 11 (a) and 11 (b).

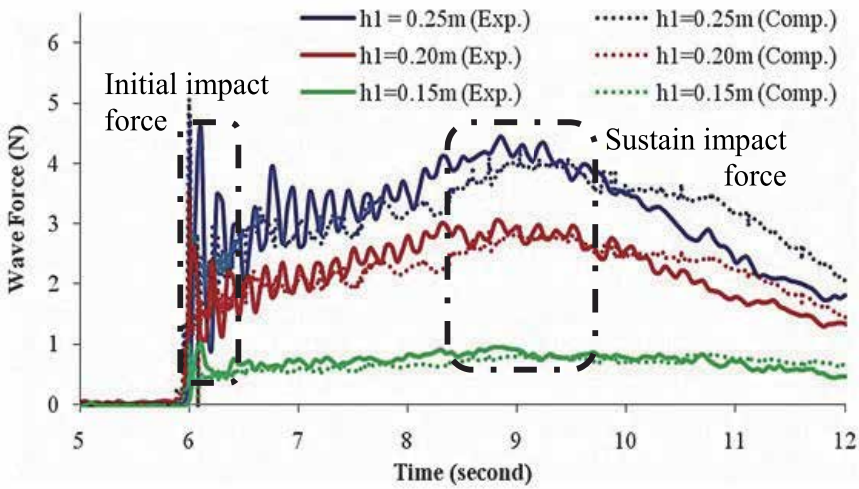

Fig. 10. Wave force profile acting on cylindrical structure.

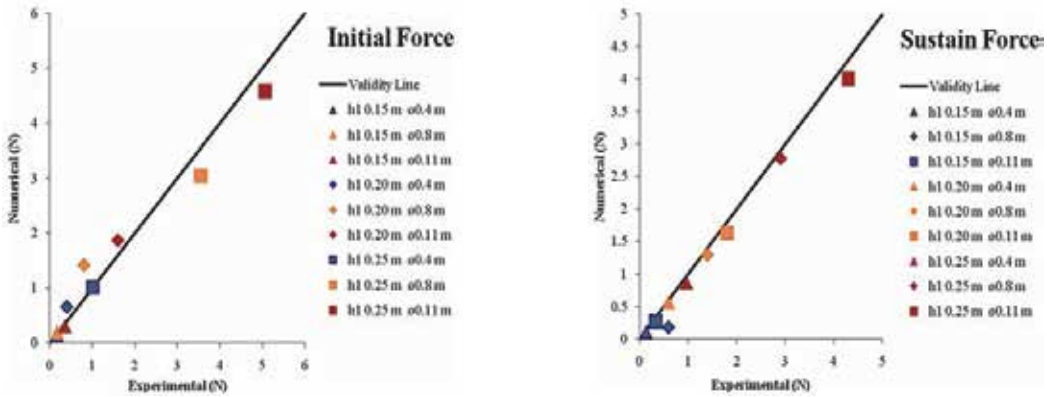

(a) (b)

Fig. 11. Validation of maximum wave forces: (a) initial wave forces, and (b) sustain wave forces

Good agreement can be seen both in maximum initial force and maximum sustain one in the wide range of bore height. The correlation of maximum initial force is slightly lower compare to sustain one. It is due to the recording of peak values of initial impact force mainly depend on the sampling frequency of data in experimental or computational time interval in numerical simulation.

4.1.2.4 Pressure profiles

Fig. 12 shows the pressure profile of attached pressure gauge on the front face of cylindrical structure. With the 0.08m of structure diameter and 0.2m of impoundment height, this figure shows that pressure at the bottom section (Z_5) received the highest pressure, and the pressure value decrease along upper section (Z_1). Even though the initial pressure seems blurred in this case, the sustain pressure can be observed well.

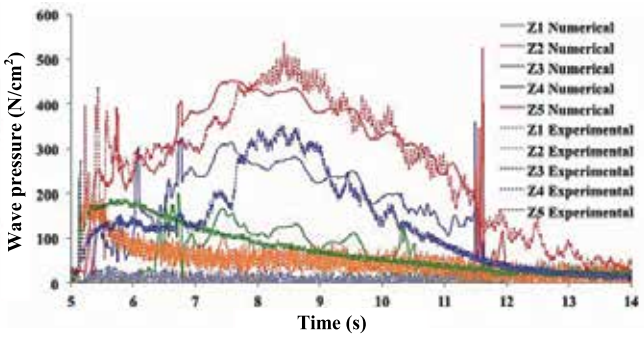

Fig. 12. Wave velocity profiles beside of cylindrical structure

The comparison between experimental and numerical results shows that numerical seems taking longer time on achieving maximum pressure (t=8.5 on Z_5) compare to experimental ones (t=7.7 on Z_5). Some spikes are also recorded on the tail of pressure profile in the computed results due to the instability of numerical simulation during complex conditions, which could be minimalized by setting up larger grid size. Overall, these comparisons show that fairly good agreement can be obtained between numerical and experimental results, both in the maximum value and the profile trend.

4.2 Cylindrical weir effects

4.2.1 Characteristic of water surface elevation

As seen in **Fig. 13**, the existence of cylindrical weir delays the arrival of tsunami wave inside weir area for a moment, and it decrease the initial water depth (t=4.5s-5s). However, after the depth of wave exceeds the weir height, the water surface level in the case with weir existence increases higher compare to without weir case. It is due to weir acts as water container and tends to kept water inside while the sustain waves are continuously flowing above it.

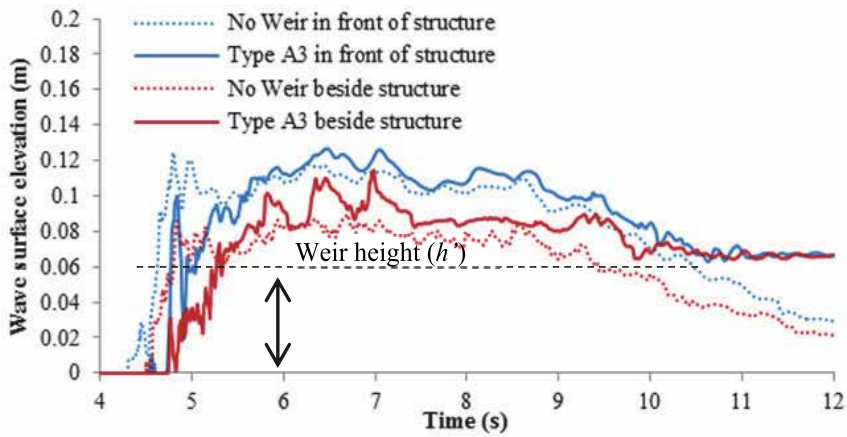

Fig. 13. Wave surface elevation profiles in front and beside cylindrical structure inside the weir area

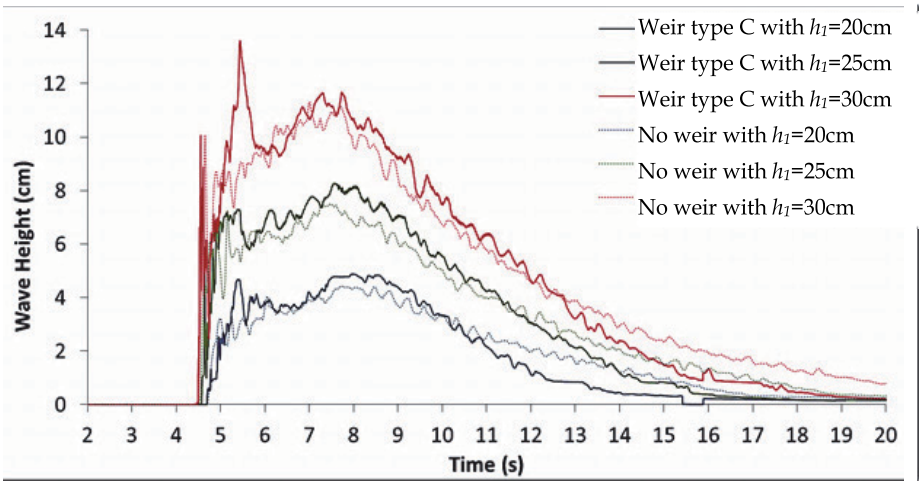

Fig. 14. Wave surface elevation profiles beside the cylindrical structure outside the weir area

The existence of weir tends to increase water surface elevation, not only inside the weir area, but also outside of it. Fig. 14 supports the evidence of increasing water depth despite of impoundment height.

4.2.2 Characteristic of velocities

The wave velocity profile just outside weir (x=+0.16m) and inside weir (x=+0.19m) in the case of no weir and weir Type A_3 can be seen in Fig. 15. This profile is recorded at Z=+0.05m above the dike with h_1=0.25m. The weir existence cause several fluctuations in the beginning of measurement as an indication of complex motion occurs. Further, the weir existence also tends to reduce velocities at both inside and outside weir due to blocked wave passage.

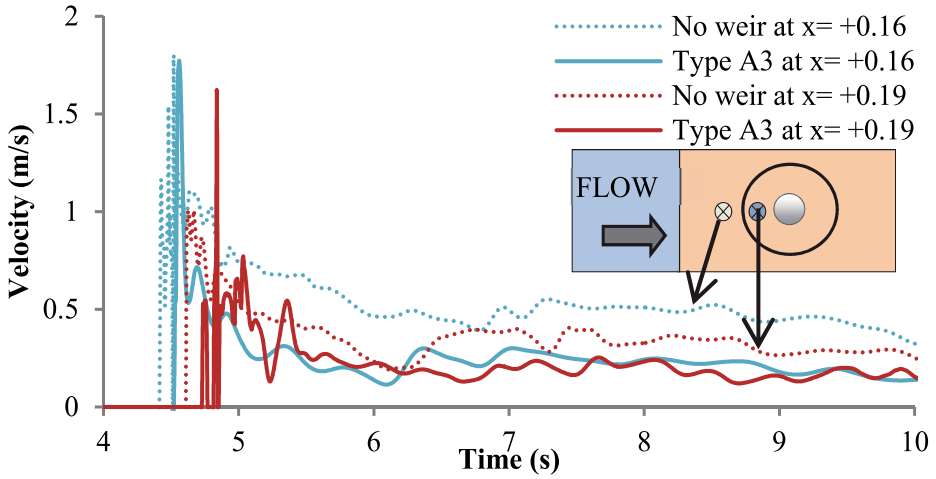

Fig. 15. Wave surface elevation profiles just in front and inside cylindrical weir

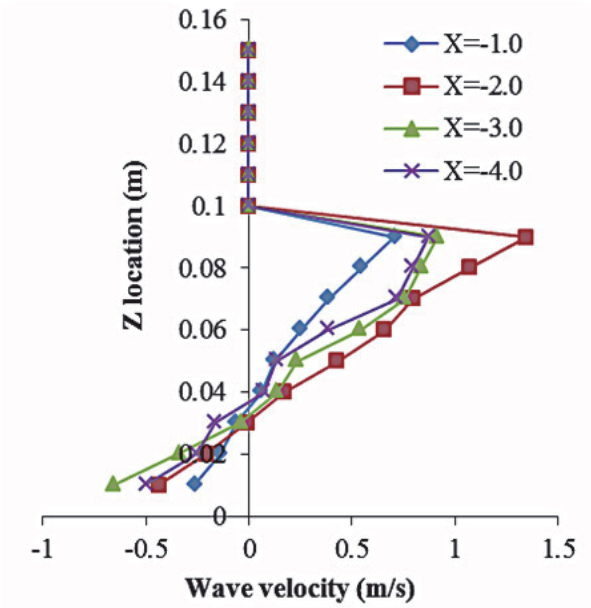

Fig. 16. Vertical distribution of wave velocity

Fig. 16 show the vertical distribution of maximum wave velocity at several location in front of structure, while Fig. 17 shows the horizontal distribution of maximum wave velocity at the bottom section, middle section and top section of structure. Fig. 16 clearly indicates the increase amount of velocity from bottom to top. The highest positive velocity occurs at x=-0.02m from structure, just after the overtopped wave hit the dike. While the negative ones, which indicate the opposite direction of x+, occurs at the bottom section of 0.03m in front of structure.

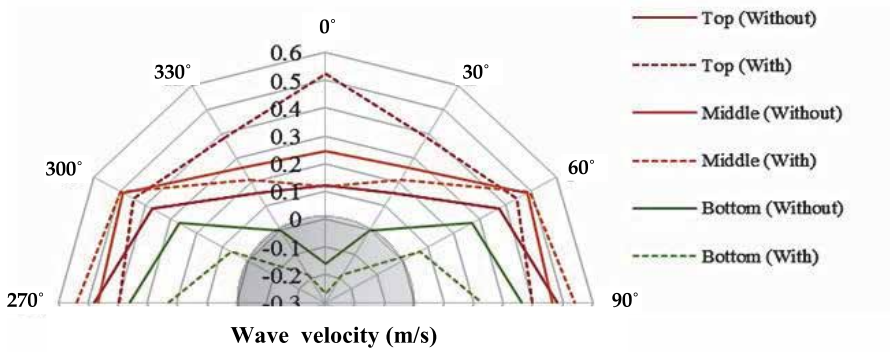

Fig. 17. Horizontal distribution of wave velocity

Fig. 17 shows that the weir existence tends to significantly increase the velocity at the top section, in front of structure. However the magnitude of increasing velocity is decreasing along circumferential direction. At the bottom section, the existence of weir causes the reduction of velocity at all circumferential faces.

4.2.3 Characteristic of pressures

The effect of the weir to the pressure mainly depends on the weir attributes, i.e. height and diameter. Fig. 18 shows the normalized pressure acting on the structure with various weir height to understand the effect of weir height in case of larger overtopped wave, i.e. h_1=0.30m.

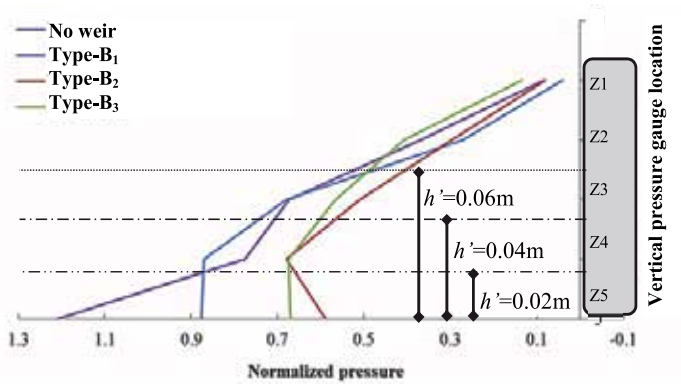

Fig. 18. Distribution of maximum sustain wave pressure on various weir height with h_1=0.30m

(a) (b)

Fig. 19. Snapshots of inundation wave against weir Type B_2 with: (a) h_1=0.03m caused large weir overtopping and (b) h_1=0.02m caused small weir overtopping

Fig. 18 shows the vertical distribution of pressure with the normalized pressure as the horizontal axis versus location of pressure gauges as the vertical axis. Weir height successfully reduces the pressure magnitude at the bottom section in all weir height cases, especially in weir Type B_2 and B_3. As can be seen in Fig. 19 (a), weir protects the bottom section of structure from the direct hit of initial impact. However, the reduction effect becomes less effective toward the upper section, i.e. middle and top section. The smaller differences between the case of with and without weir at the middle sections are caused by the increase water surface elevation on the front face of structure due to cylindrical weir existence. Fig 19(b) shows that h1=0.02m caused the small overtopped wave above weir. The vertical pressure distribution characteristic acting on the structure at this condition is similar with the larger overtopped cases.

Meanwhile, the effect of weir diameter can be described base on the amount of overtopped wave above protective weir. The vertical distribution of wave pressure in case of large overtopped wave is shown in Fig. 20 (a), while in case of small overtopped ones is shown in Fig. 20 (b). Both figures use cylindrical structure with 0.04m of diameter with various weir diameters, i.e. 0.26m, 0.22m and 0.16m. It means that the space size between inner face of cylindrical weir and outer face of cylindrical structure are 0.11m, 0.10m and 0.06m for Type A_1, type B_1 and type C_1 respectively.

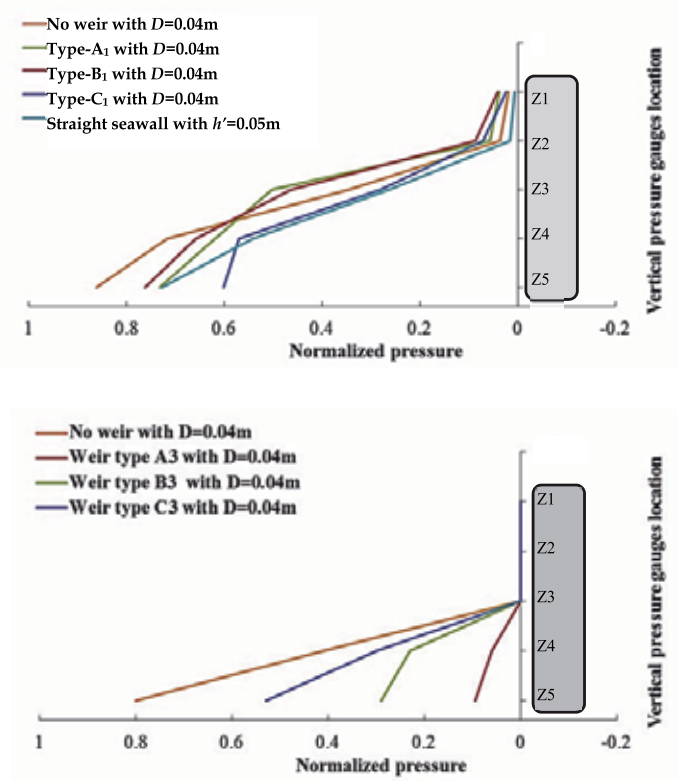

Fig. 20. Distribution of maximum sustain wave pressure on various weir diameter with: (a) larger overtopped wave h_1=0.25m, and (b) small overtopped wave h_1=0.20m

In case of larger wave overtopped, smaller space size, i.e. weir Type C_1, tended to the effectively reduce the wave pressure. The limited space between weir and structure cause wave difficult to accelerate their motion. In Fig. 20 (a), the establishment of straight seawall with height 0.05m at the dike corner (Wijatmiko and Keisuke, 2010b) have similar effect to the existence of smaller weir diameter. Seawall height cause shallower inundation depth due to small-overtopped wave and seawall location give adequate space for the wave to adjust their motion after hitting the dike.

Meanwhile in the smaller wave overtopped cases, the wider weir causes the pressure against structure significantly reduce. It is because with the similar volume of overtopped water flow, the wider diameter caused the inundation depth become shallower in the comparison with smaller weir diameter.

The horizontal distribution of maximum sustain wave pressure at the several vertical locations can be seen in Fig. 21(a), 21(b) and 21(c). The maximum water surface elevation around the cylindrical structure was 0.12m, therefore z=+0.01m represents bottom section, z=+0.05m is the middle section and z=+0.09m is the top section. 0 degree in the chart axis indicates the front face of structure, which is parallel to the direction of incoming wave, while the 90 degree and 270 degree indicate side face of the cylindrical structure.

As seen in Fig. 21, pressures at the front side of cylindrical structure are reduced due to the existence of weir in this section. However, this reduction effect becomes smaller along circumferential direction. While at the middle and top section, the existence of weir tend to increase the pressure magnitude due to the increase of water depth around cylindrical structure.

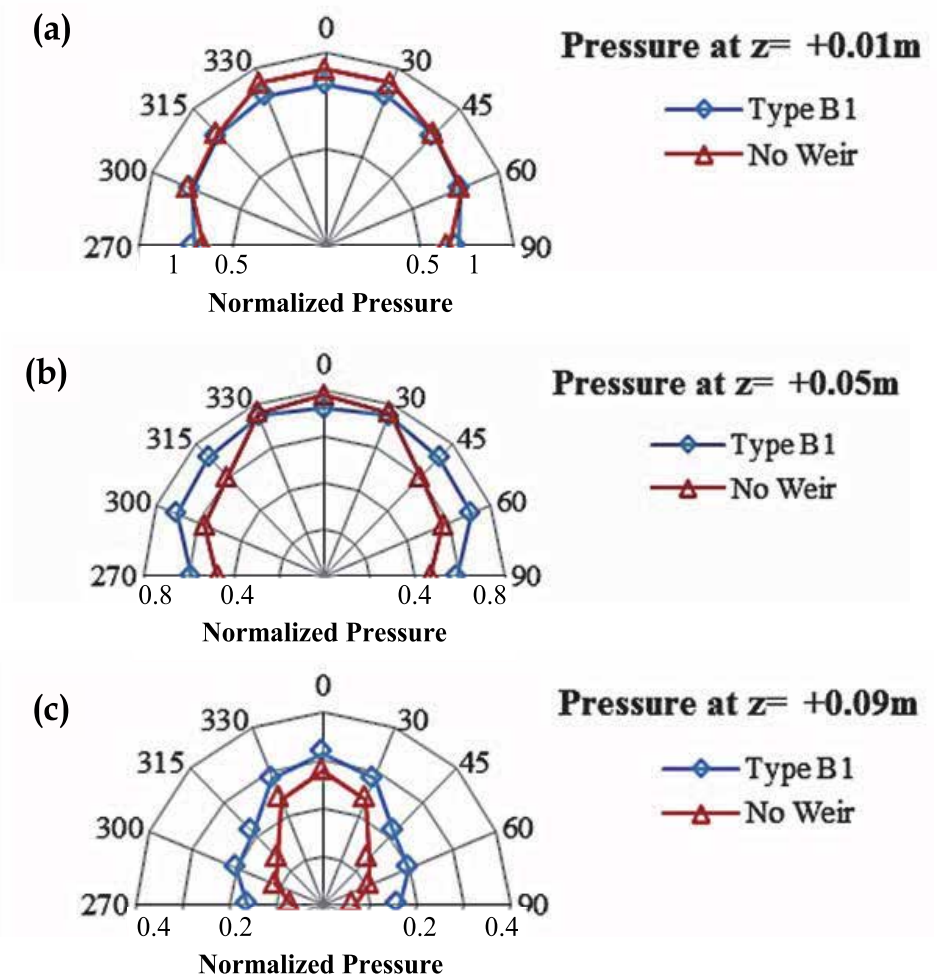

Fig. 21. Horizontal wave pressure distribution on without weir and weir type B_1 case: (a) at top section, (b) at middle section and (c) at bottom section.

4.2.4 Characteristic of forces

Weir existence reduces wave force in all impoundment height and all weir diameters cases. In addition, the reduction effect varies depending on the space between weir and structure. Higher force at Type B_1 in the cases of larger overtopped wave (h_1=0.25m and h_1=0.03m) are caused by direct hit by overtopped flow to the cylindrical structure, while the limited space between weir and structure cause significant reduction of wave forces at Type C_1, as seen in Fig. 22.

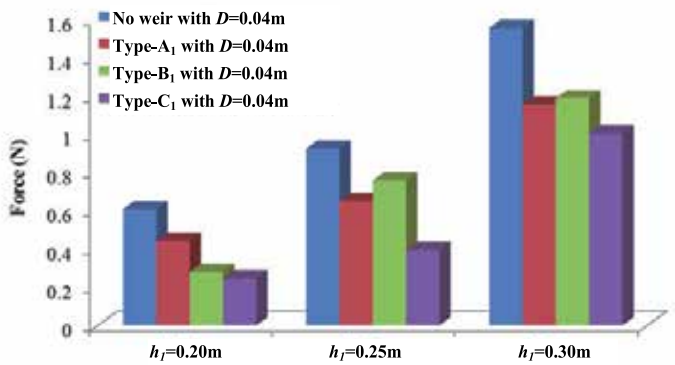

Fig. 22. Maximum sustain wave force

Meanwhile in the smaller overtopped wave case (h_1=0.02m), the shallower inundation depth inside weir cause the significant reduction of wave force. In these cases, the larger weir diameter, which means the closer weir to the dike corner, cause amount of overtopped wave inside the weir becomes larger compare to smaller ones.

5. Conclusions

The interactions between a single bore and cylindrical structure with cylindrical weir, supposed as oil tank barrier, are investigated through experimental and numerical study. Analytical equation to obtain the input velocities profile from the water surface elevation is introduced as well. Good agreements are confirmed in the physical principal quantities between experimental and numerical simulation both in the simple flat bottom and complex slope bottom conditions.

The existence of cylindrical weir tends to delay the arrival time of wave inside the weir area, and increases the water surface level around structure. In addition, weir tends to effectively reduce velocity at the bottom section, but in the contrary there are increasing velocities at upper section due to series of successive wave flowing above cylindrical weir. The reduction effects on velocity at the bottom section may provide some advantages for mitigating the scouring problems.

At the vertical pressure distributions, cylindrical weir also effectively reduces wave pressure at the bottom section. However, the reduction effect becomes smaller along higher section. While at the horizontal pressure distribution, the cylindrical weir tends to reduce pressure at the front face of structure. Furthermore, the weir configuration, i.e. weir height and weir diameter, and the level of overtopped wave play important role on the pressure and force magnitude.

6. Acknowledgment

This study was carried out by the financial support of Ministry of Education, Culture, Sport, Science, and Technology of Japan through Monbuka-gakusho scholarship. The authors would like to thank you Dr. Sakakiyama, T. for allowing us to use their experimental data. The numerical source codes used in this study are developed by research group, which are organized by Coastal Development Institute of Technology (CDIT). Some materials in this chapter are summarized from Wijatmiko and Murakami, 2010a, 2010b, 2011. All contributions are acknowledged.

7. References

Arikawa, T., and T. Yamano (2008). Large Scale Simulation on Impulsice Wave Pressure by using CADMAS SURF/3D, *Annual Journal of Civil Engineering in the Ocean (JSCE)*, Vol. 55, pp.26-30 (in Japanese)

Dangerous Goods Safety Management (2003). Spills Containment and Clean-up Measures for Dangerous Goods and Combustible Liquids. *Dangerous Goods Safety Management Act 2001*, Queensland Government Counter Disaster and Rescue Services.

Federal Emergency Management Agency (2008). Guidelines for Design of Structures for Vertical Evacuation from Tsunamis, FEMA, Retrived from http://www.fema.gov/library/viewRecord.do?id=3463

Fukui, Y., S. Hidehiko, M. Nakamura, and Y. Sasaki (1962a). Study on Tsunami, *Annual Journal of Coastal Engineering in Japan*, Vol. 9, pp. 44-49 (in Japanese).

Goto,H., H. Ikari, K. Tonomo, T. Shibata, T. Harada, and A. Mizoe (2009). Numerical Analysis on Drifting Behavior of Container on Apron due to Tsunami by Particle Method, *Annual Journal of Civil Engineering in the Ocean (JSCE)*, Vol. 59, pp.261-265 (in Japanese)

Haritos, N., Ngo, T., and Mendis, P. (2005). Evaluating Tsunami Wave Force on Structures, *Proceedings of International Symposium Disaster Reduction on Coasts Scientific-Sustainable-Holistic-Accesible*. Monash University, Melbourne, Australia, 2005

Hirt, C.W., and Nichols, B.D. (1981). Volume of fluid (VOF) method for dynamics of free boundaries. *Journal of Computational Physics*. Vol. 39, pp.201-225.

International Energy Agency (15 March 2011). Impact of Earthquakes and Tsunamis on Energy Sectors in Japan, In : *International Energy Agency Reports*, 20 May 2011, Available from : http://www.iea.org/files/japanfactsheet.pdf

Kawasaki, K., S. Yamaguchi, N. Hakamada, N. Mizutani, and S. Miyajima (2006). Wave Pressure Acting on Drifting Body after Collision with Bore, *Annual Journal of Civil Engineering in the Ocean (JSCE)*, Vol. 53, pp. 786-790

Lukkunaprasit, P., Ruangrassamee, A., and Thanasisathit, N. (2009). Tsunami loading on buildings with openings, *Science of Tsunami Hazard*, Vol. 28, No. 5, pp. 303-310

Mizutani, S., and F. Imamura (2001). Dynamic wave force tsunami acting on structure, *Proceeding of Internasional Tsunami Symposium*, pp. 941-948

Okada, T., T. Sugano, T. Ishikawa, T. Ohgi, S. Takai, and C. Hamabe (2004). Structural Design Method of Building for Tsunami Resistance (proposed), *Building Technology Research Institute*, The Building Center of Japan.

Palermo, D., and Nistor, I. (2008). Understanding tsunami risk to structures : a Canadian prespective, *Science of Tsunami Hazards*, Vol. 27, No. 4, pp.1-11.

Sakakiyama, T., and R. Kajima (1992). Numerical simulation of nonlinear waves interacting with permeable breakwaters. *Proceedings of the 23rd Internasional Conference on Coastal Engineer*, ASCE, pp. 1517-1530

Sakakiyama, T., S. Matsura, and M. Matsuyama (2009). Tsunami Force Acting on Oil Tanks and Buckling Analysis for Tsunami Pressure, *Journal of Disaster Research*, Vol. 4, No. 6, pp. 427-434

Tomita, T., K. Honda, and T. Kakinuma (2006). Application of three-dimensional tsunami to estimation of tsunami behavior arround structures, *Internasional Conference on Coastal Engineering*, pp. 1677-1688

Wijatmiko, I., and Murakami, K. (2010a). Numerical Simulation of Tsunami Bore Pressure on Cylindrical Structure, *Annual Journal of Civil Engineering in the Ocean (JSCE)*, Vol. 26, pp. 273-278, ISSN 0912-7348

Wijatmiko, I., and Murakami, K. (2010b). Three Dimensional Numerical Simulation of Bore Type Tsunami Propagation and Run up on to a Dike, *Journal of Hydrodynamics, Ser. B*, Vol. 22, Issue 5, Supplement 1, pp.259-264, ISSN 1001-6058

Wijatmiko, I., and Murakami, K. (2010a). Tsunami Bore Pressures and Forces Acting On the Structures Surrounded by weir, *Annual Journal of Civil Engineering in the Ocean (JSCE)*, Vol. 27, pp. 286-290, ISSN 0912-7348

Yeh, H. (2007). Design Tsunami Forces for Onshore Structures, *Journal of Disaster Research*, Vol 2, No. 6, pp. 531-536

Yeh, H. (1991). Tsunami Bore Runup, *Natural Hazard*, Vol. 4, pp.209-220.

Youngs, D.L. (1982). Time-dependent multi material flow with large fluid distraction. In : *Numerical Methods for Fluid Dynamics*, Morton, K., and Baines, M. (Eds.),pp.273-285, Academic Press, New York.

4

Using the General Gamma Distribution to Represent the Droplet Size Distribution in a Spray Model

Nwabueze G. Emekwuru
Midlands Simulation Group, School of Technology, University of Wolverhampton, United Kingdom

1. Introduction

The production of small sized droplets is the main purpose of using sprays. Sprays are produced when bulk liquid or large liquid sheets or jets are shattered in a process called atomization. In the atomization process, the shattering of the bulk liquid can occur if it is subjected to a high-velocity gas, or due to the kinetic energy of the liquid. An external device can also be used to induce these processes that lead to atomization.

Sprays occur naturally, in waterfall sprays and drizzle, for instance. Thus, they are of interest in meteorology. The industrial applications of sprays, however, are numerous. Drug applications in medical inhalers, chemical and irrigation applications in agriculture, dispersion of liquid fuels for combustion in engines, food preservation and processing applications, fire suppression, paint spraying and spray drying are just a few examples.

The proliferation of spray producing devices (atomizers) for use in the various applications of sprays has led to a keen interest in the hydrodynamics of sprays. Consequently, a lot of progress has been made with regards to spray measuring devices and numerical spray models in order to better match atomizers for particular applications, to predict, and improve the atomization process.

The process of atomization involves the production of new droplets that are of different sizes to the initial parent droplets. Thus atomizers, in practice, do not produce droplets of uniform size. To aid in evaluating sprays, some knowledge of the distribution of the droplet sizes is required. This is especially crucial in spray models as some representation of the droplet size distribution is needed in the prediction of the multi-phase flow hydrodynamics.

This chapter presents the application of a general Gamma distribution to represent the droplet size distribution in a spray model. This is a recently developed spray model in which the hydrodynamics characteristics of multi-phase flows are evaluated by calculating three moments of the droplet size distribution from transport equations and one moment from a general Gamma distribution. Three areas in this model require a particular distribution function for the droplet sizes: at the inlet conditions to describe the drag model, and at the droplet break up and collision processes. This is a novel concept as spray models normally track parcels of droplets and the Rosin-Rammler expression is commonly used for

representing droplet size distributions. The next section in this chapter presents the concept of droplet size distribution functions, including frequency curves and cumulative droplet distribution curves. The third section outlines the mathematical representation of the droplet size distribution functions, and, the various droplet size distribution functions that have been applied to the spray model. The fourth section presents the representation of droplet sizes in terms of mean diameters. In the fifth section, the application of the Gamma distribution to represent the droplet size distribution in a spray model is presented. Finally, in section six, the conclusions of the present chapter are summarised.

2. Representation of droplet size distributions

2.1 Introduction

A spray can be characterised as a grouping of droplets immersed in a gaseous environmment. As these groupings contain droplets that are of different sizes in practical atomizing conditions, atomizers do not produce droplets of uniform size. Therefore, to help in evaluating sprays, some knowledge and definition of the droplet size distribution is needed.

The spectrum of droplet sizes that can be found in sprays can vary depending on the particular atomizing process. This spectrum of droplets can be represented graphically. Droplet size histograms can be used to represent the droplet size distributions. Classifying droplet sizes and specifying the number of droplets that fall within the prescribed class limits, a number droplet size histogram can be plotted. A histogram of the volume droplet size distribution can be plotted by using the volume of the droplets within the prescribed droplet size classes. If the droplet classes in the histograms are prescribed with very small ranges, then the histograms can be developed into frequency curves. These frequency distribution curves can also be used to provide cumulative droplet distribution curves that give the percentage of the total number of droplets in the spray below the given droplet size or the percentage of the total volume of the liquid droplets contained in the spray below the given percentage of the total volume of the spray.

Thus the number distribution, $n(D)$, can be defined such that

$$\int_0^{\mathrm{d}} \mathrm{n(D)dD} \tag{1}$$

is the fraction of droplets with diameter less than d , where D is the droplet diameter.

The volume size distribution, $v(D)$, can also be defined such that

$$\int_0^{d} v(D)dD \tag{2}$$

is the fraction of the total droplet volume contained in droplets with diameter less than d, where D is the droplet diameter .

Figure 1 presents a volume frequency distribution and a cumulative volume distribution for a water spray (Emekwuru, 2007).

These droplet size distributions can be used to show how changes in the atomization conditions can affect the droplet size distribution in a spray. Thus, for instance, figure 2 shows the effect of the change in atomizing air pressure on the droplet size distribution, while figure 3 shows the effect of the distance from the spray nozzle on the droplet size distribution.

From figure 2(b), with the increase in atomizing air pressure value, there is a shift to more smaller sized droplets. The volume frequency of the larger sized droplets fall with increase in atomizing air pressure, and this is also reflected in the cumulative volume curve being skewed more to the smaller sized droplets compared to the figure 2(a). At higher atomizing air pressure values, increased droplet momentum results in increased droplet breakup and, thus, smaller droplet sizes. Figures 3(a) and 3(b) show the opposite trend to figures 2(a) and 2(b); a trend towards larger droplet sizes at locations further from the nozzle. The effects of droplet break up diminish at distances further from the nozzle, droplet coalescence becomes more important, and larger sized droplets travel further than smaller droplets as they experience less drag forces.

These droplet size distributions give an indication of not only how heterogeneous the spray droplets are, but also of the relative atomization performance of various nozzle designs and how these nozzles perform with changing operating conditions. Thus, droplet size distributions are a very good way of describing sprays.

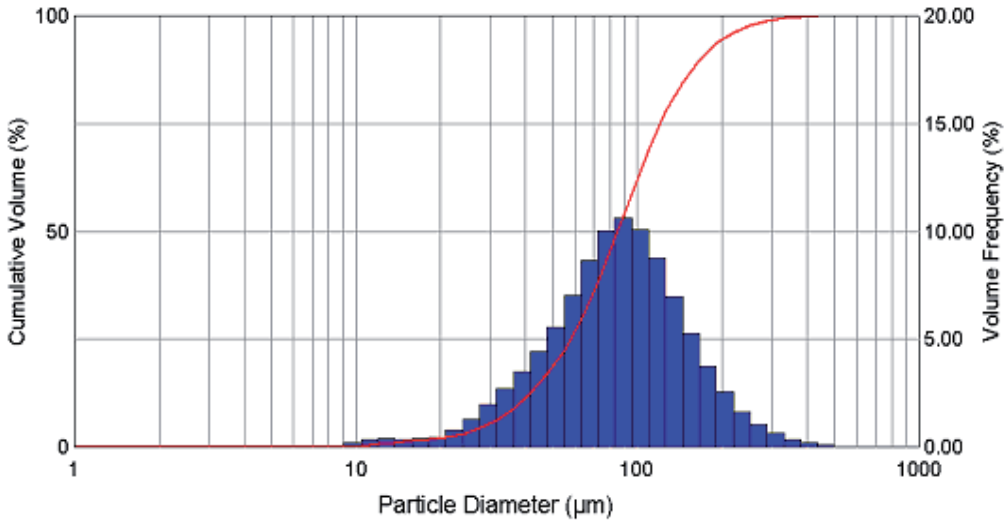

Fig. 1. Droplet size distribution showing both the cumulative volume distribution and the volume frequency distribution. These have been obtained from a water spray at 103 kPa atomizing pressure from a 3.52 mm diameter nozzle at an axial distance 275 mm from the nozzle using a laser-diffraction based droplet analyzer (Emekwuru, 2007).

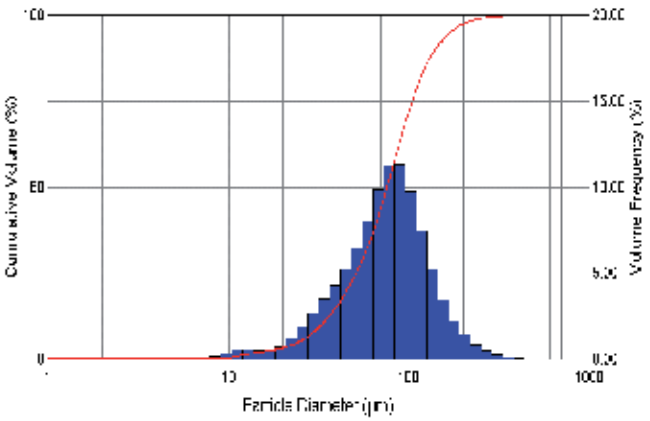

(a) 103 kPa

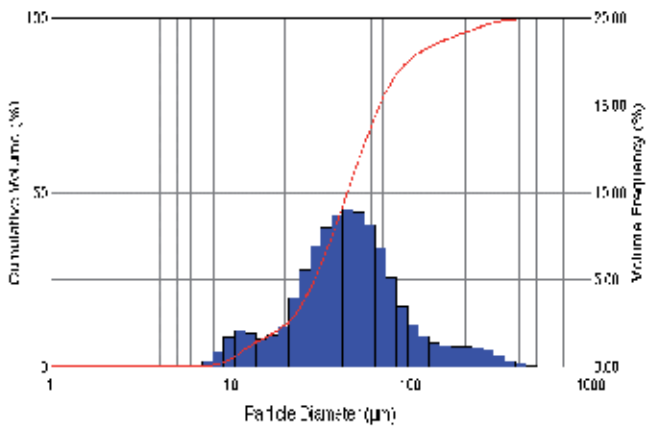

(b) 138 kPa

Fig. 2. Droplet size distribution showing both the cumulative volume distribution and the volume frequency distribution. These show the effects of the atomizing air pressure values on the droplet size distribution. (Emekwuru & Watkins, 2010a).

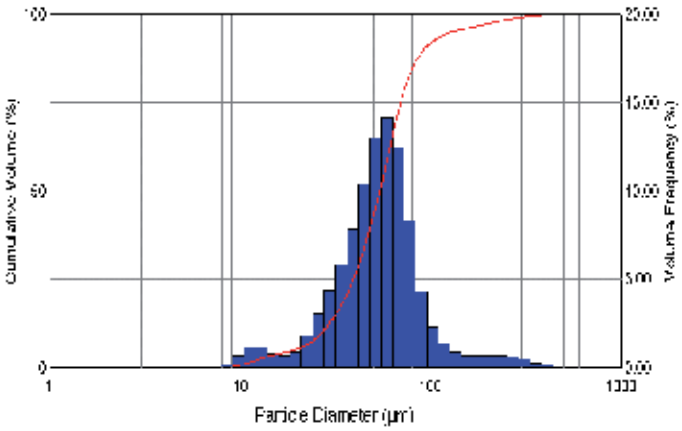

(a) 103 kPa, 150 mm.

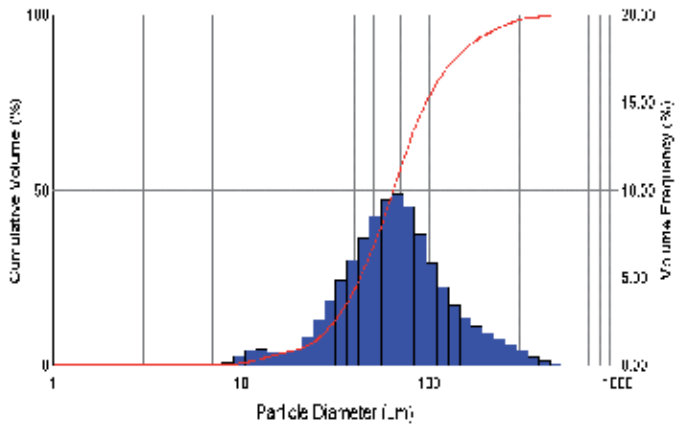

(b) 103 kPa, 200 mm.

Fig. 3. Droplet size distribution showing both the cumulative volume distribution and the volume frequency distribution. These show the effects of the axial distance from the nozzle on the droplet size distribution. (Emekwuru & Watkins, 2010a).

3. Droplet size distribution functions

As outlined in section 2, presenting the droplet size distribution graphically greatly aids in evaluating the characteristics of sprays. However, the construction of such graphs can require specialist spray measurement equipment and expertise that is not readily available to everyone with interest in spray droplet distribution characteristics. Besides, the droplet size distribution changes with both time and position, as shown in section 2, thus formulating the graphs for droplet size distributions can be involving. Therefore, many scholars have presented empirical droplet size distribution functions that attempt to give a good representation of the droplet sizes in sprays with parameters obtained from a limited knowledge of the droplet measurements. According to Miesse & Putnam (1957) if any proposed mathematical distribution function is to be able to adequately represent the droplet size distribution in a spray, it should have these qualities:

- Give a good fit to the droplet size data.
- Give a means for bringing large quantities of data together.
- Present a way of calculating mean and representative droplet diameters.
- Permit the extrapolation of the known droplet sizes to droplet sizes beyond the range of these known values.
- Ideally, beyond linking the mathematical expressions to droplet size data, provide further understanding of the basic atomization process.

Many droplet size distribution functions are in use. The *normal distribution* is based on the principle that a given droplet size occurs randomly. This distribution function is relatively easy to use but is constrained to situations where droplets occur randomly. The number distribution function $f(D)$ of the normal distribution, gives the number of droplets with a given diameter D. The expression is:

$$\frac{dN}{dD} = f(D) = \frac{1}{\sqrt{2\pi\sigma^2}} \exp\left[-\frac{\left(D - \bar{D} \right)^2}{2\sigma^2} \right] \tag{3}$$

In equation (3) , σ is the standard deviation of the values of D from a given mean value $\bar{D}$ and σ^2 is the variance.

In the *log-normal distribution*, the logarithm of the droplet diameter is used as a variable, and this is based on the normal distribution law that many droplet size distributions have been found to fit. Thus, with the logarithm of the droplet diameter as the variable, equation (3) becomes

$$\frac{dN}{dD} = f(D) = \frac{1}{\sqrt{2\pi\sigma_g{}^2}} \exp\left[-\frac{\left(\ln D - \ln \bar{D}_g \right)^2}{2\sigma_g{}^2} \right] \tag{4}$$

In equation (4) , σ_g is the geometric standard deviation of the values of D from a given number geometric mean droplet value $\overline{D}_g$ and σ^2_g is the geometric variance. These have the same significance as σ , and $\overline{D}$ in the normal distribution.

Mugele & Evans (1951) found the log-normal distribution to produce reasonable approximations to both the number and volume droplet size distribution functions. The *Nukiyama & Tanasawa distribution* (Nukiyama & Tanasawa, 1939) is also commonly used, but the expression was found to give a good fit to experimental droplet number size distributions but a poor fit to the volume size distributions (Mugele & Evans, 1951). Conversely, the same study found the *Rosin & Rammler distribution* (Rosin & Rammler, 1933), which is also widely used by scholars, a good fit to experimental droplet volume size distributions but a poor fit to number size distributions. Boulderston et al. (1981) also found that the Rosin-Rammler distribution gave a good fit to their experimental droplet volume size distribution. Other droplet distributions have been mentioned in literature, for example, the *chi-square distribution* (Hirohasu & Kadota, 1974; Bai & Gosman, 1999), a *modified log-normal distribution* (Mugele & Evans, 1951), and a *modified Rosin-Rammler function* (Rizk & Lefebvre, 1985).

There are many references on droplet size distribution functions for the interested reader, for example, Lefebvre (1989) and Mugele & Evans (1951). The rest of the section outlines the droplet size distribution functions used in the moments spray models.

3.1 Droplet size distribution functions used in the moments spray models

The moments spray model presents a novel way of characterising the complete polydisperse nature of a spray flow by evaluating the moments of the droplet size distribution. To date three types of the moments spray model have been developed based on the number of moments of the droplet size distribution that are calculated from transport equations. Different droplet size distribution functions have been used in the models. In the initial moments spray model (Beck & Watkins, 2003a), the first four moments of the of the droplet size distribution are used to describe the distribution of the of the droplet sizes. Transport equations are written for the third and fourth moments that represent the surface area and liquid volume, respectively. Thus, this model is termed the two-moments spray model.The first two moments, representing the droplet number and total radius respectively, are approximated by using a presumed distribution function. This presumed function was required to be an analytically integrable number distribution such that the volume distribution produced from the function was an approximation to the Rosin-Rammler distribution (Beck & Watkins, 2003a). The Rosin-Rammler volume distribution is defined as

$$v(r) = \left(\frac{\alpha_R}{r_R^{\alpha_R}} \right) r^{\alpha_R - 1} \exp\left(-\left(\frac{r}{r_R} \right)^{\alpha_R} \right) \tag{5}$$

where r_R is called the Rosin-Rammler mean radius, and α_R the Rosin-Rammler exponent. In this case r_R is the droplet radius for which 63% of the liquid mass is made up of droplets with smaller radii. The shape of the distribution is determind by the exponent, and Beck &

Watkins (2003a) chose an exponent such as to match a Rosin-Rammler distribution of exponent 2, because most sprays have distributions with exponents close to this value. The number distribution they found is

$$n(r) = \frac{16r}{\bar{r}_{32}^2} \exp\left(-\frac{4r}{\bar{r}_{32}}\right) \tag{6}$$

where the Sauter Mean Radius $\bar{r}_{32}$ is used because all the droplet moments are defined with respect to the droplet radii, and is not equal to the Rosin-Rammler mean radius. The volume distribution produced by this approximation is compared with the Rosin-Rammler distribution in Figure 4.

This distribution provided an adequate representation of the spray droplet size distribution in the two-moments spray model (Beck & Watkins, 2002, 2003a, 2003b).

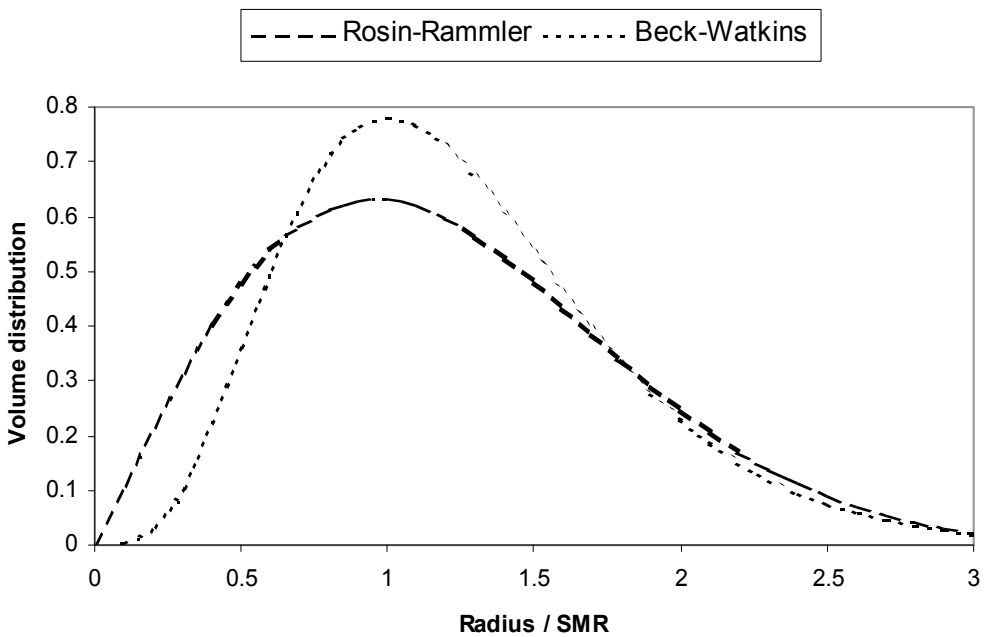

Fig. 4. Comparison of Beck-Watkins distribution used in the two moments model (Beck & Watkins, 2003a) with the Rosin-Rammler distribution of exponent 2.

The second moments model is the four-moments model of Yue & Watkins (2004). In this spray model the four moments of the droplet size distribution used in the Beck & Watkins (2002) model and their respective moment-averaged velocities are calculated from transport equations. Three areas in the spray model still require a distribution; the inlet conditions, the droplet drag model, and the droplet breakup and collision models. A Gamma distribution function is used in these sub-models. The three-moments model of Emekwuru & Watkins (2010b) is the third moments spray model, and the last three moments of the droplet size distribution are calculated from transport equations while the first moment is calculated from a Gamma distribution function which is also used for the three other areas in the spray model that require a distribution as in the four-moments model. The general Gamma distribution used in the three moments model is given by

$$n(r) = \frac{\alpha^k}{\Gamma(k) r_{32}^k} r^{k-1} e^{-\alpha(\frac{r}{r_{32}})} \tag{7}$$

where r_{32} is the Sauter mean radius and $\Gamma(k)$ is the Gamma function defined by the integral

$$\Gamma(k) = \int_0^\infty e^{-x} x^{k-1} dx \tag{8}$$

The two parameters defining the functional form are r_{32} and k.

The functional forms of equation (7) for various values of k are shown in figure (5).

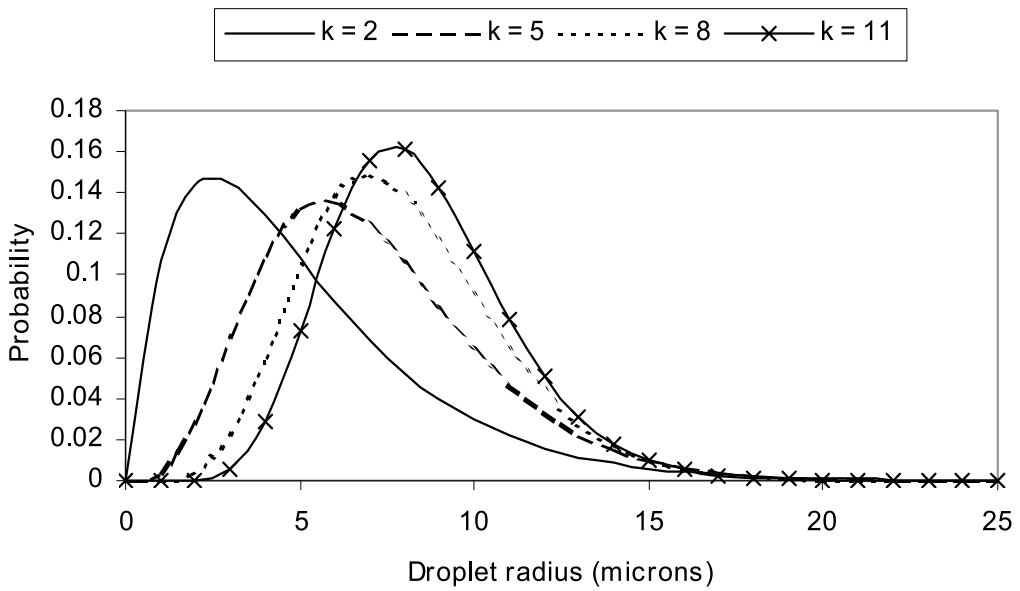

Fig. 5. Gamma distributions with r_{32} = 10μm

The results of the application of this distribution function to the three-moments spray model will be further highlighted in section 5.

4. The mean diameters concept

In practical calculations involving sprays many researchers use the mean diameters obtained from the size distributions presented in the previous sections, rather than the whole size distributions, in order to define an average droplet size in the given spray. Generally, these mean diameters can be defined thus:

$$D_{pq}^{p-q} = \frac{\int_0^\infty n(D)D^p dr}{\int_0^\infty n(D)D^q dr} \tag{9}$$

Mean diameters (from equation 9)			
p	***q***	***Symbol***	***Name***
1	0	D_{10}	Number
2	0	D_{20}	Surface area
3	0	D_{30}	Volume
2	1	D_{21}	Surface area-length
3	1	D_{31}	Volume-length
3	2	D_{32}	Sauter

Table 1. Some mean diameters

Some of the more commonly used mean diameters and their relation to equation (9) are presented in Table 1. For example, the *number mean diameter*, D_{10}, is the average value of all the droplets in the spray; the *volume mean diameter*, D_{30}, is the diameter of a droplet whose volume, when multiplied by the number of droplets in the spray, equals the the total volume of the spray; and the *Sauter mean diameter*, D_{32} is the diameter of a droplet with a ratio of volume to surface area which is similar to that of the whole spray. Mugele & Evans (1951) provide a good representation of mean diameters. Some other researchers such as Yule et al. (2000) prefer to use the volume median diameter, $D_{v,0.5}$, defined as

$$\int_0^{D_{v,0.5}} v(D)dD = 0.5 \tag{10}$$

This is akin to the concept of *representative diameters* of which some of the definitions have been presented in Table 2.

REPRESENTATIVE DIAMETERS	
$D_{0.1}$	10% of total liquid volume is in droplets of smaller diameter than this diameter
$D_{0.5}$	50% of total liquid volume is in droplets of smaller diameter than this diameter
$D_{0.9}$	90% of total liquid volume is in droplets of smaller diameter than this diameter

Table 2. Some representative diameters

Thus, the droplet size distribution function (see equations (1) & (2) for instance), can be described with the knowledge of a representative diameter and a mean diameter.

5. Application of the gamma distribution to the moments spray model

Equation (1) can be represented in terms of a droplet number probability distribution, denoted by *N(r)* where the fraction of droplets having radii between limits r_1 and r_{0-} is given by

$$\int_{r_0}^{r_1} N(r)dr \tag{11}$$

As equation (11) is a probability density function, the integral over all the droplet radii within the limits is equal to one. By multiplying by the total number of droplets per unit total volume, a multiple of this distribution, *n(r)*, can be presented , and the moments of the droplet number probability distribution is

$$Q_i = \int_0^{\infty} n(r)r^i dr \tag{12}$$

As was mentioned in section 3.1, the three moments spray model uses the first four moments, Q_0 to Q_3 , as was first used by Beck & Watkins (2003):

- Q_0 is the total number of droplets, per unit total volume.
- Q_1 is the total sum of radii of the droplets, per unit total volume.
- $4\pi Q_2$ is the total surface area of the droplets, per unit total volume.
- $\frac{4\pi Q_3}{3}$ is the total volume of the droplets, per unit total volume.

These four moments can be used to represent all the mean droplet diameters in Table 1, from D_{10} to D_{32} , and a relationship similar to equation (9) for the droplet distribution moments is

$$D_{pq}^{p-q} = \frac{2^{p-q}Q_p}{Q_q} \tag{13}$$

Sowa (1992) discusses this relationship in detail.

In the three moments spray model, the last three moments of the droplet size distribution, Q_1 to Q_3 , are obtained from transport equations. These transport equations have been described by Emekwuru & Watkins (2010b). The first moment of the droplet size distribution, Q_0 , is obtained from the Gamma size distribution function. Thus from section 3.1, the moments of equation (7) can be given as

$$Q_i = Q_0 \int_0^{\infty} \frac{\alpha^k}{\Gamma(k) r_{32}^k} r^{k+i-1} e^{-\alpha\left(\frac{r}{r_{32}}\right)} dr \tag{14}$$

By partial integration,

$$Q_3 = \frac{(k+2)}{\alpha} r_{32} Q_2 \tag{15}$$

By definition, $Q_3 = r_{32} Q_2$ thus $\alpha = k + 2$.

Therefore,

$$Q_2 = \frac{(k+1)}{(k+2)} r_{32} Q_1, \quad Q_1 = \frac{k}{(k+2)} r_{32} Q_0 \tag{16}$$

And finally Q_0 can be evaluated as

$$Q_0 = \frac{(k+2)}{k r_{32}} Q_1 \tag{17}$$

5.1 Discussion of application to water sprays

A water spray study, using a twin-fluid sprayer typically used in agricultural spraying processes, was presented by Emekwuru & Watkins (2010a). In the study, the characteristics of the water spray are defined by the droplet size data obtained using a laser-diffraction-based measuring instrument. The droplet size data measurements were taken at different atomizing air pressure values, at various axial distances from the spray nozzle, and radial distances from the spray centreline. The test results indicate that the performance of the air-atomizer depends largely on the air atomizing pressure. The nozzle diameter is 3.52 mm and the results at the 300 mm axial distance from the nozzle for different atomising air pressure values are presented in figures 6(a) to (c). Some of the conditions are presented in table 3, the complete results can be found in Emekwuru & Watkins (2010a, 2010b). The three moments model provides the capability to represent both the local droplet sizes and the local droplet size distributions. Of interest here is the comparison of the local droplet size distribution from the experimental data with the predictions from the three moments spray model. As the air atomizing pressure value is increased, the droplet sizes decrease (figures 6 (a) to (c)) as expected since droplet break up increases due to more unstable droplets resulting from higher droplet momentum and increased shear in the atomization area due to higher atomizing pressures. The volume frequency of the larger sized droplets reduces and that of the smaller sized droplets increases with these increasing air atomizing pressure values. The numerical data capture these trends. The model also captures the relatively poor atomization noticed at low air atomizing pressure cases characterised by larger droplet sizes. As the atomizing air pressure values increase, the droplet size distributions become increasingly bi-modal. The model captures this as well, though there is a difference between the observed and calculated bi-modal droplet distribution peaks.

The data from the numerical predictions suggest that, for the moments spray model, the Gamma number size distribution function can be used to model the droplet size distribution data obtained from experimental data.

The moments spray model using the general Gamma distribution to represent the droplet size distribution has also been applied to diesel spray cases (Emekwuru & Watkins, 2011) and work continues on applying this distribution to other spray cases, including combining the distribution with other droplet size distribution functions for different parts of the spray model (Emekwuru et al., 2012).

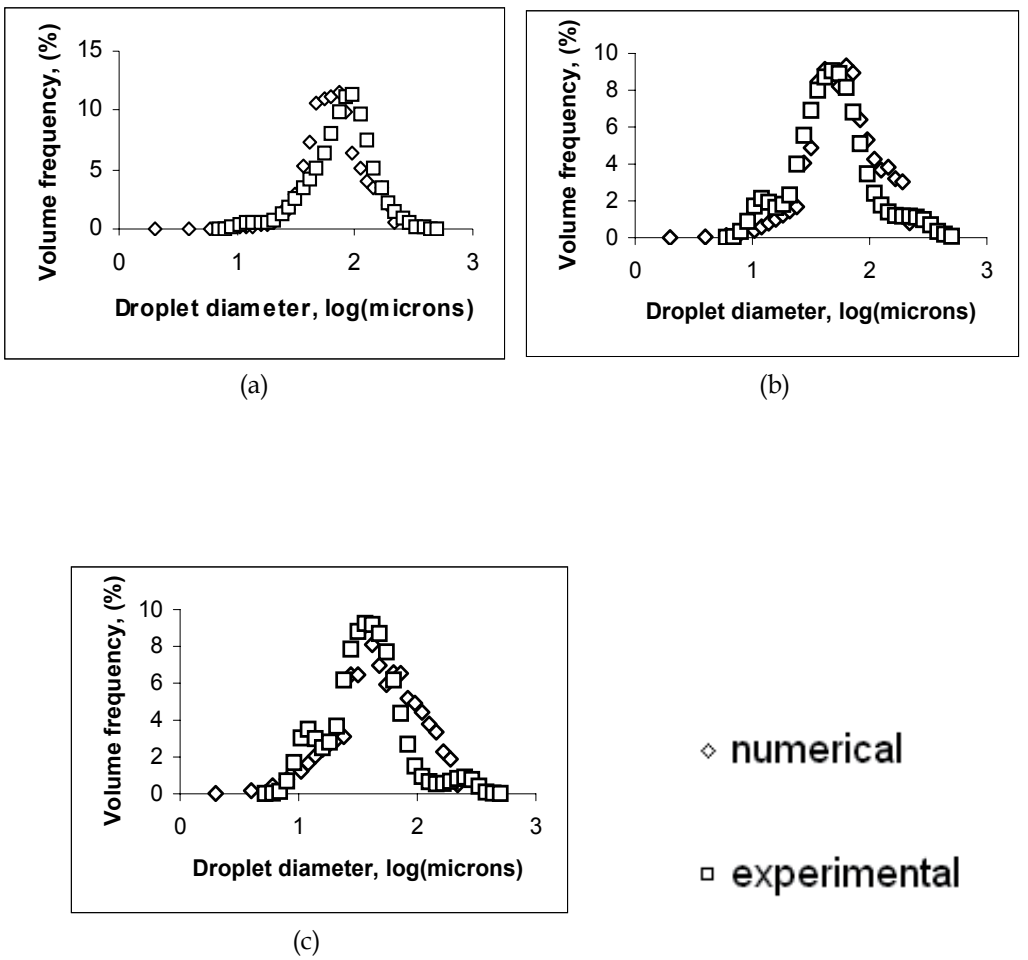

Fig. 6. Comparison of the local droplet size distribution from experimental data (Emekwuru & Watkins, 2010a) with the predictions from the three moments spray model (Emekwuru & Watkins, 2010b). The measurement location is 300 mm axial distance from the nozzle at air atomizing pressure values of (a) 103 kPa, (b) 138 kPa, and (c) 172 kPa.

Air atomizing pressure, (kPa)	103	138	172
Ambient pressure, (kPa)	100		
Injector nozzle diameter, (mm)	3.52		
Spray cone angle, (degrees)	15.94	16.25	16.46

Table 3. Some of the conditions used for the experimental (Emekwuru & Watkins, 2010a) and computational work (Emekwuru & Watkins, 2010b) presented in figure 6.

6. Conclusions

A spray can be defined as a grouping of droplets immersed in a gaseous environment. In practical conditions these groupings do not contain droplets of the same size. Thus, to help in evaluating sprays, some knowledge and definition of the droplet size distributions is necessary.

Droplet size distributions can be represented graphically as histograms, and cumulative distribution curves, but constructing such graphs can be tedious. Empirical droplet size distribution functions get round this issue by attempting to give a good representation of the droplet sizes with parameters obtained from a limited knowledge of the droplet data measurements. A number of droplet size functions exist but none can yet be judged to be a universal function for characterizing droplet size distribution in sprays. The use of these functions is useful in spray models, as some knowledge of the distribution of the droplet sizes is needed in the modelling process. The moments spray model evaluates the hydrodynamics characteristics of sprays without using droplet size classes. Instead moments of the droplet size distribution, which are calculated from transport equations and a size distribution function, are used. The application of a general Gamma distribution function to represent the droplet size distribution in a moments spray model indicate that the predictions from the model agree with experimental data, and thus is a viable distribution function to use to model the droplet size distributions in sprays. The results not only capture the changes in the local droplet size distribution with changes in the atomizing air pressure values, but also predict the shift from mono to bi-modal droplet distributions. More accurate representations of droplet size distribution functions in spray models can help in the better prediction, and hence, analysis of the hydrodynamic characteristics of sprays and spray making devices.

7. Acknowledgment

Dr. Nwabueze G. Emekwuru holds a University of Wolverhampton ERAS 2011/2012 award, which supported the publication of this work. Figures 2, 3, and 6 have been reprinted with permission from Begell House, Inc.

8. References

Bai, C., & Gosman, A.D., (1999). Prediction of spray wall impingement in reciprocating engines. *15th Annual Conf. Liquid Atomisation and Spray Systems.,* Toulouse, France, July 1999.

Beck, J.C., & Watkins, A.P. (2002). On the development of spray sub-models based on the droplet size moments. *J. Comp. Phys.,* Vol. 182, Issue 2., pp. 586-621, ISSN: 0021-9991.

Beck, J.C., & Watkins, A.P. (2003a). On the development of a spray model based on drop-size moments. *Proc. R. Soc. Lond. A*, Vol. 459, No. 2034, pp. 1365-1394, ISSN: 1471-2946.

Beck, J.C., & Watkins, A.P. (2003b). Simulation of water and other non-fuel sprays using a new spray model. *Atomization and Sprays*, Vol. 13, Issue. 1, pp. 1-26, ISSN: 1044-5110.

Boulderston, C., Ahseng, C., Yule, A.J., Felton, P.G., & Chigier, N.A., (1981). The structure of diesel injector sprays. CARL IM 81-01.

Emekwuru, N.G. (2007). Statistical Experimental Analysis of a Two-Fluid Sprayer and Its Use to Develop the Number Size Distribution Moments Model of Sprays. PhD., University of Manchester, UK.

Emekwuru, N.G., & Watkins, A.P. (2010a). Analysis of a two-fluid sprayer and its use to develop the number size distribution moments spray model, Part I: Experimental Analysis. *Atomization and Sprays*, Vol. 20, Issue 6, pp. 467-484, ISSN: 1044-5110.

Emekwuru, N.G., & Watkins, A.P. (2010b). Analysis of a two-fluid sprayer and its use to develop the number size distribution moments spray model, Part II: Computational Analysis. *Atomization and Sprays*, Vol. 20, Issue 8, pp. 653-672, ISSN: 1044-5110.

Emekwuru, N.G., & Watkins, A.P. (2011). Application of a moments spray model to solid cone diesel sprays. *JSAE Paper 20119080, SAE Paper 2011-01-1843*.

Emekwuru, N.G. (2012). A number size distribution moments based solid cone diesel spray model: Assessment of droplet breakup models based on different distribution functions. *SAE Paper 2012-01-1260*

Hiroyasu, H., & Kadota, T., (1974). Fuel droplet size distribution in diesel combustion chamber. *SAE Paper 740715.*

Lefebvre, A.H. (1989). Atomization and Sprays. *Hemisphere*. ISBN: 0-89116-603-3, New York, U.SA.

Miesse, C.C., & Putnam, A.A., (1957) Mathematical Expressions for Drop-Size Distributions, *Injection and Combustion of Liquid Fuels,* Section II, WADC Technical Report 56-344, Mattelle Memorial Institute, March.

Mugele, R.A., & Evans, H.D., (1951). Droplet Size Distributions in Sprays. *Ind. Eng. Chem.,* Vol. 43, No. 6, pp. 1317-1324.

Nukiyama, S., & Tanasawa, Y., (1939). Experiments on the Atomization of Liquids in an Air Stream, Report 3, On the Droplet-Size Distribution in an Atomized Jet, Defense Research Board, Department of National Defense, Ottawa, Canada; translated from *Trans. Soc. Mech. Eng. Jpn.,* Vol. 5, No. 18, pp. 62-67.

Rizk, N.N., & Lefebvre, A.H., (1985) Drop-Size Distribution Characteristics of Spill-Return Atomizers. *AIAA J. Propul. Power,* Vol. 1, No. 3, pp. 16-22, ISSN: 0748-4658.

Rosin, P., & Rammler, E. (1933). The Laws Governing the Fineness of Powdered Coal. *Journal of the Institute of Fuel*, Vol. 7, pp. 29-36.

Sowa, W.A. (1992). Interpreting mean drop diameters using distribution moments. *Atomization and Sprays*, Vol. 2, Issue 1, pp. 1-15, ISSN: 1044-5110.

Yue, B., & Watkins, A.P. (2004). Mathematical Development and Numerical Analysis of Further Transport Equations for the Droplet Size Moment Theory. *19th Annual Meeting of the Institute for Liquid Atomization and Spraying Systems (Europe).* Nottingham, UK, September 2004.

Yule, A.J., Sharief, R.A., Jeong, J.R., Nasr, G.G., & James, D.D. (2000). The performance characteristics of solid cone spray pressure swirl atomizers. *Atomization and Sprays,* Vol. 10, Issue. 6, pp. 627-646, ISSN: 1044-5110.

5

Well Responses in Three-Zone Linear Composite Dual-Porosity Reservoirs

Jing-Jing Guo, Lie-Hui Zhang*, Hai-Tao Wang and Qi-Guo Liu
State Key Laboratory of Reservoir Geology and Exploitation,
Southwest Petroleum University
China

1. Introduction

Naturally fractured reservoirs are composed of high flow capacity-low storage fractures and high storage-low flow capacity matrix blocks. Composite systems in this type of reservoirs can be encountered as a result of non-uniform fracture distribution, drilling, secondary or tertiary recovery projects, and stimulation programs. In general, a composite reservoir system is made up of two or more regions. Each region has its own rock and fluid properties.

In the past 25 years, a considerable theoretical effort has been made to describe the pressure behavior of this specific type of reservoir. Poon (Poon, 1984) first studied the pressure transient behavior of a composite dual-porosity reservoir by extending the Warren and Root's natural fracture model to a composite reservoir and assuming pseudo-steady-state flow in the matrix system. In 1987, Prado and Da Prat (Prado & Da Prat, 1987) presented an analytical model to describe the pressure behavior of a well completed in a reservoir wherein natural fractures occur over a limited area around the wellbore. The flow in the reservoir is treated as a composite reservoir flow problem, the region adjacent to the wellbore being considered as a fractured medium and the outer region as a homogeneous one. Wellbore storage and skin effects were included in the solution, and the flow in the fractured region was mathematically described by Warren and Root's double porosity theory. In 1991, Satman (Satman, 1991) considered a model similar to Poon's but with transient interporosity flow. He presented the early- and late-time solutions in Laplace space but did not investigate the characteristics of the solution in dimensionless form. Kikani et al. (Kikani et al., 1991) and Olarewaju (Olarewaju, 1991) proposed an analytical model for naturally fractured reservoirs with transient interporosity flow and matrix skin in a composite reservoir.

In 1999, Guo & Xiang (Guo & Xiang, 1999) extended the radial composite dual-porosity model to multi-zone condition and put forward a well test model for a composite dual-porosity oil reservoir with non-uniform thickness and lateral heterogeneity. However, they did not give the analytical solution of the model. Based on the work done by Guo, Huang &

*Corresponding author

Liu (Huang & Liu, 2006) presented an analytical solution to describe the transient pressure behavior of a naturally fractured composite gas reservoir. More recently, the transient pressure distributions in dual-porosity composite reservoirs with different outer boundaries were discussed, considering variable rate (Huang et al., 2002; Li et al., 2007; Han et al., 2007; Zhang et al., 2010a, 2010b).

The mathematical models for radial composite dual-porosity reservoirs are well developed and validated by numerous studies. However, to our knowledge, the models for a well completed in a linear composite strip reservoir with natural fractures are poorly available in the literature. The effect of the formation thickness variation on the transient response of a well in this type of reservoir configuration also does not appear to have been considered previously in the literature.

In this chapter, based on the Warren and Root's natural fracture model, a new well test model for linear composite dual-porosity reservoirs is presented, considering formation thickness and reservoir properties variations in plane. The analytical solution is obtained with one finite Fourier cosine space transformation (Farlow, 1982) and time-space Laplace transformation. By using Duhamel principle, the corresponding wellbore pressure response, together with effects of skins and wellbore storage, is obtained. The type curves are plotted with Stehfest algorithm and the impacts of relevant parameters are discussed. The model as well as the method presented in this chapter is useful in predicting production performance or analyzing production data from this type of well-reservoir system.

2. Mathematical model

Our primary interest is to consider flow in a three-zone liner composite dual-porosity reservoir. In this section, we present the detailed derivation of the mathematical model.

2.1 Assumptions

The mathematical model proposed in this chapter is based on oil reservoir conditions; it is also applicable to gas reservoirs by replacing the pressure term with a pseudo-pressure term. The key assumptions made in developing the mathematical model include:

1. A dual-porosity strip reservoir with parallel impermeable boundaries can be divided into three regions. A constant-rate line-source well is located in region I as illustrated in Fig.1. The reservoir regions on both sides of the discontinuities may have different rock and fluid properties. But each one of the three zones is homogeneous and isotropic with constant reservoir properties such as permeability and porosity.
2. The matrix system is assumed to be a medium of high storativity and low permeability. It is also assumed that production is only by virtue of the fracture system; that is, the wellbore has no direct connection with the matrix system.
3. Single-phase slightly compressible fluid and isothermal flowing.
4. Reservoir properties change at the interface. Both the width and flow resistance along the interface are neglected.
5. Laminar flow in each zone, with negligible gravitational effect and capillary effect.
6. Uniform initial reservoir pressure (p_i).
7. Pseudo-steady-state interporosity flow.

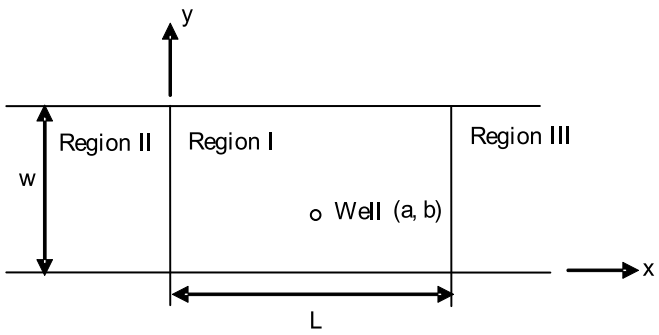

Fig. 1. Schematic of a three-zone linear composite dual-porosity reservoir

2.2 Definitions

Solutions in this chapter are presented in dimensionless form. Here, we first present the definitions of the dimensionless variables used in our derivation. All dimensionless variables are based on the properties of region I.

The dimensionless pressure for fracture system and the matrix system are defined respectively by

$$p_{Df} = \frac{2\pi k_{f1} h_1}{q\mu_1}\left(p_i - p_f\right) \tag{1}$$

$$p_{Dm} = \frac{2\pi k_{m1} h_1}{q\mu_1}\left(p_i - p_m\right) \tag{2}$$

The dimensionless time is defined by

$$t_D = \frac{k_{f1} t}{\left(\phi C_t\right)_{(f+m)1} \mu_1 r_w^2} \tag{3}$$

The dimensionless distances in the x- and y- directions are defined, respectively, by

$$x_D = \frac{x}{r_w} \tag{4}$$

$$y_D = \frac{\pi}{w_D}\frac{y}{r_w} \tag{5}$$

$$a_D = \frac{a}{r_w} \tag{6}$$

$$w_D = \frac{w}{r_w} \tag{7}$$

$$b_D = \frac{b}{r_w}\frac{\pi}{w_D} \tag{8}$$

The dimensionless variables related to the composite system are also defined in this section. The mobility ratios are defined by

$$M_{21} = \frac{k_{f2} / \mu_2}{k_{f1} / \mu_1} \tag{9}$$

and

$$M_{31} = \frac{k_{f3} / \mu_3}{k_{f1} / \mu_1} \tag{10}$$

The thickness ratios are defined as

$$h_{21} = \frac{h_2}{h_1} \tag{11}$$

and

$$h_{31} = \frac{h_3}{h_1} \tag{12}$$

The transmissibility ratios are defined as

$$\eta_{21} = \frac{k_{f2}\Big/\left(\phi C_t\right)_{(f+m)2}\mu_2}{k_{f1}\Big/\left(\phi C_t\right)_{(f+m)1}\mu_1} \tag{13}$$

and

$$\eta_{31} = \frac{k_{f3}\Big/\left(\phi C_t\right)_{(f+m)3}\mu_3}{k_{f1}\Big/\left(\phi C_t\right)_{(f+m)1}\mu_1} \tag{14}$$

As in the standard dual-porosity models, we also define the following dimensionless dual-porosity parameters. The storativity ratio is defined by

$$\omega_i = \frac{\left(\phi C_t\right)_{fi}}{\left(\phi C_t\right)_{(f+m)i}} \tag{15}$$

The interporosity flow coefficient is defined by

$$\lambda_i = \alpha \frac{k_{mi}}{k_{fi}} r_w^2 \tag{16}$$

where α is the interporosity shape factor and assumed to be identical for the three regions.

2.3 Fracture and matrix equations

Based on the assumptions and the coordinate system shown in Fig.1, the diffusivity equations governing the flow of a slightly compressible fluid in the fracture system of region I, region II and region III, respectively, are obtained by using the law of conservation of mass and are given by

$$-\nabla\cdot\left(\rho_1 v_{f1}\right)-\frac{q\delta(x-a)\delta(y-b)}{h_1}+q_1^*=\frac{\partial\left(\rho_1\phi_{f1}\right)}{\partial t}\ \text{ for }\ 0\le x\le L \tag{17}$$

$$-\nabla\cdot\left(\rho_2 v_{f2}\right)+q_2^*=\frac{\partial\left(\rho_2\phi_{f2}\right)}{\partial t}\ \text{ for }\ x\le 0 \tag{18}$$

$$-\nabla\cdot\left(\rho_3 v_{f3}\right)+q_3^*=\frac{\partial\left(\rho_3\phi_{f3}\right)}{\partial t}\ \text{ for }\ x\ge L \tag{19}$$

We now assume that Darcy's Law holds. We restrict our attention to Newtonian fluids and isothermal conditions. In this chapter, we restrict our attention to the isotropy case. Thus, the velocity of the fluid is given by

$$v_{fi}=-\frac{k_{fi}}{\mu_i}\nabla p_{fi}\quad i=1,2,3 \tag{20}$$

where the subscripts 1, 2 and 3 refer to regions I, region II and region III.

The total isothermal compressibility of the fracture system in region *i* is given by

$$C_{tfi}=\left(\frac{1}{\rho_i}\frac{\partial\rho_i}{\partial p_{fi}}\right)_{T=const}+\left(\frac{1}{\phi_i}\frac{\partial\phi_i}{\partial p_{fi}}\right)_{T=const}\quad i=1,2,3 \tag{21}$$

Insertions of the expressions on the right-hand sides of Eqs. (20) and (21) for the appropriate expressions in Eqs. (17) to (19) yield the following diffusion equations

$$\frac{\partial^2 p_{f1}}{\partial x^2}+\frac{\partial^2 p_{f1}}{\partial y^2}-\frac{q\mu_1\delta(x-a)\delta(y-b)}{k_{f1}h_1}+q_1^*=\frac{\left(\phi_f\mu C_{tf}\right)_1}{k_{f1}}\frac{\partial p_{f1}}{\partial t}\ \text{ for }\ 0\le x\le L \tag{22}$$

$$\frac{\partial^2 p_{f2}}{\partial x^2}+\frac{\partial^2 p_{f2}}{\partial y^2}+q_2^*=\frac{\left(\phi_f\mu C_{tf}\right)_2}{k_{f2}}\frac{\partial p_{f2}}{\partial t}\ \text{ for }\ x\le 0 \tag{23}$$

$$\frac{\partial^2 p_{f3}}{\partial x^2}+\frac{\partial^2 p_{f3}}{\partial y^2}+q_3^*=\frac{\left(\phi_f\mu C_{tf}\right)_3}{k_{f3}}\frac{\partial p_{f3}}{\partial t}\ \text{ for }\ x\ge L \tag{24}$$

where δ is the delta function denoting the constant-rate line-source well, and q^* is the volumetric flow rate from the matrix system to the fracture system.

Ignoring flow within the matrix system, the diffusivity equations for the matrix system of region I, region II and region III, are given by

$$\left(\phi_m C_{tm}\right)_1 \frac{\partial p_{m1}}{\partial t} + q_1^* = 0 \quad \text{for} \quad 0 \le x \le L \tag{25}$$

$$\left(\phi_m C_{tm}\right)_2 \frac{\partial p_{m2}}{\partial t} + q_2^* = 0 \quad \text{for} \quad x \le 0 \tag{26}$$

$$\left(\phi_m C_{tm}\right)_3 \frac{\partial p_{m3}}{\partial t} + q_3^* = 0 \quad \text{for} \quad x \ge L \tag{27}$$

Flow from the matrix system to the fracture system is proportional to the difference between the pressures of the two systems. If we assume pseudosteady flow from the matrix system to the fracture system (Warren and Root idealization), then we can also write

$$q_1^* = \alpha \frac{k_{m1}}{k_{f1}} \left(p_{m1} - p_{f1}\right) \tag{28}$$

$$q_2^* = \alpha \frac{k_{m2}}{k_{f2}} \left(p_{m2} - p_{f2}\right) \tag{29}$$

$$q_3^* = \alpha \frac{k_{m3}}{k_{f3}} \left(p_{m3} - p_{f3}\right) \tag{30}$$

Combining Eqs. (22) to (30), the following equations are obtained.

$$\frac{\partial^2 p_{f1}}{\partial x^2} + \frac{\partial^2 p_{f1}}{\partial y^2} - \frac{q\mu_1 \delta(x-a)\delta(y-b)}{k_{f1} h_1} + \alpha \frac{k_{m1}}{k_{f1}} \left(p_{m1} - p_{f1}\right) = \frac{\left(\phi_f \mu C_{tf}\right)_1}{k_{f1}} \frac{\partial p_{f1}}{\partial t}$$

$$\text{for} \quad 0 \le x \le L \tag{31}$$

$$\left(\phi_m C_{tm}\right)_1 \frac{\partial p_{m1}}{\partial t} + \alpha \frac{k_{m1}}{\mu_1} \left(p_{m1} - p_{f1}\right) = 0 \quad \text{for} \quad 0 \le x \le L \tag{32}$$

$$\frac{\partial^2 p_{f2}}{\partial x^2} + \frac{\partial^2 p_{f2}}{\partial y^2} + \alpha \frac{k_{m2}}{k_{f2}} \left(p_{m2} - p_{f2}\right) = \frac{\left(\phi_f \mu C_{tf}\right)_2}{k_{f2}} \frac{\partial p_{f2}}{\partial t} \quad \text{for} \quad x \le 0 \tag{33}$$

$$\left(\phi_m C_{tm}\right)_2 \frac{\partial p_{m2}}{\partial t} + \alpha \frac{k_{m2}}{\mu_2} \left(p_{m2} - p_{f2}\right) = 0 \quad \text{for} \quad x \le 0 \tag{34}$$

$$\frac{\partial^2 p_{f3}}{\partial x^2} + \frac{\partial^2 p_{f3}}{\partial y^2} + \alpha \frac{k_{m3}}{k_{f3}} \left(p_{m3} - p_{f3}\right) = \frac{\left(\phi_f \mu C_{tf}\right)_3}{k_{f3}} \frac{\partial p_{f3}}{\partial t} \quad \text{for} \quad x \ge L \tag{35}$$

$$\left(\phi_m C_{tm}\right)_3 \frac{\partial p_{m3}}{\partial t} + \alpha \frac{k_{m3}}{\mu_3}\left(p_{m3} - p_{f3}\right) = 0 \text{ for } x \geq L \tag{36}$$

Based on the definitions of dimensionless variables, Eqs. (31) to (36) can be written as

$$\frac{\partial^2 p_{Df1}}{\partial x_D^2} + \left(\frac{\pi}{w_D}\right)^2 \frac{\partial^2 p_{Df1}}{\partial y_D^2} + \frac{2\pi^2 \delta\left(x_D - a_D\right)\delta\left(y_D - b_D\right)}{w_D} = \omega_1 \frac{\partial p_{Df1}}{\partial t_D} - \lambda_1 \left(\frac{k_{f1}}{k_{m1}} p_{Dm1} - p_{Df1}\right)$$

$$\text{for } 0 \leq x_D \leq L_D \tag{37}$$

$$\lambda_1 \left(p_{Dm1} - \frac{k_{m1}}{k_{f1}} p_{Df1}\right) + \left(1 - \omega_1\right)\frac{\partial p_{Dm1}}{\partial t_D} = 0 \text{ for } 0 \leq x_D \leq L_D \tag{38}$$

$$\frac{\partial^2 p_{Df2}}{\partial x_D^2} + \left(\frac{\pi}{w_D}\right)^2 \frac{\partial^2 p_{Df2}}{\partial y_D^2} + \lambda_2 \left(\frac{k_{f1}}{k_{m1}} p_{Dm2} - p_{Df2}\right) = \frac{\omega_2}{\eta_{21}} \frac{\partial p_{Df2}}{\partial t_D} \text{ for } x_D \leq 0 \tag{39}$$

$$\lambda_2 \eta_{21} \left(p_{Dm2} - \frac{k_{m1}}{k_{f1}} p_{Df2}\right) + \left(1 - \omega_2\right)\frac{\partial p_{Dm2}}{\partial t_D} = 0 \text{ for } x_D \leq 0 \tag{40}$$

$$\frac{\partial^2 p_{Df3}}{\partial x_D^2} + \left(\frac{\pi}{w_D}\right)^2 \frac{\partial^2 p_{Df3}}{\partial y_D^2} + \lambda_3 \left(\frac{k_{f1}}{k_{m1}} p_{Dm3} - p_{Df3}\right) = \frac{\omega_3}{\eta_{31}} \frac{\partial p_{Df3}}{\partial t_D} \text{ for } x_D \geq L_D \tag{41}$$

$$\lambda_3 \eta_{31} \left(p_{Dm3} - \frac{k_{m1}}{k_{f1}} p_{Df3}\right) + \left(1 - \omega_3\right)\frac{\partial p_{Dm3}}{\partial t_D} = 0 \text{ for } x_D \geq L_D \tag{42}$$

The initial conditions can be described as

$$p_{Df1}\big|_{t_D=0} = p_{Df2}\big|_{t_D=0} = p_{Df3}\big|_{t_D=0} = 0 \tag{43}$$

and

$$p_{Dm1}\big|_{t_D=0} = p_{Dm2}\big|_{t_D=0} = p_{Dm3}\big|_{t_D=0} = 0 \tag{44}$$

The outer boundary conditions in x direction are

$$\lim_{x_D \to -\infty} p_{Df2} = 0 \tag{45}$$

and

$$\lim_{x_D \to \infty} p_{Df3} = 0 \tag{46}$$

The outer boundary conditions in y direction are

$$\left.\frac{\partial p_{Df1}}{\partial y_D}\right|_{y_D=\pi} = \left.\frac{\partial p_{Df1}}{\partial y_D}\right|_{y_D=0} = 0 \tag{47}$$

$$\left.\frac{\partial p_{Df2}}{\partial y_D}\right|_{y_D=\pi} = \left.\frac{\partial p_{Df2}}{\partial y_D}\right|_{y_D=0} = 0 \tag{48}$$

and

$$\left.\frac{\partial p_{Df3}}{\partial y_D}\right|_{y_D=\pi} = \left.\frac{\partial p_{Df3}}{\partial y_D}\right|_{y_D=0} = 0 \tag{49}$$

The pressure continuities at the interface state

$$p_{Df1}\Big|_{x_D=0} = p_{Df2}\Big|_{x_D=0} \tag{50}$$

and

$$p_{Df1}\Big|_{x_D=L_D} = p_{Df3}\Big|_{x_D=L_D} \tag{51}$$

By using the law of conservation of mass, the flow continuities at the interface satisfy

$$\left.\frac{\partial p_{Df1}}{\partial x_D}\right|_{x_D=0} = M_{21}h_{21}\left.\frac{\partial p_{Df2}}{\partial x_D}\right|_{x_D=0} \tag{52}$$

$$\left.\frac{\partial p_{Df1}}{\partial x_D}\right|_{x_D=L_D} = M_{31}h_{31}\left.\frac{\partial p_{Df3}}{\partial x_D}\right|_{x_D=L_D} \tag{53}$$

3. Model solution

The finite Fourier cosine transformation and Laplace transformation are employed to solve the dimensionless well testing model.

The finite Fourier cosine transformation is defined as (Farlow, 1982)

$$\hat{G}(m) = C_m = F\left[G(y)\right] = \int_0^{\pi} G(y)\cos(my)\,dy \tag{54}$$

where m is the Fourier variable with respect to y_D. The inverse Fourier cosine transformation is defined as

$$G(y) = F^{-1}\left[\hat{G}(m)\right] = \frac{C_0}{\pi} + \frac{2}{\pi}\sum_{m=1}^{\infty} C_m \cos(my) \tag{55}$$

The Laplace transformation is defined as

$$\overline{F}(u)=L\left[F(t)\right]=\int_0^{+\infty}F(t)e^{-ut}dt \tag{56}$$

where u is the Laplace variable with respect to time.

With Eqs. (43) and (48), the Laplace transformation with respect to t_D and the finite Fourier cosine transformation with respect to y_D of Eqs. (39) and (40) yield

$$\frac{d^2\hat{\bar{p}}_{Df2}}{dx_D^2}-\alpha_2\hat{\bar{p}}_{Df2}=0 \ \text{ for } \ x_D\le 0 \tag{57}$$

where $\alpha_2=\left(\frac{m\pi}{w_D}\right)^2+\frac{u\omega_2}{\eta_{21}}+\frac{\lambda_2 u(1-\omega_2)}{\lambda_2\eta_{21}+u(1-\omega_2)}$, $\hat{\bar{p}}_{Df2}$ is the dimensionless fracture pressure of region II in Fourier-Laplace space.

The solution to Eq. (57) with the outer boundary condition at $x_D\to-\infty$ is

$$\hat{\bar{p}}_{Df2}=Ae^{\sqrt{\alpha_2}x_D} \ \text{ for } \ x_D\le 0 \tag{58}$$

With Eqs. (43) and (49), the Laplace transformation with respect to t_D and the finite Fourier cosine transformation with respect to y_D of Eqs. (41) and (42) yield

$$\frac{d^2\hat{\bar{p}}_{Df3}}{dx_D^2}-\alpha_4\hat{\bar{p}}_{Df3}=0 \ \text{ for } \ x_D\ge L_D \tag{59}$$

where $\alpha_4=\left(\frac{m\pi}{w_D}\right)^2+\frac{u\omega_3}{\eta_{31}}+\frac{\lambda_3 u(1-\omega_3)}{\lambda_3\eta_{31}+u(1-\omega_3)}$, $\hat{\bar{p}}_{Df3}$ is the dimensionless fracture pressure of region III in Fourier-Laplace space.

The solution to Eq. (59) with the outer boundary condition at $x_D\to\infty$ is

$$\hat{\bar{p}}_{Df3}=De^{-\sqrt{\alpha_4}x_D} \ \text{ for } \ x_D\ge L_D \tag{60}$$

With Eqs. (43) and (47), the Laplace transformation with respect to t_D and the finite Fourier cosine transformation with respect to y_D of Eqs. (37) and (38) yield

$$\frac{d^2\hat{\bar{p}}_{Df1}}{dx_D^2}-\alpha_1\hat{\bar{p}}_{Df1}=\alpha_3\delta(x_D-a_D) \ \text{ for } \ 0\le x_D\le L_D \tag{61}$$

where $\alpha_1=\left(\frac{m\pi}{w_D}\right)^2+u\omega_1+\frac{\lambda_1 u(1-\omega_1)}{\lambda_1+u(1-\omega_1)}$, $\alpha_3=-\frac{2\pi^2\cos(mb_D)}{uw_D}$, $\hat{\bar{p}}_{Df1}$ is the dimensionless fracture pressure of region I in Fourier-Laplace space.

The solution of Eq. (61) is not readily accessible because of the delta function at the right hand side. The Laplace transformation of Eq. (61) with respect to x_D yields

$$s^2 W_1 - s\hat{\bar{p}}_{Df1}(x_D=0) - \frac{\partial \hat{\bar{p}}_{Df1}}{\partial x_D}(x_D=0) - \alpha_1 W_1 = \alpha_3 e^{-a_D s} \tag{62}$$

where s is the Laplace variable with respect to x_D, and W_1 refers to $\hat{\bar{p}}_{Df1}$ in Laplace space with respect to x_D. Rearranging Eq. (62) and solving for W_1 yields

$$W_1 = \frac{\alpha_3 e^{-a_D s} + \frac{\partial \hat{\bar{p}}_{Df1}}{\partial x_D}(x_D=0) + s\hat{\bar{p}}_{Df1}(x_D=0)}{s^2 - \alpha_1} \tag{63}$$

A term-by-term Laplace inversion transformation and using conditions at the interface, yields

$$\hat{\bar{p}}_{Df1}(x_D,m,u) = A\frac{e^{\sqrt{\alpha_1}x_D} + e^{-\sqrt{\alpha_1}x_D}}{2} + \frac{AM_{21}h_{21}\sqrt{\alpha_2}}{\sqrt{\alpha_1}}\frac{e^{\sqrt{\alpha_1}x_D} - e^{-\sqrt{\alpha_1}x_D}}{2} \quad \text{for } 0 \le x_D \le a_D \tag{64}$$

and

$$\begin{aligned}&\hat{\bar{p}}_{Df1}(x_D,m,u)\\ &= \frac{\alpha_3}{\sqrt{\alpha_1}}\frac{e^{\sqrt{\alpha_1}(x_D-a_D)} - e^{-\sqrt{\alpha_1}(x_D-a_D)}}{2} + A\frac{e^{\sqrt{\alpha_1}x_D} + e^{-\sqrt{\alpha_1}x_D}}{2} + \frac{AM_{21}h_{21}\sqrt{\alpha_2}}{\sqrt{\alpha_1}}\frac{e^{\sqrt{\alpha_1}x_D} - e^{-\sqrt{\alpha_1}x_D}}{2}\\ &\qquad \text{for } a_D \le x_D \le L_D\end{aligned} \tag{65}$$

With Heaviside unit step function, Eqs. (64) and (65) can be rearranged as

$$\begin{aligned}&\hat{\bar{p}}_{Df1}(x_D,m,u)\\ &= \frac{\alpha_3}{\sqrt{\alpha_1}}\frac{e^{\sqrt{\alpha_1}(x_D-a_D)} - e^{-\sqrt{\alpha_1}(x_D-a_D)}}{2}H(x_D-a_D) \qquad \text{for } 0 \le x_D \le L_D\\ &+ A\frac{e^{\sqrt{\alpha_1}x_D} + e^{-\sqrt{\alpha_1}x_D}}{2} + \frac{AM_{21}h_{21}\sqrt{\alpha_2}}{\sqrt{\alpha_1}}\frac{e^{\sqrt{\alpha_1}x_D} - e^{-\sqrt{\alpha_1}x_D}}{2}\end{aligned} \tag{66}$$

With Eq. (51) and Eq. (53), Eq. (66) yields

$$\begin{aligned}&\hat{\bar{p}}_{Df1}(x_D,m,u)\\ &= \frac{\alpha_3}{2\sqrt{\alpha_1}}\left[e^{\sqrt{\alpha_1}(x_D-a_D)} - e^{-\sqrt{\alpha_1}(x_D-a_D)}\right]H(x_D-a_D)\\ &+ \frac{\alpha_3}{2\sqrt{\alpha_1}}\frac{ge^{\sqrt{\alpha_1}(x_D-2L_D+a_D)} - e^{\sqrt{\alpha_1}(x_D-a_D)} + fge^{-\sqrt{\alpha_1}(x_D+2L_D-a_D)} - fe^{-\sqrt{\alpha_1}(x_D+a_D)}}{1+fge^{-2\sqrt{\alpha_1}L_D}}\end{aligned}$$

$$\text{for } 0 \le x_D \le L_D \tag{67}$$

where $f = \dfrac{\sqrt{\alpha_1} - M_{21}h_{21}\sqrt{\alpha_2}}{\sqrt{\alpha_1} + M_{21}h_{21}\sqrt{\alpha_2}}$, $g = \dfrac{M_{31}h_{31}\sqrt{\alpha_4} - \sqrt{\alpha_1}}{M_{31}h_{31}\sqrt{\alpha_4} + \sqrt{\alpha_1}}$.

Eq. (67) is of an exponential form in the x_D variable, and the Laplace time variable and the Fourier y_D variable are in the α terms as described above. This is a general solution that gives the pressure response at any point in the reservoir. It can be used to compute the response at the wellbore, which is done in this chapter. The dimensionless wellbore pressure drawdown then can be calculated by setting x_D=a_D-1 and y_D=b_D in Eq. (67), that is

$$\hat{\bar{p}}^{*}_{wfD}(m,u) = \frac{\alpha_3}{2\sqrt{\alpha_1}} \frac{ge^{\sqrt{\alpha_1}(2a_D - 2L_D - 1)} - e^{-\sqrt{\alpha_1}} + fge^{-\sqrt{\alpha_1}(2L_D - 1)} - fe^{\sqrt{\alpha_1}}}{1 + fge^{-2\sqrt{\alpha_1}L_D}} \tag{68}$$

The wellbore storage and skin are not included in the dimensionless wellbore pressure calculated by the above equation.

4. Computational considerations

In the preceding sections, we have developed a solution for a well in a three-zone linear composite dual-porosity reservoir. In fact, obtaining the solution for the pressure distribution is only the first step toward the computation of well responses. The major contribution of this section is to provide the means to compute the solution presented in the preceding sections.

4.1 Wellbore storage

When a well is opened, the production at surface is initially due to the expansion of the fluid stored in the wellbore, and the reservoir contribution is initially negligible. This characteristic flow regime, called the pure wellbore storage effect, can last from a few seconds to a few minutes. Then, the reservoir production starts and the sand face rate increases until it becomes the same as the surface rate. When this condition is reached, the wellbore storage has no effect any more on the bottom hole pressure response, the data describes the reservoir behavior and it can be used for transient analysis.

After any change in the well flowing conditions, there is a time lag between the surface production and the sand face rate. The effect of wellbore storage affects well pressure responses during the first instants of each test period. In this chapter, only drawdown responses are illustrated. The wellbore storage coefficient C is used to describe this process (Bourdet, 2000).

4.2 Skin

For a damaged well, an additional pressure drop Δp_s is present when the reservoir fluid enters into the well. The magnitude of Δp_s reflect the extent of reservoir damage. However, the same Δp_s can describe a low or very high damage, depending on the flow rate and the

reservoir property. For comparison between different wells, the magnitude of the pressure drop near the wellbore has to be normalized. The skin factor S, a dimensionless parameter, is introduced to normalize the pressure drop.

The wellbore pressure with effects of wellbore storage and skins in Laplace space is calculated by using Duhamel principle expressed by the following equation

$$\hat{\bar{p}}_{wfD} = \frac{u\hat{\bar{p}}^{*}_{wfD} + S}{u\left[1 + uC_D\left(u\hat{\bar{p}}^{*}_{wfD} + S\right)\right]} \tag{69}$$

where C_D is the dimensionless wellbore storage coefficient, $\hat{\bar{p}}^{*}_{wfD}$ is the dimensionless wellbore pressure drop with zero skin and wellbore storage in Laplace-Fourier space, which is calculated by Eq. (69). And $\hat{\bar{p}}_{wfD}$ is the dimensionless wellbore pressure drop incorporating wellbroe storage and skin in Laplace-Fourier space.

4.3 Finite Fourier transformation inversion

The solution presented in the preceding section is in the Laplace-Fourier domain. To obtain the wellbore pressure response in real space, an accurate Fourier inversion is needed. The Fourier cosine transformation used in this chapter is inverted numerically with Eq. (55). The convergence in numerical inversion of the Fourier transformation is assumed to be reached if the absolute value of the ratio of the sum of the m, m-1 and m-2 terms in Eq. (55) to the total sum is less than 10^{-14}. In some cases, the solution converges extremely slowly – in fact, for certain time ranges the series behave as if it is a divergent. More than 1000 terms in Eq. (55) are required at early time to achieve convergence.

4.4 Laplace transformation inversion

The Stehfest algorithm is used to invert the Laplace transformation numerically. The fundamental principle of Stehfest algorithm is given by

$$p_{wfD}\left(t_D\right) = \frac{\ln 2}{t_D}\sum_{i=1}^{N} V\left(i\right)\bar{p}_{wfD}\left[s\left(i\right)\right] \tag{70}$$

where

$$s\left(i\right) = \frac{\ln 2}{t_D} i \tag{71}$$

$$V\left(i\right) = \left(-1\right)^{\frac{N}{2}+i} \sum_{k=\left\lfloor\frac{i+1}{2}\right\rfloor}^{\min\left\{\frac{N}{2},i\right\}} \frac{k^{\frac{N}{2}+1}\left(2k\right)!}{\left(\frac{N}{2}-k\right)!\left(k!\right)^2\left(i-k\right)!\left(2k-i\right)!} \tag{72}$$

At this point, a remark on the use of the Stehfest algorithm appears to be appropriate. The accuracy of the results obtained by using the numerical inversion algorithm suggested by

Stehfest is governed by a parameter denoted by N. Briefly, the parameter N determines the number of terms to be considered in the computation of the series used to approximate the Laplace inversion of the subject function. Theoretically, the accuracy of the numerical inversion should improve as the value of N increases. In practice, however, as N becomes too large, the result suffers from rounding errors. In this chapter, the inversion of the Laplace transformation is performed using Stehfest algorithm, with n=6. This allows us to relax the convergence criteria, because for n=8 or n=10, the inverse Fourier transform would be longer to compute, as Stehfest algorithm would require a higher precision.

5. Type curves and discussions

The pressure-transient behavior of a well in a three-zone linear composite dual-porosity reservoir with varied thickness and lateral heterogeneity is presented in this section. The steps to generate the type curves are as follows

1. The finite Fourier cosine transformation is inverted numerically.
2. The Laplace transformation is inverted numerically by Stehfest algorithm.
3. Calculate the wellbore pressure responses in real space.
4. Plot the type curves (log-log graph of pressure and derivative) based on the results obtained from the steps above.

The characteristics of type curves and the effects of correlating parameters are presented as follows. It is recognized that there are a number of variables which may affect the characteristics of type curves, such as thickness ratio, mobility ratio, transmissibility ratio, well location in the reservoir (a_D and b_D) and reservoir width w_D. The effects of all these parameters on type curves are discussed in detailed in this chapter.

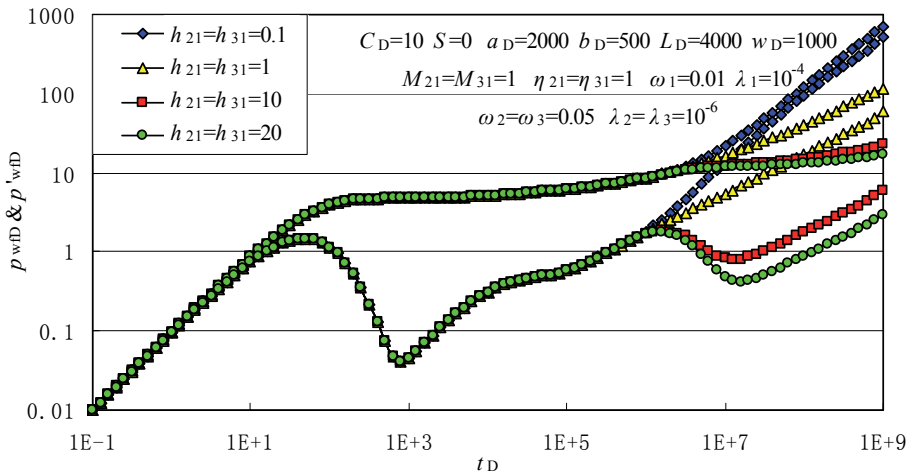

Fig. 2. Effect of thickness ratio on pressure responses for a well in a three-zone linear composite dual-porosity reservoir (h_{21}=h_{31})

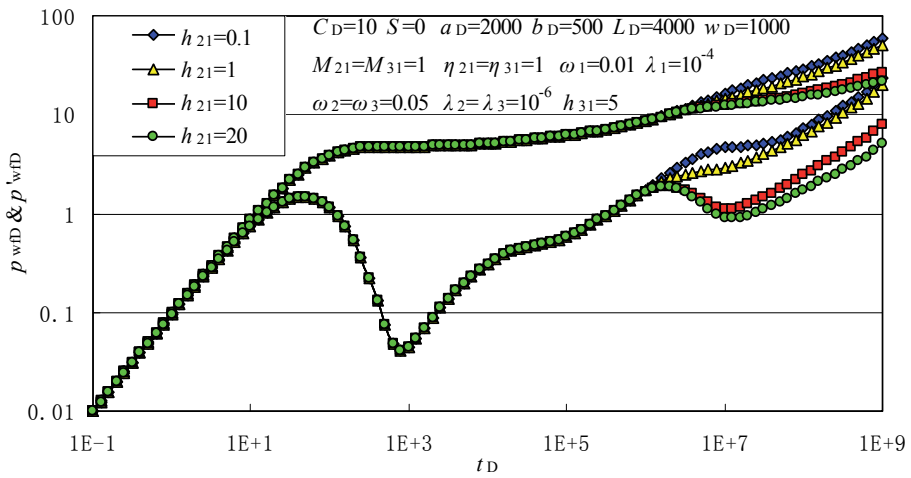

Fig. 3. Effect of thickness ratio on pressure responses for a well in a three-zone linear composite dual-porosity reservoir (h_{21}≠h_{31})

Figs.2 and 3 depict the pressure responses as a result of varied thickness ratios. Wellbore storage period, interporosity flow period and total radial flow period in region I can be observed from all the two figures. The effect of thickness ratio on type curves becomes obvious after the pressure wave reaches the interface.

It is can be seen that because the parallel impermeable boundaries are closer to the well than the facies changes, thus the derivative first displays the 1/2 slope characteristic of linear flow. Before the pressure wave reaches the interface, the wellbore pressure drawdown merely depends on reservoir properties of region I and has nothing to do with thickness ratio. Once the pressure wave reaches the interface, the following pressure behavior then is the result of average reservoir values of region I, region II and region III.

For the case the thickness ratio bigger than unit, after the pressure wave reaching the interface, the average flow capacity improves and the pressure drop consumed in fluid flow in reservoir decreases, the elevations of dimensionless pressure and pressure derivative curves get lower. The greater the thickness ratio is, the lower the pressure and pressure derivative curves are. Whereas if the thickness ratio is smaller than unit, after the pressure wave reaching the interface, the average flow capacity recedes and the pressure drop consumed in fluid flow in reservoir increases, the elevations of dimensionless pressure and pressure derivative curves get higher. The smaller the thickness ratio is, the higher the pressure and pressure derivative curves are.

In addition, Fig.2 also presents the limiting case that when the thickness of outer region (i.e. region II and III) is small enough, the derivative finally displays a unit slope instead of a 1/2 slope which is the characteristic of a closed system.

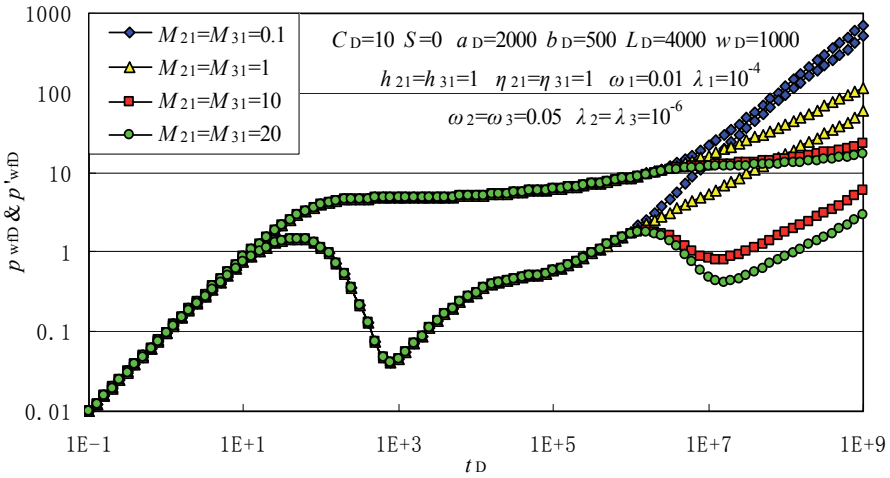

Fig. 4. Effect of mobility ratio on pressure responses for a well in a three-zone linear composite dual-porosity reservoir ($M_{21}=M_{31}$)

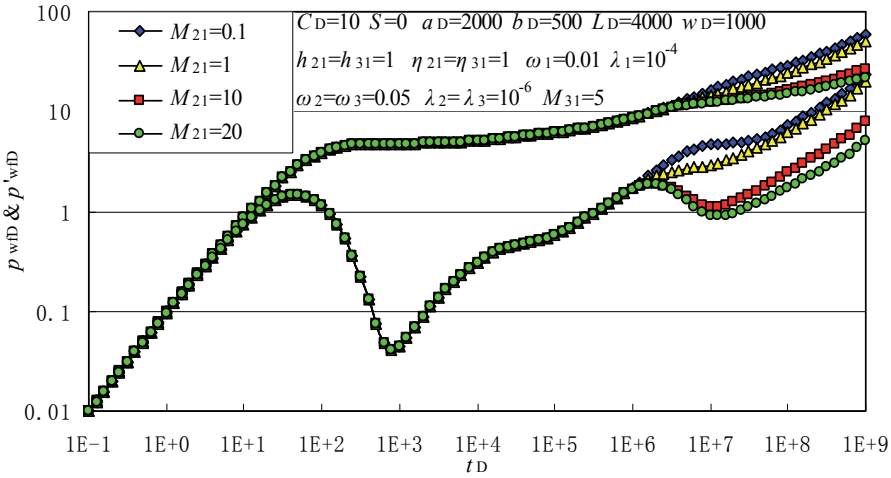

Fig. 5. Effect of mobility ratio on pressure responses for a well in a three-zone linear composite dual-porosity reservoir ($M_{21}\neq M_{31}$)

Figs.4 and 5 show the effect of mobility ratio on the pressure responses with other fixed parameters presented in the figure. It can be observed that the effect of mobility ratio is similar to that of thickness ratio. The effect of mobility ratio on type curves becomes obvious once the discontinuity is felt.

For the case the mobility ratio bigger than unit, after the pressure wave reaching the interface, the elevations of dimensionless pressure and pressure derivative curves get lower. That is because a higher mobility ratio means that the outer region is more permeable than the inner region. Thus, the pressure drop is smaller with a same time. The greater the mobility ratio is, the lower the pressure and pressure derivative curves are. In contrast, whereas if the mobility ratio is smaller than unit, after the pressure wave reaching the interface, the elevations of

dimensionless pressure and pressure derivative curves get higher. The smaller the mobility ratio is, the higher the pressure and pressure derivative curves are.

Fig.4 also presents the limiting case that when the mobility of outer region (i.e. region II and III) is small enough, the derivative finally displays a unit slope instead of a 1/2 slope which is the characteristic of a closed system.

Fig. 6 shows the effect of transmissibility ratio on the pressure responses with other fixed parameters presented in the figure. Similar flowing periods can be observed as in Figs.2 and 3. The larger the magnitude of transmissibility ratio, the higher the pressure drop after the discontinuity is felt. That is because when the mobility ratio and thickness ratio are fixed, a higher transmissibility ratio means the product of porosity and the total system compressibility of outer region is smaller than that of the inner region, i.e., the outer region is much less compressible. Thus, the pressure drop is larger with higher transmissibility ratio.

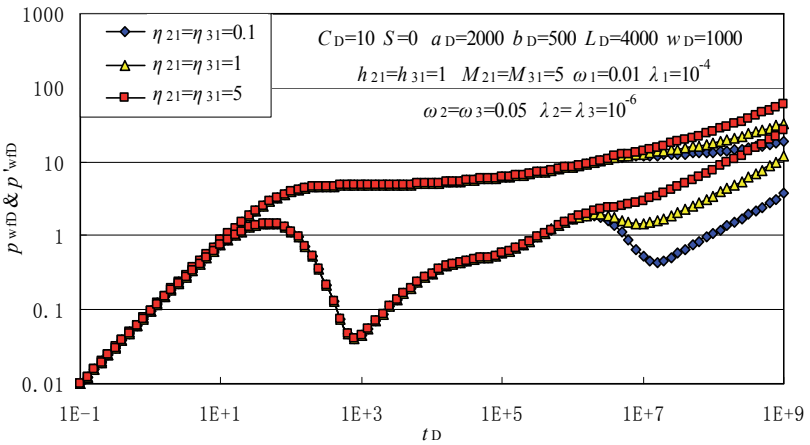

Fig. 6. Effect of transmissibility ratio on pressure responses for a well in a three-zone linear composite dual-porosity reservoir (η_{21}=η_{31})

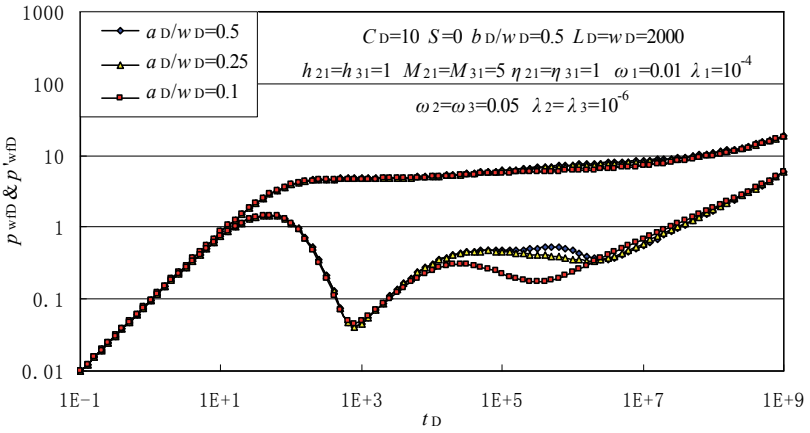

Fig. 7. Effect of well location (a_D) on pressure responses for a well in a three-zone linear composite dual-porosity reservoir

The location of the well in the reservoir is described by two parameters: a_D and b_D. Figs.7 and 8 present the effects of a_D and b_D, respectively, on the pressure transient behavior for a well in a three-zone linear composite dual-porosity reservoir with varied thickness and lateral heterogeneity.

Fig.7 presents the effect of different well locations in the x direction on the pressure transient responses with b_D/w_D=0.5 and L_D=w_D. As shown in Fig.7, wellbore storage period, interporosity flow period and total radial flow period in region I are almost identical for different values of a_D.

For the case of a_D/w_D=0.5, the well is located in the center of region I. The distances between the well and the four boundaries are equal, thus all four boundaries (two parallel impermeable boundaries and two discontinuities) are felt concurrently. After a short transition period, the derivative approached the half-slope line which is characteristic of linear flow in the total system. For a_D/w_D=0.25 and a_D/w_D=0.1, the well is closer to the discontinuity than to the impermeable boundary, so the discontinuity between region I and II is felt first as the departure of derivative from the value of 0.5. Then, the effects of two parallel impermeable boundaries are felt and the discontinuity between region I and III last. At late time, however, all curves approach linear flow behavior illustrated by the half-slope lines on the log-log graphs, irrespective of the magnitude of a_D. That is because when all discontinuities and impermeable boundaries are encountered, the fluid flow in the reservoir depends on the average properties of the linear composite reservoir, so the well location a_D has little effect on the late phase of the pressure responses.

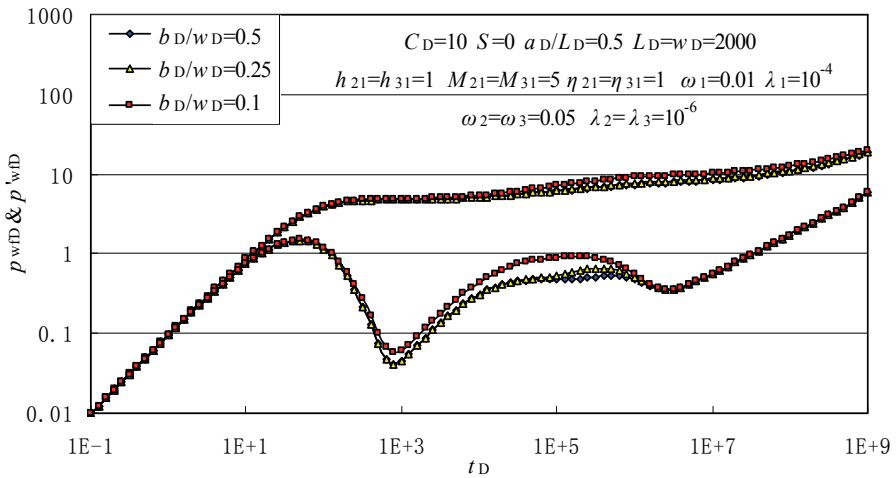

Fig. 8. Effect of well location (b_D) on pressure responses for a well in a three-zone linear composite dual-porosity reservoir

Fig.8 presents the effect of different well locations in the y direction on the pressure transient responses with a_D/L_D=0.5 and L_D=w_D. Again, the departures of the pressure derivative occur whenever one or more boundaries are felt. For example, for the case of a_D/L_D and b_D/w_D both equal to 0.5, two parallel impermeable boundaries and two discontinuities are felt at the same time. The flow in the reservoir is then dominated by the linear flow in the total system. For the case of b_D/w_D=0.25 and b_D/w_D =0.1, the effect of the lower impermeable boundary of the strip reservoir (Fig.1) is felt. At this time, flow in the reservoir is somewhat like that in an infinite reservoir with one fault boundary, thus the pressure derivative double its value to one. The doubling of constant derivative can be observed if the well is closer to one impermeable boundary. Fig.8 also illustrates that the well location b_D has little effect on the late phase of the pressure responses.

6. Conclusions

1. A new analytical solution for the pressure-transient behavior of a line-source well producing at a constant rate in a three-zone, linear composite dual-porosity reservoir is presented in Laplace-Fourier space, which takes into account the changes in reservoir thickness, wellbore storage effect and skin factor. It can easily be inverted to real space, and it is especially useful in predicting pressure performance or analyzing test data from this type of reservoir configuration.
2. Behavior of the solution at the wellbore has been analyzed with help of the pressure derivative. Sensitivity study is done and the effects of relevant parameters, such as thickness ratio, mobility ratio, transmissibility ratio, and the well location, on the pressure transient responses for a well in this type of reservoir are discussed. The late-time linear flow characteristic of strip reservoirs is observed in all curves, irrespective of mobility ratio, thickness ratio, well location or transmissibility ratio.
3. Determination of relevant parameters from the field test data is not straightforward because the pressure response depends on the property contrasts between regions and the location of the well.
4. The mathematical model proposed in this chapter is based on oil reservoir conditions; it is also applicable to gas reservoirs by replacing the pressure term with a pseudo-pressure term.
5. The model proposed in this chapter is for three-zone linear composite dual-porosity reservoirs, but could also be used for analyzing well test data from two-zone linear composite dual-porosity reservoirs.

7. Acknowledgments

This work was supported by National Science Fund for Distinguished Young Scholars of China (Grant No. 51125019), the National Program on Key Basic Research Project (973 Program, Grant No. 2011CB201005) and the Doctoral Fund of Ministry of Education of China (Grant No. 20105121110006).

8. Nomenclature

a = distance between the well and the interface between region I and II

a_D = dimensionless distance between the well and the left interface
b = y coordinate of well location
b_D = dimensionless y coordinate of well location
C_{tf1} = total fracture system compressibility of region I
C_{tf2} = total fracture system compressibility of region II
C_{tf3} = total fracture system compressibility of region III
C_{tm1} = total matrix system compressibility of region I
C_{tm2} = total matrix system compressibility of region II
C_{tm3} = total matrix system compressibility of region III
h_1 = reservoir thickness of region I
h_2 = reservoir thickness of region II
h_3 = reservoir thickness of region III
h_{21} = ratio of thickness of region II to thickness of region I
h_{31} = ratio of thickness of region III to thickness of region I
k_{f1} = fracture permeability of region I
k_{f2} = fracture permeability of region II
k_{f3} = fracture permeability of region III
k_{m1} = matrix permeability of region I
k_{m2} = matrix permeability of region II
k_{m3} = matrix permeability of region III
L = x-extent of region I
m = Fourier variable with respect to y_D
M_{21} =ratio of mobility of region II to mobility of region I
M_{31} =ratio of mobility of region III to mobility of region I
p_{Df1} = dimensionless fracture pressure of region I
p_{Df2} = dimensionless fracture pressure of region II
p_{Df3} = dimensionless fracture pressure of region III
p_{Dm1} = dimensionless matrix pressure of region I
p_{Dm2} = dimensionless matrix pressure of region II
p_{Dm3} = dimensionless matrix pressure of region III
p_{f1} = fracture pressure of region I
p_{f2} = fracture pressure of region II
p_{f3} = fracture pressure of region III
p_{m1} = matrix pressure of region I
p_{m2} = matrix pressure of region II
p_{m3} = matrix pressure of region III
p_i = initial reservoir pressure
q = flow rate at sandface
q_1^* = volumetric flow rate from the matrix system to the fracture system in region I
q_2^* = volumetric flow rate from the matrix system to the fracture system in region II
q_3^* = volumetric flow rate from the matrix system to the fracture system in region III
r_w = wellbore radius
S = skin factor

s = Laplace variable with respect to x_D
t = production time
t_D = dimensionless time
u = Laplace variable with respect to time
v_{f1} = velocity in fracture system of region I
v_{f2} = velocity in fracture system of region II
v_{f3} = velocity in fracture system of region III
w = reservoir width
w_D = dimensionless reservoir width
x = x coordinate of a point
x_D = dimensionless distance in x direction
y = y coordinate of appoint
y_D = dimensionless distance in y direction
α = shape factor
μ = fluid viscosity
ρ_1 = density of fluid in region I
ρ_2 = density of fluid in region II
ρ_3 = density of fluid in region III
ω_1 = storativity ratio of region I
ω_2 = storativity ratio of region II
ω_3 = storativity ratio of region III
λ_1 = interporosity flow coefficient of region I
λ_2 = interporosity flow coefficient of region II
λ_3 = interporosity flow coefficient of region III
ϕ_{f1} = fracture porosity of region I
ϕ_{f2} = fracture porosity of region II
ϕ_{f3} = fracture porosity of region III
ϕ_{m1} = matrix porosity of region I
ϕ_{m2} = matrix porosity of region II
ϕ_{m3} = matrix porosity of region III
δ = delta function denoting the constant-rate line-source well
η_{21} = ratio of transmissibility of region II to transmissibility of region I
η_{31} = ratio of transmissibility of region III to transmissibility of region I
Δp_s = additional pressure drop near the wellbore
p_{wfD} = wellbore pressure drop
$\hat{\bar{p}}^*_{wfD}$ =dimensionless wellbore pressure drop with zero skin and wellbore storage in Laplace-Fourier space
$\hat{\bar{p}}_{wfD}$ = dimensionless wellbore pressure drop incorporating wellbroe storage and skin in Laplace-Fourier space

8.1 Superscripts

¯ = Laplace transformation

^ = Finite Fourier cosine transformation

9. References

Bourdet, D. (2002). *Well Test Analysis: The Use of Advanced Interpretation Models* (First edition), Elsevier Science, ISBN 0-444-50968-2, Amsterdam

Farlow, S.J. (1982). *Partial Differential Equations for Scientists and Engineers*, John Wiley and Sons Inc., ISBN 0-486-97620, New York

Guo, J.C. & Xiang, K.L. (1999) Well Testing Analysis Model and Numerical Solution for a Composite Reservoir with Non-uniform Thickness and Double Media. *Well Testing*, Vol.8, No.1, pp.1-5, ISSN 1004-4388

Han, Y.L.; Huang, B.G.; Wang, N.T. & Wu, Y.M. (2007). Pressure Analysis of Double Porosity Composite Infinite Boundary Reservoir. *Drilling & Production Technology*, Vol.31, No.2, pp.83-85, ISSN 1000-7393

Huang, B.G.; Li, S.C.; Li, X.X. & Wang, N.T. (2002). Solution Analysis of The Bottom Pressure in Dual Porous Composite Reservoir. *Journal of Southwest Petroleum Institute*. Vol.24, No.6, pp. 25-27, ISSN 1674-5086

Huang, L. & Liu, Q.G. (2006). Percolation Mathematic Model in Compound Gas Reservoir with Dual Medium of Excessive Sections. *Well Testing*, Vol.15, No.4, pp.11-14, ISSN 1004-4388

Kikani, J. & Walkup, G.W. (1991). Analysis of Pressure-Transient Tests for Composite Naturally Fractured Reservoirs. *SPEFE*, Vol.6, No.2, pp. 176~182, ISSN 0885-923X

Li, R.Y.; Sun, W.T.; Li, S.C.; Huang, B.G. & Yang, H. (2007). Solution Analysis of Pressure Distribution in Composite Bounded Reservoir with Two Porous Media. *Drilling & Production Technology*. Vol.30, No.1, pp. 54~56, ISSN 1000-7393

Olarewaju J.S. & Lee W.J. (1991). Rate Behavior of Composite Dual-Porosity Reservoirs. *Paper 21703 presented at SPE Production Operations Symposium*, ISBN 978-1-55563-530-5, Oklahoma, 7-9 April 1991

Poon, D.C.C. (1984). Pressure Transient Analysis of a Composite Reservoir with Uniform Fracture Distribution, In: *SPE Paper 13384*, 1984, Availabe from http://www.onepetro.org/mslib/app/Preview.do?paperNumber=00013384&societyCode=SPE

Prado, L.R. & Da Prat, G. (1987). An Analytical Solution for Unsteady Liquid Flow in a Reservoir with a Uniformly Fractured Zone Around the Well. *Paper 16395 presented at SPE Low Permeability Reservoirs Symposium*, ISBN 978-1-55563-595-4, Denver, Colorado, 18-19 May 1987

Satman, A. (1991). Pressure-Transient Analysis of a Composite Naturally Fractured Reservoir. *SPEFE*, Vol.6, No.2, pp.169-175, ISSN 0885-923X

Zhang, L.H.; Guo, J.J. & Liu, Q.G. (2010). A Well Test Model for Stress-Sensitive and Heterogeneous Reservoir with Non-uniform Thickness. *Petroleum Science*, Vol.7, No.4, pp.524-529, ISSN 1625-5107

Zhang, L.H.; Guo, J.J. & Liu, Q.G. (2010). A New Well Test Model for a Two-zone Linear Composite Reservoir with Varied Thicknesses. *Journal of Hydrodynamics*, Vol.22, No.6, pp.804-809, ISBN 1001-6058

Part 2

The New Technology in Laboratory Experiments, Numerical Models, and Engineering Applications

6

Thermo-Hydrodynamics of Internally Heated Molten Salts for Innovative Nuclear Reactors

Lelio Luzzi, Manuele Aufiero, Antonio Cammi and Carlo Fiorina
Politecnico di Milano - Department of Energy
Enrico Fermi Centre For Nuclear Studies (CeSNEF)
Italy

1. Introduction

The problem of heat transfer in pipe flow has been extensively investigated in the past. Many different models have been proposed and adopted to predict the velocity profile, the eddy diffusivity, the temperature distributions, the friction factor and the heat transfer coefficient (Kays et al., 2004; Schlichting & Gersten, 2000). However, the majority of such studies give a description of the problem for non-internally heated fluids. Models regarding fluids with internal heat generation have been developed more than 50 years ago (Kinney & Sparrow, 1966; Poppendiek, 1954; Siegel & Sparrow, 1959), giving in most cases a partial treatment of the problem in terms of boundary conditions and heat source distribution, and relying on a turbulent flow treatment that does not seem fully satisfactory in the light of more recent investigations (Churchill, 1997; 2002; Kays, 1994; Zagarola & Smits, 1997). Internally heated fluids are of great interest in the current development of Molten Salt Reactors (MSR) (LeBlanc, 2010), included as one of the six innovative nuclear reactors selected by the Generation IV International Forum (GIF-IV, 2002) for a more sustainable version of nuclear power. MSRs are circulating fuel reactors (Nicolino et al., 2008), which employ a non-classical (fluid-type) fuel constituted by a molten halide (fluoride or chloride) salt mixture playing the distinctive role of both heat source and coolant. By adopting classical correlations for the Nusselt number (e.g., Dittus-Boelter), the heat transfer coefficient of the MSR fuel can be overestimated by a non-negligible amount (Di Marcello et al., 2008). In the case of thermal-neutron-spectrum (graphite-moderated) MSRs (LeBlanc, 2010), this has significant consequences on the core temperature predictions and on the reactor dynamic behaviour (Luzzi et al., 2011). Such influence of the heat source within the fluid cannot be neglected, and thus required proper investigation. The present chapter deals with this critical issue, first summarizing the main modelling efforts carried out by the authors (Di Marcello et al., 2010; Luzzi et al., 2010) to investigate the thermo-hydrodynamics of internally heated fluids, and then focusing on the heat transfer coefficient prediction that is relevant for analysing the molten salt behaviour encountered in MSRs.

The chapter is organized as follows. Section 2 provides a brief description of the Molten Salt Reactors, focusing on their distinctive features, in terms of both sustainability (i.e., reduced radioactive waste generation, effective use of natural resources) and safety, with respect to the traditional configuration of nuclear reactors. Section 3 deals with the study of molten salt heat transfer characteristics, which represent a key issue in the current development of MSRs. In

particular, a "generalized approach" to evaluate the steady-state temperature distribution in a representative power channel of the reactor core is presented. This approach incorporates recent formulations of turbulent flow and convection (Churchill, 1997; 2002), and is built in order to carefully take into account the molten salt mixture specificities, the reactor core power conditions and the heat transfer in the graphite core structure. In Section 4, a preliminary correlation for the Nusselt number prediction is advanced in the case of simultaneous uniform wall heat flux and internal heat generation, on the basis of the results achieved by means of the presented generalized approach. In Section 5, the main conclusions of the present study are summarized.

2. Innovative nuclear reactors based on the molten salt technology

In the recent years, there has been a growing interest in Molten Salt Reactors, which have been considered in the framework of the Generation IV International Forum (GIF-IV, 2002; 2009), because of their several potentialities and favourable features when compared with conventional solid-fuelled reactors (Forsberg et al., 2003; Furukawa et al., 2008; Hargraves & Moir, 2010; LeBlanc, 2010; Renault et al., 2010). Actually, MSRs meet many of the future goals of nuclear energy, in particular for what concerns an improved sustainability, an inherent safety, and unique characteristics in terms of actinide burning and waste reduction (Nuttin et al., 2005), while benefiting from the past experience acquired at ORNL[1] with the molten salt technology.

Different from other GIF-IV projects, a specific reference configuration for the MSR has not been identified yet (GIF-IV, 2009). Current R&D activities on MSRs are devoted to this subject and many reactor configurations have been proposed until now (Luzzi et al., 2011). A molten salt reactor can be designed considering both thermal- and fast-neutron spectrum, and can operate as incinerator or breeder or converter (Forsberg, 2002), in critical or sub-critical (i.e., driven by an external neutron source) conditions. An example of the layout of a typical MSR is given in Fig. 1. The primary molten salt mixture[2] flows through the reactor core (constituted by graphite, if a thermal-neutron-spectrum reactor is under consideration) to a primary heat exchanger, where the heat is transferred to a secondary molten salt coolant. The primary salt then flows back to the reactor core. The heat is generated inside the core directly by the primary molten salt mixture, which plays the distinctive role of both fuel and coolant. The liquid fuel salt typically enters the reactor vessel at 560°C and exits at 700°C, with a pressure of $\sim$1 atmosphere. The secondary coolant loop transfers the heat to the power cycle (a multi-reheat helium Brayton cycle or a steam Rankine cycle) or to an hydrogen production facility (Forsberg et al., 2003).

MSRs are based on a liquid fuel, so that their technology is fundamentally different from the solid fuel technologies currently in use or envisaged in future for the other GIF-IV reactor concepts. Some of the advantages specific to MSRs (for instance, in terms of safety) originate directly from this characteristic, as pointed out in the next subsection. Furthermore, these types of reactor are particularly well adapted to the thorium fuel cycle (^{232}Th-^{233}U), which

[1] See www.ornl.gov/info/library or www.energyfromthorium.com/pdf/.

[2] Typically, fluorides of fissile and/or fertile elements such as UF_4, PuF_3 and/or ThF_4 are combined with carrier salts to form fluids. The most common carrier salt proposed are mixtures of enriched (>99.99%) ^{7}LiF and BeF_2 termed "flibe". A critical assessment of the potential molten salt mixtures for MSRs can be found in (Renault et al., 2010).

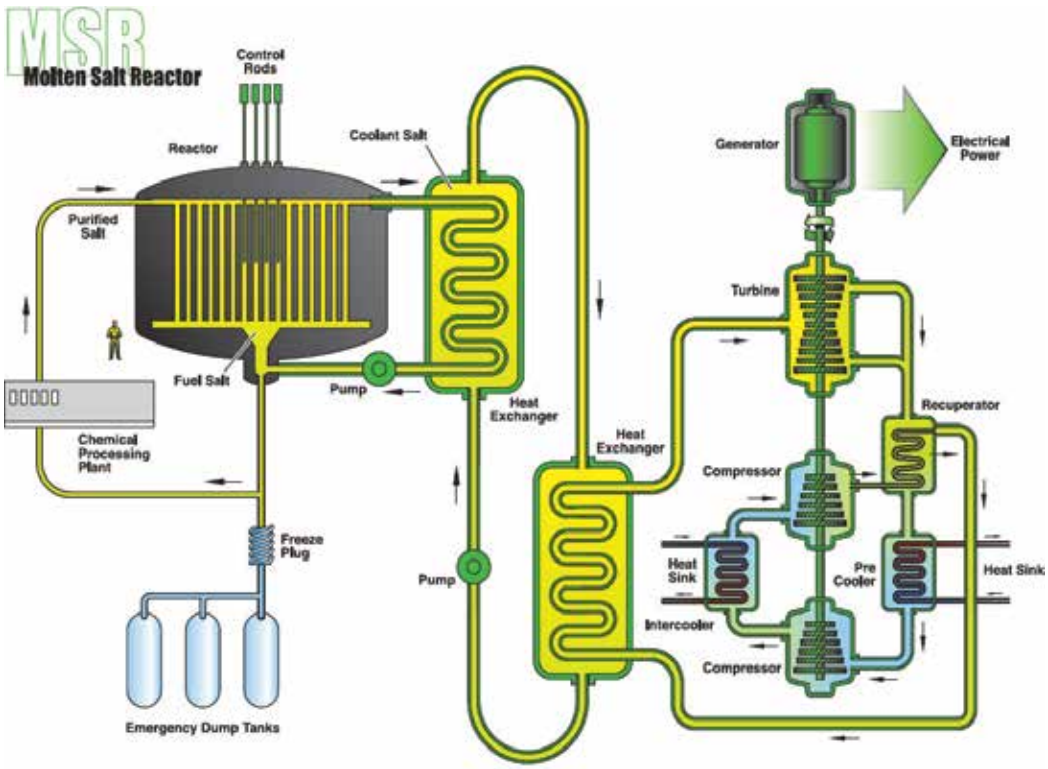

Fig. 1. Schematic representation of a typical MSR (Reproduced from (GIF-IV, 2002))

has the advantage of producing less transuranic isotopes than the uranium-plutonium fuel cycle (^{238}U-^{239}Pu) (Nuttin et al., 2005). Designs specific for the ^{232}Th-^{233}U cycle using fluoride salts have recently been termed Liquid Fluoride Thorium Reactors (LFTR). Among the most attractive features of the LFTR design is the higher sustainability of the back-end of the fuel cycle, in terms of waste profile (Hargraves & Moir, 2010). Adoption of thorium in a closed cycle (i.e., with full recycle of actinides) generates much less waste, of far less radiotoxicity (LeBlanc, 2010), which requires a few hundred years of isolated storage versus the few hundred thousand years necessary for the waste generated by the conventional once-through uranium-plutonium fuel cycle, adopted in the current Light Water Reactors (LWR). LFTRs are featured by a higher fuel cycle sustainability when compared with current LWRs also in terms of natural resource utilization, as can be appreciated looking at the volume of material handled from the front-end phase of the fuel cycle to generate a comparable amount of electric power (Fig. 2).

Besides the favourable features concerning the fuel cycle and the waste management, MSRs offer an array of other advantages in design, operation, safety and proliferation resistance over the traditional solid fuel design of nuclear reactors. A detailed review of such potentialities, as well as of the molten salt technology, is beyond the scope of the present chapter, and can be found in (Furukawa et al., 2008; LeBlanc, 2010; Luzzi et al., 2011; Renault et al., 2010). In the next subsection, the main operational and safety advantages achievable with molten salts

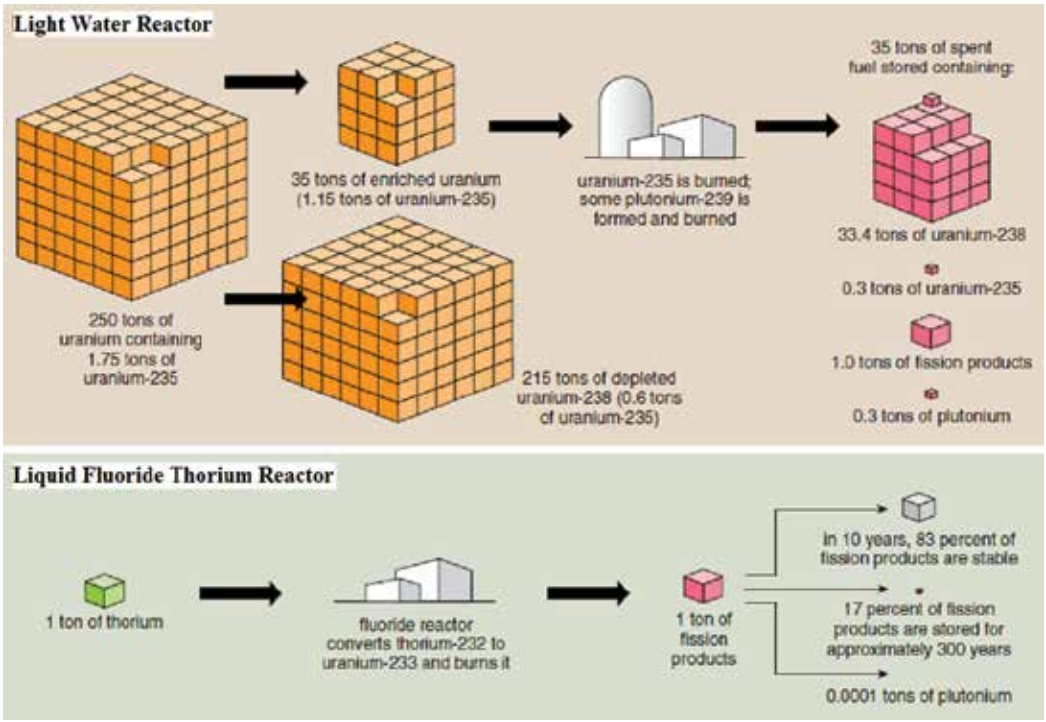

Fig. 2. Mass of material handled from beginning to end to generate comparable amounts of electric power in a LFTR and in a current LWR (Reproduced from (Hargraves & Moir, 2010))

are briefly presented, focusing the attention on the differences with respect to solid-fuelled nuclear reactors.

2.1 Operational and safety issues of MSRs

As the only liquid-fuelled reactor concept, the safety basis and characteristics of the MSR are considerably different from the other reactor concepts. This leads to different advantages, as outlined here below.

The reactor design characteristics minimize the potential for accident initiation. Unlike solid-fuelled reactors, fuel is added as needed, and consequently the reactor has almost no excess nuclear reactivity, which reduces the risk of accidental reactivity insertion. Thanks to a good neutron economy, and to the on-line fuel feeding and reprocessing (in which the fuel is cleaned up from neutron poisons such as Xe), MSRs are usually featured by low fissile inventory. Fission products (except Xe and Kr) are highly soluble in the salt and are expected to remain inside the mixture under both operating and accident conditions. The fission products, which are not soluble (e.g., Xe, Kr), are continuously and relatively easily removed from the molten fuel salt, and the potential for significant radioactivity release from the reactor is notably low.

A distinctive safety feature of the MSR design is that the primary system is at a low operating pressure even at high temperatures, due to the high boiling point ($\sim$1400°C at atmospheric pressure) of the fluoride salt mixture. This eliminates a major driving force (high pressure) for

transport of radionuclides from the reactor to the environment during an accident. Moreover, neutral pressure reduces the cost and the scale of MSR plant construction by lowering the scale of the containment requirements, because it obviates the need to contain pressure like in light water or gas cooled nuclear reactors (featured by thick walled pressure vessels). Disruption in a transport line of the primary system would not result in an explosion, but in a leak of the molten salt, which would be captured in a catch basin, where it would passively cool and harden.

The fluid nature of the fuel means that the reactor core meltdown is an irrelevant term. The liquid state of the core also enables in most emergencies a passive, thermally triggered fuel salt draining into bunkered, and geometrically sub-critical, multiple dump tanks, which are provided with passive decay heat cooling systems (see Fig. 1). Actually, at the bottom of the core, MSR designs have a freeze plug (a plug of salt, actively cooled by a fan to keep it at a temperature below the freezing point of the salt). If the fuel salt overheats and its temperature rises beyond a critical point, the freeze plug melts, and the liquid fuel overflows by gravity and is immediately evacuated from the core, pouring into the emergency dump tanks. This formidable safety tactic is only possible if the fuel is a liquid. Power is not needed to shutdown the reactor, for example by manipulating control elements, but it is needed to prevent the shutdown of the reactor.

Further characteristics of fluoride salts (both fuel and secondary system) are relevant from the safety and design/operational points of view. They are chemically inert, thermodynamically lacking the highly energetic reactions with environmental materials found in other reactor types (e.g., hot zirconium or sodium with water). In particular, the absence of water in the reactor core means no possible steam explosion or hydrogen production within the containment, as occurred in the Fukushima accident. In designs without graphite moderator, there is not even combustible material present. Moreover, molten fluoride salts are excellent coolants, with a 25% higher volumetric heat capacity than pressurized water and nearly 5 times that of liquid sodium. This results in more compact primary circuit components, like pumps and heat exchangers. They also have a much lower thermal conductivity than sodium, thus avoiding thermal shock issues. The high melting temperature ($\sim$460°C for the "flibe" mixture, LiF-BeF_2 67-33 mol%) requires operational constraints on reactor temperature to avoid freezing during the normal operating conditions or during maintenance operations, but from the safety point of view it makes molten salt accidentally escaping from the reactor vessel to immediately freeze. Liquid fluoride salts are impervious to radiation damage, which does not constitute a constraint on fuel burn-up limit as for solid-fuelled cores. Actually, they are not subject to the structural stresses of solid fuel and their ionic bonds can tolerate unlimited levels of radiation damage, while eliminating the (rather high) cost of fabricating fuel elements and the (also high) cost of periodic shutdowns to replace them. In addition, a fluid fuel permits to have a homogeneous core composition eliminating the complications connected to the refuelling strategy, which in conventional reactors comprises reshuffling of the fuel assemblies. MSRs can operate with different fissile materials and additives in the liquid fuel, proving the possibility to transmute and burn nuclear wastes such as plutonium, minor actinides and long-lived fission products (Forsberg, 2002).

As concerns inherent safety, MSR designs with fast spectrum (FS-MSRs) are characterized by a very strong negative void (expanded fuel is pushed out of the core) and temperature reactivity coefficients of fuel salt, which avoid the major design constraints required in solid-fuelled

fast reactors and, acting instantly, permit the desirable property of automatic "load following operation". Namely, under conditions of changing electricity demand (load), the reactor tends to adjust its power. Therefore, FS-MSRs can provide a high power density, while maintaining excellent passive safety characteristics (Renault et al., 2010).

In conclusion, the available evidence about the MSR features suggests that the probability and the consequences of a large accident are much smaller than those of most solid-fuelled reactors, whereas the processing system for cleaning the fuel salt and the remote maintenance of major components indicate greater concerns associated with smaller accidents. MSRs involve more intensive manipulation of highly radioactive materials than other reactor classes, and thus small spills and contamination accidents appear to be more likely with this reactor class. The salt processing technology[3] and, more in general, the "liquid salt chemistry" plays a major role in the viability demonstration of MSR concepts and requires essential R&D. Among the main issues, the following ones are worth to be mentioned: (i) the physico-chemical behaviour of coolant and fuel salts, including fission products and tritium; (ii) the compatibility of salts with structural materials for fuel and coolant circuits, as well as fuel processing materials development; (iii) the on-site fuel processing; and (iv) the maintenance, instrumentation and control of liquid salt chemistry (redox, purification, homogeneity). Further details can be found in (Delpech et al., 2010; GIF-IV, 2009). As concerns the modelling efforts, in MSRs a strong coupling between neutronics and thermal-hydraulics exists with more evidence than in solid-fuelled reactors (Cammi et al., 2011a; Křepel et al., 2007; Nicolino et al., 2008). In particular, the following two distinctive features of molten salts (acting both as circulating fuel and coolant) are of relevance for the MSR dynamics and must be properly addressed from the modelling point of view: (i) as it concerns neutronics, the concentration of delayed neutron precursors (DNP) is featured by an unusual pattern according to the fuel velocity field, and can significantly affect the neutron balance since a part of DNPs can decay outside the reactor core (Cammi et al., 2011a; Křepel et al., 2007; Nicolino et al., 2008); (ii) as it concerns thermal-hydraulics, the coolant is a fluid with internal heat generation whose heat transfer properties are considerably different from non-internally heated fluids. To this last issue are dedicated the following sections.

3. A generalized approach to the modelling of the MSR core channels

A typical configuration of a MSR core with a thermal-neutron spectrum is reported in Fig. 3a. It refers to the Molten Salt Breeder Reactor (MSBR) core (Robertson, 1971), usually considered as reference system for benchmark analyses and validation purposes (e.g., Křepel et al. (2007)). The core includes graphite blocks traversed by circular channels (Fig. 3b), through which the power generating molten salt flows. The present work is focused on heat transfer in a single-channel of the core (Fig. 3c), considering the most relevant features related to its physical behaviour modelling, while neglecting the details of the actual geometrical domain. In particular, the analysed geometry consists of a smooth circular channel with constant flow section surrounded by a solid region (represented by the graphite matrix in the specific case of interest), within which the fluid flow is hydro-dynamically developed, but thermally developing, as depicted in Fig. 3d. This situation is consistent with the flow characteristics

[3] The molten salt processing technology would include a chemical processing facility for trapping and solidifying the volatile fission products in the off-gas system, and a potential second processing system for removal of the other fission products from the fuel salt.

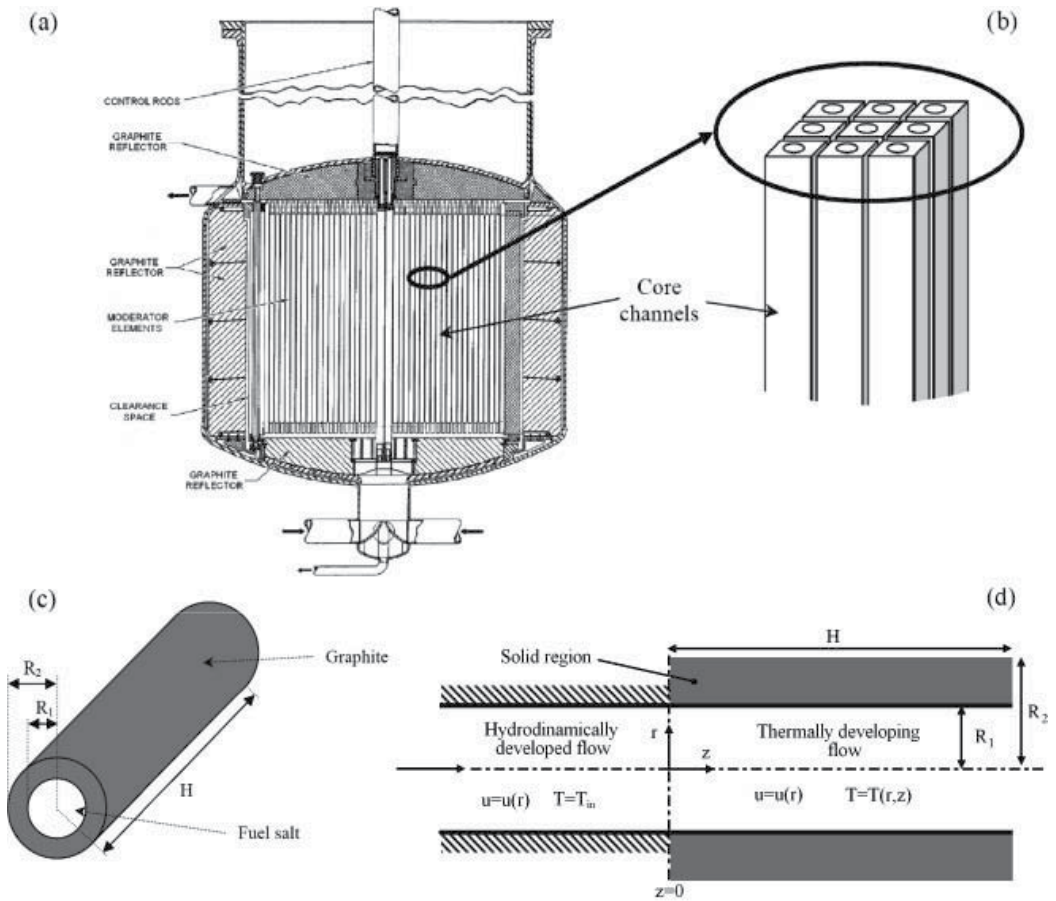

Fig. 3. Schematic representation of the core channel modelling: (a) vertical section of the reactor core; (b) simplified view of the graphite blocks; (c) cylindrical shell approximation of the single-channel; (d) analysed geometry and coordinate system

encountered in the MSR core channels, both in steady-state and transient operation (Luzzi et al., 2011). Even if the graphite blocks can be square or hexagonal shaped, it is a good approximation to model them as a cylindrical shell. In this way, the adopted geometry is axial-symmetric and the use of a two-dimensional domain is made possible.

The analysed physical situation is therefore represented by the molten salt flowing through a cylindrical channel surrounded by graphite, with both the fluid and the solid (see at the end of subsection 3.1) generating power. To properly treat the heat transfer characteristics of such a system, a "generalized approach" is undertaken. This approach treats the problem of heat transfer by forced convection of a fluid inside a circular pipe (generally known as the "Graetz problem") according to a general mathematical formulation that also considers the internal heat generation of the fluid.

In principle, the adopted model is applicable and valid for annular pipes and parallel plate channels but, in the interest of simplicity and practicality, the results are herein limited to circular pipes. The detailed derivation and numerical implementation/discussion of the solution can be found in (Di Marcello et al., 2010; Luzzi et al., 2010), hence in the next two subsections only essential parts are reproduced.

3.1 Mathematical formulation of the generalized approach

With reference to the "Graetz problem", the following expression is adopted for the energy equation:

$$u\frac{\partial T(r,z)}{\partial z} = \frac{1}{r}\frac{\partial}{\partial r}\left[r\left(\frac{\nu}{Pr}+\varepsilon_H\right)\frac{\partial T(r,z)}{\partial r}\right] + \frac{Q(r,z)}{\rho C_p} \tag{1}$$

where the time-averaged axial component of velocity (u) and the eddy diffusivity for heat (ε_H) are assumed to depend only on the radial coordinate (r). For the meaning of the other symbols, see the nomenclature in Section 7. Equation 1 is valid under the following hypotheses: (i) axial-symmetric conditions are taken into account; (ii) steady-state exists; (iii) the fluid is incompressible with no phase change, and constant physical properties; (iv) the hydrodynamic pattern is established; (v) natural convection effects are not considered; and (vi) axial conduction of heat is negligible. The last assumption has been shown by Weigand et al. (2001) to introduce a negligible error for Peclet numbers larger than 10^2. This condition is satisfied in the case of MSRs, which are typically featured by Peclet numbers greater than 10^4. The boundary conditions for Equation 1, at $r = 0$ (at the pipe centreline), must be of the second kind (see Equation 2a) because of assumption (i), while at $r = R_1$ (at the pipe wall) they can be taken as any combination of the boundary conditions of the first, second, and third kind, as expressed by Equations 2b, 2c and 2d, respectively:

$$\left.\frac{\partial T(r,z)}{\partial r}\right|_{r=0} = 0 \tag{2a}$$

$$T(R_1,z) = T_w(z) \tag{2b}$$

$$\left.-k\frac{\partial T(r,z)}{\partial r}\right|_{r=R_1} = j_w(z) \tag{2c}$$

$$T(R_1,z) - \frac{k}{h_w}\left.\frac{\partial T(r,z)}{\partial r}\right|_{r=R_1} = T_E(z) \tag{2d}$$

Finally, the boundary condition at the pipe entrance ($z = 0$) is given by Equation 3:

$$T(r,0) = T_{in}(r) \tag{3}$$

In order to get the solution of the Equation 1 with the boundary conditions 2 and 3, it is convenient to express them in a dimensionless form (see Fig. 4), and then to adopt the so-called "splitting-up procedure". Such procedure consists in splitting-up the solution of the original problem into two parts, as given by Equation 5, and can be applied by assuming that the non-homogeneous term $\Phi(Z)$ and the term $P(R,Z) = R \cdot S(R,Z)$ can be expressed in terms of q-order polynomials of the axial coordinate Z as follows:

Dimensionless form of the energy equation:

$$f(R)\frac{\partial\theta(R,Z)}{\partial Z} = \frac{1}{R}\frac{\partial}{\partial R}\left[R\cdot g(R)\frac{\partial\theta(R,Z)}{\partial R}\right] + S(R,Z) \qquad \text{in } 0 < R < 1$$

Dimensionless form of the boundary conditions:

$$\left.\frac{\partial\theta(R,Z)}{\partial R}\right|_{R=0} = 0 \qquad \theta(R,0) = \theta_{in}(R)$$

$$\alpha\theta(1,Z) - \beta\left.\frac{\partial\theta(R,Z)}{\partial R}\right|_{R=1} = \Phi(Z) \qquad \begin{cases} \text{(i)} & \alpha = 1,\ \beta = 0, & \Phi(Z) = \theta_w(Z) \text{ (first kind)} \\ \text{(ii)} & \alpha = 0,\ \beta = 1, & \Phi(Z) = J_w(Z) \text{ (second kind)} \\ \text{(iii)} & \alpha = 1,\ \beta = \frac{k}{h_w\cdot R_1}, & \Phi(Z) = \theta_E(Z) \text{ (third kind)} \end{cases}$$

Dimensionless variables:

$$R = \frac{r}{R_1} \qquad Z = \frac{2z}{Re\cdot Pr\cdot R_1} \qquad \theta(R,Z) = \frac{T(r,z) - T^*}{\Delta T}$$

$$\theta_w(Z) = \frac{T_w(z) - T^*}{\Delta T} \qquad \theta_E(Z) = \frac{T_E(z) - T^*}{\Delta T} \qquad \theta_{in}(Z) = \frac{T_{in}(z) - T^*}{\Delta T}$$

$$J_w(Z) = \frac{j_w(z)R_1}{k\cdot\Delta T} \qquad \theta_b(Z) = \frac{T_b(z) - T^*}{\Delta T} \qquad f(R) = \frac{u}{u_{avg}}$$

$$g(R) = \frac{\frac{\nu}{Pr} + \varepsilon_H}{\frac{\nu}{Pr}} \qquad S(R,Z) = \frac{Q(r,z)\cdot R_1^2}{k\cdot\Delta T} \qquad P(R,Z) = R\cdot S(R,Z)$$

Fig. 4. Dimensionless form of the Equation 1, with the boundary conditions 2 and 3, adopted in the splitting-up procedure

$$\Phi(Z) = \sum_{j=0}^{q}\Phi_j\cdot Z^j,$$

$$P(R,Z) = \sum_{j=0}^{q}P_j(R)\cdot Z^j \tag{4}$$

According to this procedure, the following final solution for the temperature field in the fluid is achieved (details can be found in Di Marcello et al. (2010)):

$$\theta(R,Z) = \sum_{j=0}^{q}\theta_j(R)\cdot Z^j + \sum_{i=1}^{\infty}C_i e^{-\mu_i^2 Z}\Psi_i(R) \tag{5}$$

where

$$C_i = \frac{\int_0^1 R\cdot[\theta_{in}(R) - \theta_0(R)]\cdot f(R)\cdot\Psi_i(R)dR}{\int_0^1 R\cdot f(R)\cdot\Psi_i^2(R)dR} \tag{6}$$

$$\theta_j(R) = \frac{1}{\alpha}\left\{\Phi_j + \beta\int_0^1 \left[P_j(R) - (j+1)Rf(R)\theta_{j+1}(R)\right]dR \right. \tag{7}$$
$$\left. +\alpha\int_0^1 \frac{1}{Rg(R)}\int_0^R \left[P_j(R') - (j+1)R'f(R')\theta_{j+1}(R')\right]dR'dR\right\}$$
$$-\int_0^R \frac{1}{Rg(R'')}\int_0^{R''} \left[P_j(R') - (j+1)R'f(R')\theta_{j+1}(R')\right]dR'dR''$$

with $j = q, q-1, q-2, ..., 1, 0$ and $\theta_{q+1}(R) = 0$. In Equation 5, $\Psi_i(R)$ and μ_i are the eigenfunctions and the eigenvalues, respectively, of the Sturm-Liouville problem represented by the differential Equation 8 with its boundary conditions 9:

$$\frac{d}{dR}\left[Rg(R)\frac{d\Psi_i(R)}{dR}\right] + \left[\mu_i^2 Rf(R)\right]\Psi_i(R) = 0 \tag{8}$$

$$\left.\frac{d\Psi_i(R)}{dR}\right|_{R=0} = 0 \tag{9a}$$

$$\alpha\Psi_i(1) - \beta\cdot g(1)\cdot\left.\frac{d\Psi_i(R)}{dR}\right|_{R=1} = 0 \tag{9b}$$

Once the temperature distribution, $\theta(R,Z)$, in the fluid flow is determined, the Nusselt number can be evaluated by means of Equations 10 and 11:

$$Nu(Z) = \frac{2}{\theta(1,Z) - \theta_b(Z)}\cdot\left.\frac{\partial\theta(R,Z)}{\partial R}\right|_{R=1} \tag{10}$$

$$\theta_b(Z) = \frac{\int_0^1 Rf(R)\theta(R,Z)dR}{\int_0^1 Rf(R)dR} \tag{11}$$

In the case of uniform internal heat generation and constant wall heat flux, the dependence of Nu on the axial coordinate vanishes when fully developed flow conditions occur (Di Marcello et al., 2010). This fact will be employed in the derivation of the heat transfer correlation form for internally heated fluids presented in subsection 4.2.

The model described above permits to evaluate in a simple and prompt way some fundamental quantities such as the distributions of temperature and the Nusselt number. It is applicable for: (i) boundary conditions (at the pipe wall) of first, second or third kind, with arbitrary axial distribution; (ii) arbitrary radial distribution of the inlet temperature, $T_{in}(r)$; and (iii) arbitrary shape of the internal heat source $Q(r,z)$ in both the radial and axial directions. The model can be implemented for both laminar and turbulent flow. In the first case, the solution can be obtained by considering the Hagen-Poiseuille parabolic velocity profile and zero eddy diffusivity ε_H, i.e.: $f(R) = 2(1-R^2)$ and $g(R) = 1$. In the second case, to obtain the velocity profile and the eddy diffusivity for the heat, both needed to solve the original Equation 1, the adoption of a formulation for turbulent flow

is required (see subsection 3.2 for details). In particular, the solution here considered includes the recent formulations of turbulent flow and convection of Churchill (1997) and was assessed for a large variety of fluids, showing that such generalized approach is able to reproduce with a good agreement the experimental data concerning heat transfer evaluations for both fully developed and thermally developing flow conditions, in a wide range of Prandtl ($10^{-2} < Pr < 10^4$) and Reynolds ($2 \cdot 10^3 < Re < 5 \cdot 10^5$) numbers, with and without internal heat generation (Luzzi et al., 2010).

The above generalized approach can be easily extended to evaluate the entire temperature field in the reactor core single-channel, by taking into account the heat conduction in the graphite matrix as well as the corresponding internal heat generation due to gamma heating and neutron irradiation. The "overall solution" (fluid + solid) of such heat transfer problem, with reference to the geometry shown in Fig. 3d, can be achieved by combining the above solution for the turbulent pipe flow of the internally heated molten salt ("Graetz problem") with the solution for the heat conduction problem in the solid region (graphite) surrounding it. The detailed derivation of the "overall solution" can be found in (Luzzi et al., 2010). The final result is shown in Fig. 5, which refers to a single-channel representative of the average steady-state conditions of the MSBR core (Robertson, 1971), shown in Fig. 3a. As far as the boundary conditions are concerned, a constant temperature (T_{in}) is imposed at the channel inlet ($z = 0$), while a convective flux condition is prescribed at the outlet ($z = H$). In the lower part of the solid annulus, at $z = 0$, the same temperature of the fluid entering the channel is fixed. Adiabatic conditions are imposed on the external radius R_2 and in correspondence of the outlet section ($z = H$). On the wall between the fluid and the solid ($r = R_1$), continuity of temperature and wall heat flux are considered.

As can be noticed in Fig. 5, a good agreement is found between the "overall solution" achieved by means of the generalized approach and a dedicated Computational Fluid Dynamics (CFD) simulation. The CFD calculation was performed by means of the finite volume software FLUENT (Fluent, 2005): (i) adopting the incompressible RANS (Reynolds Averaged Navier Stokes) equations for the fluid motion with Boussinesq's eddy viscosity hypothesis; (ii) considering the standard "$k - \varepsilon$ turbulence model" and the enhanced wall treatment approach available in FLUENT; and (iii) in steady-state and hydro-dynamically developed conditions, with reference to a two-dimensional, axial-symmetric (r, z) computational domain, in accordance with the hypotheses and the boundary conditions mentioned above. Further details concerning the mesh strategy and the numerical model are given in (Luzzi et al., 2011).

3.2 Turbulent flow formulation

As pointed out, to obtain the solution of the turbulent "Graetz problem", the reinterpretation of turbulent flow and convection of Churchill (Churchill, 1997; 2002) is considered, so that the eddy diffusivity and thus the velocity profile are expressed in terms of the local turbulent shear stress. In particular, the relationship between the eddy diffusivity for momentum, ε_M, and the dimensionless turbulent shear stress, $(\overline{u'v'})^{++}$, in hydro-dynamically developed flow, is a "one-to-one correspondence" (Churchill, 1997), as expressed in Equation 12:

$$\frac{\varepsilon_M}{\nu} = \frac{\left(\overline{u'v'}\right)^{++}}{1 - \left(\overline{u'v'}\right)^{++}} \tag{12}$$

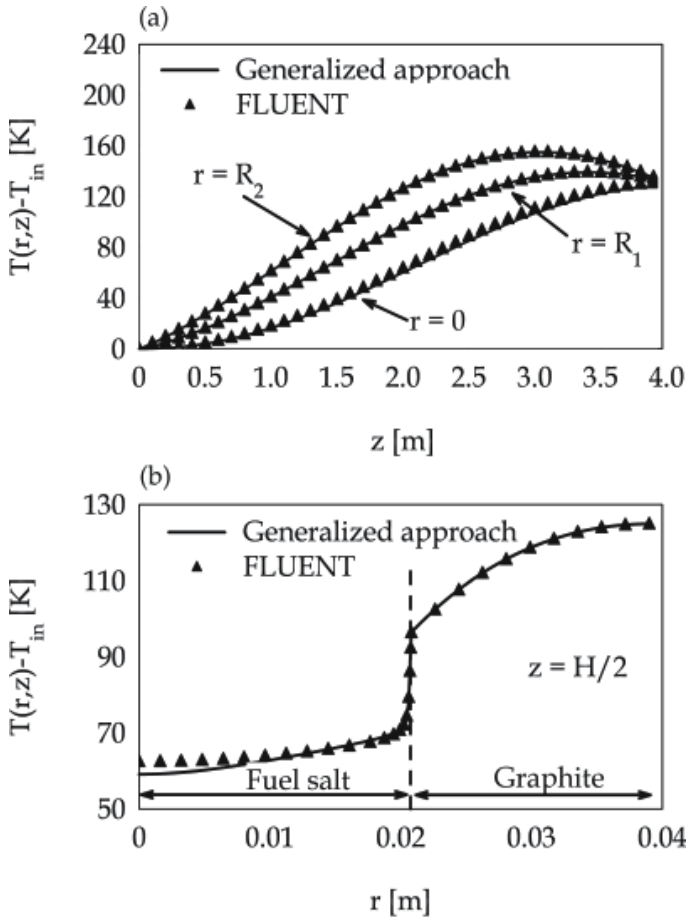

Fig. 5. Axial (a) and radial (b) temperature profile comparison

where

$$\left(\overline{u'v'}\right)^{++} = -\frac{\rho\left(\overline{u'v'}\right)}{\tau} \tag{13}$$

$$\overline{u'v'} = -\varepsilon_M\left(\frac{\partial u}{\partial y}\right) \tag{14}$$

$$\tau = \tau_w\left(1 - \frac{y}{R_1}\right) \tag{15}$$

$$\tau_w = \frac{f}{8}\rho u_{avg}^2 \tag{16}$$

From Equations 12 to 15, the velocity can be obtained as follows

$$u(R) = \frac{\tau_w R_1}{\mu}\int_R^1 R\left[1 - \left(\overline{u'v'}\right)^{++}\right]dR \tag{17}$$

It can be noticed that explicit expressions for the dimensionless turbulent shear stress and the friction factor are required in order to evaluate the velocity profile. For the first one, the following correlation, suggested by Heng et al. (1998) and based on the recent turbulent velocity measurements of Zagarola & Smits (1997), is adopted:

$$\left(\overline{u'v'}\right)^{++} = \left\{ \left| exp\left(\frac{-2.294}{y^+}\right) - \frac{2.294}{a^+}\left(1+\frac{6.95y^+}{a^+}\right)\right|^{-\frac{8}{7}} + \left[0.7\left(\frac{y^+}{10}\right)^3\right]^{-\frac{8}{7}} \right\}^{-\frac{7}{8}} \tag{18}$$

As far as the Darcy friction factor is concerned, the recent correlation proposed by Guo & Julien (2003) and expressed by Equation 19 is employed, since it predicts the values determined experimentally by Zagarola & Smits (1997) very well, and its form is preferable in terms of explicitness and simplicity:

$$f = \frac{0.3164}{Re^{\frac{1}{4}}}\left(1+\frac{Re}{4.31\cdot 10^5}\right)^{\frac{1}{8}} \tag{19}$$

Finally, in order to obtain the eddy diffusivity for heat, ε_H, which is also needed in the solution of the turbulent "Graetz problem" (Equation 1), the turbulent Prandtl number ($Pr_T = \varepsilon_M/\varepsilon_H$) is evaluated through the correlation proposed by Kays (1994), and reported in Equation 20:

$$Pr_T = 0.85 + \frac{0.7}{Pr}\left[\frac{1-\left(\overline{u'v'}\right)^{++}}{\left(\overline{u'v'}\right)^{++}}\right] \tag{20}$$

This expression was found to be in a good agreement with most experimental and computed values of the turbulent Prandtl number (Kays, 1994).

Fig. 6 shows the comparison in terms of velocity profile between the use of Equation 17 (in the generalized approach) and a CFD calculation performed by means of FLUENT, with reference to the MSBR case (see subsection 3.1). As a result, a general good agreement is found. A more complete study for different Reynolds numbers and different turbulence models is available in (Luzzi et al., 2010). It is worth pointing out that a proper evaluation of the molten salt velocity field is a relevant aspect for what concerns the dynamic behaviour of the MSRs, due to the drift of DNPs and their distribution inside the fluid (Cammi et al., 2011b).

4. Derivation of a heat transfer correlation for the MSR core channels

In the previous section, a detailed treatment of the heat transfer for internally heated fluids has been presented. Treatments of this kind, as well as dedicated CFD codes, can be used to deeply investigate the heat transfer process in many engineering applications. Nevertheless, when dealing with complex systems, computational requirements make often impossible the direct application of such techniques. This is particularly the case for the set-up of models dedicated to the transient analysis of graphite-moderated MSRs, where the reactor core is actually composed by thousands of channels. In this context, it can be useful to rely on a simplified treatment, such as the use of correlations able to predict the Nusselt number, and thus the heat transfer coefficient. In this section, the generalized model presented in subsection 3.1 is adopted to derive a simple correlation for the heat transfer in channels featured by internally heated fluids.

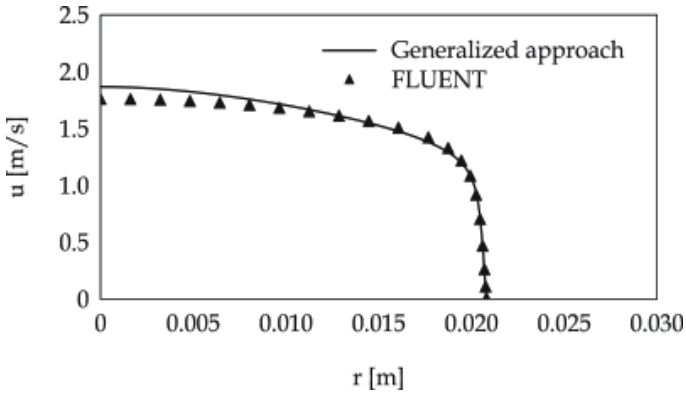

Fig. 6. Velocity profile comparison

4.1 Overview of available correlations

Molten salts are Newtonian fluids and are featured by Prandtl numbers on the order of 10. A number of correlations suitable for a wide range of Reynolds and Prandtl numbers has been proposed in the past, and can be used also for molten salts. Examples of such correlations are the following: the Dittus-Boelter (Dittus & Boelter, 1930), Colburn (Colburn, 1933), and Sieder-Tate (Sieder & Tate, 1936) correlations for turbulent flows; the Hausen (Hausen, 1959) and Gnielinski (Gnielinski, 1976) correlations, which are valid also in the transition between laminar and turbulent flow.

More recent studies have been carried out in order to increase the accuracy of the mentioned correlations for Reynolds and Prandtl numbers of interest in specific fields. As regards molten salts, the Hausen and Gnielinski correlations have been recently checked by means of a dedicated experimental facility, and a slightly modified version of the Gnielinski correlation has been proposed (Yu-ting et al., 2009). Another interesting work can be found in (Bin et al., 2009), where the Sieder-Tate and the Hausen correlations are also assessed, and a modified Sieder-Tate correlation is proposed.

All the correlations mentioned above can be used with a good degree of accuracy in many applications in the field of engineering, but they are not suitable for situations where the working fluid is featured by internal heat generation, as in the case of MSRs. Recently, it has been shown that the use of such classical correlations for predicting heat transfer in MSRs can lead to an underestimate of temperature difference between molten salt and graphite as high as 70% (Luzzi et al., 2010). Specific correlations should then be used for internally heated fluids. Some preliminary studies on the subject are available in literature (Kinney & Sparrow, 1966; Poppendiek, 1954; Siegel & Sparrow, 1959), but they are in most cases partial treatments and they do not lead to the proposal of correlations to be used for turbulent flow.

4.2 Analytical derivation of heat transfer correlation form for internally heated fluids

In this subsection, the problem of heat transfer in channels featured by internally heated fluids is treated analytically, and the general form of the Nusselt number correlation for such situation is derived under the following assumptions: (i) smooth channel with circular cross section; (ii) fully developed turbulent flow conditions; (iii) uniform internal heat generation; and (iv) constant wall heat flux. This situation can be simplified by considering it as the

superimposition of two simpler situations, i.e.: 1) a flow without internal heat generation, but featured by constant wall heat flux, which is the typical case considered by classical heat transfer correlations; and 2) a channel with adiabatic walls and internal heat generation. The possibility of such superimposition is guaranteed by the linearity (with respect to temperature) of the energy equation – see Equation 1. Hence, it is possible to compute the difference between wall and bulk temperatures as follows (see also Fig. 4):

$$(T_w - T_b)_{Q+j_w} = (T_w - T_b)_Q + (T_w - T_b)_{j_w} \tag{21}$$

In Equation 21 and in the next ones, the subscript $Q + j_w$ refers to the complete situation with both internal heat generation and wall heat flux, while the subscripts Q and j_w indicate that the temperature differences are computed in the simplified situation of internal heat generation alone (situation 1) and wall heat flux alone (situation 2), respectively. Introduction of the Equation 21 in the definition of heat transfer coefficient leads to:

$$h_w = h_{Q+j_w} = \frac{j_w}{(T_w - T_b)_Q + (T_w - T_b)_{j_w}} = \frac{1}{\frac{(T_w - T_b)_Q}{j_w} + \frac{(T_w - T_b)_{j_w}}{j_w}} = \frac{1}{h_Q^{-1} + h_{j_w}^{-1}} \tag{22}$$

It should be mentioned at this point that the term h_Q, although similar to h_{j_w} in its definition, does not represent a heat transfer coefficient. Actually, it includes in the same definition the temperatures of the situation 2 (with internal heat generation and with adiabatic walls) and the heat flux in the situation 1 (without internal heat generation). It is possible to rewrite the Equation 22 in terms of Nusselt numbers as follows:

$$Nu = Nu_{Q+j_w} = \frac{1}{Nu_Q^{-1} + Nu_{j_w}^{-1}} = Nu_{j_w} \cdot \frac{1}{1 + \frac{Nu_{j_w}}{Nu_Q}} \tag{23}$$

Equation 23 implies that the Nusselt number, in case of internally heated fluids and constant wall heat flux (Nu_{Q+j_w}), can be computed by means of classical correlations for the value of Nu_{j_w} (subsection 4.1) through the introduction of a correction factor with the form:

$$\gamma = \frac{1}{1 + \frac{Nu_{j_w}}{Nu_Q}} = \frac{1}{1 + \frac{h_{j_w}}{h_Q}} = \frac{1}{1 + \delta} \tag{24}$$

Hence, what is required is the derivation of the term δ as a function of the parameters characterizing the system. Assuming constant the properties of the fluid, it is possible to write:

$$\delta = \delta \left(C_p, \mu, \rho, k, D, u_{avg}, Q, j_w \right) \tag{25}$$

As a matter of fact, some of the dependencies appearing in Equation 25 can be made explicit by means of some physical reasoning, thus reducing the experimental/computational efforts in the derivation of a functional form for δ. By recalling the definition of δ (Equation 24), and introducing the definition of h_Q (Equation 22), it is possible to write:

$$\delta = \frac{h_{j_w}}{h_Q} = \frac{h_{j_w} (T_w - T_b)_Q}{j_w} \tag{26}$$

where h_{j_w} and $(T_w - T_b)_Q$ are independent of j_w. Moreover, the term $(T_w - T_b)_Q$ is directly proportional to Q – see for example (Poppendiek, 1954). It follows:

$$\delta = \frac{h_{j_w} (T_w - T_b)_Q}{j_w} = \frac{Q}{j_w} \varphi \left(C_p, \mu, \rho, k, D, u_{avg} \right) \tag{27}$$

in which the dependence on two parameters has been made explicit. Use of Π-theorem (Langhaar, 1962) in Equation 27 finally leads to:

$$\delta = \frac{QD}{j_w}\varphi(Pr, Re) \tag{28}$$

Summarizing, a correlation for the Nusselt number, in case of simultaneous wall heat flux and internal heat generation, must take the following form:

$$Nu_{Q+j_w} = \gamma Nu_{j_w} = \frac{1}{1+\delta}Nu_{j_w} = \frac{1}{1+\frac{QD}{j_w}\varphi(Pr, Re)}Nu_{j_w} \tag{29}$$

If Nu_{j_w} is assumed to be known from available correlations (subsection 4.1), Equation 29 allows to fully characterize the heat transfer in a channel with internal heat generation simply by finding the dependency of φ upon Reynolds and Prandtl numbers.

4.3 Derivation of a correlation for the Nusselt number in the core channels of MSRs

The results of the previous subsection are of general validity under the mentioned assumptions, and can be used to derive a correlation suitable for computing the Nusselt number in case of channels with internally heated fluids. If the classical correlations available in literature for Nu_{j_w} are adopted, what is required is just the derivation of the function $\varphi(Pr, Re)$. In case of laminar flow ($Nu_{j_w} = 48/11$), the function $\varphi(Pr, Re)$ can be analytically demonstrated to be constant and equal to 3/44 (Poppendiek, 1954), but, in case of turbulent flow, it can have a complex shape. Nevertheless, by restricting the field of application, it is reasonable to assume a simple dependence such as

$$\varphi(Pr, Re) = a_1 Pr^{a_2} Re^{a_3} \tag{30}$$

where a_1, a_2 and a_3 are constants.

At this point, it is possible to employ the generalized approach described in subsection 3.1 to evaluate the function φ and derive proper values for the constants a_1, a_2 and a_3. In particular, Equation 29 can be rearranged as

$$\varphi(Pr, Re) = \frac{j_w}{QD}\left(\frac{Nu_{j_w}}{Nu_{Q+j_w}} - 1\right) \tag{31}$$

where the Nusselt numbers can directly be computed using Equation 10.

Focusing on the situation encountered in the core channels of graphite-moderated MSRs, Reynolds numbers typically range between 10^3 and 10^5 (Luzzi et al., 2010). Consistently with the choice to use a simple correlation form like Equation 30, the investigation can be restricted to conditions of fully developed turbulence ($\mathrm{Re} \geq 10^4$). By employing Equations 31 and 10 as described above, the function φ has been evaluated for 100 different combinations of Prandtl and Reynolds numbers in the ranges $7.5 < Pr < 20$ and $10^4 < Re < 10^5$. Interpolating Equation 30 in the least square sense, the following correlation is finally achieved:

$$\varphi(Pr, Re) = 1.656 \cdot Pr^{-0.4} Re^{-0.5} \tag{32}$$

The average interpolation error results equal to 4.9%, with a maximum error equal to 10.2%. These discrepancies can be considered acceptable for preliminary calculations. It should be

mentioned that, on the basis of the same reasoning here considered, another correlation was presented in (Di Marcello et al., 2010). Such correlation was characterized by a much more complex functional form, but was able to interpolate the data provided by the generalized model with an average error of 3.5%, in the wide range $3 \cdot 10^3 < Re < 2 \cdot 10^5$ and $0.7 < Pr < 10^2$.

Adopting Equation 32, the overall correlation for the Nusselt number, in case of both internal heat generation and wall heat flux, can be written as follows:

$$Nu_{Q+j_w} = \gamma Nu_{j_w} = \frac{1}{1 + \frac{QD}{j_w}\varphi} Nu_{j_w} = \frac{1}{1 + \frac{QD}{j_w} 1.656 \cdot Pr^{-0.4} Re^{-0.5}} Nu_{j_w} \tag{33}$$

The MSBR (Fig. 3) can be selected as an example of application. The molten salt that is considered for such reactor is featured by a Prandtl number equal to 11. The Reynolds number in the core channels is on average $2 \cdot 10^4$ (Luzzi et al., 2010). According to these values, the function $\varphi(Pr, Re)$ as computed through Equation 32 results equal to $4.49 \cdot 10^{-3}$. For the MSBR, the ratio QD/j_w is on average equal to 123.4 and, consequently, the correction factor γ results equal to 0.644. This indicates that the direct use of a classical correlation for the Nusselt number would lead to an overestimate of the heat transfer coefficient on the order of 40%. In Fig. 7, the Nusselt number obtained with Equation 33 is compared with some of the correlations available in literature, for Prandtl number equal to 11 and Reynolds numbers lower than 10^5, which is the range of interest for MSRs. For both Equation 33 and Di Marcello et al. (2010), the Gnielinski correlation was used for Nu_{j_w}. The agreement between the two is clearly visible. Overestimate is instead generally observed for the classical correlations, which do not account for the internal heat generation. Such overestimate can be notable at low Reynolds numbers, where Nusselt numbers are over-predicted by as much as four times. In Fig. 7, the results obtained through the use of the CFD code FLUENT (see at the end of Section 3.1 for details) are also shown. They are in a good accordance with the proposed correlation (Equation 33).

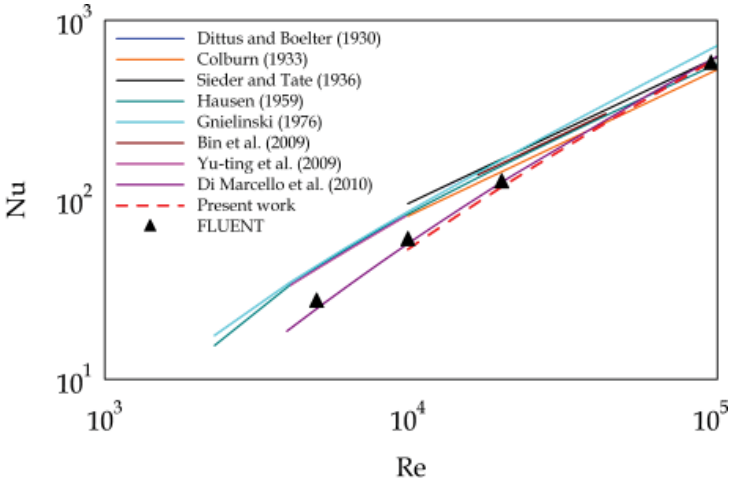

Fig. 7. Comparison among heat transfer correlations, and CFD results, in the Reynolds range of interest for MSRs (Pr=11)

4.4 Possible experimental set-up

The analytical treatment described in the previous sections can provide reasonable results in preliminary studies, but their validity can be tested only through appropriate experimental campaigns. In particular, what is of interest to assess the validity of Equation 33 is the experimental evaluation of the function $\varphi(Pr, Re)$. Equations 26 and 28, together with the definition of Nusselt number, lead to:

$$\varphi(Pr, Re) = Nu_{j_w} \frac{(T_w - T_b)_Q}{\frac{QD^2}{k}} \tag{34}$$

Assuming Nu_{j_w} as known from available correlations, what is necessary from an experimental point of view is the evaluation of the term $(T_w - T_b)_Q$. This requires a facility able to reproduce the condition of an internally heated, thermally and hydro-dynamically developed turbulent flow in a straight, circular and adiabatic channel (according to the assumptions pointed out at the beginning of subsection 4.2). The experimental set-up must be suitable for measuring wall and bulk temperatures, as well as for ensuring a uniform and precisely-known internal heat generation Q. In addition, the definition of the dependence of φ upon Prandtl and Reynolds numbers requires the capability to vary in a known way the fluid properties, as well as to vary and measure the fluid velocity.

A possible set-up for the thermal-hydraulic circuit required for the experimental analyses of interest was already adopted by Kinney & Sparrow (1966). This set-up was used to test water, but with proper modifications can be adopted also for molten salts. A schematic view of the possible experimental facility is shown in Fig. 8.

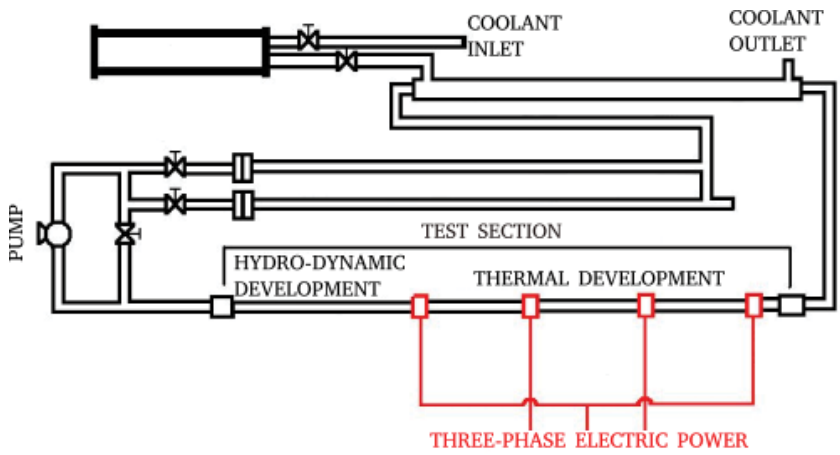

Fig. 8. Schematic view of the possible experimental facility

A closed loop is used, with a heat exchanger for cooling the working fluid, after it has been warmed in the test section. Such test section must be long enough to assure conditions of full thermal and hydro-dynamic development. Internal heating in the fluid is obtained by forcing an electrical current to flow into it. This is possible by choosing an electrically insulating material for the channel wall in the test section, and by placing electrodes at the sides of it.

In this way, the current is forced to flow longitudinally in the fluid. Adopting electricity to heat up the molten salts also solves the problem of the knowledge of the volumetric power Q, which can easily be derived by measuring the electric current in the circuit and the voltage difference at the electrodes. The velocity of the fluid can be varied by using an appropriate pump or valves, and it can be measured by means of standard techniques (e.g., Coriolis flow meter). Wall and bulk temperatures can be measured by means of thermocouples and mixing chambers. Finally, the Prandtl number can be varied by changing fluid, fluid temperature, or by using suitable "thickening" agents (Kedl, 1970).

5. Conclusion

Thermo-hydrodynamics of molten salts is a key issue in the current development of MSRs, which are featured by favourable characteristics with respect to conventional solid-fuelled reactors, due to the peculiarity of a nuclear fuel serving also as coolant, as discussed in Section 2. In this study, a "generalized approach" was undertaken for the "turbulent Graetz problem", with reference to fluids flowing through smooth and straight circular pipes, within which internal heat generation occurs, consistently with the flow characteristics encountered in MSRs. Such generalized model, which incorporates recent formulations of turbulent flow and convection, represents an original contribution in the field of thermo-hydrodynamics, and allows to consider boundary conditions of the first, second and third kind, with arbitrary axial distribution, arbitrary inlet temperature radial distribution and arbitrary variations of internal heat source in both the radial and axial directions. The "overall solution" (molten salt + graphite) presented in Section 3 is thought to be useful under the following two respects: (i) it provides an insight into the heat transfer characteristics of graphite-moderated MSR core channels, as shown for the reference case of the MSBR; (ii) it permits to evaluate in a simple and prompt way some fundamental quantities (i.e., the distributions of temperature and velocity, and the Nusselt number). Moreover, the presented generalized model offers a useful validation framework for assessing CFD codes (Luzzi et al., 2011) and can be an important interpretative support of numerical solutions in steady-state conditions, in the prospect of more complex, multi-physics (thermo-hydrodynamics + neutronics) analyses of graphite-moderated MSR core channels (Cammi et al., 2011a;b). In Section 4, the analytical derivation of the heat transfer correlation form for internally heated fluids was discussed, and a preliminary correlation for the Nusselt number prediction was advanced in the case of simultaneous uniform wall heat flux and internal heat generation, on the basis of the results achieved by means of the "generalized approach". Such correlation, which includes the range of Prandtl and Reynolds numbers of interest for molten salts, provides a simple description of the heat transfer for internally heated fluids, showing that the use of classical correlations (without internal heat generation) for predicting heat transfer in MSRs can lead to an underestimate of graphite temperatures. Although obtained through a detailed analytical treatment, the proposed Nusselt number correlation needs to be verified on experimental grounds. To this purpose, the testing facility and the procedure required for its validation have finally been discussed in brief.

6. Acknowledgment

Authors express their gratitude to Dr. Valentino Di Marcello for performing some of the computations used in this study.

7. Nomenclature

Latin symbols

a^+	dimensionless pipe/channel radius $\{= R_1 \cdot (\tau_w \cdot \rho)^{1/2}/\mu\}$
a_1, a_2, a_3	coefficients of Equation 30
C_i	coefficients defined by Equation 6
C_p	specific heat, $J \cdot kg^{-1} \cdot K^{-1}$
D	pipe/channel diameter, m $\{= 2R_1\}$
f	Darcy friction factor
$f(R), g(R)$	functions defined in Fig. 4
h, h_w	heat transfer coefficient, $W \cdot m^{-2} \cdot K^{-1}$
H	pipe/channel axial length, m
j	integer number
$j_w(z)$	wall heat flux, $W \cdot m^{-2}$
$J_w(Z)$	dimensionless wall heat flux
k	thermal conductivity of the fluid (molten salt), $W \cdot m^{-1} \cdot K^{-1}$
Nu	Nusselt number
$P(R, Z)$	function defined in Fig. 4 $\{= R \cdot S(R, Z)\}$
$P_j(R)$	j^{th} coefficient of the polynomial expansion of $P(R, Z)$
Pr	molecular Prandtl number
Pr_T	turbulent Prandtl number
q	order of the polynomial expansion of $P(R, Z)$ and $\Phi(Z)$
Q	heat source, $W \cdot m^{-3}$
r	radial coordinate, m
R	dimensionless radial coordinate $\{= r/R_1\}$
R_1	pipe radius/inner radius of the solid (graphite), m
R_2	outer radius of the solid (graphite), m
Re	Reynolds number
$S(R, Z)$	dimensionless internal heat source defined in Fig. 4
t	time, s
T	temperature, K
T^*	reference temperature, K
T_b	bulk (or mixed-mean) temperature, K
$T_E(z)$	external environment temperature, K
$T_{in}(r)$	inlet temperature, K
$T_w(z)$	wall temperature, K
u	axial component of velocity, $m \cdot s^{-1}$
u'	fluctuation in axial component of velocity, $m \cdot s^{-1}$
u_{avg}	average velocity in the pipe/channel section, $m \cdot s^{-1}$
$u_{in}(r)$	axial component of velocity at the pipe/channel inlet, $m \cdot s^{-1}$
$\overline{u'v'}$	time-averaged value of $u'v'$, $m^2 \cdot s^{-2}$
$(\overline{u'v'})^{++}$	dimensionless turbulent shear stress
v'	fluctuation in radial component of velocity, $m \cdot s^{-1}$
y	distance from the wall, m
y^+	dimensionless distance from the wall $\{= y \cdot (\tau_w \cdot \rho)^{1/2}/\mu\}$
z	axial coordinate, m
Z	dimensionless axial coordinate

Greek symbols

α, β	dimensionless coefficients defining the kind of boundary condition at wall
γ	correction factor defined by Equation 24
δ	ratio defined as $(Nu_{j_w}/Nu_Q) = (h_{j_w}/h_Q)$
ΔT	reference temperature difference, K
ε_H	eddy diffusivity for heat, $m^2 \cdot s^{-1}$
ε_M	eddy diffusivity for momentum, $m^2 \cdot s^{-1}$
$\theta(R, Z)$	dimensionless temperature
$\theta_b(Z)$	dimensionless bulk (or mixed-mean) temperature
$\theta_E(Z)$	dimensionless external environment temperature
$\theta_{in}(R)$	dimensionless inlet temperature
$\theta_j(R)$	functions defined by Equation 7
$\theta_w(Z)$	dimensionless wall temperature
$\theta_0(R)$	dimensionless reference temperature
μ	dynamic viscosity, $kg \cdot m^{-1} \cdot s^{-1} \{= \rho \cdot \nu\}$
μ_i	i^{th} eigenvalue of the Sturm-Liouville problem defined by Equation 8
ρ	density, $kg \cdot m^{-3}$
τ	total shear stress, Pa
τ_w	wall shear stress, Pa
ν	kinematic viscosity, $m^2 \cdot s^{-1}$
φ	function of Re and Pr, defined as $(j_w \cdot \delta)/(Q \cdot D)$
Φ_j	j^{th} coefficient of the polynomial expansion of $\Phi(Z)$
$\Phi(Z)$	function defining the dimensionless boundary condition at wall
$\Psi_i(R)$	i^{th} eigenfunction of the Sturm-Liouville problem given by Equations 8 and 9

Subscripts

$()_{j_w}$	case of wall heat flux alone (no internal heat generation)
$()_Q$	case of internal heat generation alone (adiabatic wall)
$()_{Q+j_w}$	general case of both wall heat flux and internal heat generation

8. References

Bin, L.; Yu-ting, W.; Chong-fang, M.; Meng, Y. & Hang, G. (2009). Turbulent convective heat transfer with molten salt in a circular pipe. *International Communications in Heat and Mass Transfer*, Vol.36, No.9, pp. 912-916, ISSN 0735-1933

Cammi, A.; Di Marcello, V.; Luzzi, L.; Memoli, V. & Ricotti, M.E. (2011a). A multi-physics modelling approach to the dynamics of Molten Salt Reactors. *Annals of Nuclear Energy*, Vol.38, No.6, pp. 1356-1372, ISSN 0306-4549

Cammi, A.; Fiorina, C.; Guerrieri, C. & Luzzi, L. (2011b). Dimensional effects in the modelling of MSR dynamics: moving on from simplified schemes of analysis to a multi-physics modelling approach. *Nuclear Engineering and Design*, doi:10.1016/j.nucengdes.2011.08.002 (in press), ISSN 0029-5493

Churchill, S.W. (1997). New simplified models and formulations for turbulent flow and convection. *AIChE Journal*, Vol.43, No.5, pp. 1125-1140, ISSN 1547-5905

Churchill, S.W. (2002). A reinterpretation of the turbulent Prandtl number. *Engineering Chemistry Research*, Vol.41, No.25, pp. 6393-6401, ISSN 0888-5885

Colburn, A.P. (1933). A method of correlating forced convection heat transfer data and a comparison with fluid friction. *Transactions of the American Institute of Chemical Engineers*, Vol.29, pp. 174-210, ISSN 0096-7408

Delpech, S.; Cabet, C.; Slim, C. & Picard, G. (2010). Molten fluorides for nuclear applications. *Materials Today*, Vol.13, No12., pp. 34-41, ISSN 1369-7021

Di Marcello, V.; Cammi, A. & Luzzi, L. (2008). Analysis of thermal-hydraulic behaviour of the molten salt nuclear fuel, *Proceedings of the International Conference Nuclear Energy for New Europe*, pp. 301.1-301.10, ISBN 978-961-6207-29-4, Portorož, Slovenia, September 8-11, 2008

Di Marcello, V.; Cammi, A. & Luzzi, L. (2010). A Generalized Approach to Heat Transfer in Pipe Flow with Internal Heat Generation. *Chemical Engineering Science*,Vol.65, No.3, pp. 1301-1310, ISSN 0009-2509

Dittus, F.W. & Boelter, L.M.K. (1930). Heat Transfer in Automobile Radiators of the Tubular Type. *University of California publications in engineering*, Vol.2, No.13, pp. 443-461, ISSN 0096-9311

Fluent, 2005. FLUENT® 6.2 User's Guide, Fluent Inc.

Forsberg, C.W. (2002). Molten salt reactors (MSRs), *Proceedings of the Americas Nuclear Energy Symposium*, Miami, FL, USA, October 16-18, 2002

Forsberg, C.W.; Peterson, P.F. & Pickard, P.S. (2003). Molten-Salt-Cooled Advanced High-Temperature Reactor for Production of Hydrogen and Electricity. *Nuclear Technology*, Vol.144, No.3, (December 2003), pp. 289-302, ISSN 0029-5450

Furukawa, K.; Arakawa, K.; Erbay, L.B.; Ito, Y.; Kato, Y.; Kiyavitskaya, H.; Lecocq, A.; Mitachi, K.; Moir, R.; Numata, H.; Pleasant, J.P.; Sato, Y.; Shimazu, Y.; Simonenco, V.A.; Sood, D.D.; Urban, C. & Yoshioka, R. (2008). A road map for the realization of global-scale thorium breeding fuel cycle by single molten-fluoride flow. *Energy Conversion and Management*, Vol.49, No.7, pp. 1832-1848, ISSN 0196-8904

GIF-IV (2002). A Technology Roadmap for Generation IV Nuclear Energy Systems. Technical Report, GIF-002-00, US DOE Nuclear Energy Research Advisory Committee and the Generation IV International Forum

GIF-IV (2009). Generation IV International Forum 2009 Annual Report, Available from http://www.gen-4.org/PDFs/GIF-2009-Annual-Report.pdf

Gnielinski, V. (1976). New equations for heat and mass transfer in turbulent pipe and channel flow. *International Chemical Engineering*, Vol.16, No.2, pp. 359-367, ISSN 0020-6318

Guo, J. & Julien, P.Y. (2003). Modified log-wake law for turbulent flow in smooth pipes. *Journal of Hydraulic Research*, Vol.16, No.2, pp. 359-367, ISSN 0020-6318

Hargraves, R. & Moir, R. (2010). Liquid Fluoride Thorium Reactors. *American Scientist*, Vol.98, No.4, (July-August 2010), pp. 304-313, ISSN 0003-0996

Hausen, H. (1959). Neue Gleichungen für die Wärmeübertragung bei freier odererzwungener Strömung (new equations for heat transfer in free or forced flow). *Allgemein Wärmetechnik*,Vol.9, No. 4/5, pp. 75-79, ISSN 0002-5976

Heng, L.; Chan, C. & Churchill, S.W. (1998). Essentially exact characteristic of turbulent convection in a round tube. *Chemical Engineering Journal*, Vol.71, No.3, pp. 163-173, ISSN 1385-8947

Kays, W.M. (1994). Turbulent Prandtl number – Where are we?. *Journal of Heat Transfer, Transaction of the ASME*, Vol.116, No.2, pp. 284-295, ISSN 0022-1481

Kays, W.M.; Crawford, M.E. & Weigand, B. (2004). *Convective Heat and Mass Transfer*, McGraw-Hill Inc., ISBN 0070337217, New York.

Kedl, R.J. (1970). Fluid dynamic studies of the Molten-Salt Reactor Experiment (MSRE) core. Technical Report, ORNL-TM-3229, Available from http://www.energyfromthorium.com/pdf/ORNL-TM-3229.pdf

Kinney, R.B. & Sparrow, E.M. (1966). Turbulent pipe flow of an internally heat generating fluid. *Journal of Heat Transfer, Transaction of the ASME*, Vol.88C, No.3, pp. 314-322, ISSN 0022-1481

Křepel, J.; Rohde, U.; Grundmann, U. & Weiss, F.P. (2007). DYN3D-MSR spatial dynamics code for molten salt reactors. *Annals of Nuclear Energy*, Vol.34, No.6, pp. 449-462, ISSN 0306-4549

Langhaar, H.L. (1962). *Dimensional analysis and theory of models*, John Wiley & Sons, ISBN 0882756826, New York.

LeBlanc, D. (2010). Molten salt reactors: a new beginning for an old idea. *Nuclear Engineering and Design*, Vol.240, No.6, pp. 1644-1656, ISSN 0029-5493

Luzzi, L.; Cammi, A.; Di Marcello, V. & Fiorina, C. (2010). An Approach for the Modelling and the Analysis of the MSR Thermo-Hydrodynamic Behaviour. *Chemical Engineering Science*, Vol.65, No.16, pp. 4873-4883, ISSN 0009-2509

Luzzi, L.; Di Marcello, V. & Cammi, A. (2011). *Multi-Physics Approach to the Modelling and Analysis of Molten Salt Reactors*, Nova Science Publishers, Inc., ISBN 978-1-61470-000-5, Hauppauge, NY.

Nicolino, C.; Lapenta, G.; Dulla, S. & Ravetto, P. (2008). Coupled dynamics in the physics of molten salt reactors. *Annals of Nuclear Energy*, Vol.35, No.2, pp. 314-322, ISSN 0306-4549

Nuttin, A.; Heuer, D.; Billebaud, A.; Brissot, R.; Le Brun, C.; Liatard, E.; Loiseaux, J.-M.; Mathieu, L.; Meplan, O.; Merle-Lucotte, E.; Nifenecker, H.; Perdu, F. & David, S. (2005). Potential of thorium molten salt reactors detailed calculations and concept evolution with a view to large scale energy production. *Progress in Nuclear Energy*, Vol.46, No.1, pp. 77-99, ISSN 0149-1970

Poppendiek, H.F. (1954). Forced-convection heat transfer in pipes with volume-heat sources within the fluids. *Chemical Engineering Progress Symposium Series*, Vol.50, No.11, pp. 93-104, ISSN 0069-2948

Renault, C.; Delpech, S.; Merle-Lucotte, E.; Konings, R.; Hron, M. & Ignatiev, V. (2010). The Molten Salt Reactor: R&D Status and Perspectives in Europe, *Proceedings of the 7th European Commission Conference on Euratom research and training in reactor systems*, pp. 384-399, ISBN 13- 978-92-79-13302-2, Prague, Czech Republic, June 22-24, 2009

Robertson, R.C. (1971). Conceptual design study of a single-fluid molten-salt breeder reactor. Technical Report, ORNL-4541, Available from http://www.energyfromthorium.com/pdf/ORNL-4541.pdf

Schlichting, H. & Gersten, K. (2000). *Boundary Layer Theory*, Springer, ISBN 3-540-66270-7, New York.

Sieder, E.N. & Tate, G.E. (1936). Heat transfer and pressure drop of liquids in tubes. *Industrial & Engineering Chemistry*, Vol.28, No.12, pp.1429-1435, ISSN 0888-5885

Siegel, R. & Sparrow, E.M. (1959). Turbulent flow in a circular tube with arbitrary internal heat source and wall heat transfer. *Journal of Heat Transfer, Transaction of the ASME*, Vol.81C, No.1, pp. 280-290, ISSN 0022-1481

Weigand, B.; Kanzamar, M. & Beer, H. (2001). The extended Graetz problem with piecewise constant wall heat flux for pipe and channel flows. *International Journal of Heat and Mass Transfer*, Vol.44, No.20, pp. 3941-3952, ISSN 0017-9310

Yu-ting, W.; Bin, L.; Chong-fang, M.; Meng, Y. & Hang, G. (2009). Convective heat transfer in the laminar-turbulent transition region with molten salt in a circular tube. *Experimental Thermal and Fluid Science*, Vol.33, No.7, pp. 1128-1132, ISSN 0894-1777

Zagarola, M.V. & Smits, A.J. (1997). Scaling of the mean velocity profile for turbulent pipe flow. *Physical Review Letters*, Vol.78, No.2, pp. 239-242, ISSN 0031-9007

7

Measurement of Multiphase Flow Characteristics Via Image Analysis Techniques: The Fluidization Case Study

Antonio Busciglio, Giuseppa Vella and Giorgio Micale
Universitá degli Studi di Palermo
Italy

1. Introduction

In recent years, thanks to the continuous development of digital imaging systems and digital image processing, a great number of researchers have chosen digital visual methods to be applied in the field of experimental fluid dynamics. These kinds of techniques play a fundamental role in analysis and data acquisition for multiphase flows such as gas-solid, gas-liquid, solid-liquid flows, where the observation of inter-phase boundaries is relatively simple.

In this chapter, an overview on some imaging-based experimental techniques for the analysis of complex multiphase systems is reported. In particular, some techniques aimed at the study fluidization dynamics will be analyzed and discussed, as developed by our research group.

Fluidization occurs when the forces exerted by a fluid passing through a bed of particles counteract the particle weight. At this stage, the bed on the whole is just supported by the flowing gas and acquires fluid-like properties, free to flow and deform, keeping a horizontal level when tilted and allowing low-density objects to float on the bed surface. For most of the cases of gas-solid fluidization, fluid velocity increments beyond incipient fluidization are accompanied by the formation of bubbles, or cavities with hardly any solid particles in them. In general, gas flow beyond incipient fluidization mostly reports to bubble flow. Aggregation of solid particles into a dense continuous phase, making room for the passage of most of the gas in excess of incipient fluidization through a bubbling discontinuous phase, bespeaks the two phase nature of gas-solid fluidization. Such a phenomenon of gas-solid systems was designated aggregative.

Much has been written about bubbling phenomena in fluidized beds over the last years. In fact a good understanding of the bubble hydrodynamics is necessary to understand bubble-related phenomena such as solid mixing and segregation, reaction conversion, heat transfer and particle entrainment in beds operated in the bubbling regime. The size, shape and velocity of bubbles and relevant flow patterns are of key interest in bubbling hydrodynamics.

The adoption of image analysis techniques can be in principle fully automated and made robust for measurement of the complex fluid dynamic behavior of fluidized systems. By in-house development of a suitable software, it is possible to get a total control over every single step of the procedure and every single parameter involved in the calculations, thus achieving a higher level of reliability of the data so far obtained. Thanks to the high level

of automation, it is possible to simultaneously compute a large number of data, allowing at the same time a meaningful statistical analysis that is intrinsically necessary given the chaotic nature of the source data.

The first technique reported is an original technique based on the back-lighting of 2-dimensional fluidized bed for the measurement of gas bubbles rising up through the dense granular phase of a fluidized bed. The main problems during the development of this particular technique are due to the set up of the light panel, and the setting up of camera, in order to obtain the best level of contrast between bubbles and emulsion phase, limiting in any case the possible over-exposition of images. Moreover, some care must be taken in the choice of threshold values for the discrimination of bubble phase from emulsion phase. A careful choice of camera setting allows to perform measurement of time dependent quantities (for which high image acquisition rates are generally necessary) and quasi-steady state properties measurements (for which, conversely, long experiments times and low image acquisition rates can be used). After data acquisition, a number of examples of derived quantities measured will be shown, together with the basic principles adopted for the derivation. Of course, most of the examples are here reported for the case of fluidized beds, but could be adapted for the measurement of other multiphase systems.

The second technique here reported allows the measurement of the solid phase behavior in a bubbling fluidized bed, by means of front-lighting of a granular bed of glass white particles in which a small amount of black corundum particles are dispersed as a seed for the application of a velocimetry technique akin to the PIV technique used for flow field measurement in single phase systems. The main problems encountered are connected with the set-up of a fast acquisition system and the image processing, in order to isolate the motion of tracers for subsequent velocity measurements.

The third technique here reported deals with the measurement of mixing pattern and dynamics measurements of two differently colored particles (having the same density but different size), allowing for the first description of mixing dynamics of the bed with non-intrusive technique. The main problems to be faced are due to the solid-phase occupied pixels identification and in the translation of luminance data into mixing-extent data. This shall pass through advanced color-image analysis.

2. Experimental set-up

For the case study here presented 2-D fluid-bed reactor was adopted in order to attain full visualization of the flow characteristics within the bed itself. The adoption of a 2D bed, in which bed thickness is quite smaller than the other dimensions allows easy visualization of bubble dynamics and solid-phase dynamics, as will be further discussed in the following sections devoted to the presentation of imaging techniques. Moreover, 2D data can be readily used for the validation of CFD codes and models (Busciglio et al., 2009) without the need for full 3D, time-consuming simulations.

The 2D fluid-bed facility reactor (size: 250 (w) x 1200 (h) x $10(t)\,mm$) adopted for the experiments presented in this contribution is made of aluminium and equipped with glass walls at front and back. Sintered plastic porous distributor is placed at the bottom of the particle bed, providing large enough pressure drop to avoid dynamic coupling between gas fluxes within the bed and the wind box placed below the distributor to guarantee uniform gas distribution. Further details on the gas supply system can be found elsewhere (Busciglio et al., 2008). The settled bed height was generally set to twice the bed width.

For the measurement of bubbling dynamics characteristics or emulsion phase velocity, experimental data (i.e. bed images) were acquired after full steady state was achieved, in order to avoid measuring bubble behavior during the initial mixing of powders. Conversely, for the measurement of mixing dynamics of powder mixtures, images were taken of the mixing transient itself, in a condition very far from steady state that will be discussed more in detail in the following. In all cases, the observation was focused on the whole bed, without selecting any particular region of interest, to allow a full field analysis of the fluidization dynamics.

The bubble-related flow structures were visualized with the aid of a back-lighting device and recorded by a digital camcorder (mvBlueFox 121c), placed opposite to the bed. Continuous high intensity uniform illumination was obtained by placing six fluorescent lamps at the back side of the bed. The experimental system was also equipped for high intensity front-lighting of the bed, that was adopted for the measurement of solid-phase related measurement (mixing dynamics and velocity field). In the case of front-lighting, a careful positioning of the lamps (often coupled with the adoption of some kind of diffusing-light device) is needed to avoid any shadow or refection that could infer the measurements. Conversely, this problem is practically non-existent when back-lighting is adopted.

The digital visual acquisition system allowed to collect images of the bed at different frequencies ranging from 1 to 70 *fps*, see Fig.1. The choice of the correct frame rate mainly depends on the time scale of the phenomena under investigation. As an example, bubble characterization needs the lowest frame rate, in order to take images of different bubbles instead of different images of the same bubble rising through the bed. Conversely, bubble velocity measurements need large frame rates, in the order of 30 to 60 fps, in order to make bubble tracking algorithm (that is able to follow the the same bubble in different subsequent frames) reliable enough.

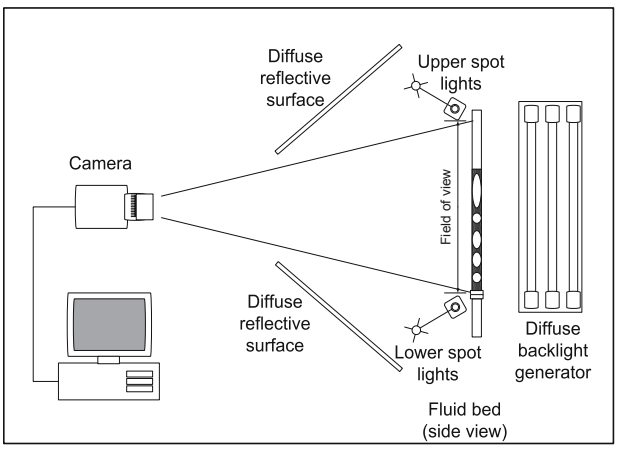

Fig. 1. Fluid bed experimental set-up: optical scheme.

In all cases, the flow dynamics were analyzed and processed using purposely developed digital image analysis routines. In order to automate the image acquisition and data processing procedure, all in-house routines were developed using the Matlab image processing toolbox.

3. Bubbles measurements

Mixing of powders and solid-fluid contact efficiency within the bed is driven by the particle-free voids of bubbles that form when the gas flow rate exceeds the superficial velocity of minimum bubbling. The bubbles ensure that the particles are circulated throughout the bed so that properties and process condition could be considered as uniform.

Many characteristic features of fluidized beds, as well as the fluidization quality in general, are highly dependent on the distribution of bubbles and their physical properties. Therefore the measurement of bubble characteristics and their distribution over the entire cross-section of fluidized beds is of great practical importance in understanding the overall fluid dynamics of the reactors as this is necessary for their design and scale-up. In particular bubble size, velocity, shapes and flow patterns are of key interest in bubbling hydrodynamics. These properties have been extensively measured experimentally by various methods. The experimental methods and finding have been summarized in several review articles (Cheremisinoff, 1986; Davidson et al., 1985).

Different techniques have been employed to experimentally measure bubble parameters. These can be broadly classified into two categories depending on the nature and position of the sensors used: (i) intrusive techniques and (ii) non-intrusive techniques. The intrusive techniques such as resistance, inductance, impedance, piezoelectric or thermal probes were extensively used and could provide accurate measurements. However such probes were expected to alter the nature of local fluidization due to their intrusiveness and moreover they were required to move through the whole volume of the fluidized bed in order to map the entire flow field of the reactor. Conversely, non intrusive techniques enable good visual observation without interfering with fluidization dynamics. These include photographic, X-ray radiography, light scattering, laser techniques, positron emission tomography, electrical capacitance tomography, optical tomography, ultrasonic tomography, positron emission particle tracking and particle image velocimetry.

In recent years a great number of researchers have chosen digital visual methods to be applied in the field of experimental fluid dynamics (Boemer et al., 1998; Gera & Gautam, 1995; Hull et al., 1999; Lim & Agarwal, 1990; Mudde et al., 1994). This technique results an important method, in particular for the analysis of bubble properties, as it provides rigorous and detailed information about the flow structure of the entire bed without interfering with flow dynamics. Digital visual methods can only be effectively used in pseudo-two-dimensional beds, as in this case bubbles can be easily observed. The use of Digital Image Analysis Technique (DIAT) in fluidized bed studies was pioneered by Lim and co-workers (Lim & Agarwal, 1992; Lim et al., 1990; 1993) and their works were summarized by Agarwal et al. (1997).

Hull et al. (1999) reported an experimental data on bubble characteristics averaged size and rise velocity were obtained using digital image analysis method from two-dimensional (thin) bubbling fluidized beds with and without simulated horizontal tube bundles. These data were used to develop semi-empirical correlations for bubble size and rise velocity. Caicedo et al. (2003) used image analysis technique to show that bubble aspect ratio and shape factor in a 2D gas-solid fluidized bed where in generally normally distributed. A wider experimental campaign was performed by Shen et al. (2004) an original image analysis technique. The authors were able to measure several bubble properties such as size and rise velocity, axial and radial distribution of bubbles and gas through flow, in order to develop suitable correlations for bubble diameter and rise velocity in 2D beds.

In the late works by Lim and co-workers (Lim et al., 2006; 2007), digital image analysis was adopted to study bubble void fraction in the frequency domain and together with relevant statistical analysis, showing how frequency-domain statistics could be useful for inferring the bed fluidization quality.

In the paper by Busciglio et al. (2008), digital image analysis technique was developed to study the hydrodynamics of a two dimensional bubbling fluidized bed. The technique allows for the simultaneous measurements of the most significant bubble properties, *i.e.* bubble size and bubble velocity distributions, bed height and bubble-phase hold-up, by means of a purposely developed software. Notably, the same authors (Busciglio et al., 2009) applied successfully their technique to both experimental data and, for the first time, to computational results, as obtained by a commercial CFD code. In particular, the use of the very same data analysis technique to both sets of data allows for a fully consistent quantitative comparison of the very same physical quantities, overcoming the well known problem of comparison sensitivity to the differences in the experimental measurement techniques and numerical post-processing computations.

Laverman et al. (2008) studied the hydrodynamics of an experimental freely bubbling pseudo 2-D fluidized bed coupling Particle Image Velocimetry and Digital Image Analysis. This technique allowed to investigate the mutual interaction between the bubble and emulsion phase in detail. Similar techniques, in which PIV and image analysis techniques were coupled together were also adopted by Sánchez-Delgado et al. (2008) and Sánchez-Delgado et al. (2010)

The work by Asegehegn and co-workers (Asegehegn et al., 2011a;b) used a back-lighting based image analysis technique to study 2D gas fluidized beds with and without a dense tube bank, comparing by means of the same technique both experimental and numerical results.

3.1 Image analysis technique

The aim of the present section is to present the technique used for the analysis of bubbling fluidization on the basis of digital image processing. The digital image analysis technique (DIAT) developed comprises acquiring images using a camcorder and then processing and analyzing the images using an in-house routine. The in-house routine was developed with the help of the Matlab 7.3 (The MathWorks inc.), using the Image Processing Toolbox to fully automate the procedure of image processing.

Bubbles were detected because they transmit light emitted at the back of the bed which reaches the camera. Thus white areas represent bubbles while the remaining black area indicates the emulsion phase, as can be clearly seen in Fig.2.

Once recalled the image to analyze, the routine works through some simple steps:

- Thresholding of the original RGB image to obtain a binary image of the bed. This allows the discrimination of the bubble phase from the dense phase of the bed;
- Indexing of all individual regions inside the area of interest;
- Filtering of false bubbles and peripheral voids;
- Property recording of each region inside the area of interest.

In particular the thresholding procedure is used to transform a greyscale image (in which any pixel assumes values ranging from 0 to 1) into a binary one, suitable for object identification. This is an important step in discriminating a bubble from the rest of the bed. Bubble

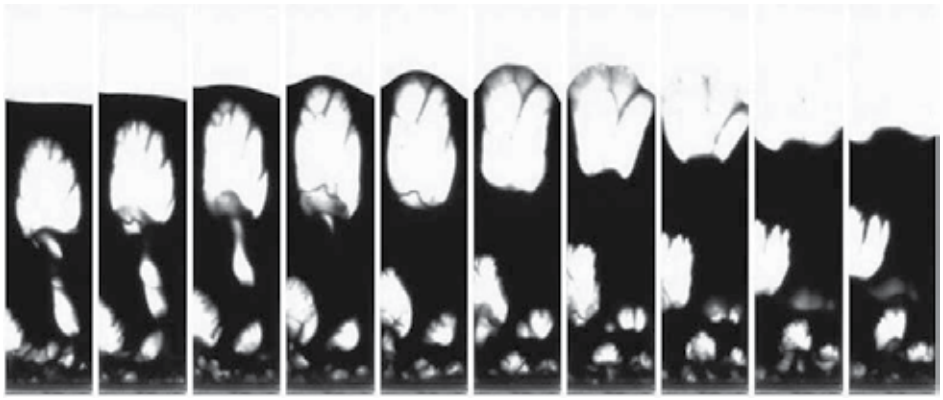

Fig. 2. Typical snapshot sequence obtained by bed back-lighting (glass particles, $U = 0.18\,m/s$, $d_p = 212 - 250\,\mu m$).

discrimination is usually done with the help of a threshold value for the pixel intensity of the grayscale images. The problem is thus converted in finding a correlation between pixel luminance, ranging from 0.0 to 1.0 and voidage, ranging from 0.4 to 1.0. The conventional distinction between the emulsion phase and the bubble phase is set at a voidage value of 0.80 (Yates et al., 1994). If the relation between luminance and voidage were assumed linear, a luminance threshold value of about 0.67 would be used. However a linear correlation does not hold true in describing the phenomenon of light transmission across a fluid bed, where typically a Beer-Lambert law applies (Boemer et al., 1998; Brucato & Rizzuti, 1997a;b; Rizzuti & Yue, 1983; Yates et al., 1994; Yue et al., 1986). On the other hand, the very wide and flat valley between the peaks in the bimodal distribution of gray-level, shown in Fig.3, ensures that the choice of any arbitrary value of luminance threshold in the range of $0.4 - 0.8$ influences in a marginal way the bubble property measurements. This is equivalent to use the so called entropy method (Kapur et al., 1985). For the images used in this work, this condition holds true, and the threshold value can be chosen using different considerations. In the left part of Fig.3 a typical gray-scale bed image is shown, while a typical gray level distribution is shown in the center of the same figure. The threshold value, in this case can be chosen at any point in the range of $0.3 - 0.8$, resulting in negligible influence of threshold value on bubble size measurement.

The binary image thus obtained is then subdivided (labeled) into different components, based upon connectivity analysis. For each bubble present in the image, its relevant area, equivalent diameter, and centroids coordinates are computed as reported in Eqns.1 and 2.

$$A_b = \sum b\,(x,y) \tag{1}$$

Bubble centroid coordinates can be computed as follow:

$$\begin{aligned} x_c &= \int\int xb\,(x,y)\,dxdy \\ y_c &= \int\int yb\,(x,y)\,dxdy \end{aligned} \tag{2}$$

where the integrals are extended to the area occupied by the analyzed bubble. Equivalent diameter is then calculated from the knowledge of bubble area.

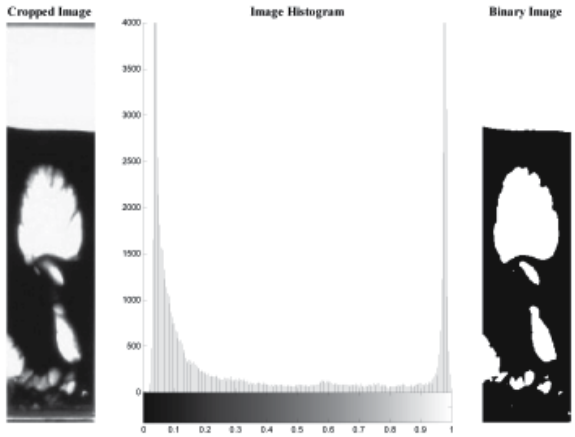

Fig. 3. Original image (left), gray level histogram (center) and threshold image (right).

Distances and areas expressed in pixels can be easily converted in metric distances and areas by multiplying with suitable scale factors preliminarily determined by a set of still calibration images. Notably, for bubble size and position measurement, very low values of frame rate can be adopted, typically 1 fps, in order to avoid measuring the same bubble in different positions within the bed.

Filtering of false bubbles is necessary because of the recirculation of solid particles inside each bubble rising through the bed. In high contrast images, this phenomenon appears in the form of high solid concentration zones at the bottom of the bubble. In the thresholding step this can lead to the appearance of a bubble followed by a constellation of small bubbles following the first one at the same velocity. The presence of the above mentioned false bubbles and peripheral voids, *i.e.* rising voids adherent to the lateral walls and bubbles bursting at the top of the bed, have been carefully excluded from the statistical analysis of bubble properties.

Once bubble in each frame were analyzed, it is possible to compute bubble velocity. This was accomplished adopting a self developed Lagrangian Velocimetry Technique (LVT), (Busciglio et al., 2008). The Lagrangian velocimetry technique (LVT) developed uses a very simple tracking algorithm to follow the displacement of each bubble in two (or more) subsequent frames. Of course, the higher the frame rate, the more accurate the bubble tracking will result. For bubble velocity measurement, a frame rate of 60 fps was found to be well suited.

By adopting the LVT procedure it is possible to obtain:

- Distribution (cloud) of bubble rise velocities and average velocity as function of equivalent diameter;
- Distribution (cloud) of bubble lateral velocities as function of equivalent diameter;
- Distribution of bubble rise angle (probability plot);
- Statistical distribution of velocity coefficients ϕ for each bubble, where the bubble velocity is given by $U_b = \phi(gD_b)^{0.5}$.

Once the bubbles rising up through the bed are indexed, it is possible follow the time evolution of each property of each bubble through its path along the bed.

This quantities alone can not be directly used for bubbling regime characterization, but a further step of data post-processing is needed to assess fluidized bed behavior. In the following, the raw data obtained will be discussed, together with some of the numerical and statistical methods adopted for translation of large amount of raw data into information useful for fluidization quality characterization.

3.2 Typical results

Bed height and overall bubble hold up data are the simplest data to be obtained. In particular, in Fig.4 it is possible to observe the characteristic saw-tooth shaped fluctuations of the free surface of the bed, due to the eruption of bubbles. Bubble hold up data are computed by dividing the sum of bubble projected areas in each frame by the total area occupied by the bed (this last being computed as the overall image area minus the freeboard projected area). It must be observed that the bed expansion dynamic and the relevant bubble hold-up dynamic, even if similar, are linked to rather different phenomena. In fact, overall bed expansion depends on both the extent of the bubble phase content and the average expansion of the emulsion phase (including, for example small non-visible bubbles, and the expanded cloud region surrounding the bubbles), while bubble hold-up measures just bubble overall content within the bed.

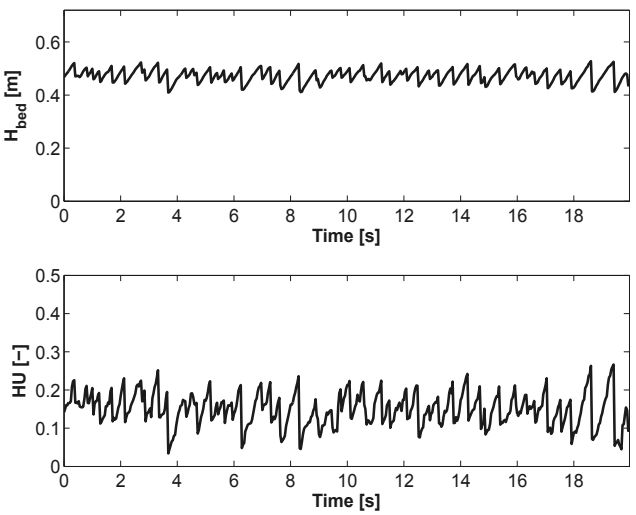

Fig. 4. Typical measurement of bed height and instantaneous average bubble hold-up (glass particles, $U = 0.18\,m/s$, $d_p = 212 - 250\,\mu m$).

Bubble equivalent diameters can be conveniently reported as function of bubble distance from distributor, since bubble size is expected to grow along its path through the bed because of coalescence phenomena. The full set of data are presented in Fig.5(a) in raw cloudy form, in order to highlight the complex bubble behavior along bed height. The adoption of an average curve with indication of its variance would not account for the richness of the raw data. Conversely, the cloudy data presented allow the visualization of the small bubbles that are inside the bed even at the highest elevations, while an average curve, even if with variance, could not show such characteristic and complexity.

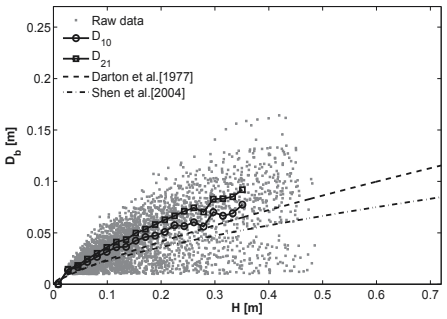

(a) Diameter evolution as a function of the distance above the distributor

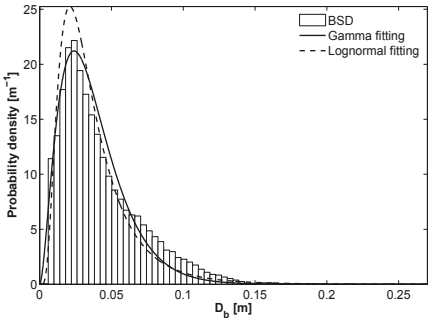

(b) Typical bubble size distribution

Fig. 5. Typical measurement of bubble size distributions (glass particles, $U = 0.18\,m/s$, $d_p = 212 - 250\,\mu m$).

On the whole the experimental data show a characteristic increase in bubble diameter, with an upper envelope of data approximately following a power law, in accordance with the analysis by Darton et al. (1977). However, the presence of a wide distribution of bubble sizes is evident at all elevations of the bed, as a result of the splitting and/or nucleation phenomena. This results are in agreement with the finding of Hulme & Kantzas (2004), in which large data scattering on bubble diameter *vs.* distance above the distributor was shown.

A different way for bubbling characterization passes through the analysis of the overall bubble size distribution (BSD). Some experimental distributions of bubble equivalent size distribution on the whole bed are reported in Fig5(b). The experimental distributions show a characteristic positive skewness of the distributions at all inlet gas velocities, in accordance with relevant literature data (Argyriou et al., 1971; Lim et al., 1990; Liu & Clark, 1995; Morooka et al., 1972; Rowe & Yacono, 1975; van Lare et al., 1997; Werther, 1974a;b). Thanks to the huge number of data available from image analysis technique, it is possible to observe that both Gamma and Log-normal distributions generally adopted in literature give rise to poor agreement with the experimental data for bubbles larger than $5\,cm$. This effect is probably linked to an oversimplification of the phenomena, that need more sophisticated analysis techniques to be better characterized (Busciglio et al., 2010).

Once the boundary between emulsion phase and bubble phase has been chosen, as already discussed in relevant chapter, the bubble hold up ϵ_b (or HU) can be simply defined as:

$$\epsilon_b = \frac{\int_V V_b dV}{\int_V V_b dV + \int_V V_{emulsion} dV} \tag{3}$$

To define the local gas hold-up, it is sufficient to define a proper control volume inside the whole system, and computing the limit for control volume towards zero.

$$\epsilon_{b,loc} = \lim_{V \to 0} \frac{\int_V V_b dV}{V} \tag{4}$$

To compute the time averaged local gas hold-up:

$$\epsilon_{b,av,loc} = \frac{1}{T}\int_0^T \lim_{V\to 0}\frac{\int_V V_b dV}{V} \tag{5}$$

If the control volume is infinitesimal, it can not admit the contemporary presence of both phases, thus the local hold up can be replaced with an instantaneous phase indicator:

$$\epsilon_{b,av,loc} \equiv \Phi(x,y) = \begin{cases} 1 \Leftrightarrow (x,y) \in V_{bubble} \\ 0 \Leftrightarrow (x,y) \notin V_{bubble} \end{cases} \tag{6}$$

$$\epsilon_{b,av,loc}(x,y) = \frac{1}{T}\int_0^T \Phi(x,y)\, dt \tag{7}$$

This definition of phase indicator is immediately applicable to compute local time averaged maps of gas hold-up by the means of digital image analysis techniques. We have to consider the images that can be obtained by the image analysis based on binarized images of the back-lighted fluidized bed already described. If we assume to assign to gas-phase occupied pixels a unitary luminance value, and zero luminance value otherwise, it is simple to observe that luminance value $b(x,y)$ exactly coincides with the gas phase indicator $\Phi(x,y)$ above defined.

The analysis of experimental time averaged bubble phase hold-up, shown in Fig.6(a), allows the visual observation of preferential bubble paths along the bed, with a typical reverse-Y shaped pattern starting near the bottom of the bed and developing in the upper regions of the bed. The reverse-Y shaped pattern is due to the coalescence-driven bubble dynamics prevailing after bubble nucleation in the proximity of the distributor in the intermediate region of the bed.

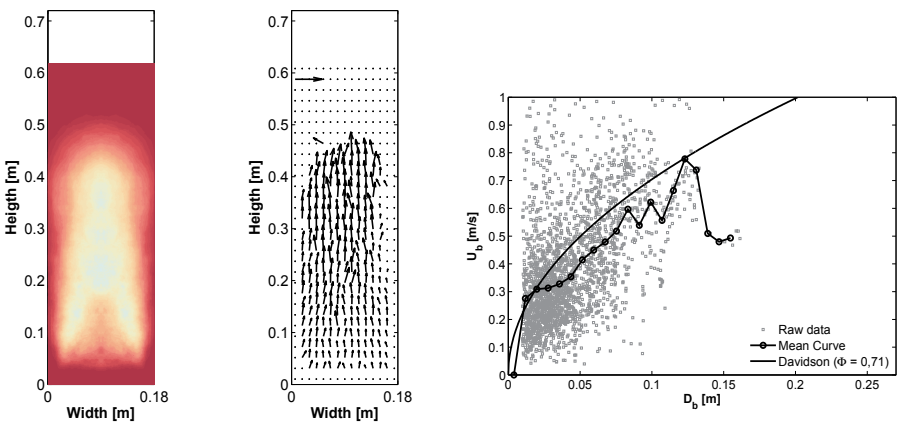

(a) Bubble hold-up (b) Bubble velocity field (c) Bubble rise velocity

Fig. 6. Bubble hold-up map and velocity field (glass particles, $d_p = 212 - 250\,\mu m$, $U = 0.18\,m/s$).

The analysis of experimental data on average rise velocity as a function of bubble equivalent diameter reported in Fig.6(c) shows a behavior different trend than expectation, *i.e.* than that of the well accepted Davidson equation $u_b = \phi\sqrt{g\,d_b}$. At smaller diameters, the average rise velocities are larger than those predicted, while at the larger diameters the experimental data are quite noisy. In the mid-range of diameters, the data trend follow correctly the square-root law expected, but velocity is somewhat smaller than that deriving form a velocity coefficient of $\phi = 0.71$ as proposed by Darton, and a velocity coefficient of $\phi = 0.58$ should be adopted. These findings can be all explained if the bubbling conditions adopted for experiments are recalled. In a few words, the systems investigated ranged from poorly bubbling to highly slugging system. The more intense the bubbling regime, the stronger are bubble-to-bubble interactions within the bed. On this basis, it is easy to imagine that small bubbles velocities are largely influenced by interaction with larger bubbles, that tend to accelerate them toward coalescence. At the same time, it is clearly very difficult to accurately measure the velocity of large, high-interacting bubbles, because of the chaotic motion of their boundary due to coalescence phenomena, bubble splitting phenomena and deformation along their path along the bed.

The experimental data on bubble rise velocity can also be put in the form of bubble vector plot, as reported in Figs.6(b). The plots can be obtained by suitable time averaging of instantaneous bubble velocity maps. In accordance to the previous discussions, bubble trajectories would be slightly oriented toward the center of the bed in the lower part of the bed and then vertically directed in the upper section of the bed. Moreover, the velocity field plots confirm the evidence for the local bubble hold-up maps shown in Figs.6(a). These latter allow for the visualization of preferential bubble paths along the bed height, whereas the former relates the relevant bubble average velocities to preferential paths.

4. Particle Image Velocimetry

Digital Image Analysis (DIA) and Particle Image Velocimetry (PIV) are two of the most common techniques applied to 2-D fluidized beds to analyze the bubble and emulsion phases. 2-D fluidized beds allow for bubble visualization, making it possible to obtain relevant bubble parameters to characterize the bubbling behavior of the fluidized bed. Additionally, the emulsion phase velocity can be characterized using the PIV technique. PIV is a non-intrusive technique for the measurement of an instantaneous velocity field in one plane of a flow.

In particular Bokkers et al. (2004) studied mixing and segregation induced by a single bubble injected in a fluidized bed at incipient fluidization conditions and in freely bubbling fluidized beds. PIV was applied to obtain the ensemble averaged particle velocity profile in the vicinity of a bubble in dense gas-solid fluidized systems. Laverman et al. (2008) combined the DIA and the PIV techniques to study the bubble behavior (local bubble size and velocity distribution and bubble fraction) and to characterize the emulsion phase profiles (in a pseudo-2-D bed because of the required visual accessibility).

Sánchez-Delgado et al. (2008) presented an experimental study to characterize ascending bubbles and granular velocity in the dense phase of a 2-D fluidized bed. They studied the time-averaged bubble concentration in a 2-Dfluidized bed to characterize the behavior of fluidized beds with different bed aspect ratios and superficial gas velocities. They also applied a PIV method to characterize the particle velocity vectors, collecting information on the location of the recirculation regions within the emulsion phase. The same authors presented also an investigation of the perturbations induced by the bubbles in a 2-D fluidized

bed developing a combination of DIA and PIV (Sánchez-Delgado et al., 2010) to distinguish the dense phase from the bubble phase and obtain the time-averaged velocity of the dense phase as well as the proportion of time that a region was occupied by a bubble.

Particle Image Velocimetry and Digital Image Analysis were used by Agarwal et al. (2011) to study the effect of inlet gas jets located at the distributor in rectangular fluidized beds. Experiments were conducted with varying distributor types and bed media to understand the motion of particles and jets in the grid-zone region of a fluidized bed.

Hernàndez-Jimènez et al. (2011) reported simulation and experimental results of the hydrodynamics of a two-dimensional, bubbling air-fluidized bed. The experimental results have been obtained by means of DIA and PIV techniques applied on a real bubbling fluidized bed to ensure its two-dimensional behavior. This study examines and compares not only the bubble hydrodynamics and dense-phase probability within the bed, but also the time-averaged vertical and horizontal component of the dense-phase velocity, the air throughflow and the instantaneous interaction between bubbles and dense-phase.

In this section we report some details about an original technique adopted for the measurement of the solid phase behavior in a bubbling fluidized bed (based on front-lighting of a granular bed of glass white particles in which a small amount of dispersed black corundum particles) for the application of a velocimetry technique akin to the PIV technique used for flow field measurement in single phase systems.

The PIV technique is able to statistically measure the main particle displacement within two subsequent frames. In traditional PIV the flow is visualized by seeding it with small tracer particles that perfectly follow the flow, in this case the utilized tracer particles are black corundum particles seeding in a granular bed of glass white particles. High intensity front-lighting of the system, coupled with light diffusers (in order to minimize shadows or reflection in the front wall of the bed) and higher frame rates (in the order of $70\,fps$) with respect to those adopted in the case of bubble-dynamic measurement must be adopted. The resulting typical images are reported in Fig.7. Notably, in the rear wall of the bed a yellow panel was placed in order to better isolate bubble-occupied pixels.

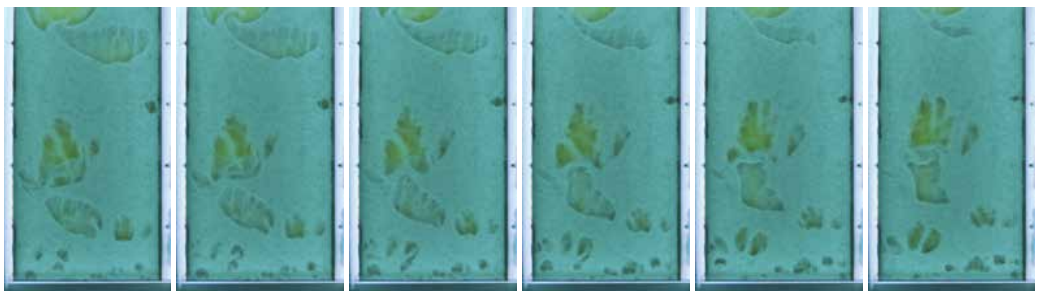

(a) (b) (c) (d) (e) (f)

Fig. 7. Snapshot sequence of a PIV-ready fluidized bed taken at $\Delta t = 1/70\,s$, (glass particles with corundum tracers, $U = 0.27\,m/s$, $d_p = 212 - 250\,\mu m$).

Two subsequent images of the flow, separated by a short time delay, Δt, are divided into small interrogation areas. Cross-correlation analysis is used to determine the displacement of the tracer particles in each interrogation area between the first and second image. The mean tracer velocity in each interrogation area can be then determined since the time delay is known. The

main tasks of image analysis in this case is to discard of bubbles from the subsequent analysis and to enhance the seed particles in the image. Cross-correlation can then be performed by means of commercial softwares or GNU-licensed software (for the present investigation, the MPIV software developed under Matlab by Nobuhito Mori, distributed under GNU - General Public License is adopted).

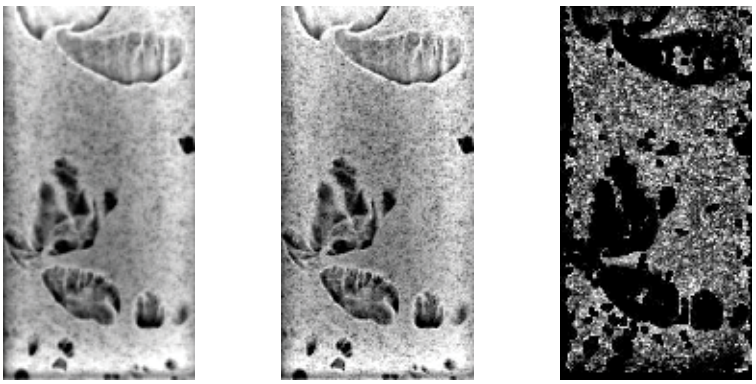

Fig. 8. Steps of image processing for PIV application to solid particles velocity measurements. From left to right: (a) cropped and adjusted image; (b) sharpened image; (c) bottom hat transform to minimize illumination non uniformity effects with final bubble elimination.

Bubble identification is needed to neglect particle velocities in highly diluted regions of the bed, *i.e.* inside the gas bubbles. In fact, these regions are characterized by high-particles velocities due to particles spouting from the bubble wake and particle raining from the bubble ceiling. Nevertheless, this velocities belong to few particles with respect to those pertaining to the emulsion phase. On this basis, a reliable measurement of particle velocities have to be restricted to emulsion phase particles. Of course, the seed particle enhancing is needed to make cross-correlation analysis more accurate.

The ideal image for PIV procedure is that in which seed particles give rise to a single illuminated pixel and zero-value pixel otherwise. This is of course a condition very far from the raw images of our system reported in Fig.7. The first step of the image analysis routine consist in the conversion of the acquired image into the relevant greyscale image and relevant exposure adjustment. The result of this operation is reported in Fig.8.a. Notably, bubbles are clearly visible. Then the image is suitably filtered to increase their contrast and increase sharpening, therefore obtaining the image reported in Fig.8.b. Bubbles are then isolated by conversion into a binary images by means of the entropy method (Kapur et al., 1985). At the same time, a bottom-hat morphological transform is applied to the enhanced image, in order to highlight the out-of-background structures. By setting to zero the value of bubble phase-occupied pixels, the final image suitable for PIV procedure is obtained (Fig.8.c). This finally allows the discrimination of bubble phase from the dense phase of the bed and the discrimination of tracer particles.

Then, the images are post processed with the help of the MPIV software under Matlab 7.3 environment. In particular the imaged, is subdivided into a macro areas of 16x16 pixels,

and in each area the mean displacement vector of tracer particles along x and y directions is measured.

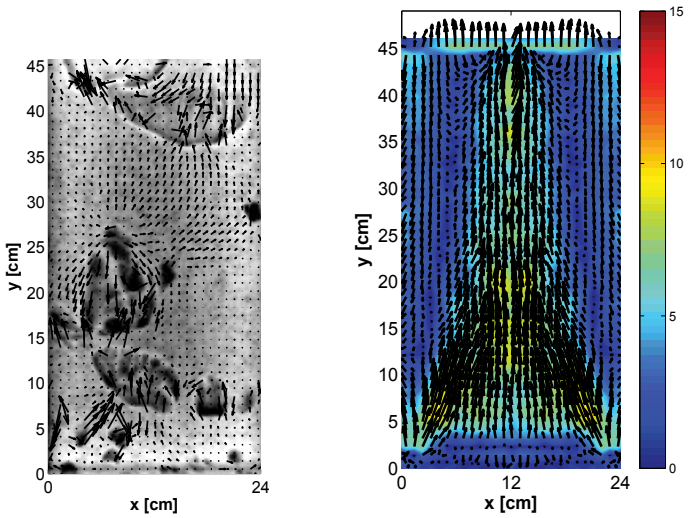

(a) (b)

Fig. 9. Typical results of PIV processing (glass particles with corundum tracers, $U = 0.27\,m/s$, $d_p = 212 - 250\,\mu m$).

In Fig.9.(a), a typical instantaneous velocity field so far obtained is reported, superimposed to the raw image of the system, where it is possible to observe the particle velocity field around each bubble. In Fig.9.(b), the relevant time-averaged velocity plot is reported, highlighting the high-upward mean velocity zone near the center of the bed together with the low-downward mean velocity regions located at the lateral walls.

5. Mixing and segregation dynamics analysis

The fluidization behavior of mixed powder with different diameter or density strongly depends on the nature and composition of the mixture. One of the main characteristics of fluidized mixed powders is the possible onset of segregation or mixing dynamics, depending on inlet gas velocity and particle characteristics. In particular, the heavier (or larger) particles, hereafter referred as jetsam component, show the tendency to segregate toward the bottom of the bed, while the lighter (or smaller), hereafter referred as flotsam component, float above of the segregated particles (Rowe & Yacono, 1975).

The particle mixing characteristics of gas fluidized bed of binary system (i.e. composed of particles with different sizes and/or densities) is of great importance because it is an important factor for the prediction of the bed performance which relates with fluidization quality (Formisani et al., 2008b). Researchers have extensively investigated how dissimilar fluidized particles mix and segregate, aiming at predicting the behavior and understanding the underlying mechanisms of mixing and segregation (Clarke et al., 2007; Formisani et al., 2008a;b). Most of the experimental studies that appear in the literature on polydispersed

fluidized mixtures tried to characterize these systems determining the minimum fluid velocity necessary to fully fluidized them, (Formisani, 1991; Formisani et al., 2001; Noda et al., 1986; Rowe & Yacono, 1976), or studying their dynamics by means of pressure probes (Marzocchella et al., 2000; Olivieri et al., 2004; 2006).

Mostoufi & Chaouki (2000) studied solids behavior by processing the obtained data by a Radioactive Particle Tracking (RPT) technique. In a different paper, the same authors (Mostoufi & Chaouki, 2001) studied the effective diffusivity of solid particles in both bubbling and turbulent regimes. Fennel et al. (2005) used Magnetic Resonance Imaging to studying the rate of axial mixing in a vertical direction of a small plug of solids throughout a fluidized bed of different solids. Humekawa et al. (2005) used X-ray and neutron radiography to studying segregation phenomena. Huang et al. (2008) determined the axial and radial solids dispersion coefficients by a two-dimensional unsteady state dispersion model.

Very few works actually deals with the measurements of segregation or mixing dynamics in bi-dispersed fluidized beds. Leaper et al. (2004) and Bosma & Hoffmann (2003) investigated the dynamics of formation of de-fluidized jetsam layers in fluidized beds, Prasad Babu & Krishnaiah (2005) studied the dynamics of defluidized jetsam layer during segregation of binary heterogeneous mixtures in small continuous-fed reactor. Goldschmidt et al. (2003) developed an experimental technique based on digital image analysis to measure bed expansion and segregation dynamics in dense gas-fluidized beds, in order to validate CFD simulation of mono-disperse and binary mixtures fluid beds. This technique allowed the authors to measure, through the use of differently colored particles and RGB images decomposition, the extent of mixing and segregation. Jang et al. (2010) reported a study on mixing-segregation phenomena in a gas fluidized bed of binary density system performed by analysis of the residence time distribution and mixing degree. The authors also considered axial concentration distribution of jetsam particle and residence time distributions of solids, finally assessing mixing characteristics from the relationship between the residence time and the mixing degree analyzed by sieve test.

In this section we report a new experimental technique, hereafter referred as Mixing and Segregation Dynamics Analysis (Mi.Se.D.A.), based on Digital Image Analysis for the measurement of the mixing behavior in a bi-dispersed 2D fluidized bed.

Corundum particles of different size and colors were used for the present investigation (black corundum particles having $d_p = 212 - 250\,\mu m$, referred to as flotsam component and white corundum particles having $d_p = 500 - 600\,\mu m$, referred to as jetsam component). Mixing patterns of the powders were visualized with the aid of a purposely arranged front-lighting device and recorded by a digital camcorder (MVBlueFox). For a better recognition of bubbles, a flat yellow panel was placed in contact with the rear wall of the bed.

Two types of experiments were performed:

- Transient mixing dynamics of segregated powder (jetsam placed at the bottom, flotsam placed at the top of the settled bed).
- Transient segregation dynamics of completely mixed powders.

The technique is based on advanced color images analysis of a bi-dispersed system with powders of different colors. In Fig.10, a typical sequence of snapshots of the bed during mixing experiment is shown. The use of different colored powders allows a clear qualitative recognition of the initial mixed condition and its evolution with time, i.e. the decrease with

time of the settled jetsam layer at the bottom of the bed and the trails of white particles carried by bubbles, especially in the first snapshots. The Image Analysis Technique here proposed is aimed at obtaining quantitative information on the mixing/segregation dynamics. The first problem to tackle is that of recognizing bubbles in the bed, that are clearly detectable by means of visual observation.

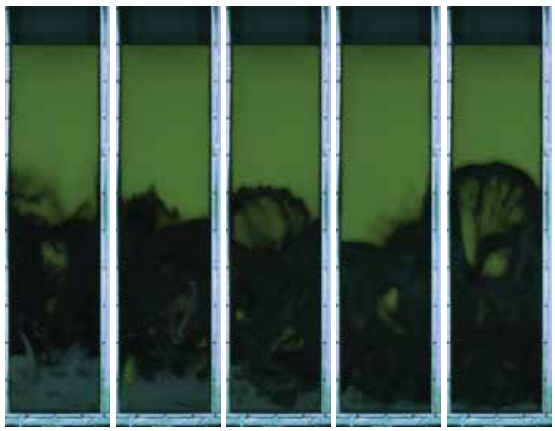

(a) (b) (c) (d) (e)

Fig. 10. Snapshots of a mixing system taken at $\Delta t = 5\,s$.

The technique is based on a suitable color decomposition of raw images acquired with the above discussed experimental set-up and on subsequent analysis of flotsam concentration dispersion and segregation in a fluidized bed. Two main problems has to be tackled in order to obtain reliable information on mixing or segregation dynamics of powders by means of image analysis:

1. Identification of the solid phase in which composition-related measure must be taken: the images are taken during the vigorous bubbling of the bed, and each color measurement must be limited to pixel belonging to solid phase only;
2. Identification sufficiently reliable relation between image characteristics and bed composition in order to obtain data on the dynamics of bed homogenization or segregation.

It is worth noting that a calibration procedure is not strictly needed when analyzing mixing dynamics, once previously discussed problems are solved. As a matter of fact, it is sufficient to measure a generic quantity monotonically dependent on bed composition to obtain sufficient information on the transitory dynamics from initial to final state of bed homogenization, regardless of the link between actual composition (expressed for example in flotsam weight percentage) and the relevant measure adopted.

Each image is taken and saved by the camera in RGB color space (Red Green Blue), that can be suitably decomposed, as reported in Fig.11(a).

As it can be clearly seen, given the original colors of the adopted powders (near to black and white), each color channel contains similar information. Qualitative analysis of mixing or segregation can be still performed, but such a color decomposition after some trials was found

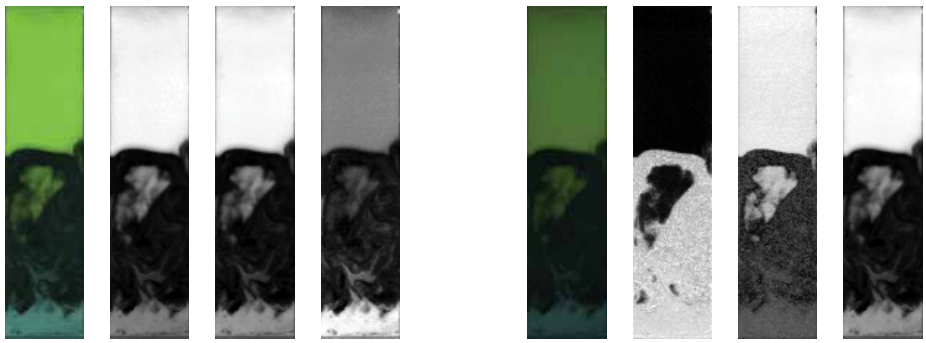

(a) RGB (red, green, blue) decomposition (b) HSV (hue, saturation, value) decomposition

Fig. 11. Typical original image and intensity plot of relevant decomposed channels in RGB and HSV space, corundum particles in mixing mode, $X = 0.5w/w$ in flotsam component, $U = 0.503\,m/s$.

unsuitable for automatic robust image analysis, even if an example of *RGB* based process was previously developed (Goldschmidt et al., 2003). It was therefore chosen to adopt a different color space for image analysis, *i.e.* the *HSV* (Hue, Saturation, Value) color space. Notably *HSV* is one of the most common cylindrical-coordinate representations of points in an *RGB* color model, which rearrange the geometry of *RGB* in an attempt to be more perceptually relevant than the *RGB* representation itself. The composite image after transformation is of course equal to that previously presented in RGB color space, but its decomposition in single components shows quite different characteristics, as can be observed in Fig.11(b).

As a matter of fact, the hue channel appears to be suitable for the identification of freeboard and bubbles, *i.e.* all bubbles that create a nearly free-of-solid region in the bed that makes yellow panel visible through the bed. A simple threshold value can be chosen by means of entropy method (Kapur et al., 1985) to suitably identify such bubbles. It is therefore possible to generate a logical mask of gas-phase occupied pixels, to be neglected in subsequent analysis of solid phase mixing behavior, as can be seen in Fig.12.

In Fig.12 the relevant distributions of Value in solid phase occupied pixels for a typical experimental case is also reported at two different stages of mixing process. The Value channel was chosen to analyze composition dynamics within the bed, being able to maximize the difference between flotsam and jetsam particles, as already seen in Fig.11(b). This kind of image is somehow proportional to relevant composition map, but, as already discussed, this should not affect mixing or segregation dynamics assessment.

Once the instantaneous Value maps are obtained, the relevant Value distribution can be computed. For the investigated systems, two Value distributions are reported in Fig.12 at two different times. As it is possible to observe for example in Fig.12.(a), in the initial distribution a single peak is observed, because solids are almost uniformly mixed in the early stages of segregation process. Increasing observation time, a strong bimodality clearly occurs in the distribution, because of segregation. Notably, in a fluidized system under mixing conditions,

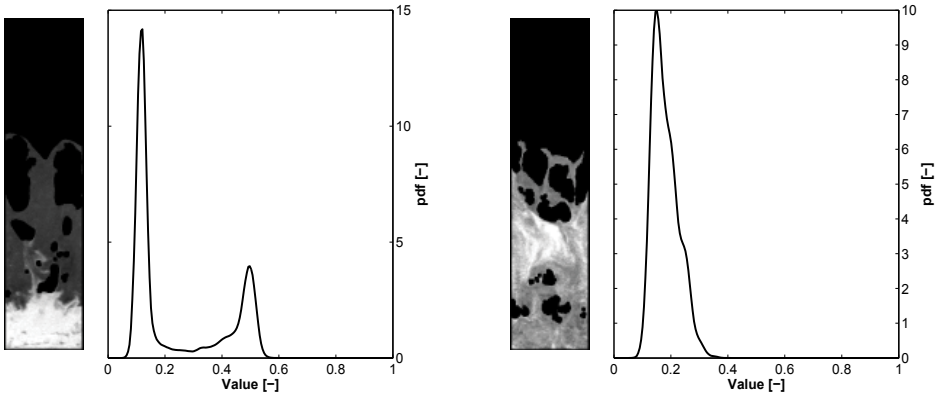

(a) $t = 0\,s$ (b) $t = 50\,s$

Fig. 12. Value channel with superimposed mask of non-solid phase occupied pixels and relevant distributions of hue values at two different times, corundum particles in mixing mode, $X = 0.5 w/w$ in flotsam component, $U = 0.503\,m/s$.

the opposite phenomena occurs, *i.e.* a bimodal distribution is found in early stages while a single peak is measured at the end of segregation.

In Fig.13.(a) it is possible to observe the gradual change from a single peaked to a bimodal distribution with time in a segregation experiment. Notably, the steady state reported in Fig.13.(b) highlights that experimental distribution is well fitted with weighted sums of Gaussian distribution.

Notably, the steady state distribution reported shows that a degree of inhomogeneity still exists for both segregated phases. This is likely to be due to both experimental noise and not perfect segregation, but this is not of crucial importance in dynamics measurements.

Conversely, in Fig.14.(a) it is possible to observe the gradual change from a bimodal to a single peaked distribution with time in a mixing experiment. In this case, the steady state distribution reported in Fig.14.(b) has been fitted with a single Gaussian curve that accounts with sufficient accuracy the main characteristics of the experimental distribution. The difference between model and experimental curve is likely to be due to local inhomogeneities still present in the mixed system.

On this basis, a composition chart could be obtained by comparing the parameters of fitted curves (*i.e.* mean value and relevant standard deviation of each peak analyzed) with the known composition of segregated regions and perfectly mixed regions, as shown in Fig.15(a), even if not strictly needed.

As it can be seen, a clear relation can be observed between mean value of mixed powders and composition, that should allow the reconstruction of composition maps from value maps. Nevertheless, the analysis of standard deviations reported in Fig.15(b) shows that the relatively high values of standard deviations (especially for mixed systems, as already discussed), coupled with some low value differences (especially at higher compositions) between segregated flotsam average value and relevant mixed average value does not encourage the translation of Value maps into composition maps, since uncertainties in such

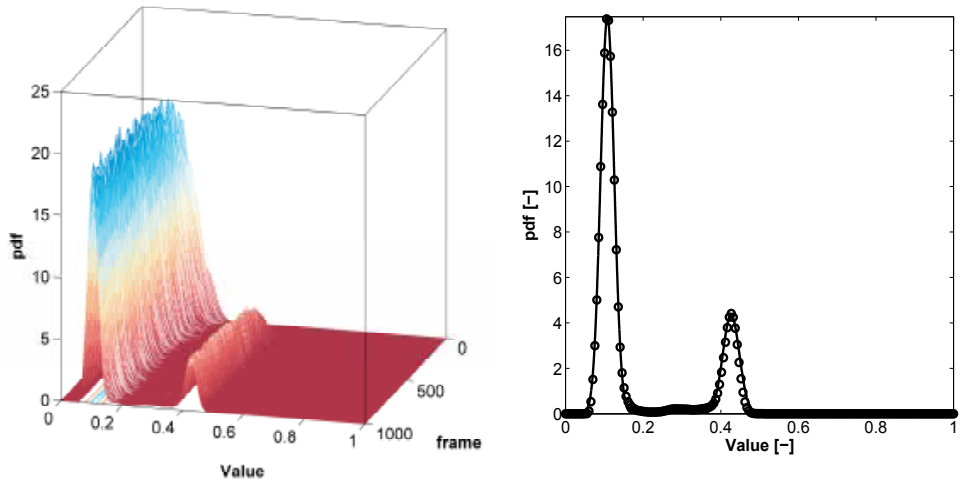

(a) (b)

Fig. 13. Value Distribution evolution with time for a segregation experiment ($X = 0.5w/w$ in flotsam component, $U = 0.38\,m/s$) and relevant steady state distribution.

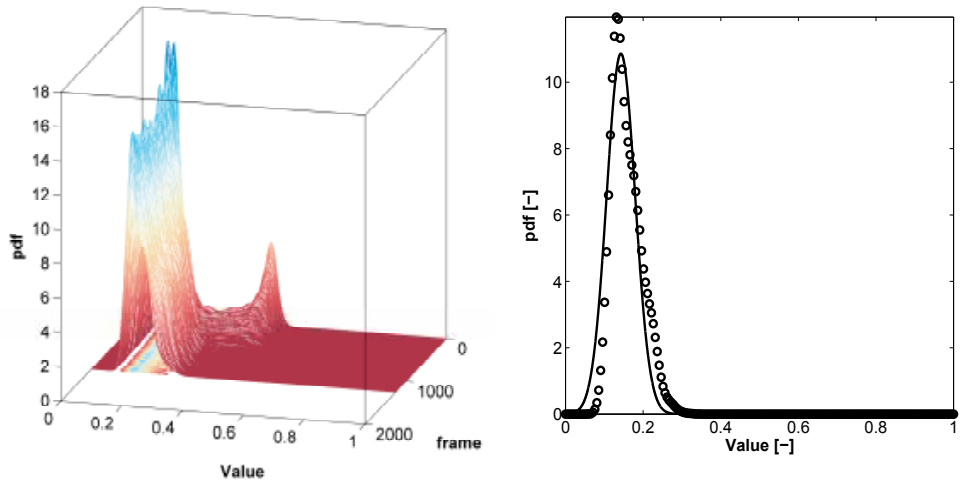

(a) (b)

Fig. 14. Value Distribution evolution with time for a mixing experiment ($X = 0.5w/w$ in flotsam component, $U = 0.503\,m/s$) and relevant steady state distribution.

a calibration would probably introduce unnecessary errors in the measurements of mixing dynamics.

On this basis, the mixing extent was chosen to be solely measured by means of Value distribution analysis. In particular, the polydispersity index was found to be the best suited to

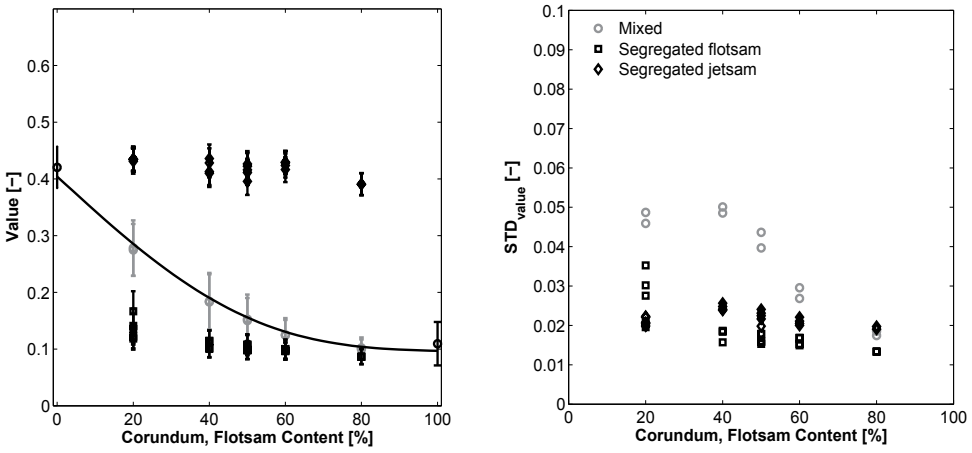

(a) Mean values (b) STD values

Fig. 15. Value and standard composition chart for all cases.

follow the mixing extent over time. The instantaneous polydispersity index $PI(t)$ of the Value distribution can be readily expressed as the ratio:

$$PI(t) = \frac{\overline{V(t)}_{21}}{\overline{V(t)}_{10}} \tag{8}$$

where the generic average value $\overline{V(t)}_{i,j}$ is simply obtained from the measured Value distribution (pdf) as:

$$\overline{V(t)}_{i,j} = \frac{\int_0^\infty V^i \cdot pdf\,(V)\,\mathrm{d}V}{\int_0^\infty V^j \cdot pdf\,(V)\,\mathrm{d}V} \tag{9}$$

In Fig.16, the typical evolution of polydispersity index as a function of time is shown for the cases of mixing (Fig.16(a)) and segregating (Fig.16(b)) system. Notably, the experimental data show a steep decrease (increase) of PI in the first stages of mixing (segregation), that finally tend to a constant value. It is worth noting the large difference in time scale between mixing end segregation dynamics, the former being in the order of tenth of seconds, the latter in the order of hundreds of seconds. Notably, the deviation from final steady state value can be used to define the mixing time as the time required to cover a variation from initial value of the polydispersity index equal to a known percentage of the whole range. In particular the θ_{95} and θ_{99} times are computed and reported in Fig.16, the former indicating that 95% of the evolution of polydispersity index from initial to final state has been run, the latter indicating a 99% evolution.

The strong difference in mixing and segregation time-scale is substantially a new result, that can be accurately addressed in the future. It is likely to be due to the different mechanism of the phenomena involved, being mixing dynamics mainly bubble-driven and

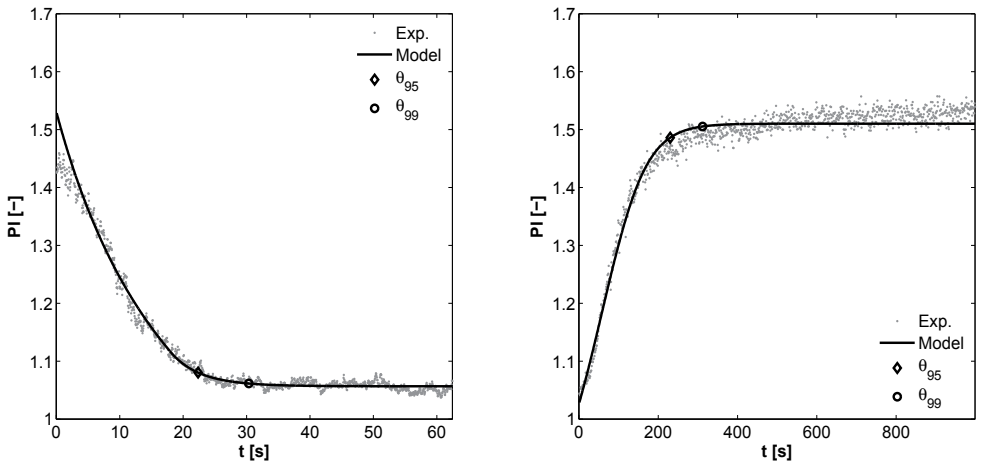

(a) Mixing, $U = 0.503\,m/s$ (b) Segregation, $U = 0.38\,m/s$

Fig. 16. Examples of polydispersity index evolution with time, $X = 0.5w/w$ in flotsam component.

segregation dynamics linked to slow percolation of jetsam particles through the emulsion phase toward the distributor. Of course, several other experiments have to be performed, and the phenomenon quantified. Notably, these first results were achieved thanks to the Mi.Se.D.A. technique, since the previously adopted techniques for measuring the mixing extent (mainly based on the frozen bed technique, that need the fluid inlet to be stopped and the powder composition analyzed layer by layer) make transient measurements impossible. Conversely, the adoption of image-analysis based techniques allows for the set-up of even large experimental campaigns relatively easy.

6. Conclusions

In this chapter, three different ways of using digital image analysis for fluid dynamic measurements were proposed. All techniques here reported were adopted to study different characteristics of a 2D gas-solid fluidized bed.

Notably, very different quantities can be accurately measured by simply changing illumination set-up and camera settings, ranging from bubble dynamics to solid-phase dynamics.

Image analysis techniques are able to combine ease of measurement, accuracy, non-intrusivity and cost saving.

7. References

Agarwal, G., Lattimer, B., Ekkad, S. & Vandsburger, U. (2011). Influence of multiple gas inlet jets on fluidized bed hydrodynamics using particle image velocimetry and digital image analysis, *Powder Technol.* 214: 122–134.

Agarwal, P., Hull, A. & Lim, K. (1997). *Digital image analysis techniques for the study of bubbling fluidized*, Elsevier, Amsterdam.

Argyriou, D., List, H. & Shinnar, R. (1971). Bubble growth by coalescence in gas fluidized beds, *AIChE J.* 17: 122–130.

Asegehegn, T., Schreiber, M. & Krautz, H. (2011a). Investigation of bubble behavior in fluidized beds with and without immersed horizontal tubes using a digital image analysis technique, *Powder Technol.* 210: 248–260.

Asegehegn, T., Schreiber, M. & Krautz, H. (2011b). Numerical simulation and experimental validation of bubble behavior in 2d gas-solid fluidized beds with immersed horizontal tubes, *Chem. Eng. Sci.* 66: 5410–5427.

Boemer, A., Qi, H. & Renz, U. (1998). Verification of eulerian simulation of spontaneous bubble formation in a fluidized bed, *Chem. Eng. Sci.* pp. 1835–1846.

Bokkers, G., van Sint Annaland, M. & Kuipers, J. (2004). Mixing and segregation in a bidisperse gas-solid fluidized bed: a numerical and experimental study, *Powder Technol.* 140: 176–186.

Bosma, J. & Hoffmann, A. (2003). On the capacity of continuous powder classification in a gas-fluidized bed with horizontal sieve-like baffles, *Powder Technol.* 134: 1–15.

Brucato, A. & Rizzuti, L. (1997a). Simplified modelling of radiant fields in heterogeneous photoreactors. 1. case of zero reflectance, *Ind. Eng. Chem. Res.* 36: 4740–4747.

Brucato, A. & Rizzuti, L. (1997b). Simplified modelling of radiant fields in heterogeneous photoreactors. 2. Limiting two-flux model for the case of reflectance greater than zero, *Ind. Eng. Chem. Res.* 36: 4748–4755.

Busciglio, A., Vella, G., Micale, G. & Rizzuti, L. (2008). Analysis of the bubbling behaviour of 2d gas solid fluidized beds. Part I. Digital Image Analysis Technique, *Chem. Eng. J.* 140: 398–413.

Busciglio, A., Vella, G., Micale, G. & Rizzuti, L. (2009). Analysis of the bubbling behaviour of 2d gas solid fluidized beds. part II. Comparison between experiments and numerical simulations via digital image analysis technique, *Chem. Eng. J.* 148: 145–163.

Busciglio, A., Vella, G., Micale, G. & Rizzuti, L. (2010). Experimental analysis of bubble size distributions in 2D gas fluidized beds, *Chem. Eng. Sci.* 65(16): 4782–4791.

Caicedo, G., Marquéz, J., Ruíz, M. & Soler, J. (2003). A study on the behaviour of a 2D gas-solid fluidized bed using digital image analysis, *Chem. Eng. Process.* 42: 9–14.

Cheremisinoff, N. P. (1986). Review of experimental methods for studying the hydrodynamics of gas-solid fluidized beds, *Ind. Eng. Chem. Process Des. Dev.* 25: 329–351.

Clarke, K., Pugsley, T. & Hill, G. (2007). Fluidization of moist sawdust in binary particle systems in a gasï£¡solid fluidized bed, *Chem. Eng. Sci.* 60: 6909–6918.

Darton, R., LaNauze, R., Davidson, J. & Harrison, D. (1977). Bubble growth due to coalescence in fluidized beds, *Trans. Instn. Chem. Engrs.* 55: 274–280.

Davidson, J., Clift, R. & Harrison, D. (eds) (1985). *Fluidization (2nd Edn.)*, Academic Press, New York USA.

Fennel, P., Davidson, J., Dennis, J., Gladden, L., Hayhurst, A., Mantle, M., Muller, C., Rees, A., Scott, S. & Sederman, A. (2005). A study of the mixing of solids in gas-fluidized beds, using ultra-fast MRI, *Chem. Eng. Sci.* 60: 2085–2088.

Formisani, B. (1991). Packing and fluidisation properties of binary mixtures of spherical particles, *Powder Technol.* 66: 259–264.

Formisani, B., De Cristoforo, G. & Girimonte, R. (2001). A fundamental approach to the phenomenology of fluidization of size segregating binary mixtures of solids, *Chem. Eng. Sci.* 56: 109–119.

Formisani, B., Girimonte, R. & Longo, T. (2008a). The fluidization process of binary mixtures of solids: Development of the approach based on the fluidization velocity interval, *Powder Technol.* 185: 97–108.

Formisani, B., Girimonte, R. & Longo, T. (2008b). The fluidization pattern of density segregating binary mixtures, *Chem. Eng. Res. Des.* 86: 344–348.

Gera, D. & Gautam, M. (1995). Bubble rise velocity in two-dimensional fluidized beds, *Powder Technol.* 84: 283–285.

Goldschmidt, M., Link, J., Mellema, S. & Kuipers, J. (2003). Digital image analysis measurements of bed expansion and segregation dynamics in dense gas-fluidized beds, *Powder Technol.* 138: 135–159.

Hernàndez-Jimènez, F., Sànchez-Delgado, S., Gòmez-Garcìa, A. & Acosta-Iborra, A. (2011). Comparison between two-fluid model simulations and particle image analysis and velocimetry (PIV) results for a two-dimensional gas-solid fluidized bed, *Chem. Eng. Sci.* 66: 3753–3772.

Huang, C., Wang, Y. & Wei, F. (2008). Solid mixing behavior in a nano-agglomerate fluidized bed, *Powder Technol.* 182: 334–341.

Hull, A., Chen, Z., Fritz, J. & Agarwal, P. (1999). Influence of horizontal tube tanks on the behaviour of bubbling fluidized beds. 1. Bubble hydrodynamics, *Powder Technol.* 103: 230–242.

Hulme, I. & Kantzas, A. (2004). Determination of bubble diameter and axial velocity for a polyethylene fluidized bed using X-ray fluoroscopy, *Powder Technol.* 147: 20–33.

Humekawa, H., Furui, S., Oshima, Y., Okura, M., Ozawa, M. & Takenaka, N. (2005). Quantitative measurement of segregation phenomena in a binary-mixture fluidized bed by neutron radiography, *Nuclear Instruments and Methods in Physics research A* 542: 219–225.

Jang, H., Park, T. & Cha, W. (2010). Mixing-segregation phenomena of binary system in a fluidized bed, *Journal of Industrial and Engineering Chemistry* 16: 390–394.

Kapur, J., Sahoo, P. & Wong, A. (1985). A new method for gray-level picture thresholding using the entropy of the histogram, *Comput. Graphics Image Process.* 29: 273–285.

Laverman, J., Roghair, I. & Van Sint Annaland, M. (2008). Investigation into the hydrodynamics of gas-solid fluidized beds using particle image velocimetry coupled with digital image analysis, *Can. J. Chem. Eng.* 86(3): 523–535.

Leaper, M., Seville, J., Hilal, N., Kingman, S. & Burbidge, A. (2004). Investigating the dynamics of segregation of high jetsam binary batch fluidized bed systems, *Chemical Engineering and Processing* 43: 187–192.

Lim, C., Gilbertson, M. & Harrison, A. (2006). Measurement and simulation of bubbling fluidized beds, *Powder Technol.* 170: 167-177.

Lim, C., Gilbertson, M. & Harrison, A. (2007). Bubble distribution and behaviour in bubbling fluidized beds, *Chem. Eng. Sci.* 62: 56–69.

Lim, K. & Agarwal, P. (1990). Conversion of pierced lengths measured at a probe to bubble size measures: an assessment of the geometrical probability approach and bubble shape models, *Powder Technol.* 63: 205–219.

Lim, K. & Agarwal, P. (eds) (1992). *Bubble velocity in fluidized beds: the effect of non-vertical bubble rise on its measurements using submersible probes and its relationship with bubble size*, Vol. 69.

Lim, K., Agarwal, P. & O Neill, B. (1990). Measurement and modelling of bubble parameters in a two-dimensional gas-fluidized bed using image analysis, *Powder Technol.* 60: 159–171.

Lim, K., Agarwal, P. & O'Neill, B. (1993). Mixing of homogeneous solids in bubbling fluidized beds: Theoretical modelling and experimental investigation using digital image analysis, *Chem. Eng. Sci.* 48(12): 2251–2265.

Liu, W. & Clark, N. (1995). Relationship between distributions of chord lengths and distribution of bubble sizes including their statistical parameters, *Int. J. Multiphase flow* 21(6): 1073–1089.

Marzocchella, A., Salatino, P., Di Pastena, V. & Lirer, L. (2000). Transient fluidization and segregation of binary mixtures of particles, *AIChE J.* 46: 2175–2182.

Morooka, S., Tajima, K. & Miyauchi, T. (1972). Behavior of gas bubble in fluid beds, *Int. Chem. Eng.* 12: 168–174.

Mostoufi, N. & Chaouki, J. (2000). On the axial movement of solids in gas-solids fluidized beds, *Trans. IChemE* 78(A): 912–921.

Mostoufi, N. & Chaouki, J. (2001). Local solid mixing in gas solid fluidized beds, *Powder Technol.* 114: 23–31.

Mudde, R., Schulte, H. & van der Akker, H. (1994). Analysis of a bubbling 2-D gas-fluidized bed using image processing, *Powder Technol.* 81: 149–159.

Noda, K., Uchida, S., Makinno, T. & Kamo, K. (1986). Minimum fluidization velocity of binary mixture of particles with large size ratio, *Powder Technol.* 46: 149–154.

Olivieri, G., Marzocchella, A. & Salatino, P. (2004). Segregation of fluidized binary mixtures of granular solids, *AIChE J.* 50: 3095–3106.

Olivieri, G., Marzocchella, A. & Salatino, P. (2006). A fluid-bed continuous classifier of polydisperse granular solids, *Proc. of the 2006 AIChE Spring National Meeting,Orlando, USA*.

Prasad Babu, M. & Krishnaiah, K. (2005). Dynamics of jetsam layer in continuous segregation of binary heterogeneous particles in gas-solid fluidized bed, *Powder Technol.* 160: 114–120.

Rizzuti, L. & Yue, P. (1983). The measurement of light transmission through an irradiated fluidised bed, *Chem. Eng. Sci.* 38(8): 1241–1249.

Rowe, P. & Yacono, C. (1975). The distribution of bubble size in gas fluidized beds, *Trans. Instn. Chem. Engrs.* 53: 59–60.

Rowe, P. & Yacono, C. (1976). The bubbling behaviour of fine powders when fluidised, *Chem. Eng. Sci.* 31: 1179–1192.

Shen, L., Johnsson, F. & Leckner, B. (2004). Digital image analysis of hydrodynamics two-dimensional bubbling fluidized beds, *Chem. Eng. Sci.* 52: 2607–2617.

Sánchez-Delgado, S., Almendros-Ibáñez, J., Soria-Verdugo, A., Santana, D. & Ruiz-Rivas, U. (2008). Coherent structure and bubble-particle velocity in 2-D fluidized beds, *Proceeding of the 9th International Conference on Circulating Fluidized Beds.*, pp. 1007–1012.

Sánchez-Delgado, S., Marugán-Cruz, C., Acosta-Iborra, A. & Santana, D. (2010). Dense-phase velocity fluctuation in a 2-D fluidized bed, *Powder Tech.* 200: 37–45.

van Lare, C., Piepers, H., Schoonderbeek, J. & Thoenes, D. (1997). Investigation on bubble characteristics in a gas fluidized bed, *Chem. Eng. Sci.* 52: 829–841.

Werther, J. (1974a). Bubbles in gas fluidized beds - part I, *Trans. Instn. Chem. Engrs.* 52: 149–159.

Werther, J. (1974b). Bubbles in gas fluidized beds - part II, *Trans. Instn. Chem. Engrs.* 52: 160-169.

Yates, J., Cheesman, d. & Sergeev, Y. (1994). Experimental observations of voidage distribution around bubbles in a fluidized bed, *Chem. Eng Sci.* 49: 1885–1895.

Yue, P., Rizzuti, L. & Augugliaro, V. (1986). Bubble phase voidage and dense phase voidage in thin two dimensional fluidized bed, *Chem. Eng Sci.* 41(1): 171–177.

8

Hydrodynamically Confined Flow Devices

Alar Ainla, Gavin Jeffries and Aldo Jesorka*
Chalmers University of Technology, Göteborg, Sweden

1. Introduction

Microfluidic technology is a fast growing branch of microdevice development, which has its origin in the dot matrix printing principle demonstrated by R. Elmqvist of the German Siemens AG in the 1950s. In this "ink jet" concept, droplets are formed from a stream of ink ejected from a microscale opening. The drop formation is characterized by a stream breakup mechanism discovered nearly a century earlier by Lord Rayleigh[1]. It took another twenty years from the initial proof of principle until the first commercial inkjet printer was produced and marketed by IBM in the mid 1970s. It has to be noted that the inkjet printer technology remains the most successful commercial microfluidic application to date.

However, advances in the application of microflow technology were also made in other fields, most notably in chemistry and the biosciences. Microfluidic devices for handling nano- and picolitre volumes of liquids are now commonplace, and have proven to greatly benefit molecular biology, proteomics, DNA analysis, and various branches of analytical chemistry. Microfluidic devices are also frequently used to address the chemical foundations of technological applications, which is often difficult to achieve on the bulk scale. The desire to confine chemical and biological functions to the micrometer sized channels arose mainly from the need to reduce sample size and reagent consumption and to lower fabrication costs, integrate a large number of processing steps, such as mixing, chemical binding and purification, and facilitate interfacing and handling. The drive to integrate various on-chip detection schemes with sample handling and analyte separation led to a new highly integrated class of microfluidic devices, the micro-total analysis systems (μTAS). Such devices require typically between 100 nl and 10 μl of liquid for processing and analysis. The dynamics of liquid flows in microscale channels is quite complex, and deviates significantly from macroscopic flows[2]. The major differences between microscale and macroscopic (bulk) fluid flows arise from the large surface to volume ratio, low Reynolds number effects and noncontinuum molecular effects. In addition, multiscale and multiphysics effects have to be considered when simulating microflow phenomena[3]. As microflows are typically laminar, several streams of fluid can flow in parallel in the same channel without converging into each other. Diffusion dominates the exchange of molecular species in those parallel streams, and equilibration is achieved on a short timescale of seconds to

*Corresponding author

minutes. This feature allows for diffusional mixing as the sole mode of transport between flows, and can be used to control separation and the progress of chemical reactions. Flows can be generated by electroosmotic pumping, capillary forces, or by means of applying pressure. Each method has advantages and disadvantages; a practical choice depends on the type of sample, the interfacing requirements and the detection principle desired.

Closed-channel microfluidics can rightfully be considered an established, often highly beneficial method for the processing of small sample volumes for applications within biology, chemistry and biotechnology, with high potential to reach into medicine and diagnostics in the near future. Recent technological developments, such as droplet microfluidics, and low-cost production processes are expected to facilitate this development further. The fabrication of microfluidic devices is generally achieved through top-down micro-construction techniques: traditional lithography of quartz, glass and silicon substrates, soft lithography using various polymers, and layered (laminate) technologies, for example utilizing paper or polymeric thin films[4].

However, in many important instances closed channel microfluidic device are not a suitable solution, even though sample size and other requirements are in the optimal range. For example, it is difficult or often impossible to interact with surfaces or surface adhered objects, such as single cells or tissue slices. Cells have to be introduced into the channel structure, manipulated to the desired position, kept alive under controlled conditions, and exchanged or removed from the channels. Growing cells in microscale channels is subject to limits imposed by the diffusion-dominated material transport in confined volumes, which can have a detrimental effect on cell growth. Moreover, the spatially controlled delivery of small amounts of liquid to a surface, for instance in order to create defined patterns or achieve surface functionalization, pushes closed channel designs to the limit. An elegant practical solution to many problems is offered by a new microflow concept, which uses a dynamically defined open volume principle rather than pre-defined, closed channels for confinement and delivery of fluids.

2. Hydrodynamically confined flow devices

Hydrodynamically confined flow (HCF), also occasionally referred to as hydrodynamically confined microflow (HCM) devices, are a modern class of microfluidic flow cells, where a small, moving volume of fluid is spatially confined within another, significantly larger fluid volume. The two liquids are physically in contact, separated only by means of a dynamically created virtual boundary. This boundary can be achieved, for example, by two adjacent microflow channels. One channel serves as injection port or outlet (positive pressure), where liquid is introduced into an open volume, and one as aspiration port or inlet (negative pressure), through which liquid is removed. As some surrounding liquid is also being removed from the fluid bulk, a laminar flow envelope results, which confines the liquid between inlet and outlet. Material transport across the boundary is only possible by diffusion. There is only a relatively small number of HCF devices present in the literature, as this novel class of devices has just started to progress into a research area[5-14]. The contributions of the different research groups are summarized in table 1. For reference, the technologically related devices, which do not employ hydrodynamic confinement, but feature similar channel arrangements and in/out-flows, creating an exposed liquid volume,

are included. They can be considered milestones in the development of the HCF devices, and have their own interesting set of applications, for example in electrochemical surface analysis and in parallel assay technology. Highlighted in the table are geometries, channel arrangement, interface and positioning, and the major material. Typical materials are silicon, glass and polymers, most dominating the silicone elastomer poly(dimethyl siloxane), or PDMS.

Figure 1 shows three example concepts of hydrodynamically confined flow devices, the microfluidic multipurpose probe (MFP), the vertical microfluidic probe (vMFP), and the multifunctional micropipette (MFπ), pioneered by two different research groups. Figure 1(A), depicts schematically the microfluidic probe developed by Junker *et al.* from IBM. From design and idea, but not necessarily from principle, it can be considered a descendant of IBM's classic ink jet printing technology[5]. The device consists of a flat silicon plate of cm^2 dimensions with two central orifices on a central mesa-like structure, one for solution inlet and one for outlet (with respect to the open bath). For operation, it is arranged parallel to the surface of interest, and submerged in a shallow bath of fluid. It is held at a fixed distance of a few micrometers by four protruding posts. The plate is interfaced by supply tubes, and can be positioned by a micromanipulation device. When positive pressure is applied to the injection port, and negative pressure (moderate vaccum) to the aspiration port, a stream of liquid moves through the bath and creates a defined volume of fluid, which is spatially confined to the region between surface and silicon mesa. The red color represents the inflow (injection) into, and the blue color the outflow (aspiration) from the open volume. A small part of the open volume is also drawn into the outflow channel. It has to be noted that this open volume component is typically the major share of the total inflow volume, which is fundamental to define the hydrodynamic confinement. In this two-cannel device, the close proximity of the surface is preferred to prevent fluid from escaping the confinement. The lower panel in fig. 1A displays the bottom plate of the device together with an enlarged view of the mesa.

Figure 1D shows a photograph of this device, as presented in the original publications. In fig. 1B a structural modification of the MFP is schematically displayed, termed the vertical microfluidic probe (vMFP)[13]. The large silicon bottom plate of the earlier design has been replaced by a rhombic Si/glass composite with a flat, polished tip, which can be clamped and interfaced to the supplies by a matching sealing holder. In order to achieve efficient interaction of the out-flowing liquid with the surface, this design still requires parallel alignment of the channel outlet plane with the surface. The generation of the confined volume is commensurate to the MFP, fluid circulation is also achieved through tubing and syringe pumps. Fig. 1E is a series of photographs, showing the two individual holder parts, the rhombic silicon chip and the fully assembled device.

Both MFP and vMFP are fabricated from silicon or bonded silicon/glass. These devices are optically intransparent and can be used under a microscope only with limitations. Even more disadvantageous is the vertical positioning in upright microscopes, which limits the compatibility with microscopy stations to some extent. The vertical probe eliminates some of the problems, since it is rather small and partly transparent. Inverse microscopes are accessible, even though a means of precise positioning might be advisable, such as a motorized stage. The solution depicted in Fig 1C overcomes these disadvantages by both using a transparent material combination and a design which allows angled positioning.

Authors	Confinement[1]	Architecture	Major Material	Channel matrix	Exposure area (μm x μm)	Application angle	Supply system	Other features. Comments
Juncker et al.[15]	None (conformal)	Planar	Si	2 x 1 (x4)	500 x 80	Planar. Fixed	On-chip wells and capillary pumps	
Cesaro-Tadic et al.[16]	None (conformal)	Planar	Si	2 x 1 (x11)	1000 x 30	Planar. Fixed	On-chip wells and capillary pump	
Smith et al. /Wasatch[17]	None (conformal)	Vertical	PDMS	2 x 1 (x48)	400 x 600	Perpendicular (90°). Fixed	On-chip wells and pressure drive	
Chen et al.[18]	None (conformal)	Vertical	PDMS	2 x 1	200 x 200	Perpendicular (90°). Fixed	External from syringe pumps	Connected to external analysis
Routenberg et al.[19]	None (conformal)	Planar	PDMS	2 x 1	~500x500	Planar. Fixed	Syringe	
Delamarche et al. WO2004050245	Hydrophilic/-phobic (dry)	Planar	Si	2 x 1	180 x 60	Planar. Fixed	On-chip wells and capillary pump	
Momotenko et al.[20]	Flow ratio (dry)	Vertical	PET	2 x 1	~Ø100	Variable angle	External from syringe pumps	Integrated carbon, Ag/AgCl electrodes
Juncker et al.[5]	Hydrodynamic (immersed)	Planar	Si	2 x 1	~Ø50-100	Planar. Fixed	External from syringe pumps	
Lovchik et al.[6]	Hydrodynamic (immersed)	Planar	Si	2 x 1	~Ø50-100	Planar. Fixed	External from syringe pumps	
Christ et al.[11]	Hydrodynamic (immersed)	Planar	Si	2 x 1	~Ø300-900	Planar. Fixed	External from syringe pumps	Syringe pumps have diff. manometer
Queval et al.[7]	Hydrodynamic (immersed)	Vertical	PDMS	3 x 2	~Ø40-100	Perpendicular (90°). Fixed	External from syringe pumps	
Kaigala et al.[13]	Hydrodynamic (immersed)	Vertical	Si/glass	2 x 1 or 3 x 1	10-10'000 (area)	Perpendicular (90°). Fixed	External from syringe pumps	Immersion liquid supply and injection
Ainla et al.[8]	Hydrodynamic (immersed)	Vertical	PDMS	3 x 1	30 x 10 – 120 x 120	Variable angle	On-chip wells and pressure drive	

[1]Technologically related flow principles (no hydrodynamic confinement) are included for reference.

Table 1. Summary of publications of HCF devices and related exposed-volume microflow technologies.

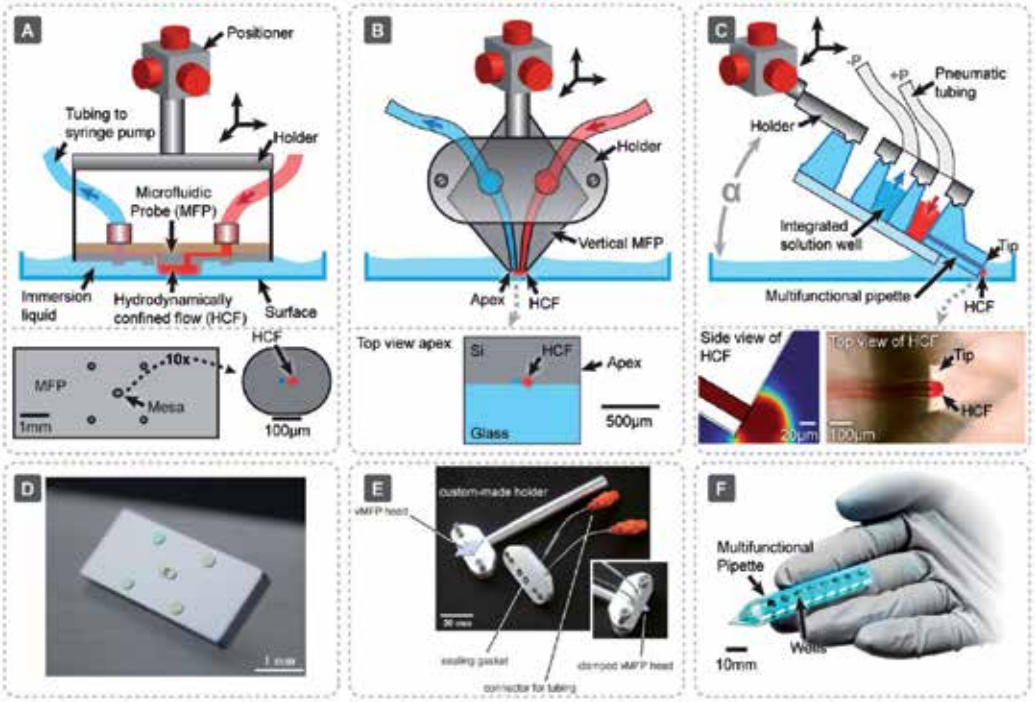

Fig. 1. Hydrodynamically confined flow devices. A) The microfluidic multipurpose probe[5-6], fabricated from a planar silicon dice. It features one inlet (injection port) and one outlet (aspiration port) and is applied in parallel orientation to the surface. B) The vertical microfluidic probe[13], constructed from a bonded silicon-glass quadrilateral, held in place by a holding clamp. It is identical in channel arrangement and function to the MFP, but is more straightforward to fabricate. The channel outlet face of the chip is also oriented parallel to the surface of interest, such that the surface is in full contact with the confined volume. C) The multifunctional pipette[21], fabricated as a bonded PDMS-glass composite. This device creates a hydrodynamically confined volume at the tip of a pipette-shaped device, which is pressurized via on-chip wells and a holding interface. This device can be positioned at an angle α to the surface, since the three channel design with one injection port and two adjacent aspiration ports is supported by the thin membrane, which assures close surface proximity. D-E) Photographs of the devices of A-C, as shown in the original publications. D) Reprinted with permission from ref. [6]. Copyright 2009 Institute of Physics. E) Reprinted with permission from ref. [13]. Copyright 2011 American Chemical Society.

The multifunctional pipette (MFπ) is a three-channel device, which uses one central injection, and two adjacent in-plane aspiration ports. An important functional feature of the device is the 10-30 µm thin transparent bottom plane, which allows close proximity to the surface and to objects of interest located thereupon. The pipette is historically related to a previously published hard-materials design, which used a set of two coaxial glass pipettes to achieve a fountain pen-like function[22]. This inspiring concept allows the contamination-free delivery of a liquid to an arbitrary volume element in an open bath, avoiding accumulating contamination of the bath by the inflowing liquid. The material however, being brittle and difficult to process, makes the larger-scale production of this solution

delivery device more than problematic. There are also severe drawbacks with respect to applying the needle-like device in close proximity to a surface. Small errors in positioning can instantly break the delicate assembly. In contrast, the MFπ tip is (currently) entirely made from PDMS elastomer, and can be repeatedly brought in contact with the surface without loss of integrity. The flow profile generated by the three-channel arrangement is comparable to the one provided by the coaxial fountain pen. It allows free-standing operation, since no fluid can escape the hydrodynamic confinement within the recirculation zone created at the very tip. Direct contact to the surface is no longer required. The lower panel in fig. 1A shows a side view (FEM simulation of the concentration profile at the channel outlet) and a top view, which visualize the three channel arrangement by means of a red colored liquid. The device further features on-chip fluid reservoirs. Externally it only requires pressure supplied through an interface/holder. This pipette opens interesting opportunities in biosciences, pharmacology and clinical research, since the device can be co-located with additional probing equipment under ordinary microscopes, and allows highly localized interaction of a chemical or biochemical stimulant with surface-adhered cells and tissue in dish cultures.

All three hydrodynamically confined flow devices have individual design strengths, which make them attractive research instruments in particular application areas. Each of the concepts requires a different set of microfabrication techniques for fabrication and assembly, owing to the materials requirements and most likely, availability of processing equipment and expertise. In the following section we give an illustrated overview over the three different fabrication routes and compare their performance.

3. Fabrication strategies

3.1 The microfluidic probe

The fabrication of the MFP follows a multi-step fabrication route based on traditional silicon processing techniques (figure 2). Bonding to a PDMS block is employed to obtain closed channel structures. The original publication reports use of double-side-polished silicon wafers as starting material. Three UV-photolithography steps, targeting both sides of the wafer, and two deep-reactive-ion etching (DRIE) steps are required to fabricate the relatively complex structure. After initial photolithography, the top channel structure is etched into the wafer (figure 2, left panel). The wafer is then turned upside-down, and a protective silicon dioxide layer is deposited, photolithographically patterned and etched to pre-define the bottom mesa and the support pillars. A third photolithography step follows to place two orifices for the following first DRIE step (figure 2, middle panel). After removal of the resist layer, and ashing resist residue, a second DRIE step on the same wafer side produces the bottom mesa and the support pillars. The top channel structure is then activated by an oxygen plasma, and bonded to a PDMS slab in order to close the device and provide an interface to the liquid supply lines.

The elastomeric rubber not only tightly bonds chemically to the silicon surface, it also allows for pushing thin plastic tubes or fused silica capillaries into stamped-out holes, effectively sealing the tubes without additional measures.

Chips with a surface area of about 3 x 7 mm^2 are diced, interfaced with tubing and placed in a holding clamp for application to desired surfaces. Further details on the fabrication

strategy are provided in a previous publication of the authors on two-level microfluidic networks for patterning surfaces[23].

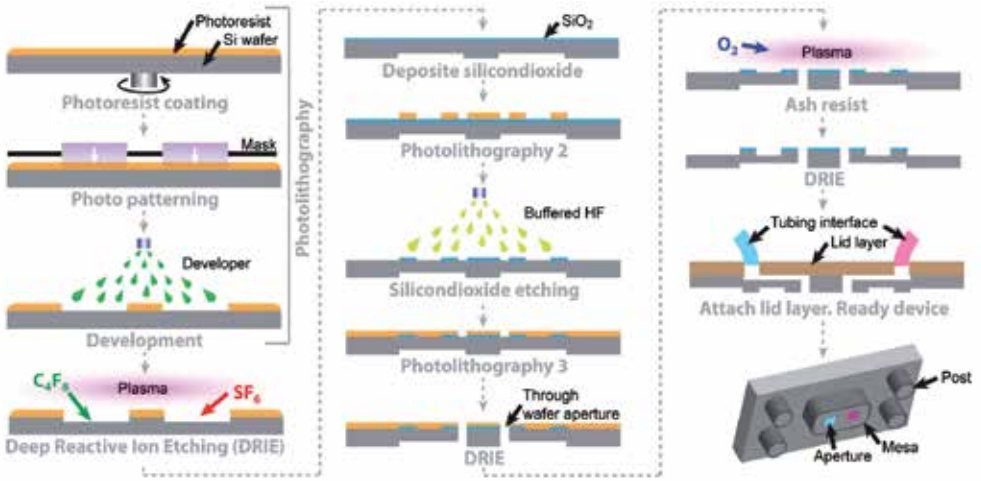

Fig. 2. Schematic fabrication procedure for the MFP, consisting of essentially three photolithography and two DRIE steps. Double-side-polished silicon wafers are used for the procedure. The left panel depicts the fabrication of the upper side of the chip, producing the horizontal channels for liquid supply to the through holes. The middle panel shows the SiO_2 fabrication to define the locations for mesa and support pillars, as well as the first DRIE step to open the vertical channels. Two additional photolithography steps are required. The right panel shows the removal of resist, and the second DRIE step in order to fabricate the bottom geometries. Also shown are the interfacing strategy by means of tubing or fused silica capillaries embedded in a PDMS lid layer, and a three-dimensional representation of the chip, with slightly exaggerated bottom features. Injection and aspiration port are depicted in red and blue, respectively, according to figure 1.

3.2 The vertical microfluidic probe

The vMFP has been designed based upon the microfluidic probe discussed above, in order to overcome critical inadequacies with respect to practical application and implementation of the original device concept. The MFP, being functionally closely related to the ink-jet print head, is associated with a number of systematic and fabrication related problems, which have been addressed by the authors in their latest study[13]. They successfully address artifacts of the earlier technology, including the inability to pattern surfaces in liquid environments, and limitations imposed by the physics of liquid ejection, which restrict the range of geometrically defined confinements of chemicals on surfaces. Above all, the fabrication of the vMFP has been largely simplified by eliminating photolithography steps and introducing some more facile, yet unconventional fabrication steps. Figure 3 depicts the full procedure. A disadvantage in comparison to the MFP is the limited flexibility with respect to the number and arrangement of channels.

vMFP heads are designed as silicon/glass hybrids, with the channel structures etched as 20 mm deep groves into the 400 μm thick silicon side. A slightly thicker glass slide of identical dimensions is anodically bonded to the silicon in order to obtain closed three dimensional channels. Since the channels are no longer located on the planar silicon face, but on one of the two sharp points of a rhombic chip geometry, which requires a finish by lapping and polishing, the risk of contamination of the channels by silicon dust particles had to be addressed. A solution to the problem was achieved through filling the channels with a low melting point wax prior to the mechanical polishing. The wax has to be removed afterwards by submerging the device in an organic solvent, such as heptane, for several hours. The authors do not detail the performance of this unconventional fabrication step, for example whether there is a wax film remaining on the channel walls, if rinsing steps are of advantage, or other details. The left panel in fig. 3 shows the initial procedure, including the first photolithography step, which defines the channel groves. The middle panel depicts the second photolithography (implicit, see figure 2), wax filling, and dicing. Lapping, polishing of the channel edges and wax removal is shown in the right panel, together with a perspective drawing of the polished tip of the device. It is clear that this procedure requires less instrument time and processing effort, in comparison to the fabrication scheme for the MFP, but wax filling and solvent treatment raises questions with regard to reproducibility and remaining traces of the wax in the channels after fabrication. From a functional point of view, this device is clearly easier to interface and integrate. It has a smaller footprint of approximately 1 mm^2, which suggest better positioning ability, even though the need for parallel alignment of the channel exit plane to the surface makes it difficult to integrate with conventional light or confocal microscopes. The original publication therefore includes a schematic drawing of the recommended setup for the probe, which includes a two-axis positioning table and tilt-adjustment mechanics. Also discussed are extensions to the flow circuitry, for example a three channel design which features two aspiration channels and is thereby similar to the MFп in arrangement. The authors introduce concepts of on-chip filter structures, designed to eliminate the threat of inflow-channel clogging by aspirated material from the surrounding volume.

Design, fabrication and advanced features of the vMFP represent a significant step forward from the MFP. The vMFP is a versatile research device, which unfortunately still requires a specialized stage for mounting and operation. This is particularly important, as the effective surface distance must be set as small as 1-30 μm in order to successfully superfuse surface structures. However, the authors rightfully point out that the in-plane design allows for most simple integration of one or more functional elements such as resistive heaters, surface printed electrodes, or sensors. They have also demonstrated that by means of side channels, immersion liquid dispensing can be integrated into the probe design. The probe clearly meets several of the challenges imposed upon dynamic fluid confinement devices, but unsolved issues remain. Important concerns arise with respect to integration with existing microscopy stations, which is particularly pressing when live cells and tissue cultures are under investigation, as well as to the somewhat limiting parallel arrangement of the channel exit plane towards the surface. These limitations are probably not easily addressable, as the material and integration options are the fundamental characteristics of these HCF chip variants.

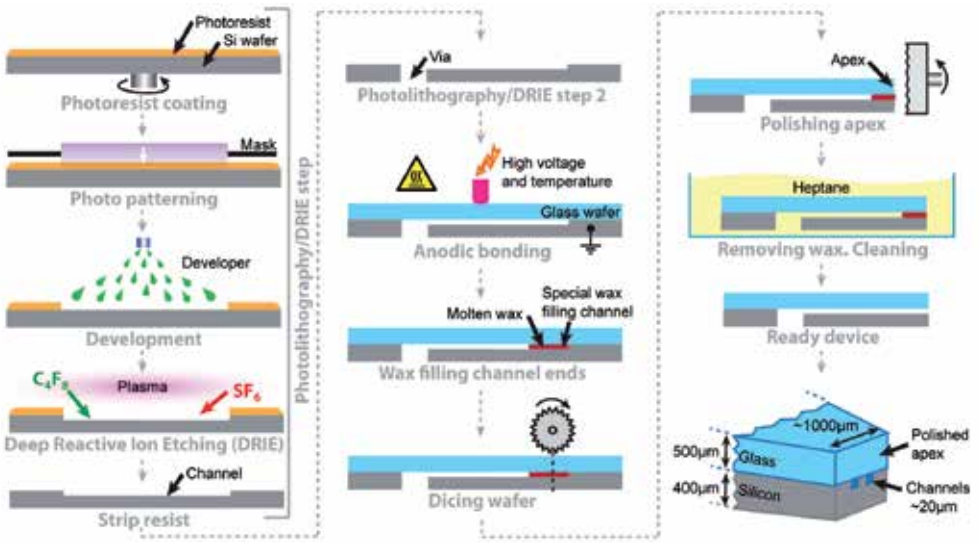

Fig. 3. Fabrication procedure for the vMFP, comprising two photolithography and DRIE steps to define the channels and vias, bonding and polishing. The left panel depicts the first photolithography and DRIE steps performed on a silicon wafer, which define the channel groves. The middle channel depicts the opening of vias by a second photolithography/DRIE round. The second PL (*cf.* fig. 2) is not shown in detail. Subsequently a glass wafer is anodically bonded onto the silicon, and the channels are closed with a low melting point wax, which is drawn into the structure by capillary forces. In the next step, as shown in the right panel, the bonded wafer is diced, and the apex of the rhombic chip is mechanically lapped and polished. Typically, several stacked dices are polished at the same time. The final step involves removal of the wax by submerging the dices in an organic solvent, which dissolves the hydrocarbon based filling. The left panel also schematically shows a perspective of the flat apex with the channels. The shape and dimensions of the chip are apparent from the photograph of the full device in fig. 1D.

3.3 The multifunctional pipette

With replica molding in PDMS a different approach was chosen to fabricate the third type of HCF device, the multifunctional pipette[8]. The device was designed to utilize three-channel recirculation, with two aspiration ports and one injection channel. The injection zone forms a free-standing dynamic fluid boundary, which prevents the escape of injected fluid and thus eliminates cross-contamination. With on-chip solution wells and a network of flow channels defined by the replica molding master, it allows complex chemical signals to be generated and applied at cellular and sub-cellular dimensions. The most important design feature is a thin PDMS membrane bottom plane of the device, fabricated by spin-coating of a pre-mixed PDMS membrane, and subsequent curing and plasma-bonding. The distinct advantage of replica molding, a form of soft-lithography, is the simple fabrication protocol, which does not even strictly require clean-room conditions. Soft lithography, in brief, employs a liquid pre-polymer and a fabrication master, which is typically a silicon wafer with the channel structure and alignment

marks microfabricated on the surface. Such a master can be produced by photolithography, typically employing a negative resist, or by DRIE if a very large number of replication cycles desired. Photoresist tends to lift off the surface after several cycles, but allows more rapid changes in master design. The choice of pre-polymer includes a number of possible materials, most commonly a mixture of silicon polymers and a cross-linking catalyst. The multifunctional pipette fabrication was performed using a commercially available poly-dimethyl siloxane (Sylgard 184 by Dow Corning), which is readily cured above 65 °C, and of low enough viscosity to allow spin coating for membrane manufacture. PDMS mixing, casting and curing was carried out in an ambient environment in a laminar flow hood, which can be placed in a standard chemical laboratory. Figure 4 illustrates the fabrication procedure. PDMS is mixed from two components and filled into a steel or plastics chamber in order to produce the top part of the pipette, including the on chip wells for solution storage and supply. The chamber consists of a top and bottom part, and is designed to minimize the entrapment of air bubbles. The bottom part of the chamber holds the fabrication master, defining the channel structures, typically for up to 20 pipettes. The resulting PDMS slab is ready to be bonded to the thin bottom layer, which will seal the channel groves and define the minimum distance of the channels to the surface. The membrane is spin coated onto a surface-treated (anti-adhesion hydrophobization) silicon wafer. Both the membrane-carrying wafer and the PDMS-filled chamber are exposed to elevated temperature (95 °C for 1 hour), which cross-links the PDMS pre-polymer and forms an elastomeric soft-solid (fig. 4, left panel). The PDMS slab is removed from the chamber, and the well bottoms are stamped out with a sharp ø 1mm hole puncher. The slab is subsequently plasma bonded to the membrane-carrying wafer to form an array of devices, which is peeled off and separated into individual pieces. The tip of each pipette tip is finally cut vertically with microscopic precision along the cutting marks defined in the PDMS structure, opening the channels (fig. 4, middle panel). To stabilize the device structure, a 1 mm thick borosilicate microscope glass cover slip, cut to pipette dimensions of approximately 8.5 x 54 mm, is plasma-bonded to the bottom of the device. The right panel shows these final steps together with a schematic perspective of the pipette tip with the channel exit region.

This soft lithography based fabrication process is by far the least complex of the three fabrication routes presented. Of distinct advantage are a) the on-chip wells, which drastically reduce dead volume and facilitate handling and interfacing, and b) the possibility to incorporate complex microfluidic circuitry into the pipette, such as mixers, gradient generation and fluid switching stages. For most purposes, the MFп is clamped in a metal or plastic pressure manifold, which can be combined with a holding arm to interface to micromanipulation hardware. The free standing pipette is typically applied at an angle (cf. fig. 1), allowing direct integration with common microscope setups, for example brightfield upright or inverse microscopy stations.

Table 2 summarizes several essential fabrication requirements, design characteristics and application features for direct comparison. Currently, each of the technologies has a number of functional advantages, but also up-scaling limitations, which can most likely be addressed in the future. For example, the strong benefits of the MFп with respect to cheap material and facile production without dedicated cleanroom environment have to be traded

off against the inherently limited compatibility of the soft PDMS polymer towards organic solvents. This disadvantage might not be overly limiting in studies of biological material such as single cells and tissue, since buffered aqueous solutions rather than organic media are typically used in these experiments. It is clear that the use of other materials is possible, and will become subject to future investigation. The MFP allows for arbitrary channel positioning and channel shapes, as the openings are generated by DRIE, which gives a certain advantage over the other two concepts, in particular the MFII, which is currently restricted to linear arrays of rectangular channels.

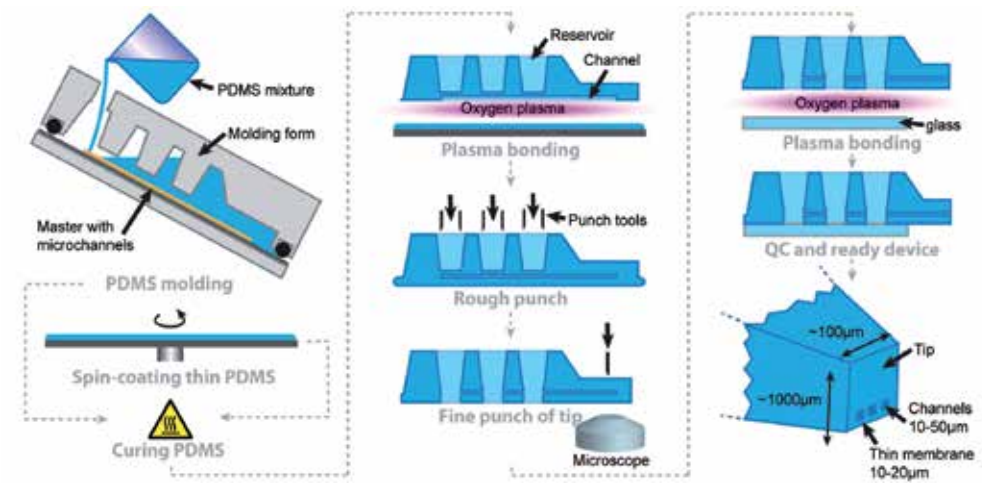

Fig. 4. Fabrication procedure for the MFII. The soft lithography procedure starts from a PDMS pre-polymer mixture, which is filled into a molding chamber. The master is a silicon wafer with the channels embossed, typically generated by SU-8 photolithography. This yields a PDMS slab with imprinted channel groves, which need to be closed to obtain a functioning device. For that purpose a thin PDMS membrane is fabricated by spin coating (left panel). The PDMS slab is removed from the molding form, and oxygen plasma bonded to the membrane. Holes are punched through the structure in order to connect the channels with the well interior, and the tip is cut off after alignment under a microscope (middle panel). A glass support is finally bonded to the underside, leaving only a 5 mm end at the pipette tip uncovered (right panel). The bottom part of the right panel also shows schematically the pipette tip obtained by the fabrication procedure. The thin membrane at the underside of the device defines the distance to the surface.

4. Application examples

Each of the devices discussed above was conceptualized to provide one or more solution(s) to technological challenges, and to make processes or scientific experiments feasible which were previously difficult or impossible to perform. While strongly interrelated in principle, the differences in design and implementation necessarily assign each device its own range of applications. While the silicon based probes are useful mainly for chemical surface processing, such as staining, etching or decorating surface areas or surface-attached objects, even cell cultures, the MFп has its strong side in single cell handling, superfusion and direct or indirect support of other probing or sensing devices. Figure 5 shows application examples for all three devices. In the original publication[5], several different application examples were provided. Continuous variation of the scanning velocity of the MFP was utilized to create local concentration gradients, useful for example for patterning surfaces with biomolecules, such as proteins. In another example, a MFP with 24 µm separated 40×40 µm apertures was positioned 15–20 µm above a substrate covered with fixed NIH3T3 fibroblast cells, and the cells were exposed to a solution of a membrane soluble fluorescent dye (fig. 5A). The selective detachment and collection of a single living cell from a surface was also demonstrated.

The beneficial use of the MFP is not only limited to experiments in cell biology and related areas, but might also find application in chemistry, micro fabrication and surface processing. Maskless lithography is an efficient technique for patterning or modifying planar surfaces with micrometer resolution. Fig. 5B shows an example where a MFP heads was used to write a hole pattern into a 3 µm thick AZ4562 (positive) photoresist layer, dispensing AZ400K developer as process liquid from the MFP. The shape of the spots is here determined by the geometry of the HCF region. In fig. 5C the application of the vMFP for localized chemistry on live cell cultures is demonstrated. Selected surface areas were treated with hypochlorite solution by means of the probe. The procedure chemically destroys the cells, which is apparent from the morphological changes (shrinkage/detachment), and can be additionally visualized with trypan blue solution, which selectively stains dead cells [13]. Fig. 5D shows an example of simultaneous use of the MFп and an additional probe, here a carbon fiber microelectrode, used to electroporate single cells for substance delivery. In the experiment the pipette re-circulates a solution of a compound which cannot penetrate the cell boundary, unless pores are opened in the membrane. This pore opening is achieved by applying an electrical pulse via a co-localized electrode. The MFп ensures delivery of the fluorescent material only to the selected cell, and allows for repeated experiments on many different cells in the same culture.

The original publication presented a number of additional applications for the concept, including dose response determinations of pharmacological compounds on selected cells, cell-protrusion formation by chemical means and measurements of ion channel activities on individual cells[8]. Most of these application examples demonstrate clearly the potential of the different HCF devices, as they address experimental problems in the biosciences or fabrication related requirements that could not be conveniently solved by traditional glass pipette methods, closed channel microfluidic chips or other kinds of microdevice technology.

Aspect	Microfluidic Multipurpose Probe (MFP)[5]	Vertical Microfluidic Probe (vMFP)[13]	Multifunctional Pipette (MFп)[8]
Functional advantages	Flexible channel geometries and positions. It is possible to use arbitrary channel shapes and positioning on 2D. Recirculation in thin cleft results in sharper HCF boundaries and smaller possible spot size	Recirculation in thin cleft results in sharper HCF boundaries and smaller possible spot size	Application under angle allows combination with other probes and pipettes. Less shadowing by the device. Integrated wells reduce contamination risk, sample requirement and dead volumes. On-chip integrated microfluidic circuitries.
Optimal for	Chemical surface processing	Chemical surface processing	Single-cell manipulation experiments
Fabrication summary	3 photolithography steps (2 alignment steps) 1 HF etching 2 DRIE processes 1 dicing 1 lid bonding	2 photolithography steps (1 alignment step) 2 DRIE processes 1 anodic bonding 1 wax filling 1 dicing (+1 alignment) 1 polishing step	1 soft-lithographic molding 1 spin-coating 1 curing 1 punching 2 plasma bonding steps 1 glass alignment 1 tip punch (+1 alignment)
Limiting steps for up-scaling	Lid bonding to PDMS	Polishing	Glass alignment and tip punch
Special equipment required	Spin-coater, Mask-aligner, DRIE plasma processor, dicing machine	Spin-coater, Mask-aligner, DRIE plasma processor, bonder, dicing machine	Spin-coater, simple molding-form, hole puncher, O_2 plasma chamber
Recommended /required environment	Cleanroom	Cleanroom	Laminar flow hood
Requirements for new design	3 photomasks	2 photomasks	1 master (can be directly written or with 1 photomask)
Overall limits	Expensive equipment required. Expensive to introduce new design (3 masks). Device covers sample - other probes and transmission imaging not possible. Tubing interface.	Expensive equipment required. Limited to linear array of rectangular channels. Device covers sample - other probes and transmission imaging not possible. Tubing interface.	Easy to fabricate only linear array of rectangular channels. Soft material may deform slightly if pressure is applied. Limited to aqueous solutions.
Fabrication advantages	Flexibility for 2D channel arrangements	Simple fabrication method for hard material device. Low cost to introduce new fluidic design	Very simple fabrication method for soft materials. Equipment requirements low (all low-cost equipment). Low cost & time to introduce new fluidic design.

Table 2. Comparison of hydrodynamic flow confinement devices (application and fabrication aspects)

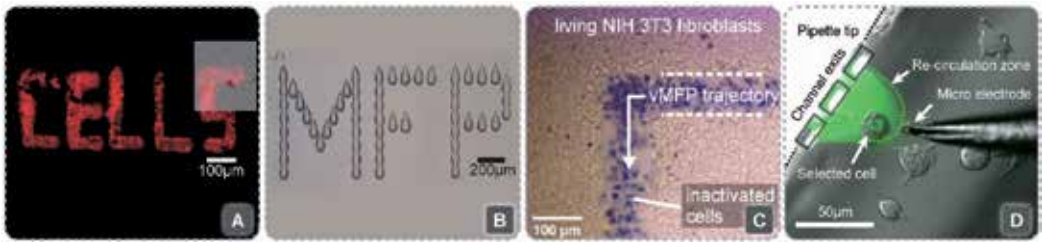

Fig. 5. Application examples of the HCF devices. A. Contact-free processing of selected adherent cells performed using the microfluidic probe. The image is a fluorescence micrograph, showing the red fluorescence of a stained fixed fibroblast cells. A selected population of cells was locally treated with a fluorescent membrane label. The inset is an overlay of transmission optical and fluorescence microscopy images, demonstrating that only the cells targeted by the MFP are affected[5]. Reprinted with permission from ref. [5]. Copyright 2005 Nature Publishing Group. **B.** Optical micrograph demonstrating local processing (developing) of a 3 µm thick positive photoresist film using the MFP[6]. Reprinted with permission from ref. [6]. Copyright 2009 Institute of Physics. **C.** Optical micrograph showing selective inactivation of fibroblasts using 2.5% sodium hypochlorite as processing liquid, applied with a vertical microfluidic probe head. Reprinted with permission from ref. [13]. Copyright 2011 American Chemical Society. **D.** Overlay of fluorescence and optical micrographs showing the application of the MFπ to a single cell electroporation experiment in combination with a carbon fiber microelectrode. The green fluorescence light is emitted by the water soluble dye fluorescein, which is diffusing into the selected cell after pore formation (unpublished).

5. Summary and outlook

Hydrodynamically confined flow devices represent a modern approach to localized solution delivery within a fluid environment. They have already shown great potential to enable new experimental techniques in the life sciences, where conventional channel microfluidics cannot be applied. There are severe challenges associated with performing experimental studies on biological cells in closed microflow devices. Some arise directly from unfavorable properties of the materials used in device fabrication, while others are connected to limited compatibility of living cells with microfluidic channel confinement. HCF devices overcome many of these limitations, and provide in addition pathways to previously impossible studies. In the second half of the last decade, several interesting technological approaches to HCF devices have been developed, some -inspired by inkjet technology, others on glass pipette methodology or droplet microfluidics. This diverse background is very much reflected in the fabrication methods employed to produce the individual devices, ranging from multistep silicon processing to soft lithography.

The theoretical understanding of the properties of hydrodynamically confined flows is still far from complete, but experimentally validated modeling techniques have recently appeared, investigating the influence of geometry, flow rate, and other parameters, on flow properties. These studies provide essential data for future HCF device development. Lately, more refined designs, which make the application in single cell and tissue studies very convenient, have been introduced. Advanced application examples from within surface

processing, pharmacology, membrane protein science and drug delivery have already emerged. They also indicate, as is expected, that the trend moves towards integration of more and more complex fluid processing functionality, including mixing, multiplexing, and diluting capacities, into the devices. These new generation devices are promising to become routine tools in bioscience research areas where single cell and tissue cultures are probed. There is also a strong possibility that the re-circulated fluid stream can be on-chip processed and analyzed for minute amounts of chemicals released from the stimulated cells and slices, a scenario which is tightly coupled to the progressively improving sensitivity of bioanalytical techniques. In order to support this development, the current microfabrication technologies employed to produce HCF devices have to be developed accordingly. The difficulties and bottlenecks, which limit production scale-up, have to be addressed in a timely manner. It can be anticipated that the traditional silicon-based processing methodologies, which are still commonly used, will be largely replaced by more rapid and cost effective processes.

6. References

[1] Strutt, J. W. L. R. Proceedings of the London Mathematical society 1878, 10, 4.

[2] Squires, T. M.; Quake, S. R. *Reviews of Modern Physics* 2005, *77*, 977.

[3] George Karniadakis, A. B., Narayan Aluru *Microflows and Nanoflows: Fundamentals and Simulation* Springer: New York, 2005.

[4] Weigl, B. H.; Bardell, R. L.; Cabrera, C. R. *Adv. Drug Delivery Rev.* 2003, *55*, 349.

[5] Juncker, D.; Schmid, H.; Delamarche, E. *Nat. Mater.* 2005, *4*, 622.

[6] Lovchik, R. D.; Drechsler, U.; Delamarche, E. *Journal of Micromechanics and Microengineering* 2009, *19*, 8.

[7] Queval, A.; Ghattamaneni, N. R.; Perrault, C. M.; Gill, R.; Mirzaei, M.; McKinney, R. A.; Juncker, D. *Lab Chip* 2009, *10*, 326.

[8] Ainla, A.; Jansson, E. T.; Stepanyants, N.; Orwar, O.; Jesorka, A. *Anal. Chem.* 2010, *82*, 4529.

[9] Perrault, C. M.; Qasaimeh, M. A.; Brastaviceanu, T.; Anderson, K.; Kabakibo, Y.; Juncker, D. *Rev. Sci. Instrum.* 2010, *81*, 8.

[10] Sun, M.; Fang, Q. *Lab Chip* 2010, *10*, 2864.

[11] Christ, K. V.; Turner, K. T. *Lab Chip* 2011, *11*, 1491.

[12] Cortes-Salazar, F.; Momotenko, D.; Girault, H. H.; Lesch, A.; Wittstock, G. *Anal. Chem.* 2011, *83*, 1493.

[13] Kaigala, G. V.; Lovchik, R. D.; Drechsler, U.; Delamarche, E. *Langmuir* 2011, *27*, 5686.

[14] Tang, Y. T.; Kim, J.; Lopez-Valdes, H. E.; Brennan, K. C.; Ju, Y. S. *Lab Chip* 2011, *11*, 2247.

[15] Juncker, D.; Schmid, H.; Drechsler, U.; Wolf, H.; Wolf, M.; Michel, B.; de Rooij, N.; Delamarche, E. *Anal. Chem.* 2002, *74*, 6139.

[16] Cesaro-Tadic, S.; Dernick, G.; Juncker, D.; Buurman, G.; Kropshofer, H.; Michel, B.; Fattinger, C.; Delamarche, E. *Lab Chip* 2004, *4*, 563.

[17] Smith, K. A.; Gale, B. K.; Conboy, J. C. *Anal. Chem.* 2008, *80*, 7980.

[18] Chen, D.; Du, W.; Liu, Y.; Liu, W.; Kuznetsov, A.; Mendez, F. E.; Philipson, L. H.; Ismagilov, R. F. *Proc. Natl. Acad. Sci. U. S. A.* 2008, *105*, 16843.

[19] Routenberg, D. A.; Reed, M. A. *Lab Chip* 2009, *10*, 123.

[20] Momotenko, D.; Cortes-Salazar, F.; Lesch, A.; Wittstock, G.; Girault, H. H. *Anal. Chem.* 2011, *83*, 5275.
[21] Ainla, A. J., Gavin D. M.; Brune, Ralf; Orwar, Owe and Jesorka, Aldo *Lab on a Chip - Miniaturisation for Chemistry and Biology (in press)* 2011.
[22] Feinerman, O.; Moses, E. *J. Neurosci. Methods* 2003, *127*, 75.
[23] Juncker, D.; Schmid, H.; Bernard, A.; Caelen, I.; Michel, B.; de Rooij, N.; Delamarche, E. *Journal of Micromechanics and Microengineering* 2001, *11*, 532.

9

Actual Problems of Hydrodynamics at Internal Not-Isothermal Flows in Fields of Mass Forces

Sergey Kharlamov
[1]*Theoretical Mechanics of National Research Tomsk State University,*
[2]*National Research Tomsk Polytechnic University,*
[3]*International Scientific and Educational Laboratory "Oil&Gas Hydrodynamics and Heat Transfer", Tomsk, Russia*

1. Introduction

1.1 General characteristic of problems in an investigation of complicated conjugated turbulent flows

Almost all flows that represent practical interest are turbulent. Turbulent flows are always complex, three-dimensional, unstable in small and irregular. The main feature of turbulence is concluded in the intensive mixing caused by hydrodynamic pulsations. Turbulent fluctuations bring large contribution in transfer of momentum, heat and mass, and, hence, have defining influence on distributions of velocity, temperature and specific concentrations in all motion fields.

At present in connection with fast rates of computer facilities perfection the interest in methods of turbulent transfer modeling has considerably grown. As turbulence is influenced by many factors it is natural that the simple procedures of calculation including empirical formulas have considerably low chance of the realistic description. They are useful only to very specific, simple problems and give integrated information only, but not the details necessary for practice.

Full representation about turbulence characteristics can be received from multidimensional numerical calculations. However the majority of such calculations can be executed only with attraction of model approximations. There are various possibilities for the turbulence description: direct numerical simulation (DNS), large eddy simulation (LES) and the statistical modeling in terms of turbulence models.

Now because of restrictions in computer performance and memory DNS is possible only for flows with rather low Reynolds numbers. However DNS method is very useful in description of turbulent structure as it is capable to give the full information about the flow pattern and to participate in estimation of turbulent models efficiency. DNS application features can be found in [1, 2].

As a result of decision of problem connected with integration of Navier-Stokes equations by DNS methods, LES method had developed, in which flow scales larger than sizes of cells are

calculated directly from the equations, and small-scale are subjected to modeling one way or the other. Papers using this ideology can be found in [3, 4]. This approach is also applied in investigation of practical problems. LES gives detailed enough picture and undoubtedly has good prospects for development in the near future.

At consideration of statistical fields (averaged fields) of required characteristics the momentum approach have recently received a wide distribution, and also a method of application of the approximate empirical relationships and purely heuristic assumptions which reliability has no doubts in some special cases. Unlike LES, statistical models of turbulence cover all spectrums of flow turbulent scales.

With the limits of momentum approach we can mark out 3 main ways of turbulence modeling. Two of them use the concept of eddy viscosity, suggesting turbulent Reynolds stresses $\overline{u_i' u_j'}$ proportional to average velocity gradients with coefficient ν_t (eddy viscosity) that defines turbulent transfer intensity. Third approach is based on direct calculation of Reynolds stresses from differential equations and known as full scheme of closure at second moment level. Models of first two types are zero-, one-, two-parametric ones, third type are models of Reynolds stresses transfer (RANS-models).

Application of eddy viscosity allows finding solutions, suitable only in concrete conditions. Complicated turbulent flow often met in engineering applications (combustion chambers of rocket engines, currents in aircraft engines, chemical lasers etc.), demand to use more generalized methods in modeling.

Practical requirements in studying of shear flows promoted formation of tendency to construct technological models of turbulent transfer containing transport equations for the one-point correlation moments of the second and third orders, and also some equations for the two-point moments. In this way practical requirements have allowed to escape from deeply empirical approaches to generally semi empirical RANS-models. Such models are essentially more reliable at studying phenomena in systems and devices with complex geometry, and also in the processes complicated with flow swirling. Insufficient approbation of these models defines necessity of their wide testing. The greatest contribution in investigation of this question has been brought by B.E. Launder, K. Hanjalic, W. Rodi, R.M.C. So, S. Elghobashi, N. Shima, V.A. Kolovandin, A.F. Kurbatsky, E.P. Volchkov, J.V. Lapin and others. From the viewpoint of reliable numerical techniques creation the majority of models do not look universal. The problem of multiple parameter model design is conjugated with expansion of experimental data bank containing data on turbulent structure which are inconsistent now.

In the present chapter the ideas of noted above authors are developed. All considered problems belong to the case of turbulent flows of inert and reacting gas mixes in channels, and developed mathematical models are based on use of essentially subsonic velocities approach. Within the limits of this approach pulsation of density are rigidly correlated with temperature fluctuations.

1.2 Stages of RANS-models construction

The basis of modern RANS-models has been put 40 years ago in works of J.C. Rotty [5], P.Y. Chou [6] and later B.I. Davidov [7, 8]. These investigations have defined the first stage of

RANS-models formulation, the critical analysis of which became possible only after ten years, with the invention of powerful computers corresponding these purposes. Publications of C.P. Donaldson [9], C.W. Hirt [10], B.J. Daley, F.H. Harlow [11] have defined second, qualitatively new stage in works on closure of Reynolds stresses equations. These investigations have convinced that difficulties of the numerical evaluation of all nonlinear differential transport equations in partial derivatives for turbulent stress tensor components are quite surmountable. And closure of flow governing equations is technically possible. From this time the active investigation on improvement of first RANS-models is in progress. It should finally finish with creation of a universal and reliable basis for calculation of wide spectrum of streams containing, in particular, flow curvature, separation, swirling, recirculated zones etc. This level of closure indeed provides the big flexibility and allows creating models, applicable in wide range of defining parameters variations. During the last years it became possible to predict some bright effects in complicated turbulent shear flows: occurrence of secondary flows in channels created by turbulence [12, 13], sensitivity turbulent near-wall fluxes to streamlines longitudinal curvature [14], etc. However we can meet works (for example, [15]) stating unsatisfactory description of flows with buoyancy forces in terms of RANS-models. Given results show it is necessary to search new approaches in closure methodology. Now some of models already get traits, corresponding to the new stage in carrying out of such works. There are already available results making conclusions about the evolution of Reynolds stresses in a developing shear flow.

The given work is focused on research of so-called complex turbulent flows. These are inert and chemically reacting swirled flows widespread in technique. Till now in such problems (for example, about mixing of internal swirled streams) turbulent models of eddy viscosity type were applied only. The considerable efforts [16–20] directed on overcoming of lacks of scalar viscosity models (the main ones are big inaccuracies of calculated size and intensity of recirculation zones in strongly swirled flows [16, 17, 21] and impossibility of calculation by means of various two-parametric models of the experimentally observed flow generated by a combination of free and forced eddies [16, 17]) have been undertaken. In the variety of two-parametric models $k\varepsilon$ - model of W.P. Jones - B.E. Launder [22] is the most popular, mainly because of its simplicity and small computer expenditures on its implementation. Indeed, many direct flows, particularly boundary layers and streams in channels with chemical reactions have been successfully calculated on the basis of $k\varepsilon$ - models [23]. Inconsistence of $k\varepsilon$-models in case of internal swirled flows is probably specified with defectiveness of assumption about the anisotropic character of turbulent transfer. In due time D.G. Lilley and N.A. Chigier [24] shown that in strongly swirled flows eddy viscosity cannot be considered as a scalar. Modifications of $k\varepsilon$ - models taking into consideration the anisotropy significantly increase calculations accuracy [25, 26], but not being universal. These models cannot be used in calculation of three dimensional flows.

In general it is expedient to pay attention to works on large eddy modeling [29, 30], and also on use of Reynolds stress transfer models [31, 32] because of presence of noted lacks of $k\varepsilon$ - models and models of eddy viscosity. In such models turbulent stresses are found out from the solution of model corresponding balance equations which are the equations in partial derivatives. Meanwhile calculated time essentially increases. It is connected with necessity of additional integration of at least six and more equations. More simple models with algebraic relationships for stresses (RSAM) which describe anisotropy without the above-

stated costs, can serve in some cases as an intermediate link between $k\varepsilon$ - models and RANS-models. We will notice that application of RSAM has a success in calculations of the thin shear layers not complicated with strong swirled effects [17, 18]. By this time only a few applications of RANS - models to calculation of the swirled flows are known. Basically they concern streams [31, 32] where their application also has not been done without problems. In connection with stated above it is necessary to estimate perspectives of RANS - models and urgency of development and application of RSAM -models [33-37] for calculation of internal flows with and without swirling.

1.3 Shear flows in mass forces fields and features of its investigation

Two main properties of rotating flows allocate them into a special group of motions of liquid and gas: the *first* is a creation of centrifugal forces field suppressing action of gravity; the *second* one is modification of near-wall flow structure and transfer mechanisms in peripheral areas. These properties are purposefully used in design of swirling-type furnaces, combustion chambers, separators, hydro-cyclones etc. These mechanisms define recirculation, eddy core precession, power- and energy division.

The influence of rotation essentially changes turbulent momentum, heat and mass transfer characteristics. In this way, according to [36], in a rotated flow hydraulic resistance can exceed its direct-flow analogue in 5 times. Bibliographic analysis (in particular, [36-41]) allows to allocate questions of swirled streams stability investigation in separate group. For swirling-type devices using strongly twisted flows both average velocity field structure and turbulence structure appears insufficiently investigate.

The main difficulty in studying of swirled flows is connected with occurrence of spatial vortex structures, capable to change the intensity of exchange processes [37]. The character of swirled influence on a flow depends on the way it is created. A variety of swirled ways (rotating pipe, vane twirlers on channel inlet, tangential gas admission, tape and screw twirlers etc.) complicates the process of experimental data generalization and creates problems in analysis of transfer mechanisms. In this connection in applications it is possible to meet criterial dependences received as result of generalization of given concrete experiments, but excluding some effects found out in experiment with another swirler. In such cases the reference to mathematical model is especially valuable.

Numerous investigations of the swirled flows in internal systems should be divided into two groups depending on whether rotation is created by walls of a pipe or provided with the device located on inlet of a channel. The given classification is convenient both for laminar and turbulent rotating flows which are analyzed in the given chapter.

1.4 Main purposes of investigation

The chapter is devoted to discussion of results of complex physico-mathematical and numerical modelling of hydrodynamics and heat transfer of strongly swirled internal laminarising flows. The purpose is to establish relationships of swirled decay on channel length and reconfiguration of rotating non-isothermal flows in direct-flow in technical devices with any configuration of a wall.

Besides, research objectives are focused on the following problems:

- Possibilities of detailed studying of complex shear flows are shown on the basis of the analysis and generalization of the modern data of theoretical and an experimental research of spatial laminar and turbulent flows in pipes and channels with/without mass centrifugal forces and with attraction of statistical second-order turbulence models (full transport equations for the one-point homogeneous and mixed correlation second-order moments of velocity and scalar field pulsations; algebraic models for Reynolds's stresses and specific turbulent heat fluxes (F. Boysen, E. Erdogan), and also separate two-parametrical models with transport equations for dissipation characteristic times of thermal and dynamic fields (C. Spezial, T.P. Sommer, R.M.C. So), integral scale of energy containing eddies (G. Glushko, S. Kharlamov) turbulence kinetic energy dissipation (B. Launder, B. Sharma) [42-46].
- Develop an effective and universal numerical procedure for calculation of non-isothermal flows of viscous media in channels with complicated wall in conditions of various swirled ways.
- Investigate details of developing swirled and direct-flow non-isothermal flows in pipes with sudden expansion, confuser-diffuser sections with rotating and stationary wall.
- Create a database of exact quantitative distributions of average and pulsating parameters of the specified above channel configurations.

It is necessary to notice that numerical investigations of problems are executed with attraction of the original technique including modern and seldom used in practice of applied researches statistical second-order turbulence models with transport equations for full Reynolds stress tensor components, specific scalar turbulent fluxes, and also some two-parametrical models with differential equations for dissipation characteristic times of thermal and dynamic fields. Ideas of combined SIMPLE algorithm [47] and splitting method on physical processes [48, 49] are the purpose for optimization and decrease of time expenses for convergence of numerical algorithm in calculations of intensive reverse flows. Moreover the last algorithm represents generalization of L.M. Simuni' ideas [50, 51] for the case of swirled flow.

By means of the given technique problems of laminar and turbulent direct and locally swirled at inlet flow and heat transfer in constant and variable (on pipe length) cross-section of pipe rotating around its longitudinal axis are solved.

In the chapter it is reported on calculated results of problem about turbulent flow of liquid and gas and heat transfer in pipes including confuser-diffuser sections with constant and moved wall in order to illustrate the ambiguity and specificity of influence of swirled way on flow structure and to extend conceptions about the application field of favorable properties of rotating flows in technological processes

Let's notice that the choice of given configurations of convective heat transfer is caused by their wide spread in industrial devices. Besides, researches of kinematic and heat- and hydrodynamic characteristics distributions for the specified modes is important from the point of view of operated technological process organization.

1.5 Scientific novelty of the obtained results is following:

- Computing procedure of the direct-flow and swirled laminar and turbulent isothermal and non-isothermal flows of liquids and gases in pipes and channels is developed on

the basis of SIMPLE algorithm and the generalized Simuni's method for case of variable in a radial direction longitudinal pressure gradient;

- Numerical modeling of complex shear flows in pipes is carried out with following motion conditions:
- A variable on pipe length cross-section area (sudden expansion, narrowing);
- With account of rotation: a local swirled method in the input field and moved wall (rotation of a pipe around the longitudinal axis);
- Heat carrier through confuser and diffuser sections with stationary and rotating wall.
- Substantiation and introduction in practice of swirled turbulent flow calculations under second-order multiple parameter models with transport equations for dissipation time scales of thermal and dynamic fields, integrated scale of turbulence is executed.

1.6 Practical importance

In this work it is presented scientific and technical information on distributions of temperature and velocity fields and its correlations in basic realization schemes of swirled flows in internal systems which are of great importance at testing and calibration of complicated program complexes for modeling of the spatial flows used for engineering calculations. It is important for creating new technological processes and devices for intensification of flows and heat transfer in power systems and industrial-scale plants.

1.7 Reliability of investigation results

Validity of scientific conclusions and summaries presented in this chapter follows from adequacy of used mathematical models and methods of numerical computation. It is proved by experimental results and theoretical data of other authors and calculations with use of commercial software packages.

2. Complex simulation of swirled turbulent flows in channels at any configuration of wall

One of early studies of swirled laminar flow structure was F. Levi's work [37-41] executed in 1929. Subsequently the data obtained by V.M.Kasyanov [52], V.I. Kravtsov [53], A.White [54], G.Y.Kuo [55] and others, has allowed to establish some general laws of wall influence on flow characteristics. It is found out: a steady rotating near-wall layer; flow non-rotative core; a reverse flow zone about a wall (high rotation velocities of pipe, constant flow rate), elongation of axial velocity profile along the axis and also decrease in thermal and dynamic flow influence on a wall. More complex structure is formed by rotating walls in annular channels - there are specific zones of separation [56, 57] and vortexes sliding on wall.

In process of perfection of experimental base and computing facilities it began possible to perform research of swirled turbulent flows at a qualitatively new level. This level is prepared by efforts of many experts. In Russia these scientists are V.K. Schukin [58, 59], A.A. Khalatov[60], V.E. Nakoryakov [61-63], A.M. Lipanov [64-67], E.P. Volchkov [68-70], S.V. Alekseenko [71-73], P.I. Geshev [74-76], V.V. Salomatov [77], V.M. Fomin [78-80], A.R. Dorokhov [81-84], V.A. Arhipov [85]; in the world - D.G. Lilley [24, 86], A.K. Gupta [37], M.T .Abujelala [86], K. Kikuyama [87-90], B.E. Launder [91] and other. The analysis of bibliographic data on swirled flows (for example, [37, 60, 92, 93]) shows: 1) the special role is

played by anisotropic spatial vortex structures of screw structure in transfer processes at presence of swirling; 2) full research of various swirled modes is necessary despite relative progress in understanding of the phenomena in swirled flows (e.g. vortex disintegration, mixture and burning delay etc.); 3) there is no uniform full position concerning influence of buoyancy forces, chemical reactions and the form of walls of channel on mechanisms of turbulent transfer of mass, momentum and heat in swirled flows; 4) works on model elaborations of a turbulent transfer and flexible and economic numerical methods are actual; 5) two-parametric models of kε and κL type, modified on rotation and using of S. Patankar's algorithm are very popular in numerical calculations and technical applications [47, 94]; 6) it is possible to establish and explain distinctive features of swirled flow in short pipes, knowing laws of distribution of average velocity, pressure and pulsating characteristics fields; 7) we can observe obvious deficiency of reliable experimental data containing detailed information on swirled lows. It is explained by imperfection of existing measurement methods and ways of processing of the received results; 8) the good tool for the analysis of swirled flows are models with differential transport equations for Reynolds stress tensor (RANS-models).

Swirled flows are often take place in channels of variable cross-section (e.g. pipeline networks with confuser-diffuser sections, inserts of sudden contraction/expansion, combustion chambers (CC)) for maximization of factor of fuel combustion completeness, stabilization of combustion, intensification of transfer processes of heat, mass and momentum in allocated areas on length of power devices. Necessity of processes intensification leads to necessity of application of swirling various configuration (e.g. with rotary guide blades). Presence of such adaptations frequently complicates modeling process of transfer phenomena. Thus, in [95] author marks formation of two backflow zones at channel axis, one of them is in immediate proximity from the swirler, and the other - at some removal. Considering small size of the first backflow zone and insignificance of axial velocity component between zones it has been noticed that such flow picture can be defined only by the swirler design [96] which is widely used in modern CC. In [97] it is also shown that swirler's blades' curvature considerably influences the sizes of recirculation zones. The sizes and location of backflow zones define CC qualitative characteristics. It is well-known the basic part of a combustible mixture burns down in these zones. When fuel particles have not time to burn down in backflow zones, we can obtain redistribution of high temperatures in CC. It is necessary to investigate features of the swirled flow in details in order to learn how to operate correctly work of such devices. That's why the mathematical modeling is more widely used at recent times at studying of flows in CC [37, 98].

However, flows in real CC are three-dimensional and multiphase, chemical reactions accompanied by radiation. It is difficult to model all these processes in complex consequently simplified models [99]. The factor raising requirements to modeling of turbulent momentum flux in CC is correct calculation of recirculation areas. These areas are characterized by a strong flow curvature, presence of complicated vortex structures, high intensity of turbulence caused by existence of internal shear layers. Complexity of flow inside and near to recirculation area opposes experimental investigations - it is indicated by absence of the wide and full measurement results in literature. The majority of works available now [100] contains data on the measured integral parameters, such, as length of recirculation zone [101] or heat-transfer coefficient along considered section [102]. It is necessary to notice that near-wall flow in

recirculation zone differs from classical turbulent flux in boundary layer in many aspects: pulsating velocity profiles has no maximum in boundary area [103-105]; in profiles of average velocity there is no logarithmic layer where the usual parity between average velocity, distance to wall and dynamic velocity (so-called law of wall [103, 105-108] would take place); values of Reynolds shear stresses are small near to a wall [106, 109]; generation and transport of turbulence kinetic energy in near-wall area are insignificant [107].

2.1 Some general summaries on hydrodynamic investigation of complicated shear conjugated and swirled flows

1. Axisymmetric swirled liquid flow experiences both stabilising and destabilising action caused by swirling. Let's explain this statement. Stabilization effect is connected with occurrence of additional turbulence destruction, destabilizing action is caused by curvature of average flow characteristics' profiles under swirling influence. A characteristic example of interaction between zones with stabilizing and destabilizing effects is flow in axially rotating channel. Thus, in inlet area, because of small thickness of boundary layer, rotation of liquid quickly decreases from the maximal values at the wall of rotating pipe to zero out of boundary layer. Near the wall because of high values of average tangent shear additional turbulence generation (destabilizing effect of rotation) takes place. Down flow formation of completely developed flow mode with constant inclination of a full velocity vector to flow axis leads turbulence generation by tangential velocity component equals zero (effective area of stabilizing effect). Between the areas specified above there is the transformation zone which size depends on a number of parameters, among them are ones characterizing the entering flow, and Reynolds number. The similar facts are resulted in [45, 87-90] where it is also noticed that in rotating channel flows because of discrepancy of average stress and shear surfaces nonzero distributions of turbulent shear stress are formed.

Investigation of full friction coefficient $|\tau_w| = (\tau_{xr}^2 + \tau_{r\varphi}^2)^{0,5}$ behavior shows that the role of tangential frictional component $\tau_{r\varphi} = \mu r \left.\frac{\partial (W/r)}{\partial r}\right|_{r=R}$ becomes appreciable at swirling parameter Ro>0.5, increase in friction with Ro growth can be significant (up to 4-5 times) already beginning from Ro>0.5 under moderate Re (Re≥5·10⁴).

2. The basic distinctions in qualitative and quantitative estimations of swirled flow parameters, executed till recent times, have been connected with unbalanced modeling. In many models effects of rotation were considered by means of updating relations defining mixing length, and no references to pulsating structure analysis have been done. However, only average momentum equations are not enough of the description of rotation effects. That's why application of RANS-models is reasonable.
3. At superposition of rotation on axial flow the stream becomes essentially anisotropic (diagonal elements of Reynolds stress tensor significantly differ and transversal turbulent momentum transfer begin to quickly disproportionally grow in comparison with transfer in other directions).
4. Strong flow rotation leads to reduction of turbulence intensity in a flow core in comparison with direct-flow, its simultaneous intensification in near-wall areas takes place.

5. Flow rotation changes condition of initially isotropic turbulence.

In summary it seems suitable to make notice concerning prospects of turbulent swirled flows modeling which is shared by many experts both in Russia and abroad. Thus, according to C.G. Spezial [110], no any of known closure models of second order can truly predict nature of turbulent developing flow with strong rotation (Ro>> 1). Authors of some latest works (for example, [111]) are not so categorical in estimations of the given approach, though as a whole they confirm necessity of updating known versions of the complicated RANS-models. Our point of view is that full universality from RANS-models certainly cannot be demanded, however, works on the further universality of these models are necessary as they are the unique tool for studying complex shear flows. But experimental analysis of these complicated flows is complicated or impossible.

2.2 Heat transfer in swirled flows and its estimation in technical applications

Early studies of heat transfer in swirled flows, carried out more than seventy years ago, have shown possibility of its essential intensification. The large quantity of works on heat transfer in single-phase swirled flows is executed to the present time. Detailed bibliography representing foreign publications, is given in [112], Russian- in [113-120]. A number of successful criterial dependencies for heat transfer calculation in single-phase media can be found in [113-120]. Note worthily that heat transfer problems in laminar swirled flows are presented not so widely, as in turbulent ones. Publications of last years on heat transfer intensification in laminar mode in internal systems show [121-123] that in particular cases increase in heat exchange reaches 200–400 % (a wire spiral section [122], screw rolling on [123] etc.) in comparison with smooth tube, and the effect of intensification amplifies with reduction of step and height growth of rolling-on and wire helix. Presence of such features on the internal surface is capable to form laminar mode with macro eddies and cause intensification up to 700 %.

The insufficient number of criterial dependencies used for the estimation of heat transfer in laminar flow, and its discrepancy [121], leads to actualization of construction of universal relation of following kind:

$$\mathrm{Nu}=f(\mathrm{Re}, \mathrm{Pr}, \mathrm{Gr}, l/R, \mathrm{Ro}, \mathrm{K_{ц}}), \tag{1}$$

where $\mathrm{Re}=U_0D/\nu$, $\mathrm{Pr}=\nu/a$, $\mathrm{Gr}=g\beta\Delta Tl^3/\nu^2$, $\mathrm{Ro}=W_0/U_0$, $\mathrm{K_{ц}}=\Omega W/g$ ($\mathrm{K_{ц}}$ considers influence of centrifugal forces field on liquid flow nature caused by its density variability).

Results of experimental investigations of flows in rotating pipe [124] have shown that increase in heat exchange caused by rotation is well characterized by dependency:

$$\mathrm{Ko}=\mathrm{Nu}/[\mathrm{Pr}^{0,43}\,\mathrm{Gr}^{0,1}(\mathrm{Pr_l}/\mathrm{Pr_w})^{0,25}\varepsilon_l], \tag{2}$$

where ε_l – correction, depending on relation between longitudinal $(\frac{UD}{\nu})$ and rotational $(\frac{\Omega R^2}{\nu})$ Reynolds numbers, indices «l», «w» in Prandtl criteria correspond to liquid and wall respectively.

For a viscous-gravitational mode it was possible to generalize experimental data and to find Ko, entering in (5) in the form $\mathrm{Ko}/\mathrm{Ko}_0 = f(\mathrm{Ro}, \mathrm{K}_{\text{ц}})$ which, despite its proximity, works with success in heat transfer analysis of electric machines with flow cooling:

$$\mathrm{Ko}\big/\mathrm{Ko}_0 = 1{,}75 \cdot \mathrm{K}_{\text{ц}}^{\,0{,}18} \cdot \mathrm{Ro}^{0{,}33}, \tag{3}$$

where index "o" corresponds to absence of rotation.

From (3) follows [124] that influence of rotation effects, connected with Rossby criterion Ro, on heat exchange is stronger, than effects of centrifugal displacement.

Special role of centrifugal forces in intensification of convective heat exchange of swirled turbulent flow was marked also in [125, 126]. Analysis of experimental data [126] shows that turbulent self-similar flow in swirled conditions appears at much smaller Re values, than at direct-flow liquid motion in cylindrical pipe.

Heat transfer in damped turbulent flow in pipes with a twisting insert of constant step, investigated in [120], needs construction of criterial dependencies, uniform for direct-flow and swirled streams. In such parities we use Reynolds's effective number

$$\mathrm{Re}^{*} = \mathrm{Re} \cdot [1 + (W/U)^2]^{0{,}5} = \mathrm{Re} \cdot (1 + \mathrm{tg}^2\alpha)^{0{,}5}, \tag{4}$$

where U – bulk velocity, W – tangential velocity.

In conditions of $\mathrm{Pr} \approx 1$ and when assumptions about energy dissipation neglection are fair, i.e. similarity of velocity and temperature fields of swirled flow takes place, heat transfer is defined by boundary layer condition. Therefore, it is expedient to search for correlation of Nusselt number Nu and friction factor with Re^* that according to [120] look like

$$\mathrm{Nu} = 0{,}021 \cdot (\mathrm{Re}^{*})^{0{,}8} \cdot \mathrm{Pr}_f^{0{,}45} \cdot \left(\frac{\mathrm{Pr}_w}{\mathrm{Pr}_f}\right)^{0{,}25}; \quad \varsigma = 0{,}316 \cdot \mathrm{Re}^{*-0{,}25} \tag{5}$$

These dependences are good enough correlate with experimental data [127]. Influence of additional turbulization is considered in the mentioned work. Measurements are performed on water and liquid metal at $\mathrm{Re}=10^4 \div 5 \cdot 10^4$, rolling-on step S=50÷238 mm, and are carefully described by following relation (M.A.Mikheyev's transformed formula with additive ε_l):

$$\mathrm{Nu} = 0{,}021 \cdot \mathrm{Re}^{0{,}8} \cdot \mathrm{Pr}_f^{0{,}43} \cdot \left(\frac{\mathrm{Pr}_w}{\mathrm{Pr}_f}\right)^{0{,}25} \cdot \varepsilon_l, \tag{6}$$

$$\varepsilon_l = 1 + A \cdot \left(\frac{D}{S}\right)^n / \mathrm{Re}^m. \tag{7}$$

where A, m, n are constants (A=1.13·10^5, m=1.2, n=1).

Throughout experimental researches of strongly swirled decay turbulent flows in [118] for air heat transfer in a cylindrical pipe with swirl chamber on inlet the following formula is offered

$$\mathrm{St} = 0,047 \cdot \mathrm{Re}_x^{-0,2} \cdot \mathrm{Pr}^{-0,6} \cdot (\cos\varphi_0)^{-0,6}, \tag{8}$$

where St= $\alpha_x/(\rho c_p U_{av})$ – Stanton number, U_{av} – averaged gas velocity, φ_0 – twist angle. Underline that (11) is quite satisfactory in range: $\mathrm{Re}_x=10^5 \div 10^6$.

The works noted in this paragraph in the majority are experimental. Theoretical results can be found in [119, 128, 129]. Thus, in [128] heat transfer characteristics of turbulent decay swirled flow are analytically investigated. Swirling is carried out by means of short profiled plates placed on workspace inlet. On the basis of solution in the form of series of swirled flow equations obtained from the Navier-Stokes equations with application of asymptotic analysis, the following dependencies for heat transfer characteristics are defined:

$$\alpha_x = \frac{\lambda}{D}[0,023(c_\alpha \mathrm{Re})^{0,8} \cdot \mathrm{Pr}^{0,4} + 0,114 \cdot (2 \cdot W_w^2 \cdot \mathrm{Re}^2 \cdot c_\beta \Delta T \cdot \mathrm{Pr})^{0,5}] \cdot (\frac{T_w}{T_{av}})^{-0,5}, \tag{9}$$

where α_x – heat transfer coefficient; λ – heat conductivity coefficient; D – channel diameter; Re, Pr – Reynolds and Prandtl number; ΔT и T_w/T_{av} – temperature drop and temperature factor respectively, $c_\alpha = (U^2 + W^2)^{0,5}/U$ (U, W – dimensionless local axial and circumferential velocities), c_β - volumetric thermal-expansion coefficient, W_w – dimensionless local tangential velocity on the wall, obtained by extrapolation of W values on the wall through the viscous sublayer, T_{av} – average gas temperature.

Heat transfer in short rotating channel under $\mathrm{Re}_T^{**} = idem$, according to [130], can be successfully forecasted with relation:

$$\mathrm{St}/\mathrm{St}_0 = \Psi_T \Psi_\varphi \tag{10}$$

where St_0 – Stanton number for non-gradient isothermal flow, St – Stanton number under current conditions, ψ_T, ψ_φ - non-isothermal and rotational indicators.

Noteworthy that the law (10) generalized for inlet part of rotating pipe transforms into dependency:

$$\mathrm{St} = \frac{0,012(1 - 0,715\mathrm{Re}_\varphi/\mathrm{Re}_{in})}{\mathrm{Re}_T^{**0,25}\,\mathrm{Pr}\,\psi_W^{0,5}}, \tag{11}$$

where Re_φ – Reynolds number calculated with use of pipe rotation velocity, Re_{in} – with use of averaged bulk velocity, Re_T^{**} – with use of energy thickness of boundary layer, $\Psi_W = T_w/T_0$ – temperature factor. Under $\Psi_W = 1 \div 3$, $\mathrm{Re}_\varphi/\mathrm{Re}_{вх} = 0 \div 1$ in first approximation we obtain

$$\Psi_\phi = 1 - 0,715\frac{\mathrm{Re}_\varphi}{\mathrm{Re}_{in}}, \Psi_T \approx \frac{2}{\Psi_W + 1}. \tag{12}$$

Calculations of $\mathrm{St}/\mathrm{St}_0$ according to the suggested relations show that in range $\mathrm{Re}_\varphi/\mathrm{Re}_{вх} = 0 \div 0,8$, there is small nonlinear dependency of the complex from $\Psi_\varphi \approx f(\frac{\mathrm{Re}_\varphi}{\mathrm{Re}_{\theta x}})$.

Agreement between calculated and experimental data is satisfactory.

In conclusion of the short bibliographic analysis of the problem let's notice that relaminarization effects in rotating technical systems and its behavior at extreme operating conditions have not received sufficient illumination in the class of prediction problems of flows complicated by swirling. Last three decades are noted by interest growth in research of "fine" structure of decay rotating and direct-flow streams in devices with complex boundary. As well as in construction of adequate mathematical models of continuous media dynamic behavior, in creation of new effective detection and calculation procedures of nonlinear effects in technological processes complicated by swirling and changes of working substance structure.

3. Laminar direct and swirled flow and heat transfer investigation in pipes and channels with complicated boundary

3.1 General physical and mathematical problem definition

There are investigated non-isothermal flows of an incompressible liquid and weakly compressible gas in pipes with variable cross-section under the influence of mass forces caused by both local swirling of a stream in inlet and swirling caused by pipe rotation around its longitudinal axis. The following equations representing conservation laws of mass (1), momentum (2) - (4) and energy (5) which in axisymmetric statement and cylindrical coordinate system is presented for modeling of such flows and heat transfer:

$$\frac{\partial U}{\partial x}+\frac{1}{r}\frac{\partial (rV)}{\partial r}=0; \tag{1}$$

$$\frac{\partial}{\partial x}\left[\rho UU-\mu\frac{\partial U}{\partial x}\right]+\frac{1}{r}\frac{\partial}{\partial r}\left[r\left(\rho VU-\mu\frac{\partial U}{\partial r}\right)\right]=-\frac{\partial p}{\partial x}; \tag{2}$$

$$\frac{\partial}{\partial x}\left[\rho UV-\mu\frac{\partial V}{\partial x}\right]+\frac{1}{r}\frac{\partial}{\partial r}\left[r\left(\rho VV-\mu\frac{\partial V}{\partial r}\right)\right]=-\frac{\partial p}{\partial r}+\left\{\rho\frac{W^2}{r}-\mu\frac{V}{r^2}\right\}; \tag{3}$$

$$\frac{\partial}{\partial x}\left[\rho UW-\mu\frac{\partial W}{\partial x}\right]+\frac{1}{r}\frac{\partial}{\partial r}\left[r\left(\rho VW-\mu\frac{\partial W}{\partial r}\right)\right]=\qquad\left\{-\rho\frac{VW}{r}-\mu\frac{W}{r^2}\right\}; \tag{4}$$

$$\frac{\partial}{\partial x}\left[\rho UT-a\frac{\partial T}{\partial x}\right]+\frac{1}{r}\frac{\partial}{\partial r}\left[r\left(\rho VT-a\frac{\partial T}{\partial r}\right)\right]=S_T; \tag{5}$$

Designations are standard in notation of the equations (1) - (5).

Solution of governing equation system (1) - (5) is carried out with attraction of numerical technique based on combined SIMPLE algorithm and method of simultaneous finding of longitudinal pressure gradient with a velocity field, originally offered by L.M. Simuni [50] and generalized on a case of its variability in radial direction [45, 51] for research of spatial deformed flows caused by swirling and/or expansion/narrowing of cross-section section. In the given chapter problems of laminar direct-flow and swirled flow and heat transfer with walls in pipes and channels with any configuration of boundary wall are considered.

The matter of technique is following. Calculated workspace is covered by finite-difference spaced grid. Functions T, U, V, W and pressure correction are calculated according to standard SIMPLE procedure with implementation of upwind scheme and TDMA method.

Discrete analogs are calculated by variable direction method which uses TDMA method on each step for the solution of system of linear algebraic equations.

Complicated pipe geometry definition is made on a uniform grid by switched off control volume approach so that the remained operating control volumes made considered irregular area.

The way of blocking of unnecessary control volumes consists in defining of great values for source components in discrete analog. Thus it is probably to assign known value (e.g. for velocity value a zero or for temperature T_w) in the switched off control volumes.

In conditions of combined algorithm we accept that numerical integration of governing equation system and closure equations (for turbulent flow) is performed on the basis of economic implicit finite-difference schemes of second order accuracy for axial and radial coordinate steps, splitting schemes both for independent variables and physical processes and TDMA method. In a radial direction we use grid concentration under the logarithmic law that provides high resolution of the grid in near-wall areas. The features of given algorithm consist in the following. For cases of small swirled intensity, small heights of the ledge (when there is no reverse flows) the marched method is used. Further this algorithm is generalized on modes with high intensity swirling, but its essence, still, consists in allocation of marched variables and in simultaneous calculation of velocity field and pressure gradient. As a result the algorithm generalizing ideas of L.M. Simuni does not concede in calculated speed to algorithms of the numerical solution of two-dimensional boundary layer problems.

The idea of sharing of SIMPLE algorithm with generalized algorithm of L.M. Simuni is defined by necessity of optimization and decrease of time expenses on numerical decision convergence at intensive reverse flows in channels with high values of swirl intensity (Ro), flow velocity (Re), ledge heights (h/d). So, in the areas where there are features caused by reverse flows, calculation is carried out with SIMPLE algorithm, in other areas - with L.M. Simuni's algorithm. Calculations show that this combined method demands less time in comparison with original SIMPLE algorithm when obtaining steady solution of intensively swirled non-isothermal flows in pipes and channels with complicated boundary.

Possibilities of numerical algorithm are illustrated with some test examples, each of them serves for correct estimation of flow calculation under the influence of one of the factors – flow swirling at the inlet and in rotating pipe, as well presence of separated flows caused by channel irregular geometry. We notice that the offered numerical algorithm is tested on numerous flows.

3.2 Results of flow and heat transfer calculation in cylindrical pipe locally swirled in flow inlet region

Boundary conditions for governing equations integration are following:

At the inlet into the pipe the uniform profile of velocity axial component is set, flow swirled is carried out under the law of solid body. The temperature of entering stream is constant and equals T_0:

$$U|_{x=0} = U_0;\ \ V|_{x=0} = 0;\ \ W|_{x=0} = W_0 \cdot \frac{r}{R}\left(1 - \left(\frac{r}{R}\right)^m\right);\ T|_{x=0} = T_0; \qquad (6)$$

Here values of U_0 и W_0 are defined from dimensionless parameters of Reynolds ($Re=U_0 \cdot D/\nu$) and swirling intensity ($Ro=\Omega \cdot R/U_0=W_0/U_0$). Value of exponent *m=const*.

At the wall - equality of velocity vector components to zero. The temperature on a wall is accepted constant and equal T_w. *On an exit* - "soft" boundary conditions (equality to zero of derivative all sizes in an axial direction) are set.

At the axis - symmetry conditions: equality of axial velocity and temperature derivative in radial direction to zero; equality of radial and tangential components of velocity vector to zero.

In this part results are presented for wide range of flow parameters: Re=10-1000 and Ro=0-20. It is shown that local entrance swirling gives central recirculated zones (fig.5). Zones of returnable flows are characterised by swirling parameters and Reynolds number (fig.1).

There are big losses of pressure in comparison with a direct-flow flow at increasing of coefficient friction on a pipe wall (fig.2), caused by additional shear stress in the swirled flow. Distributions of Nusselt number (fig.3) and temperature fields (fig.4) show heat transfer intensification on an initial site of a pipe with increase of flow swirling.

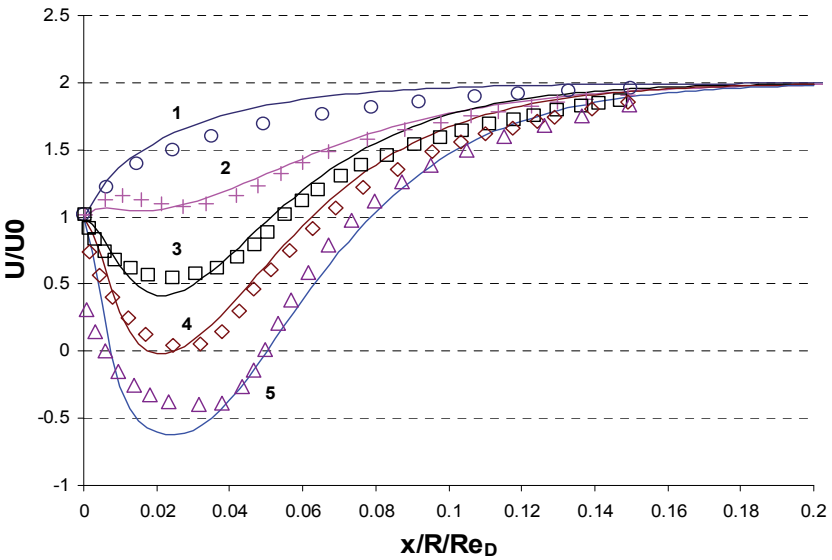

Fig. 1. Distribution of relative axial velocity U/U_0 versus normalized length ($x/R/Re_D$) at various values of swirling parameter $Ro = \Omega R/U_0$. Lines are calculation, symbols are Shnajderman M. F and Ershov's A.I data [131]: 1-Ro=0; 2-2; 3-3; 4-4; 5-6.

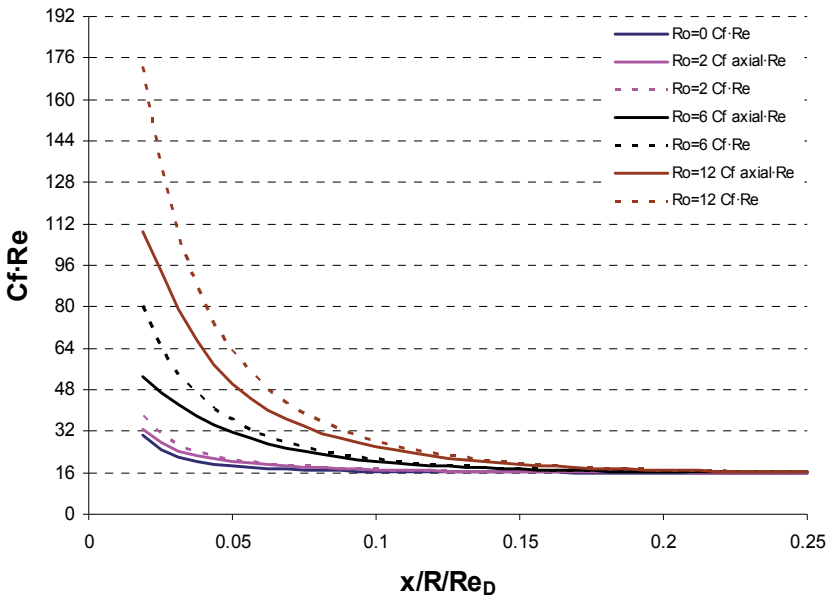

Fig. 2. Distribution of full coefficient friction (dotted lines) and coefficient friction with the account only axial component of velocity (solid line) versus the normalized length of the channel ($x/R/Re_D$) at various swirling. (This is local swirling on an input).

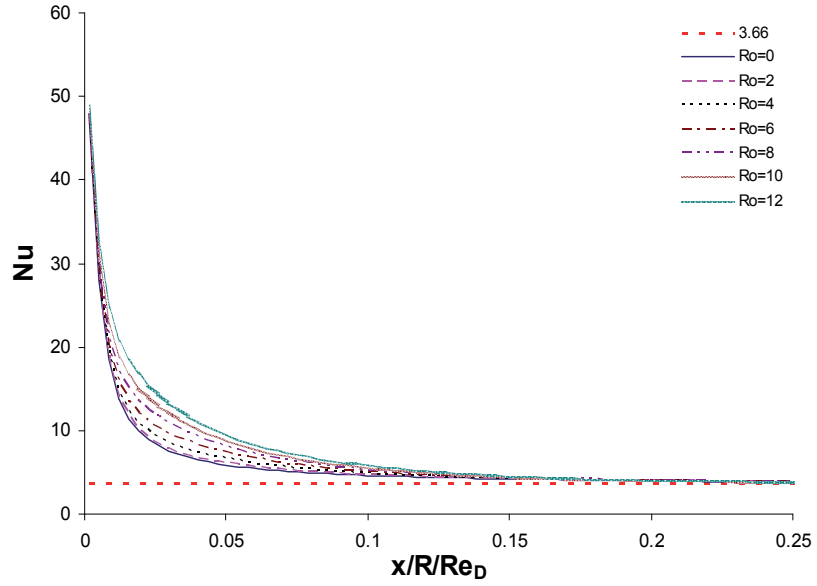

Fig. 3. Distribution of Nusselt number versus swirled parameter and normalized length of the channel ($x/R/Re_D$). (Data is local swirling on an input).

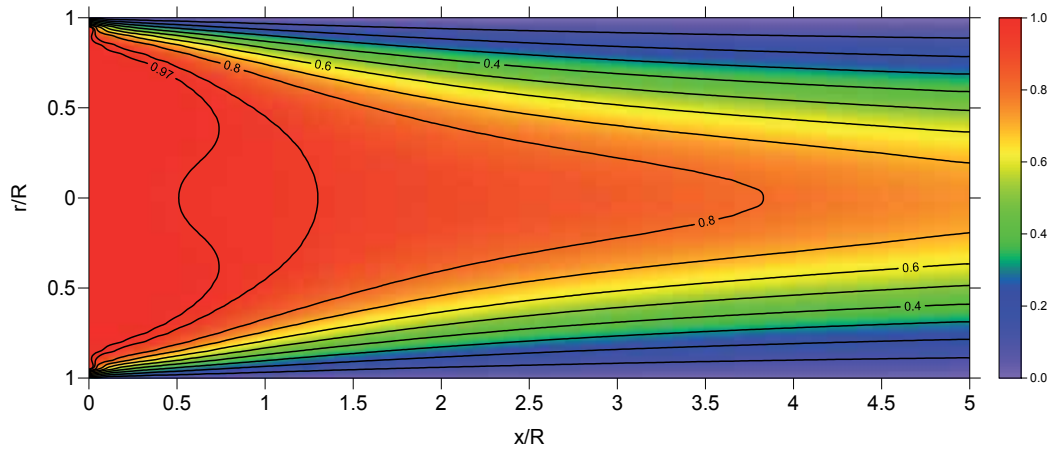

Fig. 4. Isolines and a field of temperature values $(T-T_w) / (T_0-T_w)$ at Re=20 and Ro=10

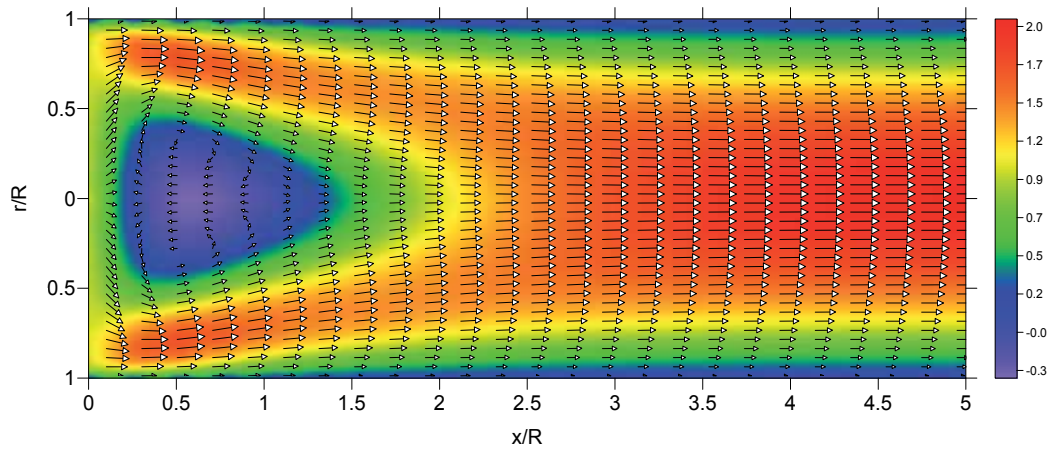

Fig. 5. A field of values of axial components of velocity U/U_0 (colour) and a vector field of a flow (arrows) in the channel with local swirling on an input (Re=20 and Ro=10).

3.3 Research of flows in rotating pipes

Let's notice, that data about influence of swirling on hydrodynamics in the conditions of complex shear flow are small and inconsistent. Nevertheless, it is possible to establish some general properties of flows in pipes with a rotating wall round the longitudinal axis. Interest to similar flows is caused by organisation of laminarizing flows under the influence of rotating effects and keeping of heat transfer extensification mode on lengthy sites.

For the purpose of explanation of details of such process problems about a laminar flow and heat transfer in pipes were originally solved.

The formulation of boundary conditions in such problem is reduced to the following. *At the input*: there are the developed profile of axial component of velocity vector and absence (equality to zero) of radial and tangential components of velocity. T_0 is flowing stream uniform temperature.

$$U\big|_{x=0} = 2 \cdot U_0 \left(1 - \left(\frac{r}{R} \right)^2 \right); \; V\big|_{x=0} = 0; \; W\big|_{x=0} = 0; \; T\big|_{x=0} = T_0; \tag{7}$$

At the pipe wall we have conditions of absence of axial and radial components of velocity vector at $r=R$. Tangential velocity component on a wall is equal to pipe velocity rotation W_0. *At the exit* there are "soft" boundary conditions, *at the axis* - symmetry conditions.

Calculation procedure included actions with consecutive working off of blocks: the decision of a problem on isothermal and not-isothermal flows with constants and variables thermo physical properties in a range of defining parameters- Re=10-1000, Ro=0-12.

Comparisons with available calculated data (fig.6 and fig.7) and their analysis allow doing following conclusions:

- flow in a rotating pipe is characterised by occurrence of zones of returnable stream near the wall on an initial pipe site and profile elongation of axial components of velocity vector in comparison with Poiseuille profile. Flow intensity and recirculated zone size in near-wall flow essentially depend on pipe rotation velocity and Reynolds number;

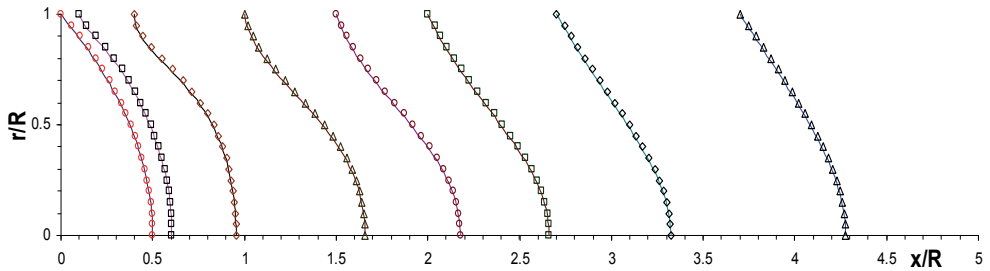

Fig. 6. Development of axial component of velocity vector U/U_0 on channel length (Reynolds number - Re=20; swirled intensity - Ro=5.22; this is case of rotating pipe wall. Lines - calculation, symbols - data [132]).

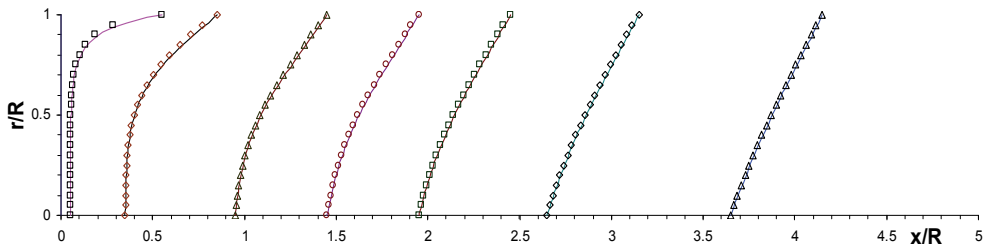

Fig. 7. Development of velocity tangential profile W/U_0 on channel length (Reynolds number - Re=20; swirlied intensity - Ro=5.22; this is case of rotated pipe. Lines - calculation, symbols - data [132]).

- shear stress caused by rotation ($\tau_{\varphi r}$), completely prevails in value of coefficient friction on a wall of rotating pipe; the full coefficient friction (fig.8) also increases with increasing of swirling parameter;
- distributions of Nusselt number (fig.9) and temperature fields show extensification of heat transfer processes in rotating pipe flow. And since some distance from an input the temperature profile is arranged under change of a velocity profile in the near wall fields. Also it is observed smaller fullness of temperature profile at the wall in comparison with a direct-flow stream. Some calculated results illustrating this process, are presented below.

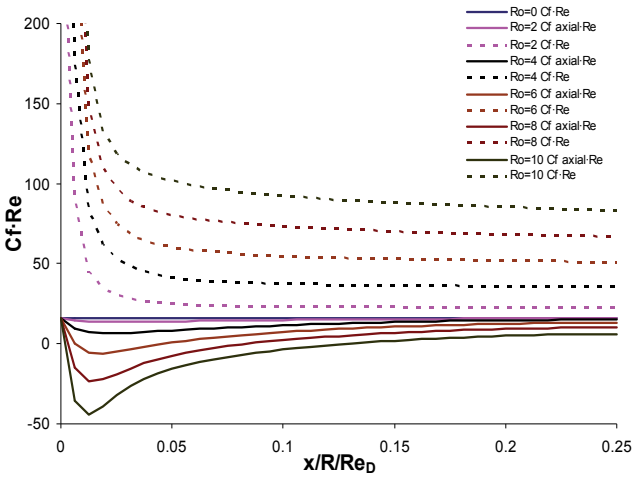

Fig. 8. Distribution of full coefficient friction (dotted lines) and coefficient friction with the account only axial component of velocity vector (solid lines) versus normalized channel length ($x/(RRe_D)$) at various swirling parameters (rotating pipe).

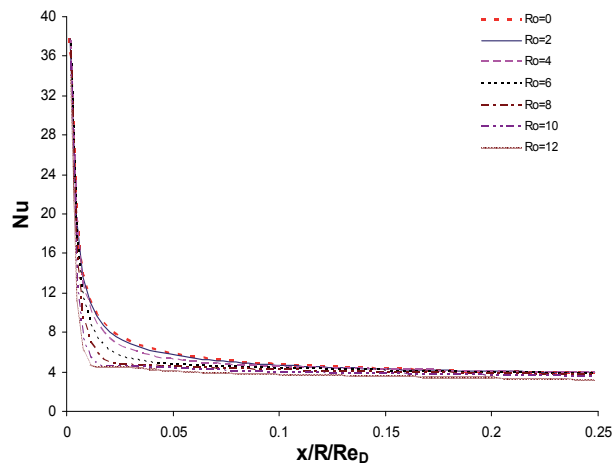

Fig. 9. Distribution of Nusselt number versus swirling parameter and nornalized channel length ($x/(RRe_D)$). (rotating pipe).

3.4 Investigations of hydrodynamics and heat transfer for a flows in channels with complex geometry

Not-isothermal subsonic fluid flow in pipes of variable cross-section section is analysed. It is supposed, that generally the flow at the input is considered completely developed. The stream flows into a pipe with uniform temperature T_0. T_w is temperature at the wall; components of velocity vector are accepted equal to zero (no-slipping conditions). At the axis - symmetry conditions, at the exit - "soft" boundary conditions.

Here, presented calculation of channel configurations shows that modelling of flows in internal systems with irregular geometry will quite well be co-ordinated with results of calculations and experiments of other authors [133]. Calculations of flows in pipes with sudden expansion at the input h/R=0.5 show presence of stream separation and formation of eddies at once behind a ledge in that kind in which it has been presented in experimental papers and numerical researches of other authors.

Calculated results of some flows illustrating possibilities of algorithm in a prediction of direct-flow and swirled streams in the conditions of irregular pipe geometry are more low given.

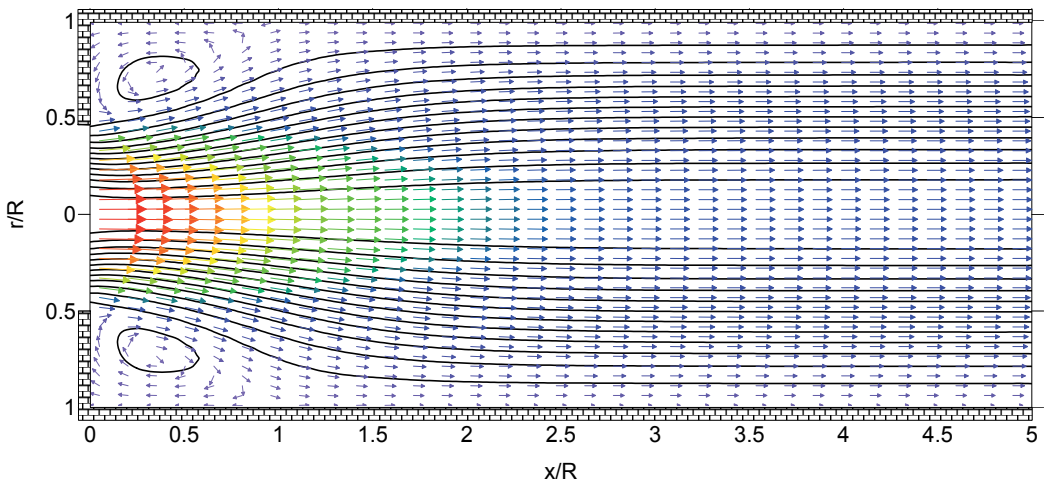

Fig. 10. Streamlines and vector field at a flow in the channel with sudden expansion. Calculation is executed at Re=20 and h/R=0.

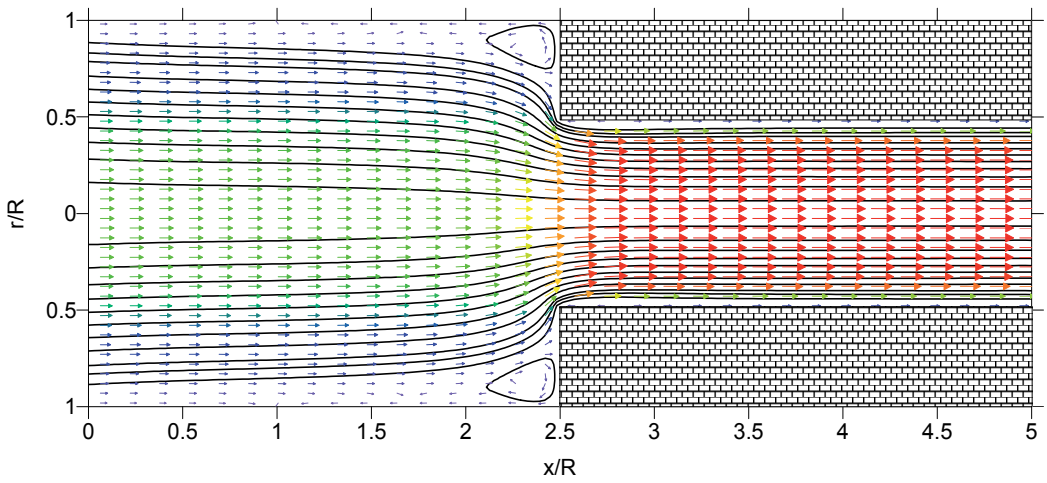

Fig. 11. Streamlines and vector field at channel flow with sudden narrowing (Re=1600 and h/R=0.5).

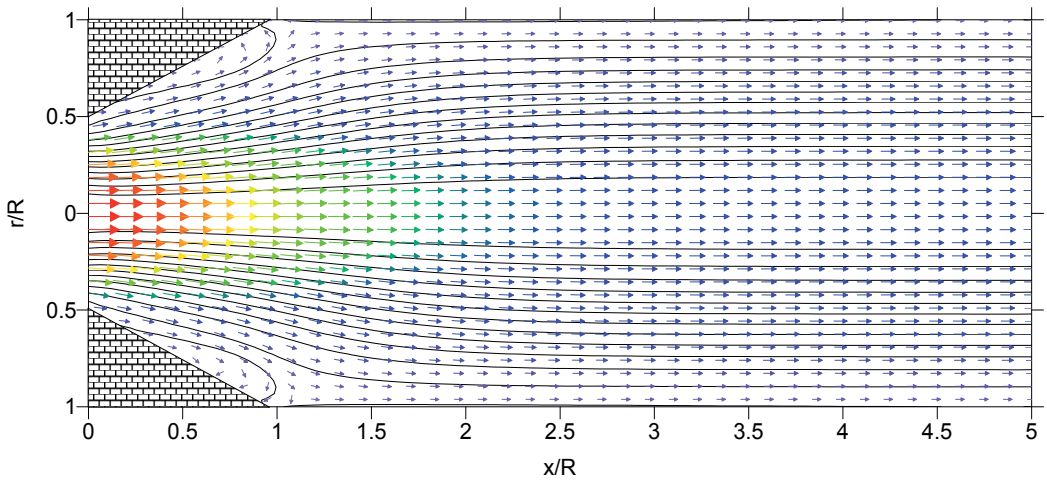

Fig. 12. Streamlines and a vector field at a channel flow with gradual expansion (Re=20, h/R=0.5, $\alpha = 30^{o}$

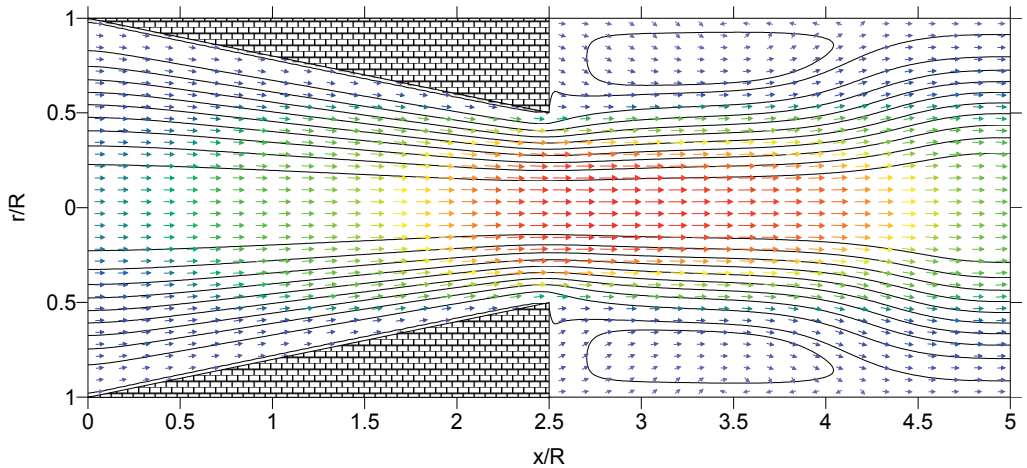

Fig. 13. Streamlines and a vector field in the channel flow with gradual narrowing to the channel middle (Re=20, h_R/R=0.5, h_x/L=0.5).

The main practice interest in calculations of similar configurations and corresponding estimations of algorithm possibilities in prediction of transfer mechanisms of momentum, heat and mass are connected with problems of peripheral recirculated zones definition in fields behind the obstacles representing of confuser and diffuser sections. Calculations show that the size of recirculated zones will well be co-ordinated with experiments. This circumstance allows hoping for the correct description of complex flows with similar geometry in the conditions of influence of mass inertial forces.

3.5 Detailed analysis of spatial swirled flows in channels of complex form

In this work it is established that joint influence on flow of swirling and features of pipe geometry conducts to combination of these effects accompanying each type of a flow separately. So, in channel stream swirled locally at input and including section of sudden expansion the occurrence of central recirculated zones (CRZ) causes reduction of peripheral recirculated zones (PRZ) and shifts reattachment more close to an input (Fig. 14).

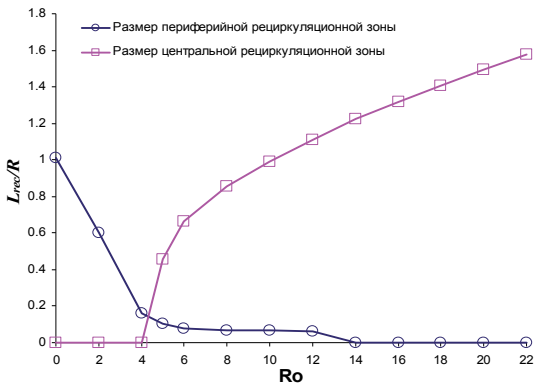

Fig. 14. Comparison of peripheral recirculated zones and central recirculated zones at combined effects of local swirling at the input and channel sudden expansion (h/R=0.5).

Some results illustrating reorganisation of vector velocity field in channels of the complex form are presented in fig. 15.

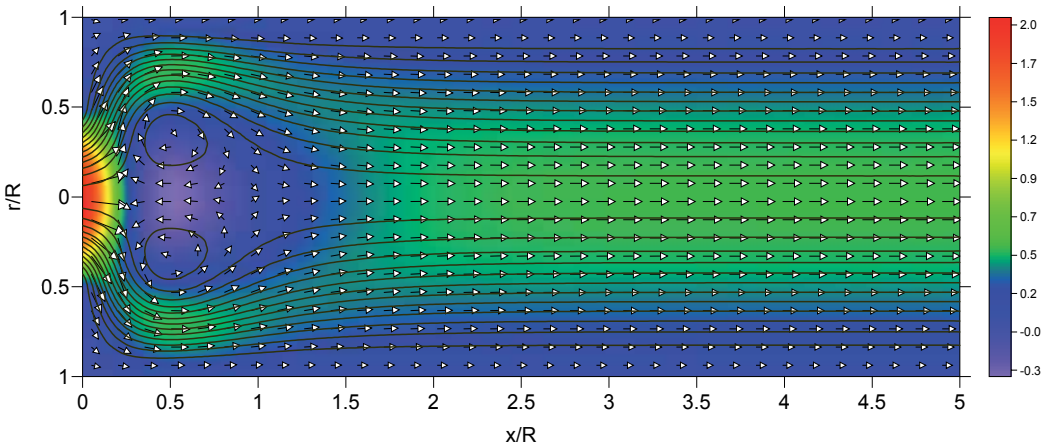

Fig. 15. Streamlines and a vector field of swirled flow at the input in conditions of suddenly extending pipe (Re=20, h/R=0.5, Ro=6).

4. Detailed modelling of structure of turbulent swirled stream

Researches of the turbulent flows complicated of non-isothermarlity, swirling, variability of properties of the heat-carrier, any wall configuration, combustion are multifaceted and multi-aspect. Publications in this direction are numerous. However, among authors of significant publications (and they mentioned above in paragraphs 2,3) concerning swirled flows at action of centrifugal mass forces and their applications in technics it is necessary to allocate some last results of the Russian scientists. So, considering the big contribution of Russian school of mechanical engineers to problems of the turbulence description, it is necessary to notice that results of last decades are reflected by successes in use of momentum approach (MA), large eddy simulation (LES), direct numerical simulation (DNS) with use of full Navier-Stokes equations, and also on the basis of the approach with application of the generalised hydrodynamic equations (GHE).

Among the specified directions actively developed last years, papers executed by B.V.Alekseev [134-141], A.M. Lipanov [142], O.M. Belotserkovskiy [143], J.V. Lapin, M.H.Strelets [144-146], A.F. Kurbatsky [147-150], B.P. Golovnay [151] are rather appreciable.

B.V.Alekseev's papers representing the elaboration of Boltzmann' ideas give the beginning of the original approach of turbulence analysis from kinetic positions. In classical understanding turbulence is described by Navier-Stokes model with characteristic for it irregularity of changing of thermo-dynamic parameters and wide range of scales of pulsing sizes. Lacks of such model of flow are connected with the absence in these equations of Kolmagorov' fluctuations. Hence, defining equations is problematic to consider as the equations which have been written down concerning actual magnitudes. In this sense on the basis of Boltzmann' equation the generalised hydrodynamic equations (GHE) received by B.V.Alekseev are more perfect and universal. These equations take into account the total spectrum of Kolmagorov' pulsations and allow to model the vortical flows in a wide range of Reynolds numbers,

including regimes of laminar and turbulent transitions. Some possibilities of the numerical description of vortical flows by means of GHE, containing physical viscosity are shown for example in [137]. It is noticed, that in comparison with the data received on difference schemes for Navier-Stokes equations, GHEquations look more preferable. In [138] the prospects are outlined for development of the kinetic and hydrodynamic theory of liquids taking into account change of functions of distribution on characteristic flow scales of an order of time of fluctuation of particles. In [139] the generalised Boltzmann kinetic theory is applied to a conclusion and research of the dispersive equations of plasma in absence of a magnetic field. In [136] the full system of the hydrodynamic equations is resulted at the level of Chapman-Enskog generalised equations (GECE). Small-scale turbulent fluctuations within the limits of model (GECE) are given in tables to [134]. In [140, 141] some problems are solved about distribution of sound speed and attenuation, shock wave structure. Despite appeal and novelty of ideas of the description of turbulence by B.V.Alekseev's equations (GHE), these equations are still poorly studied and while there is no confidence of possibilities of application of the given approach for the decision of practical problems. As any new theory it rejects already settled representations that Navier-Stokes equations are theoretical base for the turbulence description. However, as always happens in such cases, after long disputes in this occasion obviously there will be a heavy question of using of GHEquations and Navier-Stokes equations.

In direct numerical simulation (DNS) on the basis of full Navier-Stokes equations considerable successes are reached by A.M. Lipanov [142], O.M. Belotserkovskiy [143]. Calculations are executed at big Reynolds numbers (to 10^5) for the three-dimensional channel with jump of the area of cross-section section at the input with use of rather small steps on space and time, and also schemes of a high order of accuracy.

Within the given direction O.M. Belotserkovsky investigated a wide class of problems about free turbulent flows in jets, traces with effects of a separation, laminar and turbulent transition, and the transition phenomena to chaos.

Recently momentum approach actively develops in turbulent mechanics. To this approach a lot of attention is given in groups, which are managed by J.V. Lapin [144-146], A.F. Kurbatsky [147-150], B.P. Golovnya [151] etc. Efforts of these groups define successes of Low-Reynolds modelling, and also achievement in working out of practical versions of turbulent models in various complex cases.

In [144] Yu.V. Lapin has shown possibilities of following models: algebraic – T.Cebeci-S.Smit; semidifferential - John-King, Horton; differential - A.N. Sekundov, Spalart-Allmaras; B.Launder-B.Sharma, C.Chien (k ε); Menter (k ω) [for a class of problems about flows on flat or axisymmetric surfaces with sign-variable (sign-constant) gradients of pressure within the limits of a return method of the decision of the equations of turbulent boundary layer]. It is established, that in flows with a favourable (negative) gradient of pressure the greatest divergence between models and experience is observed in a prediction of longitudinal change of coefficient friction. Here, the best data are available for models of T.Cebeci-S.Smit, A.N.Sekundov-G.S.Glushko-S.N.Kharlamov, Menter.

At an adverse (positive) gradient of pressure models of Horton, A.N.Sekundov and Menter are allocated. (k-ε) models are unsuitable in calculation of flows of the given class. Menter's model gives good characteristics in calculation of effects of deceleration and a separation in comparison with analyzed models.

All models are reproduced only qualitatively accelerated or slowed down flows. The chosen models do not provide the exact description in the analysis of non-equilibrium boundary layers with a sign-variable pressure gradient.

In [145] the new algebraic model of turbulence is offered. In that paper results of model testing on a class of flows with adverse gradients of pressure are presented. These data show that the offered model does not concede to differential two-parametrical kε–, kω– turbulent models.

In [146] the Reynolds Stresses Algebraic Model (RSAM) of Vallin-Johansson with kε-base of Chen and kω of Wilcox in the conditions of flow with sign-constant pressure gradient is analysed. In comparison with classical models of Chen, Wilcox at work with RSAM-models their high sensitivity to the task of initial data, a choice of basic base is found out. It is underlined, that advantages of RSAM-models concern first of all calculation of pulsated parameters though accuracy of a prediction of components of kinetic energy of turbulence leaves much to be desired.

In [147, 148] Kurbatsky A.F. presents RANS-, RSAM-models and a numerical method to calculation of structure of a turbulent flow with an obstacle in the form of a ledge on a flat wall. In order to determine special zones (a separation, attachment, etc.) the models are involved, capable to reproduce anisotropic character of turbulence, behaviour of full tensor of Reynolds stresses in the fields near wall. Calculations show that quantitative divergences are considerable because of anisotropy of flow and proximity of used expressions for eddy viscosity. The correct description of fine structure can be received on the base of RANS-models.

Papers [149, 150] present calculated results of statistic characteristics of scalar turbulent field in channels in the conditions of the direct-flow and swirled stream. In these papers features of the description of transport heat and momentum processes at a wall with inclusion of data about time scales of thermal and dynamic turbulence are analyzed and also problems of construction of the balance equations for the given scales.

In [151] B.P.Golovnya offers original ($\overline{t'^2}, \varepsilon_t, k, \varepsilon$)-model to calculation near-wall turbulence. The model considers viscous effects, damping of walls in turbulent interactions. The model is tested on flows of type of boundary layer and is quite correct to forecast of complex flow.

Now the scientific direction connected with use of moment approach and theory of interpenetrating media in the decision of practically important problems about modelling of transfer processes and heat- and masstransfer in two-phased multicomponent systems "particle-gas" fruitfully enough develops. Here interesting results are received by M.A. Pakhomov, S.N. Kharlamov [152, 153]. So, in [152] the character of particle interaction and channel wall is analyzed in detail in frameworks of continuous model of gas-dispersed media. The assumption is entered about division of particles on falling and reflected fractions. Turbulent processes are described by L.V. Kondratiev model which is generalised on a case of presence several particle fractions. The model allows receiving the correct description of flow on dynamic and thermal characteristics.

In [152, 153] within the limits of Euler-Lagrange approach the mathematical model for a turbulent flow of multicomponent homogeneous and heterogeneous mixes in channels is

formulated and compared with numerous experiment data. Problems of detailed modelling of turbulent structure of the carrying media in the near-wall fields on the basis of popular two-parametrical turbulent models are investigated. On the basis of developed continuous models are studied the effects connected with influence of gravitational forces on parameters of not-isothermal turbulent gas suspension flow in the vertical channel in flow regimes of lifting and lowering. Intensification mechanisms of heat transfer are in details investigated at lowering of a disperse mix.

In the theoretical description of turbulence the main problems are the choice of models, methods of realisation of numerical algorithms, creation of steady numerical schemes of integration of the multidimensional transport equations, construction of approaching difference grids and so on. On these questions authors [45, 51, 146, 149,152, 153] receive new results. In particular, original multiple parameter dynamic and thermal turbulent models turbulence with $(\mathrm{k,L}, \tau, \omega, \nu_{\mathrm{t}}, \overline{t'^2}, \varepsilon_{\overline{t'^2}})$ - parameters are developed. These models are included the multiscale factor of dissipation of scalar and dynamic fluctuated fields [153], and also a method oriented pseudo-convection [45, 51]. Advantages of this method are connected with simplicity of calculation of the developed and non-stationary spatial flows with high Reynolds numbers at the expense of original representation of convective transfer by finite-difference approximation of the second order of accuracy. The offered way of introduction of pseudo-convection allows to by pass problems with numerical diffusion. The constructed iterative process provides stability of the decision at pseudo-additive disappearance (at convergence of iterations) and allows to connect advantages of finite-difference approximations of convective terms by the scheme against a stream, having the first order accuracy, to approximation by the scheme with the central differences of the second order of accuracy.

4.1 Remarks and conclusions to modelling of structure of turbulence in complex shear flows

Two-parametric *kL-*, *kε-*, *kω-* turbulent models of B.E. Launder, B.I. Sharma [46], M.V. Rubezin [154], G.S. Glushko [44,155] certainly are worthy from the point of view of maintenance of high accuracy of calculations and moderate expenses of an estimated time. However, these compromise models have considerable lacks. First, calculated time of these models is much more calculated time of simple one-parametrical models. Secondly, there is no satisfactory consent in the description of essentially anisotropic movement. Besides, in order to combine the theory and experiment the permanent investigations on updating of such models is conducted.

Possibilities of two-parametrical models are rather limited, but they provide the successful description concerning simple flows. Thus, it is necessary to notice that use of constant values c_μ does not provide true predictions in shear layers. Corrections are required on a case of small values of Reynolds number at the analysis of near-wall flows. Also those or other model modifications are required for the exact description of flows within boundary layers on the curved surfaces. Models of this class can work in the analysis of two-dimensional flows with a separation, rotation, curvature at corresponding selection of dependence $c_\mu \approx f\left(P, \varepsilon, gradU, \overline{u_i' u_j'}\right)$. The modified versions are comprehensible in not

swirled recirculated flows (except reattachment of a flow), in swirled flows without separation. There are good results in a prediction of flow behaviour in external area of strongly swirled stream at the account by turbulent model of eddy anisotropic properties. In spite of utility of existing models at designing of technical devices, essential improvements of numerical techniques and models of physical process are necessary in order to predict correctly of the complex shear flow behaviour existing in real conditions. Thus, it is required to improve accuracy of the description of transport turbulent processes of averaged characteristics of scalar quantities, in particular, concentration of reacting mixes, interactions of turbulence and chemical reactions.

In view of unsatisfactory speed and an insufficient memory size of modern computers, at numerical modelling of turbulence have important values of achievement in the field of producing capacity of computers. However, possibilities of computer calculated speed-up have a limit on each of concrete stages of computer engineering development. Therefore we can expect reception of the detailed and important information about complex shear flows interesting to appendices, from introduction of RANS - RSAM-models in calculated schemes. Thus, it is necessary to notice that for the present there are problems with realisation of RANS-, RSAM-models (low processing speed for calculation of the big data level) that limits their wide application.

RSAM-turbulent models have been developed for the purpose of expenses reduction by the decision of the differential equations in RANS-models. In special cases RANS-models are reduced to algebraic relationships for stresses through introduction of simplifying assumptions for convective and diffusive terms in the transport equations for Reynolds stresses. RSAM-models are used together with $k\varepsilon$ -, kL - or $k\ \omega$ -equations in the form expanding two-parametrical model. Additional effects (curvature of streamlines, rotation, buoyancy etc.) are considered in these relationships through sourced terms.

Averaged parameters of flow field, calculated on the RSAM-models, are close to data on two-parametrical models.

In simple flows all components of Reynolds stresses calculate precisely enough on the base of these models. In the analysis of near-wall shear layers the model corrections are required for registration of little turbulent Reynolds numbers at a wall. Various model modifications are required for calculation of complex flows (camber, concavity, complex surface).

Generally, the decision of system of the algebraic equations for stresses represents not trivial problem. From here there are many numerical techniques on using of RSAM-models in practice of engineering calculations. However, the transport equations for Reynolds stresses can be solved effectively with increasing of computer efficiency and development of calculated methods. Then RSAM-models will lose urgency.

Last twenty years considerable progress in turbulence modelling is connected with possibility of the detailed analysis of complex flows on the base of RANS-models. RANS-models application is interfaced to difficulties especially concerning modelling of unknown terms (redistribution, diffusion, dissipation) though the advantages of these models caused by their ability precisely to predict not only averaged characteristics, but also fine structure. Modern experience shows that application of RANS-models with $k\varepsilon$ - or kL-base almost invariably conducts to good results in the description of complex shear flows. The low-

Reynolds and high-Reynolds versions of RANS-models distinguish depending on applicability to concrete conditions of a flow. The high-Reynolds turbulent models use out of viscous sublayer and buffer zone $\left(y^+ > 50\right)$. Such models do not describe effects of molecular viscosity. Therefore, they often unite with the wall law.

Until recently in the majority of practical appendices calculations on $k\varepsilon$ - and RANS-models did not cover of near-wall area, because of problems of the definition of high gradients in this zone and bad validity of these models which are not using of damping relationships. It is necessary to notice, that unlike of High-Reynolds model versions, the low-Reynolds closing is studied poorly enough, especially for complex flows. And it is a subject of intensive researches on turbulent modelling.

Most likely, now the version of RANS-model offered by B.E. Launder, K. Hanjalic [156-158], M.M. Gibson [154, 159-161], D. Najot [162, 163] is considered as most developed one. And near-wall influence on correlation between pressure pulsations and deformation velocity tensor pulsation occurs in this version

These RANS-ε-models have good proved from the point of view of enough exact description of many features of a flow (velocity fields of the basic and secondary flows, shear components of Reynolds stresses full tensor). However, almost all versions of RANS-models with base in the form of ε-equation are not satisfactory in a prediction of the big maximum of autocorrelations of pulsations of axial velocity component $\overline{u'^2}$ and concerning of positive value of normal pressure at a wall. The analysis of having papers shows, that considerable efforts on improvement of models, construction of effective procedures of anisotropic near-wall field flow are necessary to receive a universal variant of turbulent equations closing at level of the second moments. Introduction of the complicated forms for a term representing correlation of pressure-deformations considerably strengthen a realizability of RANS-models and define correct behaviour of turbulence about near the wall. In [164] B.E. Launder underlines, that preservation of terms to the third order in a fast part of a redistributing term appears sufficient for modelling of near-wall behaviour of turbulence. Besides, a series of researches on diffusive modelling for $\overline{u_i'u_j'}$-equations shows possibility of use of more simple form of gradient type for D_{ij} without accuracy loss in comparison with the complex form of diffusion approximation. We will notice that theoretically more proved RANS-models still are not used in practical calculations, despite their obvious advantages. Therefore the further wide testing of these models for the purpose of their reasonable use in engineering practice is necessary.

Thus, the decision of averaged Reynolds equations together with turbulent model is represented to more economic, rather than calculations on LES modelling. Nevertheless, for challenges (chemically reacting systems, aerodynamic effects of the big speeds etc.) the estimated time can be lasting many hours on modern computers.

4.2 Physical and mathematical models of flow and heat transfer

In this part developed turbulent gas flow and heat transfer in cylindrical pipes and channels with constant and weak-changeable cross-section section is considered. It is supposed, that

the stream is one-component chemically inert media. Movement is axisymmetrical and carried out in absence of external forces, gravity and volume sources of heat. Temperature drops can be considerable so, that it is necessary to consider variability of thermo physic characteristics of a working fluid from temperature.

The system of the equations defining a flow and heat transfer includes the equation of continuity, movement (Reynolds full equations), energy and a condition and looks like, which is presented in tensor form:

$$\frac{\partial(\rho U_j)}{\partial x_j} = 0; \tag{1}$$

$$\frac{\partial(\rho U_i U_j)}{\partial x_j} = -\frac{\partial p_1}{\partial x_i} + \frac{\partial}{\partial x_j}(\mu \frac{\partial U_i}{\partial x_j} - \rho \overline{u_i' u_j'}) + \frac{\partial}{\partial x_j}[\mu(\frac{\partial U_j}{\partial x_i} - \frac{2}{3}\frac{\partial U_i}{\partial x_i}\delta_{ij})]; \tag{2}$$

$$c_p \frac{\partial(\rho U_i T)}{\partial x_i} = \frac{\partial}{\partial x_i}(\lambda \frac{\partial T}{\partial x_i} - \rho c_p \overline{u_i' t'}) + \mu(\frac{\partial U_i}{\partial x_j} + \frac{\partial U_j}{\partial x_i})\frac{\partial U_i}{\partial x_j} + \mu(\overline{\frac{\partial u_i'}{\partial x_j}\frac{\partial u_i'}{\partial x_j}} + \overline{\frac{\partial u_j'}{\partial x_i}\frac{\partial u_i'}{\partial x_j}}); \tag{3}$$

$$p_0 = \rho R_0 T; \tag{4}$$

The used designations in these equations (1) - (4) are standard, all values are averaged ones (Reynolds averaging). For closing of the defining equations the model of turbulence with the equations of balance of the one-point correlation moments of the second order of pulsations of velocity field ($\overline{u_i' u_j'}$) and temperatures ($\overline{u_i' t'}$) is involved.

4.3 Formulation of the low-Reynolds versions of transfer model for Reynolds stresses in incompressible media

Transfer equations for turbulent stresses in a stationary incompressible flow have following form [165]:

$$U_k \frac{\partial \overline{u_i' u_j'}}{\partial x_k} = \frac{\partial}{\partial x_k}(\nu \frac{\partial \overline{u_i' u_j'}}{\partial x_k}) - \overline{u_i' u_k'}\frac{\partial U_j}{\partial x_k} - \overline{u_j' u_k'}\frac{\partial U_i}{\partial x_k} + D_{ij} + R_{ij} - \varepsilon_{ij} \quad (i, j = \overline{1,3}), \tag{5}$$

where D_{ij}, R_{ij}, ε_{ij}, – accordingly turbulent diffusion, redistribution and dissipation, line over terms is Reynolds averaging.

On principle questions of term modelling of the higher orders (diffusion, redistribution, dissipation) we have no discrepancies with Y.G. Lai, R.M.K. So's approach [166]. Moreover, we practically remain system of coefficients of RANS-models. However, in representation of diffusive term we have entered a damping analogically by M. Prudhomme, S. Elgobashi [167]. Despite the made remark of the general character, the structure of modelled terms will be lower shown.

Turbulent diffusion is modelled with use of representation of K. Hanjalic [157] modified on near-wall field by using of damping function $f_\mu(\mathrm{Re}_t)$, taken on $k\varepsilon$ –model B.E. Launder- B.I. Sharma [46]:

$$D_{ij} = \frac{\partial}{\partial x_k}[c_s f_\mu(\mathrm{Re}_t)\frac{k}{\varepsilon}(\overline{u_i'u_m'}\frac{\partial \overline{u_j'u_k'}}{\partial x_m} + \overline{u_j'u_m'}\frac{\partial \overline{u_k'u_i'}}{\partial x_m} + \overline{u_k'u_m'}\frac{\partial \overline{u_i'u_j'}}{\partial x_m})], \quad (6)$$

where c_s = 0,15; $f_\mu(\mathrm{Re}_t)=\exp[-3{,}4/(1+\mathrm{Re}'_t/50)^2]$, $\mathrm{Re}'_t=k^2/(\nu\varepsilon)$.

Y.G. Lai, R.M.C. So accept for redistributing term [166]:

$$R_{ij} = \overline{\frac{p'}{\rho}(\frac{\partial u_i'}{\partial x_j} + \frac{\partial u_j'}{\partial x_i})} = R_{ij,1} + R_{ij,2} + R_{ij,w} \quad (7)$$

where it is used according to the of J.C. Rotta's approach [5]

$$\mathrm{R}_{ij,1} = -\alpha_0^* \varepsilon\, a_{ij},\ a_{ij} \equiv (\frac{\overline{u_i'u_j'}}{k} - \frac{2}{3}\delta_{ij}),\ \alpha_0^* = 1{,}17; \quad (8)$$

and it is accepted according to B.E. Launder [137, 145]

$$R_{ij,2} = \alpha(P_{ij} - \frac{2}{3}\delta_{ij}P) + \beta(Q_{ij} - \frac{2}{3}\delta_{ij}P) + \gamma k S_{ij}; \quad (9)$$

$$\alpha = -\frac{(c_{R2}+8)}{11}, \beta = -\frac{(8c_{R2}-2)}{11}, \gamma = -\frac{2(30c_{R2}-2)}{55}, c_{R2} = 0{,}3;$$

$$P_{ij} = -\overline{u_i'u_k'}\frac{\partial U_j}{\partial x_k} - \overline{u_j'u_k'}\frac{\partial U_i}{\partial x_k};$$

$$P \equiv \frac{1}{2}P_{kk}, Q_{ij} = -(\overline{u_i'u_k'}\frac{\partial U_k}{\partial x_j} + \overline{u_j'u_k'}\frac{\partial U_k}{\partial x_i}), S_{ij} = \frac{1}{2}(\frac{\partial U_i}{\partial x_j} + \frac{\partial U_j}{\partial x_i}).$$

Effects of "near-wall an echo" are entered on the basis of Y.G. Lai, R.M.C. So, B.E. Launder's structural relationship [156,166]:

$$\mathrm{R}_{ij,w} = f_w [\alpha_0^* \varepsilon\, a_{ij} + \alpha^*(\mathrm{P}_{ij} - (2/3)\delta_{ij}\mathrm{P}) - \frac{\varepsilon}{k}(\overline{u_i'u_j'}n_k n_j + \overline{u_j'u_k'}n_k n_i)]], \alpha^* = 0{,}45, \quad (10)$$

where we use V.I. Kvon's damping function in form:

$$f_w(\mathrm{Re}_t) = 1 - \exp(-\sigma_2 \mathrm{Re}_t^2) + \sigma_3 \mathrm{Re}_t^{1.5} \exp(-\sigma_1 \mathrm{Re}_t^2),\ \mathrm{Re}_t = k^{0,5}L/\nu, \quad (11)$$

$$\sigma_1 = 4\cdot 10^{-4},\ \sigma_2 = 2{,}1\cdot 10^{-4},\ \sigma_3 = 2\cdot 10^{-2}.$$

According to Y.G. Lai, R.M.C. So [166], as model of dissipative term can be accepted:

$$\varepsilon_{ij} = \frac{2}{3}\varepsilon(1-f_{w,1})\delta_{ij} + f_{w,1}\frac{\varepsilon}{k}[\overline{u_i'u_j'} + \overline{u_i'u_k'}n_k n_j + \overline{u_j'u_k'}n_k n_i + n_i n_j \overline{u_k'u_l'}n_k n_l] / [1 + 3\overline{u_k'u_l'}n_k n_l / 2k], \quad f_{w,1} = \exp[-(\mathrm{Re}_t'/150)^2]. \quad (12)$$

Relationships (12) are designed in such a manner that their use does not impose restrictions on value of an isotropic component of dissipation ε and basically for it any model can be used. As such model the transport equation for ε is used in all published papers. If to mean of the low-Reynolds number closure the decision of the equation for ε is connected with the known difficulties expressed in instability of computing process. The last is defined first of all by that of near-wall extremum in distribution ε is too close at a surface: $y^+_{max}\approx 5$ (in auto modelling internal currents). Such complexity is absent in models of the high-Reynolds number closure. As in this case the zone containing an extremum is out of calculated field. It is known also, that the turbulence scale changes monotonously at approach to a wall. Therefore the calculated algorithm of near-wall flows leaning against use of the equations for turbulence scale differs computing stability. Further we will use such equation as basic one to transport models of Reynolds stresses.

Proceeding from physical reasons the dissipation of an isotropic part of turbulence should be function of only scalar characteristics of fluctuated values and also viscosity:

$$\varepsilon=\varepsilon(\nu, k, L, l_D, \dots), \tag{13}$$

where ν is kinematic viscosity, k is kinetic energy of turbulence, L is integrated scale of turbulence, l_D is dissipative scale.

We should write down following expression for the dissipation of turbulent kinetic energy generalising experience of calculations of near-wall flows:

$$\frac{\varepsilon}{k}=c_{\varepsilon 1}f_{1\varepsilon}(\mathrm{Re}_t)\frac{\nu}{L^2}+c_{\varepsilon 2}f_{2\varepsilon}(\mathrm{Re}_t)\frac{\sqrt{k}}{L} \tag{14}$$

where $c_{\varepsilon 1}$, $c_{\varepsilon 2}$ are constants; $f_{1\varepsilon}$, $f_{2\varepsilon}$ are some individual functions:

$$f_{1\varepsilon}(\mathrm{Re}_t),\quad f_{2\varepsilon}(\mathrm{Re}_t)\in[0,1];\quad \mathrm{Re}_t\in[0,\infty).$$

The relationship (14) can be considered as "the condition equation" of two time scales for an isotropic part of turbulence.

If $f_{1\varepsilon}$ to take for identical unit, and $f_{2\varepsilon}$ is V.I.Kvon's damping function (11):

$$f_{1\varepsilon}(\mathrm{Re}_t)=1,\quad f_{2\varepsilon}(\mathrm{Re}_t)\equiv f_w(\mathrm{Re}_t) \tag{15}$$

And to accept $c_{\varepsilon 1}$=3,93; $c_{\varepsilon 2}$ =0,31 that relationship (14) will describe wide enough class of internal near-wall flows. Let's use further relationships (14), (15), and for L we will be received transport equation.

4.4 Equation for turbulent scale

Spatial distribution of linear integrated scale of turbulence L we will find from a following equation:

$$U_j\frac{\partial L}{\partial x_j}=\frac{\partial}{\partial x_j}(\nu\frac{\partial L}{\partial x_j})+D_L+P_L-\varepsilon_L. \tag{16}$$

At construction of modelling relationship for turbulent diffusion D_L (in this equation for L) the B.J. Daly, F.H. Harlow's modified gradient forms are used [11, 156]. They are presented taking into account influence of a wall by means of introduction of damping function $f_\mu(\mathrm{Re}'_t)$ and new value of a constant c_{sL}:

$$D_L = \frac{\partial}{\partial x_j}\left(c_{sL} f_\mu \overline{u'_i u'_j} \frac{L}{\sqrt{k}} \frac{\partial L}{\partial x_i}\right);\ c_{sL}=1{,}1; \tag{17}$$

Generation P_L is represented a combination of terms from Reynolds normal and tangential stresses:

$$P_L = c'_{1L}\frac{L}{k}P_n - c''_{1L}\frac{L}{k}P_\tau \tag{18}$$

where $P_\tau = -\sum_{i\neq j}\overline{u'_i u'_j}\frac{\partial U_i}{\partial x_j}$; $P_n = P_k - P_\tau$, $P_k = -\overline{u'_i u'_j}\frac{\partial U_i}{\partial x_j}$ is generation of turbulent kinetic energy, c'_{L1} =20; c''_{L1} =0,7.

The structure of dissipative term ε_L is similar to a form offered by A.N. Sekundov [168]. However, here we enter the correction on the account of influence of curvature of streamlines:

$$\varepsilon_L = -c_{Lf} c^*_{2L} k^{0,5}\left(1 - \frac{L^2}{x_n^2}\right). \tag{19}$$

where $c_{Lf}=c_{3L}+c_{4l}/\mathrm{Re}_t$; c_{3L}=0,3; c_{4L}=1,75; $c^*_{2L} = \max(0{,}3; c_{2L}f_s)$; c_{2L}=0,29; $f_s=(1+a_1\cdot\mathrm{Ri})\cdot[1-a_2\exp(-\mathrm{Re}_t^2/2)]$; $a_1\cdot$=0,74; a_2 =0,2; $\mathrm{Ri}=\frac{(W/r)\partial W/\partial r}{[(\partial U/\partial r)^2+(\partial W/\partial r)^2]}$.

Values of presented constants a_1, a_2 are found for developing swirled flows in pipes as result of optimum conformity of the given calculations and D.R. Veske's to measurements [169].

In practice instead of direct use of six equations (5) it is more convenient to work with three equations for Reynolds shear stresses, the equation for autocorrelation of a pulsation of axial velocity $\overline{u'^2}$, and also the transport equation for quantity $z=\overline{v'^2}-\overline{w'^2}$ and the equation for $k=(\overline{u'^2}+\overline{v'^2}+\overline{w'^2})/2$, finding after their integration $\overline{v'^2}=k+(z-\overline{u'^2})/2$ and $\overline{w'^2}=\overline{v'^2}-z$.

More low in 4.5 the transport model of turbulent fluxes of momentum and heat also will be formulated. This model includes as basic base of two-parametrical turbulent dynamic and thermal models with parameters: kinetic energy of turbulence (k), characteristic time of velocity pulsations (τ), intensity of temperature pulsations and its dissipation. These two-parameter models together with version of RANS-model will make the expanded version of "RANS-FLUXES"-model used in the present paper for the analysis of internal flows and heat- and mass transfer in the conditions of the direct-flow and swirled flows.

4.5 RANS-turbulent model with dynamic kτ-base

We will use tensor view for the purpose of simplicity of representation of the model equations and its closing parities. Approximated relationships for the description of the higher order terms (turbulent diffusion, redistribution, viscous dissipation) are used in a kind, offered by A.F. Kurbatsky's [150], J. Potta [5], B. Kolovandin [170], B. Launder [171], B. Petukhov [172], and generalised by us on base from kτ-equations. Taking into account remarks, the model has following view (values of constants are received as a result of numerical optimisation of calculations).

$$\frac{D\overline{u_i'u_j'}}{Dt}=\frac{\partial}{\partial x_\alpha}\left[(\nu+c_{\mu1}f_\mu\overline{u_i'u_j'}\tau)\frac{\partial\overline{u_i'u_j'}}{\partial x_\alpha}\right]-\frac{d_2}{\tau}\left(\overline{u_i'u_j'}-\frac{2}{3}k\delta_{ij}\right)-$$
$$-d_3\nu\frac{\overline{u_i'u_j'}}{\tau^2k}-\frac{2}{3}d_4\frac{k}{\tau}\delta_{ij}+P_{ij}-\frac{\partial\nu}{\partial x_\alpha}\frac{\partial\overline{u_i'u_j'}}{\partial x_\alpha}; \tag{20}$$

$$\frac{D\overline{u_i't'}}{Dt}=\frac{\partial}{\partial x_\alpha}\left[\left(\nu+\frac{(a-\nu)}{(n_i+2)}+c_{\mu\theta}f_{\mu\theta}\overline{u_i'u_j'}\tau\right)\frac{\partial\overline{u_i't'}}{\partial x_\alpha}\right]-c_2\frac{1}{\tau}\overline{u_i't'}-$$
$$-c_3(\nu+a)\frac{\overline{u_i't'}}{l^2_{\overline{u_i't'}}}-\overline{u_i'u_\alpha'}\frac{\partial T}{\partial x_\alpha}-\overline{u_\alpha't'}\frac{\partial U_i}{\partial x_\alpha}-\frac{\partial\nu}{\partial x_\alpha}\frac{\partial\overline{u_i't'}}{\partial x_\alpha}; \tag{21}$$

$$\frac{Dk}{Dt}=\frac{\partial}{\partial x_i}\left[\left(\nu+c_{\mu2}f_\mu\overline{u_i'u_j'}\tau\right)\frac{\partial k}{\partial x_i}\right]-c_{k1}\overline{u_i'u_j'}\frac{\partial U_i}{\partial x_j}-\frac{k}{\tau}; \tag{22}$$

$$\frac{D\tau}{Dt}=\frac{\partial}{\partial x_i}\left[\left(\nu+c_{\mu2}f_\mu\overline{u'_iu'_j}\tau\right)\frac{\partial\tau}{\partial x_i}\right]-\frac{2}{\tau}\left(\nu+c_{\mu2}f_\mu\overline{u'_iu'_j}\tau\right)\frac{\partial\tau}{\partial x_i}\frac{\partial\tau}{\partial x_i}+$$
$$+\left(c_{\varepsilon2}f_2-1\right)-\left(1-c_{\varepsilon1}\right)\frac{\tau}{k}\overline{u'_iu'_j}\frac{\partial U_i}{\partial x_j}+\frac{2}{k}\left(\nu+c_{\mu2}f_\mu\overline{u'_iu'_j}\tau\right)\frac{\partial k}{\partial x_i}\frac{\partial\tau}{\partial x_i}. \tag{23}$$

Here it is designated:

$$\frac{D}{Dt}=U\frac{\partial}{\partial x}+V\frac{\partial}{\partial r};\quad a=\frac{\nu}{\mathrm{Pr}};\quad P_{ij}=-\overline{u_i'u_\alpha'}\frac{\partial U_j}{\partial x_\alpha}-\overline{u_j'u_\alpha'}\frac{\partial U_i}{\partial x_\alpha}; \tag{24}$$

$$f_\mu=(1+3.45/\sqrt{\mathrm{Re}_t})\left[1-\exp\left(-y^+/85\right)\right];\quad f_{\mu\theta}=f_\mu f(\mathrm{Pr});\quad f(\mathrm{Pr})=0.5\cdot\left(1+0.871/\sqrt{\mathrm{Pr}}\right); \tag{25}$$

$$f_2=\left[1-\exp\left(\frac{-y^+}{4.9}\right)\right]^2;\quad \mathrm{Re}_t=k\tau/\nu\quad l_{\overline{u_i't'}}=f(\mathrm{Pr})\tau\sqrt{k}; \tag{26}$$

$$c_{k1}=0.9;\ c_{d1}=1.853;\ c_{d2}=0.83;\ c_{d3}=1.7;\ c_{d4}=1.44;d_2=1.4;\ d_3=140;\ d_4=0.7;$$
$$c_{\mu\theta}=0.15;\ c_\mu=0.09;\ c_{\mu1}=0.225;\ c_{\mu2}=0.066; \tag{27}$$
$$c_{\varepsilon1}=1.44;\ c_{\varepsilon2}=1.7;$$

The defining equations (1) - (27) are integrated under following boundary conditions. At the input ($X=0$) - homogeneous profiles of averaged and fluctuated values, at the exit ($X=X_K$) - so-called "soft" boundary conditions for all required parameters are set. At the wall ($r=R$) - absence of flow for hydrodynamic values and thermal stability for averaged temperatures ($T=T_w$ or $q_w=const$), the turbulent heat flux is too small. At the axis ($r=0$) - a condition of symmetry for all values, except shear stresses and a radial heat flux.

The decision of the defining equations is based on use of implicit finite-difference schemes, splitting schemes on physical processes with the subsequent application of TDMA-methods and an establishment method on march variable t (time). For this purpose of the equation (1) - (27) are represented in a non-stationary form. Iterative process proceeds until at carrying out of iterations the convergence on a friction and heat transfer with accuracy in 0.1 % will not be reached. The decision is under construction on non-uniform grids with a condensation of mesh nodes at a wall and an axis. Approximation of derivatives is carried out with the second order of accuracy concerning steps to radial and axial directions.

4.6 Results and their discussion

In this part of paper the calculated data of local velocities U, V, W, Reynolds stresses $\overline{u'^2}, \overline{v'^2}, \overline{w'^2}, \overline{u'v'}, \overline{u'w'}, \overline{v'w'}$, and also kinetic energy k, integrated scale of turbulent pulsations L, characteristic time of pulsations of velocity τ, integrated parameters of the swirled flow were analyzed: $tg\,\varphi_w = \tau_{\varphi w} / \tau_{xw}$, $\Phi=M / (R \cdot F)$, where $\tau\varphi_w$, τ_{xw} are shear stresses at the wall in azimuthal and axial directions accordingly.

Second parameter entered by N. Khiger and D. Bar [173] expresses the swirled flow intensity in any section. Now this parameter is widely used in the characteristic of rotary and axial impulses. Validation of the presented mathematical model is executed with attraction of experimental data [169, 174-176]. The main geometrical and flow dynamic characteristics were defined by following parameters: Re=5000÷100000; D=2R=0.01÷0.5m; x_k = (20÷500) D; Ro = (Ω R)/U_0=0.1÷5, Tu = (0.01÷01) %; L_0 = (0.02÷0.1) ·R. Working media is natural gas, air, water, oil. Here x_k is the co-ordinate defining length of the pipeline, the channel, Ro - dimensionless swirled parameter (Rossby number), Ω is angular velocity of rotation of a flow/wall of a pipe, Tu is intensity of turbulence ($\frac{\sqrt{\frac{1}{3}\sum_{i=1}^{3}\overline{u_i'^2}}}{U_0}$), "0" are noted by an index of size on an input in the channel.

The given researches *of moderately swirled* turbulent flow, feature of changes of its fine structure are presented on fig. 1, 2. Calculated distributions of axial velocity U/U_0 (fig. 1), normal a component of Reynolds stresses $\sqrt{\overline{u'^2}} / U_0, \sqrt{\overline{v'^2}} / U_0, \sqrt{\overline{w'^2}} / U_0$ (fig. 2) depending on dimensionless cross-section co-ordinate (y/R) in the allocated section of a pipe x/D=4 at various values of Rossby number Ro (line 1 is Ro=0, 2-0, 3-1) are compared to experiments [174, 175] (Re=50000, D=0.0762m). It is visible, that the theory and experiment consent quite

satisfactory. The swirling intensifies of turbulent transfer at a wall, causing big fullness of profile U (a line 3), connected with sharper radial gradient. The intensity of swirling is considerable in a vicinity of an input. Therefore here the swirled flow effect is brightly shown. It is expressed that at a channel surface the axial flow velocity exceeds averaged flow rate velocity. In the field of an axis we observe a zone of less moving flows ("failure" on a profile of axial velocity), which is transformed in a zone of returnable flows at higher Ro. In near-wall field the mass velocity decreases with removal from an input at swirling decay, and in axial zone, on the contrary, increases. The direct-flow stream is observed in the end of a hydrodynamic initial site x ≈ (80÷100) D.

Results show that radial velocity V is practically zero at Ro=0. By the way it increases with increase of Rossby number Ro though still the order of its value at chosen Ro is less a than order of axial and tangential velocities. In all cases velocity is directed to an axis, and its maximum decreases with growth x/D, being displaced in a flow core. It is seen that mode of quasi-solid rotation remains with almost linear distribution of tangential velocity in the field 0.05≤y/R≤1 at channel length x/D≈4. These data can be use for the approached estimations of a thickness of a buffer layer. Calculations show that W/U0 profile deformation well predicts by experiment [175] for near-wall zone with growth Ro. The location of maximum value of tangential velocity is displaced to a pipe wall with increase Ro, and the maximum converges to an axis at swirling decay conditions. Swirling influence on components of Reynolds stresses is well visible from fig. 2. Turbulent generation of tangential velocity takes place on all section of the channel.

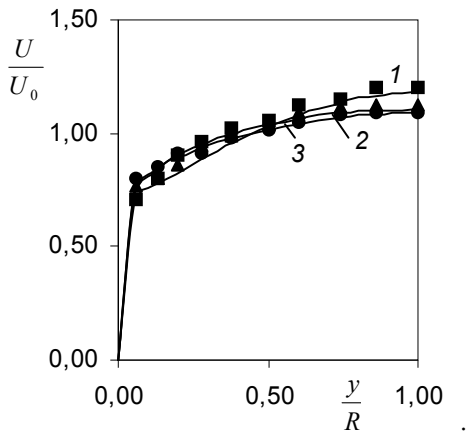

Fig. 1. Radial distribution of U/U_0 axial velocity in section x/D =4 at various swirling parameter Ro. Calculation is line, symbols are experiment [174, 175]: Ro = 0 (1, ■), 0.5 - (2, ▲), 1 - (3, ●).

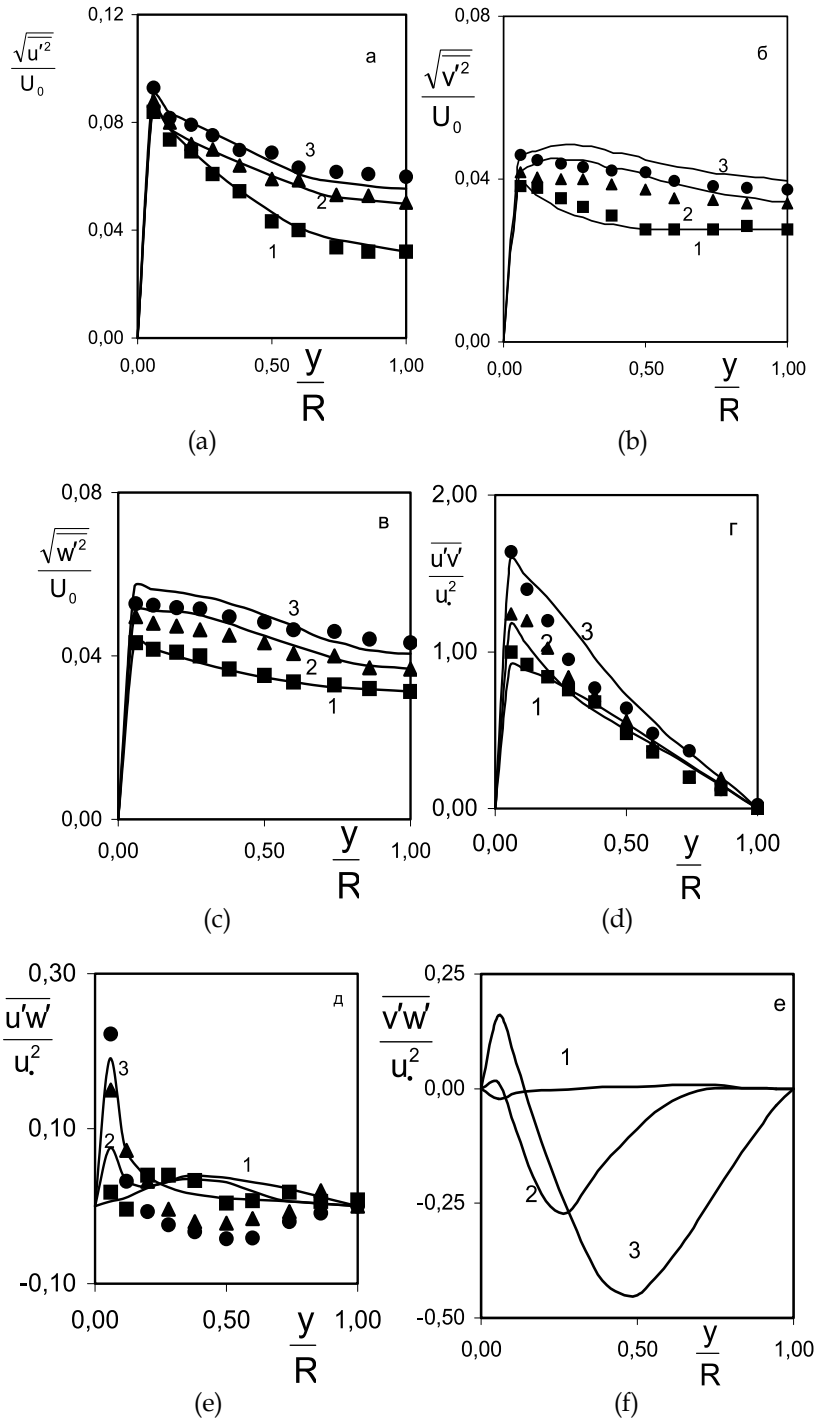

Fig. 2. Radial distributions of correlations of velocity pulsations $\overline{u_i' u_j'}$ in channel section x/D=4 at various parameters Ro. Designations are analogically to fig. 1.

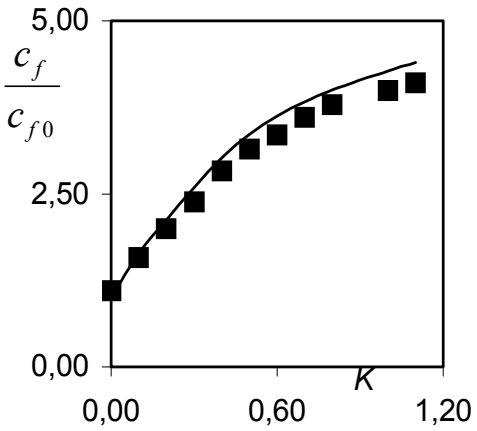

Fig. 3. Relative values of coefficient friction c_f/c_{f0} versus swirled parameter Ro in section x/D=4. Symbols are data [175], lines are calculation.

Calculations have shown, that the swirling is found the strongest influence on axial and radial component of Reynolds stresses $\overline{u'^2}$, $\overline{v'^2}$. These parameters essentially increase in an average part of the channel (lines 2, 3, fig. 2 (a)). At the direct-flow and swirled flows the theory will well be co-ordinated for component $\overline{u'^2}, \overline{w'^2}$. Increasing of Rossby number (Ro) conducts to formation of more homogeneous profiles of normal Reynolds stresses in comparison with case Ro=0 (a line 1). Such behaviour is caused by presence of generation of turbulent energy, connected with tangential averaged velocity which relative contribution grows in process of movement from a wall to a channel axis. Growth of velocity autocorrelations with increase Ro, and, hence, values of pulsations of these components leads to increase in values of mixed correlation $\overline{u'v'}$ on all section of the channel. Such intensification will quantitatively be co-ordinated with measurements [175]. In a direct-flow stream of correlation $\overline{u'w'}, \overline{v'w'}$ are practically equal to zero. Therefore the neglect is admissible by these components in majority channel parts. However, raised values $\overline{u'w'}$ are observed directly at a wall. Swirling causes essential growth of correlation $\overline{u'w'}$ directly at a wall, i.e. within a thickness of a buffer zone. In the given field $\overline{u'v'}, \overline{u'w'}$ correlations can be commensurable at big number Ro. Our data show that $\overline{v'w'}$ on a site x/D≤4 already at Ro=1 becomes commensurable for $\overline{u'v'}$. Such behaviour testifies to essential influence of swirling on turbulent structure of a flow. On fig. 3 relative change of coefficient friction c_f/c_{f0} in the allocated section of the channel (x/D) with growth of Ro (line is calculation, $c_f = 2\tau_{xw}/(\rho U_0^2), c_{f0}$ is a friction in a direct-flow stream, symbol is experiment [175]). It is visible that flow swirling is capable to intensify essentially dynamic processes (to 4 times on friction at Ro=1). Similar picture is noted in [58, 29, 176].

So, the turbulent scale has lengthier formative channel zone in comparison with a case of axial movement (approximately on 15÷20 %). Pressure distribution in a flow corresponds to complex character of reorganisation of axial and tangential velocities on pipe section: in

near-wall field movement is carried out with a negative longitudinal gradient of pressure, at the axis - with positive, and at a surface the module of a longitudinal gradient is less, than on an axis. With swirling degeneration the distribution of pressure more and more corresponds to a direct-flow stream on a hydrodynamic initial site.

On a channel site x/D≈2÷4 distributions U, W component of velocity, statistical pressure are defined by swirling intensity in considered section (parameters - Φ, $\tau\varphi_w$, τ_{xw}) and does not depend on the swirling law at the input. It will qualitatively be co-ordinated with data [58, 169, 176]. Identity of profiles of axial and tangential velocities takes place at uniform parameters Φ in pipes of various diameters in the specified zone (flow of air, water, natural gas). It allows speaking about Higir's parameter, as about criterion of hydrodynamic similarity of the swirled flows. Stream rotation influences turbulent structure mainly through additional generation of velocity pulsations and growth all of them correlations. The gradient of tangential velocity component and character of its change at a wall lend to revealing of local zones of active and passive action of centrifugal forces on fluctuated flow. It is confirmed also with data [58, 29, 177, 169].

Data of calculations of strongly twirled currents. It is known [58, 37, 178, 177, 169] that there is an intensive zone of returnable currents in such movement in a flow core. Existence of such zone is caused by attenuation of rotary movement and pressure increase on a pipe axis at removal from entrance area. Dynamics of strongly swirled stream was investigated earlier in pipes of constant and variable sections (for example, [177, 179]). Similar experimental papers can serve as a material for model validations. At the same time mathematical models allow to study in details physics of the swirled flow in the conditions complicating statement of experience: a short site of oil- and gas pipelines, intensive swirling, non-isothermality and so on.

In the present paper the estimation of working capacity of RANS-L-turbulent model is spent by comparison of calculated results with data [169, 176, 179]. Experiments are selected for flows at high values of Ro (Ro=3÷7). Calculations are executed at following values of parameters: Re = (2÷5) $\cdot 10^4$, D=0.03-0.4m, x_k = (10÷300) D.

So, on fig. 4 distributions of normal components of Reynolds stresses ($\overline{u'^2}, \overline{v'^2}, \overline{w'^2}$) on cross-section co-ordinate y/R in various sections on length of a pipe are presented at Ro=3 in comparison with data [169]. Symbols are experiment, line is calculation. It is necessary to notice, that the given mode answers a flow with the expressed tendency to formation of a zone of return currents. So, at x/D=0.35 in the field of a flow axis we have value $U_s/U_0 = 0.25$. close to experiment. The analysis of averaged velocity field shows that radial gradient of pressure gives the basic influence on formation of dynamic structure at Ro≈3. From fig. 4 it is visible, that the swirling intensity decays and values of autocorrelations $\overline{u'^2}, \overline{v'^2}, \overline{w'^2}$ decrease in process of stream advancement on length of channel. And, as well as in case of moderated swirling, the influence of rotation is more essential to correlations $\overline{u'^2}, \overline{v'^2}$ (fig. 4 a, b). Autocorrelation $\overline{v'^2}$ in the field of 0.35 ≤ x/D≤5.1 falls almost in 2 times. To section x/D≈50 the reorganisation of swirled flow in direct-flow is observed (lines 4, 5). Shear stresses tend to distributions of completely developed turbulent flow which is established in sections x/D=100÷150 (profile $\overline{u'v'}$ becomes linear). There is a satisfactory consent under statistical characteristics of

turbulence with experimental data for all field of a flow. However, the divergence of near-wall values $\overline{u'w'}$ (approximately in 2 times) is observed in a zone 0.3≤x/D≤5, which is levelled on the channel length. It is connected with influence of a real swirled way not considered in mathematical model. Distributions of W/U_0 depending on radial co-ordinate y/R for an experimental mode [179] (Re≈20000, Ro=6) are represented on fig. 5 for the purpose of an illustration of features of swirling decay on length of the channel. Such strongly swirled flow forms the expressed zone of return stream which according to calculations has the size (18÷20) D. The features of a flow connected with vortex, in input section (x/D=2) were modelled by the task of experimental distributions of velocity and pressure as initial parameters (line is 1, symbol is ■). From fig. 5 follows the consent of theory (calculation) and experiment is satisfactory on sites (x/D≤7). In distal channel fields the intensity of tangential flow at a wall lower, than according to experiments (fig. 5, lines 6-8). Thus, quality of effect of swirling influence on velocity component W remains. Such position in structure of strongly swirled stream will qualitatively be co-ordinated with data of papers [177, 169, 176, 179].

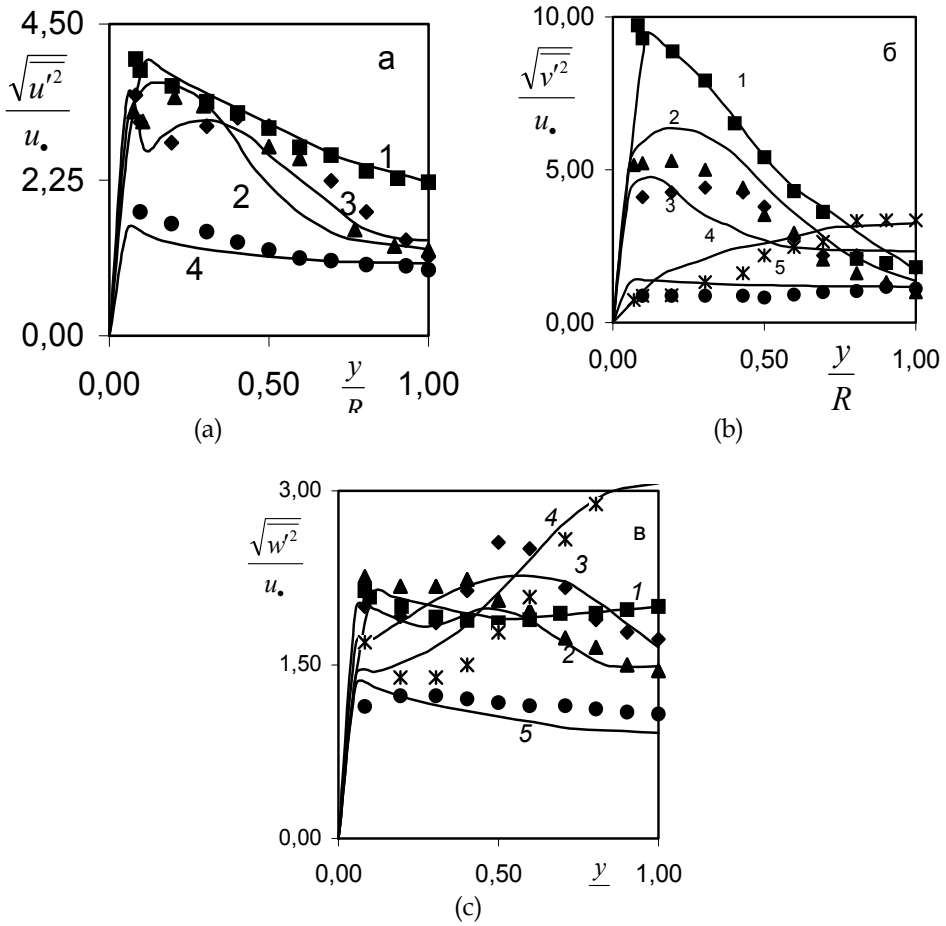

Fig. 4. Radial distributions of pulsated intensity of normal velocity components (axial – a, radial – b, tangential - c) at Ro=3 in an entrance site. Here, line - calculation, symbols - data [169]: ■ - x/D=0.35, ▲ - 5.1, ♦ - 10, * - 50, ● - 100.

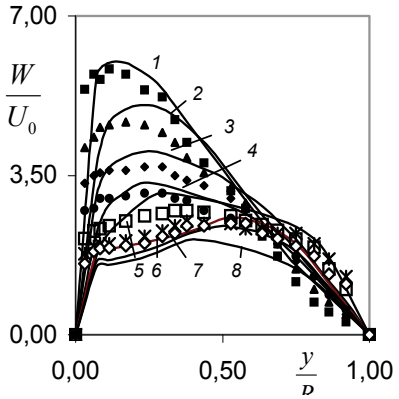

Fig. 5. Radial profiles of relative tangential velocity in an entrance site at K=6. Here, line - calculation, symbols - data [179: 1] - x/D=0 (■), 2-2 (▲), 3 - 4.5 (♦), 4 - 7.05 (●), 5 - 10.6 (○), 6 - 14.1 (*), 7 - 16.1 (□), 8 - 18.1.

As a whole, calculations show that rotation of media essentially rises turbulent mixing in a flow core. And active growth of hydrodynamic pulsations is observed in sections close to an input in a viscous sublayer and a buffer zone. Then, in process of movement, the intensification zone of pulsated flows moves in axial field. There is a liquidation of zones to a return flow in process of swirled decay. And it is established inflow of liquid mass to a core from a wall, caused by boundary layer increase. Changes in turbulent structure, in the sizes of zones of returnable flows are well predicted by RANS-L-turbulent model. Realized comparisons of calculations and experiments about the direct-flow and swirled flows on short and lengthy sites of pipelines speak about reliability of a numerical method, profitability and efficiency of RANS-L-turbulent model in the analysis of complex shear flows.

5. Conclusion

The number of important configurations of convective heat transfer in technical devices is consistently studied with use of methods of mathematical and numerical modelling of complex shear internal flows. In given chapter the development and a substantiation of complex multiple parameter turbulent models of the second order for a component of full tensor of Reynolds stresses and specific scalar fluxes with original basic bases from the transport equations for scales of dissipative dynamic and thermal times is presented for calculations of turbulent convective swirled and direct-flow streams.

By results of the presented research it is possible to do following conclusions.

1. Results of calculation of Navier-Stokes and Reynolds full equations with reference to areas of complex wall configuration (sudden expansion, narrowing, confuser-diffuser sections) with the account of heat transfer, turbulence, presence of mass inertial forces (swirling is carried out by a method of local swirling in the field of an input and method of a rotating wall of a pipe round the longitudinal axis). Calculations are executed for within the limits of models of stationary laminar and turbulent subsonic, chemically inert, not isothermal axisymmetric flows and on base of finite-difference calculated

technique - joined algorithms of SIMPLE and L.M. Simuni's approach. It is noted this approach is generalised on a case variable on radius of a longitudinal gradient of pressure.

2. The technique is characterised by working off of modules with consequence use of SIMPLE algorithm in calculations of the strong swirled laminar and turbulent flows (Ro> 4, h/d=0.5 - flows in pipes with local swirling in the field of an input; Ro> 2, h/d=0.5 - a rotating wall) and L.M.Simuni's generalised algorithm (other cases).
3. Big series of comparative test calculations is executed for cases isothermal and not isothermal, laminar and turbulent axisymmetrical flows in cylindrical pipes with complex surface (confuser-diffuser sections, sections of expansion - narrowing). It is established, that results of calculation are in the satisfactory consent with known data of other authors.
4. Calculations are carried out for swirled isothermal and not isothermal turbulent flows with attraction of modern closing schemes of the second order. These schemes include the transport equations for a component of full tensor of Reynolds stresses, specific turbulent thermal fluxes and basic bases from two-parametrical kL, $k\tau$ dynamic and thermal models with the equations for dissipative times of scalar and dynamic fields, integrated scale of turbulence.
5. Hydrodynamics and heat transfer is in details analysed by a rotating wall in conditions of flow laminarisation in pipes. Conclusion is presented about perspectives of using of the second order closures in calculations of local anisotropic turbulence on RANS-, RSAM- models.
6. The obtained data have the important applied significance about development of turbulent structure of incompressible liquid and weak-compressed gas in the conditions of action of mass inertial forces. The received results make *a databank* for construction of the general theory of rotating turbulent flows and universal statistical models for turbulent momentum and heat transfer in internal systems.

6. Acknowledgement

Author expresses gratitude to your pupil, V.Yu. Kim, Ph.D. in Mech. Engng, associator professor, Department of Theoretical Mechanics, Faculty of Mechanics&Mathematics, Tomsk State University, who is kindly presented some data for publication.

7. References

[1] Rai M.M., Moin P. Direct numerical simulation of transition and turbulence in a spatially evolving boundary layer // AIAA Paper 91-1607. 1991.

[2] Rodi W., Mansour N.N., Michelassi V. One-equation near-wall turbulence modeling with the aid of direct simulation data // Journal of Fluids Engineering. 1993. Vol.115. P.195-205.

[3] Werner A., Wengle H. Large-eddy simulation of turbulent flow over and around a cube in a plane channel // Proceedings of the 8th Symposium on Turbulent Shear Flows. Munich. Germany. 1991.

[4] Piomelli U., Moin P., Ferziger J.H. Model consistanecy in the large-eddy simulation of turbulent channel flow// The Physics of Fluids. 1988. Vol. 31. P. 1884-1891.

[5] Rotta J.C. Statistische Theorie Nichthomogener Turbulenz// Zeitschrift fur Physik. 1951. Vol. 129. №5. P. 547- 572; Vol. 131. №1. P. 51-77.
[6] Chou P.Y. On the Velocity Correlations and the Solution of the Equations of Turbulent Fluctuations// Quarterly Journal of Applied Mathematics. 1945. Vol. 3. P. 31-38.
[7] Davidov B.I. To statistical dynamics of incompressible turbulent liquid (in Russian) // Reports of USSR Academy of Sciences. 1959. Vol. 127. No. 4. Pp. 768-771.
[8] Davidov B.I. To statistical dynamics of incompressible turbulent liquid (in Russian) // Reports of USSR Academy of Sciences. 1961. Vol. 136. No. 1. Pp. 47-50.
[9] Donaldson C. do P. A computer study of boundary layer transition // AIAA Journal. 1969. Vol.7. P. 271-278.
[10] Hirt C.W. Generalized Turbulent Transport Equations. Los Alamos Scientific Laboratory. 1969.
[11] Daly B.J., Harlow F.H. Transport Equations in Turbulence // The Physics of Fluids. 1970. Vol. 13. № 11. P. 2634-2649.
[12] Naot D., Shavit A., Wolfshtein M. Numerical Calculation of Reynolds stresses in a square duct with secondary flow// Warme Stoffubertrag. 1974. Vol.7. P. 151-165.
[13] Launder B.E., Ying W.M. The prediction of flow and heat transfer in ducts of square cross-section// Proceedings of the Institution of Mechanical Engineering. London. 1973. №187. P. 37 - 73.
[14] Irwin H.P., Arnot-Smith P. Prediction of the effect of streamline curvature on turbulence// The Physics of Fluids. 1975. Vol.18. P. 264-276.
[15] Pope S.B., Whitelaw J.H. The calculation of near wake flows// The Journal of Fluid Mechanics. 1976. Vol. 73. P. 9-18.
[16] Sloan D.G., Smith P.J., Smoot L.D. Modeling of Swirl in Turbulent Flow System// Progress in Energy and Combustion Science. 1986. Vol. 12. P. 163-250.
[17] Sturgess G.J., Syed S.A. Calculation of Confined Swirling Flows // AIAA Paper 85-0060. 1985.
[18] Hendrix, Brighton. Calculation of influence of swirl and initial turbulence kinetic energy on bounded flow mixing (in Russian) // Theoretical foundations of engineering calculations 1975. No. 1. Pp. 156-163.
[19] Kubo, Goldwin. Numerical calculation of swirled turbulent flow // Theoretical foundations of engineering calculations. 1975. No. 3. Pp. 127-133.
[20] Ramos J.I. Turbulent Non-reacting Swirling Flows // AIAA Journal. 1984. Vol. 22. № 6. P. 846-847.
[21] Srinivasan R., Mongia H.C. Numerical Computations of Swirling Recirculating Flow; Final Report // NASA CR-165196. 1980.
[22] Jones W.P., Launder B.E. The Prediction of Laminarization With a Two-Equation Model of Turbulence// International Journal of Heat and Mass Transfer. 1972. Vol. 15. P. 301-314.
[23] Bradshaw P., Cebeci T., Whitelaw J.H. Engineering Calculation Methods for Turbulent Flow. N.Y. Academic Press. 1981.
[24] Lilley D.G., Chigier N.A. Nonisotropic Turbulent Stress Distribution in Swirling Flows from Mean Value Distributions // International Journal of Heat and Mass Transfer. 1971. Vol. 14. P. 573-585.
[25] Kobayashi T., Yoda M. Modified $(k-\varepsilon)$ Model for Turbulent Swirling Flow in a Straight Pipe // JSME International Journal. 1987. Vol. 30. № 259. P. 66-71.

[26] Sander G.F., Lilley D.G. The Performance of an Annual Vane Swirler // AIAA Paper 83-1326. 1983. June 27-29. Seattle. Washington.
[27] Moin P., Kim J. Numerical Investigation of Turbulent Channel Flow // Journal of Fluid Mechanics. 1982. Vol. 118. P. 341-377.
[28] Horiuti K. Comparison of Conservative and Rotational Forms in Large Eddy Simulation of Turbulent Channel Flow // Journal of Computational Physics. 1987. Vol. 71. P. 343-370.
[29] Launder B.E., Morse A. Numerical calculation of axisymmetric free shear flows with use of closure for stresses (in Russian) // Turbulent shear flows. Moscow: Mechanical Engineering, 1982. Pp. 291-310.
[30] Gibson H.H., Younis B.A. Calculation of Swirling Jets with a Reynolds Stress Closure // The Physics of Fluids. 1986. Vol. 29. № 1. P. 38-48.
[31] Sindir M.M. Effects of Expansion Ratio on the Calculation of Parallel-Walled Backward-Facing Step Flows: Comparison of Four Models of Turbulence // ASME Paper 83-Fe-10. 1983.
[32] Gibson M.M. An Algebraic Stress and Heat Flux Model for Turbulent Shear Flow with Streamline Curvature// International Journal of Heat and Mass Transfer. 1978. Vol. 21. P. 1609-1617.
[33] Rodi W. A new Algebraic Relation for Calculating the Reynolds Stress// ZAMM. 1976. Vol. 56. P. 219-221.
[34] Boysan F., Erdogan E., Ewan B., Swithenbank J. Numerical Prediction of Strongly Swirling Confined Turbulent Flows with an Algebraic Reynolds Stress Closure/ Intl. Rept., Dept. of Chemical Engineering and Fuel Technology. University of Sheffield. England. Rept. HIC 365, 1981.
[35] Boysan F., Ayers W.H., Swithenbank J. A Fundamental Mathematical Modelling Approach to Cyclone Design// Transactions of the Institute of Chemical Engineers. 1982. Vol. 60. P. 222-230.
[36] Vyisochin V.A., Safronov V.A. Experimental investigation of operating mode of vortex tube (in Russian) // Engineering-Physical Journal. Vol. 44. No. 12. Pp. 235-242.
[37] Swirled flows (in Russian) / Translation from English / Gunta A., Lilley D., Sired N.M.: Mir, 1987. 588 p.
[38] Goldshtick M.A. Vortex flows (in Russian). Novosibirsk: Science, 1981. 366 p.
[39] Smulskiy A.A. Aerodynamics and processes in swirl chambers (in Russian). Novosibirsk: Science, 1992. 300 p.
[40] Ternovskiy I.G., Kutepov A.M. Hydraulic cycloning (in Russian). Moscow: Science, 1994. 350 p.
[41] Khalatov A.A. Theory and practice of swirled flows (in Russian). Kiev, Naukova Dumka, 1989. 180 p.
[42] Zeierman S., Wolfshtein M. Turbulent Time Scale for Turbulent Flow Calculations // AIAA Journal. 1986. Vol.24. №10. P. 1606-1610
[43] Chien W.L., Lien F.S., Leschziner M.A. Computational Modelling of Turbulent Flow in Turbomachine Passage with Low-Re Two-equation Models // Computational Fluid Dynamics. 1994. P. 517-524.
[44] Glushko G.S. Differential equation for turbulence scale and calculation of turbulent boundary layer at flat plate // Turbulent Flows. Moscow: Science, 1970. Pp. 37-44.

[45] Kharlamov S.N., Kim V.Yu. Spatial Vortical Flows in Fields of Action of Centrifugal Mass Forces. Rome, Italy: Publ. House "Ionta", 2010. 112p.
[46] Launder B.E., Sharma B.I. Application of the energy-dissipation model of turbulence to the calculation of flow near a spinning disc// Letters Heat Mass Transfer. 1974. Vol. 1. P. 131-138.
[47] Patankar S. Computation of Conduction and Duct Flow Heat Transfer (in Rissian), under the editorship of V.D. Vilenskiy. Moscow, Energoatomizdat, 1984, 152 p.
[48] Yanenko N.N. Fractional step method for solution of many-dimensional tasks of mathematical physics (in Russian). Novosibirsk: Science, 1967. Pp. 345-351.
[49] Martchuk G.I. Methods of computational mathematics (in Russian). Moscow: Science, 1981. – 416 p.
[50] Simuni L.M. Computation of problem of non-isothermal motion of viscous liquid in flat pipe (in Russian) // Engineering-Physical Journal, Vol. 10, No. 1, 1966. Pp. 86-91.
[51] Kharlamov S.N. Mathematical Modelling of Thermo- and Hydrodynamical Processes in Pipelines. Rome, Italy: Publ. House "Ionta", 2010. 263p.
[52] Kasyanov V.M. Laminar liquid flow through the rotating direct pipe of round cross-section (in Russian) // Proceedings of MNN. 1951. Vol. 11. Pp.65-72.
[53] Kravtsov V.I. Influence of centrifugal forces at liquid flow character in pipes (in Russian) // Proceedings of Vedeneev VNIIG. 1951.Vol. 11. Pp. 23-31.
[54] White A. Flow of fluid in an axially rotating pipe // Journal of Mechanical Engineering Science. 1964. Vol. 6. №1. P. 145-152.
[55] Kuo G.Y., Iida H.T., Taylor J.H., Kreith F. Heat transfer in flow through rotating ducts // Transactions of the ASME. Ser.C. 1960. Vol. 82. №2. P. 54-68.
[56] Tretyakov V.V., Yagodkin V.I. Computation of laminar swirled flow in circular channel (in Russian) // Engineering-Physical Journal 1978. T. 34. №2. C. 273 - 280.
[57] Galin N.M., Raznyak V. Hydrodynamics and heat exchange in channels with unsteady walls (in Russian) // Proceedings of Moscow Energy Institute: Investigation of heat exchange processes in power and cryogenic plants. 1983. No. 616. Pp. 86-95.
[58] Schukin V.K., Khalatov A.A. Heat exchange, mass exchange and hydrodynamics on swirled flows in bulk forces fields (in Russian). - Moscow: Mechanical Engineering, 1982. 200 p.
[59] Schukin V.K. Heat exchange and hydrodynamics of inner flows in bulk forces fields (in Russian). - Moscow: Mechanical Engineering, 1980. 240 p.
[60] Khalatov A.A. etc. Heat and mass transfer, thermal-hydraulicperformance of vortex and swirling flows / (in Russian). Kiev, ITTF NASU, 2005. 500 p.
[61] Nakoryakov V.E., Gorin A.V. Heat and mass transfer in two-phase systems (in Russian). Novosibirsk: Institute of Thermal Physics, Siberian branch of Academy of Sciences, 1994. 413 p.
[62] Burundukov A.P., Galitseyskiy B.M., Dreytser G.A., Kashinskiy O.N., Kostyuk V.V., Nakoryakov V.E. Non-stationary heat and hydrodynamic processes in single phase and two-phase systems (in Russian) // Novosibirsk: Preprint Institute of Thermal Physics, Siberian branch of Academy of Sciences, 1989. No. 209. 110 p.
[63] Nakoryakov V.E., Grigoryeva N.I., Lezhnin S.I., Potaturkina L.V. Processes of combined heat and mass exchange under film absorption and bubble desorption (in Russian) // Novosibirsk: Preprint Institute of Thermal Physics, Siberian branch of Academy of Sciences, 1993. No. 266-93. 36 p.

[64] Lipanov A.M., Bobryshev V.P., Aliev A.V., Spiridonov F.F., Lisitsa V.D. Numerical experiment in theory of SRM (in Russian). Ekaterinburg: Science, 1994. 301 p.

[65] Lipanov A.M., Kisarov Yu.F., Kluchnikov I.G. Numerical simulation of eddy structure evolution in separated flows (in Russian) // Mathematical Simulation. 1994. No. 6. Pp. 13-23.

[66] Bulgakov V.K., Lipanov A.M., Roslov A.M. Computation of turbulent separated flows in channels with sudden expansion (in Russian) // Proceedings of higher education. Aircraft mechanics. 1990. No. 1. Pp. 37-40.

[67] Aliev A.V., Lipanov A.M., Lukin A.N. Mathematical simulation of inner hydrodynamics, heat and mass exchange and physicochemical conversions in systems with reacting porous medium (in Russian) // Methods of numerical experiment in engineering practice. 1992. No. 2. Pp. 16-31.

[68] Volchkov E.P., Matovich M., Oka S., Spotar S.Yu.,Chokhar I.A. Investigation of turbulent swirled flows with LD (in Russian) // Novosibirsk: Preprint Institute of Thermal Physics, Siberian branch of Academy of Sciences, 1989. No. 200. 37 p.

[69] Volchkov E.P., Dvornikov N.A., Terekhov V.I. Turbulent heat exchange in boundary layer in rotating systems (in Russian) // Heat and mass exchange. Minsk International Forum. May, 24-27, 1988. Selected reports. 1-2. Part 1. Minsk, 1989. Pp. 48-55.

[70] Volchkov E.P., Semenov S.V., Terekhov V.I. Turbulent heat exchange at vortex chamber end surface (in Russian) // Engineering-physical journal. 1988 Vol. 56. No. 2. Pp. 181-188.

[71] Alekseenko S.V., Protsaylo M.Y., Sryvkov S.V., Shtok S.I. Experimental investigation of swirled flow in chamber of square cross-section (in Russian) // Thermal physics processes simulation. Krasnoarsk: Krasnoyarsk State University press, 1989. Pp. 33-53.

[72] Alekseenko S.V., Borisov V.I., Goryachev V.D., Kozelev M.V. Three-dimensional numerical and experimental simulation of aerodynamics in combustion chamber of modern boiler units in isothermal conditions (in Russian) // Thermal physics and aeromechanics. 1994. Vol. 1. No. 4. Pp. 347- 354.

[73] Alekseenko S.V., Kuibin P.A., Okulov V.L., Shtork S.I. Large –scale vortex structures in intensively swirling flows.// Proceedings of the conference "Experimental and numerical visualization". ASME. 1995. Vol. 218. P. 181-188.

[74] Geshev P.I. Wall heat conductivity influence on turbulent Prandtl number value in viscous sublayer (in Russian) // Engineering-Physical Journal. 1978. Vol. 35. No. 2. Pp. 292-296.

[75] Geshev P.I. Linear model of near-wall turbulent transfer (in Russian). Preprint No. 73-81. 40 p.

[76] Veretentsev A.N., Geshev P.I., Kuybin P.A., Rudyak V.Y. On evolution of eddy-particle method applicable to separated flow description // Journal of Computational Mathematics and Mathematical Physics (in Russian). 1989. Vol. 29. No. 6. Pp. 878 - 887.

[77] Salomatov V.V. Calculation methods of non-linear processes of heat transfer (in Russian). Part 2. Tomsk: Tomsk State University press, 1978. 183 p.

[78] Grishin A.M., Fomin V.M. Conjugate and non-stationary problems of reacting media mechanics (in Russian). Novosibirsk: Science, 1984. 318 p.

[79] Fomin V.M., Fedorov A.V., Voroztsov E.V. Motion of gas and coal particle mixture in mines subject to desorption phenomenon (in Russian) // Aeromechanics. Moscow: Science, 1976. Pp. 316 – 327.

[80] Kovalnogov S.A., Fomin V.M., Shapovalov G.K. Investigation of near-wall pressure pulsations under passive operation with interaction of compression shock and boundary layer (in Russian) // Scientific notes of Central Aerohydrodynamic Institute. 1988. Vol. 19. No. 4. Pp. 116-121.

[81] Dorokhov A.R., Zhukov V.I. Similarity and self-similarity in film and swirled flows (in Russian)// Proceedings of Siberian branch of Academy of Sciences of USSR. Technics series. 1989. No. 1. Pp. 65-70.

[82] Burdukov A.P., Dorokhov A.R., Kazakov V.I., Kirsanov A.A. Mass exchange in liquid phase of centrifugal-bubble layer (in Russian) // Siberian Applied Physics Journal. 1993. No. 5. Pp. 11 – 16.

[83] Shilyaev M.I., Dorokhov A.R., Titov L.V. On heat exchange in viscous gas flow in narrow gap between rotating cylinders (in Russian) // Proceedings of Siberian branch of Academy of Sciences of USSR. Technics series. 1990. No. 1. Pp. 27-32.

[84] Shilyaev M.I., Dorokhov A.R., Titov L.V. Integral method for hydrodynamics and heat exchange calculation of viscous gas flow between rotating cylinders (in Russian) // Proceedings of Siberian branch of Academy of Sciences of USSR. Technics series. 1989. No. 6. Pp. 16-21.

[85] Arkhipov V.A. Analysis of stationary operating modes of power reactor of ideal mixing (in Russian) // Phusics of Combustion and Explosion. 1990. Vol. 26. No. 2. Pp. 83 – 87.

[86] Abujelala M.T., Lilley D.G. Liminations and empirical extensions of the k-ε model as applied to turbulent confined swirling fiows // AIAA Paper. 1984. N 441. 11p.

[87] Kikyama K. et al. Flow in a Rotating Pipe. (A Calculation of Flow in the Satureted Region)// Transactions of the Japan Society of Mechanical Engineers. 1982. Vol. 48. P. 1431–1438.

[88] Nishibori K., Kikuyama K., Murakami M. Laminarization of turbulent flow in the inlet region of an axially rotating pipe// Bull. JSME. 1987. Vol. 30. №260. P. 255-262.

[89] Kikuyama K., Murakami M., Nishiboki K. Development of three – dimensional turbulent boundary layers in an axially rotating pipe// Journal of Fluid Engineering. 1983. № 105. P. 154-160.

[90] Murakami M., Kikuyama K. Turbulent flow in axially rotating pipes // Journal of Fluid Engineering. 1980. № 102. P. 97-103.

[91] Morse A. Axisymmetric free shear flows with and without swirl. Ph.D.Thesis. University of London. 1980. 410p.

[92] Okulov V.L. The velocity field induced by vortex filament with cylindrial and conic supporting surface// Russian J. of Eng. Thermophysics. 1995. Vol. 5. №2. P. 63-75.

[93] Rinck K.J., Beer H. Numerical Calculation of the Fully Developed Turbulent Flow in an Axially Rotating Pipe With a Second-Moment Closure // Transactions of the ASME. Journal of Fluids Engineering. 1998. Vol. 120. P.274-279.

[94] Patankar S.V., Spalding D.B. A Calculation Procedure for Heat, Mass and Momentum Transfer in Three-Dimensional Parabolic Flows // International Journal of the Heat and Mass Transfer. 1972. Vol.15. P. 1787-1806.

[95] So R.M.PP., Ahmed S.A., Mongia H.PP. Jet characteristics on Confined Swirling Flow// Experiments in Fluids. 1985. Vol. 3. P. 221-230.
[96] Lefevr A. Processes in combustion chambers of gas turbine engines (in Russian). - Moscow: Mir, 1986. 531 p.
[97] Kilik E. Better Swirl Generation by Using Curved Vane Swirlers// AIAA Paper 85-1087. 1985.
[98] Jones W.P., Whitelaw J.H. Calculation Method for Reacting Turbulent Flows: A Review// Combustion and Flame. 1982. Vol. 48. P. 1-26.
[99] Boysan F., Ayers W.H., Swithenbank Y., Pan Z. Three Dimensional Model of Spray Combustion in Gas Turbine Combustors// Journal of Energy. 1982. Vol. 6. P. 368-375.
[100] Davenport U.D., Satton E.P. Separated and adjoint flows in near-wall area (in Russian)// Aerospace Technics. 1991. No. 5. Pp. 49-58.
[101] Arie M., Rouse H. Experiments in two-dimensional flow over a normal wall // Journal of Fluid Mechanics. 1956. № 1-2. P. 129-141.
[102] Krall K.M., Sparrow E.M. Turbulent heat transfer in the separated, reattached and redevelopment regions of a circular pipe // Journal of Heat Transfer. 1966. Vol. 88. № 1. P. 131-136.
[103] Adams E.W., Johnston J.P. Flow Structure in the Near-Wall Zone of a Turbulent Separated Flow // AIAA Journal. 1988. Vol. 26. № 8. P. 932-939.
[104] Shiloh K., Shivaprasad B.G., Simpson R.L. The Structure of a Separating Turbulent Boundary Layer. Part 3. Traverse Velocity Measurements // Journal of Fluid Mechanics. 1981. Vol. 113. P. 75-90.
[105] Ruderuch R., Fernholz H.H. An Experimental Investigation of a Turbulent Shear Flow with Separation, Reverse Flow and Reattachment // Journal of Fluid Mechanics. 1989. Vol. 163. P. 283-322.
[106] Simpson R.L., Chew Y.T., Shivaprasad B.G. The Structure of a Separating Turbulent Boundary Layer. Part I. Mean Flow and Reynolds Stresses // Journal of Fluid Mechanics. 1981. Vol. 113. P. 23-51.
[107] Simpson R.L., Chew Y.T., Shivaprasad B.G. The Structure of a Separating Turbulent Boundary Layer. Part II. Order Turbulence Results // Journal of Fluid Mechanics. 1981. Vol. 113. P. 53-72.
[108] Dianat M., Casto I.P. Measurements in Separating Boundary Layers // AIAA Journal. 1989. Vol. 27. № 6. P. 719-724.
[109] Stevenson W.H., Thompson H.D., Graid R.R. Laser Velocimeter Measurements in Highly Turbulent Recalculating Flows// Journal of Fluid Engineering. Transactions of the ASME. 1984. Vol. 106. P. 173-180.
[110] Speziale PP.G. Second – Order Closure Models for Rotating Turbulent Flows//Quarterly of Applied Mathematics. 1987. Vol. 45. №4. P. 721–733.
[111] Kurbatskiy A.F., Poroseva S.V., Yakovenko S.N. Calculations of turbulent flow statistical characteristics in rotating cylindrical pipe (in Russian) // Thermal Physics of High Temperatures. 1995.Vol. 133. No. 5. Pp. 738-748.
[112] Bergles A.E. Recent development in convective heat transfer augmentation// Applied Mech. Rev. 1973. Vol. 26. P. 675-682.

[113] Volchkov E.P., Dvornikov N.A., Spotar S.Y., Terekhov V.I. Turbulent friction and heat exchange in pipe under flow swirling (in Russian) // Applied Mechanics and Technical Physics. 1987. No. 2. Pp. 70-77.
[114] Thorsen R.S., Landis F. Friction and heat transfer characteristic in turbulent swirl flow subjected to large transverse temperature gradients// Transaction of ASME. Journal of Heat Transfer. 1968. Vol. 90. P. 81-90.
[115] Lopina R.F., Bergles A.E. Heat transfer and pressure drop in tape – generated swirl flow of single phase water// Transactions of the ASME. Journal of Heat Transfer. 1969. Vol. 91. P. 434-442.
[116] Kovalnogov A.F., Schukin V.K. Heat exchange and hydraulic resistance in pipes with vane swirlers (in Russian) // Engineering-Physical Journal. 1968. Vol. 14. No. 2. Pp. 239-247.
[117] Goldobeev V.I., Schukin V.K., Khalatov A.A., Yakshin A.P. Heat emission in inlet part of a pipe under half-way gas flow swirling at inlet (in Russian) // Proceedings of Higher Education. Aircraft Mechanics. 1973. No. 4. Pp. 108- 113.
[118] Burdukov A.P., Boger A.F., Dorokhov A.R. Heat exchange to swirled air flow in cylindrical channel (in Russian) // Heat Physics and Aeromechanics. 1994. Vol. 1. No. 1. Pp. 25-28.
[119] Algifri A.H., Bhardwaj R.K., Rao Y.V.N. Heat transfer in turbulent decaying swirl flow in a circular pipe// International Journal of Heat and Mass Transfer. 1988. Vol. 31. №8. P. 1563- 1568.
[120] Gostintsev Y.A. Heat and mass exchange and hydraulic resistance at rotating liquid flow along pipe (in Russian) // Proceedings of Academy of Sciences of USSR. Fluid Mechanics. 1968. No. 5. Pp. 115-119.
[121] Kuo G.Y., Iida H.T., Taylor J.H., Kreith F. Heat transfer in flow through rotating ducts // Transactions of the ASME. Ser.PP. 1960. Vol. 82. №2. P. 54-68.
[122] Utavar S.V., Radzha R.M. Intensification of heat exchange in laminar flows in pipes with wire spiral inserts (in Russian) // Heat Transfer. 1985. No. 4. Pp. 160-164.
[123] Nazmeev Y.G. Heat exchange intensification in viscous liquid flow in pipes with screw rolling-on (in Russian) // Heat power engineering. 1965. No. 2. Pp. 59-62.
[124] Borisenko A.I., Kostikov O.N., Chumachenko V.I. Experimental investigation of heat emission of liquid flow in pipe rotgating around its axis // Aerodynamics and heat transfer in electric machines (in Russian). Kharkov, 1974. Issue 4. Pp. 63-71.
[125] Delyagin G.N. Convective heat exchange in swirld flow under pressure (in Russian) // Proceedings of Fossil Fuels Institute. 1962. Vol. 19. Pp. 24-34.
[126] Kreith F., Margolis D. Heat transfer and friction in turbulent vortex flow// Appl. Sci. Res. 1959. Vol. 8. P. 457-473.
[127] Ibragimov M.F., Nomofilov E.V., Subbotin V.I. Heat emission and hydraulic resistance of liquid screw motion in pipe (in Russian) // Heat Power Engineering. 1961. No. 7. Pp. 57-60.
[128] Algifri A.H., Bhardwaj R.K. Prediction of the heat transfer for decaying turbulent swirl flow in a tube// International Journal of Heat and Mass Transfer. 1985. Vol. 28. №9. P. 1637-1643.
[129] Hirai S., Takagi T. Prediction of heat transfer deterioration in turbulent swirling pipe flow// Proceedings of the 2nd ASME/JSME Thermal Engineering Joint Conference. 1987. P.181-187.

[130] Buznik V.M., Geller Z.I., Pimenov A.K., Fedorovskiy A.N. Investigation of heat exchange at inlet region of rotating pipe to turbulent air flow (in Russian) // Heat Power Engineering. 1967. No. 4. Pp. 53-58.

[131] Schneidermann M.F., Ershov A.I. About the flow swirling influence at velocity and nemperature distributions in round pipe (in Russian) // Engineering-Physical Journal. 1975. Vol. 28. No. 4. Pp. 630 - 635.

[132] Lavan Z., Nielsen H., Fejer A.A. Separation and Flow Reversal in Swirling Flows in Circular Ducts// The physics of fluids. 1969. V12. N2.P. 1747-1757

[133] Hammad K. J., Ötügen M. V., Arik E. B. A PIV study of the laminar axisymmetric sudden expansion flow// Experiments in fluids. 1999. № 26.P. 266-272.

[134] Alekseev B.V. Integrated Boltzmann physical kinetics (in Russian) // Thermal Physics of High Temperatures. 1997. Vol. 35, No. 3. Pp.129-146.

[135] Alekseev B.V. Generalized Boltzmann physical kinetics in 2 volumes (in Russian). Moscow: M.V. Lomonosov Moscow State Academy of Fine Chemical Technology Press, 1997. Vol. 1. –147 p.; Vol. 2 –152 p.

[136] Alekseev B.V. Investigation of charged particles' distribution curve by the instrumentality of generalized Boltzmann equation // Thermal Physics of High Temperatures. 1995. Vol. 33, No. 6. Pp. 838-846.

[137] Alekseev B.V., Mikhailov V.V. Investigation of swirled flows of compressible gas on the basis of generalized hydrodynamic equations (in Russian) // Thermal Physics of High Temperatures. 1999. Vol. 37, No. 2. Pp.274-283.

[138] Alekseev B.V. To kinetic and hydrodynamic theory of liqids (in Russian) // Thermal Physics of High Temperatures. 1998. Vol .36, No. 2. Pp. 215-222.

[139] Alekseev B.V. Plasma dispersion equation in generalized Boltzmann kinetic theory (in Russian) // Thermal Physics of High Temperatures. 2000. Vol. 38, No. 3. Pp. 374-380.

[140] Alekseev B.V. Sound propagation investigation in terms of generalized Navier-Stokes equations (in Russian) // Proceedings of Academy of Sciences of USSR. 1990. Vol. 313, No. 5. Pp. 1078-1083.

[141] Alekseev B.V., Polev V.V. Calculation of shock wave structure with hydrodynamics equations of enhanced accuracy (in Russian) // Thermal Physics of High Temperatures. 1990. Vol. 28, No. 6. Pp. 614-623.

[142] Lipanov A.M., Kisarov Y.F., Kluchnikov I.G. Class of finite-difference schemes of high order of accuracy for direct simulation of turbulent flows under Reynolds number 10^5. Application of mathematical simulation for solution of problems in science and technology (in Russian). Izhevsk: Institute of Applied Mechanics, Ural branch of Academy of Sciences, 1996. Pp. 86-102.

[143] Belotserkovskiy O.M., Oparin A.M. Numerical experiment in turbulence: From order to chaos in Russia. Moscow: Science, 2000. 233 p.

[144] Garbaruk A.V., Lapin Y.V., Strelets M.Kh. Application of inverse method of boundary layer equations solution or turbulence model testing (in Russian) // Thermal Physics of High Temperatures. 1998. Vol. 36, No. 4. Pp. 607-616.

[145] Garbaruk A.V., Lapin Y.V., Strelets M.Kh. Simple turbulence algebraic model for calculation of turbulent boundary layer with positive pressure gradient (in Russian) // Thermal Physics of High Temperatures. 1999. Vol. 37, No. 1. Pp. 87-91.

[146] Garbaruk A.V., Lapin Y.V., Strelets M.Kh. Estimation of abilities of explicit algebraic models of Reynolds stresses in calculation near-wall turbulent boundary layers // Thermal Physics of High Temperatures. 1999. Vol. 37, No. 6. Pp. 920-927.

[147] Kurbatskiy A.F., Yakovenko S.N. Simulation of turbulent flow structure around the obstacle with sharp edges in flat channel. Turbulence models (in Russian) // Thermal Physics of High Temperatures. 1998. Vol. 36, No. 6. Pp. 927-932.

[148] Kurbatskiy A.F., Yakovenko S.N. Simulation of turbulent flow structure around the obstacle with sharp edges in flat channel. Simulation results (in Russian) // Thermal Physics of High Temperatures. 1999. Vol. 37, No. 1. Pp. 98-115.

[149] Kurbatskiy A.F., Казаков A.B. Explicit algebraic model of turbulent heat transfer for developed flow in rotating round pipe (in Russian) // Heat Physics and Aeromechanics. 1999. Vol. 6, No. 2. Pp. 247-257.

[150] Kurbatskiy A.F. Transport equations for time scale of turbulent scalar field (in Russian) // Thermal Physics of High Temperatures. 1999. Vol. 37, No. 4. Pp. 589-594.

[151] Golovnya B.P. To question of near-wall correction inclusion in turbulence model of k□ type in calculation of flows in boundary layer (in Russian) // Thermal Physics of High Temperatures. 2000. Vol. 38, No. 2. Pp. 257-261.

[152] Terekhov V.I., Pakhomov M.A. Yeat and mass transfer and hydrodynamics in gas-drop flows (in Russian). Novosibirsk: Novosibirsk State Technical University Press, 2009. -284 p.

[153] Kharlamov S.N. Mathematical models of inhomogeneous anisotropic turbulence in internal flows (in Russian), Tomsk: Tomsk University Publishing House, 2001.-448p.

[154] Wilcox D.S., Rubesin M.W. Progress in Turbulence Modeling for Complex Flow fields Including the Effect of Compressibility. NASA TP1517. 1980.

[155] Glushko G.S. Certain features of turbulent flows of incompressible liquid with transversal shift (in Russian) // Proceedings of Academy of Sciences of USSR. Fluid Mechanics. 1971. No. 4. Pp. 128-136.

[156] Launder B.E., Reece G.J., Rodi W. Progress in the Development of Reynolds-Stress Turbulence Model// Journal of Fluid Mechanics. 1975. Vol. 68. P. 537-566.

[157] Hanjalic K., Launder B.E. Contribution Towards a Reynolds-Stress Closure for Low-Reynolds-Number Turbulence// Journal of Fluid Mechanics. 1976. Vol.74. Pt.4. P. 593-610.

[158] Launder B.E., Shima N. 2-Moment Closure for the near-wall sublayer: Development and Application // AIAA Journal. 1989. Vol. 27. P. 1319-1325.

[159] Gibson M.M. An Algebraic Stress and Heat Flux Model for Turbulent Shear Flow with Streamline Curvature// International Journal of Heat and Mass Transfer. 1978. Vol. 21. P. 1609-1617.

[160] Gibson M.M., Launder B.E. Ground Effects on Pressure Fluctuations in the Atmospheric Boundary // Journal of Fluid Mechanics. 1978. Vol. 86. P. 491-509.

[161] Gibson M.M., Unis B.A. Simulation of deformed turbulent of near-wall flow (in Russian) // Aerospace Technics. 1983. Vol. 1. No. 3. Pp. 67-74.

[162] Naot D., Shavit A., Wolfshtein M. Interactions Between Components of the Turbulent Velocity Correlations Tensor// Israel Journal of Technology. 1970. Vol.8. P. 259-267.

[163] Naot D., Rodi W. Numerical Simulation of Second Currents in Open Channel Flow with an Algebraic Stress Turbulence Model/ University of Karlsruhe. West Germany. Rept. SFB80 /T/ 181. 1981.
[164] Launder B.E., Li S.P. On the Elimination of Wall-Topography Parameters from 2-Moment Closure // The Physics of Fluids. 1994. Vol.6. P. 999-1006.
[165] Belov I.A., Kudryavtsev N.A. Heat emission and resistance of pipe packages (in Russian). Leningrad: Energoatomizdat, 1987. 223 p.
[166] Lai Y.G., So R.M.C. Near-wall modelling of turbulent heat fluxes// International Journal of the Heat and Mass Transfer. 1990. Vol.33. №7. P. 1429-1440.
[167] Prud'homme M., Elghobashi S. Turbulent heat transfer near the reattachment of flow stream of a sudden pipe expansion// Numerical Heat Transfer. 1986. Vol.10. P. 349-368.
[168] Abramovich G.N., Krasheninnikov S.V., Sekundov A.N. Turbulent flows under interaction of volume forces and non-self-similarity (in Russian). Moscow: Mechanical Engineering, 1975. 95 p.
[169] Veske D.R., Sturov G.E. Experimental investigation of turbulent swirled flow in cylindrical pipe (in Russian) // Proceedings of Siberian branch of Academy of Sciences of USSR. Technics series. 1972. No. 13. Issue 3. Pp.3-10.
[170] Kolovandin B.A. Correlational modeling of transfer processes in turbulent shear flows (in Russian). Preprint. Academy of Sciences of BSSR. Institute of Heat and Mass Exchange. Minsk, 1982. No. 5. 60 p.
[171] Launder B.E. Second - Moment Closure and its use in modelling turbulent industrial flows // International Journal of the Numerical Methods in Fluids. 1989. Vol. 9. P. 963-979.
[172] Petukhov B.S. Heat exchange problems. Selected proceedings (in Russian). Moscow: Science, 1987. 278 p.
[173] Khigir N.A., Ber D. Velocity and static pressure distribution in swirled air flows escaping circular and expanding nozzles (in Russian) // Theoretical Basis of Engineering Calculations. -1964. No. 4. P. 54-61.
[174] Anwer, M., So, R.M.C. Study of Sublayer Bursting in a Bend // AIAA Pap. 1988. V.88. -P.3581-3588.
[175] Anwer, M., So, R.M.C. Rotation Effects on a Fully- developed Turbulent Pipe Flow// Experiment in Fluids. 1989. -№8. -P.33-40.
[176] Yajnik, K., Subbaiah, M. Experiments on Swirling Turbulent Flow// J. Fluid Mech. 1973. V.60. Pt.4. -P.665-667.
[177] Yamada, M. The Study of Mixing and Combustion in Swirling Flows/ Master's Thesis. Osaka University. 1982.
[178] Kline, S.J., Cantwel,l B., Lilley, G.M. Complex Turbulent Flow: Comparison of Computation and Experiment. Stanford Univ. Press. Stanford. CA. 1982.
[179] Burdukov A.P., Dorokhov A.R., Zhukov V.I. Investigation of swirled flow in cylindrical channel with smooth inlet (in Russian) // Proceedings of Siberian branch of Academy of Sciences of USSR. Technics series. - 1986. – No. 10. –Issue 2. - P. 60-63.

10

Numerical Wave Flumes Based on Smoothed Particle Hydrodynamics

Jinhai Zheng[1*], Gang Wang[1], Chi Zhang[2] and Yingqi Liu[2]
[1]*State Key Laboratory of Hydrology-Water Resources and Hydraulic Engineering, Hohai University, Nanjing,*
[2]*College of Harbour, Coastal and Offshore Engineering, Hohai University, Nanjing, China*

1. Introduction

Numerical simulation using computers or computational simulation has increasingly become a very important approach for solving complex practical problems in engineering and science. It translates a physical problem into a discrete set of mathematical description, recreates and solves the problem on a computer, and reveals phenomena virtually according to the requirements of the analysts. With the help of increasing computer power less and less assumptions are necessary and problems can be solved with more details. Numerical simulations are replacing expensive, time-consuming and difficult experiments in laboratories more and more. Furthermore, the numerical tools are often more useful than the traditional experimental methods in terms of providing insightful and complete information that cannot be directly measured or observed, or difficult to acquire via other means.

Hydraulic engineering is defined as the branch of civil engineering dealing with the use and control of water in motion. Numerical simulation is an important tool to understand the motion of water. For fluid motion, it can be described by a set of partial differential equations in time and space. Pressure, and a velocity component for every used dimension, is the only main independent field variables. With enough initial and boundary conditions the equations can be solved giving the pressure and velocity at every point, at every time. In most cases analytical solutions are not available. However, when space is discretized into cells (regular or irregular), and time is divided in a finite number of steps, the solution can be found by numerical integration. There are many ways to discretize the continuous governing equations, and the discretization techniques may be different for different numerical methods.

Traditional numerical methods, such as the finite difference method, the finite volume method and the finite element method, are based on Eulerian grids, which is that the grid is fixed and the fluid is flowing through it. The finite difference method uses a fixed rectangular grid and discretizes the equations using Taylor Series expansion. This method

*Corresponding author

was used historically due to its ease of programming and accurate results but tends to rely on a fairly regular mesh. It therefore does not handle large deformations or complex problems well. Recently, the method discretized the equations in generalized curvilinear coordinates has also been developed to adapt computations to irregularly shaped boundaries and make computations more efficient. The finite volume method discretizes the domain into a number of finite volumes and integrates the governing equations over each of these. This method is popular amongst fluid dynamics researchers because integrals are applied separately within each volume. One applies the conservation principle (volume integration) and exploits the Gauss Green theorem to turn a volume problem into a surface one; the rate of change of one property inside a control volume can now be assessed by the computation of the property fluxes at the boundaries. A structured grid is not required when using this method giving it an advantage due to the effort saved. The finite element method divides the domain up into elements (usually in the form of basic geometric shapes, such as triangular grids). The numerical solution is also determined by integration albeit a weighed integration and shape functions are also used to express the value of a property continuously as a combination of the cell nodal values. An attractive feature of the finite element method is that it is well suited to handling complicated geometries and generally considered to be very robust.

Despite these conventional grid-based numerical methods have got the great success in computational fluid dynamics for engineering and science problems, they suffer from some inherent difficulties in many aspects, which limit their applications to many problems. One drawback is capturing the position of the free surface, and it is difficult to predict when it changes rapidly in time. A multiply defined free surface as in overtopping waves is harder or even impossible to predict for these methods.

Smoothed Particle Hydrodynamics (SPH) is a pure Lagrangian, meshfree method, which was conceived in 1977 by Gingold and Monaghan[1] and independently by Lucy[2] for modeling astrophysical phenomena, and later widely extended for applications to problems of continuum solid and fluid mechanics. The basic idea of SPH is to use the collective motions of large number of particles to represent a flow in a Lagrangian way rather than Eulerian way. In a particle approach, the governing equations are discretized and solved with respect to the individual particles filled within the computational domain. This method is conceptually simple without adding new physics and high accuracy can be achieved by increasing number of particles.

To date, the SPH becomes increasingly popular and finds wide applications in computational fluid mechanics, including free surface flow[3], porous flow[4], landslide-induced flow[5] and fluid-structure interactions[6]. In particular, the SPH method has been adapted in a variety of numerical wave flumes for studying green water overtopping[7-8], wave breaking in the surf zone[9-10], and wave-structure interaction[11-13]. The most attracting feature of SPH for wave modeling is that it naturally needs no special approach for dealing with the free surface. It is meshfree and every particle at the free surface can be easily tracked in the Lagrangian frame. When conducting a numerical wave flume involved with flow separation and large deformation, this appears a significant advantage over other traditional Eulerian methods, including those based on the Reynolds Averaged Navier-Stokes (RANS) equations[14], large eddy simulation[15-16], and Laplace models[17]. Those models commonly need an additional treatment to capture the free surface on a fixed

Eulerian grid, such as the Volume Of Fluid (VOF) method or the MAC method. Moreover, those Eulerian solvers often suffer from the numerical diffusion arising from the fixed-point interpolations of advection terms. In the Lagrangian description of SPH simulations, this problem is avoided. Besides, the SPH can handle rotational flows with vortices and turbulence.

Despite its remarkable advances for simulation of violent free-surface fluid flows, the most critical drawback of SPH which limits the future applications is its extreme demand for CPU time. As was pointed out by Dalrymple and Rogers[9], the SPH method is not suitable to model large regions at the present state of art, since a large number of particles and rather small time step are often required to obtain satisfactory resolution. One of the most important factors resulting in the long CPU time is a searching process for the nearest neighboring particles for every given particle, which should be updated at each time step, called the Nearest Neighboring Particle Search (NNPS). The efficiency of NNPS method thus dominates the overall computational cost. The earliest and simplest NNPS method is the Direct Search Method (DSM), which directly computes the distances between each pair of particles to find the smallest one. Clearly, the computation order would be $O(N^2)$ (where N is the total number of particles) for this method. A variety of improvements have been made to decrease the count of operations in this process. Monaghan[18] proposed the Link-List Method (LLM), which divides all particles into rectangle grids. When searching the nearest particles of a certain particle, only those within the same grid as this one and within 8 adjacent grids around are taken into consideration. However, this method behaves poor if the density of particles is largely non-uniform over the whole domain. Hernquist and Katz[19] developed a hierarchical tree method which reduced the computation order to $O(N \cdot \log N)$. Mihai et al.[20] used a static grid system with variable spatial steps and successfully decreased the computation order to $O(N)$. Those improvements are, however, still far away from satisfactory, regarding the considerably increasing number of particles needed in wider applications of SPH method. Recently, Zheng et al.[21] proposed a new NNPS method, named as the Inner and Outer Particles Searching (IOPS) method. The method distinguishes itself from others by introducing concepts of inner and outer grids, which significantly enhances the computation efficiency compared with the DSM and the method of Mihai et al.[20].

In this paper, section 2 introduces the development of a SPH numerical wave flume based on the Navier-Stokes equations, following by a description of the IOPS method that enhances the SPH method. Section 3 validates the numerical results, which are compared with the analytical solutions, other methods and experiment data. Section 4 applies the SPH method for a wide range of solitary wave propagation problems such as the impact of waves on structures, wave run-up and rundown and breaking on a planar slope. Finally in section 5, conclusions about SPH are drawn and further improvements are recommended.

2. Numerical method

The basic concept of SPH method is to treat a flow as a sum of moving particles. Each particle has its own physical quantities such as mass, velocity, density and pressure gradient. During flow motions, all particles change their positions and corresponding properties with time. The SPH model then solves the trajectory of each particle. Through the

use of integral interpolations, the field variables are expressed by integrals approximated by summation interpolations over neighboring particles. Firstly, the functions of variables at an arbitrary location are transformed into integral forms, referred to the kernel approximation. Secondly, those integral expressions are approximated by summations of variables of relevant scattered particles.

2.1 Kernel approximation

In a continuous variable field, any function can be expressed in terms of its values at a set of particles by use of a weighting function

$$A(r)=\int_{\Omega} A(r')\delta(r-r')\mathrm{d}r' \tag{1.1}$$

and

$$\delta(r-r')=\begin{cases}1, & r=r'\\ 0, & r\neq r'\end{cases} \tag{1.2}$$

where A is the function with respect to the spatial tensor, Ω denotes the computational domain, and $\delta(r-r')$ is Dirac delta function. Replacing the Dirac delta function by a kernel W, leads to

$$A(r)=\int_{\Omega} A(r')W(r-r',h)\mathrm{d}r' \tag{1.3}$$

where h is the smoothing length which controls the size of the area around a given particle where the contribution from other particles cannot be neglected, and W is a cubic spline kernel. Representing the approximation process with a sign of <> and introducing the gradient of $A(r)$, we get

$$\langle \nabla A(r)\rangle=\int_{\Omega}\left[\nabla A(r')\right]W(r-r',h)\mathrm{d}r' \tag{1.4}$$

Equation (1.4) can be written as

$$\langle \nabla A(r)\rangle\approx-\int_{\Omega} A(r')\nabla W(r-r',h)\mathrm{d}r' \tag{1.5}$$

provided that the filtering range kh is inside the computational domain Ω .

Note that, if the filtering range extends beyond the computational domain, Eq. (1.5) will break down for the lack of particles and a special treatment should be applied at the boundary[22].

2.2 Particle approximation

If the number of particles constructing the whole domain is N, Eq.(1.5) can be approximated

by a summation, given as

$$\langle \nabla A(r) \rangle \approx -\sum_{b=1}^{N} \frac{m_b}{\rho_b} A(r_b) \nabla W(r - r_b, h) \tag{1.6}$$

where r, m and ρ represent the spatial vector, mass and density of an individual particle, respectively. Subscript b represents the index number.

It can be seen from Eq.(1.6) that the variable A at the point r is affected by all N particles in the computation domain. In practice, the influence of kernel is restricted to a radial distance of an order of kh. That means only the particles within this distance (so-called neighboring particles) are considered to contribute to the summation in Eq.(1.6). While particles keep moving with flow motions, the relative positions of all particles should be calculated to find the effective particles for each point at every time step. This work is done by the NNPS method.

2.3 IOPS method

This section describes in detail the concept and implementation of the IOPS method proposed in this study. The IOPS method saves the computational time by shifting most of advanced CPU operations (e.g., multiplication, division) into simple addition operations. Firstly, each individual particle is marked by the so-called inner and outer grids. Secondly, for a given particle inside the domain, the particles in its filtering control unit in the inner grid is marked. Finally, the distances between this particle and other particles in the filtering control unit are computed to find the nearest neighboring particles.

If the number of particles is N and the number of inner grids is m for the whole domain, the number of particles in each inner grid would be N/m. Figure 1 shows the grid structures. Overlaps can be seen between boundaries of neighboring outer grids. The number of particles in each outer grid is larger than that in each inner grid. When total number of particles is relatively large, however, that difference can be neglected in the estimation of computational effort. Therefore, the computation order of marking all particles by inner and outer grids is $O(2\times N\times m)$.

For a given particle in an inner grid, a square filtering control unit is defined with its side length of kh. Then, particles belonging to both the filtering unit and the outer grid are marked, with a computation order of $O(N^2/m^2)$. For the whole domain, that is $O(N^2/m)$. Till now, only particles inside the filtering control unit need to be considered to search the nearest neighboring ones. The computation order for this process appears a constant and can no longer be reduced. Eventually, it is easy to find that the smallest total computation order can only be obtained when $2\times N\times m+N^2/m$ is smallest. That is when $m=\sqrt{N/2}$, we get the minimum CPU time consuming.

To highlight the efficiency of the IOPS method, the CPU time required for a single searching process using the present method, DSM and the method of Mihai et al.[20] are illustrated in Figure 2. The x-axis represents the total number of particles and the y-axis represents the CPU time. All numerical experiments in this paper were carried out on a PC with a CPU 1.83 GHz. An obvious advancement of IOPS over other two methods can be found, with a

computation order of $O(N)$. In particular, unlike those two methods, the good behavior of IOPS is not significantly affected by increasing number of particles even for extreme large values. For 205,000 particles, only a CPU time of 4.2 s is needed to complete a searching using the IOPS. This improvement releases the SPH applications for practical purposes to a considerable extent.

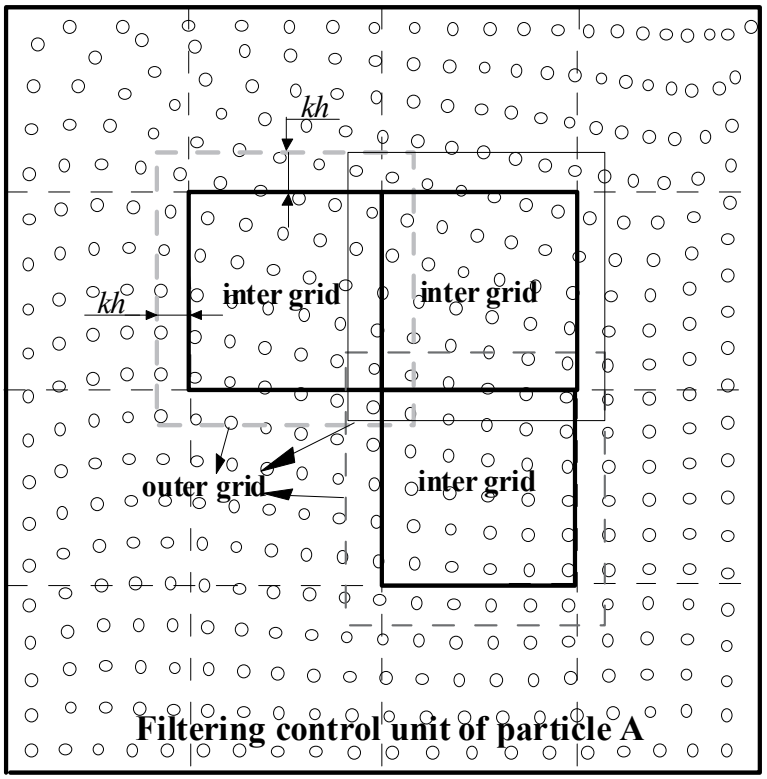

Fig. 1. Grid structure in the IOPS method

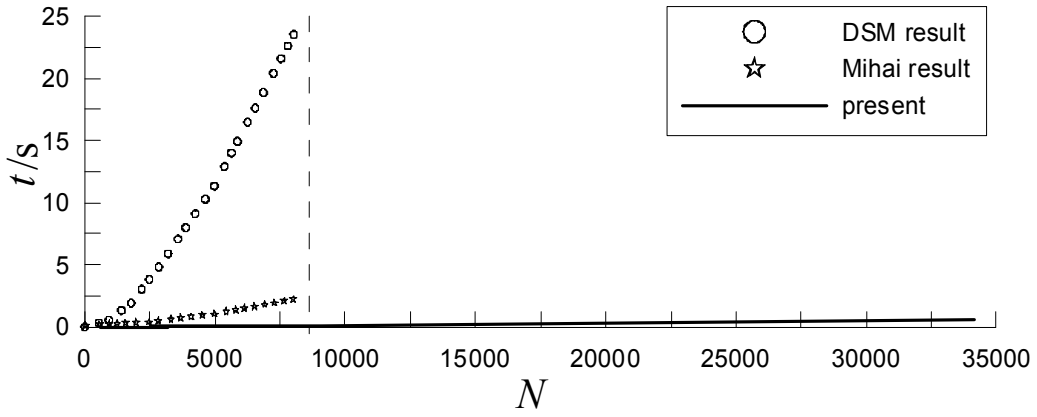

Fig. 2. Comparisons of CPU time required for a single searching by three NNPS methods

2.4 Numerical wave flume

In Lagrangian form, the conservation of mass and the conservation of momentum for a Newtonian incompressible fluid can be expressed as

$$\frac{\mathrm{d}\rho}{\mathrm{d}t} + \rho\nabla\cdot\mathbf{u} = 0 \tag{1.7}$$

$$\frac{\mathrm{d}\mathbf{u}}{\mathrm{d}t} = F - \frac{1}{\rho}\nabla p + \nu\nabla^2\mathbf{u} \tag{1.8}$$

where **u** is the particle velocity tensor, p the fluid pressure, ν the kinematic viscosity, F the body force per unit mass.

The pressure of each particle is obtained from the equation of state. By artificially enhancing the fluid compressibility, the following form is proposed

$$p = \frac{\rho_0 c_0^2}{\gamma}\left[\left(\frac{\rho}{\rho_0}\right)^{\gamma} - 1\right] \tag{1.9}$$

where ρ_0 is a reference density which is usually taken as the density of the fluid at the free surface, c_0 the speed of sound which is set much lower than its correct value to maintain numerical stability, γ the polytropic constant, usually set to be 7 for water.

At the free surface, the Dirichlet condition is applied according to Koshizukar et al.[23]. If the density calculated at particle a satisfies the following criterion

$$\rho_a < \beta\rho_0 \tag{1.10}$$

then the particle is regarded as a free-surface particle (constant β = 0.8 - 0.98) for which a density equal to ρ_0 is imposed. This treatment is based on the fact that the calculated particle density on the free surface drops abruptly for the lack of particles in the outer region of the free surface.

For the fixed solid boundary, a method involving fixed wall particles and mirror particles are used[24], as shown in Figure 3. Additional repulsive forces are imposed to wall particles to balance the pressure of inner fluid particles and prevent them from penetrating the wall. Several lines of mirror particles are placed on the outer side of the wall with their pressure setting equal to that of neighboring wall particles. The symmetrical nature of mirror particles ensures the pressure balance at the fixed boundary and makes the homogeneous Neumann condition applied.

3. Model results

3.1 Dam breaking

The study of the waves caused by the failure of a dam has attracted significant interest. This can be attributed to the significant consequences of dam failure particularly in cases where dams are located upstream of large conurbations, where the population has mostly grown

considerable since the dam's original construction. Along with the significance of the consequences, the challenges of adequately capturing the physics of the problem and the difficulty of solving the associated equations mathematically have attracted the attention of researchers. In the past similar simulations have been executed with the Marker-and-Cell method (MAC)[25] and the mesh-based Volume-of-Fluid method (VOF)[26]. These approaches have shown some benefits, but the resolution of the free surface is neither straightforward nor entirely accurate. Increased accuracy may be obtained using adaptive meshing, but at a significant cost. This style of dam failure has recently attracted the attention of researchers using SPH in particular, which is very suitable to describe this problem with a fast varying water level.

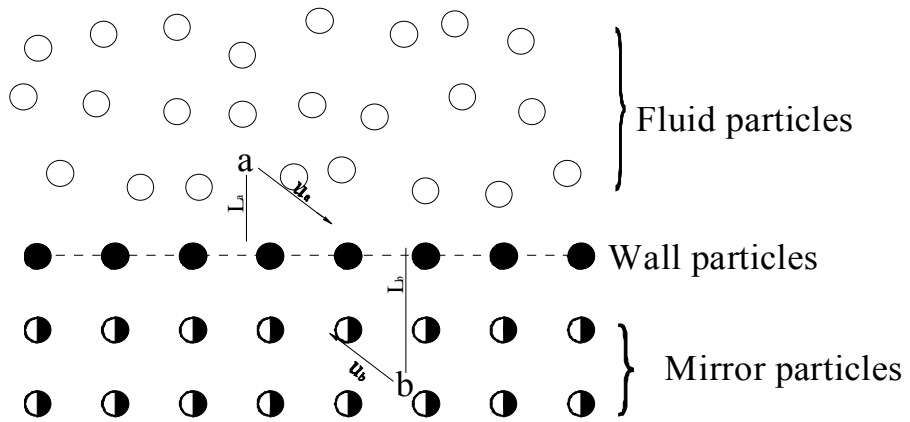

Fig. 3. Particle setting at the fixed solid boundary

A rectangular water column with a width of 0.1 m and a height of 0.2 m is confined between two vertical walls. At the beginning of the simulation, the right wall is instantaneously removed and the water is allowed to collapse due to gravity and flow out along the dry horizontal bed. In computation, a total number of N = 20× 40 of particles are configured, corresponding to an initial particle spacing of 0.005 m. A constant time step of 0.0005s is used. The kinematic viscosity is $\nu = 10^{-6}$ kg·ms^{-1}. A cubic spline kernel is employed and the smoothing length is 1.2 × 2 times of the initial particle spacing.

The particle snapshots of flow at different times t = 0.05s, t = 0.1s, t =0.15s, and t = 0.18s are shown in Figure 4. The fluid is firstly squeezed out at the bottom of the column, and then the top of the column moves down. The simulated free surfaces are consistent to those computed by Shao and Lo[27]. The leading edges of flow strictly follow the wall boundary at all moments, indicating that the pressure of fluid particles in the dry-wet transition region is correctly estimated. Figure 5 shows the position of leading edge $X = x / H$ versus the normalized time $T = t\sqrt{g / H}$ in the present simulation, as well as the results from experiments [27-28], the VOF method[26], and the MAC method[25]. Good agreements are found. The velocity field at t = 0.15s is illustrated in Figure 6. As is shown, the particle velocities in the water jet are relatively large due to strong pressure gradient, while those in the inner flow column remain almost static due to particle-particle interactions and the small pressure gradients there.

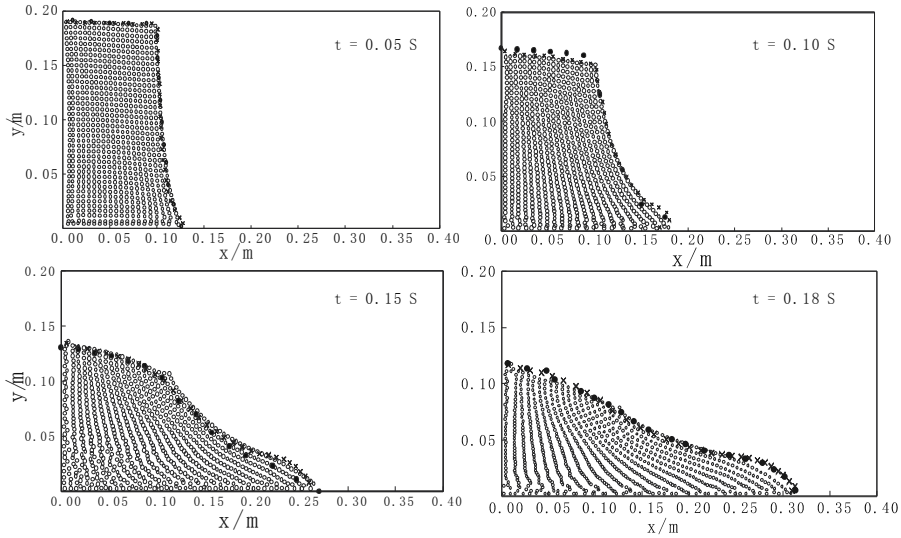

Fig. 4. Particle snapshots after dam breaking at t = 0.05s, t = 0.10s, t = 0.15s and t = 0.18s.

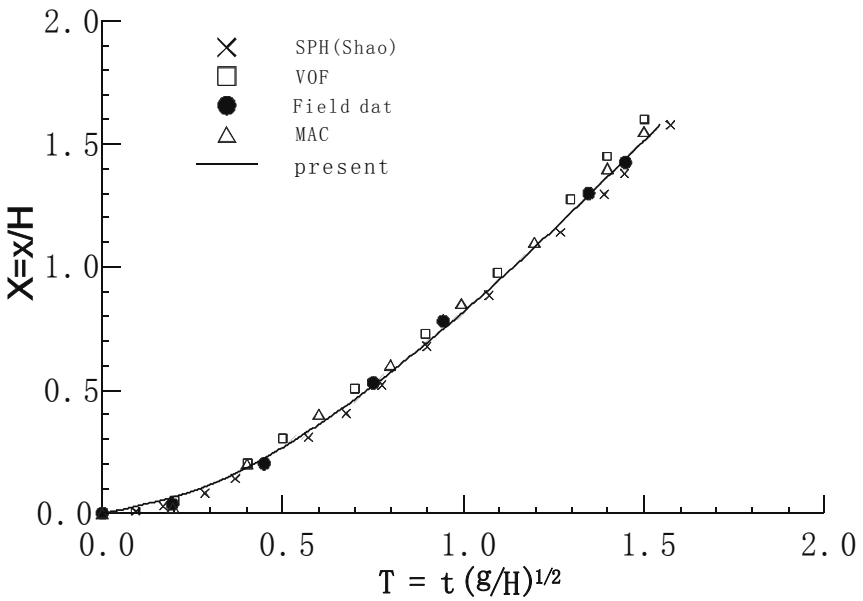

Fig. 5. Relationship between the normalized time T and the leading edge X for dam-breaking flow.

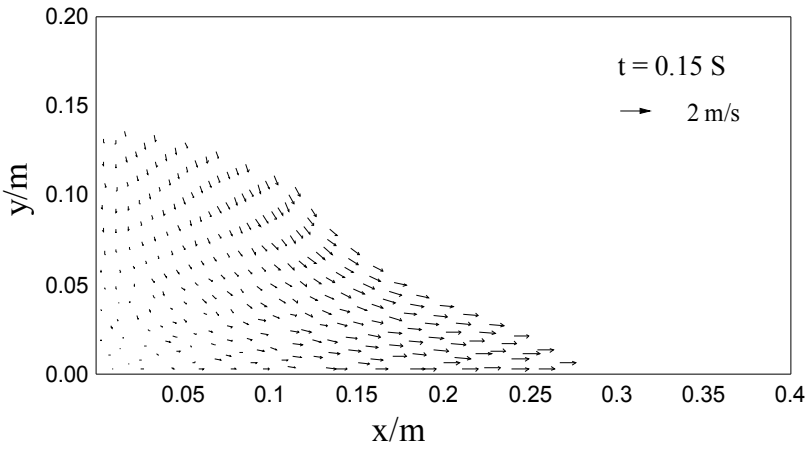

Fig. 6. Velocity field at t = 0.15 s for dam-breaking flow.

3.2 Solitary waves

The transmission of long waves is an important problem in tsunami engineering. Tsunamis can often be simplified as solitary wave or combinations of negative and positive solitary-like waves. In this case, the SPH numerical wave flume is applied to simulate the generation and propagation of a solitary wave with a wave height of 0.018 m over a plane bed. The layout of the flume setup is shown in Figure 7. The flume has a height of 0.2 m and a length of 5 m, which is approximately 4-5 times of the wave length. The initial water depth is 0.1 m. In computation, 80,000 fluid particles are used with an initial spacing of 0.025 m. The smoothing length is 0.006 m. The kinematic viscosity is $\nu = 10^{-6}$ kg·ms^{-1} as the same as in the first case. The propagation of solitary waves during a time scale of 5 s is simulated with a constant time step of 0.0002 s. To reproduce the movement of the experimental wavemaker, the wave-making paddle at the left boundary of tank is represented by a vertical set of particles with prescribed oscillatory frequency and amplitude derived from the first-order solution of the Boussinesq equation[29]

$$\xi = \sqrt{\frac{4Hd}{3}} \tanh\left[\sqrt{\frac{4H}{3d^3}}(ct - \xi)\right] \tag{1.11}$$

where H is the wave height, d the water depth, and c the wave celerity.

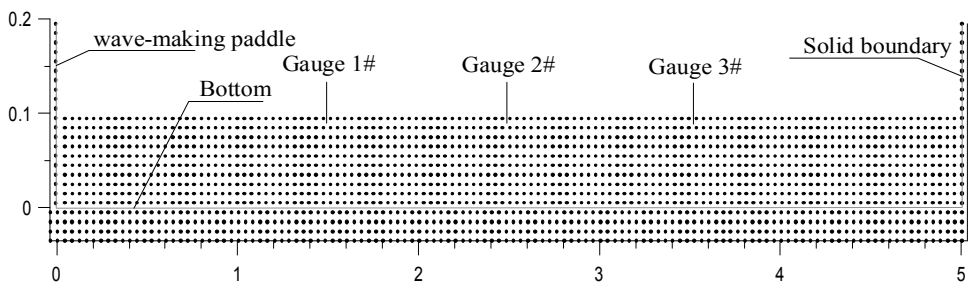

Fig. 7. Layout of numerical wave flume for solitary wave.

The time-evolution of surface elevation at three measuring points x = 1.5m, x = 2.5m and x = 3.5m are collected to verify the numerical results, as shown in Figure 8. The three surface profiles show the good consistency. For each point, the surface elevation remains stationary before wave passing through it and the peak value of surface displays no significant deviation from other two points. That means a stable pressure field is obtained in computation. The observed time lag between two adjacent points is 0.917 s, and the corresponding calculated wave celerity is 1.09 m/s, which agrees well with the analytical value of 1.08 m/s.

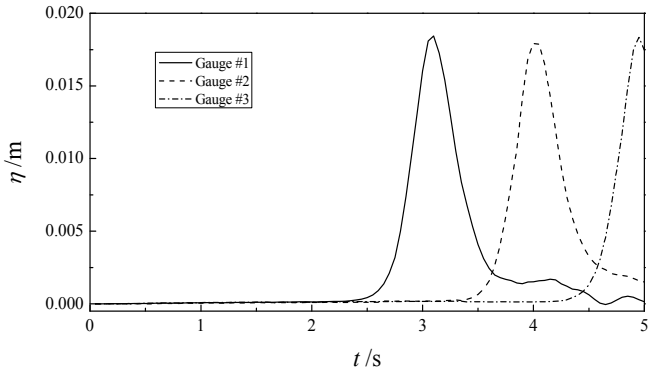

Fig. 8. Time-series of free surface elevation at three measuring points for solitary wave.

Figure 9 presents the simulated free surface at t = 4s, as well as the first-order Boussinesq solution. The overall agreement is satisfactory. The calculated profile is steeper than the theoretical result in front of wave crest while milder behind it, which is due to the kinematic viscosity included in the numerical model but not presented in the analytical solution.

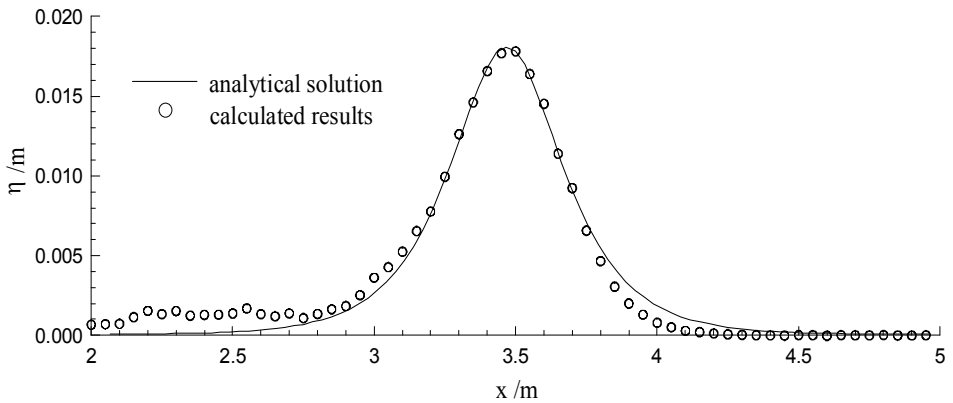

Fig. 9. Free surface variation at t = 4s for solitary wave.

Figure 10 illustrates the velocity field at t = 3s. Realistic result is shown. The horizontal velocity increases with decreasing depth with its peak value locating at the wave crest, where the vertical velocity is negligible. In the water column where wave has passed through, some minor disturbances are found. Nevertheless, generally realistic distributions of both value and direction of velocity are maintained for the whole domain, justifying the ability of the numerical wave flume developed in the present study.

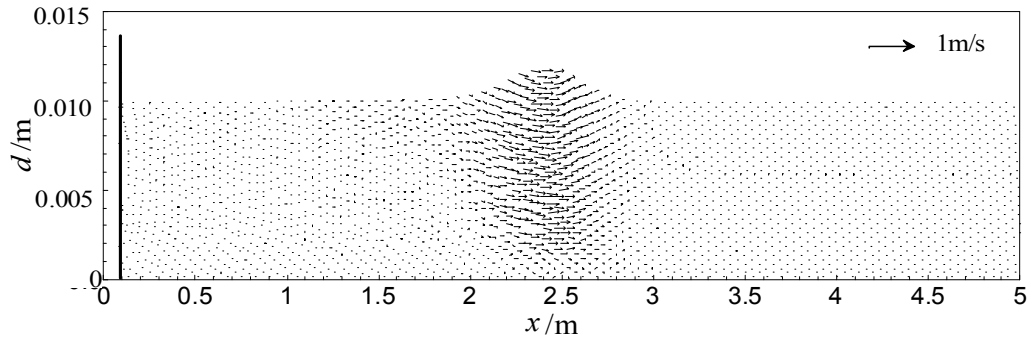

Fig. 10. Velocity field at t = 3 s for solitary wave.

3.3 Regular and irregular waves

The numerical flume has a length of 5 m and a height of 1 m, as well as an initial water depth of 0.65 m, as shown in Figure 11. A 0.9 m high wavemaker is placed at the left boundary of flume to generate irregular waves, and an artificially absorbing sponge layer is configured in the right flume section from 13 m to 16 m. The particle setting in the SPH method is the same as in the case of solitary wave. The time-series of surface elevation are recorded at seven points located at 7.5 m, 8 m, 8.5 m, 9 m, 9.5 m, 10.0 m and 10.5 m along the horizontal axis.

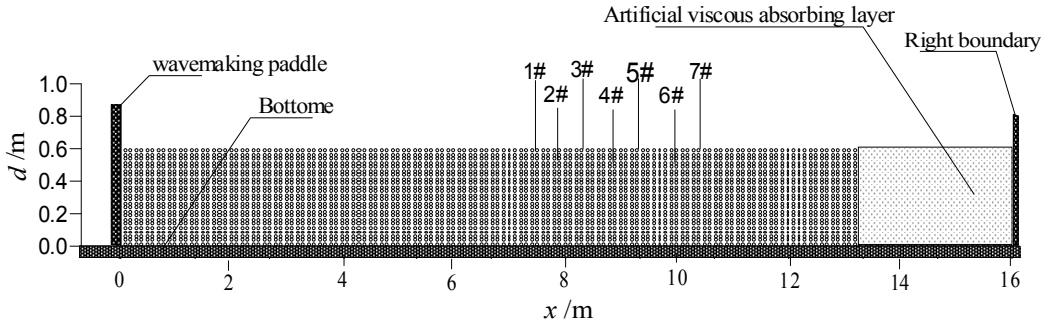

Fig. 11. Layout of numerical wave flume for irregular waves.

3.3.1 Regular waves

For small amplitude waves, it satisfied linearized forms of the kinematic and dynamic free surface boundary conditions, and the shape can be simplified as the sinusoidal form. When wave amplitude increases beyond certain range, the linear wave theory may become inadequate, and the nonlinearity should be considered. Usually, the second-order Stokes wave theory is used to described large amplitude waves, and the wave profile is

$$\eta = \frac{H}{2}\cos(kx-\sigma t) + \frac{H^2 k}{16}\frac{\cosh kh}{\sinh^3 kh}(2+\cosh 2kh)\cos 2(kx-\sigma t) \tag{1.12}$$

where H is height, k is the wave number and σ is the wave angular frequency.

The wave-making paddle at the left boundary oscillates following the method derived by Flick and Guza[30]. Ten successive regular waves with period T = 1s and wave height H = 0.1 m are generated. Figure 12 shows the elevation of the surface at gauges #1, #2, #3 and #4, the line is the second-order Stokes theoretic elevation and the crosses are the results from SPH. Before the first wave reaches the first measurement point, the free surface is not disturbed and keeps stationary, and the wave profile at #1 gets a steady state after 5s. The profile is much more peaked at the crests and flatter at the troughs than the sinusoidal form. Due to the artificial viscosity, the amplitude is decreasing slightly over space. The simulated time lag between #1 and #4 is 0.96s, and the corresponding calculated celerity is 1.60m/s, which is very close to the analytical value 1.54m/s.

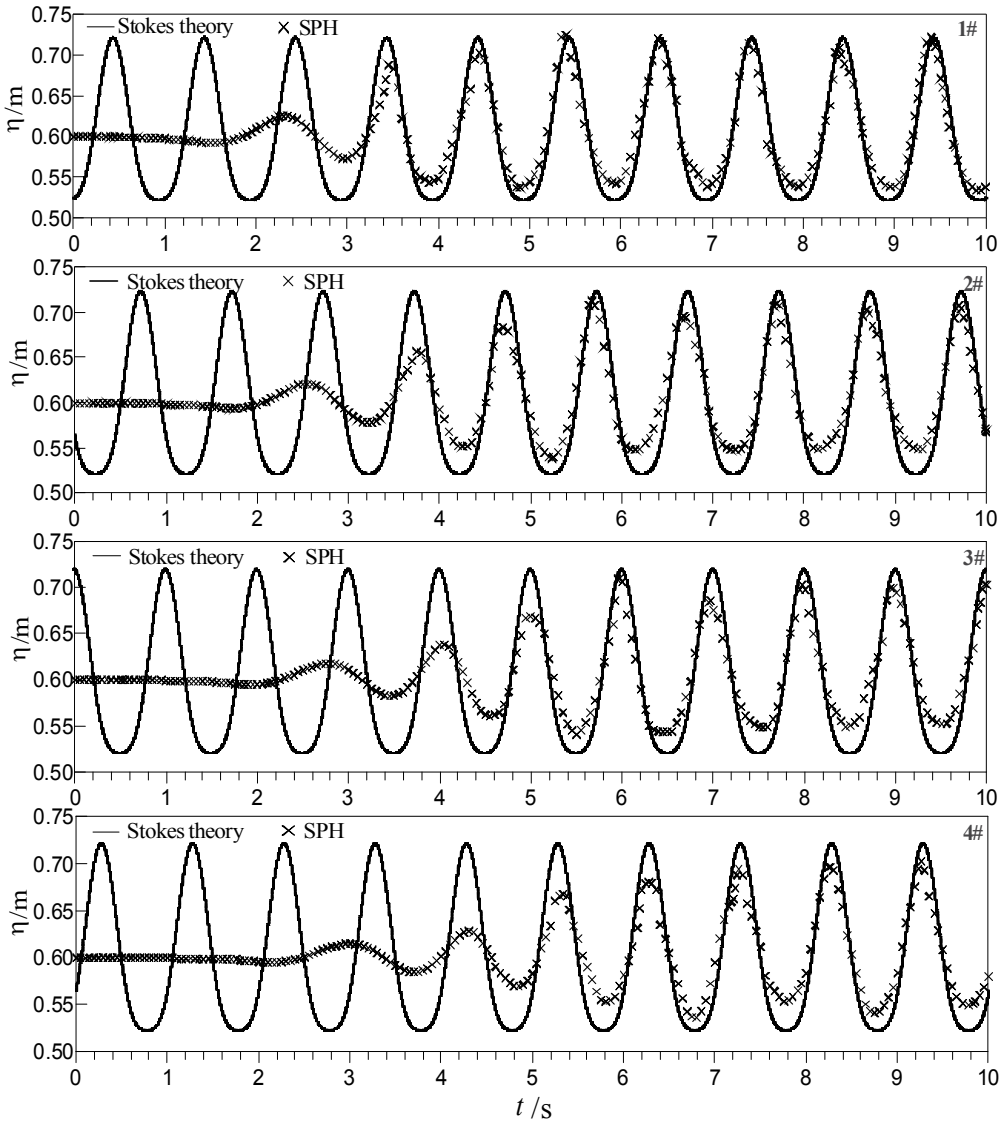

Fig. 12. Comparison of time-series of surface elevation for regular wave generation.

3.3.2 Irregular waves

The wavemaker signal for irregular waves in the experiment of Cox and Ortega[31] is employed in this test. As is shown in Figure 12, it is composed of 4 wave cycles with different frequencies and amplitudes, which gives rise to sharp discontinuities in the transitions between different cycles. These discontinuities will lead to unexpected numerical instabilities. In this study, we follow the approach of Gomez-Gesteira et al.[7], who used a filter function to smooth the signal in the transitions. If the wave-making paddle moves with amplitude A_i and frequency f_i in the interval $t \in [t_i, t_{i+1}]$ with amplitude A_{i+1} and frequency f_{i+1} in the interval $t \in [t_{i+1}, t_{i+2}]$, for any time $t \in [(t_i + t_{i+1})/2, (t_{i+1} + t_{i+2})/2]$, the movement of wavemaker can be described by

$$x(t) = smf_1(t) A_i \sin[f_i(t - t_i)] + smf_2(t) A_{i+1} \sin[f_{i+1}(t - t_{i+1})] \tag{1.13}$$

$$u(t) = smf_1(t) A_i f_i \cos[f_i(t - t_i)] + smf_2(t) A_{i+1} f_{i+1} \cos[f_{i+1}(t - t_{i+1})] \tag{1.14}$$

where smf_1 and smf_2 are smoothing functions expressed as

$$smf_1(t) = 0.5\{-\tanh[(t - t_{i+1}) \cdot \max(f_i + f_{i+1})] + 1\} \tag{1.15}$$

$$smf_2(t) = 0.5\{\tanh[(t - t_{i+1}) \cdot \max(f_i + f_{i+1})] + 1\} \tag{1.16}$$

The smoothed time-series of wavemaker position and velocity are displayed in Figure 13. With this method, a continuous signal is obtained for the numerical experiment.

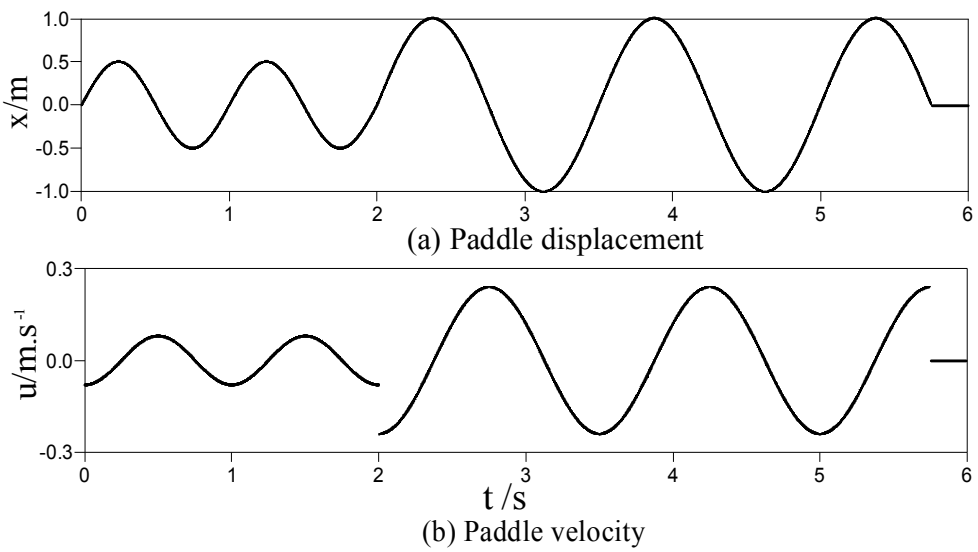

Fig. 13. Original wavemaker signal from Cox and Ortega[31].

Figure 14 presents the comparisons of free surface variations at gauges #1, #2, #3, #4, #5 and #6 between experimental data of Cox and Ortega[31] for the case without a deck, the SPH simulation results from present study and Gomez-Gesteira et al. model[7] (hereafter GGM). The simulated profiles are in generally good agreements with the GGM results and the measurements, both in amplitude and phase, although there are some slight discrepancies between numerical and experimental results for secondary peaks. These discrepancies are probably due to the smoothing effects of wavemaker signal. Particularly for the phase of the first wave and the height of the highest wave, the present model provides fitter results to the observation than GGM's.

Figure 15 shows the particle snapshots in the righter region of flume at t = 11s, t = 13s and t = 15s . The primary aim of this figure is to examine the efficiency of the sponge layer in the model. Waves enter the sponge layer (x =13m ~16m) at t = 13s and begin to dissipate energy in this region. At t = 15s, the surface variation is undistinguishable, indicating that most of wave energy has been effectively absorbed due to the viscous effect in the sponge layer.

It can be reasonably concluded that the SPH numerical wave flume developed in this paper is capable of generating reliable irregular wave trains and reproducing their propagations with good stability and boundary descriptions. Numerical results show the improvements over that of GGM to a reasonable extent. Moreover, only 25 min is needed to complete the computation for this case. This does benefit from the more efficient inner and outer particle searching technique proposed by Zheng et al.[3].

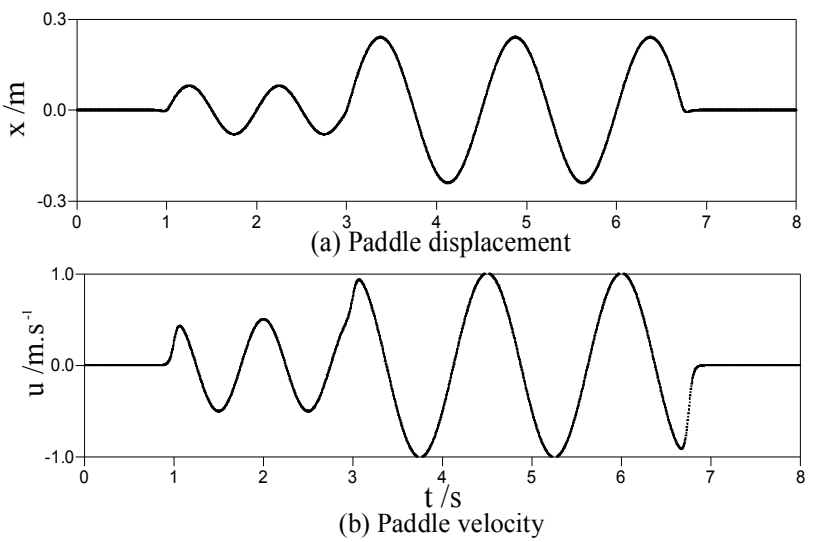

Fig. 14. Wavemaker signal smoothed by the method of Gomez-Gesteira et al.[7].

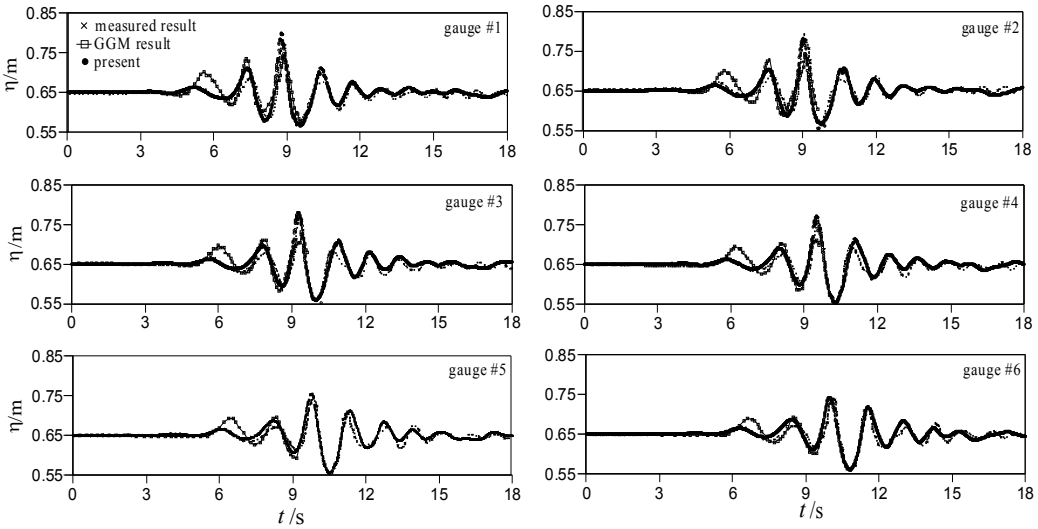

Fig. 15. Comparisons of time-series of surface elevation for irregular wave generation.

4. Application

Since the SPH model has demonstrated an ability to provide numerical solutions to problems such as dam breaking and the generations of solitary waves and irregular waves, this section applies the numerical method for a wide range of solitary wave propagation problems such as the impact of waves on structures, wave run-up and rundown and breaking on a planar slope.

4.1 The run up of a solitary wave on a vertical wall

In many cases, the wave forces on the structure are always related to the structure stability analysis, which in earlier days was mainly made with the use of empirical formulas established on limited number of experimental tests. With the use of SPH method, it is possible to calculate the wave forces on the structure directly. The layout of the flume setup is similar to Figure 7; the length is reduced to 2m to save the calculation time, and the height is increased to 0.3m to prevent the wave running over the wall. Chan and Street [32] have investigated the run-up of solitary waves over the vertical wall by the MAC method and experiments. In order to compare with their results, simulations are carried out with the initial water depth d = 0.2m.

The wave run-up induced by solitary waves with different heights is shown in Figure 16. Clearly, the SPH method yields results that are in excellent agreement with experiments and the MAC method. The run up of a solitary wave on a vertical wall is almost as large as three times of the incident wave height, which is larger than the height of standing waves. Successive stages of wave propagation are shown in Figure 17 and the contour lines of the pressure are shown in Figure 18 for the case H/d = 0.19. Solitary waves propagate keeping a permanent waveform without any breaking. The total pressure is similar to the hydrostatic pressure when solitary waves run up and down.

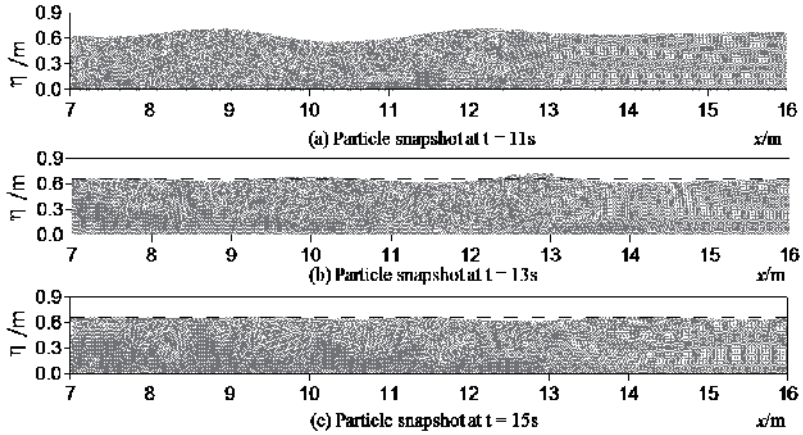

Fig. 16. Particle snapshots for irregular waves.

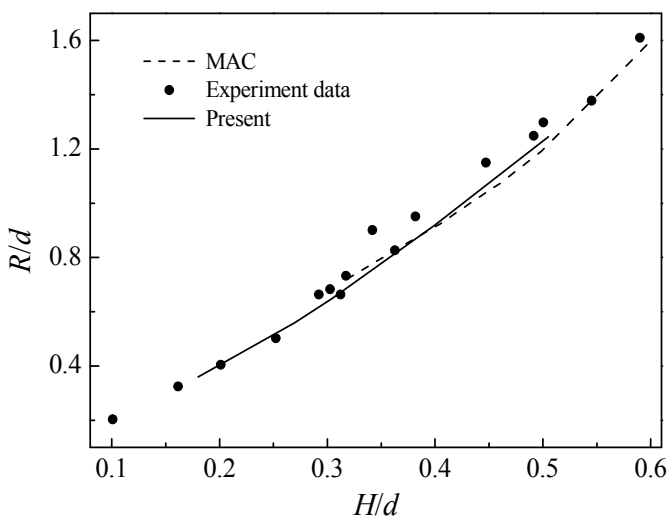

Fig. 17. Wave run up on a vertical wall.

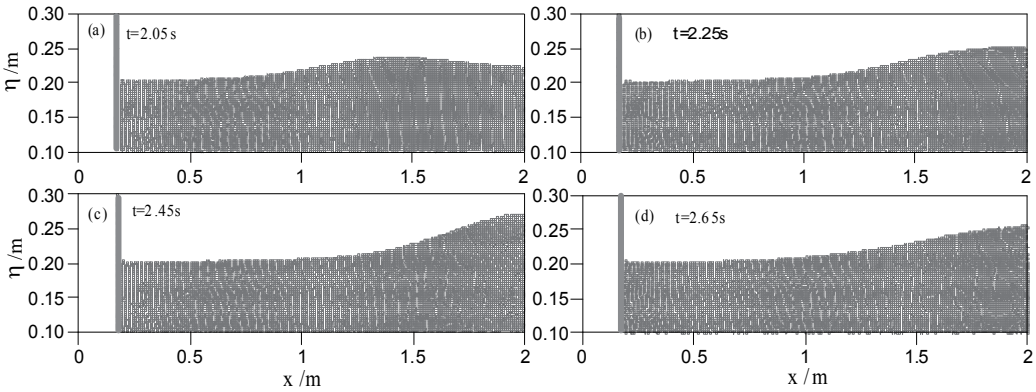

Fig. 18. Particle snapshots for the impact of solitary waves on a vertical wall.

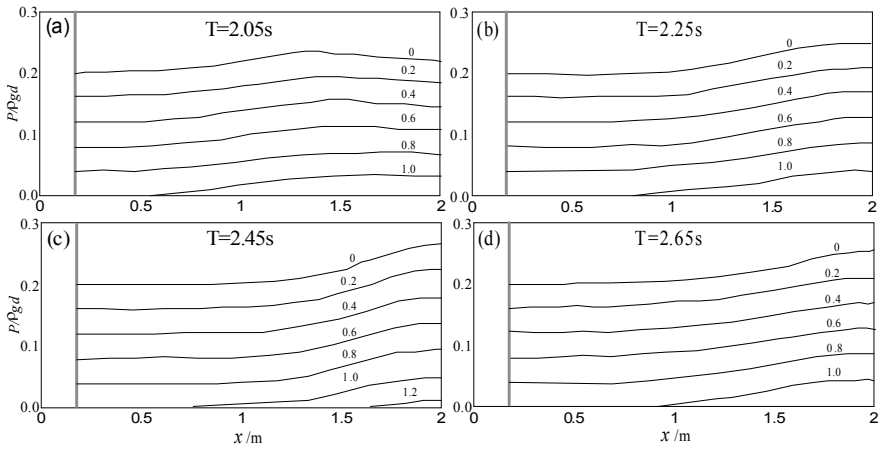

Fig. 19. Pressure distribution.

4.2 Run-up of solitary waves on sloping beaches

The evolution of long waves on a beach is a classic problem in hydrodynamics, and there have been numerous attempts at modeling wave amplification and run-up on sloping beaches. The numerical flume has a length of 8.5m and a height of 0.4m with the initial water depth d = 0.21m, and a beach inclined an angle 2.88^o to the horizontal direction (the slope $s \approx 1/20$) is placed 2m away from the wave-making paddle. A solitary wave with the height of 0.0588m is generated by the paddle following the equation(1.11). Our computational domain represents a 1:10 prototype of Synolakis'[33] experimental setup. In computation, 37,877 fluid particles are used with an initial spacing 0.005m with the smoothing length 0.006m and the kinematic viscosity $\nu = 10^{-6}$m/s^2. A total simulation time of 8s has been considered with an approximate time step of 0.0001s.

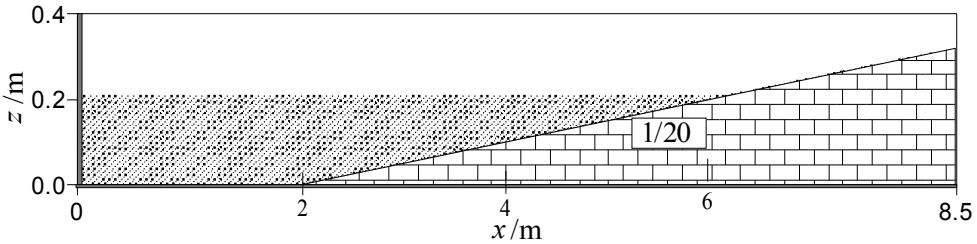

Fig. 20. Layout of numerical flume for run-up of solitary waves on sloping beaches.

The profiles normalized by water depth d versus the normalized time $\tau = t\sqrt{g/d}$ are present in Figure 20. As the wave paddle in the simulation is moved forward to the beach, our results need to be shifted $\Delta\tau$ = 8.958276 to compare with the experiment data. The wave has evolved asymmetric at τ = 15, the front becomes very steep and the height increases to 0.14m much larger than the incident height; The profile becomes vertical and the wave begins to break at τ = 20; the wave has topped over the water below and breaking quickly at τ = 30, then forces the volume to climb up to the beach; the wave runs up to the maximum at τ = 45. Overall, the numerical results and the laboratory data equally well before and after breaking.

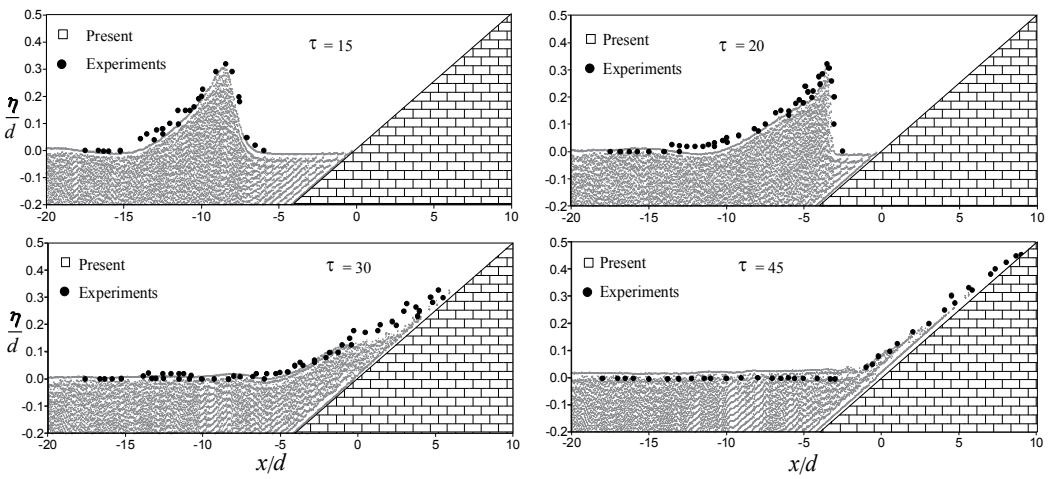

Fig. 21. The clime of a solitary wave with H/d = 0.28 up a 1:20 beach.

5. Conclusions and recommendations

In this paper the application of the SPH method for numerical wave flumes is presented. SPH is a mesh-less method in which particles are used to simulate the fluid. The method has the advantage of solving the governing equations by a Lagrangian approach. By employing an IOPS technique in the SPH simulation, the computation time has been reduced effectively, which improves the method to apply to larger study areas. Several cases are used to investigate its performance, including dam breaking, generation and propagation of solitary wave and irregular wave. Numerical results are in good agreements with theoretical solutions, experimental data and results provided in previous studies. It is concluded that the SPH numerical wave flume with the IOPS method can reproduce the generation and

propagation of realistic waves in a physical tank, which could act as the foundation for further studies involving more complicated flows.

SPH has the potential to replace traditional grid based numerical methods in many applications but more research is needed in order to raise its accuracy and adaptability. Although the IOPS technique has improved the SPH's efficiency, the calculation time is still large especially for a large number of particles. It may be reduced with a more sophisticated interaction find algorithm. Parallelization of the code can also decrease the calculation times significantly. Furthermore, the artificial viscosity keeps the simulation stable, but frequently too dissipative than reality. The improvement of the viscosity model needs further study.

6. References

[1] Gingold, R.A. and Monaghan, J.J., 1977. Smoothed particle hydrodynamics - Theory and application to non-spherical stars. Monthly Notices of the Royal Astronomical Society, 181: 375-389.

[2] Lucy, L.B., 1977. A numerical approach to the testing of the fission hypothesis. Astronomical Journal, 82: 1013-1024.

[3] Zheng, K. et al., 2009. Numerical simulations of water wave dynamics based on SPH methods. Journal of Hydrodynamics, Ser. B, 21(6): 843-850.

[4] Chu, Y. and Lu, W.-q., 2009. Porescale SPH simulation of flow in porous media. Journal of Engineering Thermophysics, 30(3): 437-440.

[5] Ataie-Ashtiani, B. and Shobeyri, G., 2008. Numerical simulation of landslide impulsive waves by incompressible smoothed particle hydrodynamics. International Journal for Numerical Methods in Fluids, 56(2): 209-232.

[6] Xu, Q.-x. and Shen, R.-y., 2008. Fluid-Structure Interaction of Hydrodynamic Damper During the Rush into the Water Channel. Journal of Hydrodynamics, Ser. B, 20(5): 583-590.

[7] Gómez-Gesteira, M., Cerqueiro, D., Crespo, C. and Dalrymple, R.A., 2005. Green water overtopping analyzed with a SPH model. Ocean Engineering, 32(2): 223-238.

[8] Shao, S. et al., 2006. Simulation of wave overtopping by an incompressible SPH model. Coastal Engineering, 53(9): 723-735.

[9] Dalrymple, R.A. and Rogers, B.D., 2006. Numerical modeling of water waves with the SPH method. Coastal Engineering, 53(2-3): 141-147.

[10] Khayyer, A., Gotoh, H. and Shao, S.D., 2008. Corrected Incompressible SPH method for accurate water-surface tracking in breaking waves. Coastal Engineering, 55(3): 236-250.

[11] Gong, K., Liu, H. and Wang, B.-l., 2009. Water entry of a wedge based on SPH model with an improved boundary treatment. Journal of Hydrodynamics, Ser. B, 21(6): 750-757.

[12] SHAO, S., 2005. SPH simulation of solitary wave interaction with a curtain-type breakwater. Journal of Hydraulic Research, 43(4): 366-375.

[13] Gómez-Gesteira, M. and Robert A. Dalrymple, 2004. Using a Three-Dimensional Smoothed Particle Hydrodynamics Method for Wave Impact on a Tall Structure. Journal of Waterway, Port, Coastal, and Ocean Engineering, 130(2): 63-69.

[14] Lv, B., Jin, S. and Ai, C.-f., 2010. A conservative unstructured staggered grid scheme for incompressible Navier-Stokes equations. Journal of Hydrodynamics, Ser. B, 22(2): 173-184.
[15] Christensen, E.D. and Deigaard, R., 2001. Large eddy simulation of breaking waves. Coastal Engineering, 42(1): 53-86.
[16] Zou, L., Lin, Y.-f. and Lam, K., 2008. Large-eddy simulation of flow around cylinder arrays at a subcritical reynolds number. Journal of Hydrodynamics, Ser. B, 20(4): 403-413.
[17] Da-peng, S. and Yu-cheng, L., 2000. Wave damping absorber in numerical wave tank and calculation of wave transformation. China Ocean Engineering, 18(2): 46-50.
[18] Monaghan, J.J., 1985. Particle methods for hydrodynamics. Computer Physics reports, 3(2): 71-124.
[19] Hernquist, L. and Katz, N., 1989. TREESPH - A unification of SPH with the hierarchical tree method. Astrophysical Journal Supplement Series 70: 419-446.
[20] Mihai, B., Marty, L. and Nathan, Q., 2004. Grid-assisted particle search in smoothed particle hydrodynamics, Galway faculty of Engineering Research Day.
[21] Zheng, J.-h., Soe, M.M., Zhang, C. and Hsu, T.-W., 2010. Numerical wave flume with improved smoothed particle hydrodynamics. Journal of Hydrodynamics, Ser. B, 22(6): 773-781.
[22] Liu, G.R. and Liu, M.B., 2003. Smoothed particle hydrodynamics: a meshfree particle method. World Scientific, Singapore, 472 pp.
[23] Koshizuka, S., Nobe, A. and Oka, Y., 1998. Numerical analysis of breaking waves using the moving particle semi-implicit method. International Journal for Numerical Methods in Fluids, 26(7): 751-769.
[24] Violeau, D. and Issa, R., 2007. Numerical modelling of complex turbulent free-surface flows with the SPH method: an overview. International Journal for Numerical Methods in Fluids, 53(2): 277-304.
[25] Harlow, F.H. and Welch, J.E., 1965. Numerical Calculation of Time−Dependent Viscous Incompressible Flow of Fluid with Free Surface Physics of Fluids, 8(12): 2182-2189.
[26] Hirt, C.W. and Nichols, B.D., 1981. Volume of fluid (VOF) method for the dynamics of free boundaries. Journal of Computational Physics, 39(1): 201-225.
[27] Shao, S. and Lo, E.Y.M., 2003. Incompressible SPH method for simulating Newtonian and non-Newtonian flows with a free surface. Advances in Water Resources, 26(7): 787-800.
[28] Martin, J.C. and Moyce, W.J., 1952. Some gravity wave problems in the motion of perfect liquids. Part IV. An Experimental Study of the Collapse of Liquid Columns on a Rigid Horizontal Plane. Philosophical Transactions of the Royal Society of London. Series A, Mathematical and Physical Sciences, 244(882): 312-324.
[29] Synolakis, C.E., 1990. Generation of long waves in laboratory. Journal of Waterway, Port, Coastal and Ocean Engineering, 116(Compendex): 252-266.
[30] Flick, R.E. and Guza, R.T., 1980. Paddle generated waves in laboratory channels. Journal of the Waterway, Port, Coastal and Ocean Division, Proceedings of the American Society of Civil Engineers, 106(Compendex): 79-97.
[31] Cox, D.T. and Ortega, J.A., 2002. Laboratory observations of green water overtopping a fixed deck. Ocean Engineering, 29(14): 1827-1840.

[32] Chan, R.K.C. and Street, R.L., 1970. A computer study of finite-amplitude water waves. Journal of Computational Physics, 6(1): 68-94.
[33] Synolakis, C.E., 1987. The runup of solitary waves. Journal of Fluid Mechanics, 185: 523-545.

11

Lattice Boltzmann Simulation for Shallow Water Flow Applications

Mapundi K. Banda[1] and Mohammed Seaid[2]
[1]*School of Computational and Applied Mathematics, University of the Witwatersrand*
[2]*School of Engineering and Computing Sciences, University of Durham*
[1]*South Africa*
[2]*United Kingdom*

1. Introduction

Under the influence of gravity, many free-surface flows can be modelled by the well-known shallow water equations under the assumption that the vertical scale is much smaller than any typical horizontal scale and the pressure is hydrostatic. These equations can be derived from the depth-averaged incompressible Navier-Stokes equations and usually include continuity and momentum equations. Hence, the applications of depth-averaged models include a wide spectrum of phenomena in hydraulic flows such as ocean circulation modelling Salmon (1999a) and wind-driven ocean circulation Zhong et al. (2005) to name but a few. Simulation of such real-world flow problems is not trivial since the geometry can be complex and the topography irregular. Numerical methods based on the finite difference, the finite volume or the finite element methods have been applied to simulate the shallow water equations, refer to Bermúdez & Vázquez (1994); Kurganov & Levy (2002); LeVeque (1998); Stansby & Zhou (1998); Toro (1992); Vázquez-Cendón (1999); Vukovic & Sopta (2002); Xing & Shu (2006); Zhou (1995) among others. For most of these approaches, the treatment of bed slopes and friction forces often cause numerical difficulties in obtaining accurate solutions, see, for example, Bermúdez & Vázquez (1994); LeVeque (1998); Vázquez-Cendón (1999). In addition the extension of these schemes to complex geometries is not trivial, refer to Benkhaldoun et al. (2007), for example. Some of these approaches are very expensive if one considers real flows Vukovic & Sopta (2002). Since the problems are posed at a large scale it has been the aim of practitioners to develop a simple and accurate representation of the source terms in order to simulate practical shallow water flows without relying on upwind discretization or Riemann problem solvers, refer to Benkhaldoun et al. (2009; 2010); Benkhaldoun & Seaïd (2010) and references therein for these alternatives. The idea of this chapter will be to give the reader a self-contained introduction of the developments and the implementation of the shallow water lattice Boltzmann approach. In this chapter the lattice Boltzmann method will be applied to the simulation of depth-averaged models in flow hydraulics and dispersion Banda et al. (2009); Klar et al. (2008); Seaïd & Thömmes (2009); Thömmes et al. (2007). It can be pointed out that the shallow water equations referred to in this discussion are viscous and also account for the effects of bed slope, bed friction, Coriolis forces and wind stresses in two-dimensional simulations Dellar (2002); Salmon (1999a); Zhou (2002). The practical aspects

of the method will be emphasized. In addition the methods for coupling the shallow water flow to other mass balance equations like pollutant transport and temperature dispersion will also be discussed. Considerations will also be made for new developments in the fields and further possible extensions.

The lattice Boltzmann (LB) method, also popularly referred to as LBM, is an alternative numerical tool for simulating fluid flows Chen & Doolen (1998). The method is based on statistical physics and models the fluid flow by tracking the evolution of the distribution functions of the fluid particles in discrete phase space. The essential approach in the LB method lies in the recovery of macroscopic fluid flows from the microscopic flow behaviour of the particle movement or the mesoscopic evolution of particle distributions. The basic idea is to replace the nonlinear differential equations of macroscopic fluid dynamics by a simplified description modeled on the kinetic theory of gases. Furthermore, the LBM offers several desirable properties such as linear convection terms and nearest-neighbor stencils. On a structured mesh, the LBM can be implemented in a two-stage procedure namely, a collision operator evaluation which involves only local operations, and an advection operation where values are transported to adjacent lattice points without performing any computations. In this chapter, the dynamics of the two different but dependent models namely, (i) a depth-averaged hydrodynamic model defining the flow, and (ii) a depth-averaged advection-diffusion model defining the transport of the pollutant/temperature are solved by an LBM with two distribution functions modelling the dynamics of the hydrodynamic flow and the pollutant concentration or temperature, respectively, will be discussed. To obtain the hydrodynamic behaviour, the Chapman-Enskog expansion which exploits a small mean free path approximation to describe slowly varying solutions of the underlying kinetic equations, is undertaken Zhou (2004). The method has been proven to be effective for simulating flows in complicated geometries and implementation on parallel computer architectures Kandhai et al. (1998). Furthermore, the method has become an alternative to other numerical methods like finite difference, finite element and finite volume methods in computational fluid dynamics.

As such the LB method has found a wide range of applications in a variety of fields, which include numerical simulation of shallow water equations. The LB method has been successfully adopted to simulate shallow water equations which describe wind-driven ocean circulation Salmon (1999a); Zhong et al. (2005), to model three-dimensional planetary geostrophic equations Salmon (1999b), and to study atmospheric circulation of the northern hemisphere with ideal boundary conditions Feng et al. (2002). In Klar et al. (2008); Thömmes et al. (2007), a practical study of the LBM for shallow water flows and pollutant dispersion by tidal flow problems in complex geometry and irregular bathymetry was presented. The bathymetry is given either by an analytical function or by data points in a two-dimensional domain. In the dispersion of pollutants Banda et al. (2009) the flow characteristics and concentration profiles of dispersive species will be discussed in detail. It can be noted that all above LB methods have been mainly applied to the isothermal shallow water flows and no thermal sources have been accounted for. In Seaïd & Thömmes (2009), a presentation of shallow water equations involving thermal sources has been made.

In the next section a brief discussion of the shallow water equations will be presented. This will be followed by Section 3 in which the practical details of implementing the LBM will be presented. Section 4 will present numerical results. The chapter concludes with Section 5.

2. Shallow water equations in hydraulics with coupling to dispersion

In this section a brief discussion of the derivation of the shallow water equations will be presented. This will be extended to the modelling of pollutant and temperature dispersion. In general, modelling of fluid flow with dispersion on a free-surface requires two sets of coupled partial differential equations. The first set of equations describes the water motion on the free-surface flow while, the second set of equations models the distribution of a pollutant or temperature on the water free-surface.

The flow is governed by the depth-averaged Navier-Stokes equations involving several assumptions including (i) the domain is shallow enough to ignore the vertical effects, (ii) the pressure is hydrostatic, (iii) all the water properties are assumed to be constant with the exception that in temperature dispersion the density is temperature dependent, which is accounted for using the Boussinesq approximation, and (iv) viscous dissipation of energy is ignored and any radiative heat losses are assumed to have occurred over a time scale small compared with that which characterizes the flow motion.

2.1 Equations of depth-averaged models in hydraulics

The starting point for the discussion of depth-averaged models in hydraulic flows is the three-dimensional incompressible Navier-Stokes equations,

$$\frac{\partial u}{\partial x}+\frac{\partial v}{\partial y}+\frac{\partial w}{\partial z}=0, \tag{1a}$$

$$\frac{\partial u}{\partial t}+u\frac{\partial u}{\partial x}+v\frac{\partial u}{\partial y}+w\frac{\partial u}{\partial z}+\frac{1}{\rho}\frac{\partial p}{\partial x}=\nu_H\Delta u+\frac{\partial}{\partial z}\left(\nu_V\frac{\partial u}{\partial z}\right)-\Omega v, \tag{1b}$$

$$\frac{\partial v}{\partial t}+u\frac{\partial v}{\partial x}+v\frac{\partial v}{\partial y}+w\frac{\partial v}{\partial z}+\frac{1}{\rho}\frac{\partial p}{\partial y}=\nu_H\Delta v+\frac{\partial}{\partial z}\left(\nu_V\frac{\partial v}{\partial z}\right)+\Omega u, \tag{1c}$$

$$\frac{\partial w}{\partial t}+u\frac{\partial w}{\partial x}+v\frac{\partial w}{\partial y}+w\frac{\partial w}{\partial z}+\frac{1}{\rho}\frac{\partial p}{\partial z}=\nu_H\Delta w+\frac{\partial}{\partial z}\left(\nu_V\frac{\partial w}{\partial z}\right)-g, \tag{1d}$$

where t is the time variable, $(x,y,z)^T$ are the space coordinates, ρ the density, $(u,v,w)^T$ the velocity field, p the pressure, Ω the Coriolis parameter defined by $\Omega = 2\omega\sin\phi$, with ω denoting the angular velocity of the earth and ϕ is the geographic latitude, g is the gravitational force, ν_H and ν_V are the coefficients of horizontal and vertical viscosity, respectively. In (1), $\Delta = \frac{\partial^2}{\partial x^2}+\frac{\partial^2}{\partial y^2}$ denotes the two-dimensional Laplace operator. In most shallow water models, the ratio of vertical length scale to horizontal length scale is very small. As a consequence, the horizontal viscosity terms are typically orders of magnitude smaller than the vertical viscosity terms and their effect is normally small and obscured by numerical diffusion. Therefore, most models either neglect these terms or simply use a constant horizontal viscosity coefficient. In addition, assuming that the pressure is hydrostatic, the momentum equation in the vertical direction (1d) degenerates into the following form

$$\frac{1}{\rho}\frac{\partial p}{\partial z}=-g. \tag{2}$$

Integrating vertically the continuity equation (1a) from the bottom topography $z = Z$ to the free surface $z = h + Z$, and using the kinematic condition at the free surface leads to the free

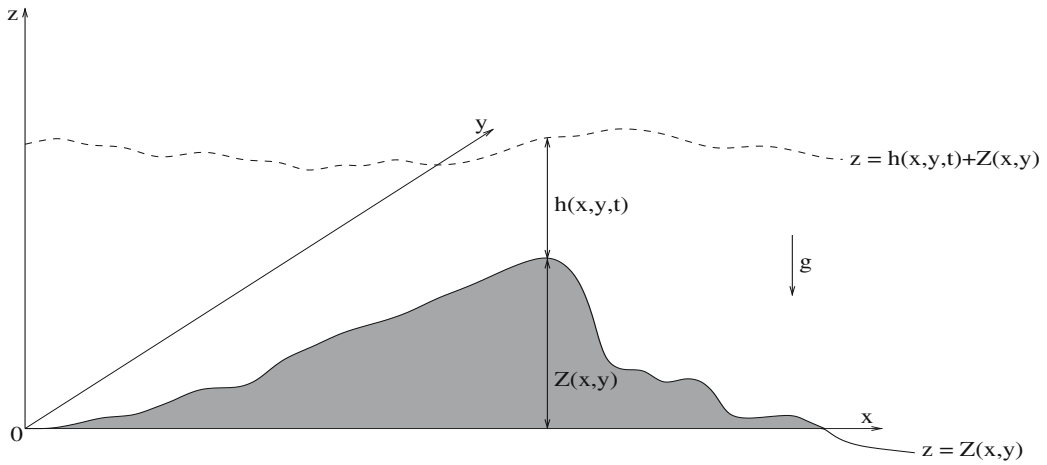

Fig. 1. Vertical section of the hydraulic domain and notations.

surface equation

$$\frac{\partial}{\partial t}(h+Z)+\frac{\partial}{\partial x}\left(\int_Z^{h+Z} u\,dz\right)+\frac{\partial}{\partial y}\left(\int_Z^{h+Z} v\,dz\right)=0, \tag{3}$$

where $h(x,y,t)+Z(x,y)$ is the water surface elevation and $Z(x,y)$ is the bed or bottom as depicted in Figure 1. The boundary conditions at the water free surface are specified by the prescribed wind stresses $\mathcal{T}_x^W$ and $\mathcal{T}_y^W$

$$\nu_V\frac{\partial u}{\partial z}=\mathcal{T}_x^W, \qquad \nu_V\frac{\partial v}{\partial z}=\mathcal{T}_y^W. \tag{4}$$

The wind stresses $\mathcal{T}_x^W$ and $\mathcal{T}_y^W$ are given by a quadratic function of the wind velocity $(W_x,W_y)^T$ as

$$\mathcal{T}_x^W=C_W W_x\sqrt{W_x^2+W_y^2}, \qquad \mathcal{T}_y^W=C_W W_y\sqrt{W_x^2+W_y^2}, \tag{5}$$

where C_W is the coefficient of wind friction defined by Bermúdez & Vázquez (1994) as

$$C_W=\rho_a\left(0.75+0.067\sqrt{W_x^2+W_y^2}\right)\times 10^{-3},$$

for example. Here, ρ_a denotes the density of ambient air. The boundary conditions at the bottom are given by expressing the bottom stress in terms of the velocity components taken from values of the layer adjacent to the sediment-water interface. The bottom stress can be related to the turbulent law of the wall, a drag coefficient associated with quadratic velocity or using a Manning-Chezy formula such as

$$-\nu_V\frac{\partial u}{\partial z}=\mathcal{T}_x^b, \qquad -\nu_V\frac{\partial v}{\partial z}=\mathcal{T}_y^b, \tag{6}$$

where $\mathcal{T}_x^b$ and $\mathcal{T}_y^b$ are the bed shear stresses defined by the depth-averaged velocities as

$$\mathcal{T}_x^b=g\frac{u\sqrt{u^2+v^2}}{C_z^2}, \qquad \mathcal{T}_y^b=g\frac{v\sqrt{u^2+v^2}}{C_z^2}. \tag{7}$$

The coefficient $C_z = h^{1/6}/\eta$ is the Chezy friction coefficient, and η denotes the Manning roughness coefficient at the bed. Thus, using the free surface equation (3) and the boundary conditions (4) and (6), and after standard approximations on convective terms, the two-dimensional vertically averaged system of shallow water equations rewritten in conservative form is obtained as

$$\begin{aligned}
&\frac{\partial h}{\partial t} + \frac{\partial (hU)}{\partial x} + \frac{\partial (hV)}{\partial y} = 0, \\
&\frac{\partial (hU)}{\partial t} + \frac{\partial}{\partial x}\left(hU^2 + \frac{1}{2}gh^2\right) + \frac{\partial}{\partial y}(hUV) = -gh\frac{\partial Z}{\partial x} + \nu_H \Delta (hU) + \frac{\mathcal{T}_x^W}{h} - \frac{\mathcal{T}_x^b}{h} - \Omega V, \\
&\frac{\partial (hV)}{\partial t} + \frac{\partial}{\partial x}(hUV) + \frac{\partial}{\partial y}\left(hV^2 + \frac{1}{2}gh^2\right) = -gh\frac{\partial Z}{\partial y} + \nu_H \Delta (hV) + \frac{\mathcal{T}_y^W}{h} - \frac{\mathcal{T}_y^b}{h} + \Omega U,
\end{aligned} \tag{8}$$

where U and V are the depth-averaged horizontal velocities in x- and y-direction given by

$$U = \frac{1}{h}\int_Z^{h+Z} u\, dz, \qquad V = \frac{1}{h}\int_Z^{h+Z} v\, dz.$$

Note that the system (8) has been widely used in the literature to model physical phenomena of water flows such as flood waves, dam breaks, tidal flows in an estuary and coastal water regions, and bore wave propagation in rivers, among others.

2.2 Equations for free-surface flow with temperature distribution

The starting point for the derivation of the free-surface flow model with temperature distribution is the three-dimensional incompressible Navier-Stokes/Boussinesq equations,

$$\frac{\partial u}{\partial x} + \frac{\partial v}{\partial y} + \frac{\partial w}{\partial z} = 0, \tag{9a}$$

$$\frac{\partial u}{\partial t} + u\frac{\partial u}{\partial x} + v\frac{\partial u}{\partial y} + w\frac{\partial u}{\partial z} + \frac{1}{\rho}\frac{\partial p}{\partial x} = \nu_H \Delta u + \frac{\partial}{\partial z}\left(\nu_V \frac{\partial u}{\partial z}\right) - \Omega v, \tag{9b}$$

$$\frac{\partial v}{\partial t} + u\frac{\partial v}{\partial x} + v\frac{\partial v}{\partial y} + w\frac{\partial v}{\partial z} + \frac{1}{\rho}\frac{\partial p}{\partial y} = \nu_H \Delta v + \frac{\partial}{\partial z}\left(\nu_V \frac{\partial v}{\partial z}\right) + \Omega u, \tag{9c}$$

$$\frac{\partial w}{\partial t} + u\frac{\partial w}{\partial x} + v\frac{\partial w}{\partial y} + w\frac{\partial w}{\partial z} + \frac{1}{\rho}\frac{\partial p}{\partial z} = \nu_H \Delta w + \frac{\partial}{\partial z}\left(\nu_V \frac{\partial w}{\partial z}\right) - g + F, \tag{9d}$$

where the variables have the same meaning as in (1). In (9), the force term F is given according to the Boussinesq approximation as

$$F = g\alpha(T - T_\infty), \tag{10}$$

where α is the thermal expansion coefficient and T_∞ is the reference temperature. In addition, assuming that the pressure is hydrostatic, the momentum equation in the vertical direction (9d) reduces to the following form

$$\frac{1}{\rho}\frac{\partial p}{\partial z} = -g + g\alpha\,(T - T_\infty)\,. \tag{11}$$

Integrating vertically the continuity equation (9a) and using the kinematic condition at the free surface leads to the free-surface equation as presented above in (3).

Thus, using the free surface equation (3) and the boundary conditions (5) and (6), and after standard approximations on convective terms, the two-dimensional vertically averaged system of shallow water equations rewritten in conservative form is obtained as

$$\begin{aligned}
\frac{\partial h}{\partial t}+\frac{\partial (hU)}{\partial x}+\frac{\partial (hV)}{\partial y} &= 0,\\
\frac{\partial (hU)}{\partial t}+\frac{\partial}{\partial x}\left(hU^2+\frac{1}{2}g'h^2\right)+\frac{\partial}{\partial y}(hUV) &= -g'h\frac{\partial Z}{\partial x}-g\alpha h\frac{\partial (h\Theta)}{\partial x}+\nu\Delta(hU)\\
&\quad +\frac{\mathcal{T}_x^W}{\rho}-\frac{\mathcal{T}_x^b}{\rho}-\Omega hV, \qquad (12)\\
\frac{\partial (hV)}{\partial t}+\frac{\partial}{\partial x}(hUV)+\frac{\partial}{\partial y}\left(hV^2+\frac{1}{2}g'h^2\right) &= -g'h\frac{\partial Z}{\partial y}-g\alpha h\frac{\partial (h\Theta)}{\partial y}+\nu\Delta(hV)\\
&\quad +\frac{\mathcal{T}_y^W}{\rho}-\frac{\mathcal{T}_y^b}{\rho}+\Omega hU,
\end{aligned}$$

where $g' = g(1+\alpha T_\infty)$, Θ is the depth-averaged temperature, U and V are the depth-averaged horizontal velocities in x- and y-direction given by

$$\Theta=\frac{1}{h}\int_Z^{h+Z} T\,dz, \qquad U=\frac{1}{h}\int_Z^{h+Z} u\,dz, \qquad V=\frac{1}{h}\int_Z^{h+Z} v\,dz.$$

Numerical treatment of the equations (8) or (12) often presents difficulties due to their nonlinear form, hyperbolic nature of the homogeneous system, and presence of complex source terms particularly the differential terms involving irregular topography. Therefore, the treatment of topography and friction source terms is of major importance in many practical applications of shallow water models. These could be a source of numerical instability and may produce nonphysical oscillations mainly because dicretizations of the flux and source terms are not well balanced in their reconstruction Bermúdez & Vázquez (1994); Toro (2001); Vázquez-Cendón (1999); Vukovic & Sopta (2002).

The shallow water equations (8) or (12) have to be solved in a bounded spatial domain with smooth boundaries endowed with given initial and boundary conditions along with a prescribed bed elevation. In practice, these conditions are problem dependent and their discussion is postponed until Section 4 where numerical examples are discussed.

2.3 Equations for pollutant or temperature dispersion

To model solute or heat transport by water flows, equations (8) or (12) are coupled to the depth-averaged convection-diffusion equation of the form

$$\frac{\partial h\Theta}{\partial t}+\frac{\partial}{\partial x}(hU\Theta)+\frac{\partial}{\partial y}(hV\Theta)=\nu_C\Delta(h\Theta)+hQ, \qquad (13)$$

where Θ is the depth-averaged pollution concentration or temperature, Q is the depth-averaged source, and ν_C is the diffusion coefficient. In practical situations the eddy viscosity ν_C and the eddy thermal diffusivity coefficients depend on water temperature, water salinity, water depth, flow velocity, bottom roughness and wind, compare Bartzokas (1985); LaCasce & Mahadevan (2006) for more discussions. For the purpose of the work presented in this Chapter, the problem of the evaluation of eddy diffusion coefficients is not considered.

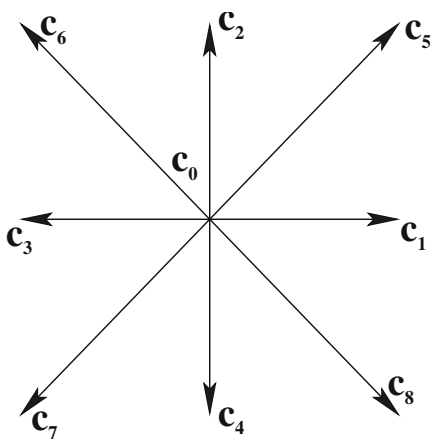

Fig. 2. The nine-velocity model in the D2Q9 lattice model.

3. The Lattice Boltzmann Method (LBM)

The central idea of the LBM is the discretization of the kinetic equation formulated for a two-dimensional geometry as

$$\frac{\partial f_i}{\partial t} + \mathbf{e}_i \cdot \nabla f_i = J_i + F_i, \qquad i = 1, 2, \ldots, N, \tag{14}$$

where f_i is the particle distribution function which denotes the number of particles at the lattice node $\mathbf{x} = (x, y)^T$ and time t moving in direction i with velocity $\mathbf{e}_i$ along the lattice $\Delta x = \Delta y = \|\mathbf{e}_i\| \Delta t$ connecting the nearest neighbors and N is the total number of directions in a lattice. In (14), J_i represents the collision term and F_i includes the effects of external forces. Using the single time relaxation of the Bhatnagar-Gross-Krook (BGK) approach Bhatnagar et al. (1954), the discrete Boltzmann equation takes the form

$$\frac{\partial f_i}{\partial t} + \mathbf{e}_i \cdot \nabla f_i = -\frac{1}{\tau_f}\left[f_i - f_i^{eq}\right] + F_i, \tag{15}$$

where τ_f is the relaxation time and f_i^{eq} is the equilibrium distribution function.

In the current work the D2Q9 square lattice model Qian et al. (1992), as depicted in Figure 2 is considered. The nine velocities $\mathbf{e}_i$ in the D2Q9 lattice are defined by

$$\mathbf{e}_0 = \begin{pmatrix} 0 \\ 0 \end{pmatrix} c, \quad \mathbf{e}_1 = \begin{pmatrix} 1 \\ 0 \end{pmatrix} c, \quad \mathbf{e}_2 = \begin{pmatrix} 0 \\ 1 \end{pmatrix} c, \quad \mathbf{e}_3 = \begin{pmatrix} -1 \\ 0 \end{pmatrix} c, \quad \mathbf{e}_4 = \begin{pmatrix} 0 \\ -1 \end{pmatrix} c,$$

$$\mathbf{e}_5 = \begin{pmatrix} 1 \\ 1 \end{pmatrix} c, \quad \mathbf{e}_6 = \begin{pmatrix} -1 \\ 1 \end{pmatrix} c, \quad \mathbf{e}_7 = \begin{pmatrix} -1 \\ -1 \end{pmatrix} c, \quad \mathbf{e}_8 = \begin{pmatrix} 1 \\ -1 \end{pmatrix} c,$$

where $c = \Delta x / \Delta t = \Delta y / \Delta t$. Here, Δt is chosen such that the particles travel one lattice

spacing during the time step. The corresponding weights w_i to the above velocities are

$$w_i = \begin{cases} \dfrac{4}{9}, & i = 0, \\ \dfrac{1}{9}, & i = 1,2,3,4, \\ \dfrac{1}{36}, & i = 5,6,7,8. \end{cases} \tag{16}$$

The choice of relaxation time, τ_f, and equilibrium distribution function, f_i^{eq}, in (15) depends on the macroscopic equations under study. Next, the formulation of these parameters for the shallow water equations (8) or (12) and the convection-diffusion equation (13) are described.

3.1 Lattice Boltzmann discretization for the shallow water equations

For the shallow water equations (8) or (12), the equilibrium distribution function f_i^{eq} depends on the water depth h and the velocity field $\mathbf{u} = (U, V)^T$ which are recovered by

$$h(\mathbf{x}, t) = \sum_{i=0}^{N-1} f_i(\mathbf{x}, t), \qquad h(\mathbf{x}, t)\mathbf{u}(\mathbf{x}, t) = \sum_{i=0}^{N-1} \mathbf{e}_i f_i(\mathbf{x}, t). \tag{17}$$

For the D2Q9 lattice, the equilibrium function f_i^{eq} in (15) is defined as Dellar (2002); Salmon (1999a)

$$f_i^{eq}(h, \mathbf{u}) = \begin{cases} h - w_0 h \left(\dfrac{15}{2} gh - \dfrac{3}{2}\mathbf{u}^2 \right), & i = 0, \\ w_i h \left(\dfrac{3}{2} gh + 3\mathbf{e}_i \cdot \mathbf{u} + \dfrac{9}{2}(\mathbf{e}_i \cdot \mathbf{u})^2 - \dfrac{3}{2}\mathbf{u}^2 \right), & i = 1, \ldots, 8, \end{cases} \tag{18}$$

with the weight factors w_i in (16). It is easy to verify that the local equilibrium function satisfies the following conditions

$$\sum_{i=0}^{8} f_i^{eq} = h, \qquad \sum_{i=0}^{8} \mathbf{e}_i f_i^{eq} = h\mathbf{u}, \qquad \sum_{i=0}^{8} \mathbf{e}_i \otimes \mathbf{e}_i f_i^{eq} = \frac{1}{2} gh^2 \mathbf{I} + h\mathbf{u} \otimes \mathbf{u}, \tag{19}$$

where $\mathbf{I}$ denotes the 2×2 identity matrix. The central idea in the LBM lies essentially in the recovery of the macroscopic flow behaviour from the mesoscopic flow picture of the particle movement Salmon (1999a).

After discretization, equation (15) can be written as

$$f_i(\mathbf{x} + \mathbf{e}_i \Delta t, t + \Delta t) = f_i(\mathbf{x}, t) - \frac{\Delta t}{\tau_f} \left[f_i - f_i^{eq} \right] + 3\Delta t w_i \mathbf{e}_i \cdot \mathbf{F}, \tag{20}$$

where τ_f is the relaxation time for the flow simulation and $\mathbf{F}$ represents the force term in the shallow water equations (8) or (12), for example

$$\mathbf{F} = \begin{pmatrix} -gh \dfrac{\partial Z}{\partial x} + \dfrac{\mathcal{T}_x^W}{h} - \dfrac{\mathcal{T}_x^b}{h} - \Omega V \\ -gh \dfrac{\partial Z}{\partial y} + \dfrac{\mathcal{T}_y^W}{h} - \dfrac{\mathcal{T}_y^b}{h} + \Omega U \end{pmatrix}. \tag{21}$$

By applying Taylor expansion and the Chapman-Enskog procedure to equation (20), it can be shown that the solution of the discrete lattice Boltzmann equation (20) with the equilibrium distribution (18) results in the solution of the shallow water equations (8) or (12). For details on this multi-scale expansion, the reader is referred to Dellar (2002); Salmon (1999a); Zhong et al. (2005).

In this LBM implementation, the relaxation time is determined by the physical viscosity in (8) and the time step through the formula

$$\tau_f = \frac{3\nu_H}{c^2} + \frac{\Delta t}{2}. \tag{22}$$

In the lattice Boltzmann method, equation (20) is solved in two steps: collision and streaming. In the collision step, the equations for each direction are relaxed toward equilibrium distributions with forcing

$$\tilde{f}_i(\mathbf{x}, t) = f_i(\mathbf{x}, t) - \frac{\Delta t}{\tau_f}\left[f_i - f_i^{eq}\right] + 3\Delta t w_i \mathbf{e}_i \cdot \mathbf{F}.$$

Then, at the streaming step, the distributions move to the neighboring nodes

$$f_i(\mathbf{x} + \mathbf{e}_i\Delta t, t + \Delta t) = \tilde{f}_i(\mathbf{x}, t)$$

3.2 Lattice Boltzmann discretization of the convection-diffusion equation

The LBM for convection-diffusion equation (13) is derived using a similar approach as the one used for the shallow water equations (8) or (12). Hence, starting from equation (15) and using the D2Q9 lattice from Figure 2, a lattice Boltzmann discretization of the convection-diffusion equation is

$$g_i(\mathbf{x} + \mathbf{e}_i\Delta t, t + \Delta t) - g_i(\mathbf{x}, t) = -\frac{\Delta t}{\tau_g}\left[g_i - g_i^{eq}\right] + \Delta t \mathcal{Q}_i, \tag{23}$$

where g_i is the distribution function, τ_g is the relaxation time and $\mathcal{Q}_i$ is the source term associated with the convection-diffusion equation (13). In (23), g_i^{eq} is an equilibrium distribution function satisfying the following conditions

$$\sum_{i=0}^{8} g_i = \sum_{i=0}^{8} g_i^{eq} = h\Theta, \qquad \sum_{i=0}^{8} \mathbf{e}_i g_i = \sum_{i=0}^{8} \mathbf{e}_i g_i^{eq} = \mathbf{u}h\Theta. \tag{24}$$

To process equation (23), a relaxation time and equilibrium function are required. For the convection-diffusion equation, the equilibrium function is given by

$$g_i^{eq} = w_i h\Theta\Big[1 + 3\mathbf{e}_i \cdot \mathbf{u}\Big], \tag{25}$$

where the lattice weights w_i are defined in (16). For this selection, the source term in (23) is set to

$$\mathcal{Q}_i = w_i h Q. \tag{26}$$

It should be noted that the convection-diffusion equation (13) can be obtained from equation (23) using the Chapman-Enskog expansion. Details on these derivations were given in Banda et al. (2009); Klar et al. (2008); Thömmes et al. (2007).

The relaxation time is defined by the diffusion coefficient in (13) as well as the time step

$$\tau_g = \frac{3\nu_C}{c^2} + \frac{\Delta t}{2}. \tag{27}$$

Notice that conditions (22) and (27) establish a relation between the diffusion coefficient and the relaxation time used in the LBM simulations.

3.3 Implementation and boundary conditions

The computational domain is discretized by a square lattice using the D2Q9 model with 9 velocities as shown in Figure 2. The scheme to advance the solution from the time t_n to the next time t_{n+1} can be implemented based on the following steps:

Step 1. Equilibrium functions:

- **1.a.** Using the water depth and velocity at time t_n, compute from (18) the equilibrium function f_i^{eq}, $i = 0, 1, \ldots, 8$.
- **1.b.** Using the concentration (and velocity from shallow water equations) at time t_n, compute from (25) the equilibrium function g_i^{eq}, $i = 0, 1, \ldots, 8$.

Step 2. Distribution functions:

- **2.a.** Calculate the distribution function f_i, $i = 0, 1, \ldots, 8$, using the lattice Boltzmann equation (20) with an appropriate relaxation time τ_f and impose the corresponding boundary conditions.
- **2.b.** Calculate the distribution function g_i, $i = 0, 1, \ldots, 8$, using the lattice Boltzmann equation (23) with relaxation time τ_g and impose the corresponding boundary conditions.

Step 3. Solution reconstructions:

- **3.a.** Update the water depth and velocity using the equations (17).
- **3.b.** Update the concentration using equations (24).

Step 4. Change the time $t_n \longrightarrow t_{n+1}$, go to **Step 2** and repeat until the stopping criterion is reached.

The time evolution is stopped in **Step 4** either when a fixed time is reached for instationary problems, or by comparing the deviation between two consecutive solutions for steady problems.

The implementation of boundary conditions in the LBM has a crucial impact on the accuracy and stability of the method, see Gallivan et al. (1997); Zou & He (2002) for more discussions. When no-slip boundary conditions are imposed at walls the bounce-back rule is usually used in the lattice Boltzmann algorithm. At a boundary point x_b, populations f_i of links $\mathbf{e}_i$ which intersect the boundary and point out of the fluid domain are simply reflected (bounce-back) since they cannot participate in the normal propagation step

$$f_{i^*}(\mathbf{x}_b, t + \Delta t) = f_i(\mathbf{x}_b, t), \qquad \text{index } i^* \text{ s.t.} \quad \mathbf{e}_{i^*} = -\mathbf{e}_i.$$

Flow boundary conditions for the height, h, and/or the velocities, (U, V), are needed at the inlet and the outlet of computational domains. When the height h_l is prescribed at the left boundary, the three distributions f_1, f_5 and f_8 are unknown. The techniques described in Zhou (2002); Zou & He (2002) for flat interfaces to implement these boundary conditions in

the framework of LBM can be used. Assuming that $V = 0$, the velocity in x-direction can be recovered from the relation

$$h_l U = h_l - \Big(f_0 + f_2 + f_4 + 2(f_3 + f_6 + f_7)\Big),$$

and the unknown distributions are defined as

$$\begin{aligned} f_1 &= f_3 + \frac{2}{3} h_l U, \\ f_5 &= f_7 - \frac{1}{2}(f_2 - f_4) + \frac{1}{6} h_l U, \\ f_8 &= f_6 + \frac{1}{2}(f_2 - f_4) + \frac{1}{6} h_l U. \end{aligned} \tag{28}$$

Neumann boundary conditions are implemented by imposing the equilibrium distribution corresponding to the prescribed height, h_l, and the velocity of the nearest neighbor in direction of the normal, (U_n, V_n)

$$f_i = f_i^{eq}\left(h_l, U_n, V_n\right), \qquad i = 0, 1 \ldots, 8.$$

Dirichlet boundary conditions for a prescribed concentration/temperature Θ_0 can be imposed by the equilibrium for the unknown populations

$$g_i = g_i^{eq}\left(\Theta_0, U, V\right), \qquad i = 0, 1 \ldots, 8.$$

Neumann boundary conditions in convection-diffusion problems are implemented in a similar way by prescribing the concentration of the neighbour node Θ_n at the boundary

$$g_i = g_i^{eq}\left(\Theta_n, U, V\right), \qquad i = 0, 1 \ldots, 8.$$

For more details on implementation of general boundary conditions in LBM, the reader is referred to Gallivan et al. (1997); Klar et al. (2008); Zou & He (2002) and further references therein. General details on the implementation of an LB method for irregular domains can also be found in der Sman & Ernst (2000); Mei et al. (1999) among others.

4. Numerical examples and results

In this section a practical study of the LB method to shallow water problems on complex geometry and irregular bathymetry is presented. The bathymetry is given either by an analytical function or by data points in a two-dimensional domain. The aim of this section is to test the accuracy, efficiency and study challenges for the LB approach for practical situations. Numerical results for several test cases will be presented. To verify this approach, the problem of mean flow in the Strait of Gibraltar has also been used as a test example. This latter example presents a challenge to numerical schemes because of its irregular geometry, complex bathymetry and presence of bottom friction and wind stresses. The results obtained are competitive in comparison with other approaches that solve the macroscopic equations using direct discretization methods. They are obtained without consideration for well-balancing, or adaptive grids and other technical details as is the case with other approaches. The term well-balanced schemes refers to those methods that require special treatment of the source terms such that the discretization of the flux gradients is balanced with the one used for the source terms. For more details on well-balanced schemes for shallow water equations

the reader is referred to LeVeque (1998); Vázquez-Cendón (1999); Xing & Shu (2006), while references on adaptive methods for solving shallow water equations can be found in Ambrosi (1999), among others. The findings in this section inform applied scientists to consider the LB method as an alternative practical numerical scheme for solving flow problems modelled by the shallow water equations. For all the results presented in this section, the gravity acceleration is set to $g = 9.81\ m/s^2$, the relaxation times τ_f and τ_g are fixed and time steps are selected according to conditions (22) and (27).

4.1 Verification of the method using the hydraulic model

To verify the performance and accuracy of the LBM, the one-dimensional shallow water equations with known analytical solutions are considered. In the current simulations, the bed friction, Coriolis forces and wind stresses are neglected in equations (8). It should be pointed out that a two-dimensional LBM code has been used to reproduce numerical solutions for the one-dimensional problems. Therefore, boundary conditions in the y-direction have to be supplied for the two-dimensional code. For these test examples, the dimension in y-direction is fixed to 50 lattice points and periodic boundary conditions are assumed on the upper and lower walls. Thereafter tests will be performed on flow through the Strait of Gibraltar.

4.1.1 Lake-at-rest example

The benchmark problem of a lake at rest proposed in Bermúdez & Vázquez (1994) to test the conservation property of numerical methods for shallow water equations is solved. The lake bed is irregular, so this test example is a good illustration of the significance of the source term treatment for practical applications to natural water-courses. It is expected that the water free-surface remains constant and the water velocity should be zero at all times. The LBM is executed using $\tau_f = 0.6$, $c = 200\ m/s$ and the results are displayed at the time $t = 10800\ s$.

Figure 3 shows the free water surface along with the lake bed. In this figure a close-up of the free surface is included for better insight. As can be seen, small perturbations appear on the free surface. The amplitude of these perturbations decreases as the number of lattice points increases. A comparison of the relative errors on a sequence of grids reveals nearly first-order convergence of the water level $h + z$ (see Table 1). The relative error is computed using the maximum norm

$$e_h = \frac{\max_i(h_i - z_i - H_{\text{ref}})}{H_{\text{ref}}},$$

where $H_{\text{ref}} = 16\ m$ is the reference height of the water surface in this case. On a mesh with 320 lattice points along the channel length, the amplitude of perturbations is of the order of $0.1\ m$. The error of $0.3\ m$ on the grid with 80 nodes seen in Figure 3 corresponds to a relative error of 2%, and one can argue if this is sufficiently small. In general, on the one hand, the LBM is a simple scheme that is easily implemented but one needs a finer grid, while more sophisticated schemes can use a coarser grid to achieve the same accuracy. On the other hand, one wishes to simulate an application with a complex geometry where more elaborate schemes are difficult to implement, while this is not a significant problem for LBM. It can be mentioned that the performance of the LBM approach is very attractive since the computed solution remains stable and accurate even when coarse lattices are used without solving Riemann problems or reconstructing upwind fluxes or requiring complicated techniques to balance the source terms and flux gradients as those reported in Vázquez-Cendón (1999).

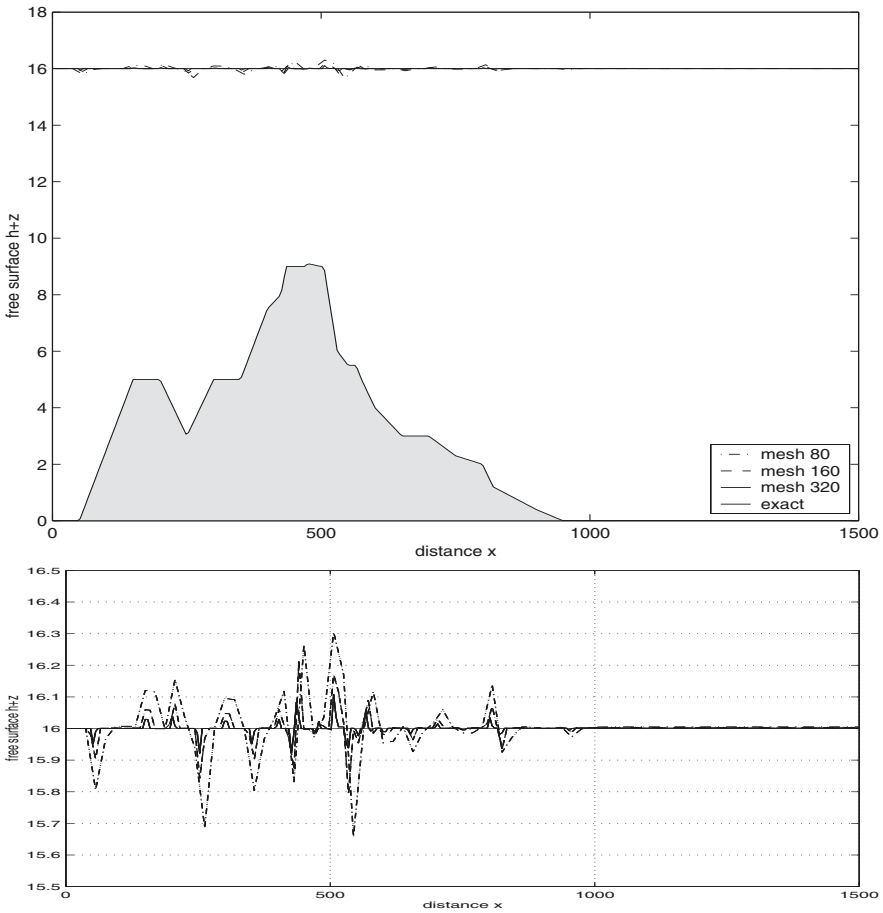

Fig. 3. The free-surface for the lake at rest on different meshes at time $t = 10800\ s$.

δx	e_h
$\frac{1}{80}$	0.0191
$\frac{1}{160}$	0.0133
$\frac{1}{320}$	0.0067

Table 1. Relative error of the free surface $h + z$ for the lake at rest on different meshes at time t=10800s. The convergence order obtained from a least squares fit is $p = 1.09$. Here $\delta x = \Delta x / L$ is the cell size Δx relative to the domain length $L = 1500\ m$.

4.1.2 Tidal wave flow

Secondly, the problem of a tidal wave flow in a frictionless ($C_b = 0$) channel with length, $L = 14$Km is considered. The bottom topography is analytically defined by

$$Z(x) = 10 + \frac{40x}{L} + 10\sin\left(\pi\left(\frac{4x}{L} - \frac{1}{2}\right)\right).$$

The initial conditions for the water height and velocity are

$$h(x,0) = 60.5 - Z(x), \qquad u(x,0) = 0.$$

At the channel inflow and outflow, respectively, the following

$$h(0,t) = 64.5 - 4\sin\left(\pi\left(\frac{4t}{86400} + \frac{1}{2}\right)\right), \qquad u_1(L,t) = 0,$$

are prescribed.

Following Bermúdez & Vázquez (1994), an asymptotic analytical solution for this example can be developed as

$$h(x,t) = 64.5 - Z(x) - 4\sin\left(\pi\left(\frac{4t}{86400} + \frac{1}{2}\right)\right),$$
$$u_1(x,t) = \frac{(x-L)\,\pi}{5400h(x,t)}\cos\left(\pi\left(\frac{4t}{86400} + \frac{1}{2}\right)\right).$$

This asymptotic analytical solution is used to quantify the results obtained by the LB method. The relative L^∞-, L^1- and L^2-error norms are defined as

$$\|\mathbf{e}\|_{L^\infty} = \frac{\max_{ij}\left|e_{ij}^n\right|}{\max_{ij}\left|u_{ij}^n\right|}, \qquad \|\mathbf{e}\|_{L^1} = \frac{\sum_{ij}\left|e_{ij}^n\right|}{\sum_{ij}\left|u_{ij}^n\right|}, \qquad \|\mathbf{e}\|_{L^2} = \frac{\sqrt{\sum_{ij}\left|e_{ij}^n\right|^2}}{\sqrt{\sum_{ij}\left|u_{ij}^n\right|^2}},$$

where $e_{ij}^n = u_{ij}^n - u(x_i, y_j, t_n)$ is the error between the numerical solution, u_{ij}^n, and the analytical solution, $u(x_i, y_j, t_n)$, at time t_n and lattice point (x_i, y_j). For the LB method, $\tau_f = 0.6$, $c = 200$m/s is used and the results are displayed at time $t = 9117.5$s. For this test example the ratio $U/c = 0.0009$. In Figure 4 the error norms for the velocity solution using four uniform lattices with sizes $\Delta x = \Delta y = 56$m, 28m, 14m and 7m are plotted. Logarithmic scales are used on the x- and y-axis. It is easy to verify that decreasing the lattice size results in a decrease of all error norms. As expected the LB method shows a first-order accuracy for this test example. The velocity values corresponding to the considered lattices are plotted along the analytical solution as shown in Figure 5. Grid convergence is clearly observed in this figure. Only a small difference between the LB solutions obtained with lattice resolution $\Delta x = \Delta y = 7$m and the asymptotic analytical solution is observed.

Figure 6 presents the numerical and analytical solutions for the free surface at the simulation time $t = 9117.5$s using $\Delta x = \Delta y = 7$m. There is an excellent agreement between the numerical results obtained by the LB method and the asymptotic analytical solution.

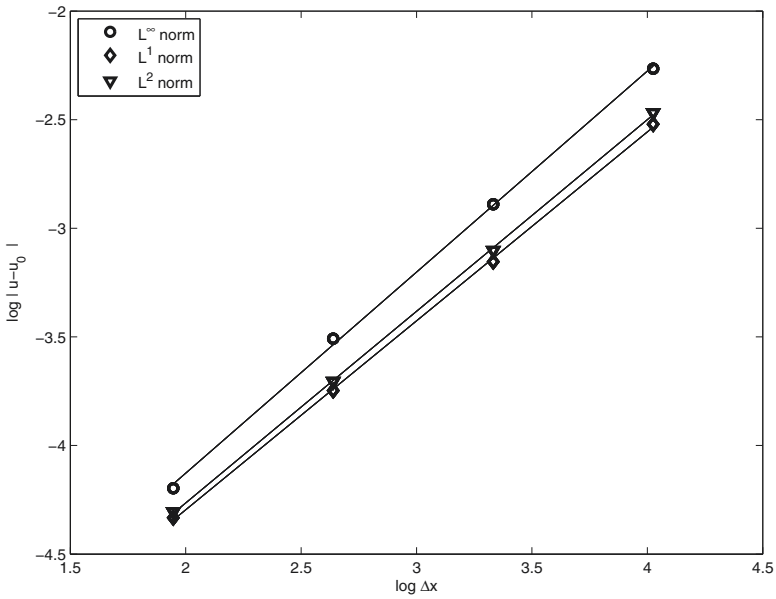

Fig. 4. Grid convergence for the tidal wave flow at time $t = 9117.5$s.

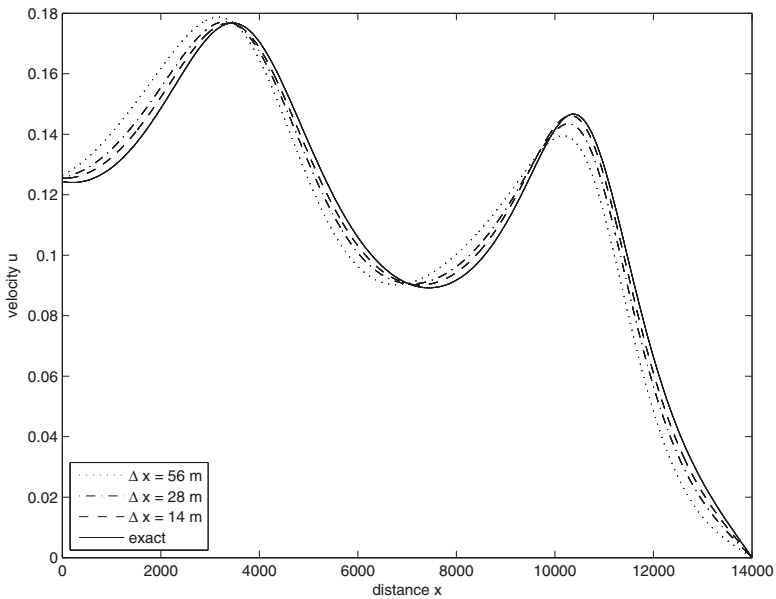

Fig. 5. Velocity plots for the tidal wave flow on different meshes at time $t = 9117.5$s.

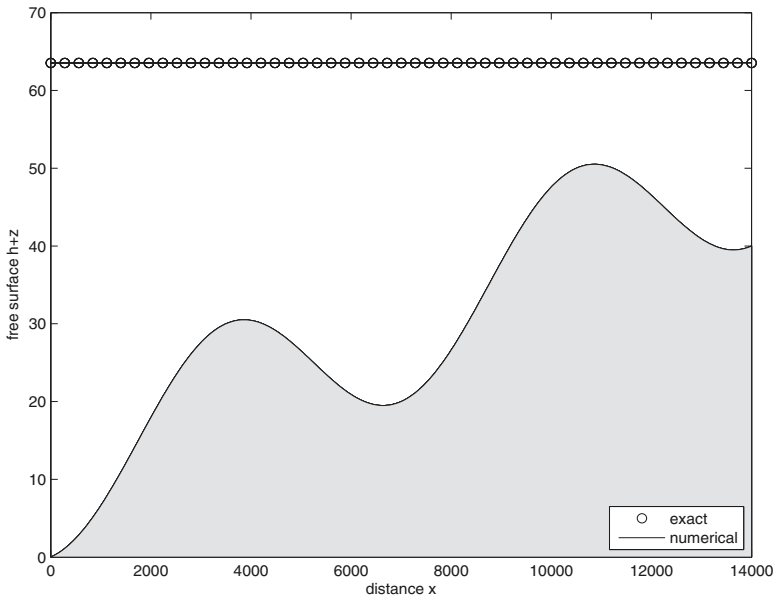

Fig. 6. Numerical and analytical free surface for the tidal wave flow at time $t = 9117.5$s.

4.1.3 Mean flow in the Strait of Gibraltar

The next application is the problem of mean flow in the Strait of Gibraltar. The schematic description of the Strait of Gibraltar is given in Figure 7. The system is bounded to the North and South by the Iberian and African continental forelands, respectively, and to the West and East by the Atlantic Ocean and the Mediterranean sea, respectively. This test problem is chosen because it presents a true practical test of lattice Boltzmann shallow water flow for two major reasons. Firstly, the Strait of Gibraltar's domain is a large-scale domain including high gradients of the bathymetry and well-defined shelf regions. Secondly, the Strait contains complex fully two-dimensional flow structures, which present a challenge in the shallow water modelling. The Strait of Gibraltar has also been the subject of numerous investigations such as water circulation, hydrodynamic processes and tides, compare Almazán et al. (1988); González & Sánchez-Arcilla (1995); Lafuente et al. (1990); Tejedor et al. (1999) among others. In all these references, the simulation domain is restricted by the Tangier-Barbate axis from the Atlantic Ocean and the Ceuta-Algeciras axis from the Mediterranean sea, see Figure 7. A schematic map of the Strait of Gibraltar is depicted in Figure 7 along with the main locations and ports. In geographical coordinates, the Strait is $35^o45'$ to $36^o15'$ N latitude and $5^o15'$ to $6^o05'$ W longitude. This domain is taken in numerical simulations mainly because measured data is usually provided by stations located on the above mentioned cities. The main objective in this numerical example is to test the capability of the LB method to handle complex geometry and irregular topography.

The bathymetry of the Strait is obtained from González & Sánchez-Arcilla (1995) and it is depicted in Figure 8. In this figure ten equally spaced bathymetric contourlines are shown. It is evident that the bathymetry is not smooth and exhibits irregular features with different length scales. For instance, two bumps with minimum bathymetric values of 997m and 463m are localized in the vicinity of the eastern exit of the Strait and the Caraminal Sill,

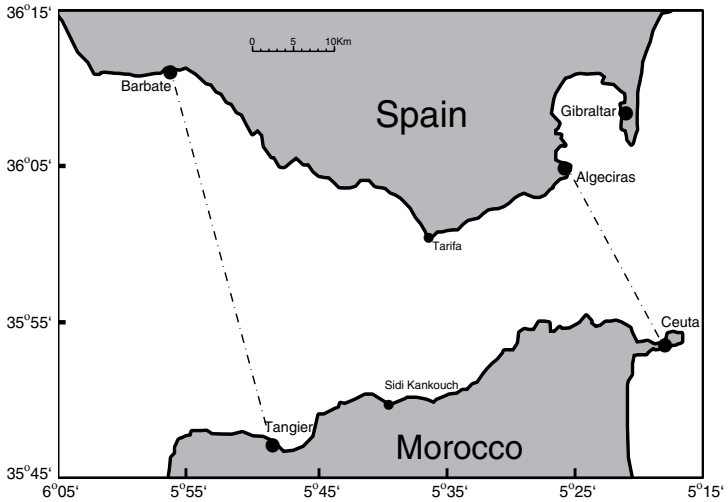

Fig. 7. The Strait of Gibraltar map in geographical coordinates along with the main locations. The considered computational domain is marked by dashed lines.

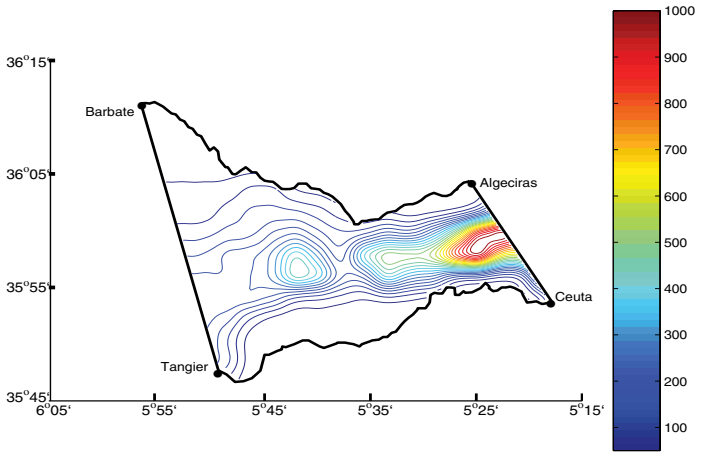

Fig. 8. Bathymetry contours for the domain under study in the Strait of Gibraltar. The water depth is given in meters.

respectively. All simulations used a constant Manning coefficient of $n_b = 0.012\text{s/m}^{1/3}$, a Coriolis parameter of $\Omega = 8.55 \times 10^{-5}\text{s}^{-1}$, and a typical value for the horizontal eddy viscosity of $\nu = 100\text{m}^2/\text{s}$ known in the literature, see for example González & Sánchez-Arcilla (1995); Tejedor et al. (1999). A no-slip boundary condition for velocity variables was applied to the coastal boundaries. At the open boundaries, Neumann boundary conditions are imposed for the velocity, and the water elevation is prescribed as a periodic function of time using the main semidiurnal and diurnal tides. The tidal constants at the open boundary lattice nodes were calculated by interpolation from those measured at the coastal stations Tangier and Barbate on the western end and the coastal stations Ceuta and Algeciras on the eastern end of the Strait with data listed in Table 2.

Station	Tide k	A_k $[m]$	ω_k $[rad/s]$	φ_k $[^\circ]$
Tangier	M_2	0.680	1.4052×10^{-4}	-67.00
	S_2	0.250	1.4544×10^{-4}	-90.00
	N_2	0.130	1.3788×10^{-4}	-56.00
	K_1	0.060	7.2921×10^{-5}	-80.00
Barbate	M_2	0.762	1.4052×10^{-4}	-53.50
	S_2	0.279	1.4544×10^{-4}	-77.00
	N_2	0.160	1.3788×10^{-4}	-37.00
	K_1	0.027	7.2921×10^{-5}	-59.00
Ceuta	M_2	0.288	1.4052×10^{-4}	-55.02
	S_2	0.105	1.4544×10^{-4}	-76.13
	N_2	0.071	1.3788×10^{-4}	-37.38
	K_1	0.038	7.2921×10^{-5}	-147.72
Algeciras	M_2	0.323	1.4052×10^{-4}	-34.80
	S_2	0.121	1.4544×10^{-4}	-65.76
	N_2	0.075	1.3788×10^{-4}	-34.96
	K_1	0.025	7.2921×10^{-5}	-129.72

Table 2. Parameters of tidal waves in the stations considered in the present study.

The main astronomical tidal constituents in the Strait of Gibraltar are the semidiurnal M_2, S_2 and N_2 tides, and the diurnal K_1 tide. Thus, in this computational study, the boundary conditions on open boundaries are prescribed as

$$h = h_0 + A_{M_2}\cos\left(\omega_{M_2}t + \varphi_{M_2}\right) + A_{S_2}\cos\left(\omega_{S_2}t + \varphi_{S_2}\right) + A_{N_2}\cos\left(\omega_{N_2}t + \varphi_{N_2}\right) + A_{K_1}\cos\left(\omega_{K_1}t + \varphi_{K_1}\right), \tag{29}$$

where A_k is the wave amplitude, ω_k the angular frequency and φ_k the tide phase for the tide k, $k = M_2$, S_2, N_2 or K_1. In (29), h_0 is the averaged water elevation set to 3m.

Initially, the flow was at rest and two weeks of real time were simulated. At the end of the simulation time the velocity fields were sampled for each tidal simulation at four different times $t = 0$, $t = T/4$, $t = T/2$ and $t = 3T/4$, where T represents the period of the considered tidal wave.

First the lattice dependence of the solutions was examined. To this end, the LB code using the M_2 tidal conditions on three different meshes with lattice sizes $\Delta x = \Delta y =$ 500m, 250m and 125m was executed. In Figure 9 the cross sections of the water height at mid-width of the Strait at times $t = T/4$ and $t = 3T/4$ are shown. It is evident that, for this flow regime, the results obtained on the coarse lattice of 500m show differences to those obtained on the fine lattice of 125m. These differences noticeably decrease for the lattice of 250m. For instance, the discrepancies in the maximum water height on the lattices with sizes 250m and 125m are less than 1.92% and 2.34% at $t = T/4$ and $t = 3T/4$, respectively. Similar results, not reported here, were obtained for the water velocity and for the other tidal waves. Therefore, bearing in mind the relatively small differences on the results from a lattice with size 125m and 250m at the expense of rather significant increase in the computational costs, the lattice with size 250m

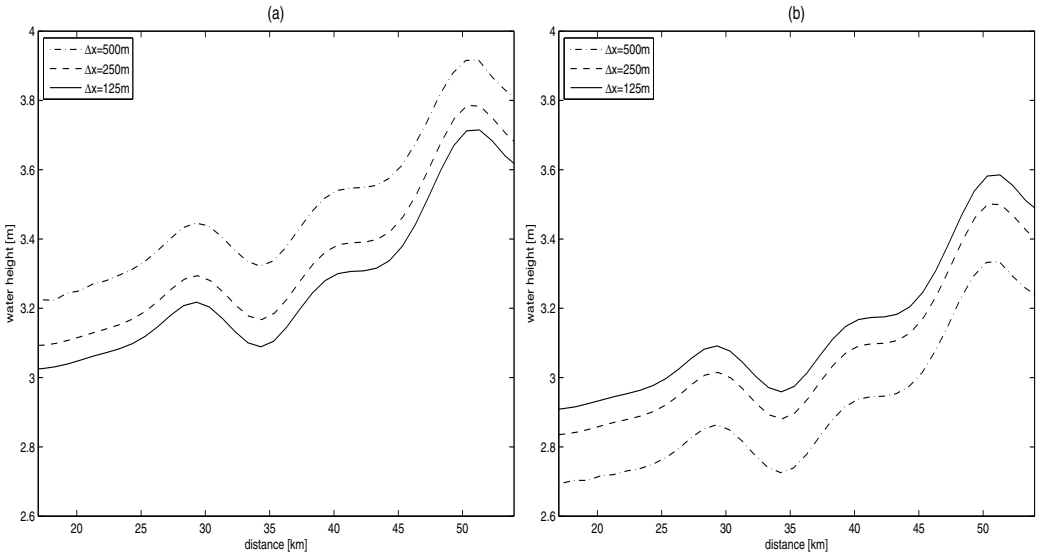

Fig. 9. Water height using the M_2 tidal wave on different meshes. (a) $t = T/4$ and (b) $t = 3T/4$.

was believed to be adequate to obtain reasonable results subject to minimal lattice effects. Hence, the results presented herein are based on the mesh with lattice size $\Delta x = \Delta y = 250$m.

The computed velocity fields using the parameters of the semidiurnal M_2, S_2 and N_2 tidal waves are presented in Figure 10, Figure 11 and Figure 12, respectively. The results for the diurnal K_1 tidal wave are presented in Thömmes et al. (2007). The results at four different times using the corresponding time period of each tide are displayed. Once the period is completed, dynamics of the water flow are repeated reproducing analogous velocity fields. The results show different aspects in the flow generated using tidal conditions for the semidiurnal M_2, S_2 and N_2 tidal waves. Using the conditions for the semidiurnal tides, the flow exhibits a recirculating zone of different magnitudes near the Craminal Sill. At later time, before the period is completed, the flow generated by semidiurnal M_2, S_2 and N_2 tidal waves changes the direction pointing towards the Atlantic Ocean. A recirculating flow region is also detected on the top eastern exits of the Strait near Algeciras. Similar features have also been reported in Almazán et al. (1988); González & Sánchez-Arcilla (1995). The lattice Boltzmann shallow water model performs well for this test problem since it does not diffuse the moving fronts and no spurious oscillations have been observed near steep gradients of the flow field in the computational domain. It can be clearly seen that the complicated flow structures on the Caraminal Sill and near Tarifa narrows and Tangier basin are being captured by the LB method. In addition, the presented results clearly indicate that the method is suitable for the prediction of mean flow in the Strait of Gibraltar.

Finally, computational cost, in terms of CPU seconds per time step, is 0.22s for each simulation using the M_2, S_2, N_2 and K_1 tidal waves. Approximately 2×10^6 time steps were needed to reach the real time of two weeks in a solution. All the computations were performed on a Pentium IV 2.66 GHz having 1Gb of RAM. Considering the computational cost and the accuracy achieved, the LB algorithm can be considered as a competitive alternative to the

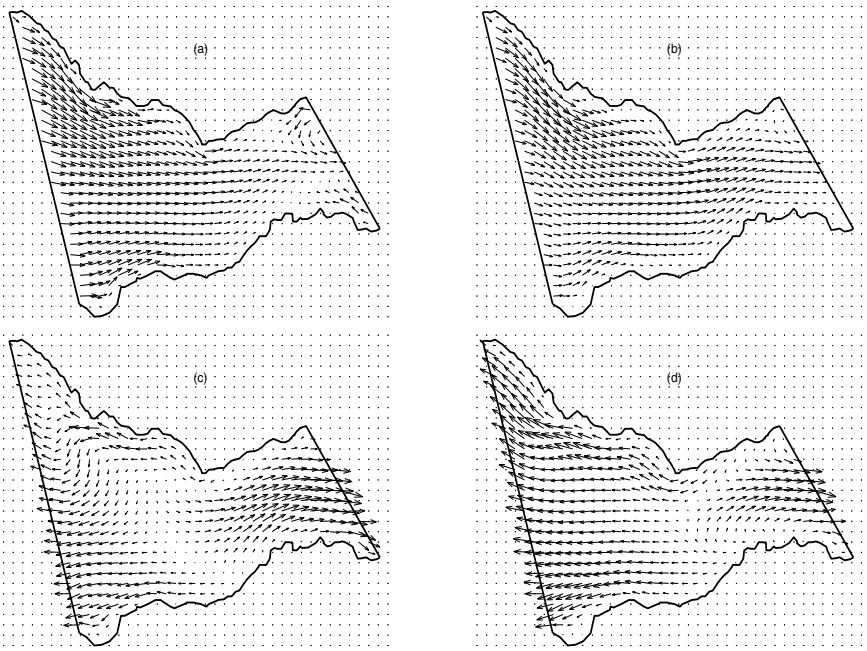

Fig. 10. Results using the M_2 tidal wave. (a) $t = 0$, (b) $t = T/4$, (c) $t = T/2$, and (d) $t = 3T/4$.

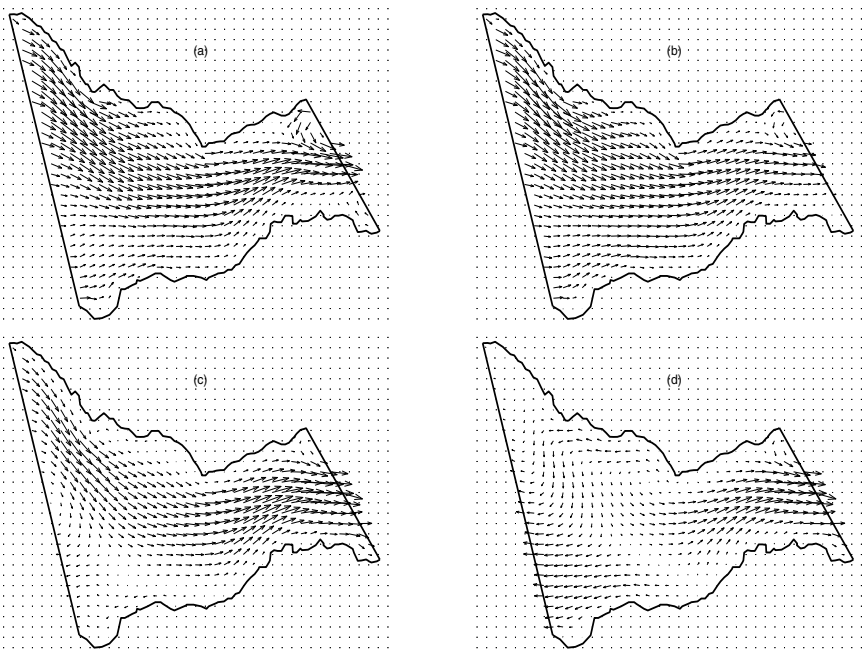

Fig. 11. Results using the S_2 tidal wave. (a) $t = 0$, (b) $t = T/4$, (c) $t = T/2$, and (d) $t = 3T/4$.

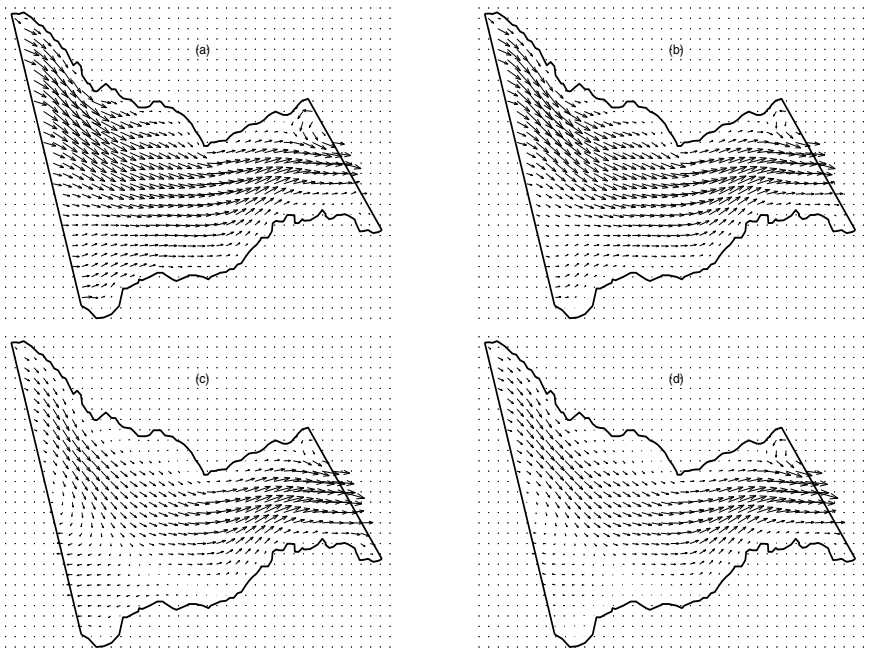

Fig. 12. Results using the N_2 tidal wave. (a) $t = 0$, (b) $t = T/4$, (c) $t = T/2$, and (d) $t = 3T/4$.

finite volume methods widely used in the literature to perform numerical studies on shallow water flows, in terms of both numerical accuracy and computational cost.

4.2 Application to pollutant transport

Recently, the authors in Banda et al. (2009) extended this method to pollutant transport by the shallow water flows. The behaviour of the pollutant is investigated especially in connection with a non-flat topography and the surface stress originated by the shear of blowing winds. Firstly, the accuracy and convergence features of the LB method are verified. Finally, the LB method is applied to the simulation of a contamination event taking place in the Strait of Gibraltar.

4.2.1 Pollutant transport in a squared cavity

A problem of convection-diffusion of a pollutant transport in a 9000 $m \times 9000$ m squared cavity with bottom slopes given by

$$\partial_x Z = \partial_y Z = -0.001$$

is solved. The Manning resistance coefficient is set to $n_b = 0.025\ s/m^{1/3}$. As in Komatsu et al. (1997), uniform flow velocities $u_1 = u_2 = 0.5\ m/s$ are imposed as well as uniform flow water depth $(h + Z)$ as initial condition. The initial condition for the pollutant concentration is given by the superposition of two Gaussian pulses centered, respectively, at $(x_1 = 1400\ m, y_1 = 1400\ m)$ and $(x_2 = 2400\ m, y_2 = 2400\ m)$,

$$C(0,x,y) = C_1 \exp\left(-\frac{(x-x_1)^2 + (y-y_1)^2}{\sigma_1^2}\right) + C_2 \exp\left(-\frac{(x-x_2)^2 + (y-y_2)^2}{\sigma_2^2}\right),$$

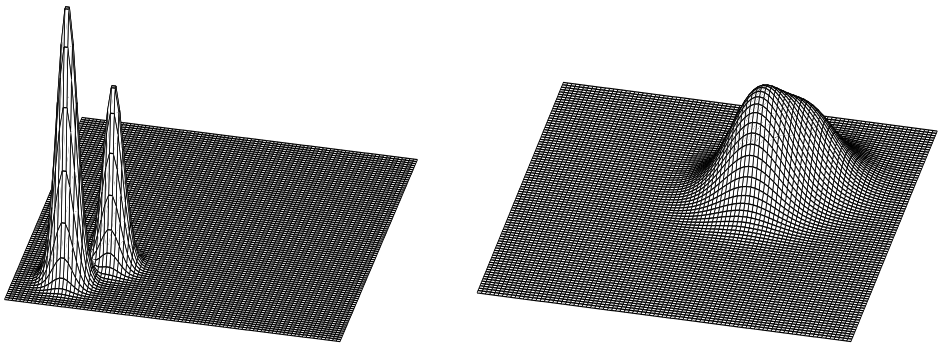

Fig. 13. Initial concentration distribution (left) and final result at $t = 4600\ s$ (right).

where $C_1 = 10$, $C_2 = 6.5$ and $\sigma_1 = \sigma_2 = 264$. For this example, the pollutant concentration is a wave that moves along the diagonal cross-section $x = y$ with the constant speed $u_1 = u_2 = 0.5\ m/s$. Here, the wind effects are neglected ($W_1 = W_2 = 0$) in the hydraulic equations, no source ($Q = 0$) is considered in the pollutant transport equation, and a diffusion coefficient $\nu_C = 100\ m/s^2$ is used in all LB simulations. Neumann boundary conditions are used for both hydraulic variables and pollutant concentration on all walls of the cavity. We used $\tau = 0.01$ and simulations were stopped at time $t = 4600\ s$. At this time, the pollutant concentration reaches the end corner of the cavity.

Figure 13 shows the initial concentration and the numerical result using a uniform mesh with lattice size $\Delta x = \Delta y = 50\ m$. The corresponding contour plots are presented in Figure 14. It is clear that the LB method preserves the expected transport trajectory and captures the correct dynamics. It can be remarked that due to the diffusion present in the equation of pollutant transport, the two initial pulses merge into one concentration pulse during the time process. In addition, the obtained solutions are completely free of spurious oscillations and the moving fronts are well resolved by the LB method.

In order to check the grid dependence of the LB method for this test example, in Figure 15 cross sections of the pollutant concentration in the main diagonal ($x = y$) at time $t = 4600\ s$ using different meshes are presented. Four meshes with $\Delta x = \Delta y = 200\ m$, $100\ m$, $50\ m$ and $25\ m$. are considered. For the selected pollutant conditions, a large difference in the concentration profile is detected for the coarse mesh with $\Delta x = \Delta y = 200\ m$ compared with finer meshes. This difference becomes smaller as the mesh is refined. For instance, the discrepancy in the pollutant concentration on meshes with $\Delta x = \Delta y = 50\ m$ and $\Delta x = \Delta y = 25\ m$ is less than 1%. Similar trend was observed in the hydraulic variables. Therefore, bearing in mind the slight change in the results from a mesh with $\Delta x = \Delta y = 50\ m$ and $\Delta x = \Delta y = 25\ m$ at the expense of rather significant increase in computation time, the mesh $\Delta x = \Delta y = 50\ m$ is believed to be adequate to obtain computational results (shown in Figure 13 and Figure 15) free of grid effects for the considered pollutant transport problem.

4.2.2 Pollutant transport in the Strait of Gibraltar

The Strait of Gibraltar is used heavily for shipping traffic and oil cargo. As a consequence, the Strait is considered as one of the most chronically contaminated regions, see Gómez (2003).

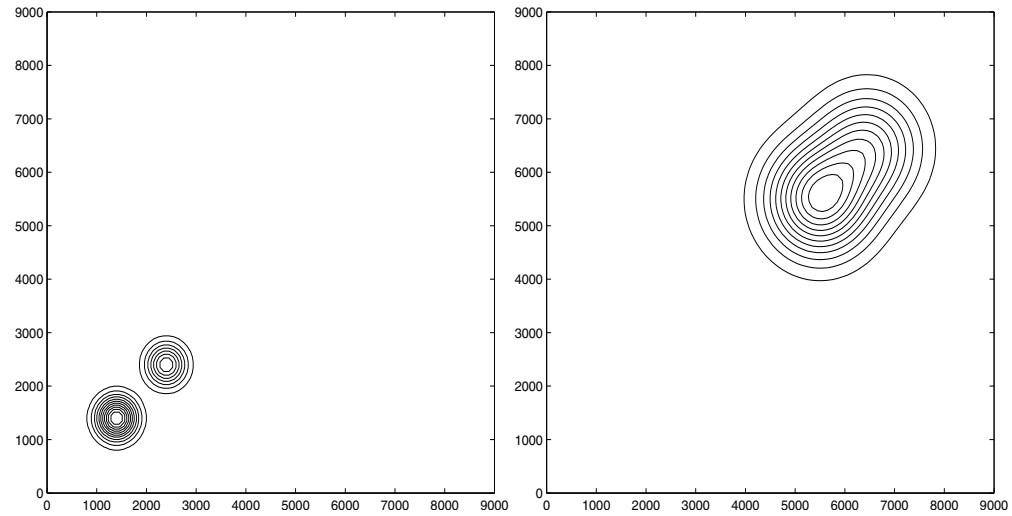

Fig. 14. Contours for initial concentration (left) and final result at $t = 4600\ s$ (right).

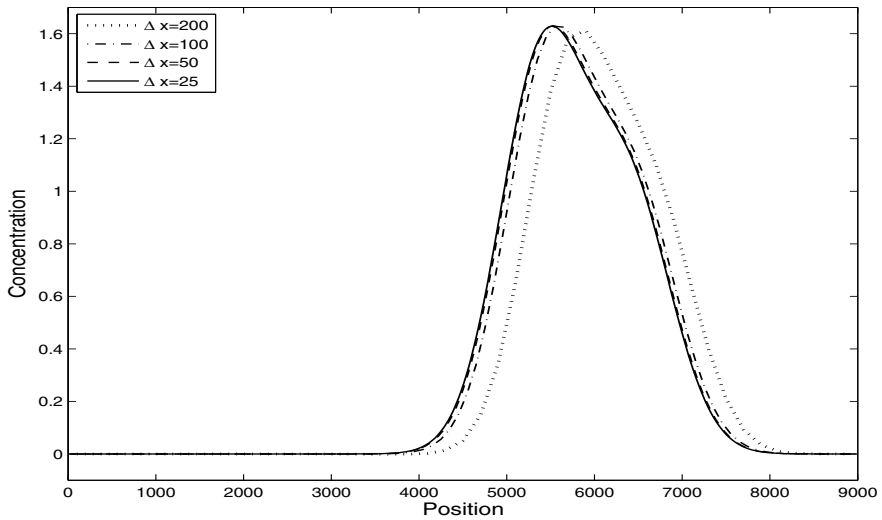

Fig. 15. Cross sections of the pollutant concentration for different meshes.

In this example the LB method will be applied to simulate a contamination event in the Strait of Gibraltar accounting for all the hydraulic effects such as friction sources, wind stresses, Coriolis forces and horizontal eddy viscosity.

Initially, the flow is assumed to be at rest and no pollutant is present *i.e.*,

$$u = v = 0, \qquad h = h_0 \qquad \text{and} \qquad \Theta = 0. \tag{30}$$

Parameters of the flow are set as in the previous subsection. A diffusion coefficient of $\nu_C = 100\ m/s^2$ is used for the pollutant transport. The contaminant source is implemented as an

indicator function of the form

$$Q(t,x,y) = \begin{cases} 1, & \text{if} \quad (x,y) \in \mathcal{D}_{release} \quad \text{and} \quad t \leq t_{release}, \\ 0, & \text{otherwise,} \end{cases}$$

where $t_{release}$ is the release time and $\mathcal{D}_{release}$ is the release region to be located in the Strait of Gibraltar. For the continuous release, $t_{release}$ corresponds to the final simulation time while for the instantaneous release, $t_{release}$ is set to 3 *hours*. In this sense, the simulations are schematic, since the number, the arrangement, and the capacities of pollution sources in the Strait of Gibraltar only partially correspond to the real situation.

The flow is initialised as in Section 4.1.3. The shallow water equations (8) are solved without pollutant release for two weeks of real time to obtain a well-developed flow. The obtained results are taken as the real initial conditions and the pollutant is injected at this stage of computation. Depending on the wind direction, three cases are simulated namely, calm situation, eastern wind and western wind Banda et al. (2009). At the end of the simulation time the velocity fields and concentration of pollutant are displayed after 1, 3 and 6 *hours* from the injection of pollutant. A mesh with lattice size $\Delta x = \Delta y = 250\ m$ is used for all the results presented in this section. A Neumann boundary condition is used for the pollutant concentration at the open boundaries and zero concentration is imposed at the coastlines of the Strait.

First a calm situation corresponding to $W_x = W_y = 0\ m/s$ is simulated. The pollutant is injected in the middle of the Strait of Gibraltar and located at $(5^o53'W, 35^o56'N)$. The simulated results are presented in Figure 16 at three separated instants from the injection of pollutant. A simple inspection of this figure reveals that the velocity field changes the direction during the time process according to the period of the considered tides. The decrease and increase of the strengths of velocities with time can also be seen in the figure. Obviously, the spread of contaminant patch on the water free-surface is very slow for both continuous and instantaneous releases. This fact can be attributed to the small velocities generated by the tidal waves and also to the periodic character of these tides. As expected, a wider spread of contaminant patch is observed for the instantaneous release than the continuous case.

Next, a pollutant transport subject to blowing wind from the east with $W_x = -1\ m/s$ and $W_y = 0\ m/s$ is considered. In contrast to the previous test example, the present pollutant transport is solved with extra velocity field due to wind. The results of the simulation for the continuous release as well as those obtained for the instantaneous release are shown in Figure 17. It is clear that the pollutant transport is influenced significantly by the action of the wind. The figure shows that the proposed LB method accurately reproduces concentration fronts. Moreover, the steep gradient in the shallow water flow and the high concentration in the convection-diffusion equation highlights the good stability and capability of the LB model to resolve pollutant transport by tidal flows.

In summary, the pollutant transport is captured accurately, the flow field is resolved reasonably well, and the concentration front is shape preserving. All these features illustrate the robustness of the LB method.

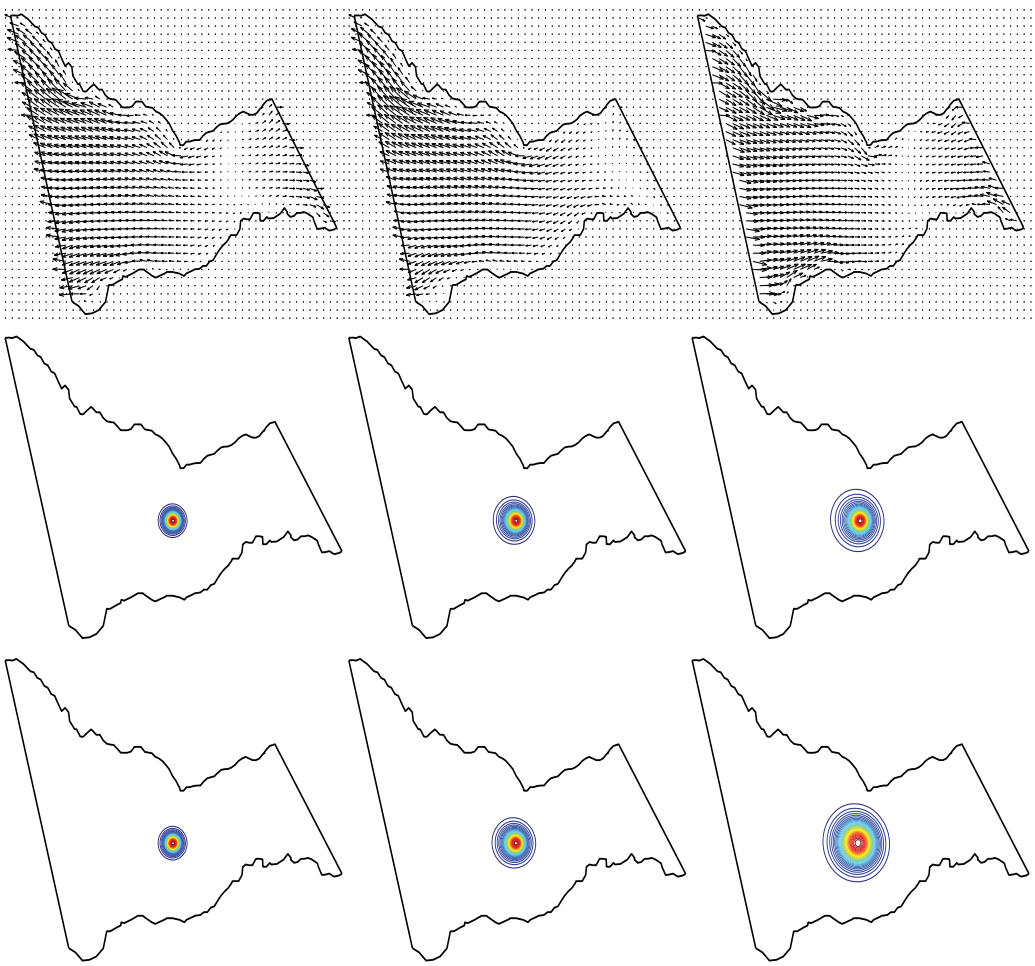

Fig. 16. Flow field (first row), concentration contours for continuous release (second row) and for instantaneous release (third row) using calm conditions at three times after the release.

4.3 Free-surface temperature in the Strait of Gibraltar

Temperature can strongly interact with hydraulics in many situations of engineering interest and neglecting its effects may have significant consequences in the overall predictions. For a discussion on the thermal effects on hydraulic flows reference is made to Chelton et al. (2001); Millán et al. (1995); Polyak et al. (1996); Samelson et al. (2006); Vargas et al. (1999) and further references can be found therein. The basic circulation in the Strait of Gibraltar consists of an upper layer of cold, fresh surface Atlantic water and an opposite deep current of warmer, salty Mediterranean outflowing water, compare Almazán et al. (1988); González & Sánchez-Arcilla (1995). The sea-surface temperatures in the Strait of Gibraltar are maxima in summer (August-September) with average values of 23-24$^{\circ}C$ and minima in winter (January-February) with averages of 11-12$^{\circ}C$. The north Atlantic water is about 5-6$^{\circ}C$ colder than the Mediterranean water, elaborate details are available in Millán et al. (1995); Polyak et al. (1996).

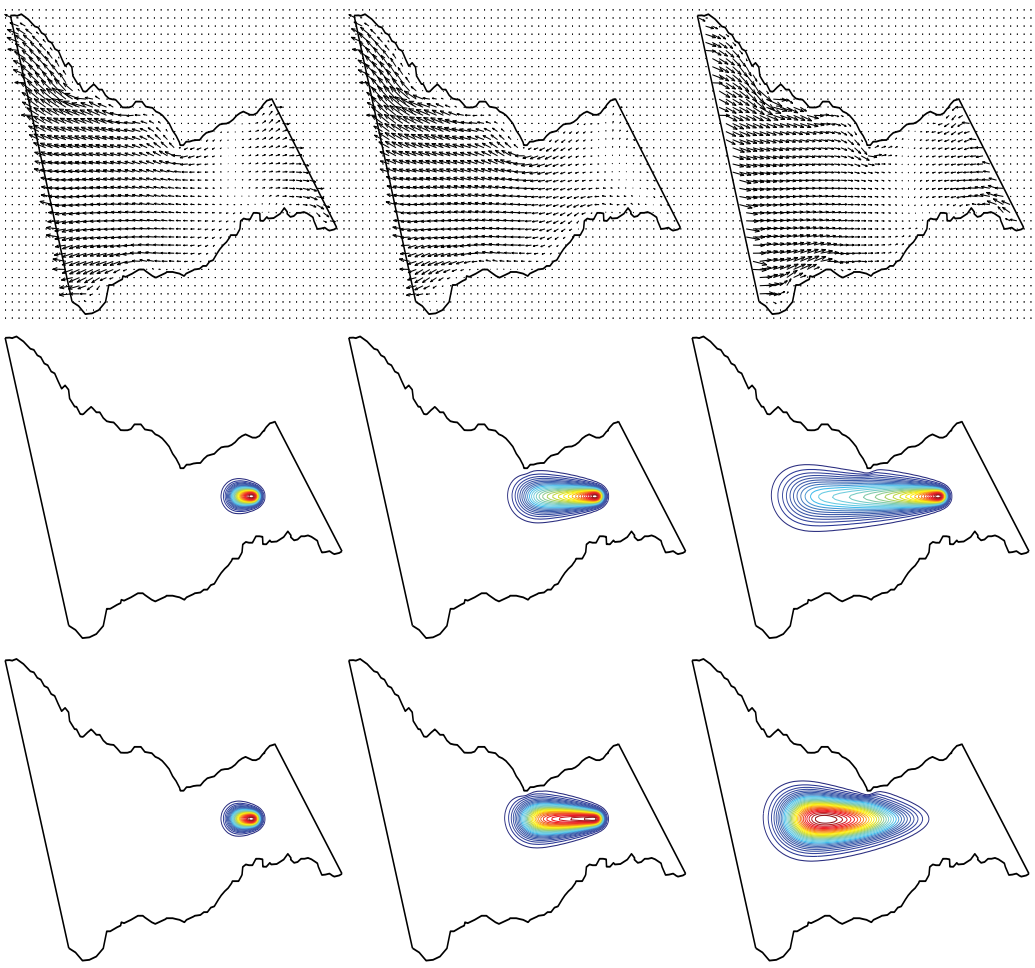

Fig. 17. Flow field (first row), concentration contours for continuous release (second row) and for instantaneous release (third row) using eastern wind at three times after the release.

In the simulations the flow parameters are set as in Section 4.1.3. As discussed above a mesh with lattice size $\Delta x = \Delta y = 250\ m$ is used for all the results presented in this section. Depending on the wind conditions, two situations are presented namely:

(i) Calm situation corresponding to $(\omega_x = 0\ m/s, \omega_y = 0\ m/s)$,

(ii) Wind blowing from the west corresponding to $(\omega_x = 1\ m/s, \omega_y = 0\ m/s)$.

Initially, the simulated flow has been at warm rest *i.e.*,

$$U = V = 0, \qquad H = H_0 \qquad \text{and} \qquad \Theta = \Theta_h, \tag{31}$$

where $\Theta_h = 23^\circ C$ is the Mediterranean temperature and the western temperature boundary of the Strait is fixed to the Ocean temperature $\Theta_c = 17^\circ C$. The shallow water equations (12) are solved without temperature dispersion for two weeks of real time to obtain a well-developed flow. The obtained results are taken as the real initial conditions and the

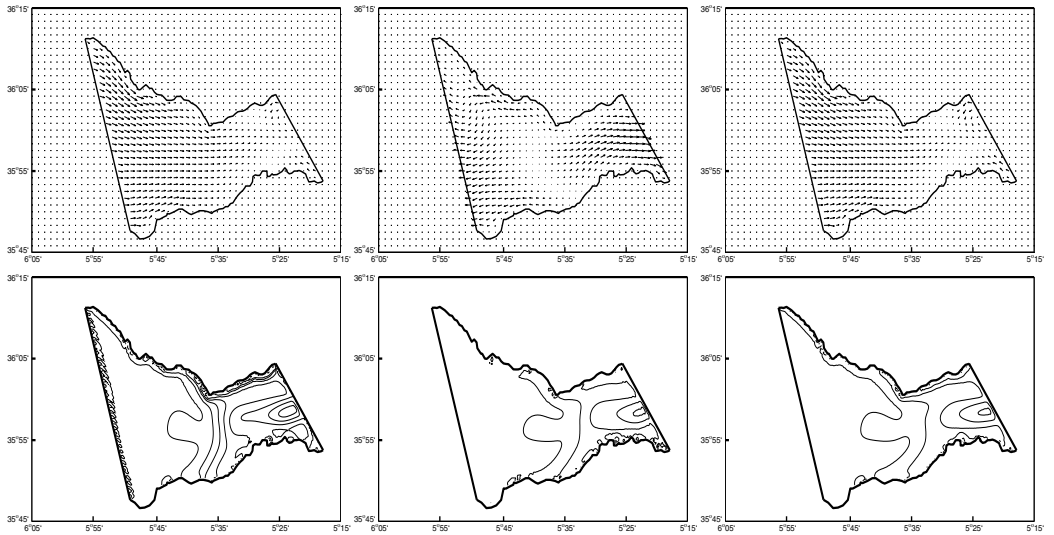

Fig. 18. Flow field (first row) and temperature contours (second row) for calm situation at three different times. From left to right $t = 12$, 18 and 24 hours.

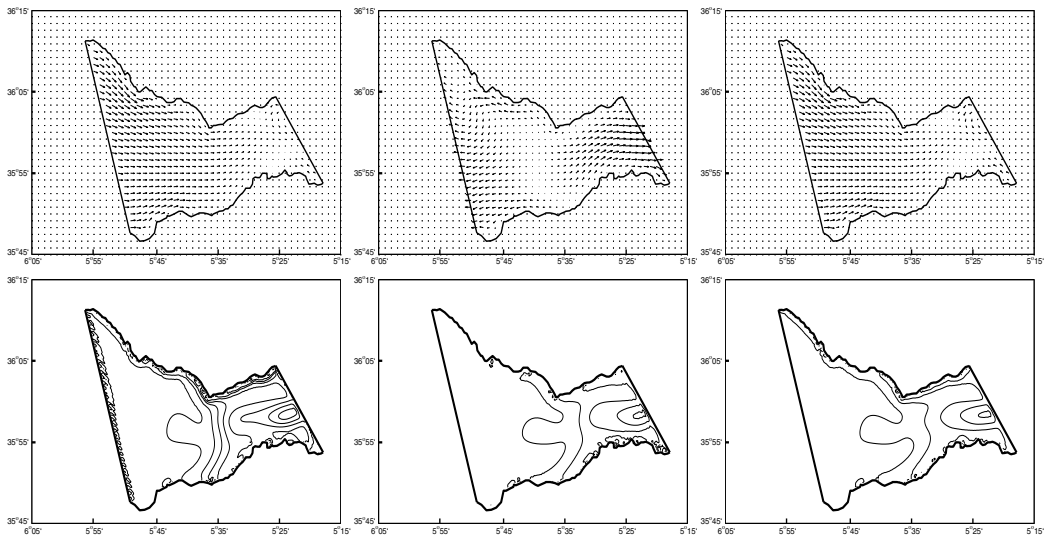

Fig. 19. The same as in Figure 18 but for a wind blowing from the west.

sea-surface temperature is included at this stage of the simulation. At the end of the simulation time the velocity fields and temperature contours are displayed after 12, 18 and 24 hours from the inclusion of sea-surface temperature.

In Figure 18 numerical results obtained using calm wind conditions are presented. Those obtained for the wind blowing from the west are displayed in Figure 19. In these figures, the velocity field is shown and 10 equi-distributed contours between Θ_c and Θ_h of the temperature at the instants $t = 12$, 18 and 24 hours. It is clear that using the conditions for the tidal waves and the considered wind situations, the flow exhibits a recirculating zone

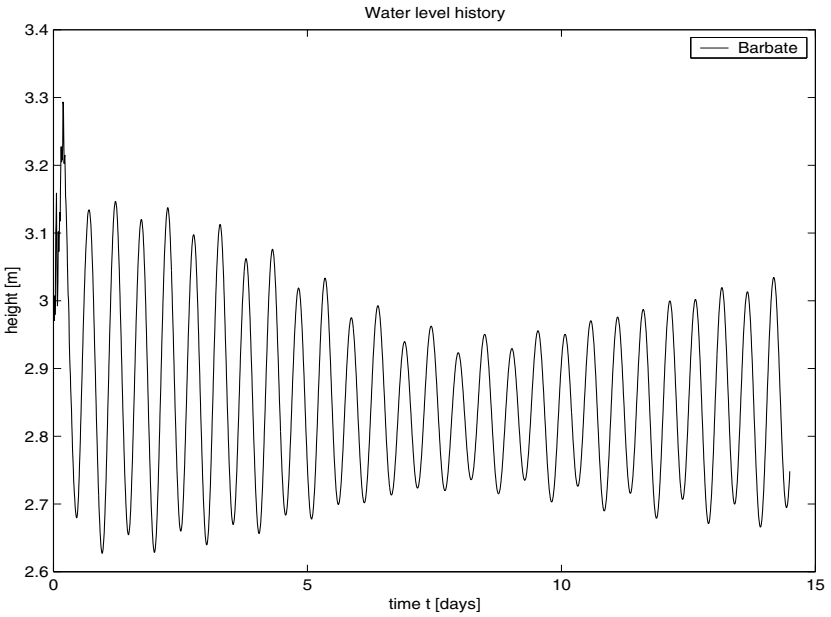

Fig. 20. Time evolution of water elevation at the Tarifa narrows.

with different order of magnitudes near the Caraminal Sill (*i.e.* the interface separating the water bodies between the Mediterranean sea and the Atlantic Ocean). At the beginning of simulation time, the water flow enters the Strait from the eastern boundary and flows towards the eastern exit of the Strait. At later time, due to tidal waves, the water flow changes the direction pointing towards the Atlantic Ocean. A recirculating flow region is also detected on the top eastern exits of the Strait near Algeciras. Similar flow behaviours have been also reported in Almazán et al. (1988); González & Sánchez-Arcilla (1995); Thömmes et al. (2007).

The effects of wind conditions are observed in the temperature distributions presented in Figure 18 and Figure 19. A boundary layer of high sea-surface temperatures has been detected on the Spanish coastal lines. For the considered tides and wind conditions, the buoyancy force has been seen to play a weak role in influencing the sea-surface tamperature in the Strait of Gibraltar which results in thinner mixing layers. In Figure 20 the time evolution of the water free-surface elevation at the Tarifa narrows for a time period of two weeks is displayed. As expected, the time series show two tidal periods with different amplitude and frequencies. They are in good agreement with those previously computed in Castro et al. (2004); Tejedor et al. (1999). Similar results not presented here, have been obtained at other locations in the Strait of Gibraltar.

It can be clearly seen that the complicated flow structures on the Caraminal Sill and near Tarifa narrows and Tangier basin are being captured by the LB method. In addition, the presented results clearly indicate that the method is suited for prediction of sea-surface temperature dispersion in the Strait of Gibraltar. It should be stressed that ideally, results from the temperature dispersion model should be compared with observations of real sea-surface temperatures in the Strait of Gibraltar. However, there are no available data until now to

carry out this work. Thus, only some hypothetical simulations have been undertaken simply to show that LB results are logical and consistent.

5. Conclusion

The most common two-dimensional lattice Boltzmann method using nine particle speeds arranged on a D2Q9 squared lattice was used to approximate numerical solutions to the shallow water equations. The model is simple, accurate, easy to implement, and can be used to solve both steady and unsteady shallow water problems. The method also provides a straightforward treatment of source terms without relying on complicated discretization techniques. Other source terms such as wind stresses or bed shear stresses can naturally be added to the lattice Boltzmann equation as force terms without special treatment. In this chapter the main focus is to demonstrate the ability of the lattice Boltzmann method to solve practical shallow water flows on non-flat beds with irregular bathymetry.

The efficiency of the method for predicting shallow water flows was assessed in the benchmark problems such as the tidal wave flow and steady flow over a hump. The results clearly indicate that the method captures the correct flow structures and reproduces results which satisfactorily agree with those available in the literature for the same test problems. To demonstrate the ability of the lattice Boltzmann method on complex practical shallow water problems, the method has been applied to the mean flow in the Strait of Gibraltar. The numerical results show correct physics in different test regimes. The influence of different spatial resolutions on the numerical results has also been discussed. Refined spatial models in which a larger number of total particles is used in the simulation can resolve more small-scale effects at the expense of long computational times. Nevertheless, flows in such complex domains can be computed, providing correct physics without the need for generating adaptive grids or complicated reconstruction of numerical fluxes using exact or approximate Riemann solvers. Overall the method shows reasonable accuracy while ensuring the required properties of the shallow water flows.

Furthermore the lattice Boltzmann method has been extended and tested for pollutant dispersion by shallow water flows. The mass, momentum and transport equations are obtained from the nine-velocity distributions of hydraulic flow and pollutant concentration variables. Two types of distribution functions have been developed for the hydraulic variables and pollutant concentration. Although lattice Boltzmann methods are very promising, they are still in the early stage of development and validation. More investigations are needed to explore the capability of lattice Boltzmann methods for more practical engineering applications in environmental fluid flows and species transport. For instance, extension of the current solver to complex geometries involving turbulent effects can also be of interest both for hydraulics and pollutant transport.

6. References

Almazán, J., Bryden, H., Kinder, T. & Parrilla, G. (1988). *Seminario Sobre la Oceanografía Física del Estrecho de Gibraltar*, SECEG, Madrid.

Ambrosi, M. M. D. (1999). Mesh adaptation strategies for shallow water flow, *Int. J. Num. Meth. Fluids.* 31: 497–512.

Banda, M., Seaïd, M. & Thömmes, G. (2009). Lattice Boltzmann simulation of dispersion in two-dimensional tidal flows, *International Journal for Numerical Methods in Engineering* 77: 878–900.

Bartzokas, A. (1985). Estimation of the eddy thermal diffusivity coefficient in water, *J. Meteorology and Atmospheric Physics* 33: 401–405.

Benkhaldoun, F., Elmahi, I. & Seaïd, M. (2007). Well-Balanced Finite Volume Schemes for Pollutant Transport by Shallow Water Equations on Unstructured Meshes, *J. Comp. Physics.* 226: 180-203.

Benkhaldoun, F., Elmahi, I. & Seaïd, M. (2009). Application of mesh-adaptation for pollutant transport by water flow, *Math. and Computers in Simul.* 79: 3415–3423.

Benkhaldoun, F., Elmahi, I. & Seaïd, M. (2010). A new finite volume method for flux-gradient and source term balancing in shallow water equations, *Computer Meth. Appl. Mech. and Engrng* 199: 49–52.

Benkhaldoun, F. & Seaïd, M. (2010). A simple finite volume method for the shallow water equations, *J. Comp. Appl. Math.* 234: 58–72.

Bermúdez, A. & Vázquez, M. (1994). Upwind methods for hyperbolic conservation laws with source terms, *Computers & Fluids* 23: 1049–1071.

Bhatnagar, P., Gross, E. & Krook, M. (1954). A model for collision process in gases, *Phys. Rev. Lett.* 94: 511–525.

Castro, M., Garcia-Rodriguez, J., Gonzalez-Vida, J., Macias, J., Pars, C. & Vazquez-Cendon, M. (2004). Numerical simulation of two-layer shallow water flows through channels with irregular geometry, *J. Comput. Phys.* 195: 202–235.

Chelton, B., Esbensen, S., Schlax, M., Thum, N., Freilich, M., Wentz, F., Gentemann, C., McPhaden, M. & Schopf, P. (2001). Observations of coupling between surface wind stress and sea surface temperature in the Eastern Tropical Pacific, *Journal of Climate.* 14: 1479–1498.

Chen, S. & Doolen, G. (1998). Lattice Boltzmann method for fluid flows, *Annual Rev. of Fluid Mech.* 30: 329–364.

Dellar, P. (2002). Non-hydrodynamic modes and a priori construction of shallow water lattice Boltzmann equations, *Phys. Rev. E (Stat. Nonlin. Soft Matter Phys.)* 65: 036309.

der Sman, R. V. & Ernst, M. H. (2000). Convection-diffusion Lattice Boltzmann scheme for irregular lattices, *J. Comput. Phys.* 160: 766–782.

Feng, S., Zhao, Y., Tsutahara, M. & Ji, Z. (2002). Lattice Boltzmann model in rotational flow field, *Chinese J. of Geophys.* 45: 170–175.

Gallivan, M., Noble, D., Georgiads, J. & Buckius, R. (1997). An evaluation of the bounce-back boundary condition for lattice Boltzmann simulations, *Int. J. Num. Meth. Fluids.* 25: 249–263.

Gómez, F. (2003). The Role of the Exchanges through the Strait of Gibraltar on the Budget of Elements in Western Mediterranean Sea: Consequences of Human-Induced Modifications, *Marine Pollution Bulletin* 46: 685–694.

González, M. & Sánchez-Arcilla, A. (1995). Un modelo numérico en elementos finitos para la corriente inducida por la marea. aplicaciones al estrecho de Gibraltar, *Revista Internacional de Métodos Numéricos para Cálculo y Diseño en Ingeniería* 11: 383–400.

Kandhai, D., Koponen, A., Hoekstra, A., Kataja, M., Timonen, J. & Sloot, P. (1998). Lattice Boltzmann hydrodynamics on parallel systems, *Comput. Phys. Commun.* 111: 14–26.

Klar, A., Seaïd, M. & Thömmes, G. (2008). Lattice Boltzmann simulation of depth-averaged models in flow hydraulics, *International Journal of Computational Fluid Dynamics* 22: 507–522.

Komatsu, T., Ogushi, K. & Asai, K. (1997). Refined numerical scheme for advective transport in diffusion simulation, *J. Hydraulic Engrng.* 123: 41–50.

Kurganov, A. & Levy, D. (2002). Central-upwind schemes for the Saint-Venant system, *Math. Model. Numer. Anal.* 36: 397–425.

LaCasce, J. & Mahadevan, A. (2006). Estimating sub-surface horizontal and vertical velocities from sea surface temperature, *J. Mar. Res.* 64: 695–721.

Lafuente, J., Almazán, J., Catillejo, F., Khribeche, A. & Hakimi, A. (1990). Sea level in the Strait of Gibraltar: Tides, *Int. Hydrogr. Rev. LXVII.* 1: 111–130.

LeVeque, R. (1998). Balancing source terms and the flux gradients in high-resolution Godunov methods: the quasi-steady wave-propagation algorithm, *J. Comput. Phys.* 146: 346–365.

Mei, R., Luo, L. & Shyy, W. (1999). An accurate curved boundary treatment in the Lattice Boltzmann method, *J. Comput. Phys.* 155: 307–330.

Millán, M., Estrela, M. & Caselles, V. (1995). Torrential precipitations on the Spanish East Coast: The role of the Mediterranean Sea surface temperature, *Atmospheric Research.* 36: 1–16.

Polyak, B., Fernández, M., Soto, M., Basov, J., Comas, I., Khain, M., Alonso, V., Agapova, B., Mazurova, G., Negredo, I., Tochitsky, A., de la Linde, V., Bogdanov, J. & Banda, N. (1996). Heat flow in the Alboran Sea, Western Mediterranean, *Tectonophysics* 263: 191–218.

Qian, Y., d'Humieres, D. & Lallemand, P. (1992). Lattice BGK models for the Navier-Stokes equation, *Europhys. Letters.* 17: 479–484.

Salmon, R. (1999a). The Lattice Boltzmann method as a basis for ocean circulation modeling, *J. Mar. Res.* 57: 503–535.

Salmon, R. (1999b). The Lattice Boltzmann solutions of the three-dimensional planetary geostrophic equations, *J. Mar. Res.* 57: 847–884.

Samelson, J. C., Skyllingstad, E., Chelton, D., Esbensen, S., O'Neill, L. & Thum, N. (2006). On the coupling of wind stress and sea surface temperature, *Journal of Climate.* 19: 1557–1566.

Seaïd, M. & Thömmes, G. (2009). Lattice Boltzmann simulation of free-surface temperature dispersion in shallow water flows, *Advances in Applied Mathematics and Mechanics* 1: 415–437.

Stansby, P. & Zhou, J. (1998). Shallow water flow solver with non-hydrostatic pressure: 2D vertical plane problems, *Int. J. Numer. Meth. Fluids* 28: 541–563.

Tejedor, L., Izquierdo, A., Kagan, B. & Sein, D. (1999). Simulation of the semidiurnal tides in the Strait of Gibraltar, *J. Geophysical Research.* 104: 13541–13557.

Thömmes, G., Seaïd, M. & Banda, M. (2007). Lattice Boltzmann methods for shallow water flow applications, *Int. J. Num. Meth. Fluids.* 55: 673–692.

Toro, E. (1992). Riemann problems and the WAF method for solving two-dimensional shallow water equations, *Phil. Trans. Roy. Soc. Lond. A* 338: 43–68.

Toro, E. (2001). *Shock-Capturing Methods for Free-Surface Shallow Flows*, Wiley & Sons.

Vargas, M., Sarhan, T., Lafuente, J. G. & Cano, N. (1999). An advection-diffusion model to explain thermal surface anomalies off Cape Trafalgar, *Bol. Inst. Esp. Oceanogr.* 15: 91–99.

Vázquez-Cendón, M. (1999). Improved treatment of source terms in upwind schemes for shallow water equations in channels with irregular geometry, *J. Comput. Phys.* 148: 497–526.

Vukovic, S. & Sopta, L. (2002). ENO and WENO schemes with the exact conservation property for one-dimensional shallow-water equations, *J. Comp. Physics.* 179: 593–621.

Xing, Y. & Shu, C. (2006). High order well-balanced finite volume WENO schemes and discontinuous Galerkin methods for a class of hyperbolic systems with source terms, *J. Comp. Physics.* 214: 567–598.

Zhong, L., Feng, S. & Gao, S. (2005). Wind-driven ocean circulation in shallow water Lattice Boltzmann model, *Adv. in Atmospheric Sci.* 22: 349–358.

Zhou (2004). *Lattice Boltzmann Methods for Shallow Water Flows*, Springer, Berlin.

Zhou, J. (1995). Velocity-depth coupling in shallow water flows, *J. Hydr. Engrg., ASCE* 10: 717–724.

Zhou, J. (2002). A Lattice Boltzmann model for the shallow water equations, *Computer methods in applied mechanics and engineering* 191: 3527–3539.

Zou, Q. & He, X. (2002). On pressure and velocity boundary condition for the Lattice Boltzmann BGK model, *Phys. Fluids* 9: 1591–1598.

12

The Numerical Simulation of Hydrodynamics of Fishing Net Cage

Yunpeng Zhao[1,*], Tiaojian Xu[1], Chunwei Bi[1],
Guohai Dong[1] and Shengcong Liu[2]
[1]*Dalian University of Technology*
[2]*Dalian Tianzheng Industry Co., Ltd*
China

1. Introduction

The aquaculture industry is playing an increasingly important role in the fish production industry as the demand for seafood increases. At present, the net cage is widely used in aquaculture industry all over the world. Because of environmental impact concerns and limited near-shore locations, more and more net cages for aquaculture will be located offshore and exposed to more waves and currents. Thus, knowledge of their hydrodynamic behavior of net cage under the action of waves and current is of great importance to the design of gravity cages in the open sea.

Techniques used to investigate the facilities have typically included the use of scaled physical and numerical models, and, where possible, field measurements. Comparing model tests and field measurement, the numerical simulation method is low in cost, saving time and being easy to manage. In this chapter, the latest progress of this technology by our research group will be introduced in detail. The contents of the progresses include the following parts: *The numerical simulation of net cage in irregular waves; The numerical simulation of multi-net cage in waves; The numerical simulation of flow through and around fishing net cage.*

2. Numerical methods

The fishing net cage is mainly composed of two parts: floating collar and fishing net. The floating collar is model as a rigid body and the fishing net is simulated as flexible body. The numerical model of net cage system is described in detail as follow.

2.1 Fishing net

By applying the lumped-mass model, the net is assumed to be a connected structure with springs and limited mass points, which are set at each knot and the centre of the mesh bar, as shown in Fig. 1. According to the Newton's second law, the motion equation of lumped mass in waves can be written as follows:

*Corresponding author

$$M\ddot{\vec{R}} = M\frac{\partial^2 \vec{R}}{\partial t^2} = \vec{F}_D + \vec{F}_I + \vec{T} + \vec{B} + \vec{W} \tag{1}$$

where $\vec{F}_D$ and $\vec{F}_I$ are the drag and inertia forces, respectively, $\ddot{\vec{R}}$ is the acceleration of mass point, $\vec{T}$ is the tension force in twine, $\vec{B}$ is the buoyancy force, and $\vec{W}$ is the gravity force. According to the research of **Zhao et al. (2008)**, the inertial force $\vec{F}_I$ on fishing net in waves is much smaller than drag force, so here it is omitted.

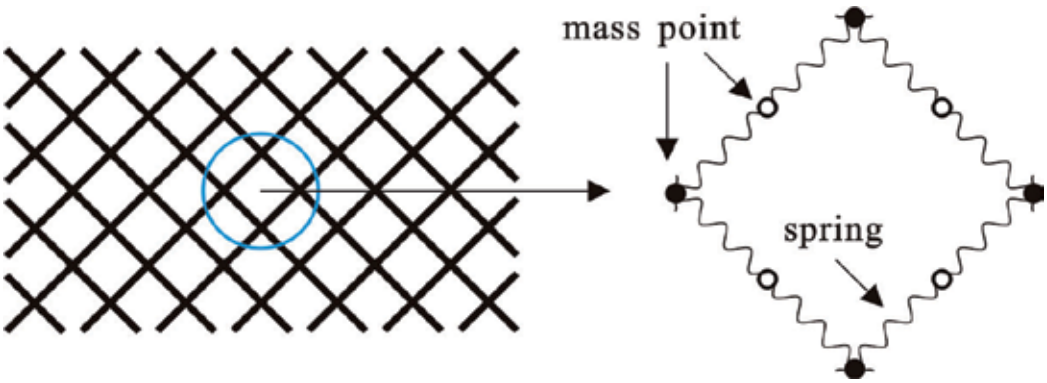

Fig. 1. Schematic of mass-spring model for net pen

The relationship between the elastic elongation of twine and tension based on **Wilson (1967)** is given by:

$$T = d^2 C_1 \varepsilon^{C_2}, \quad \varepsilon = \frac{l - l_0}{l_0} \tag{2}$$

where T is the tension force in twine, l_0 is the undeformed length of twine, l is the deformed length, d is the diameter of twine, C_1 and C_2 are the elastic constants of material which can be obtained by matching, referring to **Gerhard (1983)**. For polyethylene (PE), C_1=345.37×10^6, and C_2=1.0121; for polyamide (PA), C_1=784.9×10^6, and C_2=1.6988. The units of T and d are N and m, respectively.

To consider the direction of fluid forces acting on net mesh bar, a local coordinate system O-$\tau\eta\xi$ is defined, as described by Fig. 2. The origin of the local coordinate system is set at the centre of a mesh bar and the η axis lies on the plane including τ and V.

Besides the gravity and buoyancy, the τ component of the drag force on lumped-mass point can be obtained by Morison Equation, as follows.

$$F_{D\tau} = \frac{1}{2}\rho C_{D\tau} D l \left|\vec{V}_\tau - \vec{\dot{R}}_\tau\right| (\vec{V}_\tau - \vec{\dot{R}}_\tau) \tag{3}$$

where $C_{D\tau}$ represents the drag coefficient of the τ component, D is the diameter of twine, and l is its length. The same expression can be applied to the other drag forces ($F_{D\eta}$, $F_{D\xi}$) of η, ξ components. The drag coefficients related to Reynolds number are described in following section.

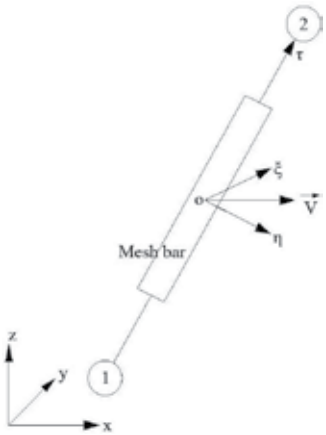

Fig. 2. Schematic diagram of the local coordinates for mesh yarns

For each mesh bar, the numerical procedure calculates the drag coefficient C_n and C_τ using a method described by **Choo and Casarella (1971)** that updates the drag coefficients based on the Reynolds number (Re_n) as follows:

$$C_n = \begin{cases} \dfrac{8\pi}{\mathrm{Re}_n s}\left(1-0.87s^{-2}\right) & \left(0<\mathrm{Re}_n\le 1\right) \\ 1.45+8.55\mathrm{Re}_n^{-0.90} & \left(1<\mathrm{Re}_n\le 30\right) \\ 1.1+4\mathrm{Re}_n^{-0.50} & \left(30<\mathrm{Re}_n\le 10^5\right) \end{cases} \tag{4}$$

$$C_\tau = \pi\mu(0.55\mathrm{Re}_n^{1/2}+0.084\mathrm{Re}_n^{2/3}) \tag{5}$$

where $Re_n=\rho V_{Rn}D/\mu$, s=-0.077215665+ln(8/Re_n), μ is the viscosity of water, C_n and C_τ are the normal and tangential drag coefficients for mesh bar, V_{Rn} is the normal component of the fluid velocity relative to the bar, and ρ is the density of water.

For the knot part, the **Fredheim and Faltinsen (2003)** suggested it could be reasonable to use a drag coefficient in the range of 1.0-2.0 when modeling the knot part as a sphere. Here C_D is set as 1.0 for the knot part.

2.2 Floating collar

2.2.1 Forces on floating collar

Although the float collar mainly consists of two concentric pipe rings and a hand rail. Float collar system is usually at the water surface and double floating pipes are the main components to withstand the wave and current induced loads. For the sake of simplicity, the float collar system is reduced to a double-column pipe structure.

When calculating the forces on float collar, the float collar is divided into many mini-segments. The forces on the whole collar can be obtained by summing the forces on each mini-segment. Fig. 3 is a sketch of a mini-segment of the float collar with a local coordinate

system defined in each mini-segment. As to the coordinate system, n and τ are in the normal and tangential directions of the mini-segment, respectively, and then v is normal to the mini-plane.

Because the tube diameter of float collar is relatively small compared to the wave length. As **Brebbia and Walker (1979)** suggested, the n component of wave-induced forces on a mini-segment can be calculated using the modified Morison equation to include relative motion between the structural element and the surrounding fluid, which is shown as follows:

$$F_n = \frac{1}{2} C_{Dn} \rho A_n \left| \vec{u}_n - \dot{\vec{R}}_n \right| \cdot (\vec{u}_n - \dot{\vec{R}}_n) + \rho V_0 \vec{a}_n + C_{mn} \rho V_0 (\vec{a}_n - \ddot{\vec{R}}_n) \tag{6}$$

where $\vec{u}_n$ and $\dot{\vec{R}}_n$ are the velocity vectors for water particles and mini-segments of the n component, respectively; $\vec{a}_n$ and $\ddot{\vec{R}}_n$ are the acceleration vectors for water particles and mini-segments of the n component, respectively; ρ is the density of water; V_0 is the water displaced volume of a mini-segment; A_n is the effective projected area of a mini-segment in the direction of the n component; and C_{Dn} and C_{mn} are the drag and added mass coefficients of the n component, respectively. The same expression can be applied to other wave-induced forces (F_τ, F_v).

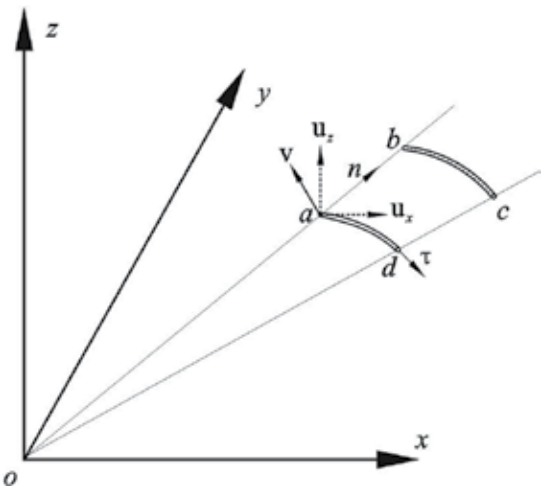

Fig. 3. Sketch of float collar mini-segment

The relationship between the mooring-line forces and elongation is determined experimentally and to be used in the numerical simulation, as follows:

$$T = 10.4 \times (\Delta S / S)^{1.132} \tag{7}$$

where ΔS is the elongation of a mooring line (m), S is the original length of the mooring line (m), and T is the tension in the mooring line (N).

Apart from the above-mentioned external force, the float collar is also subjected to gravity and buoyancy forces. Because it is easy to calculate these forces, the formulation for these forces is not given here.

2.2.2 Motion of floating collar

The three-dimensional motions of the float collar include surge-sway-heave translation and roll-pitch-yaw rotation. To obtain the motions of the float collar, two sets of coordinate systems are defined, which are the fixed-coordinate system *Oxyz*, and the body-coordinate system *G123*, as shown in the Fig. 4. Initially, axes *x*, *y* and *z* are parallel to axes 1, 2 and 3.

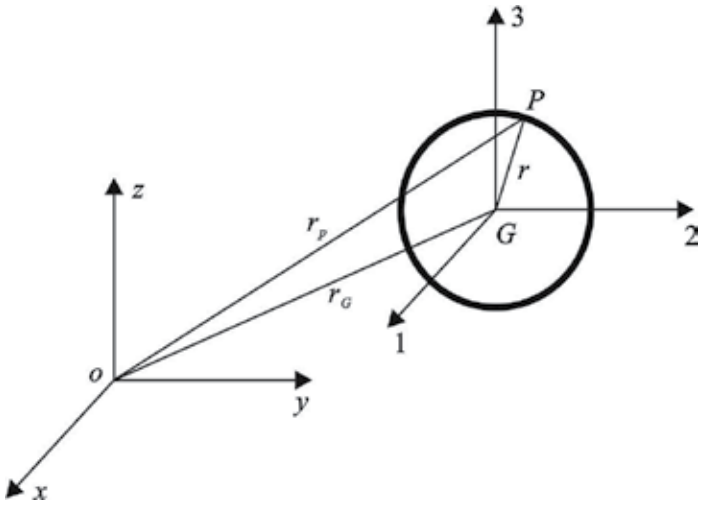

Fig. 4. Schematic of the body-coordinate system of float collar

Six degrees of freedom are required to describe the motion of float collar. According to the Newton's second law, under fixed coordinate system, the three translational equations of motion are given by:

$$\ddot{x}_G = \frac{1}{m_G}\sum_{i=1}^{N} F_{x_i}, \quad \ddot{y}_G = \frac{1}{m_G}\sum_{i=1}^{N} F_{y_i}, \quad \ddot{z}_G = \frac{1}{m_G}\sum_{i=1}^{N} F_{z_i} \tag{8}$$

where F_{xi}, F_{yi} and F_{zi} are the components of the external forces on mini-segment along fixed-coordinate axes *x*, *y* and *z*, m_G is the mass of the float collar, x_G, y_G and z_G are the acceleration of the mass centre of the float collar, and *N* is the number of mini-segments.

Axes 1, 2, 3 are principal axes with origin at the centre of the mass *G*, and thus the Euler equations of motion of a rigid body (**Bhatt and Dukkipati, 2001**) are applied. In the body-coordinate system, the three rotational equations of motion are given by:

$$\begin{gathered} I_1\frac{\partial\omega_1}{\partial t} + (I_3 - I_2)\omega_3\omega_2 = M_1, \quad I_2\frac{\partial\omega_2}{\partial t} + (I_1 - I_3)\omega_1\omega_3 = M_2 \\ I_3\frac{\partial\omega_3}{\partial t} + (I_2 - I_1)\omega_1\omega_2 = M_3 \end{gathered} \tag{9}$$

where subscripts 1, 2, 3 represent the body-coordinate axes 1, 2, 3; I_1, I_2 and I_3 are the components of the moments of inertia *I* along the three principal axes; ω_1, ω_2 and ω_3 are the components of angular velocity vector ω along the three principal axes; M_1, M_2 and M_3 are the components of the moment vector *M* along the three principal axes.

2.3 Flow around fishing net

The numerical simulation of the flow field around a plane net is based on the FLUENT software platform. The porous media model is introduced to model the plane net (see Fig. 5), and the finite volume method (FVM) is used to solve the governing equations of the numerical model. In this way, the numerical simulation of the flow field around the plane net is available.

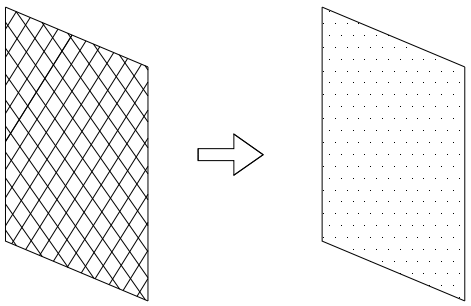

Fig. 5. Sketch of the porous media model.

2.3.1 Porous media resistance coefficients

The porous media model employs empirically determined flow resistance in the region of the porous media **(Fluent, 2006)**. For flow through the porous media, the hydrodynamic forces acting on the porous media can be expressed as follows:

$$F = S_i \lambda A \tag{10}$$

where S_i is the source term for the momentum equation in the i direction, λ is the thickness of the porous media, A is the area of the porous media, and F is the hydrodynamic force in the i direction.

When the region is outside the porous media model, $S_i = 0$. While, inside the porous media, S_i is calculated by the following equation:

$$\begin{aligned} S_i &= -\left(D_{ij}\mu u + C_{ij}\frac{1}{2}\rho |u| u \right); \\ D_{ij} &= \begin{pmatrix} D_n & 0 & 0 \\ 0 & D_t & 0 \\ 0 & 0 & D_t \end{pmatrix}, C_{ij} = \begin{pmatrix} C_n & 0 & 0 \\ 0 & C_t & 0 \\ 0 & 0 & C_t \end{pmatrix}. \end{aligned} \tag{11}$$

where D_{ij} and C_{ij} are prescribed material matrices consisting of the porous media resistance coefficients, D_n is the normal viscous resistance coefficient, D_t is the tangential viscous resistance coefficient, C_n is the normal inertial resistance coefficient, C_t is the tangential inertial resistance coefficient.

Substituting Eq. (11) into Eq. (10) provides formulas for calculating the drag force (F_d) and the lift force (F_l) of the plane net. The drag force is parallel to the flow direction, and the lift force is perpendicular to the flow direction.

$$F_d = \left(D_n \mu u + C_n \frac{1}{2} \rho |u| u \right) \lambda A \tag{12}$$

$$F_l = \left(D_t \mu u + C_t \frac{1}{2} \rho |u| u \right) \lambda A \tag{13}$$

The porous coefficients in Eq. (11) can be calculated by the data for the drag and lift forces. In a general way, the drag and lift forces of the plane net are obtained from the laboratory experiments. In addition, the forces can be calculated from the Morison equation:

$$F_d = \frac{1}{2} \rho C_d A u^2 \tag{14}$$

$$F_l = \frac{1}{2} \rho C_l A u^2 \tag{15}$$

where C_d and C_l are coefficients that can be calculated using empirical formulas proposed by **Zhan et al. (2006), Løland (1991), Aarsnes et al. (1990),** etc.

When the plane net is oriented normal to the flow, the porous coefficients (D_n and C_n) are chosen from a curve fit between drag force data of the plane net and corresponding current velocities using the least squares method. The other two coefficients (D_t and C_t) can be ignored because the lift force is equal to 0 when a=90°.

When the plane net is oriented with different attack angles (see Fig. 6), the porous coefficients should be transformed into formula (16) **(Bear, 2006)**. Then, the four porous coefficients can be obtained by minimizing the error between the theoretical values and existing data for the drag and lift forces using the least squares method, which is a common analytical method in error minimization.

$$\begin{aligned} D_n^{'} &= \frac{D_n + D_t}{2} + \frac{D_n - D_t}{2} \cos(2\alpha^{'}); D_t^{'} = \frac{D_n - D_t}{2} \sin(2\alpha^{'}); \\ C_n^{'} &= \frac{C_n + C_t}{2} + \frac{C_n - C_t}{2} \cos(2\alpha^{'}); C_t^{'} = \frac{C_n - C_t}{2} \sin(2\alpha^{'}). \end{aligned} \tag{16}$$

where $\alpha^{'} = 90^0 - \alpha$, and a is the attack angle.

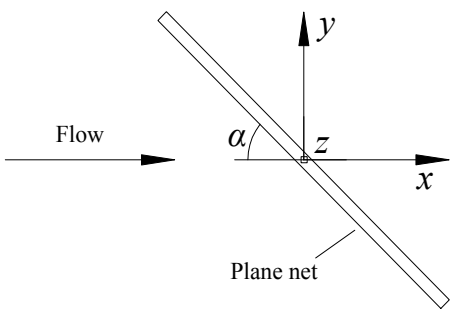

Fig. 6. Definition of attack angle (a).

2.3.2 Mesh grids and boundary conditions

An example of computational grids of a plane net at an attack angle a=90° is shown in Fig. 7. The mesh consists of unstructured tetrahedral elements that are refined in the vicinity of the porous media. The coordinate system for the numerical model is a right-handed, 3D Cartesian coordinate system, where x is positive toward the flow direction. The left boundary of the flume tank is described by the velocity-inlet boundary condition, while the right boundary is described by the outflow boundary condition. The solid surfaces of the flume tank and the free surface are modeled using the wall boundary condition (with zero shear force).

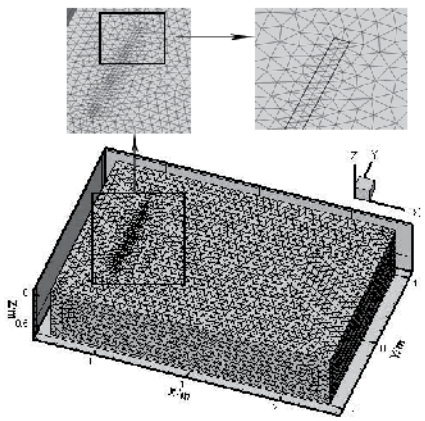

Fig. 7. Example of the computational grids.

3. Hydrodynamic simulation of net cage in irregular waves

The real sea is mainly composed of irregular waves. In this section, the hydrodynamic behavior of net cage in irregular waves is analyzed by numerical simulation and physical model test.

3.1 Irregular wave model

The linear wave theory (refer to **Zhao et al. 2007**) and random phase method are employed in the computation of irregular wave field. Based on linear wave theory, the velocity potential of the wave is given by

$$\phi = -A\frac{g}{2\pi f}\frac{\cosh k(d+z)}{\cosh kd}\sin(kx - 2\pi ft) \tag{17}$$

Surface elevation,

$$\eta = A\cos(kx - 2\pi ft) \tag{18}$$

and dispersion relation,

$$(2\pi f)^2 = gk\tanh(kd) \tag{19}$$

where A is the wave amplitude, g is gravitational acceleration, f is the wave frequency, k is the wave number (equal to $2\pi/L$), L is the wave length, d is the water depth, z is the vertical distance (positive upward) from mean-water level.

The irregular waves are generated using the random phase method as described by **Charkrabarti (1994)** which, in the time domain, is the superposition of multiple regular waves.

$$\eta(x,t)=\sum_{j=1}^{n}A_j\cos(k_jx-2\pi f_jt+\varepsilon_j) \tag{20}$$

where A_j is given by

$$A_j=\sqrt{2S(f_j)\Delta f} \tag{21}$$

where A_j and K_j are the wave amplitude and number of the individual wave components, respectively. ε_j is the uniform distributive random phase between 0 and 2π. The surface elevation time series will repeat after a given amount of time, and it is correlated with the two aspects: the number of regular waves used in the superposition and the sample length of the surface elevation. In the present study it was decided to discretize to 60 waves in the spectrum and have a length of each time series giving approximately 100 wave cycles. The input wave spectrum $S(f)$ is determined by the modified JONSWAP spectrum given by **Goda (1999)**, as follows,

$$S(f)=\beta_JH_{1/3}^2T_P^{-4}f^{-5}\exp\left[-1.25(T_Pf)^{-4}\right]\cdot\gamma^{\exp\left[-(f/f_P-1)^2/2\sigma^2\right]} \tag{22}$$

where T_P is the spectral dominant period, $T_P=T_{H1/3}/(1\text{-}0.132(\gamma+0.2)^{-0.559})$; $H_{1/3}$ and $T_{H1/3}$ are the significant wave height and period, respectively; f is the wave frequency; f_P is the spectral peak frequency; σ is the peak shape factor, σ=0.07 ($f\le f_P$), σ=0.09 ($f>f_P$), γ is the peak enhancement factor and equal to 3.3. The parameter β_J is determined by the following expression:

$$\beta_J=\frac{0.06238}{0.230+0.0336\gamma-0.185(1.9+\gamma)^{-1}}\cdot\left[1.094-0.01915\ln\gamma\right] \tag{23}$$

3.2 Physical model set up

A series of experiments of the motion response of float collar and the tension response in the mooring line were conducted in a wave-current flume at the State Key Laboratory of Coastal and Offshore Engineering, Dalian University of Technology, China. The wave-current flume is 69m long, 2m wide and 1.8m high, equipped with a random wave-maker and a current-producing system. The test setup is shown in Fig. 8. As shown in the Fig. 8, the physical model was installed in the centre of the flume. The mooring-line forces were measured by two transducers attached to the bottom of the mooring lines. The anchors on the left side are labeled for load identification. An optical measurement system for determining the float collar motions was developed. Two diodes (front and back points), numbered 1 and 2, were fixed on

the float collar for motion analysis. The movement of diodes was recorded by a CCD camera. The camera captures a series of images and transfers each frame to the computer and temporary storage. Later, specially-written software is used to search the position of diodes, which is used to calculate the float collar horizontal and vertical movements as a function of time. The geometric and mechanical properties of gravity cage model are provided in Table 1.

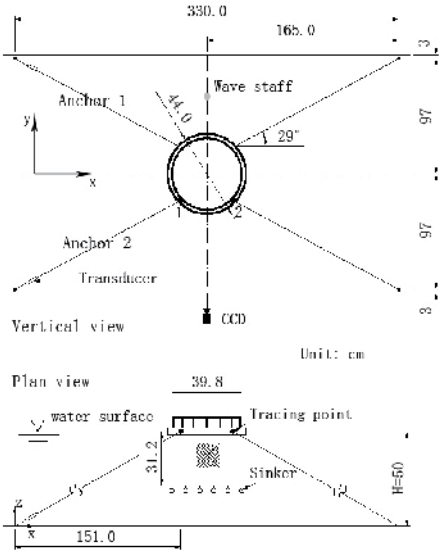

Fig. 8. Arrangement of a gravity cage model in the wave tank

Component	Parameter	value
Outer circle	Circumference(m)	1.382
	Pipe diameter(m)	0.014
	material	HDPE
Inner circle	Circumference(m)	1.250
	Pipe diameter(m)	0.014
	material	HDPE
Net	Mesh size(m)	0.041
	Twine diameter(m)	0.001
	Material	PE
Sinker	Unit mass(g)	1.8
	Number of pieces	10
	Total mass(g)	18.0
Mooring line	Length(m)	1.657
	Diameter(m)	0.00072
	Density(g/cm3)	1.14
	Pretension(N)	1.913

Table 1. Specifications of the physical model

3.3 Comparison in time domain

The numerical and physical gravity cage models were subjected to regular and irregular waves. The motion response (in surge and heave) of the float collar and the tension response in the mooring line are analyzed and compared in the time domain.

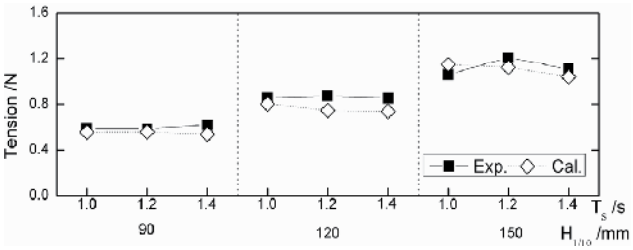

Fig. 9. Comparisons of the average of top one-tenth mooring line forces between numerical and experimental data

To examine the numerical model, quantitative comparisons are carried out between calculated and experimental results. The average of one-tenth highest mooring line tensions and cage motions are selected for comparisons. Fig. 9 shows the comparisons of the average of one-tenth highest mooring line tensions between calculated and experimental results. Fig. 10 and 11 demonstrate comparisons of the top one-tenth cage surge and heave motions between simulated and experimental results, respectively. The mean relative error of the mooring-line forces is 6.9%, and the mean relative errors of the cage surge and heave motions are 9.9% and -4.2%, respectively.

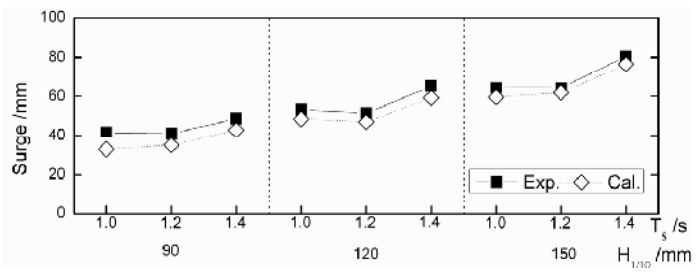

Fig. 10. Comparisons of the average of top one-tenth cage surge motions between numerical and experimental data

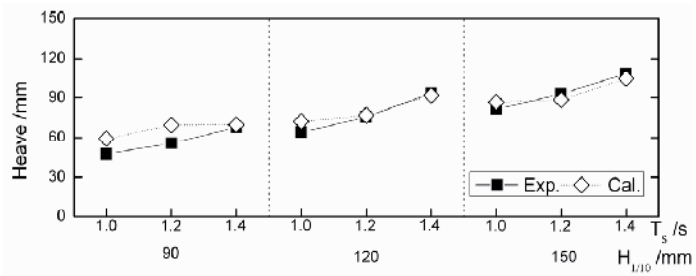

Fig. 11. Comparisons of the average of top one-tenth cage heave motions between numerical and experimental data

3.4 Comparison in frequency domain

For regular wave cases, response amplitude operators (RAOs), determined by dividing the amplitude of the response by the amplitude of the wave, are used to characterize the surge and heave motion response and the mooring-line tension response. For irregular wave cases, the transfer functions of the motion response of the float collar and the tension response in the mooring line were calculated using auto-spectral density method, and compared with the regular wave RAOs. The corresponding transfer functions are calculated as a function of frequency. Combining with statistical wave descriptions, these transfer functions can be used to yield statistics of cage dynamic response in a realistic sea conditions.

The time series of wave elevation and heave motion of float collar from the numerical simulation and physical model tests are shown in Fig. 12. In Fig. 12, the heave motion of float collar is synchronized with the wave elevation. Based on these time series, the corresponding auto-spectral density function can be obtained by using Fast Fourier Transform (FFT) method. The numerical and physical model wave spectra are shown in Fig. 13. The Fig. 13 shows that the wave spectra obtained from the numerical simulation and physical model test are similar to each other.

According to **Bendat and Peirsol (1986)**, the linear transfer functions of cage motion and tension responses can be calculated using the auto-spectral technique.

Fig. 14 shows the heave motion transfer function. In general, the motion response transfer function results for heave were characteristic of a highly damped system. At high frequencies, the cage system has no significant heave motion response to wave forcing. With the decreasing of wave frequency, the heave motion transfer function increases approaching one, indicating wave contouring behavior. This is reasonable, and it agrees with our qualitative analysis according to the common knowledge. In all cases the heave motion transfer function did not exhibit a resonant peak but tend to a value of one as the wave frequency decreases. If a resonant condition exists, it most likely occurs at the waves with frequency lower than 0.6 Hz.

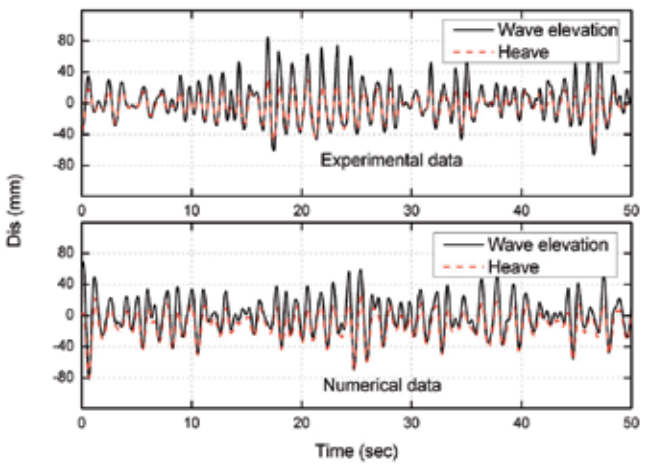

Fig. 12. The time series of wave elevation from the numerical simulation and physical model tests (the average of top one-tenth wave height $H_{1/10}$ is 0.12 m and significant wave period T_s is 1.2 s)

The surge transfer function results are presented in Fig. 15. It shows that the responses of the gravity cage in surge, obtained from the numerical simulation and physical model test, are similar with little response in high frequencies. As with heave motion response, the surge motion tends to increase slightly with decreasing wave frequency.

As shown in Fig. 16, the mooring line tension results, obtained from numerical simulation and physical model test, matched up well throughout the frequencies. The transfer functions of the mooring line tension and the cage motion in heave and surge show the same trend. As the wave frequency increases, the tension response in mooring line decreases. The numerical and physical models both predicted a mooring line tension response less than 0.02 N/mm throughout the wave frequencies.

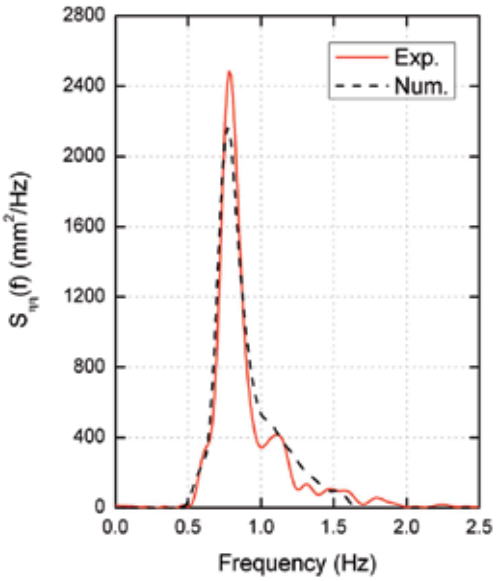

Fig. 13. The output recorded wave spectra of the numerical simulation and physical model test, (H1/10 = 0.12 m, Ts = 1.2 s).

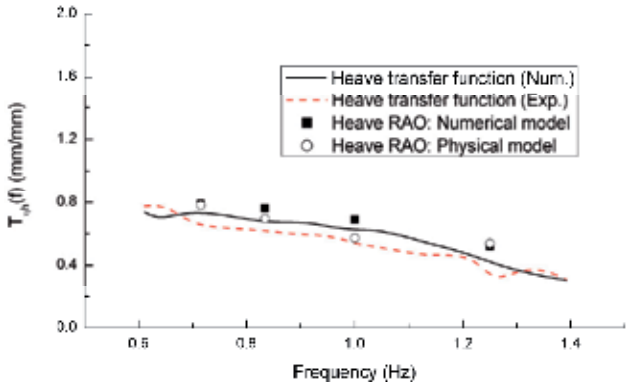

Fig. 14. Heave results from the numerical simulation (random shown by solid line; regular by squares) and physical model tests (random shown by dashed line; regular by circular dots)

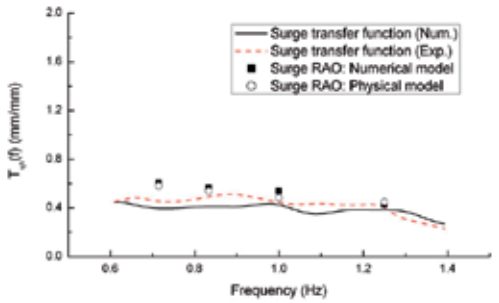

Fig. 15. Surge results from the numerical simulation (random shown by solid line; regular by squares) and physical model tests (random shown by dashed line; regular by circular dots)

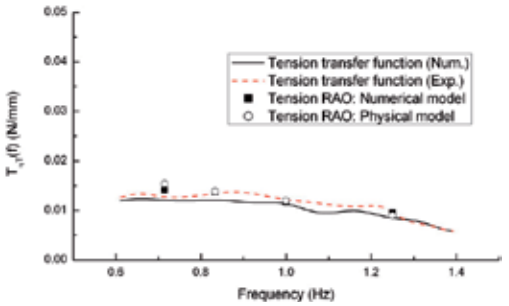

Fig. 16. Mooring line tension results from the numerical simulation (random shown by solid line; regular by squares) and physical model tests (random shown by dashed line; regular by circular dots)

4. Hydrodynamic behavior of multiple net cages

In the open sea, the large fish farm often includes multiple net cages assembly together. In this section, a numerical model of four-cage mooring structure in regular waves is presented. The effect of wave directions on mooring line tensions is analyzed.

4.1 Cage arrangement description

Mooring system is used to hold cage structures against the forces caused by waves and currents. Its design is very important for the operating and performance of cage structures. A change in the mooring system will change the internal loads on the cage systems. In this section, a four-cage system with grid mooring is analyzed. As shown in Fig. 17, four cages are arranged in two columns. Each net cage is connected to the submerged grid mooring by four bridle lines. The submerged grid mooring is attached to the sea floor by anchor lines. The direction of anchor line is perpendicular to grid line, which forms a 16 degree angle with the sea floor. The grid mooring consists of four submerged, pre-tensioned square grid (1 m × 1 m). The horizontal grid is 0.1 m below the still water surface. The pretension on the mooring system is maintained by the submerged floater at each grid corner. The diameter of floating pipe is 6.25 mm, and its density is 7.1 g/m. The diameter of net twine is 0.72 mm, and the mesh size is 11.7 mm.

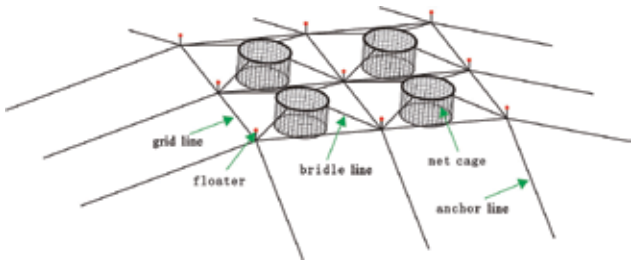

Fig. 17. Offshore grid mooring cage structure

4.2 The effect of wave direction on mooring line tension

Note that the waves propagated along various directions in the open sea, and it will affect the hydrodynamic behavior of grid mooring cage structure. Therefore, three different wave directions are considered in this section. Concerning the symmetrical characteristics of grid mooring cage structures, wave directions of 0°, 30° and 45° are chosen. Since the tension force on anchor lines is largest among the three types of mooring lines, only the maximum tension force on anchor lines is given here for the sake of clarity. Fig. 18 shows the maximum tension force on anchor lines of net cage system under the action of waves from different directions.

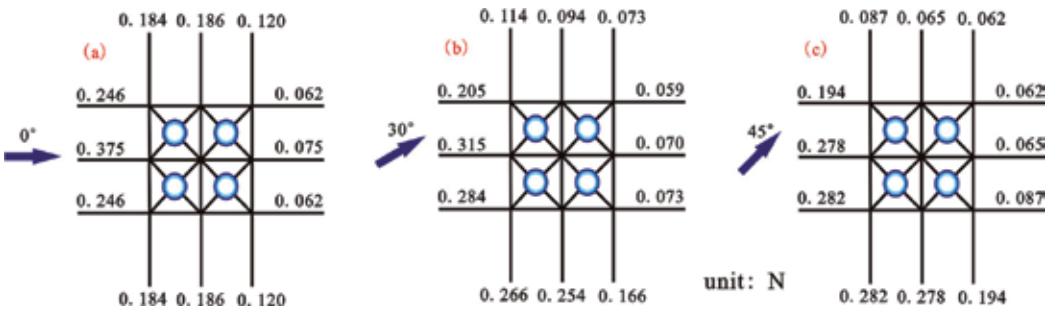

Fig. 18. The maximum tension force on anchor lines of two kinds of mooring cage structures subjected to waves from different directions.

For three different wave directions, the maximum tension forces on anchor lines are 0.375 N, 0.315 N and 0.282 N, respectively. When the wave incident angle is 0°, the left three anchor lines are main components to withstand external force on net cages. If the incident angle becomes 45°, the left three anchor lines and the bottom three anchor lines are main components to withstand the external force. Considering three kinds of wave directions, the uniformity of tension force on anchor lines is different.

When wave incident angle becomes 45°, there are more anchor lines to withstand external force on net cage. Therefore, the maximum tension force on anchor lines is smallest when wave incident angle is 45°.

For different wave incident angles, the transfer load path is different, and hence the uniformity of tension force on anchor lines is different. In the design of mooring cage structure, wave incident angle of 45° may be a good choice.

5. Numerical simulation of flow through and around fishing net cage

In this section, the flow field inside and around a gravity cage is simulated. The diameter of the cage (D) is 16 m, and the height (H) is 10 m. The cage net is knotless nylon net. The twine diameter was 2.8 mm, and the net mesh size was 29 mm. For the numerical model only the fishing net is modeled, and the effect of the float collar and sinker system on the flow field is ignored. The cylindrical cage is divided into 16 plane nets around the circumference and a bottom net (see Fig. 19). These plane nets can be described as the porous media with different attack angles. Therefore, the simulation of the flow field inside and around a gravity cage is straight forward.

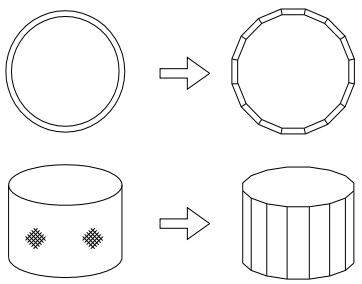

Fig. 19. Sketch of the gravity cage model.

5.1 Numerical model description

In the numerical model, the flume is 240 m long, 80 m wide and the depth of the water is 20 m. The boundary is considered large enough that the influence of the boundary condition on the flow field around the cage is negligible. The thickness of the porous media is 50 mm, and the porous coefficients are D_n=75083 m^{-2}, D_t=38307 m^{-2}, C_n=4.985 m^{-1}, and C_t=1.660 m^{-1}. The numerical simulations are performed with the incoming velocity u_0=0.5 m/s and the inlet turbulence quantities: k=1.34×10^{-4} m^2/s^2 and ε=4.76×10^{-9} m^2/s.

Four cases are modeled with different cage numbers, n=1, 2, 3 and 4, and the spacing distance between two adjacent cages is 24 m. The cages, which are located in a row along the flow direction, are centered on the width of the flume. The front cage is positioned 40 m downstream from the velocity-inlet boundary, while the others are positioned downstream successively with different cage numbers. Fig. 20 shows the sketch of one cage model.

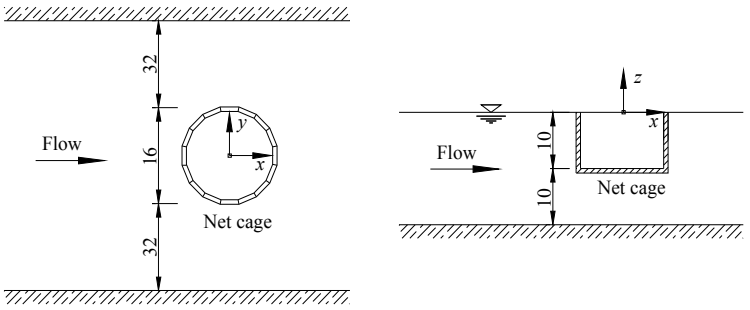

(a) horizontal view (b) vertical view

Fig. 20. Sketch of a gravity cage model (unit: m).

5.2 Simulated results

As shown in the contour plots, the velocity is approximately uniformly distributed inside the cage. There is a small region of velocity reduction upstream of the cage, while there is a rather large velocity reduction region downstream from the cage. Obvious flow velocity reduction exists along the flow direction, and the velocity reduction increases with increasing cage numbers. The width of the wake becomes narrower toward the centerline with increasing distance from the cage. The flow velocities outside the velocity reduction region are approximately 1%–10% greater than the incoming flow u_0, and more cages lead to greater flow velocity around the cages (see Fig. 21). As the cage number increases from 1 to 4, the maximum velocity reduction downstream from the cages increases from 25% to 69%. The cages influence the flow velocity distribution inside and around them. The rear cage has no influence on the flow velocity distribution inside the former cage (see Fig. 22).

Aarsnes *et al***. (1990)** combined theoretical work with the experimental work to derive formulas for flow velocity reduction of the cage nets. The formulas are as follows:

$$u = u_0 \prod_{i=1}^{n_c} r_i \,, \quad r_i = 1.0 - 0.46 C_d \tag{24}$$

where r_i is the flow velocity reduction factor, n_c is the number of upstream crossings of the cage net, and C_d is the drag coefficient of the net.

The flow velocity reduction factors u/u_0 show a good agreement and the velocity reduction trend of the numerical simulations is consistent with the results of Aarsnes's formula at different cage numbers. Fig. 23 shows the comparison results when n=4.

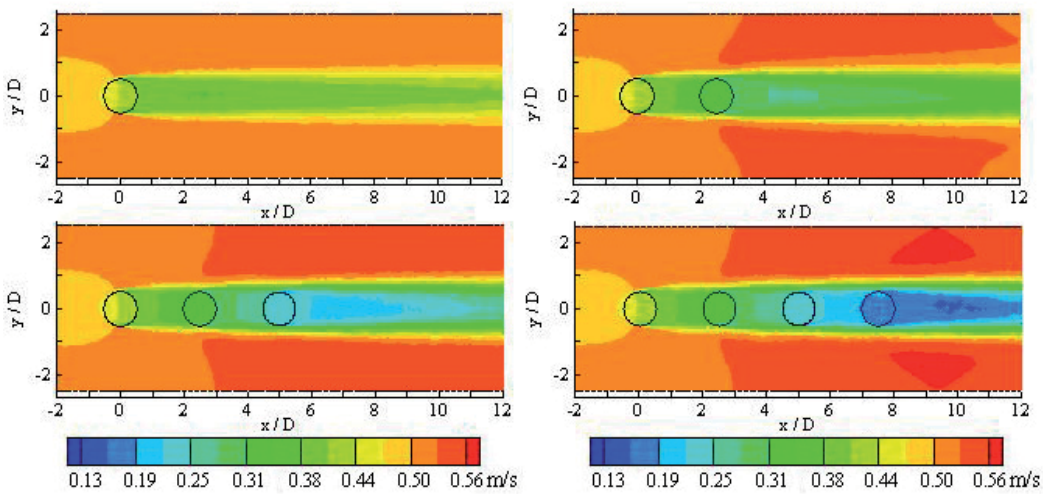

Fig. 21. Velocity distribution on a horizontal cut through the center of the cages at different cage numbers (n=1, 2, 3 and 4).

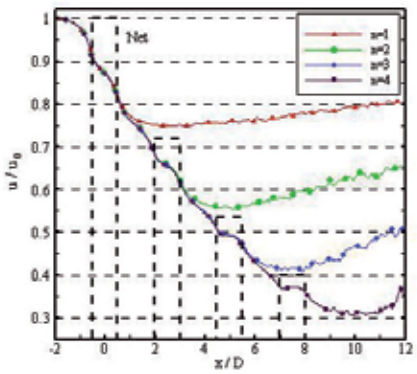

Fig. 22. Magnitude of the flow velocity u along the centerline of the cages in the x direction at different cage numbers (n=1, 2, 3 and 4).

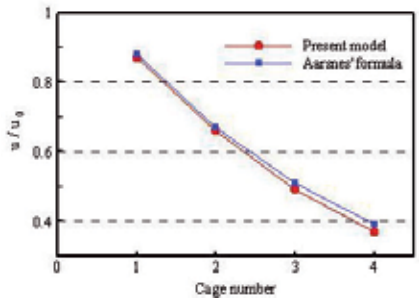

Fig. 23. Comparisons of the flow velocity reduction factor u/u_0 inside the cages between the present numerical model and Aarsnes's formula.

6. Conclusions

Three numerical models for calculating net cage in irregular waves, multi-net cage in waves and flow through fishing net cage are developed in the paper. The simulated results are in good agreement with the experimental values. Some main conclusions can be drawn as follows:

1. The gravity cage system shows a characteristic of a highly damped system with small response to high frequencies. The gravity cage surge and heave motions generally decrease as the wave frequencies increase. The heave motion is synchronized with the wave elevation. At low frequencies, the heave motion transfer function is approaching to one indicating wave contouring behavior. The transfer functions of cage motion response (heave and surge) and mooring line tension response have the same trend.
2. When the wave incident angle is 45°, the maximum tension force on anchor lines is smallest. Therefore, in the design of grid mooring cage structure, wave incident angle of 45° may be a good choice.
3. The velocity is approximately uniformly distributed inside the cage. As the cage number increases from 1 to 4, obvious flow velocity reduction exists along the flow direction, and the velocity reduction downstream from the cages increases from 25% to 69%. However, the rear cage has no influence on the flow velocity distribution inside the former cage.

7. Acknowledgments

This work was financially supported by the National Natural Science Foundation (NSFC) Project No.50809014 and 50921001, the National 863 High Technology Project No.2006AA100301, and the Specialized Research Fund for the Doctoral Program of Higher Education No.200801411094.

8. References

Aarsnes, J.V.; Rudi, H. & Løland, G. (1990). Current forces on cage, net deflection. *In: Engineering for Offshore Fish Farming*, pp. 137–152, ISBN 0727716018, Thomas Telford, London, Oct 17-18, 1990

BEAR J. (1972). *Dynamics of fluids in porous media*. America Elsevier Publishing Company, Inc., ISBN 0486656756, New York, USA

Bendat, J.S. & Peirsol, A.G. (1986). *Random Data: Analysis and Measurement Procedures* (3rd ed.), Wiley, ISBN 0471317330 ,New York

Bhatt, R.B. & Dukkipati, R.V. (2001). *Advanced dynamics*, Alpha Science International, Ltd., ISBN 184265022X, UK

Brebbia, C.A. & Walker, S. (1979). *Dynamic Analysis of Offshore Structures*, Newnes-Butterworths, ISBN 0408003936, London

Charkrabarti, S.K. (1994). *Offshore Structure Modeling*, World Scientific Publishing, ISBN 9810215126 , Singapore

Choo, Y.I. & Casarella, M.J. (1971). Hydrodynamic resistance of towed cables, *Journal of Hydronautics*, Vol. 5, No. 4, (Oct, 1971), pp. 126–131, ISSN 0022-1716

FLUENT (2006). *FLUENT 6.3 User's Guide*. Fluent Inc., Lebanon, NH, USA, Sep, 2006

Fredheim, A. & Faltinsen, O.M. (2003). Hydroelastic analysis of a fishing net in steady inflow conditions, *Proceeding of 3rd International Conference on Hydroelasticity in Marine Technology*, University of Oxford, Oxford, Great Britain, Sep, 2003

Gerhard, K. (1983). *Fiber Ropes for Fishing Gear*, FAO Fishing Manuals. Fishing News Books Ltd., Farnham, UK

Goda, Y. (1999). A comparative review on the functional forms of directional wave spectrum, *Coastal Engineering Journal*, Vol. 41, No. 1, (Mar, 1999), pp. 1–20, ISSN 0578-5634

Løland, G. (1991). *Current force on flow through fish farms*. PhD Dissertation, Division of Marine Hydrodynamics, Norwegian Institute of Technology, ISBN 82-7119-269-8, Trondheim, Norway

Wilson, B.W. (1967). Elastic characteristics of moorings, *ASCE Journal of the Waterways and Harbors*, Division 93(WW4), pp. 27–56, ISSN 0733-950X

Zhan, J.M.; Jia, X.P.; Li, Y.S.; Sun. M.G.; Guo, G.X. & Hu, Y.Z. (2006). Analytical and experimental investigation of drag on nets of fish cages, *Aquacultural Engineering*, Vol.35, No.1, pp. 91–101, ISSN 0144-8609

Zhao,Y.P. ; Li, Y.C. ; Dong, G.H. ; Gui, F.K. & Wu, H. (2008). An experimental and numerical study of hydrodynamic characteristics of submerged flexible plane nets in waves, *Aquacultural Engineering*, Vol. 38, No. 1, pp. 16–25, ISSN 0144-8609

Zhao,Y.P., Li, Y.C., Dong,G.H., Gui,F.K.(2007). A numerical study on dynamic propeties of gravity cage in combined wave-current flow. *Ocean Engineering*. Vol.34,No.(17-18), pp.2350~2363

Zhao,Y.P.,Li,Y.C.,Dong,G.,H.,Gui.,F.,K.,Teng.,B.(2009).The numerical simulation of hydrody namic behaviors of gravity cage in current and waves. *International Journal of Offshore and Polar Engineering*. Vol. 19, No.2, pp. 97-107

Dong,G.H.,Xu,T.J., Zhao,Y.P., Li,Y.C.,Gui,.F.K.(2011) Analysis of hydrodynamic behaviors of gravity net cage in irregular waves. *Ocean Engineering*.Vol.38,No.13,pp. 1545-1554

Dong,G.H.,Hao,S.H.,Zhao,Y.P., Zong,Z.,Gui,.F.K.(2010) Elastic responses of a flotation ring in water waves. *Journal of Fluids and Structures*.Vol.26, No.1, pp.176-192.

Dong,G.H.,Xu,T.J., Zhao,Y.P., Li,Y.C.,Gui,.F.K.(2010) Numerical simulation of hydrodynamic behavior of gravity cage in irregular waves. *Aquacultural Engineering,* Vol. 42, Issue 2, Pages 90-101.

Dong, G.H., Hao, S.H., Zhao, Y.P., Zong, Z.(2010).Numerical analysis of the flotation ring of a gravity-type fish cage. *Journal of Offshore Mechanics and Arctic Engineering*,Vol. 132, Issue 3,pp: 031304-1- 031304-7

Zong,Z.,Hao,S.H., Zhao,Y.P. , Dong,G.H.,Gui,.F.K.(2008). In-plane hydroelastic response of a circular ring in water waves. *Applied Ocean Research*, Vol.30,No.3,pp.208-214.

Edited by Jinhai Zheng

With the amazing advances of scientific research, Hydrodynamics - Theory and Application presents the engineering applications of hydrodynamics from many countries around the world. A wide range of topics are covered in this book, including the theoretical, experimental, and numerical investigations on various subjects related to hydrodynamic problems. The book consists of twelve chapters, each of which is edited separately and deals with a specific topic. The book is intended to be a useful reference to the readers who are working in this field.

ISBN 978-953-51-4963-7

Photo by marty8801 / iStock

IntechOpen